

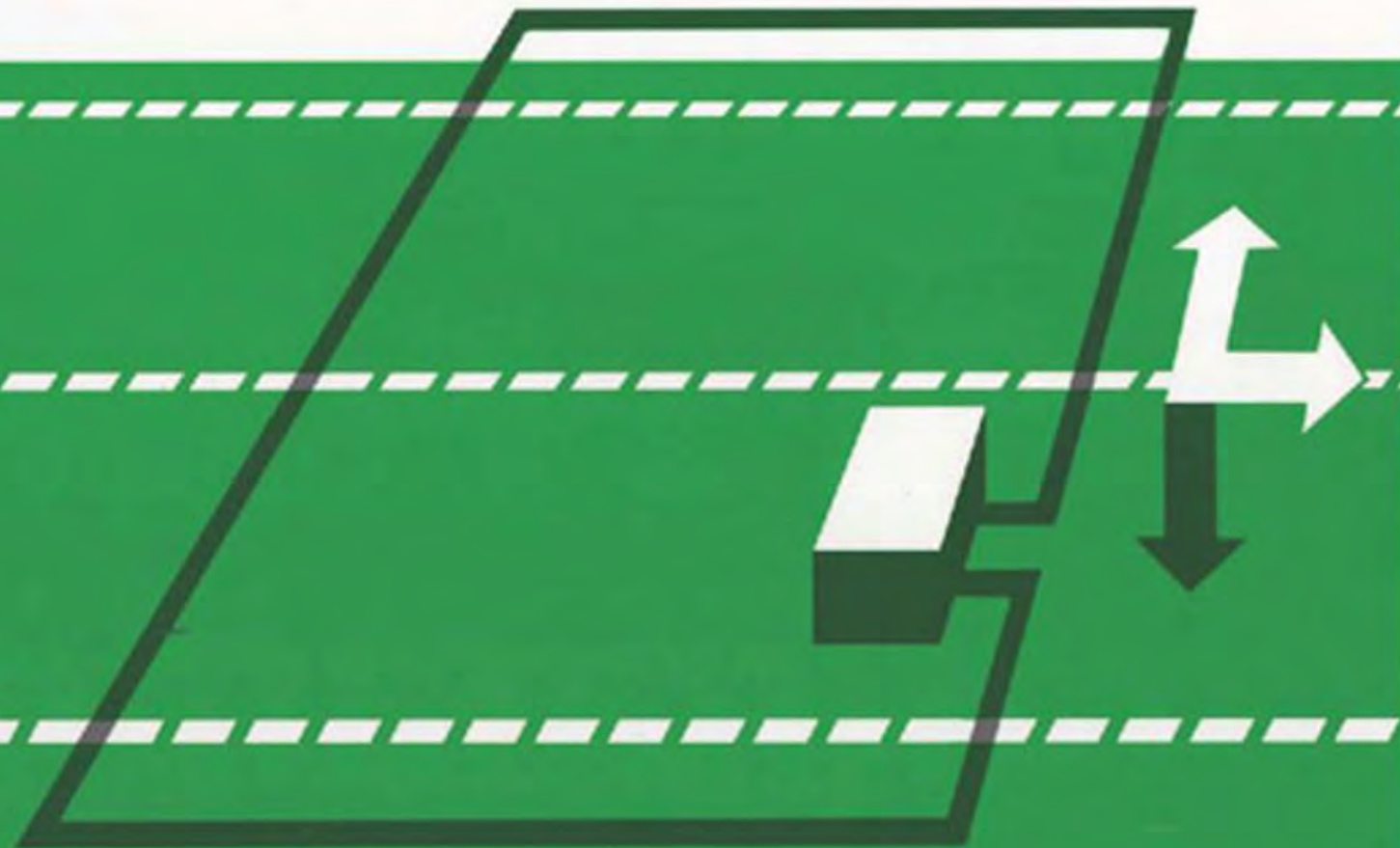
Downloaded 06/23/14 to 134.153.184.170. Redistribution subject to SEG license or copyright; see Terms of Use at <http://library.seg.org/>

**INVESTIGATIONS IN GEOPHYSICS NO. 3**

# **ELECTROMAGNETIC METHODS IN APPLIED GEOPHYSICS**

**VOLUME 1, THEORY**

**EDITED BY MISAC N. NABIGHIAN**



**SOCIETY OF EXPLORATION GEOPHYSICISTS**



**Series: Investigations in Geophysics, Volume 3**  
**E. B. Neitzel, Series Editor**

Downloaded 06/23/14 to 134.153.184.170. Redistribution subject to SEG license or copyright; see Terms of Use at <http://library.seg.org/>

# **ELECTROMAGNETIC METHODS IN APPLIED GEOPHYSICS—THEORY**

## **Volume 1**

Edited by  
**Misac N. Nabighian**

Project Editor  
**John D. Corbett**

Society of Exploration Geophysicists  
P.O. Box 702740/Tulsa, Oklahoma 74170-2740

**Electromagnetic methods in applied geophysics**

(Investigations in geophysics; v.3)

Includes biographies and index.

Contents: v.1. Theory—v.2. Applications

pts. A-B

1. Magnetic prospecting. I. Nabighian, Misac N.

II. Series: Investigations in geophysics; no. 3.

TN269.E387 1987 622'.153 87-63300

ISBN 978-0-931830-46-4 (Series)

ISBN 978-0-931830-51-8 (v. 1)

ISBN 978-1-56080-022-4 (v. 2)

ISBN 978-1-56080-069-9 (Paperback)

© 1987 by Society of Exploration Geophysicists  
All rights reserved. This book or parts hereof may  
not be reproduced in any form without permission  
in writing from the publisher.

Published 1988

Paperback 1989

Paperback reprinted 2006, 2008

Printed in the United States of America

**ELECTROMAGNETIC METHODS IN  
APPLIED GEOPHYSICS—THEORY**  
**Volume I**



**Frank C. Frischknecht (1928–1987)**

## Dedication

Dr. Frank C. Frischknecht, a pioneer in the field of airborne geophysics, was killed August 12, 1987 in a helicopter-plane collision near Ketchikan, Alaska.

Frank, born in Bicknell, Utah, on October 12, 1928, obtained a Bachelor of Science degree in Electrical Engineering (1950) and a Master of Science degree in Geophysics (1953) from the University of Utah, and later, a Master of Science degree in Geophysical Mathematics (1967) and a Doctor of Philosophy degree in Electrical Engineering Physics (1973) from the University of Colorado. He started his career with the United States Geological Society (USGS) in 1952 working on airborne geophysical instrumentation, compilation, and interpretation problems. From 1955 to 1962, Frank helped develop and test various controlled- and natural-source electromagnetic techniques for application to a variety of geological problems (i.e. investigations on floating ice islands in the Arctic, measuring molten lava on Hawaii, prospecting for minerals under glacial drift cover, etc.).

In 1966, in collaboration with Dr. George V. Keller, Frank wrote the now classic textbook "Electrical Methods in Geophysical Prospecting," and in 1967, he published the first computer generated, layered-earth theoretical EM sounding curves which guided the interpretation of a generation of airborne EM specialists. During this same period, Frank also developed an electromagnetic scale model tank which provided crucial data to test interpretation methods. These methods are internationally recognized today as standards against which theories are tested.

From 1976 to 1980 and again from 1984 to 1986, Frank served as Chief of the Branch of Electromagnetism and Geomagnetism at USGS, where he accomplished an extensive renovation of the geoelectric program and a major modernization of the geomagnetic program. In addition, he pioneered the application of mining geophysical techniques to environmental problems, including toxic waste disposal, deep well injection, and location of abandoned wells. He published extensively in all these areas. In 1986, his career achievements were recognized by the award of the Department of the Interior's Meritorious Service Award.

Frank was an effective spokesman for geophysics, and ably represented the USGS in relationships with other governmental agencies, universities, and private organizations both in the U.S. and abroad. Recognized as an international authority in geophysics, Frank lectured and conducted field studies with coworkers in Australia, Mexico, Canada, Norway, Sweden, Hungary, and Brazil; participated as a member of two scientific delegations to the Soviet Union; and acted as a scientific consultant for the United Nations in India and for the USGS-Saudi Arabian Project on airborne electromagnetic studies. Frank was a member of Society of Exploration Geophysicists, Institute of Electrical and Electronics Engineers, Inc. (Geosciences and Remote Sensing Society), American Geophysical Union, European Association of Exploration Geophysicists, Australian Society of Exploration Geophysicists, American Institute of Mining, Metallurgical and Petroleum Engineers, American Association for the Advancement of Science, and was listed in American Men and Women of Science. He served the Society of Exploration Geophysicists as an Associate Editor for GEOPHYSICS.

Several months before his untimely death, Frank was nominated for the highest honor of the Department of the Interior, the Distinguished Service Award in recognition of his outstanding accomplishments.

Frank avidly hiked and photographed. He loved the ballet, opera, symphony, and the fine arts. He was a shy person and extremely modest about his own accomplishments. He is remembered as the "gentleman geophysicist." He was a superb listener and quickly (frequently humorously) isolated the heart of problems. As a colleague said, "We will miss him, his great knowledge, dignity, and unassuming manner." It is in this spirit that we dedicate these two volumes of "EM Methods in Applied Geophysics" to Frank Frischknecht, one of their major contributors.



This page has been intentionally left blank



# CONTENTS



Foreword xv *J. D. Corbett*  
Introduction 1 *Misac N. Nabighian*

**Chapter 1 Fundamentals of the Electromagnetic Method 5**

*Charles M. Swift, Jr.*

Differences in Array Configuration	7
Differences in Transmitter Waveform	8
Differences in Techniques to Remove the Primary Field	8
Differences in Interpretive Parameter	9
The Future	10

**Chapter 2 Rock and Mineral Properties 13**

George V. Keller

Physical Laws, Electromagnetic Induction, and Rock Properties	13
Conductivity	13
Dielectric permittivity	14
Magnetic permeability	15
Properties of Minerals	22
Conductivity of metals and semiconductors	22
Dielectric properties of rockforming minerals	25
Magnetic properties of minerals	33
Piezoelectric properties of minerals	37
Properties of Rocks	37
Mixtures of conductive minerals in host rocks	43
Dielectric permittivity	44
Megascopic Considerations	48

## **Chapter 3 Resistivity Characteristics of Geologic Targets 53**

G. J. Palacky

Massive Sulfide and Magnetite Deposits	<b>56</b>
Volcanic-associated massive sulfide deposits	<b>57</b>
Other types of massive sulfide deposits	<b>68</b>
Magmatic deposits of nickel, copper, and platinum	<b>69</b>

Iron formations	70
Lineaments and Weathered Layers	72
Mapping of lithology	82
Unconformity-related uranium deposits	88
Bauxite deposits	90
Lateritic nickel deposits	92
Kimberlites	93
Mapping of lineaments	94
Geothermal exploration	96
Unconsolidated Sediments and Sedimentary Rocks	100
Unconsolidated sediments in glaciated terrains	100
Nonglacial unconsolidated sediments	106
Sedimentary rocks	106
Coal and lignite prospecting	110
Seawater, Aquifers, and Permafrost	112
Bathymetric charting	112
Mapping of freshwater-saltwater interface	114
Mapping of chemical pollution plumes	118
Permafrost	122
Conclusions	124
Acknowledgment	125
References	125

## **Chapter 4      Electromagnetic Theory for Geophysical Applications   131**

*Stanley H. Ward and Gerald W. Hohmann*

Fundamental Electromagnetism—Section 1	131
Maxwell's equations in the time domain	132
The constitutive relations	133
Maxwell's equations in the frequency domain	134
The wave equations	134
Solutions of the wave equations	137
Dispersive electrical parameters	141
Polarization vectors	142
Schelkunoff potentials	144
Boundary conditions	148
Appendix 1.1 Expressions for Operators in Three Coordinate Systems	158
Vector operators	158
Maxwell's equations	160
Mode decomposition	160
Appendix 1.2 Boundary Conditions	162
The integral forms of Maxwell's equation	162
Boundary conditions	163
Sources in Unbounded Media—Section 2	167
Scalar Green's function	167
Time-domain Green's function	169
Point source of direct current	172
Harmonic electric dipole	173
Transient electric dipole	174
Harmonic magnetic dipole	175
Transient magnetic dipole	177
Harmonic line source	178
Transient line source	180

Tensor Green's functions	180
Reflection and Refraction of Plane Waves—Section 3	183
Snell's laws	183
Fresnel's equations	186
The plane-wave impedance of an $n$ -layered isotropic earth	194
Magnetotelluric formulation for a 1-D earth	201
Finite Sources Over a Layered Half-space—Section 4	203
Complementary solution	203
General solution	205
Vertical magnetic dipole	208
Large horizontal loop	217
Horizontal magnetic dipole	223
Horizontal electric dipole	229
Long grounded wire	237
Line source of current	242
Computations	250
Boundary-value Problems in Cylindrical Coordinates—Section 5	252
Basic solutions	252
A conducting cylinder in a uniform transverse electrostatic field	255
A permeable cylinder in a uniform transverse magnetostatic field	257
A conducting permeable cylinder in a uniform alternating magnetic field	258
A conducting permeable cylinder in a uniform transient magnetic field	264
A conducting cylinder in a plane-wave electromagnetic field	265
A conducting cylinder in the field of a line source—frequency domain	269
A conducting cylinder in the field of a line source—time domain	271
Appendix 5.1 Properties of Cylinder Functions	272
Small argument asymptotes	273
Large argument asymptotes	273
Zeros of cylinder functions	274
Singularities of cylinder functions	274
The recurrence formulas	274
Boundary-value Problems in Spherical Coordinates—Section 6	276
Basic solutions	276
Alternative solution of the Helmholtz equation in spherical coordinates	279
Integral solutions in spherical coordinates	282
A conducting sphere in a uniform electrostatic field	282
A permeable sphere in a uniform magnetostatic field	285
A conducting permeable sphere in a uniform alternating magnetic field	285
A conducting permeable sphere in a uniform transient magnetic field	287
A conducting sphere in a plane-wave field	291
A conducting sphere in the field of an alternating magnetic dipole	296
A conducting sphere in the field of a transient magnetic dipole	305
Appendix 6.1 Spherical Cylinder Functions	306
Derivation of the spherical Bessel functions	307
The Schelkunoff spherical Bessel functions	307
Acknowledgment	308
References	308

## Chapter 5     Numerical Modeling for Electromagnetic Methods of Geophysics 313

*Gerald W. Hohmann*

Differential and integral equations	314
Time-domain equations	314

Frequency-domain equations	317
Direct current equations	319
Method of Weighted Residuals	321
Two-dimensional Model and Source	322
Frequency-domain differential-equation methods	322
Finite-element techniques	324
Integral equation solution	329
Time-domain finite-difference solution	334
Two-dimensional Model: Three-dimensional source	341
Zero-frequency solutions	341
EM solutions	342
Three-dimensional modeling	345
Volume integral-equation method	345
Thin-sheet solutions	351
Transient calculations	352
Differential equation solutions	357
Hybrid solutions	359
Acknowledgment	361
References	361

## **Chapter 6      Electromagnetic Physical Scale Modeling 365**

*F. C. Frischknecht*

Theory of Electromagnetic Scale Modeling	365
Types of Scale Models	372
Physical Facilities	375
Supporting structures	375
Design of tanks	376
Shielding against noise	382
Sources	386
Finite sources	386
Plane wave or uniform sources	391
Probes	394
Transmission Lines	398
Signal Processing and Data Acquisition	401
Testing and Calibration	404
Model Materials	406
Properties of materials	406
Measurement of properties of model materials	413
Review of Model Studies	418
Historical development	418
Examples of instrumentation and facilities	419
Examples of results	423
Discussion	433
References	434

## **Chapter 7      Detection of Repetitive Electromagnetic Signals 443**

*A. Becker and G. Cheng*

The Boxcar Integrator	444
-----------------------	-----

Analog Detection of Geophysical Signals	<b>450</b>
General purpose equipment	<b>450</b>
Lock-in amplifier	<b>454</b>
Digital Detection of Geophysical Signals	<b>454</b>
The digital analogy detector	<b>456</b>
Uniform stacking detector	<b>459</b>
Digital lock-in	<b>461</b>
Optimization of Dynamic Systems	<b>461</b>
Summary	<b>465</b>
Acknowledgments	<b>465</b>
References	<b>465</b>

## **Chapter 8      Inversion of Controlled-Source Electromagnetic Data    469**

*Gerald W. Hohmann and Arthur P. Raiche*

The Electromagnetic Inverse Problem	<b>470</b>
Integral equation formulation	<b>470</b>
Uniqueness	<b>471</b>
Construction of a solution	<b>472</b>
Appraisal	<b>476</b>
Model Fitting by Nonlinear Optimization	<b>479</b>
Parameter estimation	<b>479</b>
Generalized inverse of a matrix	<b>481</b>
Mathematical representation of data and parameters	<b>486</b>
Measuring inversion performance	<b>488</b>
An example of joint inversion and the use of inversion statistics	<b>490</b>
Field example	<b>494</b>
Multidimensional Inversion	<b>495</b>
Simple models	<b>495</b>
Differential equation methods	<b>496</b>
Integral equation methods	<b>499</b>
References	<b>502</b>
Index	<b>505</b>

This page has been intentionally left blank

## Foreword

During the last two decades advancements in the practice of electromagnetics (EM) methods have been tremendous. However, good recent textbooks encompassing the many techniques are virtually nonexistent.

To meet this void, a small group of Denver-based geophysicists—during a typical “attitude readjustment” session after a local meeting—agreed to promote an up-to-date textbook covering the practice of modern EM methods. The purpose was to provide a comprehensive review of the many significant advancements in method, techniques, interpretation, and modeling procedures. The text, originally conceived as an updated version of *Mining Geophysics*, Volumes I and II, would incorporate theory and practice and include a significant case history component.

The other principal members of this small group, from whom I took counsel and direction, were Edwin J. Ballantyne, Jr., H. David McLean, and Charles M. Swift, Jr. Forming an “ex officio” committee of the Mining Committee of the SEG, of which I was then Chairman, I took the concept to the SEG Executive Committee who approved its publication. The rest has become history as this volume attests.

The two volume set was organized and edited primarily through the efforts of Dr. Misac Nabighian who with entreaty, cajole, threats, and always patience and determination, brought together and edited the many parts that have made these volumes what they are. Our sincere and heartfelt gratitude is extended to Misac for his dedication and many hours of effort. Lastly, we acknowledge the continued support of the Publication Committee of the SEG and the Publication Department in Tulsa.

July, 1987

J. D. Corbett

This page has been intentionally left blank



## Introduction

*Misac N. Nabighian*

Over the last two decades there have been significant advances in electromagnetic (EM) methods of exploration, as evidenced by the extensive research carried out at various companies, universities, and government research organizations; by the large number of papers published on the subject; and by the numerous workshops on various EM topics held in conjunction with the SEG Annual Meetings.

Early EM methods were largely designed by the Scandinavians and the Canadians for exploration under glaciated Precambrian shield conditions, where the resistivities of the host rock and overburden are generally high. They did not work well in areas with conductive overburden or host rock. The lack of sophistication in data gathering and processing severely limited their exploration depth. Moreover, early EM systems were relatively heavy, cumbersome, and slow in operation.

Modern EM methods are characterized by their emphasis on deeper exploration and by their need for measurements of the response of the earth over a broad frequency range. In addition, to process the vast amount of digital data collected in the field and the inherently weaker signals originating from deeper targets, it has become necessary to rely heavily on modern computer technology. Nevertheless, most modern equipment is remarkably portable, considering its sophistication.

To properly apply EM methods to various exploration problems requires a good understanding of the physics involved and the ability to choose the optimum system for the problem at hand. The main difficulty of the EM methods is their complexity. There is a plethora of available techniques and instruments, and the results are highly dependent on the particular system used. Unfortunately, the information on various systems is scattered throughout the geophysical literature and there is no comprehensive, up-to-date treatise on the subject. Therefore, very few geophysicists are familiar with the entire spectrum of EM techniques.

These two volumes on EM methods document the solid scientific advancements of the past twenty years since the publication of the first SEG books on mining geophysics. In putting together these volumes we had two audiences in mind. First and foremost this book is written for exploration geophysicists, to help them brush up on the fundamentals of their profession and to get reacquainted with the various EM techniques in modern use. Second, it is intended for university students in applied geophysics or related sciences to provide an up-to-date treatment of EM techniques, both from a theoretical and a practical point of view. The extensive list of references at the end of each chapter and the diversity of illustrative case histories should prove invaluable for advanced further study.

Volume I presents the mathematical and physical foundations common to all EM methods, while Volume II gives a method by method treatment of principal EM techniques in common use.

The bulk of Volume I is devoted to the presentation of the theoretical basis of EM methods, to help facilitate the understanding of the physics involved and to provide a limited amount of interpretational aids. The chapters on numerical and analog modeling elaborate on ways

## Introduction

of enlarging these capabilities. The chapters on electrical properties of rocks and on the resistivity characteristics of geologic targets help envisage the different kinds of ground structures that may be dealt with and the effect of various factors on the observed conductivities of rocks. The basic principles of modern instrument design are incorporated under the heading "Detection of Repetitive Electromagnetic Signals." Finally, volume I concludes with a chapter on the principles of EM inversion, as a first step toward achieving the elusive goal of automatic interpretation of electromagnetic data.

The various EM techniques in common use are individually treated in Volume II. After a general presentation of principles of survey design and interpretation of electromagnetic techniques, individual chapters are devoted to:

- Electromagnetic profiling with dipolar systems
- Inductive large loop systems
- Electromagnetic soundings
- Time domain electromagnetic techniques
- Magnetotelluric (MT) method
- Controlled Source Audio Magnetotelluric (CSAMT) technique
- Very low frequency (VLF) techniques
- Magnetometric resistivity (MMR) methods
- High-frequency techniques (radar, etc.)
- Borehole techniques
- Airborne electromagnetic systems
- Underwater electromagnetic methods

All chapters rely heavily on the mathematical and physical foundations described in Volume I. Besides a detailed presentation of various techniques, a deliberate effort has been made to include in each chapter a number of representative case histories. As written, the book should be of interest to both mining and petroleum geophysicists who are applying EM methods and could also benefit those involved in groundwater or civil engineering applications.

The choice of topics and the manner of presentation represent a personal viewpoint. To achieve a treatment as broad in scope as possible, well known experts from the U.S. and overseas were approached to write the various chapters. Special attention was given to eliminate, as much as possible, duplication between various chapters and to achieve a reasonable uniformity in presentation. In this regard, I want to express my sincere appreciation to all contributors, for their patient understanding and cooperation during the writing of this book.

The initial idea of putting together an EM volume originated with the Mining Committee of the SEG under the leadership of Jack Corbett. I am grateful for his constant and unselfish support which has made this book possible. In addition, I want to express my deepest gratitude to Dr. Stan Ward who contributed greatly in shaping the final form of this book and for his constant encouragement and suggestions. The SEG publication staff deserves special thanks for their assistance in assembling these volumes. Without the help of Lynn Griffin, Jerry Henry, John Hyden, and Stanley Jones, this work would not have been possible. Last, but not least, I want to thank Dr. Maurie Davidson, Director of the Geophysical Department of Newmont Exploration, for actively encouraging this endeavor and Mrs. Sheryl Recker for keeping a semblance of order in an otherwise chaotic undertaking.



This page has been intentionally left blank

Downloaded 06/23/14 to 134.153.184.170. Redistribution subject to SEG license or copyright; see Terms of Use at <http://library.seg.org/>

---

---

# 1

## **Fundamentals of the Electromagnetic Method**

---

---



1

## Fundamentals of the Electromagnetic Method

*Charles M. Swift, Jr.*

Exploration geophysics is applied to obtain information about the subsurface of the earth that is not available from surface geological observations. Because the electrical resistivity of different earth materials ranges over many orders of magnitude, electromagnetic (EM) methods are used to map the subsurface resistivity structure. Applications can be at any scale—a metal detector searching for coins in beach sands, a detailed resistivity survey to map the influx of conductive seawater into a resistive aquifer, a high powered time-domain electromagnetic sounding survey to map the thickness of resistive volcanics over conductive possibly petrolierous sediments, or a magnetotelluric survey to detect anomalously conductive mantle for a dissertation. However, because most base metal massive sulfide ores are very conductive and provide a strong contrast to their host rocks, mineral exploration surveys have been the prime application of the EM methods and the mineral exploration industry has funded most of the development.

Electromagnetic (EM) methods include an initially confusing variety of techniques, survey methods, applications, and interpretation procedures, which are further complicated by a bewildering array of trade names. Each technique, however, involves the measurement of one or more electric or magnetic field components by an “EM receiver,” from some natural or artificial source of electromagnetic energy—the “EM transmitter.” A useful classification based upon this commonality of EM systems is presented as Figure 1. It is apparent that the measurement is essentially that of obtaining the transfer function of the earth. At most practical current densities, the earth is linear, so the transfer function is simply the output divided by the input. Properties of the earth are interpreted from these transfer functions in ways similar to how properties of an electrical circuit are interpreted from its transfer or system function.

Possibly the most fundamental electromagnetic method is the direct current (dc) laboratory measurement of the output voltage developed from an input current across a sample of rock. From Ohm’s law, the ratio of the voltage in volts to the current in amperes is the absolute resistivity in ohm-meters for a rock one cubic meter in volume. The resistivity technique, as categorized in Figure 1, is a generalization of the above lab measurement for arbitrary geometric configurations of the transmitter and receiver electrodes, yet by being dc, it is only a subset of the electromagnetic methods which arise when nonzero frequencies [alternating current (ac)] are utilized by the transmitter.

Based on Maxwell’s laws, an ac electromagnetic source induces secondary currents in conductive earth material. These secondary currents generate secondary magnetic fields. EM receivers measure both the primary and secondary fields. Upon normalization by the input source or by the received primary field, either the secondary or the total (primary plus sec-

ondary) field response is interpreted to yield the significant resistivity information.

Electromagnetic response, usually expressed as the secondary field or the mutual impedance between the transmitter and receiver, depends upon the frequency, the conductivity structure, and the geometric coupling between the transmitter and receiver. (Quantitatively, it will be developed in later chapters that the response can be plotted as a function of a dimensionless "response parameter,"  $\sigma\mu\omega a^2$ , where  $a$  represents a dimension usually characteristic of the target but sometimes of the array.) Response increases with increasing response parameter from zero, to a range of maximum rate of change in amplitude and maximum response in phase shift, to a saturation limit of no change. This response has been available for many years for simple earth geometries such as a layered earth, or for a sphere, a cylinder, or a thin conductive sheet target in an infinitely resistive half-space. For a complex resistivity structure, however, each conductive region will respond according to its own response parameter, and total induction will be complicated because the inducing fields for some conductors will include secondary fields from the better conductors. Development of the standard approach to EM exploration for conductive massive sulfides 25 years ago involved selecting an operating frequency for a given system that would produce a measurable response only from the massive sulfide body. Prospecting for these targets consists of systematically traversing the ground, and detecting an anomalous response over background.

The major advances in EM methods in the past 25 years have resulted from consideration of the entire resistivity structure. We now know that "current channeling" from weakly con-

**Table 1. A classification of electrical and electromagnetic systems**

Transmitter	Receiver			
	Grounded wire	Both wire and small coil	Small coil (ground)	Small coil (air)
Grounded wire				
Galvanic	Resistivity IP		Magnetometric resistivity (MMR) Magnetic IP (MIP)	
Inductive	Eltran	Controlled source AMT (CSAMT)	Some TEM systems	
Small loop			Slingram Horizontal loop EM Vertical loop EM Tilt angle method Some TEM systems Coincident loop Borehole configurations	Airborne EM Time domain towed-bird Helicopter rigid-boom
Large loop (long wire)			Large loop systems Turam Many TEM systems Borehole configurations	
Plane wave				
Vertical antenna				
Natural geomagnetic field	Telluric currents	VLF-resistivity Magnetotellurics	VLF	VLF

Notes: Grounded wires measure potential difference per length, thus electric field. Coils (or fluxgate magnetometers or SQUIDS) measure magnetic field, or its time derivative. A small loop is a 3-D source (magnetic dipole). A long wire (or the long edge of a large loop) is a 2-D source. Natural EM sources are assumed to be 1-D sources. Receivers can be frequency-domain, time domain (TEM), or both. This classification excludes the high-frequency techniques (radar, etc.).

ducting host rock can funnel current into the good conductors to produce a response altered from that of an identical conductor in free space. We have developed numerical methods to calculate forward solutions and hence realistic type curves for interpretation. And we have designed digital instrumentation to better measure the response and better process the more complex data.

Nevertheless, one “best” EM system simply does not exist for all applications. Depending upon the estimated resistivity structure including “geological noise,” the electrical noise environment, the availability of relevant interpretational aides, the familiarity of the geophysicist with a particular system, and nongeophysical constraints such as limited land accessibility and budget, any one of many systems can be the most appropriate for a given geophysical problem. The diversity of the EM systems now in use can be attributed to a number of factors as discussed in the following paragraphs: (1) different combinations of type and orientation of EM source and receiver, (2) the transmitter waveform and hence the receiver detection schemes, (3) the techniques used to subtract out the primary field, and (4) the particular form of the final parameter to interpret. 

## Differences in Array Configuration

The classification in Figure 1 includes a number of subtle but significant differences. When currents in a conductive earth are generated without the transmitter directly contacting the earth, the EM response is termed EM induction, and the resulting techniques are “inductive.” For current transmitted directly into the earth in dc resistivity, the technique is “galvanic.” Galvanic techniques depend upon good electrode contact and thus are not appropriate in areas of surface high resistivity such as dry sand or glaciers.

EM response can be induced by natural earth currents (passive techniques) or by artificial or controlled sources (active techniques). Most EM systems employ an active transmitter so that the source geometry and frequency can be controlled by the geophysicist. However, the ambient electromagnetic radiation from ionospheric oscillations (below 10 Hertz) and from lightning discharges (above 8 Hertz) is utilized as a source for the telluric, magnetotelluric, and audio-frequency magnetic (AFMAG) techniques. Advantages are the avoidance of the financial and logistical problems of a transmitter, and the availability of low frequency energy, which is expensive to generate artificially. However, sufficient signal strength is not always available, particularly in the 0.1–10 Hz frequency range.

In addition, the natural field magnetotelluric and AFMAG fields are “plane wave” sources for most all applications, which simplifies the analysis because the location of the transmitter can be ignored. In VLF (for “very low frequency” in radio jargon, although 20 kHz is a high frequency for exploration geophysics) and controlled source audio magnetotellurics, an active source is used to simulate a “far field” plane-wave source. This assumption usually holds for VLF. In CSAMT, as the receiver-transmitter separation becomes less than three skin depths ( $\delta = \sqrt{2/\sigma\mu\omega}$ ) at the low frequencies, the field becomes “near-field” rather than “far-field,” and the transmitter acts more as a local EM source than as a magnetotelluric (plane-wave) source.

Array configurations are selected in advance depending upon the application, whether for “sounding,” to measure the variation of resistivity with depth, and/or for “profiling,” to measure the variation of resistivity across the surface. Whereas in galvanic techniques depth penetration for a given resistivity structure is controlled only by the array geometry, in inductive techniques deeper penetration can also be obtained by using lower frequencies. However, lower frequencies in practice require higher power. In addition, the EM skin depth physics that allows deeper penetration will also diminish resolution. In the earth, electromagnetic wave propagation at geophysical frequencies is controlled by a diffusion equation, not a wave equation. EM waves attenuate significantly and dispersively, so resolution analogous to seismics is impossible.

In profiling, choice of a receiver-transmitter combination is usually determined by maximizing the response from the target. Best response occurs when the primary magnetic field

is perpendicular to the plane of the target, and when the long axis of the target is parallel to the primary electric field. Plane wave sources have great horizontal extent, and thus couple well with very long targets such as clay-rich shear zones. For steeply dipping targets, a horizontal loop source located on the ground away from the target generates a horizontal magnetic field in the earth for maximum coupling. A common configuration for profiling is the so-called Slingram array, a system using small coplanar loops for transmitter and receiver at a fixed separation. Another configuration for profiling is Turam, a system using a large loop transmitter and two receiver coils at a fixed separation measuring amplitude ratios and phase shifts of the two received signals. The popular modern version uses one receiver coil measuring the response with reference to the transmitted waveform. For such a large loop source, conductive ground and target conductors close to the loop can rotate and attenuate the field so that coupling away from the loop can be reduced from that anticipated in the absence of other conductors.

## Differences in Transmitter Waveform

Early EM systems using analog electronics utilized a sine wave source waveform, or a square-wave of equivalent fundamental frequency, with different frequencies, if employed, being measured as separate measurements. Square-waveforms are more common in the newer digital instrumentation, much of which utilizes synchronous detection. Most of electromagnetic theory for geophysical applications was developed in the frequency domain (see Ward, 1967, Grant and West, 1965). Measurement of some electromagnetic field component is expressed as the amplitude and phase shift (relative to the primary), or as the in-phase (real) and out-of-phase (quadrature) components. One important airborne EM system (INPUT) and some ground systems (see Keller and Frischknecht, 1965), however, measured the transient decay of the secondary field, after turn-off of the primary field.

Much of the development of the EM methods in the past twenty years has resulted from the recognition that this "time domain" measurement, measured in the absence of the primary field, offers some practical advantages to a "frequency domain" measurement. Time and frequency domain alternatives have existed for years for the induced polarization measurement in the 0.1–10 Hz frequency range. Theoretically, one transient waveform (or a "stack" of the sum of many measured waveforms) possesses the same information content as the frequency response obtained in a more time consuming fashion over many separate measurements. The time domain measurement is wide band, however, and thus is more susceptible to noise (mostly tellurics) which can be filtered out in a frequency domain measurement. Currently, the better approach for IP is debatable, and the final survey choice frequently depends upon the system with which the geophysicist is most familiar.

For EM, the better approach appears to be time domain EM [transient electromagnetic method (TEM)], particularly in areas of high surface conductivity such as Australia. A conductive environment forces an EM system to operate at lower frequencies or longer times, where the signal-to-noise ratio deteriorates. In fact, modeling has shown that the optimum time for detection of a finite target may be over a finite time window when the target response is greater than the background response of conductive host and overburden. Nevertheless, the direct measurement of the secondary field in TEM avoids the contamination of noise caused by errors in removing the primary field in FEM methods.

## Differences in Techniques to Remove the Primary Field

An accurate estimate of the secondary field requires an accurate technique to remove the primary field from the total observed field. These techniques differ according to the type of measurement, and the type of final interpretive parameter. For VLF and simple "dip-angle" configurations of the horizontal-loop EM methods, the primary field is not removed; a sec-

ondary field tilts the total primary field (from the background orientation of horizontal or vertical, respectively). Similarly for magnetotellurics, where the measured electric field can be thought of as indicating the induced EM response from the measured inducing magnetic field, no secondary field is normally considered.

For most active EM systems from simple sources, the primary field is calculated using careful geometric information from surveying in the field, then the secondary field is obtained from subtracting this theoretical estimate from the observed total field. Results are then expressed as a percent of the primary field. Deviations from zero thus reflect either anomalous secondary fields, or erroneous removal. For real primary fields, measurement of the quadrature component (or phase of the total field with respect to the primary) reveals directly the presence of a secondary field. Simple quadrature systems can therefore avoid the necessity of careful primary field removal. Thus, some early airborne systems were quadrature systems to avoid the complicated compensation systems used to monitor variations in transmitter-receiver separation due to wind and vibration. Another technique to avoid careful surveying utilizes the low-frequency asymptotic response. Secondary response is thus obtained by subtracting a low-frequency measurement from a higher-frequency measurement which includes response from some conductor whose response parameter is sufficiently high.

As mentioned, one very effective technique for avoiding this problem is to measure the transient response in the absence of the primary. All the time domain systems, including the airborne INPUT system, utilize this technique. Normalization by the transmitter moment results in units of volts/(amps times meters squared).

## Differences in Interpretive Parameter

The various EM systems yield final parameters that vary in their ease of understanding. Some yield geometric descriptions of the total field such as the tilt angle or ellipticity. Some yield a measure of the output total field normalized by the input source, the impedance. The magnetotelluric impedance can be easily transformed into the conceptually more convenient apparent resistivity. The mutual impedance between two loops can be normalized and transformed with a little more difficulty into an apparent resistivity, although some physicists prefer to consider the observed fields per se. Most EM systems yield a measure of the secondary field normalized by the local primary field to produce units of "percent of primary," or "parts per million." The diversity in data presentation can be confusing to those used to the standard presentations of gravity, magnetics, and refraction and reflection seismics.

However the EM response is presented, the geophysical interpretation involves two inter-related quantitative steps. First, the geometry of any anomalous conductor is interpreted from the spatial characteristics of the coverage—length from the anomalous extent, depth from the horizontal shape, dip from the asymmetry of response, etc. Second, the resistivity as a function of depth or the conductivity-thickness product (the conductance) of a confined conductor is interpreted from the frequency or time variation of the response. Awareness of the results of EM modeling, whether by scale models or analytic formulas or numerical computations, is critical. Forward modeling provides not only type curves for interpretive use, but also insight for increased understanding of the physics of EM induction and information for the intelligent design of field surveys. Automatic interpretation of the data to produce an appropriate and consistent resistivity structure—the inverse problem—is available for some simple geometries, and is an active research topic for the more complex earth geometries. Nevertheless, for the limited irregularly spaced measurements over a geologically heterogeneous earth in the presence of instrument and ambient noise, the ultimate act of geophysical interpretation remains an artful balance of physical understanding, awareness of the geological constraints, and pure experience.

## The Future

Electromagnetic methods are necessary and accepted in mineral exploration, in geothermal exploration, and in engineering geophysics. In petroleum exploration, electrical and electromagnetic methods have been lumped with gravity and magnetics into a nonseismic category, but recent successful applications in mapping permafrost and in determining the thickness of high resistivity basalt and overthrust carbonate sections in areas of poor seismic data have brought the EM methods into more serious consideration. (Of course, induction logging tools have been used with confidence for years by the petroleum industry, but are not usually mentioned with the surface exploration methods.) Further acceptance in petroleum exploration by explorationists not experienced in EM methods requires that any EM survey or system be explained fully and quantitatively, with an understanding of the relative capabilities and limitations of the EM technique, particularly the decreasing resolution with increasing depth of penetration.

For the near-term future, the emphasis in the application of electromagnetic methods will be on precision. Engineering applications in particular require accuracy. Moreover, the concern over cost-effectiveness now permeating all mineral and petroleum exploration programs will force geophysicists to design their EM surveys more carefully and to interpret their EM responses more precisely. The contents of this book provide a solid foundation for this work.

## References

- Grant, F.S., and West, G.F., 1965, Interpretation theory in applied geophysics: McGraw-Hill Book Co.  
Keller, G.V., and Frischknecht, F.C., 1966, Electrical methods in geophysical prospecting: Pergamon Press Inc.  
Ward, S.H., 1967, Electromagnetic theory for geophysical applications: Mining geophysics, Vol. II., Society of Exploration Geophysicists.



This page has been intentionally left blank

---

---

**2**

**Rock and Mineral  
Properties**

---

---



## Rock and Mineral Properties

*George V. Keller\**

### Physical Laws, Electromagnetic Induction, and Rock Properties

Maxwell's equations provide the starting point to obtain an understanding of how electromagnetic fields can be used to study the structure of the earth and determine its electric or magnetic properties (Maxwell, 1954; Ward and Hohmann, this volume). One equation is used to represent the fact that magnetic fields are caused by electric current flow:

$$\nabla \times \mathbf{H} = \mathbf{J} + \frac{\partial \mathbf{D}}{\partial t}, \quad (1)$$

where  $\mathbf{H}$  is the magnetic field,  $\mathbf{J}$  is the current density, and  $\mathbf{D}$  is the electric displacement. This equation represents two kinds of current flow, one ( $\mathbf{J}$ ) in which charge carriers flow through a medium without hindrance, and another,  $\partial \mathbf{D} / \partial t$ , in which charge separation, and hence an impeding electric field, arises. The first type of current is often called ohmic, or galvanic, while the second type of current is known by the name displacement current.

A second equation which represents the physical law that electric fields result from time-varying magnetic induction fields is

$$\nabla \times \mathbf{E} = - \frac{\partial \mathbf{B}}{\partial t} \quad (2)$$

where  $\mathbf{E}$  is the electric field vector and  $\mathbf{B}$  is the magnetic induction vector.

#### Conductivity

These two equations of Maxwell characterize electromagnetic field behavior very well for any application in geophysical exploration. However, as the equations are expressed above, there is no obvious relationship of the behavior of the electromagnetic field to the subsurface structure of the earth or its properties. To see where such dependencies arise, we turn to a variety of relationships known as constitutive equations.

Perhaps the most important of the constitutive equations in terms of inductive methods of geophysical prospecting is Ohm's law, relating current density to electric field intensity as

\*Department of Geophysics, Colorado School of Mines, Golden, Colorado 80401

$$\mathbf{J} = \sigma \mathbf{E}, \quad (3)$$

where  $\sigma$ , defined by this equation, is a property of the medium. The quantity has been named the electrical conductivity of the medium.

Because both the electric field intensity  $\mathbf{E}$ , and the current density  $\mathbf{J}$ , are vectors, the quantity  $\sigma$  must be a tensor, which in Cartesian coordinates will have the components

$$\sigma = \begin{vmatrix} \sigma_{xx} & \sigma_{xy} & \sigma_{xz} \\ \sigma_{yx} & \sigma_{yy} & \sigma_{yz} \\ \sigma_{zx} & \sigma_{zy} & \sigma_{zz} \end{vmatrix} \quad (4)$$

The conductivity tensor has a simple form if two of the orthogonal coordinate directions are selected to lie in the direction of maximum conductivity and minimum conductivity (the principal directions of the conductivity tensor):

$$\sigma = \begin{vmatrix} \sigma_{xx} & 0 & 0 \\ 0 & \sigma_{yy} & 0 \\ 0 & 0 & \sigma_{zz} \end{vmatrix}, \quad (5)$$

that is, the nondiagonal terms are zero. If the coordinate system is arbitrarily oriented, the off-diagonal terms will have symmetrically equal values written as

$$\sigma_{xy} = \sigma_{yx} \quad \text{and so on.} \quad (6)$$

In isotropic minerals or rocks, the three principal values of conductivity are the same. Because few earth materials have a completely symmetrical structure or composition, isotropic minerals and rocks are in the minority. Materials in which a property such as conductivity depends on the direction in which it is measured (probably the direction of the  $\mathbf{E}$  vector) are termed anisotropic. If the nonsymmetry exists at the atomic or molecular level, the anisotropy is termed intrinsic. In addition, an aggregate of otherwise isotropic mineral particles or rock units, can exhibit a dependence of average conductivity on the direction of the applied electric field, and appear to be anisotropic in bulk. Such behavior is commonly known as "structural" anisotropy.

In some rocks and minerals that exhibit uniformity of structure in a plane, two of the three principal values of conductivity are equal (normally these two are the maximum conductivity value). Such materials are termed gyroscopic.

In other applications of electrical geophysics, as in dc resistivity soundings or induced polarization surveys, the term electrical resistivity is often used. For an isotropic material, the "resistivity" is the reciprocal of the conductivity. For an anisotropic material, the resistivity tensor is the inverse of the conductivity tensor.

The conductivity of a material need not be a linear property; that is, the conductivity may be a function of current density or electric field intensity. For most earth materials, linearity of conductivity as a property is well observed. One exception which is easily recognized is the nonlinearity of current flow in air. When the electric field exceeds a threshold value, breakdown occurs, and enormous currents flow, as in a lightning stroke. In exploration, the electric field intensities generated never approach the threshold for breakdown.

Conductivity of a mineral or rock need not be a constant. Its value can change with time, temperature, pressure, and various environmental factors.

### Dielectric permittivity

In formulating the equations that bear his name, Maxwell recognized that there must be a constitutive equation which relates electric field intensity to displacement,

$$\mathbf{D} = \epsilon \mathbf{E}, \quad (7)$$

and which defines another property of the medium  $\epsilon$ , known as the dielectric permittivity. Like the conductivity, the dielectric permittivity is a tensor and most rocks and minerals are anisotropic. In contrast to conductivity, dielectric permittivity has a well defined value even in the absence of matter, this value being  $8.854 \times 10^{-12}$  Farads per meter in free space.

In the classic theory of dielectric materials, displacement is attributed to the motion of electrons, nuclei and polar molecules from neutral equilibrium positions to displaced, non-neutral positions under the effect of an applied electric field (Ioffe, 1960; Bottcher, 1952; Frolich, 1949; von Hippel, 1954 a, b). Charges separate until the Coulomb force between them balances the applied force of the electric field. Polarization of such charge carriers has been well studied and is well known.

In addition to these classic mechanisms for polarization, at the low frequencies often used in geophysical exploration a variety of other less well known polarization mechanisms are recognized. The most important in terms of its use in exploration is "induced polarization" (Sumner, 1976; Bertin and Loeb, 1976). While the induced polarization phenomenon serves as the basis for a set of exploration methods, it is becoming apparent that the same physical processes are significant in the low-frequency electromagnetic exploration methods, particularly when measurements are made with high accuracy (Wait and Debroux, 1984).

### Magnetic permeability

The third of the main constitutive equations which play a role in the application of Maxwell's equations to the earth is that which relates magnetic field strength and magnetic induction and is written as

$$\mathbf{B} = \mu \mathbf{H} \quad (8)$$

in which the quantity  $\mu$ , a third property of the medium, is defined as the magnetic permeability. This property serves as the basis for magnetic methods in geophysical exploration, but also plays an essential role in the electromagnetic methods. As with conductivity and dielectric permittivity, the magnetic permeability is a tensor quantity, and more often than not is anisotropic.

In contrast to the dielectric permittivity and conductivity properties which are usually considered independent of the applied field strengths at the levels used in exploration, magnetic permeability can have a complicated dependence on magnetic field strength (Brown, 1958; Strangway, 1967a, b). If no material is present, a free-space relationship exists between field strength and induction

$$\mathbf{B} = \mu_0 \mathbf{H}, \quad (9)$$

which defines an important quantity for use in calculations of electromagnetic field behavior

$$\mu_0 = 4\pi \times 10^{-7} \text{ H/m.} \quad (10)$$

In addition to the three constitutive equations listed similar equations exist which represent more exotic interactions between electromagnetic fields and materials. These are not normally considered in geophysical exploration, but should be mentioned for completeness. One such exotic phenomenon is that of piezoelectricity (Parkhomko, 1971). Piezoelectric polarization can be observed either in a single crystal with an appropriate internal structure, or in aggregates of crystals (rocks) with an appropriate internal structure. A fundamental feature of minerals and rocks which exhibits piezoelectricity is the absence of a center of symmetry. When the piezoelectric effect is present, there is a linear relationship between the components of the polarization intensity vector and the mechanical stress vector. Because the piezoelectric effect occurs only in anisotropic media, the modulus of piezoelectricity  $d$ , which is a physical property characterizing a rock or mineral, relates the polarization vector  $P$  to the mechanical strain tensor  $S$  and is written as

$$P = dS. \quad (11)$$

The polarization is a vector with three components and the strain is a tensor with nine components, so the modulus of piezoelectricity might have 27 components. In fact, because of symmetry of some of the components, the modulus of piezoelectricity can be written in terms of 18 components as,

	$S_{11}$	$S_{22}$	$S_{33}$	$2S_{23}$	$2S_{31}$	$2S_{12}$
$P_1$	$d_{111}$	$d_{122}$	$d_{133}$	$2d_{123}$	$2d_{131}$	$2d_{112}$
$P_2$	$d_{211}$	$d_{222}$	$d_{233}$	$2d_{223}$	$2d_{231}$	$2d_{212}$
$P_3$	$d_{311}$	$d_{322}$	$d_{333}$	$2d_{323}$	$2d_{331}$	$2d_{312}$ ,

(12)

where  $P_i$  are the components of the polarization intensity vector,  $S_{ik}$  are the components of the stress tensor, and  $d_{ikl}$  are the coefficients of proportionality, which are called the piezoelectric moduli. Data on appropriate values for the modulus of piezoelectricity are given in Parkhomenko (1971).

When a magnetic field is present, conduction currents will be diverted from their normal direction of flow in a phenomenon called the "Hall effect" (Putley, 1968),

$$\mathbf{E}_H = R \mathbf{B} \times \mathbf{J}, \quad (13)$$

where  $\mathbf{E}_H$  is the additional electric field generated by the Hall phenomenon, and  $R$  is the Hall coefficient, again a property of the material. The Hall coefficient is largest in metals and very small in other types of conductors.

Other exotic effects can be considered. Usually they exist when an electromagnetic field interacts with another force field, and energy is transferred between the two.

So far, we have considered the constitutive equations separately, so that each rock property appears to affect the electromagnetic field independently. In fact, in most applications, the physical properties defined by the first three constitutive equations combine to form a single characteristic of the medium, the "wave number," which determines the behavior of the electromagnetic field. The expression for the wave number can be developed by substituting the three constitutive equations into the two Maxwellian equations, and then expressing the latter in terms of only the magnetic and electric field strengths

$$\nabla \times \mathbf{H} = \sigma \mathbf{E} + \frac{\partial}{\partial t} (\epsilon \mathbf{E}),$$

and

$$\nabla \times \mathbf{E} = - \frac{\partial}{\partial t} (\mu \mathbf{H}). \quad (14)$$

In a separate step, and for demonstration purposes only, the time derivatives in the two equations can be replaced with the operational notation

$$\frac{\partial}{\partial t} = i\omega \quad \text{where} \quad \omega = 2\pi f. \quad (15)$$

The procedure is acceptable only if the dielectric permittivity and the magnetic permeability can be considered time-independent (independent of the history of field behavior). This excludes consideration of realistic behavior in ferromagnetic rocks. However, by using this operator representation, the Maxwellian equations become

$$\nabla \times \mathbf{H} = (\sigma + i\omega\epsilon)\mathbf{E},$$

$$\nabla \times \mathbf{E} = -i\mu\omega\mathbf{H}, \quad (16)$$

and the two fields  $\mathbf{E}$  and  $\mathbf{H}$  can be separated by simple algebraic operations

$$[\nabla^2 - i\omega\mu(\sigma + i\omega\epsilon)]\mathbf{E} = 0. \quad (17)$$

The result of this procedure is that all the rock properties and frequency group into one term which can be treated as a single parameter characterizing the interaction of the electromagnetic field with the medium.

$$k^2 = -i\omega\mu(\sigma + i\omega\epsilon) = \epsilon\mu\omega^2 - i\mu\sigma\omega. \quad (18)$$

Consider a uniform medium with properties  $\mu$ ,  $\epsilon$ , and  $\sigma$  completely filling all space. Assume a planar electromagnetic field present in this medium, in which the electric field has only an  $x$  component, the magnetic field has only a  $y$  component, and the amplitudes of the two fields vary only in the  $z$  direction. For this case, the field equations have a simple solution:

$$E_x = E_{x,0}e^{-ikz} = E_{x,0}e^{-(G_R + iG_I)z} \quad (19)$$

where  $G_R$  and  $G_I$  are the real and imaginary parts of the quantity,  $-ik$ , respectively.  $E_{x,0}$  is the strength of the electric field at some reference point in the medium, perhaps  $z = 0$ .

The real  $G_R$  and imaginary  $G_I$  parts affect the field strength differently. The real part,  $G_R$ , causes the field strength to decrease exponentially, or attenuate, in the  $+z$  direction. It is reasonable to expect that this is the direction in which the energy in the electromagnetic field is flowing, and that the reduction in strength is caused by the conversion of the energy of the electromagnetic field to heat, as conduction currents flow in the medium. In practice, we specify the attenuative characteristic of the medium in terms of the distance  $\delta$ , over which the field strength is reduced by the factor  $1/e$ . This quantity, known as the "skin depth," is defined as

$$\delta = \frac{1}{G_R}. \quad (20)$$

The imaginary part of  $G$  causes the amplitude of the field strength to vary sinusoidally with distance  $z$ , with no decrease in average strength. Each time the argument of the trigonometric functions in equation (19) increases by  $2\pi$ , the term assumes the same value. This distance,

$$\lambda = \frac{2\pi}{G_I}, \quad (21)$$

is known as the "wave length" of the propagating field.

The quantity  $k$  is known as the wave number. It is a function of three (or more) physical properties of the earth and of frequency. Frequency can be considered a design parameter, in that selection of an operating frequency is largely at the discretion of the explorationist. The behavior of the wave number with change in frequency is important to an understanding of the use of various electromagnetic methods. At very low frequencies, for which the behavior of the electromagnetic field is said to be diffusion, the wave number is approximately

$$k^2 \approx -i\sigma\mu\omega. \quad (22)$$

The dependence on dielectric permittivity disappears (we can neglect displacement currents), and the wave number has equal real and imaginary parts expressed as

$$k = \left( \frac{\omega\mu\sigma}{2} \right)^{1/2} - i \left( \frac{\omega\mu\sigma}{2} \right)^{1/2} \quad (23)$$

In one wave length, the attenuation of the field is  $2\pi$ . The field strength is large enough to measure only at a distance comparable to a few skin depths; because of this, in the low frequency range, the skin depth is also known as an “electrical unit of distance.” At frequencies low enough that the second term in the wave number can be ignored, attenuation is so rapid that radiating fields cannot be detected. This regime is known as the “inductive” regime in the application of electromagnetic methods.

In the other extreme, at high frequencies, the wave number is

$$k^2 \approx \omega^2 \mu \epsilon. \quad (24)$$

In this regime, the propagation of the electromagnetic field proceeds without significant attenuation. Wave length depends only on the dielectric constant

$$\lambda = \frac{2\pi}{\omega(\mu\epsilon)^{1/2}}. \quad (25)$$

Propagating fields can be used to measure the distance to reflecting rock masses in terms of the time required for the field to travel from a transmitter, be reflected, and travel back to a receiver—the principle of ground-probing radar.

In the intermediate range where neither displacement currents nor induction currents can be neglected, the behavior of the field is more complicated. The midpoint of this transition range is specified by the condition that

$$\frac{\sigma}{\omega\epsilon} = 1. \quad (26)$$

This condition specifies that conduction and displacement currents are of equal importance in the wave number. The ratio is known as the loss factor, since it grows in size with the importance of the conduction currents which give rise to loss of the electromagnetic field strength to heat. The loss factor is often expressed in terms of the loss tangent, defined as

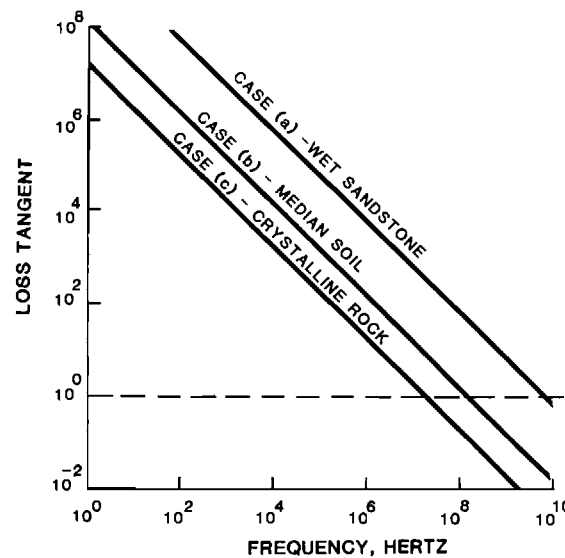


FIG. 1. Values for loss tangent of typical rocks over a geophysical range of frequencies.

$$\tan \delta = \frac{\sigma}{\omega \epsilon}. \quad (27)$$

The change in loss tangent with frequency is shown in Figure 1 for the three simple cases a, b, and c:

- a. Conductivity = 1.0 mho/meter, permittivity = 177 F/m.
- b. Conductivity = .01 mho/meter, permittivity = 88.5 F/m.
- c. Conductivity = .0001 mho/meter, permittivity = 50 F/m.

Case (a) represents a water filled sedimentary rock, case (b) represents the median rock seen at the surface in the United States, and case (c) is a water-free igneous or metamorphic rock.

The examples in Figure 1 are based on the idea that each rock can be characterized by values for dielectric constant, electrical conductivity and magnetic permeability that are independent of frequency. As will be shown in the following discussion, these properties do have values which vary with frequency, a phenomenon known as dispersion.

When the properties of a material vary with frequency, a simple physical consideration shows that each is not permitted to vary independently of the others. When an electric field at a specific frequency is applied to an element of a material, that material reacts as though it were a lumped circuit having a capacitance

$$C = \epsilon \frac{A}{\ell} \quad (28)$$

and a conductance

$$S = \sigma \frac{A}{\ell} \quad (29)$$

where  $A$  is the cross-sectional area and  $\ell$  the thickness of the sample.

If one of the elements has a value that depends on frequency, the other element must be dispersive as well. This can be argued by recognizing that if an electrical impulse were to be applied to a circuit such as that shown in Figure 2, a realizable voltage and current waveform would result. Because the time-domain waveform is simply the Fourier transform of

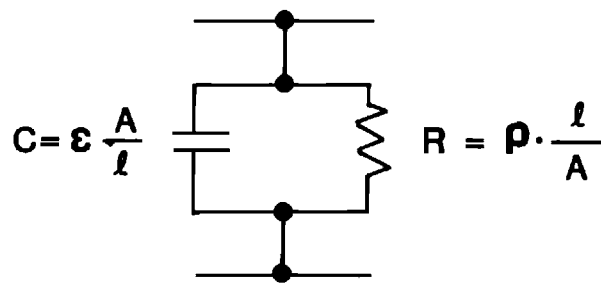


FIG. 2. Lumped circuit representation of the resistivity and dielectric permittivity of a material.

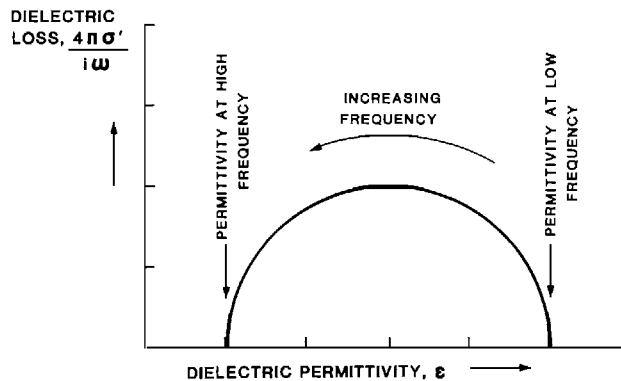


FIG. 3. A Cole-Cole plot, or plot of conductivity and permittivity in the complex plane for an ideal dispersive dielectric material. The form of the curve is a semicircle.

the impedance of the equivalent circuit,

$$Z = R + iX \quad (30)$$

where

$$R = \frac{1}{S} \quad \text{and} \quad X = \frac{1}{\omega C}.$$

This condition places restrictions on the way in which the real and imaginary parts of the impedance can vary with frequency (Papoulis, 1962, Ch. 10). Based on the Hilbert Transform, the relationship between the real and imaginary parts of the specific impedance are related as

$$X(\omega_0) = -\frac{1}{\pi} \int_{-\infty}^{\infty} \frac{R(\omega)}{\omega_0 - \omega} d\omega$$

and

$$R(\omega_0) = R(\infty) + \frac{1}{\pi} \int_{-\infty}^{\infty} \frac{X(\omega)}{\omega_0 - \omega} d\omega. \quad (31)$$

As a consequence of the nonindependence of the real and imaginary parts of the wave number, it is often desirable to examine both parts of the parameter simultaneously in a graphic presentation. This is commonly done using a Cole-Cole plot (Cole and Cole, 1941), which is a plot of the real and imaginary parts of the impedance in the complex plane. One of the simpler frequency-dependent behaviors in electrical properties is caused by electron resonance, which is characterized by simple harmonic behavior of an electron in its orbit when an oscillatory electric field is applied (see von Hippel (1954a, b) for example):

$$\epsilon - \epsilon_{\infty} = \frac{\epsilon_s - \epsilon_{\infty}}{1 + \omega^2 \tau^2}, \quad (32)$$

This behavior is shown as a plot in the complex plane in Figure 3. The form of the plot is that of a semicircle, a shape that is characteristic of simple harmonic motion. Often in dealing with real materials where the laws governing resonance are more complicated, the Cole-Cole plot has the form of an arc of a circle with the origin dropped beneath the real axis and is written as

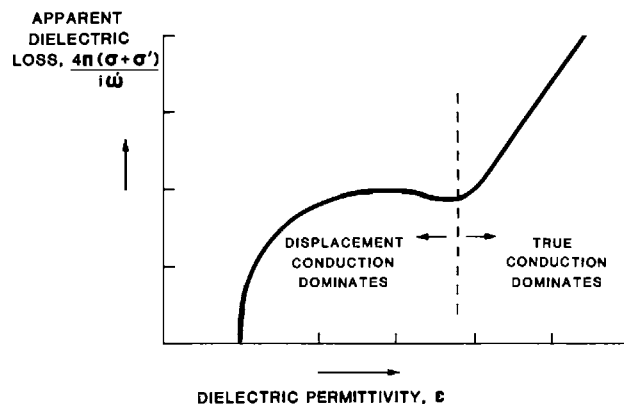


FIG. 4. Cole-Cole plot for a material which exhibits both ideal dispersion and steady conduction.

$$\epsilon = \epsilon_\infty + (\epsilon_0 - \epsilon_\infty)/(1 + i\omega\tau)^{1-\alpha}. \quad (33)$$

In the simple polarization mechanisms, the real conduction term is zero at extremely high and low frequencies; no steady conduction takes place. In real materials, there is almost always an independent conduction term. For an ideal nondispersive material, if such were to exist, with a single value of conductivity and a single value of dielectric constant, the Cole-Cole plot takes on the form shown in Figure 4. The plot has the shape of a line rising with a constant slope. Often, several conduction-polarization mechanisms are present simultaneously in a material, and the Cole-Cole plot will be a combination of several such simple shapes.

Finally, it should be noted that the three equations defining the conductivity, permittivity, and permeability of a material do not guarantee that these parameters are real; in general, equations (3), (7), and (8) permit these parameters to be complex (Olhoeft and Strangway, 1974). Thus, each tensor element would have to be characterized as

$$\begin{aligned} \mu &= \mu_R + i\mu_I \\ \epsilon &= \epsilon_R + i\epsilon_I \\ \sigma &= \sigma_R + i\sigma_I \end{aligned} \quad (34)$$

where the subscripts  $I$  and  $R$  indicate imaginary and real parts of the corresponding parameter. The necessity of considering the properties of the earth to be complex is usually avoided by using arbitrary definitions. Since the early days of electromagnetic theory, convention has incorporated the imaginary part of conductivity with the permittivity and the complex part of the permittivity with the real part of conductivity (see Hartshorn, 1927, for example).

It is usually assumed that the permeability has the value appropriate in a vacuum, and therefore, no dispersion exists which would require the use of a complex value for  $\mu_0$ . In those few cases in which rocks have a significantly different magnetic permeability, that permeability will probably exhibit dispersion over some portion of the frequency range (Miles et al., 1957; Olhoeft and Strangway, 1974). In such cases, the magnetic susceptibility is separated into real and imaginary parts as

$$\mu = \mu_R + i\mu_I. \quad (35)$$

The wave number is then written as

$$k^2 = -i\omega(\mu_R + i\mu_I)[(\sigma_R + i\sigma_I) + i\omega(\epsilon_R + i\epsilon_I)] \quad (36)$$

and can be separated into two parts, one behaving as the complex wave number for a non-dispersive magnetic susceptibility, and the other representing the dispersion in magnetic susceptibility. The loss tangent is:

$$\tan \delta_{EM} = \tan (\delta_M - \delta_E)/2 \quad (37)$$

in which

$$\tan \delta_E = \frac{\sigma_R - \omega \epsilon_I}{\sigma_I + \omega \epsilon_R} \quad (38)$$

and the magnetic loss tangent has been defined as

$$\tan \delta_M = \mu_I / \mu_R. \quad (39)$$

## Properties of Minerals

A starting point for the discussion of the electrical properties of rocks is a discussion of the properties of the individual minerals that comprise the rock. While it may never be possible to measure the properties of an individual mineral with an exploration method, it often is of interest to attempt to build a rock conceptually from minerals for which the properties are known and to predict the properties of the aggregate.

In tabulating the properties of minerals, the minerals separate naturally into two groups; (1) metals and (2) semiconductors, as opposed to insulators. The first group occurs rarely but is of great economic interest; the second group includes the common rockforming minerals and comprises the host in which the first type of mineral must be recognized. The difference between the two groups that leads to their separation into this classification is the fact that for metals and semiconductors, the conductivity is the important property, with dielectric constant being difficult to measure and rarely of any importance. On the other hand, for the insulating rockforming minerals, conductivity is rarely large enough to contribute significantly to the wave number for a rock; as a consequence, the dielectric constant is often the property most easily determined.

### Conductivity of metals and semiconductors

The physics of metals and semiconductors is covered extensively in literature (Kittel, 1953; Jones, 1956; Mott and Jones, 1958; Shuey, 1975). Metals are materials in which electrons become available for conduction with little or no excitation energy. An integral number of electrons are expected to be available per atom in conduction, and conductivity is expected to be very high. Conduction is limited only by interference between nuclear motion and the free movement of electrons under an applied electric field. Because the nuclei in a metal move about more at higher temperatures, metals are characterized by a positive coefficient of resistance with temperature. The conductivity decreases with increasing temperature. At very low temperatures, some metals (perhaps all) become superconductors. The properties of metals are well known, but native metals occur only very rarely at the surface of the earth. Copper, iron, gold, platinum, and a few other elements occur, but are far less important than the occurrence of various compounds of the same metals. A few values for conductivities of metals are given in Table 1.

Combinations of metals as alloys may also exhibit the high conductivity of pure metals. Some of the combinations of metals with arsenic, tellurium, and selenium appear to be alloys, with high conductivity typical of metals (Table 2).

The more important category of economic ore minerals, which are usually sulfides or oxides, appears to be semiconductors. In such materials, relatively high conductivity can be present, but normally, not as high as in metals. Conduction occurs by transfer of electrons

**Table 1.** Resistivities of metals and metallic minerals (zero frequency).

Refined metals at 0°C	$\rho$ (ohm-m)
Lithium	$8.5 \times 10^{-8}$
Beryllium	$5.5 \times 10^{-8}$
Sodium	$4.3 \times 10^{-8}$
Magnesium	$4.0 \times 10^{-8}$
Aluminium	$2.5 \times 10^{-8}$
Potassium	$6.3 \times 10^{-8}$
Calcium	$4.2 \times 10^{-8}$
Titanium	$83 \times 10^{-8}$
Chromium	$15.3 \times 10^{-8}$
Iron	$9.0 \times 10^{-8}$
Cobalt	$6.3 \times 10^{-8}$
Nickel	$6.3 \times 10^{-8}$
Copper	$1.6 \times 10^{-8}$
Zinc	$5.5 \times 10^{-8}$
Gallium	$41 \times 10^{-8}$
Arsenic	$35 \times 10^{-8}$
Rubidium	$11.6 \times 10^{-8}$
Strontium	$33 \times 10^{-8}$
Zirconium	$42 \times 10^{-8}$
Molybdenum	$4.3 \times 10^{-8}$
Ruthenium	$11.7 \times 10^{-8}$
Rhenium	$4.5 \times 10^{-8}$
Palladium	$10.0 \times 10^{-8}$
Silver	$1.5 \times 10^{-8}$
Cadmium	$6.7 \times 10^{-8}$
Indium	$8.5 \times 10^{-8}$
Tin	$10.0 \times 10^{-8}$
Antimony	$36 \times 10^{-8}$
Cesium	$18 \times 10^{-8}$
Barium	$59 \times 10^{-8}$
Lanthanum	$59 \times 10^{-8}$
Cerium	$71 \times 10^{-8}$
Praseodymium	$62 \times 10^{-8}$
Hafnium	$29 \times 10^{-8}$
Tantalum	$14 \times 10^{-8}$
Tungsten	$5.0 \times 10^{-8}$
Osmium	$9.1 \times 10^{-8}$
Iridium	$5.0 \times 10^{-8}$
Platinum	$9.8 \times 10^{-8}$
Gold	$2.0 \times 10^{-8}$
Tellurium	$14 \times 10^{-8}$
Lead	$19 \times 10^{-8}$
Bismuth	$100 \times 10^{-8}$
<i>Metallic minerals</i>	
Native copper	$1.2$ to $30 \times 10^{-8}$ ohm-m
Graphite (carbon)	$36$ to $100 \times 10^{-8}$ (current flow parallel to cleavage)
	$28$ to $9900 \times 10^{-6}$ (current flow across cleavage)
Ulmanite, NiSbS	$9.0$ to $120 \times 10^{-8}$
Breithauptite, NiSb	$3.0$ to $50 \times 10^{-8}$

which require some energy to be driven into conduction bands. The energy is provided by thermal agitation, and so, the conductivity of semiconducting material often is seen to increase with temperature.

Information on the electrical properties of metals and semiconductors is reported in four extensive studies, Harvey (1928), Parasnis (1956), Parkhomenko (1967), and Shuey (1975). Table 2 lists values for conductivities reported for such minerals.

**Table 2.** Resistivities of semiconducting minerals (zero frequency).

Native elements	$\rho$ (ohm-m)
Diamond (C)	2.7
Sulfides	
Argentite, $\text{Ag}_2\text{S}$	$1.5 \text{ to } 2.0 \times 10^{-3}$
Bismuthinite, $\text{Bi}_2\text{S}_3$	3 to 570
Bornite, $\text{Fe}_2\text{S}_3 \cdot n\text{Cu}_2\text{S}$	$1.6 \text{ to } 6000 \times 10^{-6}$
Chalcocite, $\text{Cu}_2\text{S}$	$80 \text{ to } 100 \times 10^{-6}$
Chalcopyrite, $\text{Fe}_2\text{S}_3 \cdot \text{Cu}_2\text{S}$	$150 \text{ to } 9000 \times 10^{-6}$
Covellite, $\text{CuS}$	$0.30 \text{ to } 83 \times 10^{-6}$
Galena, $\text{PbS}$	$6.8 \times 10^{-6} \text{ to } 9.0 \times 10^{-2}$
Haverite, $\text{MnS}_2$	10 to 20
Marcasite, $\text{FeS}_2$	$1 \text{ to } 150 \times 10^{-3}$
Metacinnabarite, 4 HgS	$2 \times 10^{-6} \text{ to } 1 \times 10^{-3}$
Millerite, $\text{NiS}$	$2 \text{ to } 4 \times 10^{-7}$
Molybdenite, $\text{MoS}_2$	0.12 to 7.5
Pentlandite, $(\text{Fe}, \text{Ni})_9\text{S}_8$	$1 \text{ to } 11 \times 10^{-6}$
Pyrrhotite, $\text{Fe}_7\text{S}_8$	$2 \text{ to } 160 \times 10^{-6}$
Pyrite, $\text{FeS}_2$	$1.2 \text{ to } 600 \times 10^{-3}$
Sphalerite, $\text{ZnS}$	$2.7 \times 10^{-3} \text{ to } 1.2 \times 10^4$
Antimony-sulfur compounds	
Berthierite, $\text{FeSb}_2\text{S}_4$	0.0083 to 2.0
Boulangerite, $\text{Pb}_5\text{Sb}_4\text{S}_{11}$	$2 \times 10^3 \text{ to } 4 \times 10^4$
Cylindrite, $\text{Pb}_3\text{Sn}_4\text{Sb}_2\text{S}_{14}$	2.5 to 60
Franckeite, $\text{Pb}_5\text{Sn}_3\text{Sb}_2\text{S}_{14}$	1.2 to 4
Hauchecornite, $\text{Ni}_9(\text{Bi}, \text{Sb})_2\text{S}_8$	$1 \text{ to } 83 \times 10^{-6}$
Jamesonite, $\text{Pb}_4\text{FeSb}_6\text{S}_{14}$	0.020 to 0.15
Tetrahedrite, $\text{Cu}_3\text{SbS}_3$	0.30 to 30,000
Arsenic-sulfur compounds	
Arsenopyrite, $\text{FeAsS}$	$20 \text{ to } 300 \times 10^{-6}$
Cobaltite, $\text{CoAsS}$	$6.5 \text{ to } 130 \times 10^{-3}$
Enargite, $\text{Cu}_3\text{AsS}_4$	$0.2 \text{ to } 40 \times 10^{-3}$
Gersdorffite, $\text{NiAsS}$	$1 \text{ to } 160 \times 10^{-6}$
Glaucodote, $(\text{Co}, \text{Fe})\text{AsS}$	$5 \text{ to } 100 \times 10^{-6}$
Antimonide	
Dyscrasite, $\text{Ag}_3\text{Sb}$	$0.12 \text{ to } 1.2 \times 10^{-6}$
Arsenides	
Allemonite, $\text{SbAs}_3$	70 to 60,000
Lollingite, $\text{FeAs}_2$	$2 \text{ to } 270 \times 10^{-6}$
Nicollite, $\text{NiAs}$	$0.1 \text{ to } 2 \times 10^{-6}$
Skutterudite, $\text{CoAs}_3$	$1 \text{ to } 400 \times 10^{-6}$
Smaltite, $\text{CoAs}_2$	$1 \text{ to } 12 \times 10^{-6}$
Tellurides	
Altaite, $\text{PbTe}$	$20 \text{ to } 200 \times 10^{-6}$
Calavarite, $\text{AuTe}_2$	$6 \text{ to } 12 \times 10^{-6}$
Coloradoite, $\text{HgTe}$	$4 \text{ to } 100 \times 10^{-6}$
Hessite, $\text{Ag}_2\text{Te}$	$4 \text{ to } 100 \times 10^{-6}$
Nagyagite, $\text{Pb}_6\text{Au}(\text{S}, \text{Te})_{14}$	$20 \text{ to } 80 \times 10^{-6}$
Sylvanite, $\text{AgAuTe}_4$	$4 \text{ to } 20 \times 10^{-6}$
Oxides	
Braunite, $\text{Mn}_2\text{O}_3$	0.16 to 1.0
Cassiterite, $\text{SnO}_2$	$4.5 \text{ to } 10^{-4} \text{ to } 10,000$
Cuprite, $\text{Cu}_2\text{O}$	10 to 50
Hollandite, $(\text{Ba}, \text{Na}, \text{K})\text{Mn}_8\text{O}_{16}$	$2 \text{ to } 100 \times 10^{-3}$
Ilmenite, $\text{FeTiO}_3$	0.001 to 4
Magnetite, $\text{Fe}_3\text{O}_4$	$52 \times 10^{-6}$
Manganite, $\text{MnO} \cdot \text{OH}$	0.018 to 0.5
Melaconite, $\text{CuO}$	6000
Psilomelane, $\text{KMnO} \cdot \text{MnO}_2 \cdot n\text{H}_2\text{O}$	0.04 to 6000
Pyrolusite, $\text{MnO}_2$	0.007 to 30
Rutile, $\text{TiO}_2$	29 to 910
Uraninite, $\text{UO}_2$	1.5 to 200

Some minerals have a wide range of conductivities reported, while others have a narrow range (see Figure 5). Although the variability may reflect to some extent the number of measurements made, there are various factors which affect the uniformity of the conductivity of a highly conducting mineral. In semiconductors, impurities may contribute electrons for conduction with low activation energy; in this case, the conductivity of a mineral is controlled by the concentration of such minor constituents, which can vary by orders of magnitude. Also, microfractures or crystal domain boundaries can impede conduction, causing measurements to be unexpectedly high.

It is unlikely that the conductivity of metals and semiconductors will change with frequency over the range of frequencies used in geophysics.

### Dielectric properties of rockforming minerals

In a strict sense, all materials that are not metals are semiconductors. However, in many materials, the energy required for activation of conduction electrons is so large that virtually no conduction takes place. Such materials are termed insulators. Most silicates, carbonates, and other common minerals fall into this category.

In insulating minerals, semiconduction is often so small that another mechanism, electrolytic conduction, dominates. Thermal agitation of the crystal lattice can displace ions from their normal positions, so that they become available for conduction when an electric field is applied. Such ions will move through the crystal lattice, and recombine when an opportunity presents itself. Electrolytic conduction in solids is described in Lidiard (1957) and in Stevel (1957).

Processes contributing to dielectric displacement and polarization have been identified as being electronic, atomic, molecular, and space charge derived in nature (von Hippel, 1954a, b).

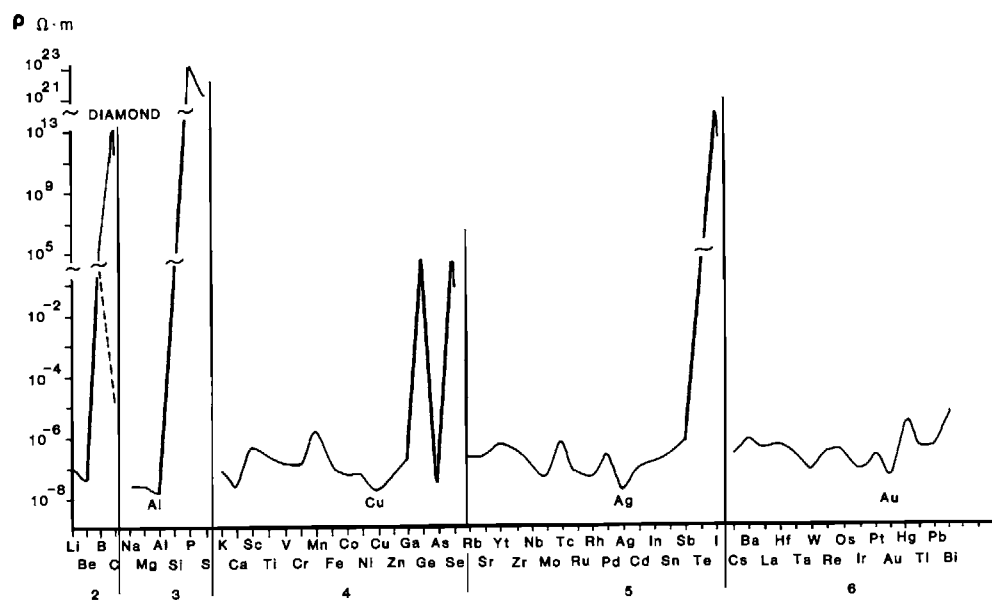


FIG. 5. Resistivity of the elemental materials as a function of atomic number.

Each process is illustrated in simplified form in Figure 6. Electrons are displaced from a neutral position with respect to the atomic nucleus when an electric field is applied, giving rise to electronic polarization. Because the charge to mass ratio is very large in electrons, the displacement of the electron population takes place very rapidly, and so, electron polarization occurs uniformly at all frequencies used in geophysics, both high and low. The electronic contribution to permittivity is easiest to evaluate at optical frequencies, because it can be derived from the index of refraction  $n$  which is easily measured;

$$K_e = n^2, \quad (40)$$

where  $K_e$  is the dielectric constant, and is taken to be the ratio of permittivity of a material to that of free space

$$K_e = \epsilon / \epsilon_0. \quad (41)$$

Some values for dielectric permittivity of minerals at optical frequencies are listed in Table 3, along with values for permittivity at lower frequencies.

At lower frequencies, including the entire range of frequencies of interest in exploration,

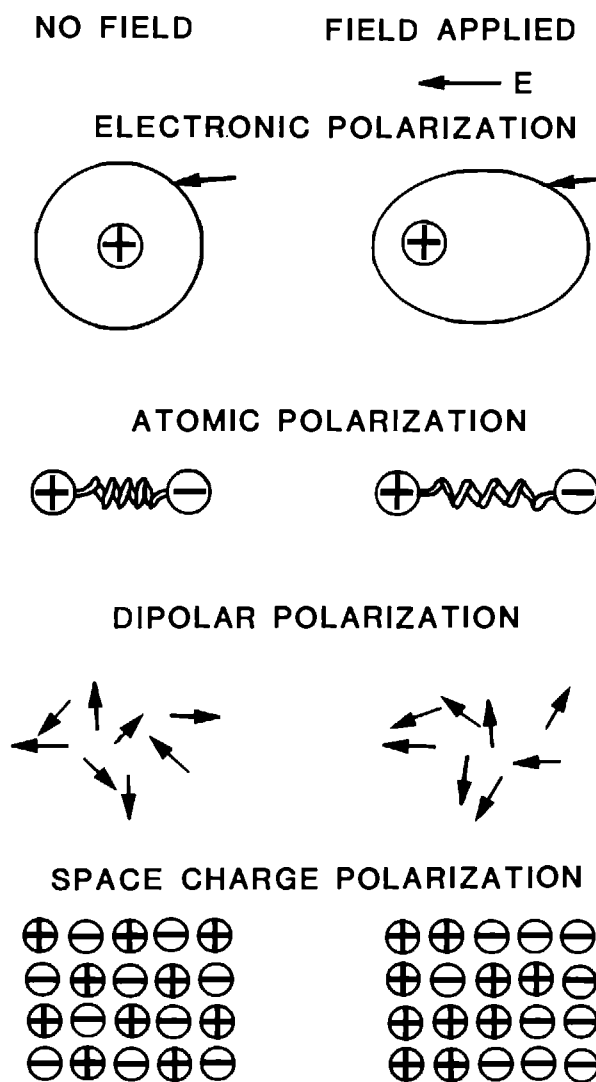


FIG. 6. Mechanisms for polarization (from von Hippel 1954 a, b).

**Table 3. Dielectric constants of minerals, rocks, and soils at high frequencies.**

Mineral or rock	Source and orientation of sample	Dielectric constant	
		Radio frequencies	Optical frequencies
Phosphate Minerals			
Apatite, $\text{Ca}_5(\text{F}, \text{Cl})(\text{PO}_4)_3$		7.40–10.47	
	Asio, Japan		
	Across optic axis	7.60	2.69
	Along optic axis	10.0	2.71
	Kamioka, Japan		
	Across optic axis	7.43	
	Along optic axis	6.07	
Vivianite, $\text{Fe}_3(\text{PO}_4)_2 \cdot 8\text{H}_2\text{O}$		6.07	2.49–2.67
Sulfate Minerals			
Anglesite, $\text{PbSO}_4$		74.0–500	3.52–3.59
Anhydrite, $\text{CaSO}_4$		5.70–6.30	
	Along a axis	—	2.48
	Along b axis	—	2.49
	Along c axis	—	2.61
Barite, $\text{BaSO}_4$		6.99–12.2	
	Along a axis	7.10	2.68
	Along b axis	8.85–10.0	2.38–2.69
	Along c axis	6.72–7.60	2.40–2.71
	Trintington, England (nine samples)		
	Along a axis	7.85 ± (0.09)	
	Along b axis	12.31 ± (0.05)	
	Along c axis	7.88 ± (0.05)	
Celestite, $\text{SrSO}_4$	Sicily		
	Along a axis	7.60	2.62
	Along b axis	—	2.64
	Along c axis	8.26	2.66
Gypsum, $\text{CaSO}_4 \cdot 12\text{H}_2\text{O}$		5.00–11.5	
	Along a axis	11.2	2.31
	Along b axis	12.0	2.32
	Along c axis	5.40	2.34
Silicate Minerals			
Analcime, $\text{NaAlSi}_2\text{O}_4 \cdot \text{H}_2\text{O}$	Tyrol	5.88	2.21
Augite, $\text{Ca}(\text{Mg}, \text{Fe}, \text{Al})(\text{Al}, \text{Si})_2\text{O}_6$		6.90–10.27	
	Along a axis	8.60	2.92
	Along b axis	6.90	2.95
	Along c axis	7.10	3.01
Beryl, $\text{Be}_3\text{Al}_2\text{Si}_6\text{O}_{18}$		5.48–7.80	
	Across optic axis	6.59	2.53
	Along optic axis	6.16	2.56
	Urals		
	Along optic axis	6.18	
	Across optic axis	5.67	
Biotite, $\text{K}(\text{Mg}, \text{Fe})_3\text{AlSi}_3\text{O}_{10}(\text{OH})_2$		6.19–9.30	
	Along a axis	—	2.50
	Along b axis	—	2.68
	Along c axis	—	2.68
Sulfide Minerals			
Galena, $\text{PbS}$		17.9	
Sphalerite, $\text{ZnS}$	Titibu, Japan	7.90	5.61 to 6.10
	Nakatatu, Japan	12.1	
	Joplin, Missouri	69.9–7.90	

Table 3. continued

Mineral or rock	Source and orientation of sample	Dielectric constant	
		Radio frequencies	Optical frequencies
	Harz, Germany	69.7–7.88	
Oxide Minerals			
Corundum, $\text{Al}_2\text{O}_3$		11.0–13.2	
	Across optic axis	—	3.10
	Across optic axis	—	3.14
Cassiterite, $\text{SnO}_2$		23.4–24.0	
	Along optic axis	—	3.98
	Across optic axis	—	4.36
Diaspore, $\text{Al}(\text{OH})$	Mituisi, Japan		
	Along a axis	7.70	2.90
	Along b axis	8.38	2.96
	Along c axis	7.27	3.05
Hematite, $\text{Fe}_2\text{O}_3$		25.0	
	Along optic axis	—	8.65
	Across optic axis	—	10.33
Rutile, $\text{TiO}_2$		31.0–170	
	Along optic axis	—	6.82
	Across optic axis	—	8.42
Anatase, $\text{TiO}_2$		425	
Halide Minerals			
Halite, $\text{NaCl}$		5.70–6.20	2.39
Flourite, $\text{CaF}_2$		6.79	2.06
	Akenobe, Japan	6.26	
	Saxony	6.61	
	Okuno, Japan	6.27	
	Switzerland	6.25	
	Durham, England	6.30	
	Freiburg, Saxony	6.60	
Sylvite, $\text{KCl}$		4.39–6.20	2.20
Carbonate Minerals			
Aragonite, $\text{CaCO}_3$	Bohemia		
	Along a axis	6.46	2.34
	Along b axis	9.72	2.82
	Along c axis	7.55	2.84
Calcite, $\text{CaCO}_3$		7.80–8.50	
	Across optic axis	—	2.21
	Along optic axis	—	2.75
Dolomite, $\text{CaMg}(\text{CO}_3)_2$		6.80–8.00	
	Across optic axis	7.53	2.28
	Along optic axis	6.11	2.85
Epidote (average of 14 samples) $\text{Ca}_2(\text{Al, Fe})_3(\text{SiO}_4)_3\text{OH}$	Tyrol		
	Along a axis	7.60 ± .13	3.01
	Along b axis	9.99 ± .14	3.11
	Along c axis	15.36 ± .04	3.17
Leucite, $\text{KAlSi}_2\text{O}_6$	Italy	7.13	
	Across optic axis	—	2.27
	Along optic axis	—	2.27
Muscovite, $\text{KAl}_3\text{Si}_3\text{O}_{10}(\text{OH})_2$		6.19–8.00	
	Along a axis	—	2.46
	Along b axis	—	2.55
	Along c axis	—	2.60
Opal, $\text{SiO}_2 \cdot n\text{H}_2\text{O}$	Bodai, Japan	7.15	2.10

Table 3. continued

Mineral or rock	Source and orientation of sample	Dielectric constant	
		Radio frequencies	Optical frequencies
Opal, var. Hyalite	Takarasaka, Japan	7.43	
Orthoclase feldspar var. adularia, $KAlSi_3O_8$	Tateyama, Japan	4.21	
	Along a axis	5.55	2.30
	Along b axis	5.80	2.33
	Along c axis	4.50	2.34
Phlogopite, $KMg_2Al_2Si_3O_{10}(OH)_2$		5.90–6.50	
	Along a axis	—	2.44
	Along b axis	—	2.58
	Along c axis	—	2.58
Plagioclase feldspar			
var. albite $Ab_{97}An_3$	Basi-bergwerk, Japan	5.58	2.33
var. albite $Ab_{99}An_1$	Switzerland	5.45	2.34
var. albite $Ab_{95}An_5$	Tyrol	5.57	2.36
var. albite $Ab_{96}An_4$	Switzerland	5.52	2.36
var. albite $Ab_{98}An_2$	Italy	5.55	2.34
var. albite $Ab_{94}An_6$	Norway	5.63	2.36
var. albite $Ab_{99}An_1$	Urals	5.55	2.33
var. albite $Ab_{98}An_2$	Bavaria	5.39	2.34
var. oligoclase $Ab_{76}An_{24}$	North Carolina	6.03	2.39
var. oligoclase $Ab_{77}An_{23}$	Norway	6.06	2.39
var. andesine $Ab_{65}An_{35}$	Norway	6.20	2.41
var. andesine $Ab_{61}An_{39}$	Korea	6.47	2.41
var. andesine $Ab_{52}An_{48}$	Nakasioti, Japan	6.30	2.43
var. labradorite $Ab_{43}An_{57}$	Labradore, Italy	6.61	2.45
var. labradorite $Ab_{45}An_{55}$	North America	6.51	2.45
var. anorthite $Ab_4An_{96}$	Otaru, Japan	7.24	2.51
var. anorthite $Ab_2An_{98}$	Tsushima, Japan	7.14	2.51
var. anorthite $Ab_7An_{93}$	Hokkaido, Japan	7.05	2.49
var. anorthite $Ab_4An_{96}$	Miyakeshima, Japan	7.15	2.49
Quartz $SiO_2$		4.19–5.00	
	Across optic axis	4.96	2.36
	Along optic axis	5.05	2.41
	Naegi, Japan		
	Normal to optic axis	4.11	
	Parallel to optic axis	4.27	
	Kinbuzan, Japan		
	Normal to optic axis	4.13	
	Parallel to optic axis	4.27	
Quartz, bipyramidal	Cumberland, Maryland		
	Normal to optic axis	4.09	
	Parallel to optic axis	4.27	
Sericite		19.55–25.35	
Sillimanite		4.80	
$Al_2SiO_5$	Along a axis	—	2.78
	Along b axis	—	2.79
	Along c axis	—	2.84
Topaz, $Al_2SiO_4(F, OH)_2$		6.30–7.60	
	Along a axis	6.65	2.66
	Along b axis	6.70	2.66
	Along c axis	6.30	2.68
	Naegi, Japan		
	Along a axis	6.31	
	Along b axis	6.43	
	Along c axis	6.27	

Table 3. continued

Mineral or rock	Source and orientation of sample	Dielectric constant	
		Radio frequencies	Optical frequencies
Tourmaline		5.60–7.10	
	Ceylon		
	Normal to optic axis	6.75	2.76
	Parallel to optic axis	5.52	2.89
	Cumberland, Maryland		
	Normal to optic axis	6.76	
	Parallel to optic axis	5.45	
Zircon, $ZrSiO_4$		8.59–12.0	~3.84

atomic polarization becomes significant. Because of the much lower charge to mass ratio of the atomic nucleous, atomic polarization responds more slowly to an applied electric field than do the electrons. Even so, polarization occurs in less than a microsecond for heavy atoms, and at frequencies near the optical range for light atoms. Inasmuch as the force which prevents an atom from undergoing continuous displacement is the bonding force within the crystal lattice, the contribution to permittivity by atomic polarization is less easily predicted than in the case of electrons. At radio frequencies and below, both atomic and electronic polarization are present. Values for permittivity of some minerals in this frequency range are listed in Table 3.

There is a useful correlation between dielectric permittivity and density, as illustrated in Figure 7.

Molecular polarization can occur in materials which contain polar molecules, or molecules that have asymmetric structures and possess a permanent dipole moment. Of the materials that occur in rocks, those which have dipolar molecules are water and hydrocarbons. In water, which is a common constituent of rock, the molecular structure is as shown in Figure 8. The hydrogen atoms, which carry an average positive charge, have a center of location that is displaced from the center of the average negative charge distribution, located at the oxygen nucleus. When an electric field is applied, the atom will tend to rotate to align itself with the direction of the applied field. During rotation, there is an effective displacement current, and on completion of rotation, a polarization will exist. The speed of rotation depends primarily on the tightness with which the water molecule is held in place. In liquid water, there is little resistance to rotation, and polarization will occur at high frequencies. In the high radio frequency range curves for the permittivity of water as a function of frequency are shown in Figure 9. In ice, also an abundant mineral, polarization occurs more slowly. Curves for the permittivity and conductivity in ice are shown in Figure 10.

Hydrates of natural gas, clathrates, are thought by some to occur as solids in many rocks, particularly in permafrost areas and in the sediments of the deep seas (Makogon, 1981). Such materials can be expected to have relatively high dielectric permittivities at low frequencies, but no definitive studies of the electrical properties of the solid gas hydrates have yet been reported.

Volume polarization occurs when free charge carriers are available in a material to move under the action of an applied field. If the material is uniform, these charge carriers give rise to a conduction current. If, as is more likely the case, the mobility of the charge carriers

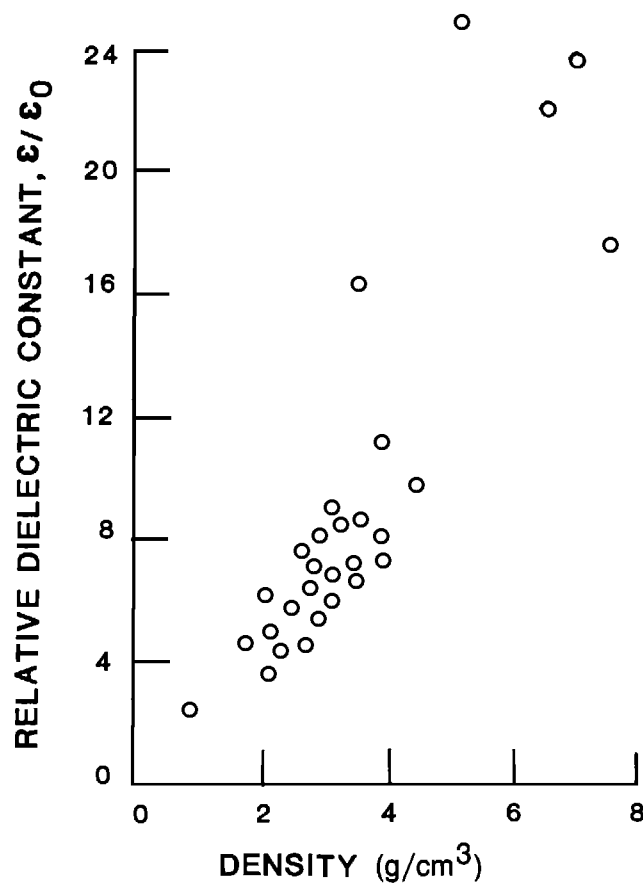


FIG. 7. Correlation between relative dielectric constant and density for a number of mineral compounds (from Parkhomenko, 1967)

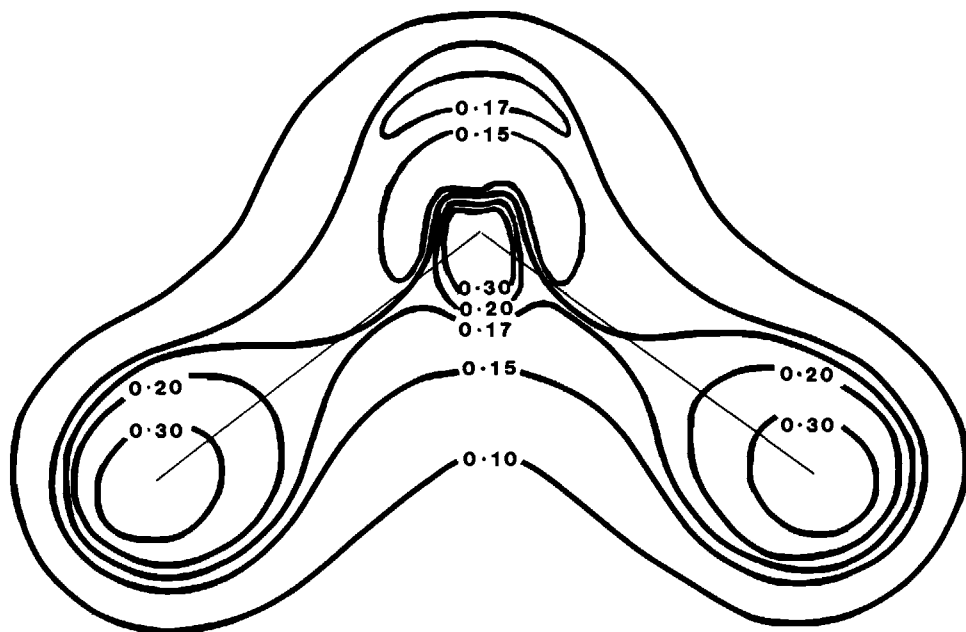


FIG. 8. Electron density contour map for the water molecule showing the density of valence electrons in the plane defined by bonding of the molecule (from Eisenberg and Kauzman, 1969)

changes from place to place because of defects in the crystal lattice or changes in crystal properties, concentrations or depletions of ions will exist at such discontinuities, giving rise to polarization. Because the mobility of ions in a solid structure is often very low, and because the distance between mobility barriers is often very long on the atomic scale, this type of polarization is very slow. Polarization appears to increase even at frequencies below 1 Hz.

Because thermal excitation plays such an important role in this type of polarization and conduction, most studies of space charge effect have been done as a function of temperature. A series of conductivity-temperature curves for several minerals are shown in Figures 11 and 12. On these plots, conductivity is plotted on a logarithmic scale, while temperature is plotted on an inverse scale. The advantage of this plotting scheme is that often the data plot as a series of straight line segments, which can be approximated with simple algebraic expressions of the form

$$\sigma = A_1 e^{-m_1/T} + A_2 e^{-m_2/T} \quad (42)$$

where  $m_i$  is the slope of a straight line segment, and  $A_i$  is the corresponding intercept value on the  $1/T = 0$  axis. The exponent represents the binding energy of the charge carrier, which is:

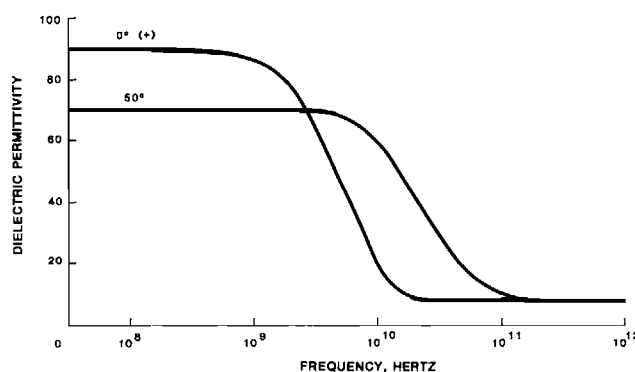


FIG. 9. Dielectric permittivity of water over frequencies at which dispersion takes place.

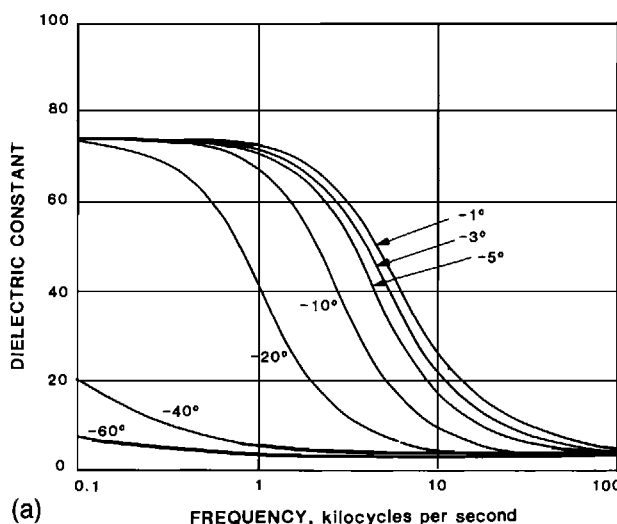


FIG. 10a. The relative dielectric constant of ice as a function of temperature and frequency (from Eisenberg and Kauzman, 1969)

$$U_i = Km_i \quad (43)$$

For the case of excitation individual ions from the lattice, where  $U$  is the binding energy,  $K$  is Kelvin's constant, and  $T$  is absolute temperature. Values for  $U_i$  are listed in Table 4.

### Magnetic properties of minerals

Magnetic permeability is not normally considered an electrical property of a material, but as shown above, its value enters into the expression for wave number, which is the fundamental parameter to consider in the behavior of electromagnetic waves.

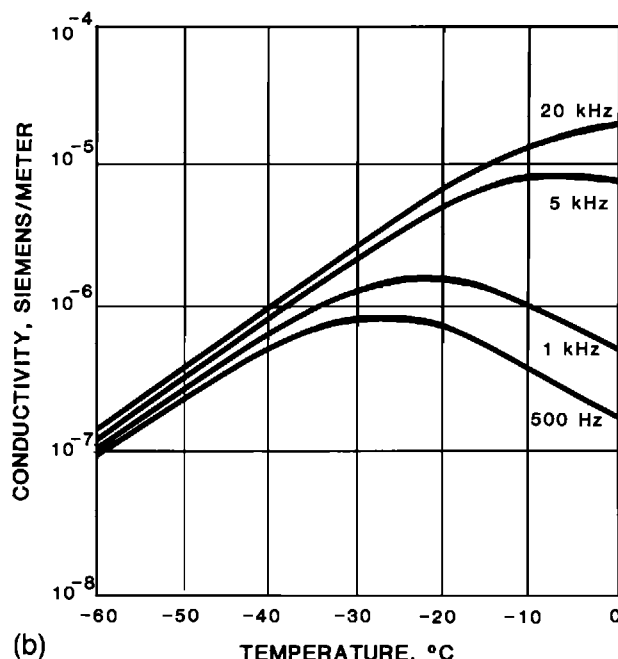


FIG. 10b. The electrical conductivity of pure ice as a function of temperature and frequency (from Eisenberg and Kauzman, 1969)

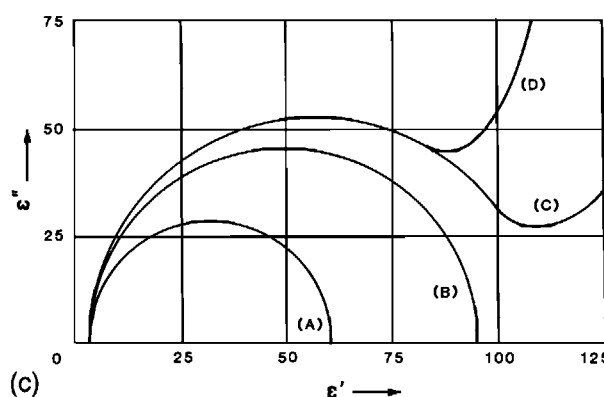


FIG. 10c. Cole-Cole plot for ice. Curve A represents a sample with a fracture plane, curve B is a sample of solid ice, and curves C and D are samples with some conductivity. Temperature is  $-10.8^{\circ}\text{C}$  (From Hasted, 1961)

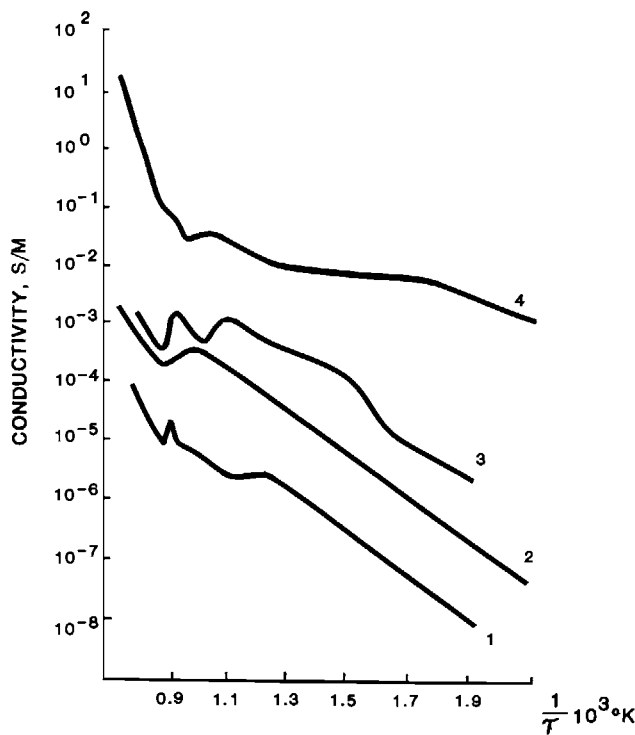


FIG. 11. Conductivity of amphibolite minerals as a function of temperature. 1. tremolite, 2., actinolite, 3., hornblende, and 4., riebeckite.

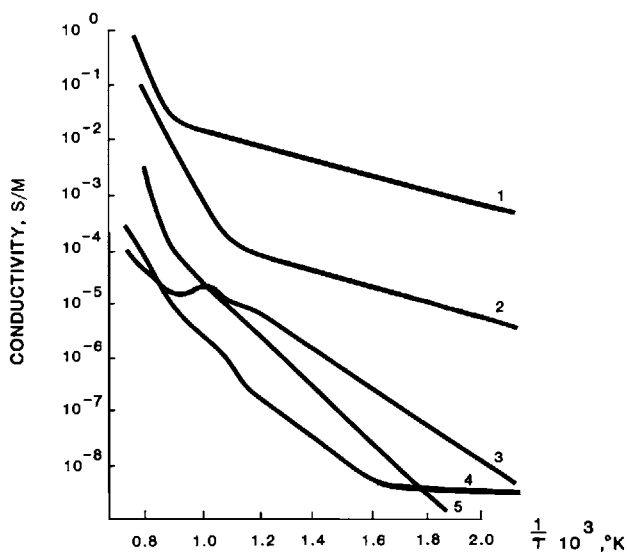


FIG. 12. Conductivity of pyroxene minerals as a function of temperature. 1. aegirine, 2., jadeite, 3., spodumene, 4., diopside, and 5., enstatite.

Most materials are diamagnetic or paramagnetic. In these materials, rotating electrons align themselves with or against the applied magnetic field. This applied field can be the static magnetic field, but in our case, we are more interested in the magnetic field comprising a time-varying electromagnetic field. These effects can be expected to occur very rapidly, just as electron polarization occurs rapidly. Moreover, the contribution to the magnetic field by such electron orbital alignments is quite small. Typical permeability values for diamagnetic and paramagnetic minerals differ from that of free space by a few tens or hundreds of parts per million (see values listed in Table 5).

A few minerals exhibit ferromagnetism, an intense magnetic polarization which can occur

**Table 4. Parameters defining the temperature dependence of resistivity in solid electrolytes.**

Rock	$A_1$	$A_2$	$U_1$	$U_2$
Granite	$5 \times 10^{-4}$ mho/cm	$10^5$ mho/cm	0.62 eV	2.5 eV
Gabbro	$7 \times 10^{-3}$	$10^5$	0.70	2.2
Basalt	$7 \times 10^{-3}$	$10^5$	0.57	2.0
Peridotite	$4 \times 10^{-2}$	$10^5$	0.81	2.3
Andesite	$6 \times 10^{-3}$		0.7	1.6

**Table 5. Susceptibility of minerals and other materials (at room temperature, unless otherwise noted).**

Material	Composition	Notes	Density (gm/cm <sup>3</sup> ) a	k	
				in 10 <sup>-6</sup> cgs/cm <sup>3</sup> b	in 10 <sup>-6</sup> cgs/gm
<b>Minerals</b>					
Hematite	$\alpha\text{Fe}_2\text{O}_3$	760°C	5.26	18,862	3,586
Wustite	FeO	20°C	5.75	41,400	7,200
Troilite	FeS	20°C	4.83	5,187	1,074
Siderite	$\text{FeCO}_3$	20°C	3.96	44,750	11,300
Corundum	$\text{Al}_2\text{O}_3$		4.02	-149	-37
Cassiterite	$\text{SnO}_2$		6.99	-287	-41
Rutile	$\text{TiO}_2$		4.25	25	5.9
Quartz	$\text{SiO}_2$		2.65	-78	-29.6
Calcite	$\text{CaCO}_3$		2.71	-103	-38
Magnesite	$\text{MgCO}_3$		3-3.4	~-100	-32
Anhydrite	$\text{MgSO}_4$	21°C	2.96	-148	-50
Galena	PbS		7.58	-637	-84
Millerite	NiS	20°C	5.5	1045	190
Rock salt	NaCl		2.16	-65	-30
<b>Metals, etc.</b>					
Gold	Au	23°C	19.3	-540	-28
Copper	Cu	23°C	8.95	-49	-5.5
Tin	Sn	gray; 7°C	5.75	-213	-37
Sodium	Na		0.97	15.5	16
Gadolinium	Gd	27°C	7.90	5,965,000	755,000
Diamond	C		3.51	-21	-5.9
				-1.8	
Graphite	C		2.1-2.2	-13	-6
				-6 to -16	
Water	$\text{H}_2\text{O}$	liquid, 100°C			-13.1
		liquid, 0°C	1.0	-12.9	-12.9
		solid (ice), 0°C	0.92	-11.7	-12.7
Oxygen	$\text{O}_2$	gas, 20°C			3449

**Table 6.** Susceptibilities of rock types, calculated from their magnetite and ilmenite content

Material	Magnetite content and susceptibility, cgs units							
	Minimum		Maximum		Average		Ilmenite, average	
	%	$k \times 10^4$	%	$k \times 10^4$	%	$k \times 10^4$	%	$k \times 10^4$
Quartz porphyries	0.0	0	1.4	4,200	0.82	2,500	0.3	410
Rhyolites	0.2	600	1.9	5,700	1.00	3,000	0.45	610
Granites	0.2	600	1.9	5,700	0.90	2,700	0.7	1000
Trachyte-syenites	0.0	0	4.6	14,000	2.04	6,100	0.7	1000
Eruptive nephelites	0.0	0	4.9	15,000	1.51	4,530	1.24	1700
Abyssal Nephelites	0.0	0	6.6	20,000	2.71	8,100	0.85	1100
Pyroxenites	0.9	3000	8.4	25,000	3.51	10,500	0.40	5400
Gabbros	0.9	3000	3.9	12,000	2.40	7,200	1.76	2400
Monzonite-latites	1.4	4200	5.6	17,000	3.58	10,700	1.60	2200
Leucite rocks	0.0	0	7.4	22,000	3.27	9,800	1.94	2600
Dacite-quartz-diorite	1.6	4800	8.0	24,000	3.48	10,400	1.94	2600
Andesites	2.6	7800	5.8	17,000	4.50	13,500	1.16	1600
Diorites	1.2	3600	7.4	22,000	3.45	10,400	2.44	4200
Peridotites	1.6	4800	7.2	22,000	4.60	13,800	1.31	1800
Basalts	2.3	6900	8.6	26,000	4.76	14,300	1.91	2600
Diabases	2.3	6900	6.3	19,000	4.35	13,100	2.70	3600

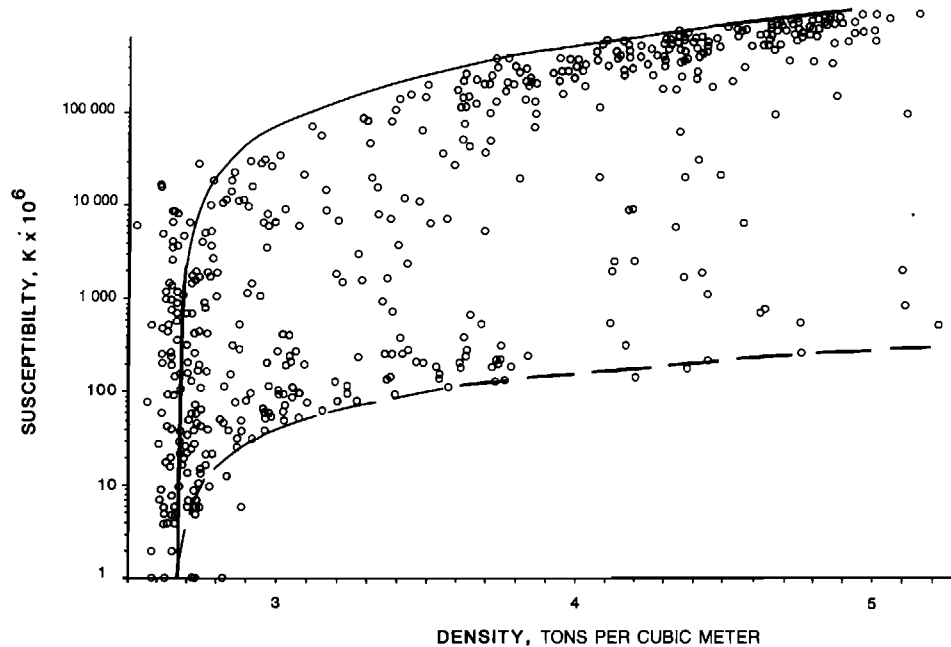


FIG. 13. Summary of magnetic susceptibility measurements (from Hansen, 1966)

Table 7. Piezoelectric effect in rocks containing nepheline.

Rock	Mineral composition, %			Piezoelectric modulus, $d_{ii}' \cdot 10^{-10}$ in cgse units		
	nephline	aegerine	others	$d_{11}'$	$d_{22}'$	$d_{33}'$
Urtite (coarse-grained)	80	20	—	30.0	15.0	10.0
Urtite	80	10	10	3.2	1.3	0.9
Eolite, fine-grained trachyoidal	45	40	15	0.5	0.4	0.27
Luyavrite (unequal grain sizes)	40	15	45	10.0	9.5	5.0
Reischorrite	—	—	—	1.4	0.6	—
Nepheline-apatite rock	—	—	—	0.8	0.7	0.7
Khibinite	—	—	—	0.3	0.2	—
Trachyoidal luyavrite	—	—	—	0.8	—	—
Trachyoidal luyavrite	—	—	—	0.4	0.4	0.32

in a material when large sections of a crystal, called magnetic domains, orient themselves in unison to provide a large enhancement of the magnetic field. Minerals that exhibit this effect include magnetite and titano-magnetite. Values for the magnetic permeability of magnetite and other magnetic minerals are listed in Table 6.

Magnetite occurs in many rocks as an accessory mineral. In most cases, the permeability of the rock is determined by the magnetite content. Figure 13 shows correlation between magnetite content and permeability.

Because the domains which organize to contribute to ferromagnetism do so relatively slowly, magnetic permeability will exhibit dispersion. Little information is available on the frequency dependence of permeability, but frequency dependence obviously will have an effect on electromagnetic field behavior. Lee (1984a, b) indicates that decay of magnetization near the source coil in a coincident loop electromagnetic system will give rise to transients that are significant in size.

#### Piezoelectric properties of minerals

Piezoelectric properties of rocks and minerals have been discussed in detail in Parkhomenko (1971). Values for the piezoelectric coefficients for minerals and rocks are listed in Table 7.

## Properties of Rocks

A rock is an aggregate of one or more types of mineral grains. The properties of a rock might be expected to be some simple combination of the properties of the mineral constituents. This is not often true, and the cause of the complexity of predicting rock properties from mineral properties is the presence of a nonmineral substance, water, in virtually all rocks. Because water has strong effects on both conductivity and dielectric permittivity, the presence of even very small amounts will dominate the behavior of conductivity and dielectric permittivity. Electrical properties of rocks are discussed extensively in Olhoeft (1980) and Collett and Katsube (1973).

The properties of water as a substance are documented in the literature (Hasted, 1961, and Eisenberg and Kauzman, 1969). Unmineralized water is a relatively poor conductor, but is

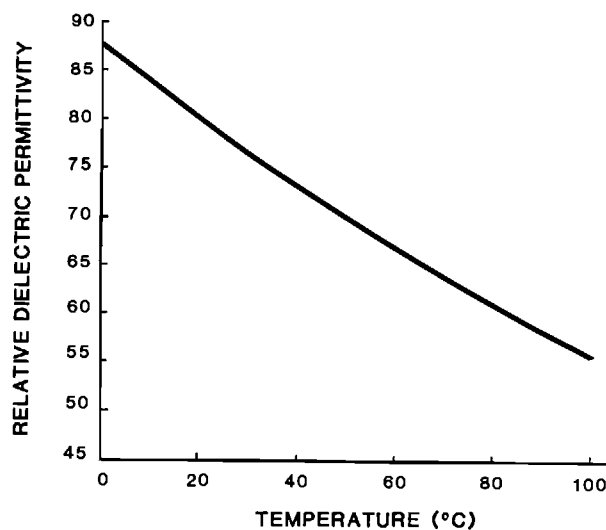


FIG. 14. Static dielectric constant of liquid water as a function of temperature (from Eisenberg and Kauzman, 1969)

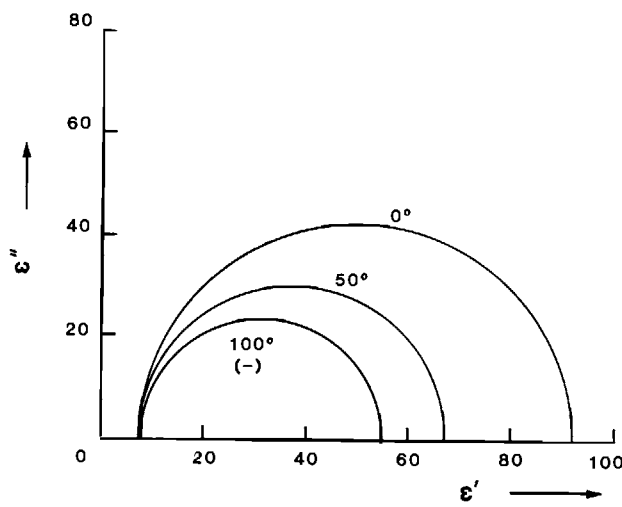


FIG. 15. Cole-Cole plots for liquid water at several temperatures.

Table 8. Ion mobilities measured\* in low concentrations at 25°C.

Ion	Mobility
H <sup>+</sup>	$36.2 \times 10^{-8}$
OH <sup>-</sup>	$20.5 \times 10^{-8}$
SO <sub>4</sub> <sup>=</sup>	$8.3 \times 10^{-8}$
Na <sup>+</sup>	$5.2 \times 10^{-8}$
Cl <sup>-</sup>	$7.9 \times 10^{-8}$
K <sup>+</sup>	$7.6 \times 10^{-8}$
NO <sub>3</sub> <sup>-</sup>	$7.4 \times 10^{-8}$
Li <sup>+</sup>	$4.0 \times 10^{-8}$
HCO <sub>3</sub> <sup>-</sup>	$4.6 \times 10^{-8}$

\*Meters per second/volts per meter.

characterized by a relatively high value of dielectric permittivity (see Figure 14). The values shown in Figure 14 are for deionized water under laboratory conditions. At relatively high frequencies, both properties exhibit dispersion; dielectric permittivity and conductivity vary with frequency. In water, molecular polarization is significant because of the nonsymmetrical distribution of electron density in the molecule. The molecule has a permanent dipole moment, such that an applied electric field will cause the molecule to rotate in the field to align its moment with the direction of the field. During rotation, a displacement current occurs, and dielectric displacement of charge accompanies the process. Since the dispersion in both properties is caused by a single process, molecular polarization, there is a specific relationship between the real and imaginary parts of the wave number. A Cole-Cole plot of the real and imaginary wave number for pure water is shown in Figure 15.

Water is a solvent, and in nature, it exists as an electrolyte with considerable amounts of ions present to add to conductivity. Ground water, the water filling the pore space of any rock, is often an electrolyte with a wide variety of salts in solutions. However, most ground waters can be categorized as belonging to one of four types, with ionic contents reflecting the origin and history of the ground water. The most common ground water is connate water, or fossil water left from the deposition of sedimentary rocks. The salinity of such water reflects the chemistry of the depositional basin, and commonly is rich in sodium chloride. Another common type of ground water is bicarbonate water. These waters usually reflect erosion on a continent, and contain a higher proportion of carbonates and calcium; they are also usually less concentrated than connate waters. In some areas, acid ground waters may be found. These acid waters are often typical of mining districts where sulfide and oxide minerals provide a source for acids on weathering.

The conductivity of an electrolytic solution depends on the mobility and number of ions in solution. Mobilities, the terminal velocity to which ions are accelerated under a constant electric field, are listed in Table 8 for some of the common ions that occur in ground water. Mobility is determined by the viscous friction to ion movement which in turn depends on temperature to some extent, and on pressure. In pore structures of rock, because of the adsorption of water and ions to the mineral surfaces, pressures can be high, and mobility significantly reduced from that in a free solution. The mobilities listed in Table 8 are valid for standard temperatures and pressures; for rocks, the mobility in place must be considered.

An important feature of the values listed in Table 8 is that most of the ions have roughly

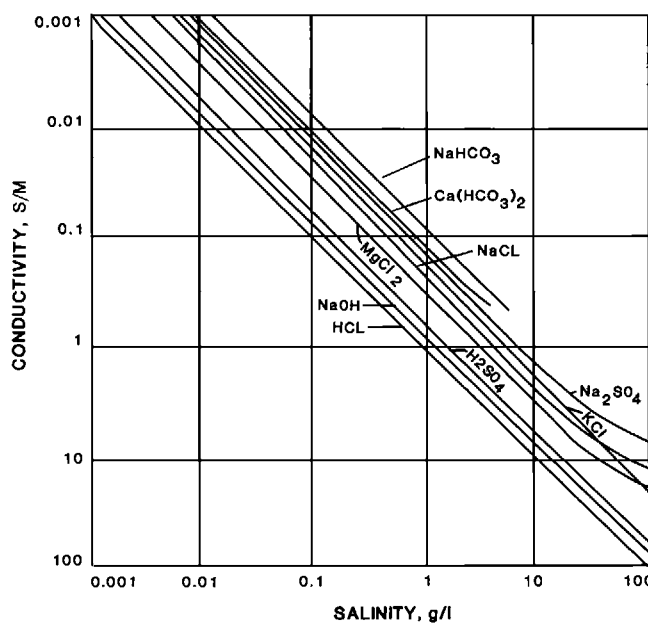


FIG. 16. Conductivity of solutions of various salts as a function of concentration. Temperature of 20° C.

the same mobilities. Hydrogen ion and hydroxyl ion are exceptions, having mobilities nearly an order of magnitude larger than the salts. For neutral ground water, each salt need not be considered separately, but the total dissolved solids can be considered as characterized by an average mobility. The conductivity of an aqueous electrolyte as a function of salt concentration is shown graphically in Figure 16 for a number of salts. The effect of temperature, which increases mobility, is shown by the curves in Figure 17 for a sodium chloride electrolyte.

Note that if only information on total dissolved solids is available, the high conductivity of rocks around an oxidizing ore body where highly acid ground water is present may be surprising.

When water is contained in a rock, water-rock interactions will make it difficult to know the salinity of the electrolyte in place. If clay minerals are present, a relatively large number of ions may be released from such minerals by ion exchange processes (Waxman and Smits, 1968). Typical ion exchange capacities for some of the clay minerals are listed in Table 9. The ions contributed by this process provide a threshold conductivity for water in the pore structure of a rock, so that a rock with quite pure water in it can appear to be moderately conductive. Figure 18 illustrates this effect.

In most rocks, water is the only constituent with significant conductivity that is present. In clay-bearing rocks, clay is sometimes considered a conducting mineral, though the clay must be wet for the conduction process to take place (Waxman and Smits, 1968). In this case, the conductivity of the rock is determined by the conductivity of the contained water, with its shape taken into account (the shape of the pore structure). Pore structures have highly complicated shapes, in terms of conventional geometries. Efforts to describe pore structures geometrically and probabilistically have been only moderately successful (Madden, 1976; Kwon and Pickett, 1975; Jackson et al. 1978).

The most satisfactory expression for the conductivity of a water-bearing rock is that attributed to Archie (1942) which is

$$\sigma = a\sigma_w W^m \quad (44)$$

where  $\sigma$  is the overall conductivity of the rock,  $\sigma_w$  is the conductivity of the electrolyte in place in the pore structure, taking into account the effects of pore pressures and ion exchange,  $W$  is the volume fraction of water present in the rock, assuming that the pore space is completely filled with water, and  $a$  and  $m$  are parameters used to force the expression to fit the behavior of a given rock.

In some rocks, part of the pore space can be occupied by a gas such as air. In this case, the above equation can be written as

$$\sigma = a\sigma_w S''\phi^m \quad (45)$$

where  $S$  is the fraction of the pore space filled with water and  $\phi$  is the volume fraction of void space in the rock.

Pore structures are complicated in form and difficult to describe geometrically, but at least three different styles of pore geometry can be recognized; (1) intergranular space in sedimentary rock, (2) fracture, joint, and microcrack pores, usually in crystalline rocks, and (3) vugs or other large, poorly interconnected pore structures, as in extrusive volcanic rocks. For a given porosity and water content, fracture porosity will result in the highest rock conductivity of the three classes because of the simpler shape of the void structures, while vuggy porosity will contribute the lowest conductivity because of the complex structure.

Most measurements have been made on sedimentary rock because of the interest in electrical properties of oil reservoir rocks, but a few studies of the conductivity-porosity relationship in igneous and crystalline rocks have been done. In each case, Archie's law seems to be a good representation of the measurements. Archie's law representations for these three classes of relationship are shown graphically in Figure 19 and algebraically in Table 10.

In exploration for geothermal systems, the conductivity of a rock which may contain conductive molten minerals has been of interest. Archie's law has been used as a starting point

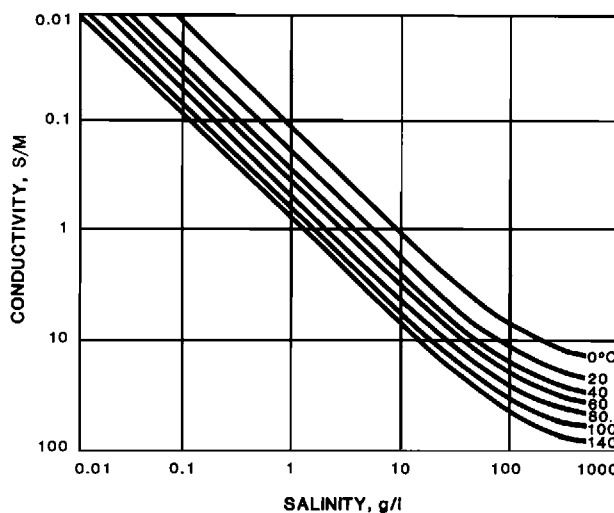


FIG. 17. Conductivity of a solution of NaCl as a function of temperature and concentration.

**Table 9. Exchange capacities of some common clay minerals.**

Clay	Exchange capacity
Kaolinite	3 to 15 m · equiv/100 g
Halloysite · 2H <sub>2</sub> O	5 to 10
Halloysite · 4H <sub>2</sub> O	40 to 50
Montmorillonite	80 to 150
Illite	10 to 40
Vermiculite	100 to 150
Chlorite	10 to 40
Attapulgite	20 to 30

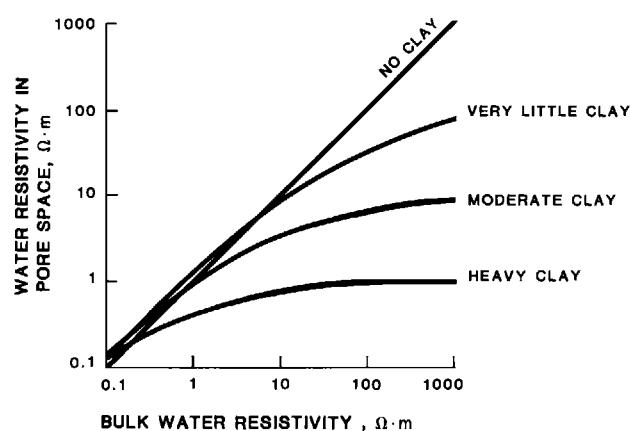


FIG. 18. Effect of salinity added by clay minerals on the apparent conductivity of the solution filling a porous rock (from Keller, 1967).

for describing the relationship between the conductivity of a partially molten rock and the melt fraction. Numerous studies of partially molten or molten systems have appeared in the literature (Shankland et al., 1981; Shankland and Waff, 1977; Tyburczy and Waff, 1983, 1985; Waff, 1974, 1976; Waff and Bulau, 1979; Waff and Weill, 1979; and Bulau et al., 1979).

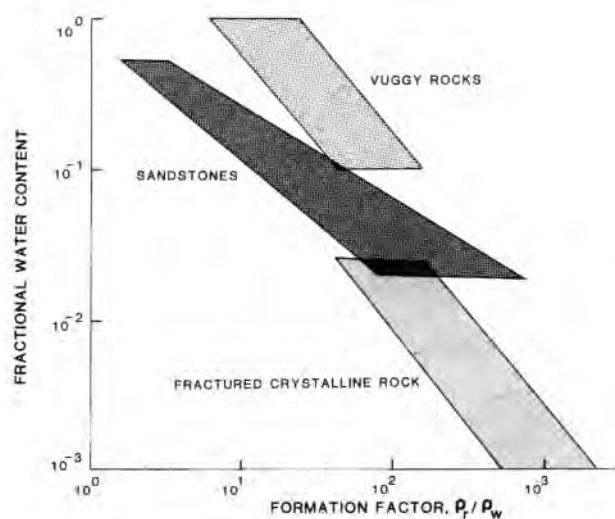


FIG. 19. Relationship between formation factor (ratio of rock resistivity to the resistivity of the water saturating it) to the amount of water in a rock for various types of pore structure.

**Table 10. Forms of Archie's law which may be used when lithology of a rock is known.**

Description of rock	a	m
Weakly-cemented detrital rocks, such as sand, sandstone, and some limestones, with a porosity range from 25 to 45%, usually Tertiary in age	0.88	1.37
Moderately well cemented sedimentary rocks, including sandstones and limestones, with a porosity range from 18 to 35%, usually Mesozoic in age	0.62	1.72
Well-cemented sedimentary rocks with a porosity range from 5% to 25%, usually Paleozoic in age	0.62	1.95
Highly porous volcanic rocks, such as tuff, aa and pahoehoe, with porosity in the range 20% to 80%	3.5	1.44
Rocks with less than 4% porosity, including dense igneous rocks and metamorphosed sedimentary rocks	1.4	1.58

### Mixtures of conductive minerals in host rocks

There is far less information available on the bulk resistivity of rocks containing highly conductive minerals than on rocks containing electrolytic conductors. As with electrolytes, the geometric style of distribution of the conducting minerals is expected to be an important factor in predicting the bulk resistivity. Very little study has been reported on the dependence of bulk resistivity on mineral habit, though it has been observed that accicular hematite can reduce the resistivity of a rock at far lower concentrations than can specular hematite. Also, it has been reported that very small concentrations of graphite can render a rock highly conductive because of its tendency to form thin continuous films along grain boundaries. Generally, however, in results of measurements on hand samples containing ore minerals, it is observed that a relatively high concentration of the ore mineral must be present before the rock in bulk becomes markedly conductive. Figure 20 shows the combined data from three extensive studies of the resistivity of ore and mineral-bearing rocks as a function of ore mineral content (Anderson, 1960; Parkhomenko, 1967, 1982; Nelson and Van Voorhis, 1983).

Another approach to examining the behavior of a rock that contains conducting mineral inclusions is by mathematical analysis, which assumes that mineral grains have some simple, easily modeled, geometric shape. Calculations were carried out in the early days of geophysics; Heiland (1946) cites a calculation by Maxwell and one by Hummel for an aggregate consisting of a medium with conductivity  $\sigma_1$  in which spherical grains of conductivity  $\sigma_2$  are imbedded in regular arrangement and in such a manner that their separation is large compared with their radius.

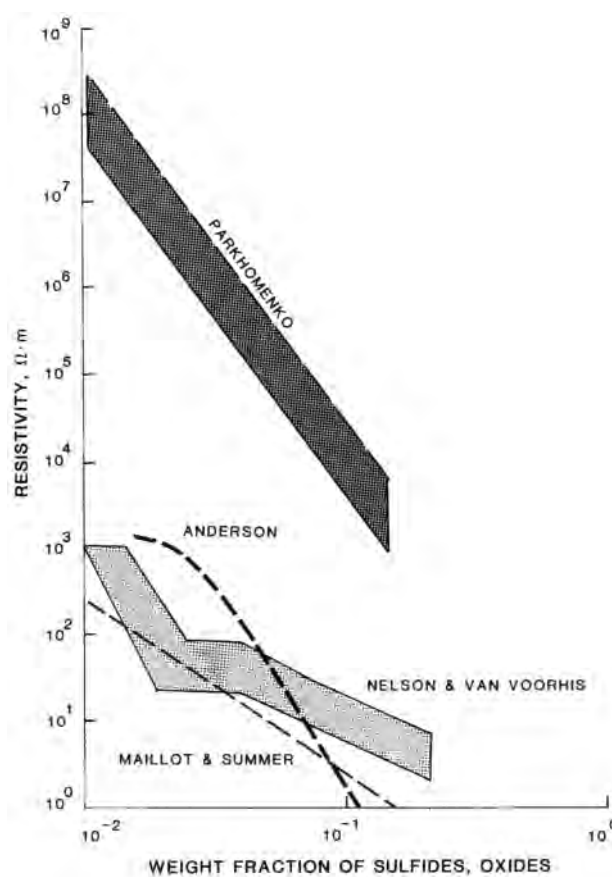


FIG. 20. Reported relationships between rock resistivity and the concentration of conducting minerals contained in that rock. Parkhomenko's data were obtained by laboratory measurement on pyritic rocks at high temperature (200°C). Anderson's measurements were done on wet samples of mineralized gabbro. The other two data sets are in situ measurements of porphyry copper ores.

$$\sigma = \frac{3\sigma_2 + 2v_1(\sigma_1 - \sigma_2)}{3\sigma_1 - v_1(\sigma_1 - \sigma_2)} \sigma_1 \quad (46)$$

where  $v_1$  is the volume fraction of conducting mineral. Because of the assumptions, this expression would apply only for quite small values of the ore mineral concentration,  $v_1$ . However, curves for the bulk conductivity as a function of the volume fraction of ore mineral and the contrast in conductivity between that mineral and the host rock (assumed to be modestly conductive because of a pervasive electrolyte content) are shown in Figure 21 for a relatively wide range of ore contents. It can be seen that isolated low concentrations of ore minerals have little effect on bulk conductivity. A similar conclusion can be drawn from a plot of observed conductivity-mineral content data in Figure 20.

Similar expressions have been developed for higher concentrations where the effect of the rest of the particles on the field about each particle must be considered, and on a wide variety of grain shapes, including spheroids, ellipsoids, and so on. Such elaboration of the problem leads to no different result than Maxwell's original formulation; isolated conductive grains do not strongly affect the overall electric properties of a rock.

### Dielectric permittivity

Because it is difficult to measure the dielectric permittivity of a conductive rock, the most credible data reported in the literature are for completely dry rocks, with no electrolytes or conducting minerals. In such cases, simple mixing rules can be used to predict the dielectric permittivity of a rock from the properties of the constituent minerals and their concentrations. von Hippel (1954a, b) reports that a logarithmic mixing rule works well for mixtures in which all minerals have the same conductivity (or all are insulators)

$$\log \epsilon = v_1 \log \epsilon_1 + v_2 \log \epsilon_2, \quad (47)$$

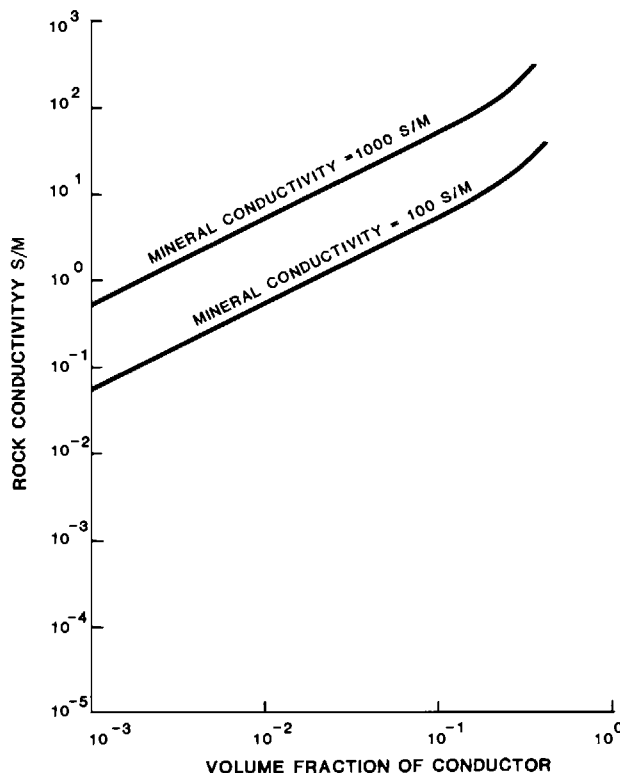


FIG. 21. Theoretically computed resistivity for spheres of one conductivity embedded in a host of another conductivity.

where  $v_1$  and  $v_2$  are the volume fractions of two constituents comprising a rock. Clearly, the formula can be extended to a larger number of constituents by adding additional terms of the same form.

Simple mixing rules cannot be applied when interfacial polarization takes place. Interfacial polarization occurs when abutting dielectric materials differ in conductivity and therefore require different voltage gradients to transconduct a current of constant density; to achieve this a charge must be present at the interface. The simplest case in which the effect of interfacial polarization can be evaluated is that of a laminated material (Maxwell, 1954). Consider a laminated material made up of two extensive sheets as indicated in Figure 22 (only two sheets are shown, but the material can consist of any number of repetitions of this basic structure with no change in the results). If the layers are electrically thin, they can be considered to react as two lumped circuits in series for a planar electromagnetic field traveling through them. By solving for the impedance of the two lumped circuits, the capacitance and conductance of the system can be found. From the capacitance, the composite dielectric permittivity can be calculated as

$$\epsilon = \frac{\tau_1 + \tau_2 - \tau + \omega^2 \tau_1 \tau_2}{\epsilon_0 (\rho_1 + \rho_2) (1 + \omega^2 \tau^2)}, \quad (48)$$

where  $\tau$  is a combination of properties of the system which acts as a time constant

$$\tau_1 = \epsilon_1 / \sigma_1, \quad \tau_2 = \epsilon_2 / \sigma_2, \quad r = d_1 / d_2$$

and

$$\tau = \frac{\epsilon_1 + \epsilon_2 r}{\tau_1 + \tau_2 r}.$$

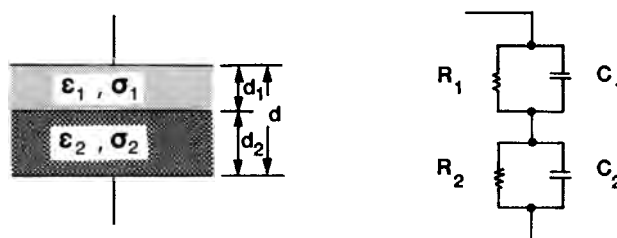


FIG. 22. Simulation of a laminated material as a lumped circuit.

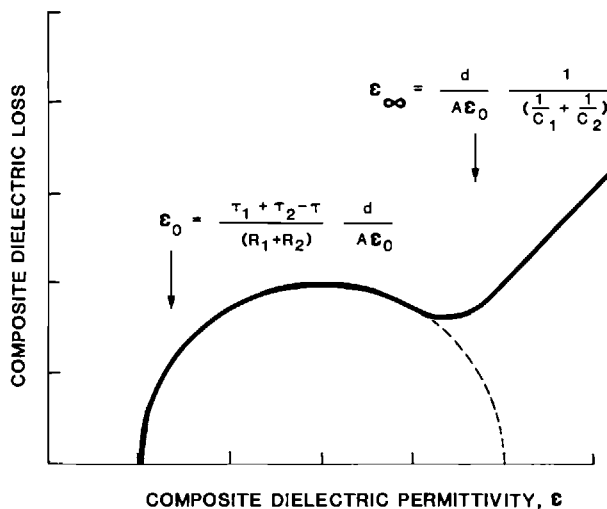


FIG. 23. Cole-Cole plot for a laminated material.

The dispersion exhibited by a laminated dielectric consisting of uniform alternating layers has the same form as the dispersion for a simple harmonic oscillator; this is demonstrated by the semicircular Cole-Cole plot shown in Figure 23, computed for a model of a rock made up of alternating layers of a conducting mineral and a less conducting, water-saturated gangue material.

Very large values of dielectric permittivity can be obtained with the proper control of the properties and proportions of materials in a laminated dielectric. If the laminated sequence consists primarily of conductive material, the composite dielectric permittivity can be greater than the permittivity of either component by a very large factor. In real rocks, the conductive component is commonly the less abundant component, and in such a case, the composite dielectric permittivity is only modestly enhanced.

Other, more complicated processes can also occur in rocks with even minor amounts of water. The largest of these effects include electrolytic polarization and polarization that occurs when current in a rock flows between one medium which is an ionic conductor and another medium which is an electronic conductor. These effects have served as a basis for an extremely important method in minerals exploration, the induced polarization method, but with improved capabilities of induction methods, as described in Nabighian (1984), it may well be necessary to include consideration of these effects on electromagnetic induction as well.

Electrolytic polarization seems to occur when the mobility of ions varies along the conduction paths in a water-laden rock. These variations in mobility are probably caused by changes in viscosity of the pore water, resulting from adsorption pressures on the mineral grains. Ions will move rapidly in open pores and less rapidly in tight pores. After a persistent current flow in one direction, ions may become more concentrated in the areas of low mobility, and less concentrated in areas of normal mobility. Then, when the applied voltage is removed, the ions will diffuse from the areas of concentration to areas of impoverishment, giving rise to a transient current discharge. The charge  $Q$  discharged in this process can be calculated from the integral of the transient voltage

$$Q = \sigma \int E(t) dt. \quad (49)$$

For very long charging periods, this discharged charge can be used to compute the limiting dc capacitance, and hence, dielectric permittivity of a rock (Keller, 1959)

$$\epsilon_{dc} = \int \frac{E(t)}{\rho E_{ss}} dt \quad (50)$$

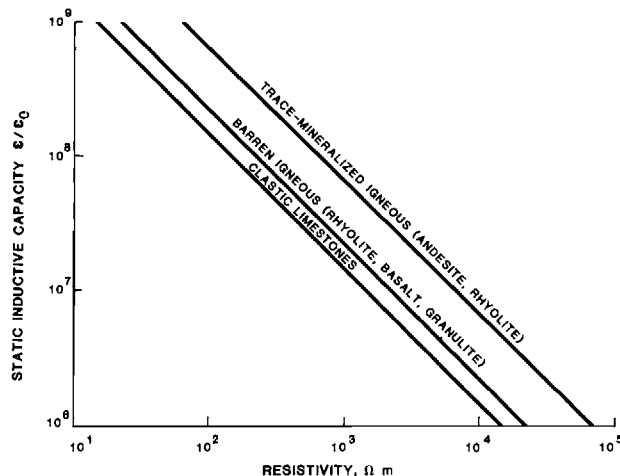


FIG. 24. Observed relationship between inductive capacity measured at low frequencies (with induced polarization present) and resistivity.

where  $E_{ss}$  is the steady-state voltage.

The polarization which occurs in a rock containing electron-conducting minerals is very similar. In order to achieve continuity of current flow from an electrolyte in the pores of a rock through electron conducting mineral grains, the chemical processes of oxidation and reduction are required. At the low current densities used in geophysical exploration, the amount of oxidation and reduction which occurs is probably quite small. Rather, ions in the electrolyte will concentrate on either side of an electron-conducting grain, forming concentration cells similar to those formed in electrolytic polarization. When excitation is removed, these concentrations will discharge, giving rise to a transient current and voltage. Again, dc dielectric permittivity can be calculated from the charge represented in a transient discharge when the excitation has been sufficiently long to saturate the polarization process.

A graphical summary of the correlation between dc dielectric permittivity and dc conductivity for a variety of rock samples is given in Figure 24.

Much of the early research on induced polarization was done using time-domain (step) techniques (Wait, 1959). In addition to providing a specification of the limiting dielectric permittivity and conductivity at low frequencies, information can also be obtained from such studies about the electrical properties at intermediate frequencies. Farnham (1947) was among the first to observe that by using a  $t^{-1/2}$  scale, graphs of voltage versus time could be linearized. This behavior is representative of processes controlled by diffusion, and the polarization process has come to be known as a Warburg impedance, in which the simple resistor-capacitor circuit representing the process contains a capacitance that varies as the square root of frequency (see Figure 25).

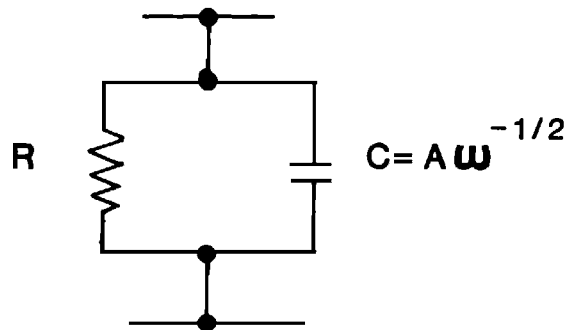


FIG. 25. Lumped circuit for a Warburg impedance.

In an alternate approach, Keller (1959) analyzed a number of observed transient discharge curves and represented them as a sum of parallel resistor-capacitor circuits with different time constants, a process originally proposed in Wagner (1913) in connection with Maxwell interfacial polarization.

## Megascopic Considerations

In exploration for ore bodies, it is not always possible to determine the conductivity of a rock mass independently of its geometry. Only in large, extensive ore bodies can the electrical properties be determined independently of the dimensions. In many cases, the ore body is not this large, and the parameters determined from field surveys are usually some combination of dimensions and electrical properties.

For tabular (two-dimensional) conductive bodies, the parameter that can be determined from inductive field surveys is the conductance,  $S$ . Unfortunately, no tabulation of these values is available in the literature for typical tabular or dike-like ore bodies; such data probably exist, and should be collected.

Three-dimensional ore bodies are probably more common than tabular ore bodies. In such cases, again, only a single summary parameter combining the geometry and the electric properties of the ore body can be determined. Kaufman and Keller (1985) pointed out that for three-dimensional bodies which can be approximated as spheres, the parameter that can be determined is a combination of dimensions and conductivity which acts as a time constant. For a spherical mass, this time constant  $\tau$ , is

$$\tau = \sigma \mu a^2 / \pi^2, \quad (51)$$

where  $a$  is the radius of the body in meters. For a disc with constant thickness, the time constant is

$$\tau = \mu S a / 5.51 \quad (52)$$

where  $S$  is the conductance in the disc, and  $a$  is its radius.

Ore bodies exist in barren or altered rock masses against which an economic ore body must be discriminated. To complete the discussion of rock properties as they apply in the induction methods of minerals prospecting, it is necessary to point out that huge volumes of data exist on the conductivities of rock masses in the form of well log libraries. The great majority of these logs are run in wells in sedimentary rocks, but significant numbers are now becoming available from crystalline and igneous rocks, which are more common hosts to mineralization.

## References

- Anderson, L. A., 1960. Electrical properties of sulfide ores in igneous and metamorphic rocks near East Union, Maine, in *Short Papers in the Geological Sciences*: Paper 400B, 125–128.
- Archie, G. E., 1942. The electrical resistivity log as an aid in determining some reservoir characteristics: Am. Inst. Min. Metallurg. Petr. Eng. Tech. Paper 1422.
- Bertin, J. and Loeb, J., 1976, Experimental and theoretical aspects of induced polarization, 2 vols.; Gebrüder Bornträger.
- Bottcher, C. J. F., 1952, Theory of electric polarisation: Elsevier Publ. Co., Inc.
- Brown, W. F., Jr., 1958, Magnetic materials, in Condon, E. U., and Odishaw, H., (Eds), *Handbook of Physics*: McGraw-Hill Book Co, 126–137.
- Bulau, J. P., Waff, H. S., and Tyburczy, J. R., 1979, Mechanical and thermodynamic constraints on fluid inclusion distribution in partial melts: J. Geophys. Res., **84**, 6102–6108.
- Bussian, A. E., 1983, Electrical conductance in a porous medium: Geophysics, **48**, 1258–1268.
- Cole, K. S., and Cole, R. H., 1941, Dispersion and adsorption in dielectrics: J. Chem. Phys., **9**, 341.
- Collett, L. S., and Katsube, T. J., 1973, Electrical parameters of rocks in developing geophysical techniques: Geophysics, **38**, 76–91.

- Eisenberg, D., and Kauzman, W., 1969, The structure and properties of water: Oxford Univ. Press, Inc.
- Farnham, F., 1947, Analysis of induced polarization measurements: USGS Open File Report.
- Frolich, H., 1949, Theory of dielectrics: Oxford Univ. Press, Inc.
- Hansen, D. A., 1966, Introduction to the search for iron ores, in Mining Geophysics, Vol. I, Soc. Explor. Geophys., 359–365.
- Hartshorn, L. 1927, A critical resume of recent work on dielectrics: J. Inst. Elec. Engr. (London), **64**, 1152–1190.
- Harvey, R. D., 1928, Electrical conductivity and polished mineral surfaces: Econ. Geol., **23**, 778–801.
- Hasted, J. B., 1961, The dielectric properties of water: Progress in Dielectrics, Vol. 3, John Wiley & Sons, Inc., 101–150.
- Heiland, C. A., 1946, Geophysical exploration, 634, Prentice-Hall, Inc.
- Ioffe, A. F., 1960, Physics of semiconductors: Academic Press Inc.
- Jackson, P. D., Taylor-Smith, D., and Stanford, P. N., 1978, Resistivity-porosity-particle shape relationships for marine sands: Geophysics, **43**, 1250–1268.
- Jones, H., 1956, Theory of electrical and thermal conductivity in metals: Handbuch der Physik, Springer-Verlag, **19**, 227–315.
- Kaufman, A. A., and Keller, G. V., 1985, Inductive Mining Prospecting Part 1, Theory: Elsevier Sci. Publ. Co., Inc.
- Keller, G. V., 1959, Analysis of some electrical transient measurements on igneous sedimentary and metamorphic rocks, in Wait, J. R. (Ed), Overvoltage research and applications: Pergamon Press, Inc., 92–111.
- Kittel, C., 1953, Introduction to solid state physics: John Wiley & Sons, Inc.
- Kwon, B. S., and Pickett, G. R., 1975, A new pore structure model and pore structure interrelationships: Soc. Prof. Well Log Analysts, **16**, 1–14.
- Lee, T., 1984a, The transient electromagnetic response of a magnetic or superparamagnetic ground: Geophysics, **49**, 854–860.
- Lee, T., 1984b, The effect of a superparamagnetic layer on the transient response of a ground: Geophys. Prospect., **32**, 480–496.
- Lidiard, A. B., 1957, Ionic conductivity: Handbuch der Physik, Springer-Verlag, **20**, 246–349.
- Madden, T. R., 1976, Random networks and mixing laws: Geophysics, **41**, 1104–1125.
- Makogon, Y. F., 1981, Hydrates of natural gas: PennWell Publ. Co.
- Maxwell, J. C., 1954, A treatise on electricity and magnetism: Dover Publ. Inc., (Reprint of third edition of 1891).
- Miles, P. A., Westphal, W. B., and von Hippel, A., 1957, Dielectric spectroscopy of ferromagnetic semiconductors: Rev. Mod. Physics, **29**, 279.
- Mott, N. F., and Jones, H., 1958, The theory of the properties of metals and alloys: Dover Publ. Inc.
- Nabighian, M. N., 1984, Foreword and introduction: Geophysics **49**, 849–853.
- Nelson, P. H., and Van Voorhis, G. D., 1983, Estimation of sulfide content from induced polarization data: Geophysics, **48**, 62–75.
- Olhoeft, G. R., 1980, Electrical properties of rocks, in Y. S. Toulakian, W. R. Judd and R. F. Roy, Eds Physical properties of rocks and minerals: McGraw-Hill Book Co., 257–330.
- Olhoeft, G. R., and Strangway, D. W., 1974, Magnetic relaxation and the electromagnetic response parameter: Geophysics, **39**, 302–311.
- Papoulis, A., 1962, The Fourier integral and its applications: McGraw Hill Book Co.
- Parasnis, D. S., 1956, The electrical resistivity of some sulfide and oxide minerals and their ores: Geophys. Prospect., **4**, 249–278.
- Parkhomenko, E. I., 1967, Electrical properties of rocks: Plenum Press.
- Parkhomenko, E. I., 1971, Electrification phenomena in Rocks: Plenum Press.
- Parkhomenko, E. I., 1982, Electrical resistivity of minerals and rocks at high temperature and pressure: Rev. of Physics and Space Physics, **29**, no 2, 193–218.
- Putley, E. H., 1968, The Hall effect and semi-conductor physics: Dover Publ. Inc.
- Shankland, T. J., O'Connell, R. J., and Waff, H. S., 1981, Geophysical constraints on partial melt in the upper mantle: Rev. Geophys., **19**, 394–406.
- Shankland, T. J., and Waff, H. S., 1977, Partial melting and electrical conductivity anomalies in the upper mantle: J. Geophys. Res., **82**, 5409–5417.
- Shuey, R. T., 1975, Semiconducting ore minerals: Elsevier Sci. Publ. Co., Inc.
- Stevell, J. M., 1957, The electrical properties of Glass: Handbuch der Physik, Springer-Verlag, **20**, 350–391.
- Strangway, D. W., 1967a, Mineral magnetism, in Mining Geophysics, Vol II, Theory: Soc. Explor. Geophys., 437–445.
- Strangway, D. W., 1967b, Magnetic characteristics of rocks, in Mining Geophysics, vol II, Theory: Soc. Explor. Geophys., 454–473.
- Sumner, J. S., 1976, Principles of induced polarization for geophysical exploration: Elsevier Sci. Publ. Co., Inc.
- Tyburczy, J. A., and Waff, H. S., 1983, Electrical conductivity of molten basalt and andesite to 25 kbars pressure—geophysical significance and implications for charge transport and melt structure: J. Geophys. Res., **88**, 2413–2430.
- Tyburczy, J. A., and Waff, H. S., 1985, High pressure electrical conductivity in naturally occurring silicate liquids, in R. N. Schock, Ed., Point defects in minerals: Am. Geophys. Union. Mono. **31**, 78–87.
- von Hippel, A. R., 1954a, Dielectric materials and applications: John Wiley & Sons, Inc.
- von Hippel, A. R., 1954b, Dielectrics and waves: John Wiley & Sons Inc.
- Waff, H. S., 1974, Theoretical considerations of electrical conductivity in partially molten mantle and

- implications for geothermometry: *J. Geophys. Res.*, **79**, 4003–4010.
- Waff, H. S., 1976, Electrical conductivity measurements on silicate melts using the loop technique: *Rev. Sci. Instr.*, **47**, 87–879.
- Waff, H. S., and Bulau, J. R., 1979, Equilibrium fluid distribution in an ultramafic partial melt under hydrostatic stress conditions: *J. Geophys. Res.*, **84**, 6109–6114.
- Waff, H. S., and Weill, D. F., 1979, Electrical conductivity of magmatic liquids; effects of temperature, oxygen fugacity and composition: *Earth and Planet. Sci. Lett.*, **28**, 189–197.
- Wagner, K. W., 1913, The theory of a heterogeneous dielectric: *Ann. Physik*, **40**, 817–855.
- Wait, J. R., (ed.), 1959, Overvoltage research and geophysical applications: Pergamon Press Inc.
- Wait, J. R., and DeBroux, P., 1984, Induced polarization in electromagnetic inductive schemes: *Geophys. Prosp.*, **32**, no 6, 1147–1154.
- Waxman, M. H., and Smits, L. J. M., 1968, Electrical conduction in oil-bearing shaly sands: *Soc. Petr. Eng. J., Trans. Am. Inst. Min. Metallurg. Petr. Eng.*, **243**, 107–122.

## References for General Reading

- Angoran, Y., and Madden, T. R., 1977, Induced polarization—a preliminary study of its chemical basis: *Geophysics*, **42**, 788–803.
- Bardeen, J., 1958, Conduction, metals and semiconductors, in Condon, E. U., and Odishaw, H. (Eds), *Handbook of Physics*: McGraw-Hill Book, Co., 73–102.
- Brace, W. F., 1971, Resistivity of saturated crustal rocks to 40 km based on laboratory measurements, in J. Heacock, Ed., *The structure and physical properties of the Earth's crust*: Am. Geophys. Union, 243–255.
- Carmichael, R. S., 1982, Magnetic properties of minerals and rocks: in Carmichael, R. S. (Ed.) *Handbook of physical properties of rocks* Vol II, CRC Press, 229–279.
- Cole, R. H., 1961, Theories of dielectric polarization and relaxation: *Progress in dielectrics*, **3**, 47–100, John Wiley & Sons, Inc.
- Collett, L. S., 1959, Laboratory investigation of overvoltage, in J. R. Wait, Ed., *Overvoltage research and geophysical applications*: Pergamon Press, 50–70.
- Dortman, N. B., Vasileva, V. I., Veinberg, A. K., Dubinchik, E. Ya., Zhdanov, V. V., Zotova, I. F., Ilaev, A. K., Trunina, V. Ya., Khoreva, B. Ya., and Sholpo, L. E., 1964, *Fizicheskiye Svoistva Gornikh Porod i Poleznikh Iskopaemikh SSSR* (Physical properties of rocks and economic mineral deposits of the USSR): Nedra.
- Duba, A., and Shankland, T. J., 1982, Free carbon and electrical conductivity in the Earth's mantle: *Geophys. Res. Lett.*, 1271–1274.
- Gerritsen, A. N., 1956, Metallic conductivity, experimental part; *Handbuch der Physik*: Springer-Verlag, **19**, 137–227.
- Greenberg, R. J., and Brace, W. F., 1969, Archie's law for rocks modeled by simple networks: *J. Geophys. Res.*, **74**, 2099–2102.
- Ibrahim, A. W., and Keller, G. V., 1981, Seismic velocities and electrical resistivity of recent volcanics and their dependence on porosity, temperature, and water saturation: *Geophysics*, **46**, 1415–1422.
- Keller, G. V., 1960, Pulse-transient behavior of brine-saturated sandstones: *U.S. Geol. Surv. Bull.* 1083-D, 111–129.
- Keller, G. V., 1963, Electrical properties in the Deep Crust: *Trans. Antennas and Propagation, Inst. Electr. Electron. Eng.*, **AP-11**, No. 3, 344–357.
- Keller, G. V., 1966, Electrical properties of rocks and minerals, in Clark, S. P., Jr. (Ed), *Handbook of physical constants*: *Geol. Soc. Am. Memoir* **97**, 553–578.
- Keller, G. V., 1968, Electrical prospecting for oil: *Quart. Colorado School of Mines*, **63**, no. 2, 268.
- Keller, G. V., 1971, Electrical characteristics of the earth's crust, in Wait, J. R. (Ed), *Electromagnetic probing in Geophysics*: Golem Press, 13–79.
- Keller, G. V., 1981, Elastic, mechanical, and electrical properties of low-porosity rocks: *The Log Analyst*, **22**, no. 6, 13–26.
- Keller, G. V., 1982, Electrical properties of rocks and minerals, in Carmichael, R. S. (Ed), *Handbook of physical properties of rocks*: Vol 1, CRC Press, 217–294.
- Klein, J. D., Biegler, T., and Horne, M. D., 1984, Mineral interface processes in the method of induced polarization: *Geophysics*, **49**, 1105–1114.
- Klein, J. D., and Shuey, R. T., 1979a, Nonlinear impedance of mineral-electrolyte interfaces, Part I, Pyrite: *Geophysics*, **43**, 1222–1234.
- Klein, J. D., and Shuey, R. T., 1979b, Nonlinear impedance of mineral-electrolyte interfaces, Part II, galena, chalcopyrite and graphite: *Geophysics*, **43**, 1235–1249.
- Kobranova, V. N., 1962, *Fizicheskiye Svoistva Gornikh Porod* (Physical Properties of Rocks): Gos-toptekhnizdat.
- Lange, J. N., 1983, Microwave properties of saturated reservoirs: *Geophysics*, **48**, 367–375.
- Lee, T., 1981, The Cole-Cole model in time-domain induced polarization: *Geophysics*, **46**, 932–933.
- Lsyne, P. C., 1983, A model for the high frequency electrical response of wet rocks: *Geophysics*, **48**, 775–786.
- Meakins, R. J., 1961, Mechanisms of dielectric absorption in solids: *Progress in dielectrics*, John Wiley & Sons, Inc., **3**, 151–202.
- Mendelson, K. S., and Cohen, M. H., 1982, The effect of grain anisotropy on the electrical properties of sedimentary rocks: *Geophysics*, **47**, 257–263.

- Mullins, C. E., and Tite, M. S., 1973, Magnetic viscosity, quadrature susceptibility, and frequency dependence of susceptibility in single-domain assemblies of magnetite and maghemite: *J. Geophys. Res.*, **78**, 804–809.
- Olhoeft, G. R., 1979, Tables of room temperature electrical properties for selected rocks and minerals with dielectric permittivity statistics: U.S. Geol. Surv. Open File Rept. 79-993.
- Olhoeft, G. R., 1985, Low-frequency electrical properties: *Geophysics*, **50**, 2492–2503.
- Pascal, H., 1983, Further discussion on attenuation and dispersion of electromagnetic wave propagation in fluid saturated porous rocks and applications to dielectric constant well logging: *Geophysics*, **48**, 1373–1380.
- Popper, P., 1959, Non-oxide ceramic dielectrics: *Progress in dielectrics*, John Wiley & Sons, Inc., **1**, 217–270.
- Sen, P. N., 1981, Relation of certain geometrical features to the dielectric anomaly of rocks: *Geophysics*, **46**, 1714–1720.
- Sen, P. N., 1984, Grain shape effects on dielectric and electrical properties of rocks: *Geophysics*, **49**, 586–587.
- Sen, P. N., Scala, C., and Cohen, M. H., 1981, A self-similar model for sedimentary rocks with application to the dielectric constant of fused glass beads: *Geophysics*, **46**, 781–795.
- Shankland, T. J., and Waff, H. S., 1974, Conductivity of fluid bearing rocks: *J. Geophys. Res.*, **79**, 4863–4868.
- Shen, L. C., Savre, W. C., Price, J. M., and Athavale, K., 1985, Dielectric properties of reservoir rocks at ultra high frequencies: *Geophysics*, **50**, 692–704.
- Strangway, D. W., Larson, E. E., and Goldstein, M., 1968, A possible cause of high magnetic stability in volcanic rocks: *J. Geophys. Res.*, **73**, no. 12, 3787–3795.
- Vincenz, S. A., 1965, Frequency dependence of magnetic susceptibility of rocks in weak alternating fields: *J. Geophys. Res.*, **70**, 1371–1378.
- Volarovich, M. P., and Parkhomenko, E. I., 1976, Electrical properties of rocks at high temperatures and pressures, in Adam, A. (Ed), *Geoelectric and geothermal studies*: Akademiai Kiado.
- von Hippel, A. R., 1958, Dielectrics, in Condon, E. U., and Odishaw, H. (Eds), *Handbook of Physics*: McGraw-Hill Book Co., 103–125.
- Walsh, J. B., and Brace, W. F., 1984, The effect of pressure on porosity and the transport properties of rock: *J. Geophys. Res.*, **89**, 9425–9432.
- Ward, S. H., and Fraser, D. C., 1967, Conduction of electricity in rocks, in *Mining Geophysics*, Vol II, Theory: Soc. Explor. Geophys. 197–223.
- Werner, S., 1945, Determinations of the magnetic susceptibility of ores and rocks from Swedish iron ore deposits: *Swedish Geol. Surv.*, **39**, 5.
- Wong, J., and Strangway, D. W., 1981, Induced polarization in disseminated sulfide ores containing elongated mineralization: *Geophysics*, **46**, 1258–1268.
- Wyllie, G., 1960, Theory of polarization absorption in dielectrics, an introductory survey: *Progress in Dielectrics*: John Wiley & Sons, Inc. **2**, 1–28.



---

---

**3**

**Resistivity Characteristics  
of Geologic Targets**

---

---



## 3

# Resistivity Characteristics of Geologic Targets

*G. J. Palacky\**

The aim of geophysical surveys is to obtain information on subsurface geology. While execution of surveys using specific techniques may differ in detail, it will almost invariably consist of three steps: surveying, data processing, and data interpretation. A successful survey will yield more information on the geological target—its existence, location, shape, size, etc. New information is obtained by interpreting geophysical data. The success of a survey depends to a large extent on decisions made before the survey initiation. An exploration geophysicist working for a mining company is often asked the following question: Can we use geophysics in prospecting for this particular commodity? If yes, what techniques should we use and how do we specify survey parameter. Decisions that are usually based on experience often cannot be justified scientifically. The proper approach would be to carry out test surveys to investigate the physical properties of the target and other bodies that might interfere with its response. In recent years, exploration geophysics has progressed beyond target finding to mapping subsurface geology.

Analyzing the sequence of geophysical survey steps as shown in Figure 1, the main flow (surveying, processing, interpretation) and the associated areas of research can be identified. To make an intelligent decision on the use of a technique, the geophysicist should have at least a rudimentary knowledge of the physical properties of the target and the surrounding media the response of which might interfere with target identification. Most physical property studies have been done in the laboratory on samples collected in the field. While this approach may be satisfactory for some geophysical methods (gravity, magnetics), it is not for others. Electrical properties of earth materials vary substantially (by several orders of magnitude) depending on whether they are measured in situ or in a laboratory. It is virtually impossible to simulate real conditions in the laboratory. An attempt can be made to recompose the original water content, but microinhomogeneities typical of many geological environments (e.g., rock fractures and their frequency and variation with depth) cannot be duplicated.

In the 1950s, when electromagnetic (EM) methods began to be used extensively in prospecting for sulfide deposits, the approach to interpretation was largely empirical. New instruments were tested over known targets (e.g., the Whistle deposit in Ontario, Canada) and if successful, they were put to routine use. Interpretation theory for a particular technique was developed later (and for some methods never—they became extinct before they drew the attention of research geophysicists). While the main thrust in instrumentation came from

\*Geological Survey of Canada, 601 Booth Street, Ottawa, Ontario, Canada K1A 0E8. Contribution No. 32686

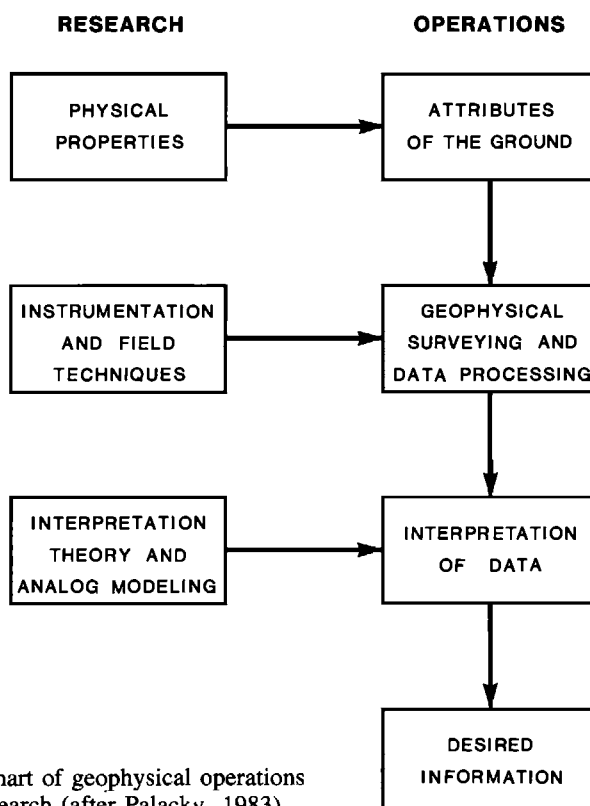


FIG. 1. Flow chart of geophysical operations and research (after Palacky, 1983).

geophysical companies, advances in interpretation originated largely in academia. As this volume demonstrates, during the last 20 years significant breakthroughs have been achieved in quantitative interpretation of EM measurements.

Chapter 1 is devoted to the "weak link" between geology and geophysics, at present the most neglected area of the exploration sequence, and describes various possible targets for EM techniques and their geologic and geophysical characteristics. Perhaps defining these targets will stimulate the development of new applications for EM methods beyond their traditional role in prospecting for massive sulfides.

In the days of simple, one-frequency EM instruments, a definition of a target (massive sulfide) overburden and host rock appeared sufficient. Massive sulfides were supposed to be highly conductive, the host rock highly resistive, and the overburden was the cause of "geologic noise." Forty years of experience with EM methods have shown that not all sulfides are highly conductive, that geologic noise carries a geologically interpretable message, and that the host rock can be conductive. In order to interpret EM data, the geophysicist has to understand, at least in principle, the nature of geologic features producing EM response. Modern EM instruments are sufficiently sensitive to measure conductivity rather than to simply indicate whether a target is conductive or not. The conductivity of sulfide deposits depends on their formation, geologic history, and weathering. Overburden can be the result of in-situ weathering, accumulation of glacial debris, or glaciolacustrine sediments. The weathered layer is in some regions an important source of several metals (nickel, tin, gold, aluminum) and EM methods can be used effectively in their prospecting.

The traditional exploration targets, volcanic-associated massive sulfide deposits, are usually highly conductive (less than  $1 \Omega \cdot m$  in most cases), even though poorly conductive and even nonconductive sulfides have been described in literature (Figure 2). Only one other earth material, graphite, overlaps substantially the resistivity range of massive sulfides (less than  $1 \Omega \cdot m$ ). Shield areas, where sulfide deposits commonly occur, are composed of igneous and metamorphic rocks, which are highly resistive (over  $1000 \Omega \cdot m$ ). Only under ideal conditions are sulfides and graphite the only conductors: i.e., no conductive weathered layer, glaciolacustrine sediments, or shear zones. While such conditions may exist in parts of the

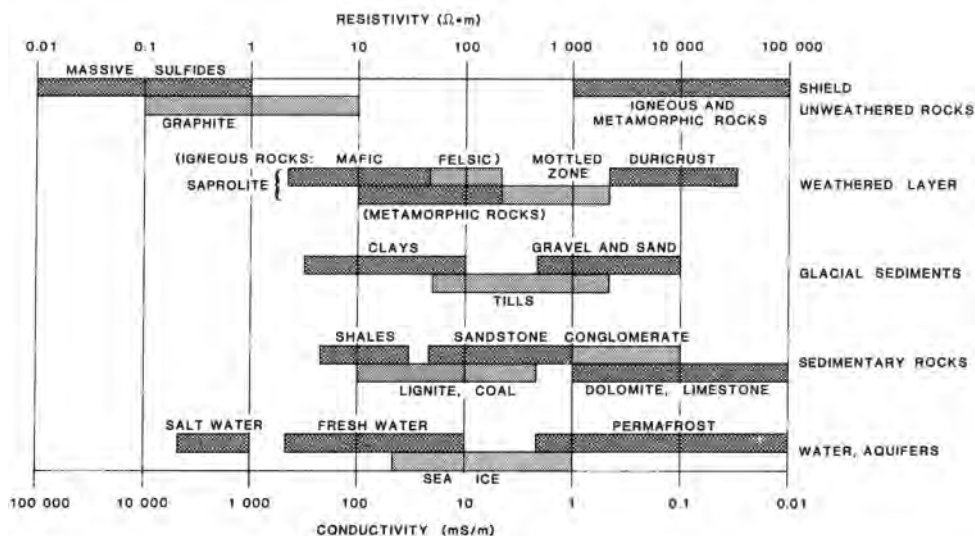


FIG. 2. Typical ranges of resistivities of earth materials.

Canadian and Fennoscandian Precambrian shields, they are not common elsewhere. In regions of the world where the weathered layer has not been removed by glacial erosion the conductance of near-surface material may reach values comparable to those of massive sulfides. As shown in Figure 2, the resistivity of saprolite, which is the most conductive component of the weathered layer developed between the water table and fresh rock, ranges between 2 and 200  $\Omega \cdot \text{m}$ . Because of its thickness, the conductance (conductivity-thickness product) of saprolite may approach that of massive sulfides. Other components of the weathered layer (progressing upward) are the less conductive mottled zone (between 200 and 2 000  $\Omega \cdot \text{m}$ ) and the resistive duricrust (between 2 000 and 30 000  $\Omega \cdot \text{m}$ ). All values given are typical and values outside these ranges can be found at many localities. Resistivities of minerals, rocks, and other earth materials have been summarized by several authors, e.g., Angenheister (1982) and McNeill (1980).

In Canada and Scandinavia, glacial or glaciolacustrine sediments cover most of the previously glaciated areas. Although the moraine sediments (gravel, sand, tills) are resistive to poorly conductive (50 to 10 000  $\Omega \cdot \text{m}$ ), clays deposited in lakes formed after the retreat of glaciers are conductive (5 to 100  $\Omega \cdot \text{m}$ ). In some areas (e.g., Abitibi clay belt), their presence has seriously hampered the use of EM in mineral exploration. However, advanced EM techniques should, in principle, permit mapping of bedrock topography, identification of the type of glacial sediment, and recognition of bedrock conductors.

In sedimentary areas, conductivity depends on clay content, porosity, dissolved mineral content, and water saturation of rocks. While clay-rich sedimentary rocks, such as shales, are always rather conductive (5 to 30  $\Omega \cdot \text{m}$ ), resistivity of most other sedimentary rocks spans several decades of  $\Omega \cdot \text{m}$ . Ranges given in Figure 2 are meant only to suggest that in most areas dolomites, limestones, and conglomerates are more resistive than shales. The resistivity of porous rocks varies with the conductivity and amount of contained water, and also with the volume and arrangement of the pores. An empirical formula describing this complex relationship was published by Archie (1942).

The presence of water, its state, and its mineral content, determine the resistivity profile in many situations (Keller, 1987, this volume). Seawater is always highly conductive (0.2



FIG. 3. Location of sites described in the section Massive sulfide and magnetite deposits (*Canada*: (1) Goldstream, British Columbia, (2) Thompson and Pipe deposits, Manitoba, (3) Temagami, Ontario, (4) Abitibi greenstone belt, Ontario-Québec, (5) Chibougamau, Québec, (6) Labrador Trough, Québec, (7) Bathurst camp, New Brunswick;

*Brazil*: (8) Lavras do Sul; *Australia*: (9) Mons Cupri, Western Australia, (10) Teutonic Bore, Western Australia, (11) Mt. Keith and Forrestania, Western Australia, (12) Mt. Isa and McArthur River, Queensland, (13) Thalanga, Queensland, (14) Elura, New South Wales, (15) Woodlawn, New South Wales, (16) Que River and Hellyer, Tasmania).

to  $1 \Omega \cdot m$ ) and its thickness can be mapped by airborne electromagnetic (AEM) techniques (shallow-water bathymetry). Sea ice is significantly more resistive than sea water (20 to  $1\,000 \Omega \cdot m$ ). In coastal areas, the extent of salt-water and fresh-water aquifers can be mapped by electrical techniques. The fact that not only NaCl but other chemical substances can make water conductive has been used in outlining chemical pollution plumes. When water-saturated ground is frozen, it becomes highly resistive. Mapping of permafrost thickness is an important application of electrical methods in Arctic regions.

Applications of EM techniques have economic significance in prospecting for mineral deposits, in groundwater exploration, and in geotechnical studies. In this paper an attempt is made to describe geological situations where detectable resistivity differences occur. ☺

## Massive Sulfide and Magnetite Deposits

Massive sulfides have been the most important exploration target for EM methods since the 1950s. In fact, most techniques have been developed for this particular application. In his introduction to the chapter "The Search for Massive Sulfides," in *Mining Geophysics I*, Ward (1966) attempted to characterize some of the Canadian sulfide types. Significant advances in economic geology during the last 20 years have changed many theories on the origin of massive sulfides. Some understanding of the basic types of massive sulfide deposits is essential for geophysicists, who are often asked to design the most effective geophysical exploration strategy. Some sulfide types are highly conductive and some are magnetic, but some may not have any geophysical signature at all. A map showing the location of massive sulfide bodies described in the text is given in Figure 3.

### Volcanic-associated massive sulfide deposits

Deposits of this type result from submarine hydrothermal activity in back-arc basins. Their contemporary formation was observed for the first time on the East Pacific Rise in the late 1970s (Francheteau et al., 1979). Fracture systems control the sulfide discharge sites and the intrusions and extrusions of igneous melts. Depending on the composition of the hydrothermal solutions and the temperature of the hydrothermal reservoir, volcanic-associated massive sulfides can be either (a) copper-zinc rich, related to the ferromagnesian mineral-feldspar assemblages of mafic rocks, or (b) zinc-lead-copper rich, related to the feldspar-mica-clay mineral assemblages of felsic rocks and/or sediments (Franklin et al., 1981). Deposits of both types are usually found along synvolcanic fractures in successions of submarine volcanic rocks. They usually occur in clusters with diameters of 20 to 40 km. The age of volcanic-associated massive sulfides ranges from 3.7 Ga to the present.

The classical volcanic-associated copper-zinc rich deposits have been described in Cyprus, where they have been mined for over 4000 years. The largest orebodies of this kind are in Canada (Kidd Creek, Ontario; Horne, Québec; Flin Flon, Manitoba), with reserves of more than 50 Mt. Elsewhere, copper-zinc rich massive sulfide orebodies tend to be rather small. The average tonnage of 50 deposits (excluding Kidd Creek and Horne) in the Abitibi greenstone belt in Canada is 4 Mt. Their average grade is 1.5 percent Cu, 3.4 percent Zn, 32 g Ag/t, and 0.8 g Au/t (Lydon et al., 1984). In Canada, such deposits account for 28 percent of the copper production, 41 percent of zinc, 39 percent of silver, and 7.5 percent of gold (1977–78 figures). The deposits occur in ophiolite sequences (Cyprus) or in greenstone belts (submarine, predominately mafic volcanic sequences). Commonly, they cluster around centers of felsic volcanism. The sulfide bodies are usually conformable, of lensoid to tabular shape, and stratigraphically underlain by discordant stringer sulfide ore and hydrothermally altered wallrock. Minerals are characteristically zoned concentrically outward from the core of the stringer zone: chalcopyrite + pyrrhotite + magnetite → pyrite → sphalerite. The principal ore minerals are sphalerite, chalcopyrite, and minor galena (Franklin et al., 1981).

Another type of volcanic-associated Cu-Zn deposit named after a classical orebody in Japan, the stratiform Besshi deposits, are associated with mafic volcanic rocks of oceanic or intra-plate geochemistry (Kanehira, 1970). Outside Japan, such deposits have been identified in the Trondheim region of Norway (Tverfjell, Killingal), in the Outokumpu region of Finland (Keretti with reserves of 33 Mt at 3.5 percent Cu and 0.5 percent Zn), and also in Canada (Goldstream, British Columbia). Chalcopyrite, pyrite, pyrrhotite, and sphalerite are the most common sulfide minerals.

The zinc-lead-copper rich volcanic-associated deposits are more important worldwide than the copper-zinc type. The classical deposits, which are of Tertiary age occur in the Kuroko Green Tuff Belt in Japan. The average size and grade of the 25 major deposits is 5.8 Mt containing 3.9 percent Zn, 0.9 percent Pb, 1.6 percent Cu, 12.2 g Ag/t, and 0.4 g Au/t (Lydon et al., 1984). Orebodies of this kind are important in the Iberian Pyrite Belt (Spain, Portugal), the Lachlan Fold Belt in Australia, and in New Brunswick in Canada. Average tonnage and grade of 29 deposits in the Bathurst Camp in New Brunswick is 8.7 Mt containing 5.4 percent Zn, 2.2 percent Pb, 0.6 percent Cu, 60 g Ag/t, and 0.5 g Au/t. The largest orebody in the camp is Brunswick No. 12. The economic importance of orebodies of this type in Canada is slightly less than of the copper-zinc type and they accounted for 22 percent of zinc, 27 percent of lead, and 19 percent of silver production. The deposits occur in submarine volcanic sequences (commonly of mafic-felsic composition) situated on continental crust. Submarine sedimentary rocks (including conductive black shales) usually constitute more than 40 percent of total succession. Zoning (concentrically outward) usually follows the sequence: chalcopyrite + pyrite + pyrrhotite → sphalerite + galena → barite.

**The Woodlawn Deposit, New South Wales.**—Geophysical characteristics have been studied systematically only at a handful of volcanic-associated massive sulfide deposits. The best descriptions come from Australia, the Woodlawn Zn-Pb-Cu orebody (Whiteley, 1981) and Elura Zn-Pb-Ag orebody (Emerson, 1980).

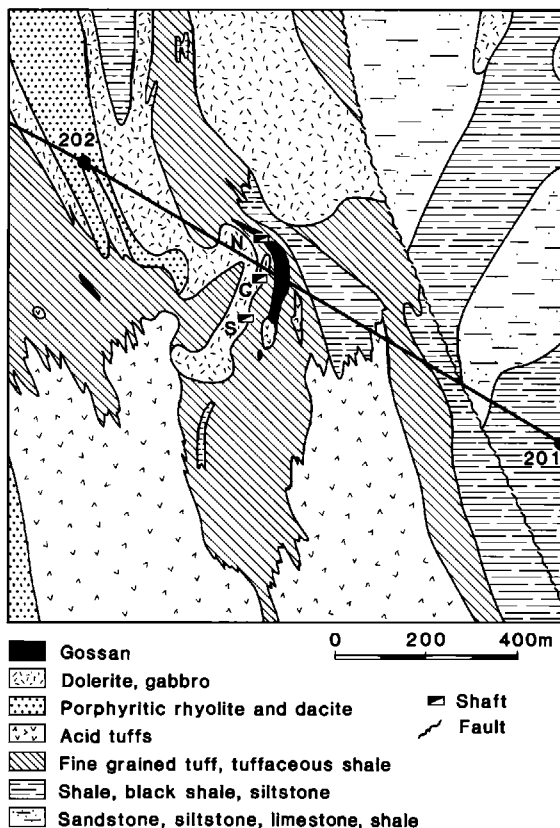


FIG. 4. Geologic map of the Woodlawn Pb-Zn-Cu volcanic-associated massive sulfide deposit, New South Wales, Australia (after Malone, 1981). Helicopter AEM data are depicted along line 201-202 in Figure 8.

The Eastern Lachlan Fold Belt is situated in eastern New South Wales. Polymetallic base metal deposits are associated with Silurian felsic volcanic rocks. Before the discovery of Woodlawn in 1970, Captain Flats was the most important deposit in the area, which produced 4 Mt of ore containing copper, lead, zinc, gold, and silver, before the reserves were mined out in 1962. Over 40 Kuroko-type massive sulfide bodies have been identified in the Belt, but only Woodlawn is mined at present. The mine is 50 km northeast of Canberra. The first successful drill hole at Woodlawn intersected 24.4 m of 18 percent Zn, 7 percent Pb, and 1.45 percent Cu. Exploration and development drilling performed in 1971 outlined reserves of 6.3 Mt of polymetallic ore (14.4 percent Zn, 5.5 percent Pb, and 1.7 percent Cu) and 3.7 Mt of copper ore (1.9 percent Cu). The mine and the mill started operation in December of 1978 (Malone and Whiteley, 1981).

Local geology is shown in Figure 4. During Middle to Late Silurian, a shallow shelf sequence of quartzose sandstone, mudstone, siltstone, and minor limestone was deposited. Woodlawn Volcanics, which contain the orebody, were deposited during a period of felsic volcanism, followed by a mafic volcanic sequence (pillow lavas, basaltic tuffs, dolerite). Both volcanic sequences are overlain by flysch sediments (sandstone, slate, and siltstone), probably of early Devonian age. The whole sequence of volcanic and sedimentary rocks has undergone low-grade metamorphism of the greenschist facies (Malone, 1981).

Figure 5 shows two east-west sections, one north-south section, and a plan at the 2 750 m level. The main massive sulfide lens has a maximum strike length of 420 m and a downdip length of 300 m. Its thickness ranges from 5 m to 45 m. The more abrupt changes in thickness appear to be associated with folding and cross-folding of the lens. The lens consists of at least 75 percent sulfides, composed in decreasing abundance of pyrite, sphalerite, galena, and chalcopyrite. The sulfides are fine-grained and well banded at the top and bottom of the

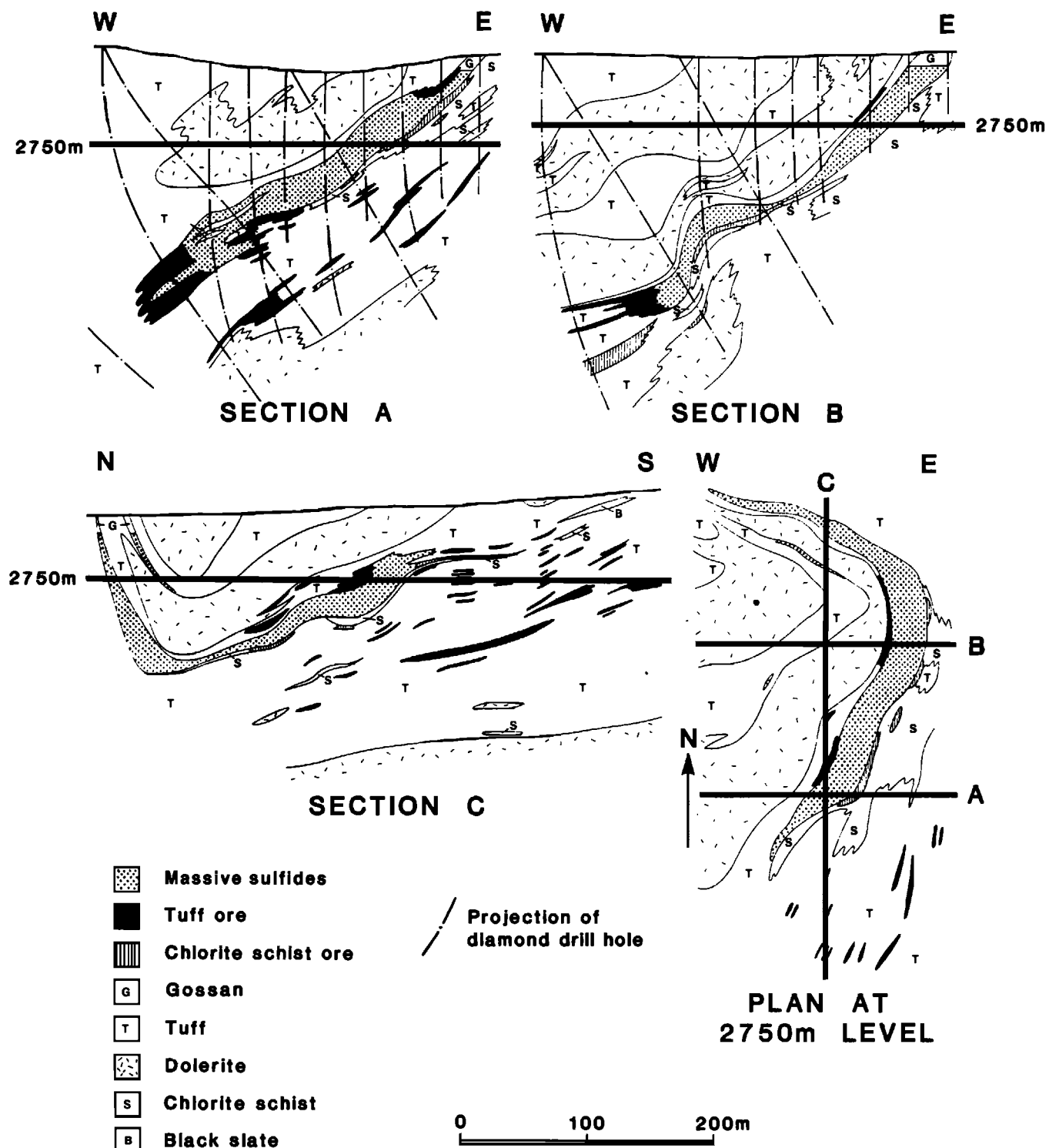


FIG. 5. Plan of the Woodlawn orebody at the 2750 m level (750 m above near sea level) and geologic sections A, B, and C, whose location is indicated in the plan (after Malone, 1981).

lens. In addition to the main orebody, there are numerous small lens of tuff ore. These are ore grade because of the abundance of sulfide stringers, which comprise 25 percent of the total volume. The enclosing volcanic rocks contain between 5 and 10 percent sulfides. As most Kuroko-type deposits, the Woodlawn orebody is nonmagnetic (Agostini et al., 1981). A residual gravity anomaly of 0.8 mgals was determined by Templeton (1981). EM methods were found to be the most effective exploration tool.

Tyne (1981) described both resistivity well-logging and resistivity measurements on unevacuated core samples and showed that a good agreement existed between the two ways of determining resistivities. Both are assumed to represent reasonably accurate in-situ resistivities. Figure 6 shows controlled core sample resistivities and the corresponding geological log. Massive sulfides appear to have resistivities between 0.1 and 5  $\Omega \cdot \text{m}$ . Pure massive sulfide samples yielded resistivities of about 0.01  $\Omega \cdot \text{m}$ , but where intercalated with tuff, their resistivity increased to the range 0.1 to 5  $\Omega \cdot \text{m}$ . Tuff ore has a resistivity of about 10  $\Omega \cdot \text{m}$ . Resistivity ranges are shown schematically in Figure 7. All nonmineralized rock types are poorly conductive, with resistivities ranging from 100  $\Omega \cdot \text{m}$  (low values for acid tuffs) to well over 10 000  $\Omega \cdot \text{m}$ . Therefore, it appears that a typical massive sulfide body would be a relatively easy exploration target, if the resistivity contrasts were considered alone. There is a well-defined gap between sulfides (less than 10  $\Omega \cdot \text{m}$ ) and all other rock types (over 100  $\Omega \cdot \text{m}$ ).

In general, complications in interpretation of electrical and EM data are frequently caused by the often highly complex shape of sulfide lenses. The Woodlawn orebody can be considered as a modestly complex target. There are massive sulfide orebodies which closely resemble a vertical plate, but there are some of exceedingly complex shapes. In exploration, it is not known *a priori* whether an anomaly is caused by a massive sulfide lens or some other conductor. Once the geologic characteristics of an area are established, an educated guess concerning the origin of a given anomaly can be made. In most mining camps, massive sulfide orebodies occur in clusters and therefore all EM anomalies close to a known mineral occurrence are of interest.

In the Woodlawn area, massive sulfides are not the only conductors and strong AEM anomalies (Input® and Dighem) are caused by black shale units, which outcrop about 1.5 km south of the deposit (Malone, 1981). The black shales, whose thickness exceeds 40 m,

©Registered Trademark of Barringer Research Ltd.

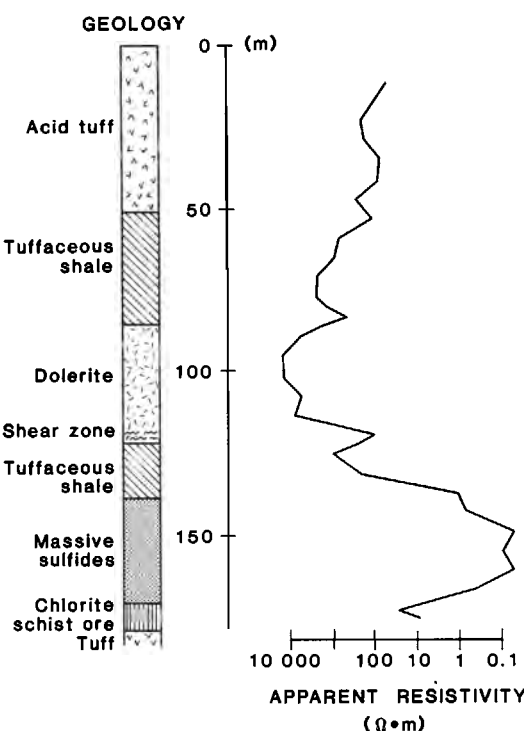


FIG. 6. Geologic log of the hole W276, Woodlawn. The apparent resistivity log was obtained with a three-electrode array ( $AM = MN = 1.5$  m), after Tyne (1981).

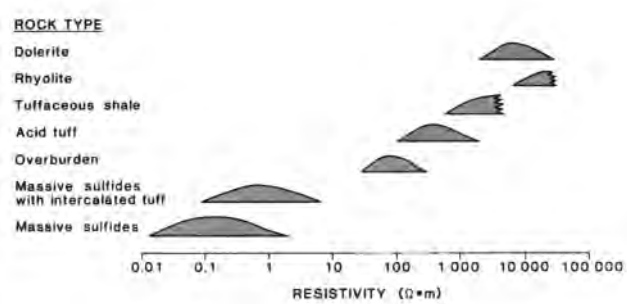


FIG. 7. Resistivity ranges for sulfides, country rocks, and overburden at Woodlawn obtained from core sample and drill hole measurements (after Tyne et al., 1981).

are in a sequence of Devonian sediments which also contain siltstones and shales. Figure 8 shows an apparent resistivity profile (location shown in Figure 4), which was calculated from Dighem AEM data (Fraser, 1981). The orebody is characterized by a well-defined anomaly ( $6 \Omega \cdot m$ ). Smaller anomalies with resistivities  $60$ – $80 \Omega \cdot m$  were recorded 300 to 700 m southeast of the orebody over the shale sequence. More conductive AEM responses due to shales were obtained at other localities, which were mapped with the Input AEM system (Pederson, 1981). Moderately conductive response ( $30$ – $50 \Omega \cdot m$ ) between fiducials 202 and 203 is most likely due to a near-surface layer resulting from weathering of grained tuffs and tuffaceous shales. As Figure 6 indicates, such rocks are quite resistive ( $100$  to  $10,000 \Omega \cdot m$ ) when fresh.

**The Elura Deposit, New South Wales.**—The Cobar mining district in central New South Wales has been an important producer of gold and base metals since 1870. Elura (located 43 km north-northwest of Cobar), which is the northernmost deposit in this mineral province, was detected by aeromagnetic surveying in 1972. After a systematic follow-up of all “bull’s eye” magnetic anomalies, this target was drilled in 1973 and 1974. After intersecting high-grade Zn-Pb-Ag massive sulfide mineralization, extensive airborne and ground geophysical test surveys were carried out over the deposit. They are described in detail in a volume edited by Emerson (1980).

There is still some disagreement about the origin of the Elura deposit, but it likely is syngenetic and volcanic-associated (Adams and Schmidt, 1980). Mineralization is hosted by a folded monotonous sequence of siltstone and shale (lower Devonian C.S.A. Siltstone unit of the Cobar Super-Group). There are no outcrops in the area and the geology is known only from drillhole data and shallow pits. The orebody has the shape of a vertical pipe (cross-section 200 by 120 m) elongated north-south. Rocks are completely weathered (oxidized) to a depth of 75 to 105 m and below that level another 12 to 36 m have been less intensely weathered. A perched aquifer whose water is highly saline (1.9 percent NaCl) is 80 m deep.

The deposit has three major mineralization types with clearly defined boundaries (Figure 9):

1. Siliceous ore envelops the whole deposit with a sheath 2 to 25 m thick. The sulfides are

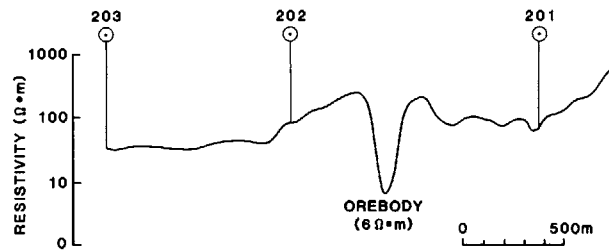


FIG. 8. Apparent resistivity profile over the Woodlawn orebody calculated from helicopter AEM data (horizontal coplanar coils at 900 Hz), after Fraser (1981).

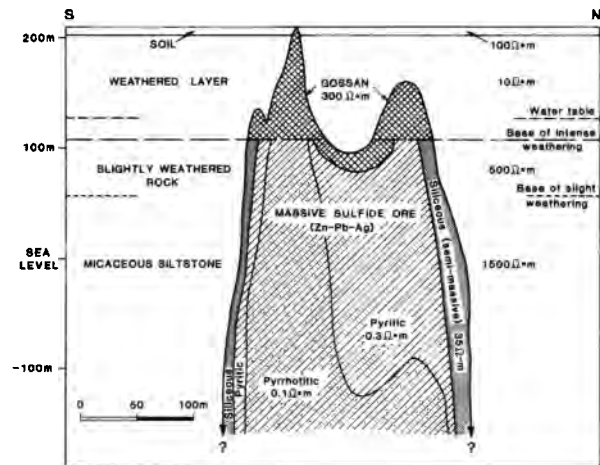


FIG. 9. North-south geologic section of the Elura Zn-Pb-Ag orebody, New South Wales, Australia. Average resistivity values from resistivity soundings and core sample measurements (after Emerson, 1980).

semimassive to disseminated, with a highly variable siliceous matrix. Because of its rather high resistivity ( $35 \Omega \cdot m$ ) and a limited thickness, this ore does not contribute to the electrical response of the orebody.

2. Pyritic ore is fine grained and contains between 70 and 90 percent massive sulfides by volume (pyrite, sphalerite, galena). Its resistivity was estimated as  $0.3 \Omega \cdot m$ .
3. Pyrrhotitic ore is slightly coarser, highly magnetic, and conductive (resistivity— $0.1 \Omega \cdot m$ ). The massive to semimassive mineralization contains 70 to 80 percent sulfides, with 40 percent pyrrhotite.

Reserves have been outlined to a depth of 510 m. The deposit contains 17 Mt of ore with average grade of 8.3 percent Zn, 5.6 percent Pb, 140 g Ag/t, and less than 0.2 percent Cu. The upper 100 m (gossan) are of no economic interest. The gossan consists of goethite and hematite. The southern gossan which outcrops is a product of weathering of massive pyrrhotitic and pyritic mineralization. The northern gossan was originally composed of brecciated siliceous mineralization. The gossan resistivity is quite variable,  $300 \Omega \cdot m$  being the mean value. Electrically, three segments can be identified in the weathered layer (Hone, 1980): resistive duricrust (about 5 m thick,  $500 \Omega \cdot m$ ), conductive saprolite ( $10 \Omega \cdot m$ ), and zone of fracturing ( $500 \Omega \cdot m$ ). The host rock has a resistivity of at least  $1500 \Omega \cdot m$ .

The Elura orebody is a difficult exploration target for most EM systems. Only wide-band time-domain ground systems (Sirotem, Newmont, Crone) could detect it (McCracken et al., 1980). Intense tropical weathering during the Tertiary created a highly conductive, 100 m thick layer, which causes a strong EM response. The orebody is detectable only at late delay times, when saprolite response is significantly reduced. No present AEM systems can penetrate this conductive layer. Tests with Input and Dighem systems were carried out in 1977 and 1979 (Staltari and Rutter, 1980).

**Mons Cupri deposit, Western Australia.**—The third example of EM response of volcanic-associated massive sulfides is from the Pilbara area in Western Australia. Gunn and Chisholm (1984) described two orebodies, Salt Creek and Mons Cupri, which are nonconductive. The deposits, which are located in the Whim Creek greenstone belt, occur in a thick pile of Archean felsic volcanic rocks and associated sediments. A longitudinal section of the Mons Cupri deposit is shown in Figure 10. Miller and Gair (1975) described the mineralization:

- (1) A stringer containing disseminated Cu-Zn sulfides, copper grades from 0.2 percent at the base to 2–4 percent immediately below the massive cap with a zinc grade of 1–3 percent, and

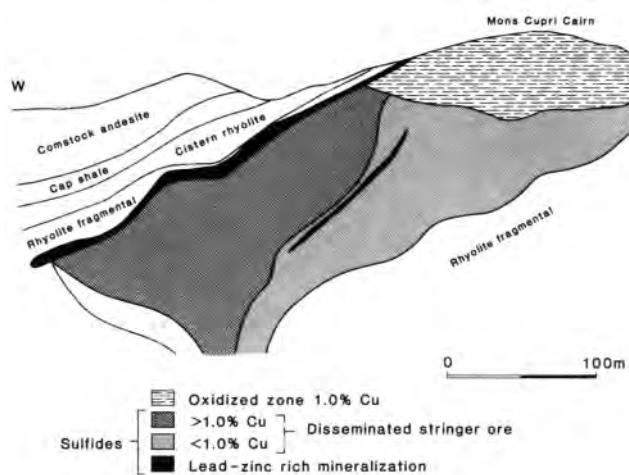


FIG. 10. East-west geologic section of the Mons Cupri Pb-Zn-Cu orebody, Western Australia. Resistivity and EM surveys could not detect sulfide mineralization which is nonconductive (after Gunn and Chisholm, 1984).

- (2) A siliceous massive zone containing chalcopyrite, galena, sphalerite, and pyrite. The grades in these massive sulfides vary: the upper 2 m are rich in zinc and lead (6.2 percent and 10.9 percent, respectively), but are poor in copper (0.5 percent). The lower 18 m are richer in copper (1.2 percent), but have less zinc and lead (6.5 percent and 5.2 percent, respectively). Ground time-domain EM measurements were carried out using Sirotem, Geonics EM-37, and Crone systems, all with negative results. The lack of EM response is explained by shielding of sulfides by silicification. Ore minerals are interbedded with silica because the deposition of mineralization is associated with the introduction of chalcedony (chert) into the system (Miller and Gair, 1975). Figure 11 shows a section of the mine pit, where the silicification of sulfides is clearly visible. Chert veins have destroyed the continuity of sulfide veins.

I have observed nonconductive volcanic-associated massive sulfide occurrences in Tasmania. Pyrite ore at the Chester mine near Zeehan is nonconductive, even though visually it appears massive. Microscopic examination has shown that individual grains are coated by a thin siliceous layer (N. Hungerford, pers. comm.). As the two described areas, Pilbara and Tasmania, represent distinct geologic environments (Archean and Cambrian volcano-sedimentary sequences, respectively), there are certainly many other regions in the world where similar conditions exist. Obviously, a study of the type of mineralization must carefully be made before deciding to rely exclusively on EM methods as the basic prospecting tool.

**Other volcanic-associated deposits in Australia.**—Use of EM techniques in outlining volcanic-associated massive sulfide deposits was described at several other localities in Australia. Fritz and Sheehan (1984) documented ground EM and physical property measurements at the Teutonic Bore Cu-Zn-Ag deposit in Western Australia (600 km northeast of Perth). The orebody is rather small (400 m strike length, 250 m depth extent, 30 m thickness, reserves 1.4 Mt), but high grade (16.4 percent Zn, 4.2 percent Cu, 203 g Ag/t). The massive sulfides are highly conductive (resistivity less than  $0.01 \Omega \cdot \text{m}$ ), but nonmagnetic. The weathered layer is 85 m thick and different resistivity values were obtained over weathered basalts and felsic rocks (20–40 and 50–150 m, respectively). Time-domain EM measurements at Teutonic Bore have been described in Buselli et al., (1986).

Irvine et al. (1985) documented the discovery of the Thalanga Zn-Pb-Cu-Ag deposit in Queensland (65 km southwest of Charters Towers). The reserves have been estimated at 5 Mt of 15 percent combined Zn + Pb + Cu. The orebody has a surface expression (limonite-goethite gossan), but ore-grade sulfides lie at a depth exceeding 200 m. Ground and airborne EM techniques clearly detected anomalies associated with the shallow, subeconomic sulfides, which have resistivity of  $0.01\text{--}1 \Omega \cdot \text{m}$ . The orebody is nonmagnetic.

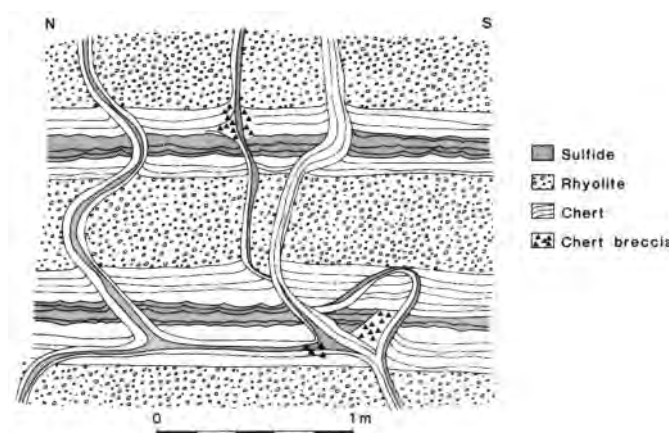


FIG. 11. A section of the Mons Cupri mine pit illustrates shielding of sulfides by silicification (after Miller and Gair, 1975).

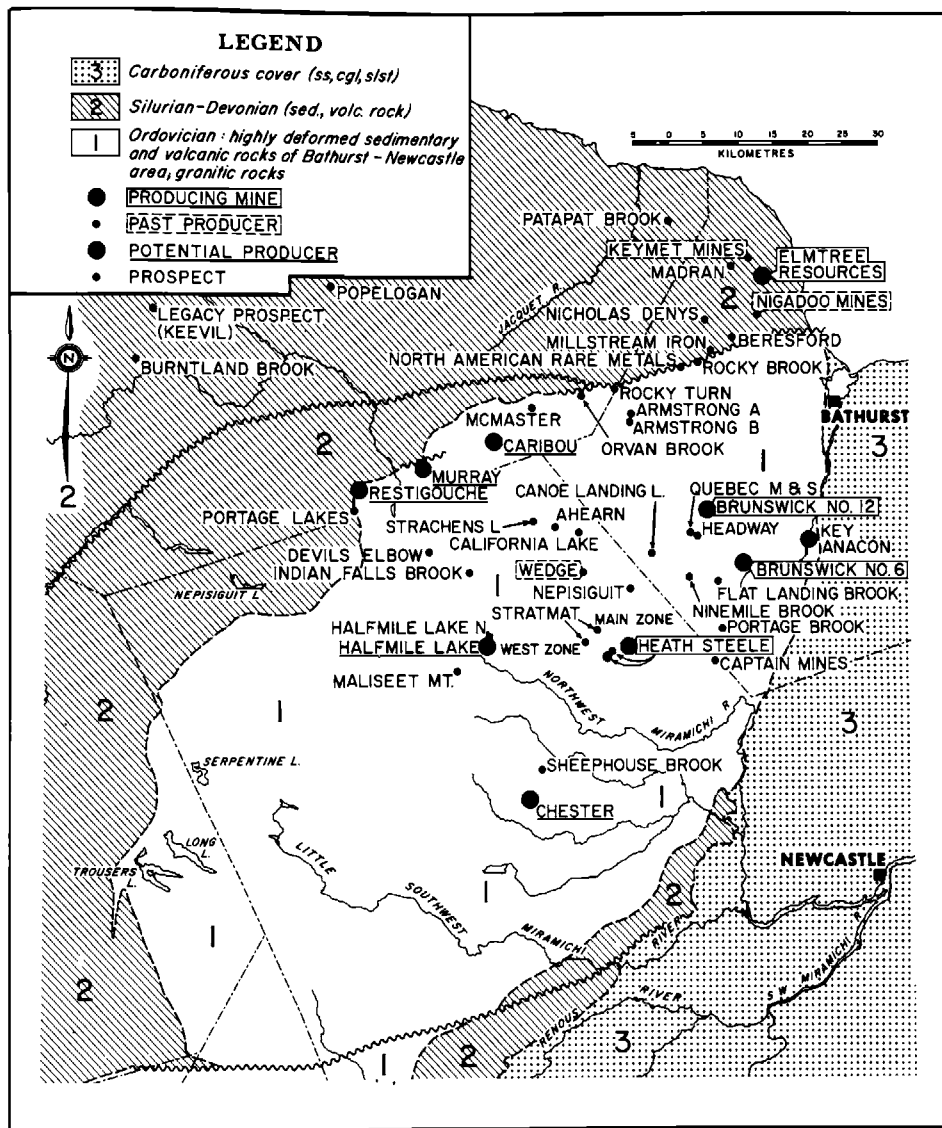


FIG. 12. Geologic map of the Bathurst mining camp, New Brunswick, Canada. In the early 1950s the first ground and airborne EM discoveries in Canada were made in this camp (after Potter, 1985).

EM techniques were instrumental in the discovery of two Pb-Zn sulfide orebodies in Tasmania, Que River (Webster and Skey, 1979) and Hellyer (Eadie et al., 1985), both about 50 km northeast of Zeehan. After early geophysical work at Que River it was concluded that the deeper lens (PQ) was nonconductive because of the large amount of sphalerite. However, subsequent surveying with more advanced EM systems indicated that the lens was conductive. Extensive use of the EM technique in the Que River area led to the discovery of the rich Hellyer deposit in 1983. The blind orebody, which has reserves of 15 Mt, is covered by more than 100 m of volcanic rocks. Technically, this discovery is considered to be the most impressive so far using EM methods in Australia.

**Prospecting for volcanic-associated massive sulfide deposits in Canada.**—Since the 1950s, airborne and ground electromagnetic techniques have been widely used in Canada in prospecting for volcanic-associated massive sulfide deposits. Most EM systems were developed specifically for this purpose (Collett, 1986). First EM discoveries were made in 1952

in the Bathurst camp, New Brunswick (the No. 6 orebody using vertical-loop ground EM and the Heath Steele mine with an AEM system). Early EM surveys in the camp were described in Ward (1957) and Brant et al. (1966). The map of the Bathurst Camp showing operating mines, deposits, and occurrences demonstrates clustering of massive sulfide bodies (Figure 12).

Another part of Canada, where extensive EM surveys have been carried out, is the Abitibi greenstone belt in northeastern Ontario and northwestern Québec. Gold and base metals have been mined in the area for almost a century, and towns such as Val d'Or, Rouyn-Noranda, Kirkland Lake, and Timmins depend almost exclusively on mining. Locally thick glaciolacustrine sediments make traditional prospecting difficult and for the last 40 years geophysical techniques have been appreciated as effective exploration tools. Numerous papers have been published describing case histories in the Abitibi greenstone belt, usually focusing on individual discoveries. Boldy (1979) gave an excellent overview of geological, geophysical, and geochemical discoveries in the Noranda district. Mobrun was the first discovery using a vehicle-borne EM system (Seigel et al., 1957). Podolsky (1966) and Salt (1966) gave account of early geophysical case histories. The more recent AEM discoveries of Magusi River, Iso, and New Inco orebodies in the Noranda camp were described in Telford and Becker (1979) and the finding of the Detour orebody was treated in Reed (1981).

In 1956, the Mattagami Syndicate carried out airborne magnetic and EM surveys over large portions of the northern Abitibi greenstone belt. Their systematic approach consisting of airborne geophysical coverage, ground geophysical surveying, and drilling became the model which has been followed not only in Canada, but elsewhere. After the early discovery of the Watson Lake orebody, several other successes followed. Paterson (1966, 1970), who described the Mattagami discoveries in detail, also compiled statistics on AEM surveys, ground follow-up, and discoveries in Canada in the period from 1955 to 1959. The study illustrates the odds of mineral prospecting. The total 800 000 km flown resulted in the identification of 100 000 AEM anomalies, of which 3 000 were followed up on the ground and 1 000 drilled. While sulfides were intersected in 800 cases, only 16 bodies were of economic interest. The statistics show a significant reduction at each decision point. The most critical one is the selection of targets for ground geophysical follow-up, when only one in 33 anomalies is carefully examined. The remaining anomalies were eliminated by "skimming" using a set of criteria based largely on experience. Let us analyze those criteria in detail and see whether they are universally valid.

An ideal massive sulfide target was supposed to satisfy four criteria: (1) to have a magnetic association, (2) to have high conductivity (or conductance), (3) to be isolated from lithologic conductors, (4) to be small (typically 500–1 000 m in strike extent).

The early AEM systems were rather crude and an accurate determination of target conductivity was difficult. In areas of conductive glaciolacustrine sediments (Abitibi clay belt) most EM anomalies were caused by clays. By selecting a target with a coinciding magnetic and EM anomaly, it was reasonably certain that the conductor was in bedrock and not in overburden. The most common magnetic mineral in volcanic-associated polymetallic massive sulfide deposits is pyrrhotite, but as explained previously, this mineral is commonly absent or it may occur as nonmagnetic polymorph. At least half of the deposits of this kind have only insignificant quantities of pyrrhotite and therefore are nonmagnetic. A clear distinction should be made between polymetallic massive sulfide orebodies and ultramafic associated nickel-copper deposits. In the Canadian geophysical literature both are described as "massive sulfides." In the latter case, pyrrhotite is always present and the deposits are invariably magnetic. Much of the earlier AEM work in Canada, particularly in Inco Ltd., was done while prospecting for nickel-copper deposits.

When the resistivity is measured on samples, massive sulfides are indeed highly conductive (Angenheister, 1982). However, their in-situ electrical properties are a function of texture and mineral composition. We have seen from the example of Mons Cupri that some massive sulfides are nonconductive. Sulfide bodies rich in pyrrhotite are usually highly conductive. Pyrrhotite, even in small quantities, forms elongated veinlets, which constitute a conduction path. Because of the presence of pyrrhotite, even bodies which appear to be composed mostly of nonconductive sphalerite can have high conductivity (e.g., Rosebery mine in Tasmania).

While chalcopyrite is highly conductive, often it is minor in the total sulfide volume. Pyrite often forms blobs which are not interconnected. Therefore, a deposit rich in pyrite may have only a low to moderate conductivity. Studies on correlation between conductivity and pyrrhotite content based on data from Québec were made in Gaucher (1983).

The third criterion concerns the conductor location. Formational conductors, usually graphitic schist or other graphite-rich rocks, are found in some areas stratigraphically and spatially distant from the volcanic centers with which massive sulfides are associated. However, the distribution of graphitic shale does not necessarily have any special relationship to the center of volcanics. On the contrary, many deposits have a close association with graphitic shale. The Kidd Creek orebody, Ontario, has a major unit of graphitic shale immediately above it, and the Westarm deposit near Flin Flon, Manitoba, is entirely within graphitic shale (J. M. Franklin, pers. comm.). The matters are even more complicated in areas where conductive saprolite formed over volcanic rocks is preserved. In complex situations, it is necessary to identify "conductors within conductors." Identification of individual conductors can be done by statistical analysis of conductivities (Palacky and Sena, 1979), or by conducting AEM surveys with multicoil and multifrequency systems. While it has been widely assumed by geophysicists that saprolite layers do not exist in Canada, their existence has been proven by recent geologic studies (e.g., Veillette and Nixon, 1982). Their presence is widespread in the Labrador Trough, where no rational interpretation of AEM data can be done without understanding the principle of clay formation in weathered layers.

Concerning the fourth criterion, it is argued that most volcanic-associated massive sulfide orebodies are indeed small (see statistics given at the beginning of this section), but who would not like to find a real "elephant"? The economic value of the Kidd Creek orebody near Timmins, Ontario, is greater than that of all small deposits in the district put together. Applying rigidly the above mentioned criteria, this world's largest volcanic-associated orebody would not have been found: it is nonmagnetic, large, and close to graphitic formations.

Other examples of orebodies where discovery and development were delayed by a number of years because of rigid application of the above mentioned criteria can be cited. Reed (1981) described the discovery of the Detour zinc-copper-silver deposit in Québec (100 km west of Mattagami) which is without magnetic expression and poorly conductive. Because of the two

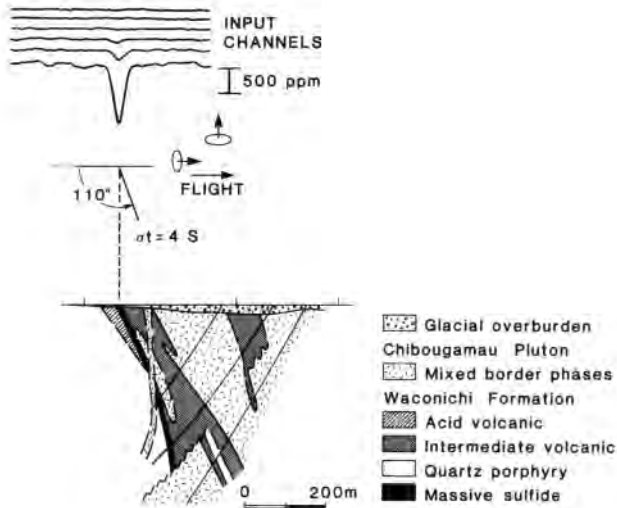


FIG. 13. Geologic section and Input AEM response of the Scott Zn-Ag-Cu volcanic-associated massive sulfide deposit, Québec, Canada (after Questor Surveys, 1984).

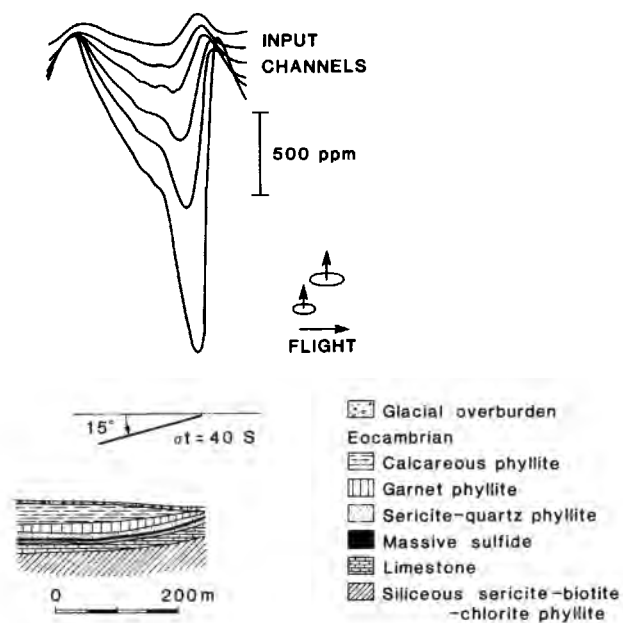


FIG. 14. Geologic section and Input AEM response of the Goldstream Cu-Zn-Ag volcanic-associated massive sulfide deposit, British Columbia, Canada (after Konings and DeCarle, 1985).

characteristics the AEM anomaly was not followed up until 1974, even though detected 16 years earlier.

As an example of a typical Canadian Shield exploration target, the Scott orebody is described. This volcanic-associated massive sulfide deposit is located 20 km west of Chibougamau, Québec, in a Precambrian greenstone belt. Massive sulfides occur at the contact of felsic and intermediate volcanic rocks of the Waconichi formation (Figure 13). The deposit, which has reserves of 680 000 t grading 6.9 percent Zn, 0.55 percent Cu, and 13.3 g Ag/t, was discovered as a result of an AEM survey (Questor Surveys, 1984). The anomaly was typical of massive sulfides: small, isolated, and with magnetic association, even though the ground follow-up identified the magnetic zone to be distinct 100 m distant from the sulfide body. The target was selected for follow-up despite its low conductance (4 S). Probably the memory of the already mentioned Detour deposit, which is located in a similar geologic environment, helped to downgrade the importance of the conductivity criterion.

The Goldstream deposit, 90 km north of Revelstoke, British Columbia, is of the Besshi type (Kanehira, 1970, Fox, 1984). Such bodies are typically tabular and stratiform. The reserves of this orebody, which is formed by 2.5 m thick layer of sulfides in Eocambrian metasediments, are 3.5 Mt grading 4.5 percent Cu, 3.1 percent Zn, and 24 g Ag/t. The deposit was discovered as a result of a helicopter Input AEM survey (Konings and De Carle, 1985). Because of the system configuration (horizontal-coil receiver) and the flat-lying geometry of the orebody, a different type of AEM response was obtained (Figure 14). The deposit is magnetic and has a rather high conductance (40 S), probably because of significant pyrrhotite content.

It has been difficult to establish consistent conductivity estimates over a number of volcanic-associated sulfide orebodies. Conductivity and conductance determinations depend significantly on the type of the EM system used. Ghosh (1972) and Palacky (1978) evaluated a number of conductance estimates based on interpretation of AEM data and came to the conclusion that only results obtained with one system are comparable. Using interpretation nomograms, Palacky (1976) estimated conductances for a number of Canadian massive sulfide deposits which were surveyed with the Input AEM system (Table 1). The conductances range from 1 to 42 S, which is virtually the whole range for which estimates can be reliably

**Table 1. Conductances of some Canadian volcanic-associated sulfide deposits**

Deposit	Type	Conductance (S)	Source
<b>Québec</b>			
Chibougamau (Chibex) (Patino)	Cu-Au	22	(1)
	Cu-Au-Ag	42	(1)
Lessard	Cu-Zn-Ag	11	(1)
Magusi River	Zn-Cu-Ag	12	(1)
New Insco	Zn-Cu-Ag	14	(1)
Scott	Zn-Cu	4	(2)
Selbaie	Zn-Cu-Ag	2	(2)
Staunton	Cu-Zn	10	(1)
<b>Ontario</b>			
Detour Lake	Au	13	(2)
Sturgeon Lake	Zn-Cu-Ag	40	(1)
<b>Manitoba</b>			
Morgan Lake	Zn	1	(2)
Rail	Cu-Zn	6	(1)
Reed Lake	Cu-Zn	10	(2)

*Source:* Estimates based on Input AEM data (1) Palacky (1976) and (2) Questor Surveys (1984)

made on the basis of Input data. The system ceases to have good discrimination for conductors with  $\sigma t$  above 40 S, and at the other extreme, bodies with  $\sigma t$  less than 1 S are only marginally detectable (Palacky and West, 1973). Pelton et al. (1978) carried out complex resistivity measurements on 26 North American mineral deposits, many of them of the massive sulfide type. They also show resistivity histograms for various types of mineralization.

In Canada, where prospecting for massive sulfide orebodies more often than not commences with an airborne geophysical campaign, the selection of AEM anomalies for ground follow-up is of utmost importance. In the future, more effective use will be made of available geologic and geochemical information, particularly in mature mining districts (Boldy, 1979). The role that geophysical techniques will play may be substantially different from the past.

As a final thought, it may be useful to analyze the development of AEM systems and their application to prospecting for massive sulfide orebodies in Canada in their historic and geographic context. In the post World War II years, there was a need to find reserves of strategic metals in politically secure areas. Canada, with its huge, largely unexplored territory was the obvious choice. A technique was needed to screen large areas fast and at a modest cost. The approach based on AEM surveying and ground follow-up satisfied these requirements and was highly successful. During the last 30 years the knowledge of Canadian geology has increased substantially. AEM methods may play an important role in systematic, government-sponsored, airborne geophysical coverage of large areas, such as greenstone belts. In Finland, such surveying was initiated in 1952 (Peltoniemi, 1982). The Government of Québec has adopted a similar policy and since 1968 over 600 000 km line AEM surveys have been flown (Lefebvre et al., 1986). The wealth of available data necessitates a new approach to interpretation; all anomalies should be analyzed, not just those thought to be related to massive sulfides.

### Other types of massive sulfide deposits

Most of the world's production of zinc and lead comes from sediment-hosted sulfide deposits (Lydon and Sangster, 1984). Among the major producing mines are Broken Hill, New South Wales, and Mount Isa, Queensland, in Australia; and Sullivan, British Columbia, and Faro, Yukon, in Canada. Also the zinc orebodies in Ireland (Silvermines, Tynagh) and Germany (Rammelsberg, Meggen) belong in this category. Compared with volcanic-associated massive sulfides, orebodies of this type are large. Thirty eight world deposits belonging to this group range from 4 to 550 Mt (average 60 Mt). Their average grades are 7.3 percent Zn, 4 percent Pb, and 48 g Ag/t. The highest mined grades are 18 percent Zn, 13 percent Pb, and 180 g Ag/t. In Canada, 45 percent of the lead, 16 percent of the zinc and 10 percent of the silver production come from this type of deposit (1977–78 figures).

Sediment-hosted sulfide deposits are the product of deposition in moderately warm (150°–250° C) brine pools, some distance away from volcanic centers. Solutions rich in zinc, lead, and silver were introduced into the pool by hydrothermal activity (Gustafson and Williams, 1981). The majority of deposits are found in thick successions of clastic sedimentary rocks, indicating proximity of continents. Prime exploration areas are second-order basins, which can be recognized by rapid lateral facies changes. Syndepositional geothermal activity is indicated by the presence of (a) volcanic rocks (local flows, or thin tuff horizons), or (b) chemical sediments of hydrothermal origin (e.g., barite, chert, Fe, and Mn rich sediments).

The deposits have the form of concordant layers of sulfides, whose lateral extent is ten to several hundreds times the layer thickness. The most common ore minerals are sphalerite and galena. Associated minerals are quartz, pyrrhotite, pyrite, chalcopyrite, marcasite, arsenopyrite, and cassiterite. The most common rocks associated with the sulfide zone are wedges of sedimentary breccia and conglomerate; chert and barite are common in the overlying sequence of chemical sediments.

Probably because of their size and lateral extent, most of the major deposits were discovered by prospectors. Geophysics has been used less often than prospecting for volcanic-associated massive sulfides. Because of their high grade and large tonnage sediment-hosted sulfide deposits constitute very attractive targets, and in principle geophysical methods can be effectively used in their exploration. Induced polarization and, to a lesser degree, EM

surveys were used in prospecting in Ireland where most of the area is covered by glacial sediments. The known orebodies are rich in sphalerite and therefore nonconductive (Seigel, 1966). Extensive AEM surveys were conducted in Queensland, Australia, in the search for Mt. Isa and McArthur River-type orebodies, which are highly conductive (N. Hungerford, pers. comm.). Unfortunately, most of this information remains in files of various exploration companies and virtually nothing has been published.

Stratabound sediment-hosted orebodies of the Mississippi Valley type are also an important source of lead and zinc, particularly in the USA. Major mines are located in the Old Lead Belt and Viburnum Trend Districts in Missouri and in the East Tennessee District. In Canada, Pine Point and Polaris Mines in North West Territories belong to this category. The size of the individual deposit ranges from 1 to 10 Mt, with a combined grade of 5 to 10 percent Pb-Zn (Sangster, 1984).

The deposits occur in platform carbonate successions. They are of highly irregular shape and consist primarily of massive sphalerite and galena. So far, economic geologists have been unable to reach a consensus on a genetic model. For geophysicists, this type of target has been difficult to find, and EM techniques have been used with no success. The prime reason for the failure is the low conductivity of galena and associated pyrite and the well-known fact that sphalerite, the prime ore mineral, is nonconductive. Conductivity obviously depends on the type and origin of the orebody, and the fact that sulfides are massive does not necessarily make them an EM target.

#### **Magmatic deposits of nickel, copper, and platinum**

Magmatic deposits account for about half of the world nickel production (the other half being extracted from lateritic deposits) and virtually the total world production of platinum. The Sudbury deposits in Canada have produced more nickel than any other district in the world (about 7 Mt). About half of the world platinum production comes from Merensky Reef Mines in South Africa. All deposits of this type are associated with mafic-ultramafic igneous rocks and their origin is syngenetic. Most are found in Precambrian greenstone belts. The origin of the Sudbury structure is still poorly understood and several hypotheses, including one of meteoritic impact origin, were put forward.

The mineralized zones usually form conformable layers or lenses. Ore may be in the form of massive or disseminated sulfides, sulfide veins, or breccia. The principal ore minerals are pentlandite and chalcopyrite, and in platinum orebodies various types of minerals of the platinum group. Pyrrhotite and pyrite, which are usually conductive, are common. The overall conductivity depends, however, upon the texture and the type of deposit.

The magmatic Ni-Cu-Pt deposits can be divided into two groups, ultramafic-associated Ni-Cu and gabbro-associated Ni-Cu-Pt. The Mt. Keith and Kambalda deposits in Western Australia, Thompson in Manitoba, Canada, and Pechenga in the USSR belong to the first group. Typical grades are 1 to 3 percent Ni and 0.1 to 0.3 percent Cu. The tonnage of the orebodies varies between 1 and 10 Mt (Eckstrand, 1984). Sudbury in Ontario, Canada, Selebi-Pikwe in Botswana, Norilsk in the USSR, and all platinum-group deposits belong to the second group. Grades range from 0.6 to 1.6 percent Ni and 0.2 to 1.3 percent Cu. Typically, the host massifs contain a number of orebodies whose tonnage may range from 100 000 t to 10 Mt. Merensky Reef deposits have grades 10–20 g Pt/t.

Electromagnetic methods have been extensively used in prospecting for ultramafic-associated Ni-Cu deposits in Manitoba, Canada. Several orebodies in the Thompson belt were discovered as a result of AEM surveying. The geology of the belt was described in detail in Peredery (1982). Dowsett (1970) documented case histories of two geophysical discoveries, Thompson and Pipe mines, where conductive sulfides are associated with peridotite. In the case of the Thompson mine, the massif is at depth, and the pyrrhotite-pentlandite-rich zones were formed at its margins. Figure 15 shows a geologic section and a geophysical profile obtained with the vertical-loop EM system (conductors are indicated by a crossover anomaly). The orebody is conductive and magnetic because of its high pyrrhotite content. The EM response can be approximated by a vertical sheet model.

The sulfide-rich zone is more complex at the Pipe mine (Figure 16), where two irregularly

shaped lenses occur within the peridotite massif. Thickening of glacial overburden over the massif is due to glacial erosion of softer peridotite. A stronger magnetic anomaly was obtained over the peridotite massif than over the iron formation. Vertical-loop EM surveys detected both sulfides lenses, but no detailed determinations of resistivity were made at the orebody.

Unlike volcanic-associated and sedimentary massive sulfides, magnetic association is an important parameter in selecting drilling targets. Magnetic pyrrhotite is almost invariably present in Ni-Cu magmatic deposits. In areas where the weathered layer has not been removed by erosion, prospecting is made more difficult by formation of highly conductive saprolite over mafic or ultramafic massifs. Such bodies will be outlined by AEM surveys, but sulfide lenses within the massifs may remain undetectable unless a broad-band EM system is used.

Interesting case histories concern the application of EM techniques in the Archean Yilgarn Block in Western Australia. Their usefulness for reconnaissance was found limited in the Kambalda camp (100 km south of Kalgoorlie) because of intense weathering, high salt concentration near the surface, and the presence of other conductive horizons (black shales). Geophysical surveys at the Mt. Keith nickel sulfide deposit (500 km north of Kalgoorlie) were described in Elliott and Staltari (1985). The thin (0.3 to 10 m) pyrrhotite-pentlandite ore zone is subvertical. Local weathering which reaches a depth of 80 m affects all EM measurements and the response due to the sulfide-zone could be seen only at late delay times (larger than 5 ms). The use of ground EM methods in detecting similar mineralization at Flying Fox, Forrestania, was described in Staples (1984). This nickel sulfide occurrence is located 380 km east of Perth. Interpretation of EM measurements was complicated by salty groundwater and a weathered layer 90 m thick.

### Iron formations

Iron formations are the world's most important source of iron. Reserves of the major ore-bodies (e.g., Carajás and Minas Gerais in Brazil) are in billions of tons. According to Gross (1984), iron formations can be divided into two groups; the Lake Superior type (more important worldwide) and the Algoma type.

Iron formations of the first type originated by chemical precipitation of iron and silica in an oxidizing environment. They consist of iron and silica rich beds, which are typically 30 to 150 m thick and have a strike length of several kilometers. The most common rock types are taconite, itabirite, and jaspilite. The principal ore minerals, magnetite, hematite, and

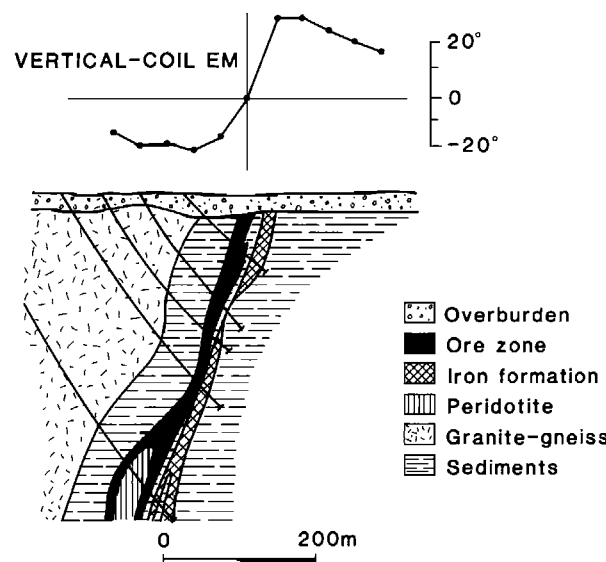


FIG. 15. Geologic section and vertical-coil ground EM response of the Thompson ultramafic-associated nickel deposit, Manitoba, Canada (after Dowsett, 1970).

goethite are associated with finely laminated chert, quartz, Fe-silicates, Fe-carbonates, and Fe-sulfides. All orebodies are syngenetic and most are Proterozoic. Algoma-type iron formations have a more direct spatial association with volcanic centers. In addition to volcanic rocks, greywacke and shale are common. Their age ranges from Precambrian to recent.

Magnetite, usually the most important mineral in iron formations, is not highly conductive, but it possesses high magnetic susceptibility. Therefore, mainly magnetic surveys have been used in prospecting. EM response depends on the dimensionless response parameter, which is a product of conductivity, magnetic susceptibility, system frequency, and two dimensions (which may represent the system or the target). More details can be found in Grant and West, 1966, and Ward and Hohmann, 1987, this volume). This complex dependency means that iron formations can also be detected by frequency-domain EM measurements. When inphase and quadrature components are measured, magnetic targets can be identified by their negative inphase response. So far, no theoretical studies have been done concerning the response of magnetic bodies in the time domain.

Only a few case histories involving EM methods have been published concerning the detection of iron formations. Palacky (1981) described the results of helicopter AEM surveys in the Precambrian shield of Rio Grande do Sul in southern Brazil. Volcanic breccia and tuff predominate in the volcano-sedimentary Hilário Formation within which iron formations frequently occur. As Figure 17 illustrates, negative inphase responses were obtained over iron formations near Lavras do Sul, 250 km west of Porto Alegre. Conductivity differences between Hilário andesite and Santa Bárbara sandstone are due to differential weathering. Because of the anomaly character (narrow, easily identifiable) EM surveys are more effective in mapping such formations than magnetic survey.

Fraser (1973) and Seguin (1975) have used the results of helicopter AEM surveys to estimate the tonnage of iron ore deposits. The first author demonstrated the technique on data from the Sherman Mine, near Temagami, 80 km north of North Bay, Ontario, Canada. The ore grade at this mine is low by world standards, 29 percent magnetite by weight and 18 percent by volume. After determination of magnetic susceptibility on hand specimens, he was able to estimate the tonnage per vertical unit of length from EM data. The difference between his estimates and the ground truth obtained by drilling was less than 10 percent.

Seguin (1975) described geophysical surveys carried out near Schefferville in the Labrador Trough, Québec, which was the most important Canadian iron ore district until its closure in 1983. EM data were used to calculate both tonnage and grade of taconite bodies. Both

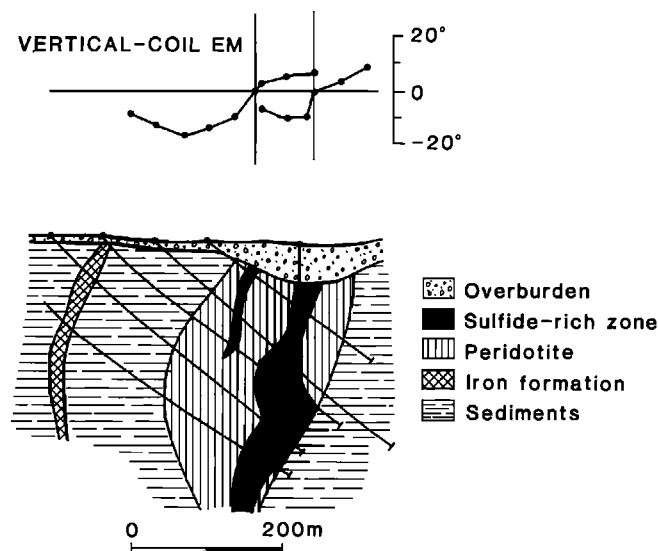


FIG. 16. Geologic section and vertical-coil ground EM response of the Pipe ultramafic-associated nickel deposit, Manitoba, Canada (after Dowsett, 1970).

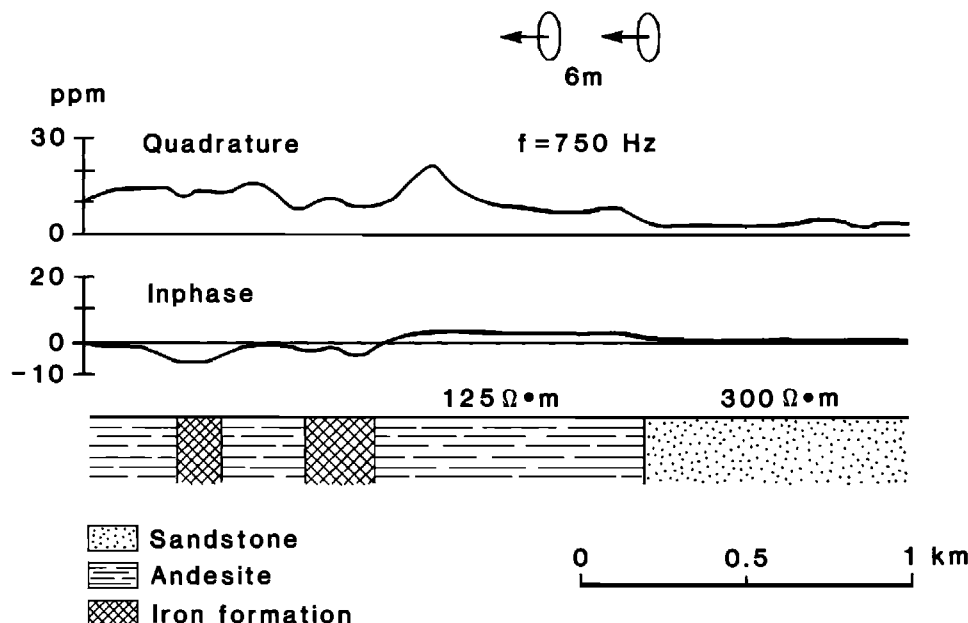


FIG. 17. Geologic section and helicopter AEM response of an iron formation, Lavras do Sul, Brazil (after Palacky, 1981).

authors agreed on the advantages of EM surveys over magnetics: (a) No remanence problems exist because of alternating primary field, (b) EM response is independent of magnetic latitude, (c) Inherently high resolution of EM surveys permits better separation of adjacent magnetic bodies.

While this application does not appear important because of the present lack of incentives to prospect for iron ore, a capability to recognize and analyze EM responses caused by iron formations is essential for a thorough interpretation of AEM survey results in greenstone belts and other geologic environments. In the Labrador Trough and the Abitibi belt, both in Canada, the number of negative inphase anomalies on helicopter EM surveys is substantial.

### Lineaments and Weathered Layers

Water-saturated clays which form as a result of weathering or hydrothermal alteration are among the most common geologic conductors. Transported and deposited clays occur in unconsolidated Quaternary lacustrine, and in fluvial and glaciolacustrine sediments. Conductive clay minerals are present also in a variety of sedimentary rocks (e.g., shales). Many mineral deposits are associated with clays (e.g., unconformity-related uranium, bauxite, lateritic nickel, and gold) and some clays are economically important on their own, [e.g. China clay (kaolin)]. Presence of clays is a useful guide to detection of kimberlites and lineaments; the knowledge of the latter is important in groundwater exploration and prospecting for hydrothermal deposits. Geothermal reservoirs are conductive because of high fluid temperature, increased porosity, and the presence of clays resulting from hydrothermal alteration. Finally,

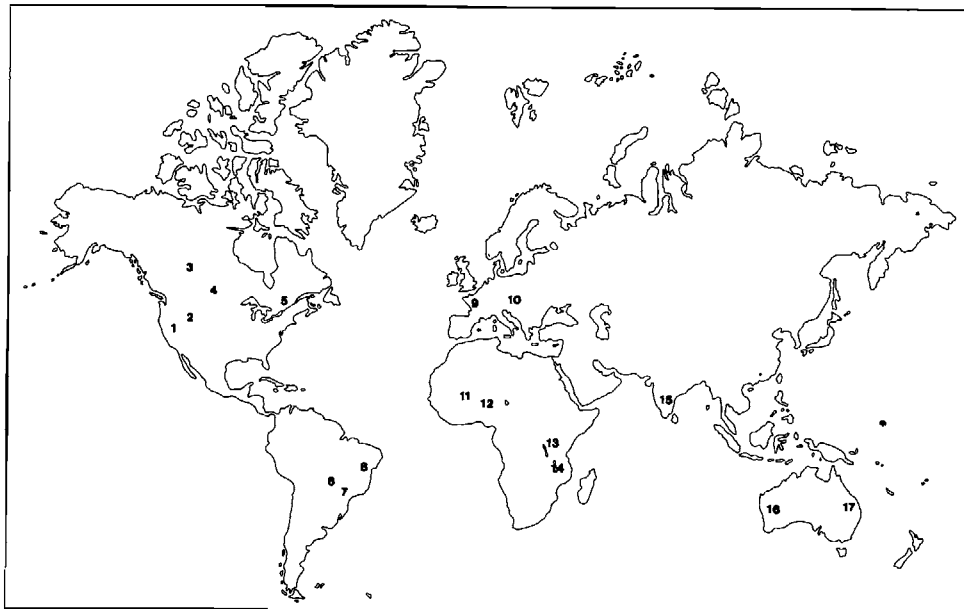


FIG. 18. Location of sites described in the section Lineaments and Weathered Layers (USA: (1) Lassen National Park, California, (2) Roosevelt Hot Springs, Utah; Canada: (3) Athabasca Basin, Saskatchewan, (4) Rice Lake greenstone belt, Manitoba, (5) Ottawa, Ontario; Brazil: (6) Canabrava and Santa Fé, Goiás, (7) Nova Lima, Minas Gerais, (8) Itapicurú greenstone belt, Bahia; Europe: (9) Bois-de-Cené, France, (10) Bakonyjákó and Pápayárvár, Hungary; Africa: (11) Mankarga and Rapadama, Burkina Faso, (12) Northern Nigeria, (13) Musongati, Burundi, (14) Tanzania; India: (15) Vikarabad, Andhra Pradesh; Australia: (16) Teutonic Bore, Western Australia, (17) Ingham, Queensland).

differential weathering, which is a function of the underlying lithology, constitutes the physical *raison d'être* of utilization of EM techniques in geologic mapping. Despite their importance and common occurrence, this group of conductors remains poorly understood and more effort should be directed at studies investigating their nature. Examples from six continents (Figure 18) illustrate the various situations, in which increased conductivity is caused, at least partly, by the presence of clays.

### Weathered layer

In many areas of exploration interest, conductive weathered layers are the source of most EM anomalies detected by airborne surveys. Deep weathering is common in most tropic and subtropic shields (Africa, Australia, Brazil, Guyanas, India). Thick weathered layers may be preserved even in regions where the present climate is not favorable to deep weathering (Canada, Scandinavia, Central Europe). AEM surveys in Australia and Brazil indicate that 50 to 95 percent of AEM anomalies in any given area are caused by weathered layers. Therefore, a good understanding of the weathering mechanism is essential for component interpretation of AEM survey results. In many arid areas (e.g., Australia and southwestern USA) the conductivity distribution is further complicated by the presence of a near-surface salt layer resulting from intense evaporation. This problem will be treated in the Sea Water, Aquifers, and Permafrost section of this paper.

The intensity and type of weathering depends on many factors including climate, lithology, topography, and groundwater regime. Physical weathering predominates in frigid and arid climatic zones, chemical weathering is prevalent in all other regions. Many areas have undergone several weathering cycles. Butt (1982) described the phases of the chemical weathering

process (Figure 19). In situation (a), the water table is at the surface and rocks have not been weathered. In case (b), a saprolite layer develops just below the water table and a thin sand layer appears at the surface. Saprolite is a material in which the original rock textures are still preserved by stable primary minerals and neo-formed secondary clays. While this definition of saprolite is standard in Australia, where most research on weathering has been done, it is not universally accepted in Europe, where the term "chloritization zone" may be more common. (Saprolite may then mean soft material higher up in the weathering sequence). In situation (c), a mottled zone forms at the top of saprolite. In this zone, mobile constituents are increasingly lost and only the most resistant primary minerals, such as chromite and zircon, are preserved. Some of the clays formed in the saprolite layer are replaced by second-generation clays, notably kaolinite. The top of saprolite is defined by the loss of primary textures, which occurs close to the water table. Situation (d) illustrates the development of a ferruginous zone whose transition from the mottled zone is marked by the presence of pisolithic concretions. The hard ferruginous zone is enriched in iron oxides, particularly hematite. Leaching under acid and oxidizing conditions can cause formation at the surface of residual sand, which consists mostly of quartz. The fully developed weathering profile is shown in (e). The weathering process is accompanied by a slow erosion resulting in lowering of the landscape, relief reduction, and filling of valleys with material eroded from the highlands. In this paper the term "regolith," which is common in Africa and North America, denotes the weathering mantle.

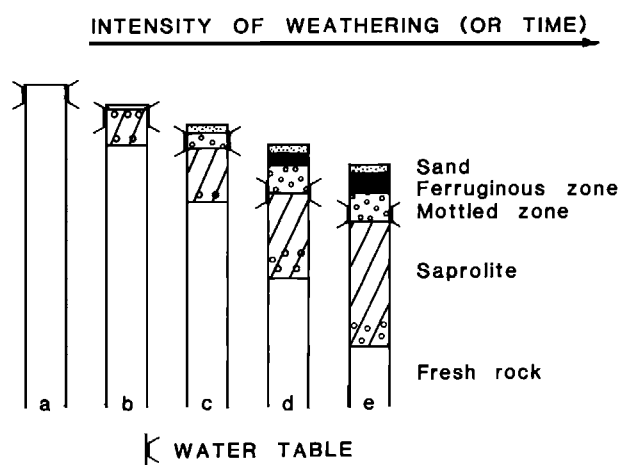


FIG. 19. Development of a complete weathering profile as a function of time or weathering intensity (after Butt, 1982).

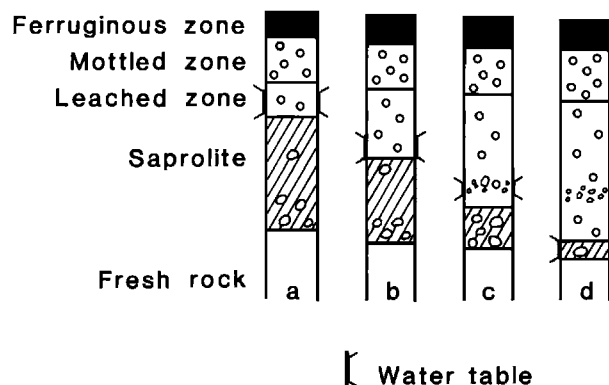


FIG. 20. Modification to the weathering profile due to declining water tables resulting from tectonic uplift (after Butt, 1982).

The weathering process will be altered, if the region becomes progressively arid or is subjected to a gradual uplift (Figure 20). The resulting lowering of the water table causes leaching of the upper part of the saprolite layer and formation of a pallid leached zone. The actual saprolite, as defined above (preservation of original rock textures), may become very thin. As the water table declines, the upper horizons are progressively exposed to oxidizing conditions. Dehydration of the uppermost ferruginous layer leads to its hardening and to the formation of duricrust (called "canga" in Brazil and "cuirasse" in West Africa). The weathering profile illustrated in Figure 20d is the result of two chemical processes; (1) laterization under a high water-table regime, followed by (2) leaching when the water-table progressively declines.

The weathering process has been described as a function of tectonic movement and climatic changes, but there are other factors determining the final outcome, notably topography and lithology. The profiles given in Figures 19 and 20 are typical of uplands. On slopes, erosion causes a continuous removal of the top of the weathered layer, particularly of the frail mottled zone, and a deposition of the material in valleys. Thus lower slopes and valleys are enriched with materials derived from the upslope.

Not all rock types are equally affected by weathering (Figure 21). Gneiss or granite are more resistant than amphibolite or some types of volcanic rocks. For igneous rocks, the weathering intensity is a function of the lithologic composition. Mafic and ultramafic rocks are more susceptible to intense chemical weathering than felsic rocks which have a higher content of resistant minerals (quartz, muscovite). Figure 22 (Bowen's reaction series) shows

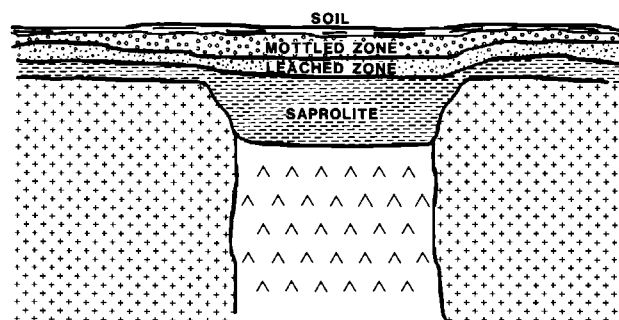


FIG. 21. Schematic geologic section of the weathered layer and its composition as a function of the underlying rock type.

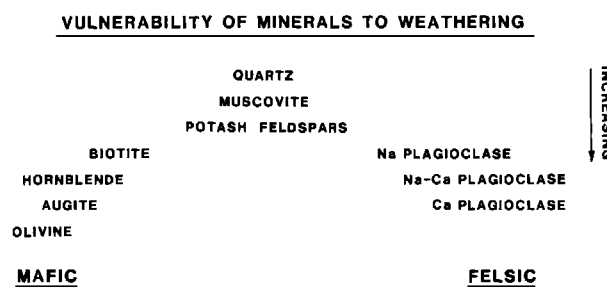


FIG. 22. Vulnerability of igneous rock-forming minerals to weathering Bowen's reaction series (after Goldich, 1938).

the vulnerability of common rock-forming minerals to weathering (increase downward). Under normal conditions, mafic minerals (olivine, augite, and hornblende) are transformed into clay minerals (chlorite, illite, smectite, vermiculite, and montmorillonite) (Ollier, 1969). Laboratory and in-situ studies have shown that water-saturated clays are conductive (Figure 2).

Conventional petrographic classifications of igneous rocks is based on their silica content (Figure 23). The less  $\text{SiO}_2$  (quartz) the rock matrix contains, the more susceptible it is to chemical reactions and to formation of conductive clays. This chemical activity takes place in the water-saturated zone—saprolite. In a given area, where all other parameters are equal (climate and topographic position), a saprolite layer formed over mafic rocks is always more conductive than one over felsic rocks.

In-situ resistivities of most fresh igneous rocks vary between 500 and 10 000  $\Omega \cdot \text{m}$  even though lower values have been recorded (e.g., Hawaiian basalts). Laboratory investigations on samples give values which are several orders of magnitude higher (Angenheister, 1982). Table 2 lists laboratory and in-situ resistivities of some igneous rock types. Relatively low values (under 1000  $\Omega \cdot \text{m}$ ) have been observed over mafic rocks (diabase, gabbro, and basalt). Intermediate to felsic rocks (granite, syenite, and diorite) have in-situ resistivities over 2 000  $\Omega \cdot \text{m}$ . Variations in resistivities determined in the laboratory were much larger and no such separation appeared possible. The resistivities of saprolite formed over igneous rocks range between 5  $\Omega \cdot \text{m}$  (basalt) and over 200  $\Omega \cdot \text{m}$  (quartz diorite).

Idealized weathering profiles over felsic and mafic igneous rocks are shown in Figure 24. As the formation of weathering profiles was explained previously, the focus will be on the composition and electrical properties of its component layers. Starting from the bottom, fresh parent rock is found with resistivity usually in excess of 500  $\Omega \cdot \text{m}$ . Immediately above is a zone of fractured rock whose mineral composition is identical to the parent rock, i.e., mostly



FIG. 23. Standard classification of igneous rocks based on their silica content. The susceptibility of rocks to weathering and saprolite conductivity increase with a decreasing quartz content.

Table 2. Resistivities of igneous rocks

Volcanic	In situ ( $\Omega \cdot \text{m}$ )	Laboratory ( $\Omega \cdot \text{m}$ )
Lava	6 000	10 000
Basalt	800	7 000
Diabase	450	10 000
Andesite		2 000
Dacite		21 000
<hr/>		
Plutonic		
Peridotite		3 000
Gabbro	490	1 500
Diorite	7 000	100 000
Syenite	2 400	30 000
Granite	4 300	20 000

Source: Average values from compilation in Angenheister (1982).  
Laboratory values are for wet rocks.

quartz, K-feldspar, biotite, and muscovite in the case of felsic rocks, and plagioclase, pyroxene, amphibole, and serpentine in the case of mafic rocks. Current resistivity and well-logging data are not sufficiently detailed to indicate whether this zone can be accurately identified by electrical measurements. Particularly in the case of soundings, an identification may be difficult, because the layer usually has a resistivity intermediate between that of fresh rock (high) and saprolite (low).

What is of importance to exploration geophysicists is that saprolites formed over mafic rocks are thick and conductive. A definite identification of saprolite as the most conductive layer in the weathered section can be found in Peric (1981). Figure 25 shows two borehole resistivity logs which were converted to conductivity to highlight the conductive layer. More such data are included in Peric's paper, which describes geophysical surveys carried out over the Musongati lateritic nickel deposit in Burundi (80 km southeast of the capital of Bujumbura). The transition from saprolite to fresh peridotite usually occurs within 1 to 3 m (top log), but appears more gradual on the lower log. Peak conductivity is about 150 mS/m, corresponding to  $6.7 \Omega \cdot \text{m}$ . Similar resistivity values were interpreted also from soundings, which indicated limit values of 5 and  $25 \Omega \cdot \text{m}$ . The average saprolite thickness is 18 m.

Resistivity soundings were carried out by Palacky and Kadekaru (1979) over basalt flows and peridotite massifs at Canabrava, Goiás, Brazil (270 km north of Brasília). A statistical analysis of the interpreted resistivities and thicknesses of the saprolite layer suggests that the difference in resistivity between the two lithologic types is statistically meaningful (Figure 26). Eight soundings over basalt indicated a mean resistivity of  $19.5 \Omega \cdot \text{m}$  with a standard deviation of  $3.7 \Omega \cdot \text{m}$ ; 13 soundings over peridotite had a mean resistivity of  $7.9 \pm 2.5 \Omega \cdot \text{m}$ . The corresponding mean thicknesses were  $10.6 \pm 3.9 \text{ m}$  for basalts and  $20.7 \pm 3.8 \text{ m}$  for peridotite. The average resistivities measured in the laboratory are  $7\,000 \Omega \cdot \text{m}$  for basalt and  $3\,000 \Omega \cdot \text{m}$  for peridotite (Angenheister, 1982).

Table 3 summarizes the values of saprolite resistivity published by several researchers. All values were obtained by interpretation of resistivity soundings, but because of different survey specifications they may not be comparable in absolute terms. Nevertheless, two facts are striking: saprolite formed over mafic rocks is generally more conductive than over felsic

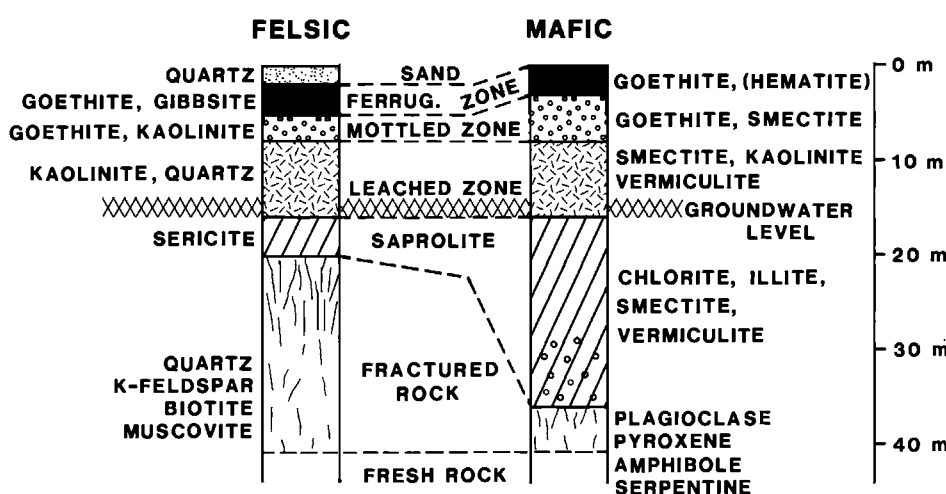


FIG. 24. Schematic weathering profiles over felsic and mafic igneous rocks. The minerals most common to each horizon are written on the sides of the columns. Mineral content of fresh rock and zone of fractured rock are the same (after Palacky, 1986).

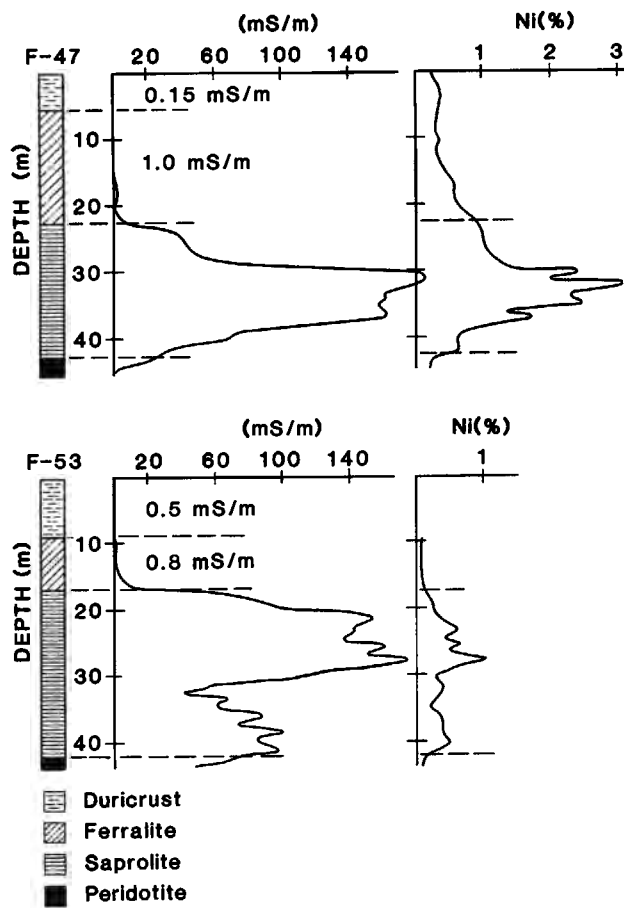


FIG. 25. Geologic logs, resistivity logs (three-electrode array, results converted to conductivity in  $\text{mS}/\text{m}$ ), and nickel content of the weathered layer at the Musongati ultramafic massif, Burundi (after Peric, 1981).

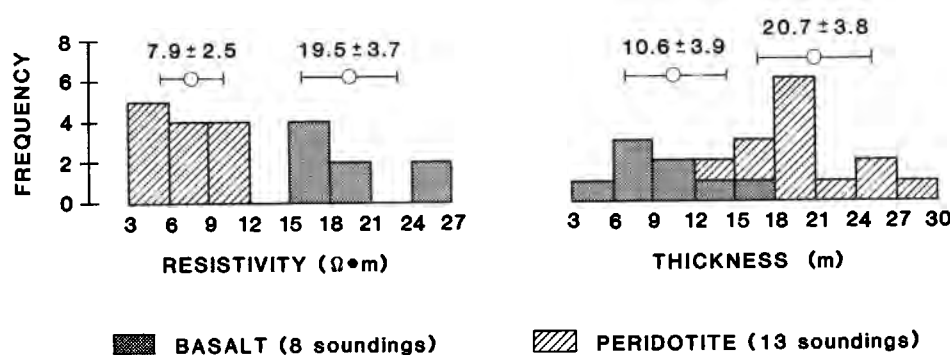


FIG. 26. Histograms of resistivity and thickness values (from resistivity soundings) over basalt and peridotite at Canabrava, Goiás, Brazil (after Palacky and Kadekara, 1979).

**Table 3.** In situ resistivities of saprolite formed over igneous rocks

Rock Type	Locality	Country	Resistivity ( $\Omega \cdot m$ )	Source
<b>Mafic</b>				
Peridotite	Canabrava	Brazil	8	(1)
Peridotite	Musongati	Burundi	10	(2)
Basalt	Vikarabad	India	5	(3)
Basalt	Ingham	Australia	5	(4)
Basalt	Santa Luz	Brazil	15	(1)
Basalt	Canabrava	Brazil	20	(1)
Basalt	Teutonic Bore	Australia	30	(3)
Dunite	Santa Fé	Brazil	50	(1)
<b>Felsic</b>				
Andesite	Teutonic Bore	Australia	100	(5)
Andesite	Lavras do Sul	Brazil	110	(6)
Granite	Sadaseopet	India	40	(3)
Granite	Santa Luz	Brazil	65	(1)
Granite	Rapadama	Burkina Faso	70	(7)
Granite	Northern Region	Nigeria	100	(8)
Quartz diorite	Nova Lima	Brazil	220	(1)

Source: (1) Palacky and Kadekaru (1979), (2) Peric (1981), (3) Poddar and Rathor (1983), (4) Birkett (1981), (5) Fritz and Sheehan (1984), (6) Palacky (1981), (7) Palacky et al. (1981), and (8) Acworth and Griffiths (1985).

**Table 4.** In situ resistivities of saprolite formed over metamorphic rocks

Rock Type	Locality	Country	Resistivity ( $\Omega \cdot m$ )	Source
Amphibolite	Rapadama	Burkina Faso	10	(1)
Amphibolite	Curaçá	Brazil	30	(2)
Amphibolite		Mali	10	(3)
Phyllite	Quatipurú	Brazil	20	(2)
Serpentinite	Quatipurú	Brazil	90	(2)
Schist		Mali	20	(3)
Schist	Mankarga	Burkina Faso	20	(1)
Schist	Nova Lima	Brazil	80	(2)
Schist	Caçapava do Sul	Brazil	130	(2)
Gneiss	Curaçá	Brazil	100	(2)
Gneiss	Raniganj	India	100	(4)

Source: (1) Palacky et al. (1981), (2) Palacky and Kadekaru (1979), (3) Engalenc (1978), and (4) Verma and Bandyopadhyay (1983)

rocks (if we consider the data from a given area, this statement is true without qualification), and the variation in resistivity between continents (South America, Africa, Asia, Australia) does not appear significant.

Unlike igneous rocks, the susceptibility of metamorphic rocks to weathering seems to depend more on rock texture than on mineral composition. Gneiss was found generally more resistant to weathering than other metamorphic rocks and the derived saprolite does not appear very conductive (Table 4). The resistivity of the saprolite layer formed over schists varies quite substantially, but most likely the rocks described as schists are not petrologically identical. Within a geographically defined region, the resistivity values did not vary by more than 50 percent.

As Figure 25 shows, conductivities of the upper two layers, ferralite (corresponding to the leached and mottled zones) and duricrust (ferruginous zone), are significantly smaller, 0.8–1 mS/m and 0.15 mS/m, respectively. The respective resistivity values are 1 000–1 250  $\Omega \cdot \text{m}$  and 6 600  $\Omega \cdot \text{m}$ . At all localities listed in Tables 3 and 4, the upper part of the weathered layer was more resistive than its lower part. However, in most instances, no further separation was made into leached zone, mottled zone, and ferruginous zone. In a medium where resistivity decreases with depth, interpretation of sounding curves is usually difficult and a good fit of measured data to theoretic curves can only be achieved if the existence of such layers is a priori known. High resistivity values (over 1 000  $\Omega \cdot \text{m}$ ), which could be ascribed to the ferruginous zone, were observed only over lateritic soils in Minas Gerais and Goiás in Brazil (localities Santa Fé, Nova Lima, and Quatipurú). Other localities in the same states had upper layer resistivities varying from 80 to 500  $\Omega \cdot \text{m}$ , suggesting absence of ferruginous zone. At Teutonic Bore, Western Australia, resistivities of the uppermost layer ranged from 100 to 1 000  $\Omega \cdot \text{m}$ , but Fritz and Sheehan (1984) gave no detailed description of the weathered layer. Acworth and Griffiths (1985) suggested the range of 500 to 5 000  $\Omega \cdot \text{m}$  as typical for duricrust in Northern Nigeria. At other places listed in Tables 3 and 4, no highly resistive layer was observed.

As an example of a complete weathering profile determined by resistivity soundings, a section is shown in Figure 27 of the nickel occurrence at Santa Fé, Goiás, 250 km west of

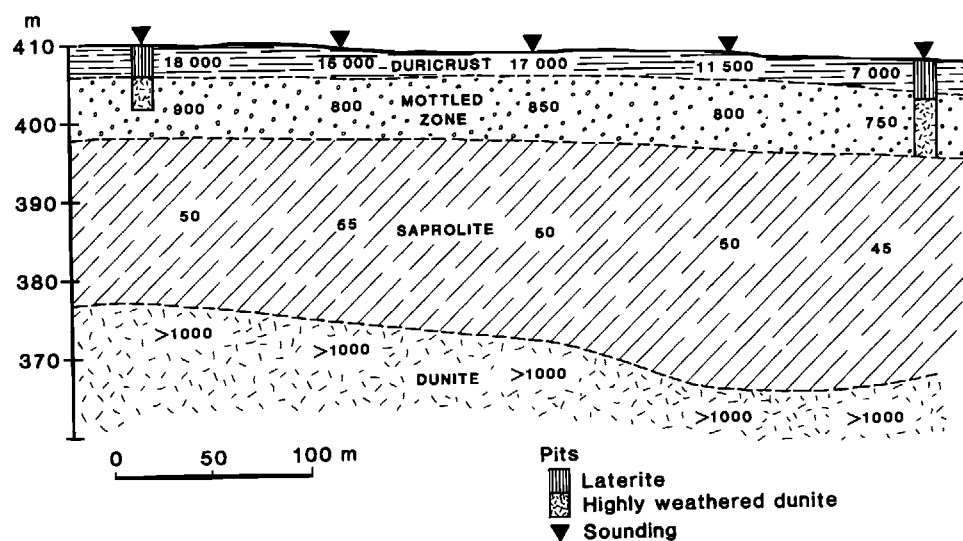


FIG. 27. Geologic section of the weathered layer at Santa Fé, Goiás, Brazil. Resistivities (in  $\Omega \cdot \text{m}$ ) and depths from interpreted resistivity soundings (after Palacky and Kakekaru, 1979).

Brasília. The dunite massif is weathered to a depth of 30 to 40 m. Saprolite is the thickest (20 m) and the most conductive ( $50 \Omega \cdot \text{m}$ ) of the zones of the weathered layer. The mottled zone formed at its top is thinner (less than 10 m) and more resistive (750 to  $900 \Omega \cdot \text{m}$ ). Unless the sounding data are interpreted with an a priori knowledge of a 4-layer model, the distinction between saprolite and mottled zone becomes blurred and the two may sometimes appear as a thick layer of resistivity of about  $100 \Omega \cdot \text{m}$ . The underlying fresh dunite is resistive (over  $700 \Omega \cdot \text{m}$ ) and the thin top layer (duricrust) is highly resistive (7 000 to 18 000  $\Omega \cdot \text{m}$ ).

Palacky and Kadekaru (1979) carried out repeated resistivity soundings at several localities in Minas Gerais, Brazil, to determine whether in-situ resistivities depend on seasonal rains. They found that only the resistivity of the upper, resistive layer was affected. The seasonal change in resistivity over Nova Lima schists is shown in Figure 28 together with the mean monthly precipitation for Belo Horizonte, the state capital, lying 80 km north. The resistivity increased from a low of  $6\,000 \Omega \cdot \text{m}$  recorded during the wet season to  $14\,000 \Omega \cdot \text{m}$  at the end of the dry season. While a duricrust was observed in many areas, the rather thick resistive layer (about 10 m) was constituted mostly by the mottled zone, where clays become more conductive when wet. As this layer is situated above the water table, clays remain dry and resistive during the dry season. The resistivity of saprolite remained constant during the repeated measurements in the 50 to  $100 \Omega \cdot \text{m}$  range for the test site ensemble.

Weathering profiles become complex, if neighboring units are of distinctly different age. Birkett (1981) conducted resistivity and EM studies in Kangaroo Hills near Ingham, Queensland, Australia (120 km northwest of Townsville). Permo-Carboniferous granite underwent substantial weathering during Cretaceous and Tertiary. Valleys were formed in which cassiterite and ilmenite sands were deposited. In the late Tertiary, the area was covered by basalt flowing from Mt. Fox volcano. In many places, the lava flows filled only the ancient valleys

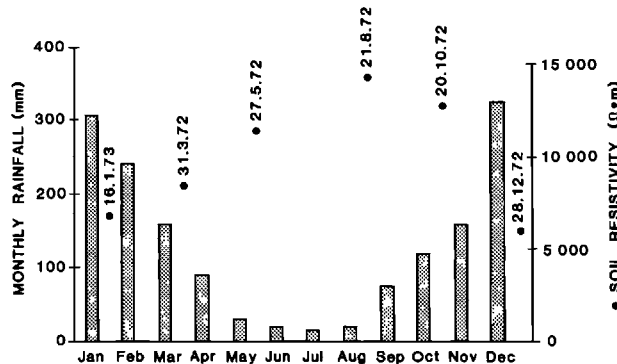


FIG. 28. Average monthly precipitation (columns) and resistivities of the top weathered horizon (ferruginous and mottled zones) determined on the indicated dates (day, month, year) at Nova Lima, Minas Gerais, Brazil (after Palacky and Kadekaru, 1979).

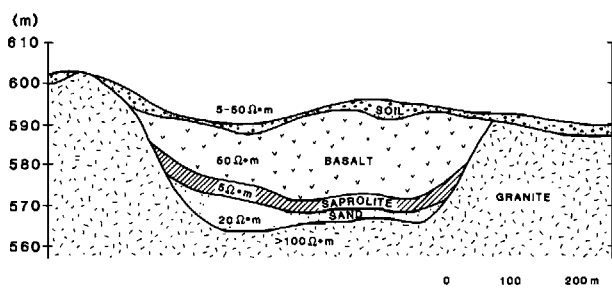


FIG. 29. Geologic section of a paleochannel at Kangaroo Hills, near Ingham, Queensland, Australia. Resistivities were determined by interpretation of resistivity soundings (after Birkett, 1981).

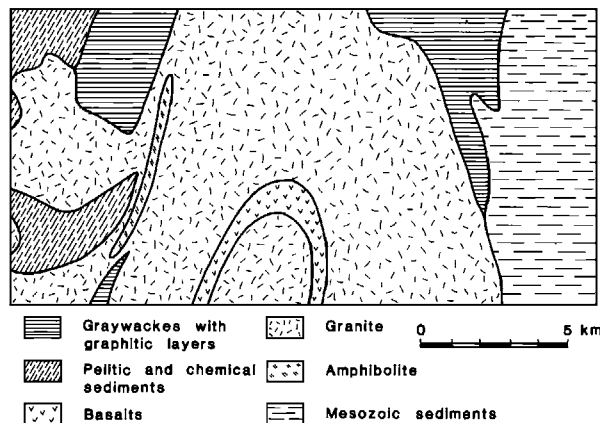


FIG. 30. Geologic map of a selected area in the Itapicurú greenstone belt, Bahia, Brazil (after Palacky, 1981).

that now show a rather peculiar resistivity layering (Figure 29). At the top of slightly fractured granite (with resistivities over  $100 \Omega \cdot m$ ) is a water-filled sand layer with resistivities around  $20 \Omega \cdot m$ . A highly conductive clay-rich layer is developed at the base of the basalt flow ( $5 \Omega \cdot m$ ). The basalt flow itself was described as only slightly weathered and, typically, it had resistivities around  $50 \Omega \cdot m$ . The soil layer is rather thin over basalt, but generally well developed over granite. In some places volcanic tuffs were deposited which weather more readily than basalt flows. Their resistivity was determined as  $5 \Omega \cdot m$ . Subsequently, ground EM surveys were used to map buried valleys which contain economic concentrations of cassiterite.

Existence of a highly conductive clay layer at the base of weathered basalts from the Vikarabad area in Andhra Pradesh, India was also described in Poddar and Rathor (1983). Cretaceous basalt flows of the Deccan Trap formation are up to 25 m thick and their resistivity ranges from 12 to  $70 \Omega \cdot m$ . Formed at their base was a 3 m thick, highly conductive interflow clay bed (resistivity 3–5  $\Omega \cdot m$ ). The basalts are covered by a few tens of centimeters of "black cotton" soil. Because of the large extent of the Deccan Trap weathered formation, this pattern is very common in India and in the past has hindered successful interpretation of airborne EM data in that country.

#### Mapping of lithology

The dependence of saprolite resistivity on the underlying lithology makes resistivity and EM methods suitable tools for geologic mapping in shield areas, where the weathered layers have not been removed by erosion. Particularly EM methods, which are fast and relatively inexpensive, have the potential of contributing significantly to overall geologic knowledge of such areas. Correlation between AEM responses and lithology had been observed (Makowiecki et al., 1965) in Tanzania, but the matter was not pursued to its logical conclusion.

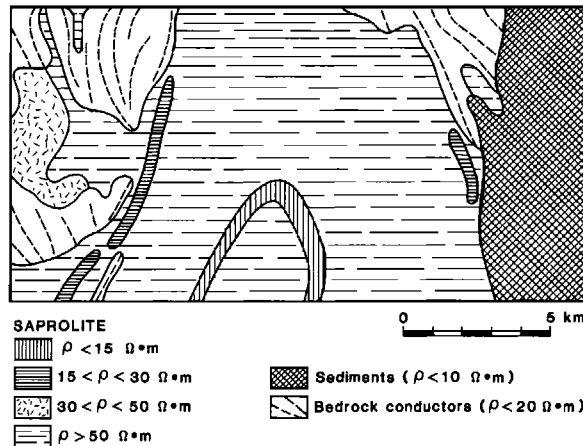


FIG. 31. Schematic map of apparent resistivity; the same area as in Figure 30. Resistivities were interpreted from Input AEM data using a homogeneous half-space model.

Palacky (1981) described application of Input and helicopter AEM surveys to geologic mapping in two areas in Brazil, the Itapicurú greenstone belt in Bahia and the Rio Grande do Sul Shield. Figure 30 is a geologic map of a part of the Itapicurú belt, 30 km north of the town of Araci, which is 180 km northwest of Salvador. The metavolcanic and metasedimentary sequence of the greenstone belt is surrounded by Archean granites. In the east, the belt is overlain by Mesozoic shale. Figure 31 depicts apparent resistivities, which were interpreted from Input AEM data using a homogeneous half-space nomogram (Palacky and West, 1973). The AEM responses could be divided into 3 categories: (1) Strong, broad anomalies over Mesozoic shale with resistivity less than  $10 \Omega \cdot m$ . Resistivity soundings in the area indicated an average value of  $7 \Omega \cdot m$  (Lima, 1979), (2) Bedrock conductors, mostly graphitic schist in the greywacke sequences. Axes of individual conductors are shown in Figure 31. (3) AEM anomalies due to saprolite. Strongest anomalies were observed over a basalt structure, with resistivities less than  $15 \Omega \cdot m$ . Medium anomalies (resistivities between  $15$  and  $30 \Omega \cdot m$ ) appeared associated with amphibolite lenses. Scattered, small-amplitude anomalies were observed locally over granite near the western edge of the map. In most of the area surveyed, no AEM response was recorded over granite. The time-domain Input system used in the survey is insensitive to bodies with resistivity in excess of  $50 \Omega \cdot m$ . Resistivity and ground EM surveys in the area indicated a resistivity range of 40 to  $100 \Omega \cdot m$  for saprolite formed over granite. By suitably selecting resistivity ranges, a resistivity map bearing a striking resemblance to geology could be compiled from AEM data. As Palacky (1981) documented, no such correlation existed in this area between magnetic maps and lithology. The results of Input AEM surveys were used in the Itapicurú greenstone belt and elsewhere in Brazil to improve geologic maps, when map quality was poor because of lack of outcrops. AEM techniques can become a powerful mapping tool in many regions of the world where similar conditions exist.

Conductive saprolite layers also exist in regions with temperate or cold climates. Paleo-weathered layers may be preserved from distant geologic past, often tens of millions of years, when the local climate was more favorable to intense chemical weathering. Figure 32 (from Palacky, 1987) illustrates the preservation of conductive material related to amphibolite and serpentinite in western France. The area depicted lies northeast of Bois-de-Cené, 30 km south of Nantes. While conductive Quaternary marine clays outcrop in the northwestern corner, the whole area is underlain by metamorphic rocks, mostly mica schists. A geologic map at the scale 1:80 000 (Bureau de Recherches Géologiques et Minières—BRGM, sheet Nantes, Île du Pilier) indicates serpentinite and amphibolite dikes, whose presence is partly obscured by loess. Superimposed on the geologic map are the flight lines and the location of Input AEM anomalies (Figure 32). Two types of AEM responses were observed (Figure 33): (1) Strong, large-amplitude anomalies associated with conductive marine clays, (2) Narrow, me-

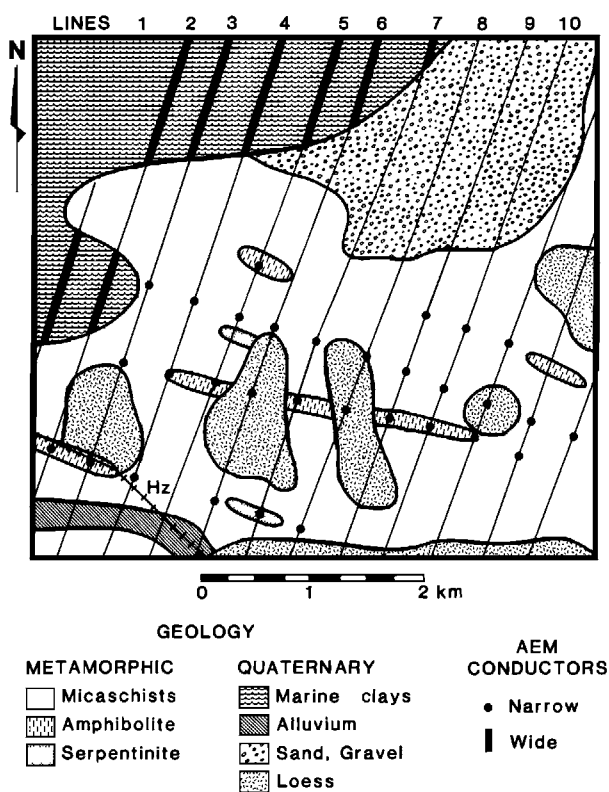


FIG. 32. Geologic map of an area near Bois-de-Cené, France. Depicted are conductors detected in the course of an Input AEM survey and the flight lines (after Palacky, 1987).

dium-to-small anomalies coinciding in many places with mapped amphibolite or serpentinite dikes. The presence of AEM anomalies suggests that the extent of such dikes is greater than traditional mapping could determine. The anomalies appear to be caused by saprolite formed over mafic-ultramafic dikes. The example shows that AEM techniques can provide new geologic information even in areas mapped in great detail. The results do not show any degradation of the EM response over resistive loess, sand, and gravel, but the continuation of dikes could not be traced under the highly conductive marine clays which almost saturated the Input response. The dikes could not be detected by airborne magnetism (Figure 33).

Until the completion of recent studies by the Geological Survey of Canada, it had been assumed that glacial erosion removed all weathered material in Canada. Evidence from drilling, and circumstantially from interpretation of AEM data, indicates that paleo-saprolites are quite common. Veillette and Nixon (1982) described thick paleo-saprolite layers (up to 26

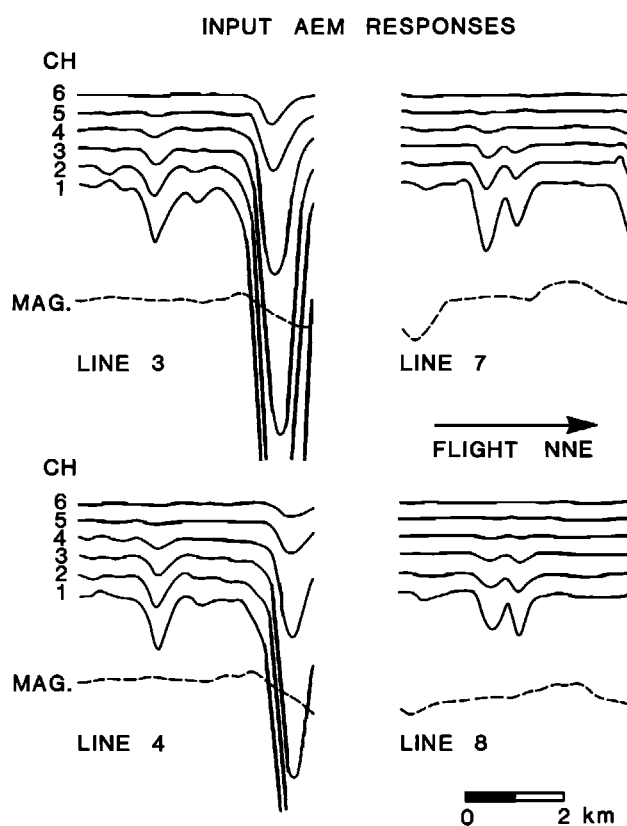


FIG. 33. Input AEM data along four lines in the Bois-de-Cené area, France. The flight line location is indicated in Figure 32 (after Palacky, 1987).

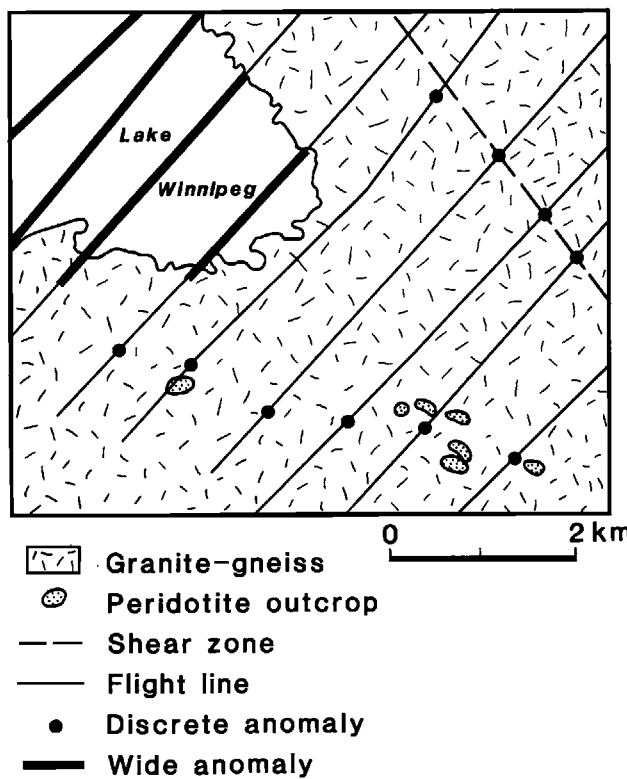


FIG. 34. Geologic map of a portion of the Project Pioneer Area 5, Rice Lake greenstone belt, Manitoba, Canada. Depicted are Input AEM conductors and the flight lines (after Dyck et al., 1975).

m) formed over metasediments and granites in New Brunswick. Figure 34 shows a geologic map and Input AEM survey results from the Pioneer project area (Area 5) in Manitoba (Dyck et al., 1975). The surveys covered five blocks in the Rice Lake greenstone belt and its contact with the Winnipigow River plutonic complex. Clear AEM anomalies are associated in all areas with peridotite and serpentinite dikes. The survey was flown in the horizontal-receiver configuration which permits separation of anomalies caused by vertical dikes and horizontal-ribbon conductors (Palacky, 1975). Consistently, the Input responses over dikes resembled horizontal ribbons rather than vertical sheets. Hence, it can be concluded that the anomalies are caused by paleo-saprolite rather than by peridotite, which is known to be resistive in its fresh state (Table 2). The area is covered by a thin layer of resistive glacial sediments. Strong AEM anomalies coinciding with lakes are caused by clayey sediments at the lake bottom.

Conductive paleo-saprolite layers may be preserved under a sedimentary cover. The Geological Survey of Canada has drilled six holes at Bells Corners, near Ottawa, Ontario, for the purpose of well-logging instrument calibration and testing (Killeen, 1986). The resistivity

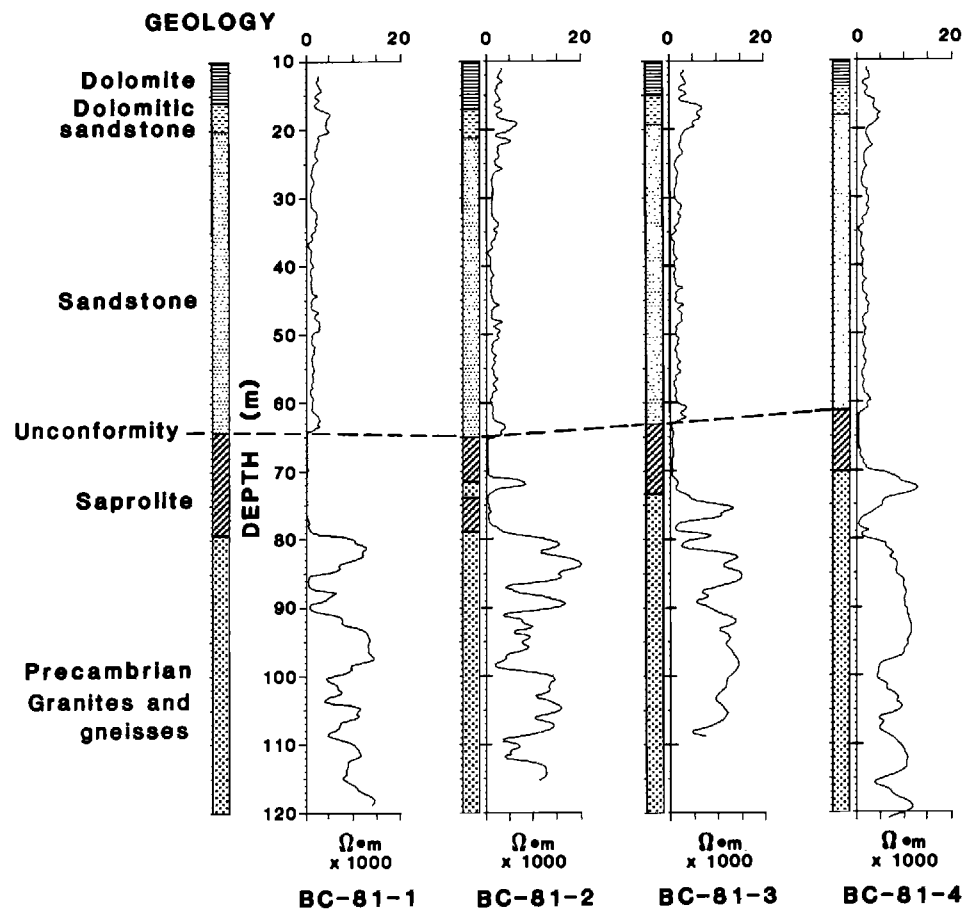


FIG. 35. Geologic and resistivity logs from the Bell's Corners test area near Ottawa, Ontario, Canada (after Killean, 1986).

logs of four of the holes are shown in Figure 35. In each hole, moderately resistive (500–1 000  $\Omega \cdot m$ ) Paleozoic sediments (dolomite, conglomerate, and sandstone) were encountered in the upper 61 to 65 m. Underneath, a conductive paleo-saprolite layer was intersected (resistivity between 80 and 200  $\Omega \cdot m$ ) which was formed by weathering of Precambrian granite and gneiss. The values are not unlike those listed for saprolite formed over granite in other parts of the world (Table 3). Fresh granite was highly resistive (2 000 to 15 000  $\Omega \cdot m$ ). The saprolite layer, which varied in thickness from 10 to 15 m, contained in one hole (BC-81-2) a more resistive intercalation.

Miller (pers. comm.) compiled a map (Figure 36) of the possible extent of paleoweathered layers formed over rocks of Aphebian age (1.8–2.5 Ga) in Canada. Existence of conductive paleo-saprolite (locally described as regolith) was confirmed by drilling in the Athabasca basin in Saskatchewan, in the Labrador Trough in Québec, and at several places in Ontario (see also the section on unconformity-related uranium deposits). Studies have been made comparing recent saprolites in Australia and Aphebian regoliths in Canada.

### Unconformity-related uranium deposits

Deposits related to the Aphebian-Helikian unconformity contain the largest reserves of uranium in Canada. The first deposit of this type, Rabbit Lake, was discovered in 1968 (Sibbald, 1983). The mine, which went into production in 1975, had rather limited reserves (18 140 t of 0.4 percent U<sub>3</sub>O<sub>8</sub>), but it focused attention of explorationists on the Athabasca Basin. Other discoveries followed in the 1970s and early 1980s. Most significant were McClean and Cigar Lake orebodies with reserves of 353 730 t of 1.8 percent U<sub>3</sub>O<sub>8</sub> and 110 000 t of 12.2 percent U<sub>3</sub>O<sub>8</sub>, respectively. The latter is the world's largest high-grade uranium deposit (Ruzicka and LeCheminant, 1986). Both were discovered as a result of AEM surveys. At present, in Canada, uranium exploration represents as equally important an application for EM methods as prospecting for massive sulfides.

Uranium deposits in northern Saskatchewan are found in a weathered layer (locally described as regolith) formed at the top of a crystalline basement and in Athabasca sediments. The basement Wollaston Group, which is Aphebian age (1.8–2.5 Ga) consists of three units (Sibbald, 1983): (1) Metapelitic unit, which commonly contains graphitic metapelite, (2) Meta-arkose unit, (3) Upper units consisting of quartzite and amphibolite. The basement rocks underwent an intense alteration (chloritization) dated at 1.6 Ga, which resulted in the formation of conductive clay minerals, particularly illite and chlorite. The thickness of the regolith depends upon the underlying lithology: about 20 m over meta-arkoses, 40 m over metasemipelites, 100 m over graphitic metapelites (Wallis et al., 1984). The alteration zone reaches a thickness of 220 m along fractures. The regolith shows a clear zonation, the upper part (leached zone) is red-purple and rich in kaolinite, the lower part (saprolite) is greenish

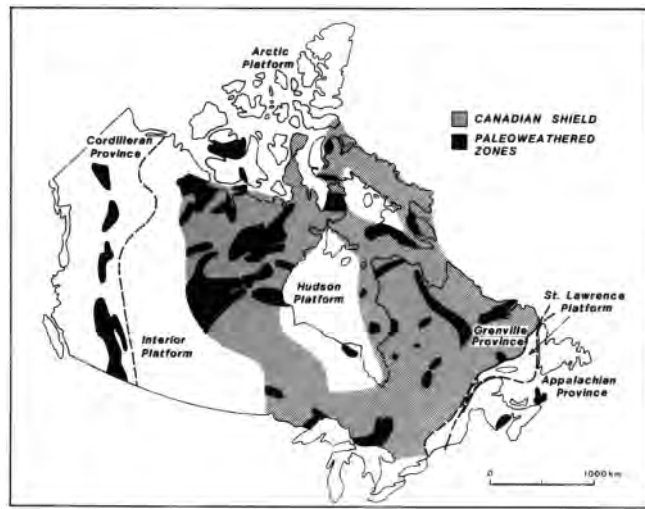


FIG. 36. Map of Canada showing the probable extent of weathered layers under Aphebian sediments (courtesy of A. R. Miller).

with illite and chlorite predominating. An alternative explanation would be to ascribe the formation of the clay-rich regolith to hydrothermal alteration rather than to intense chemical weathering, but the mentioned observations (zonation, dating, and lithology dependence) make this hypothesis unlikely.

Economic uranium mineralization occurs also in the Athabasca sandstone (Helikian age, 1.4 Ga) immediately above the unconformity. Even in single mineralized pods, reserves may be in both regolith and the Athabasca sedimentary rocks. Uranium mineralization is always related to presence of clay minerals, particularly illite, and to graphitic metapelites in the basement (Wallis et al., 1984). As both clay-rich zones and graphitic metasediments are conductive, airborne and ground EM techniques have been extensively used in prospecting (Saracoglu et al., 1983).

Fouques et al. (1986) described the discovery of the Cigar Lake deposit. AEM surveys were used to outline the conductive regolith under a cover of 400 to 450 m thick Athabasca sediments. Figure 37 shows the extent of the Input AEM anomaly in the Waterbury Lake—Cigar Lake area. Magnetic units correspond to Archean granites and the meta-arkose unit of the Wollaston group. The metapelitic and quartzite units are nonmagnetic. While the regolith overlying granites, quartzites, and meta-arkoses is rather thin and resistive, it is well developed over the metapelitic unit. Graphitic metapelites are particularly deeply weathered and even though their graphite content may be reduced (from 80 percent to less than 10 percent), Deepem surveys could be successfully used to map their extent (Figure 37). Unfortunately, no in-situ studies of electrical properties were made to determine whether EM anomalies were caused by a local thickening of the regolith, or by the underlying graphitic metapelites.

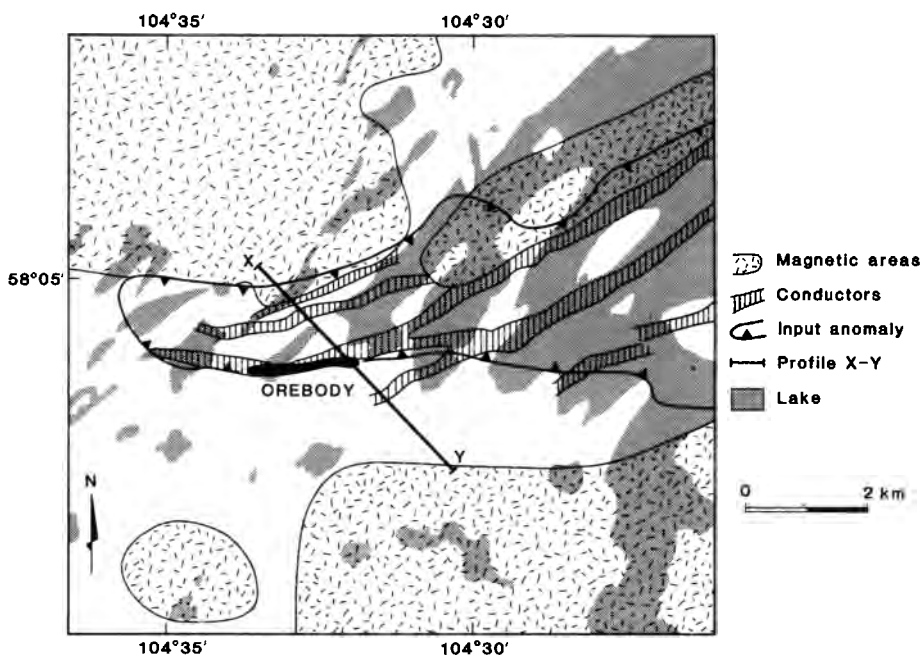


FIG. 37. Map of the Cigar Lake uranium deposit, Athabasca Basin, Saskatchewan, Canada. In addition to the orebody, which is 415 m below surface, magnetic areas, an Input AEM anomaly and Deepem conductors are depicted (after Fouques et al., 1986).

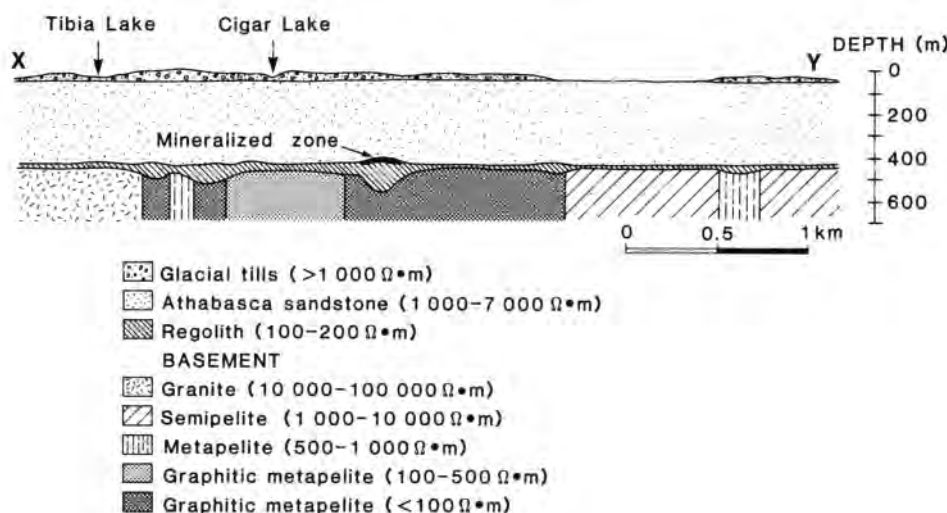


FIG. 38. Geologic section across the Cigar Lake uranium deposit (Line X-Y of Figure 42). Resistivities of the major lithologic units were estimated from CSAMT and Deepem surveys (after Fouques et al., 1986).

Figure 38 shows a geologic section (X-Y) with resistivity values interpreted from CSAMT (audio-frequency magnetotelluric) measurements (Fouques et al., 1986). While the values interpreted over till, Athabasca sandstone, and granite are consistent with experience elsewhere, those related to regolith and metapelites are based only on local data. It is virtually impossible to distinguish the EM effect of clay thickening from an increase in graphite content in metapelites because resistivities of both materials are very close. The high-grade orebody (12.2 percent  $U_3O_8$ ) is formed mostly by pitchblende which replaced the kaolin matrix. In addition to uranium, nickel and cobalt mineralization is present.

Saracoglu et al. (1983), Wallis et al. (1984), and Jagodits et al. (1986) described the McClean orebody, its discovery, geology, and geophysical surveys. Other geophysical and geochemical surveys in the Athabasca test area, which is centered on the McClean deposit, were described in a special volume (Cameron, 1983). The deposit consists of several mineralized pods, ranging from 135 500 t of ore at 2.54 percent  $U_3O_8$  (Pod 1) to 5 600 t at 0.35 percent  $U_3O_8$  (Candy Lake). The pods are aligned in two zones, McClean North and McClean South (Figure 39). AEM anomalies were associated with both zones and ground EM surveys were extensively used in their exploration (Jagodits et al., 1986). Unlike the deep Cigar Lake deposit (420 m), ground EM techniques could separate the effect of clays in the regolith and fracture zones ("electrolytic" conductors) from that of graphitic metapelites. Typical resistivity values are given in Figure 39. The McClean deposits lie below 150 to 180 m of resistive Athabasca sandstones ( $1000-7000 \Omega \cdot m$ ). Both case histories indicate that the penetration of AEM systems is greater than thought previously (over 400 m in the case of Cigar Lake orebody). The important implication is that the technique can be effectively used to outline deep flat-lying conductors such as paleoweathered layers where the overlying medium is resistive.

#### Bauxite deposits

Bauxite is formed by intense chemical weathering and leaching under tropical conditions. An important condition for its formation is a progressive lowering of the water table which results in the leaching of saprolite (Butt, 1982). Figure 20 shows a weathering profile with

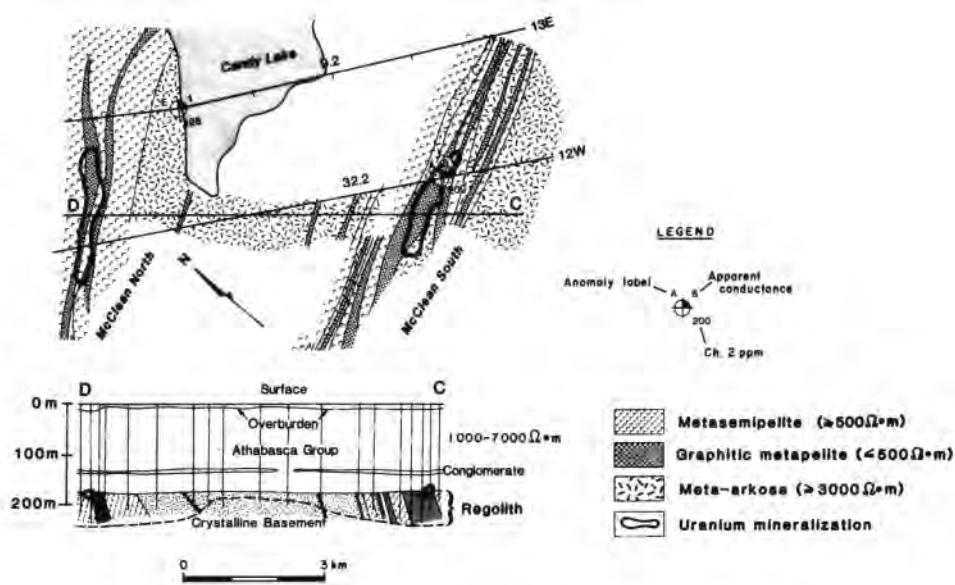


FIG. 39. Geologic map and section of the McClean uranium deposits, Athabasca Basin, Saskatchewan, Canada. Resistivities of the major lithologic units were estimated from ground EM and resistivity surveys (after Questor Surveys, 1984).

an increasingly prominent leached zone. A bauxite deposit is formed when this zone becomes rich in aluminum oxides and depleted in iron and silica. The parent rock is rather unimportant in bauxite formation and economic deposits are known to exist over various lithologic types. Bauxite ore can range from hard to soft and from dense to porous. The composition may vary substantially, but the ore is by definition within the following limits: 40 to 60 percent  $Al_2O_3$ , 1 to 10 percent  $Fe_2O_3$ , and 2 to 10 percent  $SiO_2$ .

Bauxite deposits may occur in several forms (Greig, 1970):

- (1) Extensive blankets or dome-shaped bodies on topographic highs between drainage systems (deposits in Malaysia, Brazil, and Australia).
- (2) Residual deposits on karsted limestone surfaces (Jamaica and Istria-Yugoslavia).
- (3) Secondary deposits resulting from erosion and redeposition of the first or second type (Arkansas-USA and Guinea).
- (4) Buried deposits resulting from the burial of any of the previously described types, a deposition of new sediments at their top, and possibly subsequent tectonic deformation. The deposits can be uplifted and partially eroded (France, Hungary, Dalmatia-Yugoslavia, and Guyana).

The applicability of EM methods depends on the deposit type. Their use would not be economically justified in the first case, because the deposits are virtually outcropping. The weathering profile of bauxite deposits does not significantly differ from that of nonmineralized rocks. The leached zone is generally not highly conductive (hundreds of  $\Omega \cdot m$ ). In karst areas, the contrast between bauxite and limestone should be sufficient to allow their identification. If such bauxite accumulations are buried under sediments (Case 4), EM techniques can be used as an effective exploration tool but it appears that such application has not been frequent in Western countries (Greig, 1970).

In Hungary, geophysical techniques have been used in bauxite exploration since 1933 (Kilényi and Szabó, 1985). Bauxite deposits are concentrated in the Bakony Hills, north of Lake Balatón. The ore is usually found in karstic depressions and sinkholes in Upper Triassic formations which are covered by Tertiary and Quaternary sediments. The resistivity contrast

(bauxite 100–200  $\Omega \cdot \text{m}$ , dolomite 2 000–5 000  $\Omega \cdot \text{m}$ ) usually permits identification of even minor pockets of bauxite. The selection of the technique depends on the thickness and conductivity of overlying sediments. When the overburden is thin, VLF surveying was found to be the most cost-effective approach. Figure 40 shows a VLF resistivity map from the Pápavár area, 40 km south of Györ. All holes drilled over low resistivity anomalies (less than 400  $\Omega \cdot \text{m}$ ) resulted in bauxite ore discoveries. Even though the reserves are small (usually around 100 000 t per pod), they can be mined economically. Holes drilled in areas of higher resistivity (around 800  $\Omega \cdot \text{m}$ ) were negative.

A direct detection of bauxite under 50 to 200 m thick sediments is difficult, but deep-penetration EM systems have been successfully used in Hungary. The application of a combination of geophysical methods is effectively used to map the basement relief. Bauxite bodies are known to be frequently associated with geomorphological features, such as grabens and terraces. Figure 41 shows a conductance map compiled from results of galvanic resistivity profiling. The Bakonyjákó horst north of Lake Balatón is bounded by subvertical faults, which are accurately outlined by conductance contours (12.5 S). On the downthrust sides, the thickness of sediments exceeds 300 m and bauxite deposits, even if found there, could not be profitably mined. Prospective targets are anomalies of higher conductance (10 S) on the horst.

### Lateritic nickel deposits

About half of the world production of nickel comes from lateritic deposits, which result from weathering of ultramafic massifs and accumulation of nickel in saprolite. World-class orebodies are in production in New Caledonia, Indonesia, Cuba, Colombia, and the Dominican Republic. Unfortunately, little has been published about electric properties of these deposits. Geophysicists have not paid much attention to this deposit type (Dowsett, 1970).

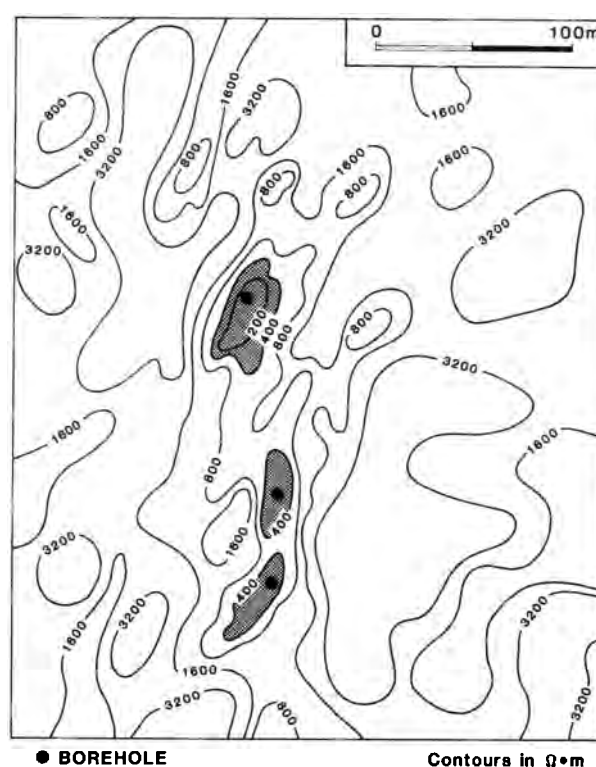


FIG. 40. Apparent resistivity map compiled from VLF data of the Pápavár bauxite deposits, Hungary. Solid circles indicate positive boreholes in which ore-grade bauxite was found (after Kilényi and Szabó, 1985).

Recently, Peric (1981) discussed the use of resistivity techniques at the Musangati deposit in Burundi; and reference to his work was made in the Weathered Layer section. Figure 25 shows resistivity logging data and also the nickel content, which reaches economic values in saprolite.

Identification of conductive saprolite layers was found to be the key to prospecting for nickel-rich zones. Geophysical data suggest that areas of high conductivity (over 400 mS/m) are rich in nickel (Figure 42). Investigation of anomalies with conductance over 2 S revealed saprolite layers over 30 m thick. Economic nickel concentrations are located primarily on slopes. At plateaus, the weathered layer is thick, but it consists mostly of ferralite, which is leached of nickeliferous minerals. The nickel grades at Musongati deposit range from 1 percent to 6 percent Ni and the indicated reserves at 90 Mt with average 1.5 percent Ni at 0.8 percent cut-off. In principle, EM surveys can be used in prospecting for saprolite nickel deposits, but not all lateritic deposits have the same characteristics, i.e., saprolite being the richest nickel zone. As Butt (1982) mentioned, under certain circumstances nickel can be reprecipitated in the leached zone.

### Kimberlites

In southern Africa, Australia, and the USSR, kimberlite pipes are an important source of diamonds. Kimberlite structures, which are circular, elliptical, or linear, resulted from an explosive breakthrough, usually at an intersection of crosscutting fractures or dikes. Kimberlite is an ultramafic igneous rock which easily weathers. In southern Africa, fresh pipe rock is given the name "hardebank," and the overlying weathered zones are called "blue ground" and "yellow ground." The upper yellow ground is rich in clays, particularly montmorillonite, which is conductive. The use of geophysical techniques in kimberlite exploration was reviewed in Gerryts (1970), Macnae (1979), and Kamara (1981). Kimberlites usually

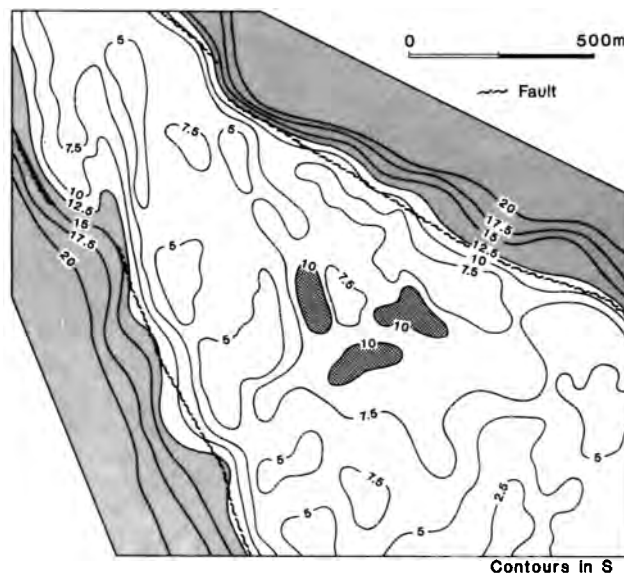


FIG. 41. Conductance map of the Bakonyjákó Horst, Hungary, which appears resistive. Conductive pockets on the horst have bauxite potential. The map was compiled from central gradient resistivity surveys (after Kilenyi and Szabó, 1985).

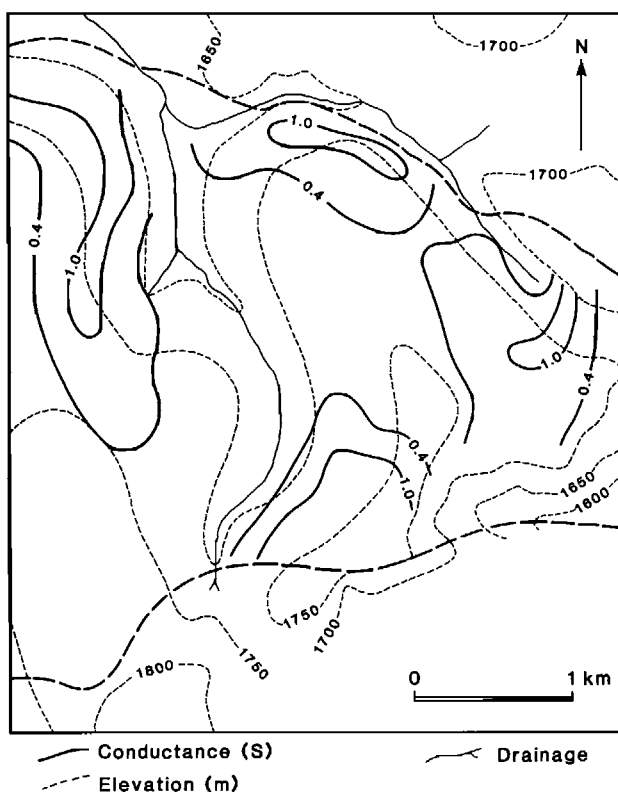


FIG. 42. Conductance map of the Musongati massif, Burundi. Values over 0.4 S indicate a well developed saprolite horizon with high nickel potential. The map was compiled from resistivity sounding data (after Peric, 1981).

contain magnetite and ilmenite, and traditionally magnetic surveys have been the most widely used exploration method. In southern Africa and Australia, where weathering is intense, its effectiveness has often been reduced and several pipes with no magnetic signature have been described. In such circumstances, AEM would appear a more suitable technique because it is able to map the conductive yellow ground. Johnson and Seigel (1986) showed the responses of three kimberlite pipes in Tanzania (Figure 43). While all three pipes produced strong AEM responses (conductivities between 160 and 320 mS/m), only two of them had associated magnetic anomalies. Macnae (1979) showed several examples of Input AEM and horizontal-loop EM responses from southern Africa. He concluded that joint AEM and magnetic surveys are the most cost-effective way to detect kimberlite in weathered terrains.

#### Mapping of lineaments

The weathering process advances faster along zones where the parent rock is fragile, e.g. shears, fractures, and lineaments. If there is no lithologic or topographic variation in weathering patterns, such zones can be easily detected by resistivity or EM techniques. A knowledge of shear and fracture zones is important in geotechnical studies, groundwater exploration, and mineral exploration. What makes lineaments more conductive is the presence of water-saturated clays resulting from weathering or hydrothermal activity, and increased fracture porosity.

In shield areas in western Africa, shear and fracture zones constitute locally important

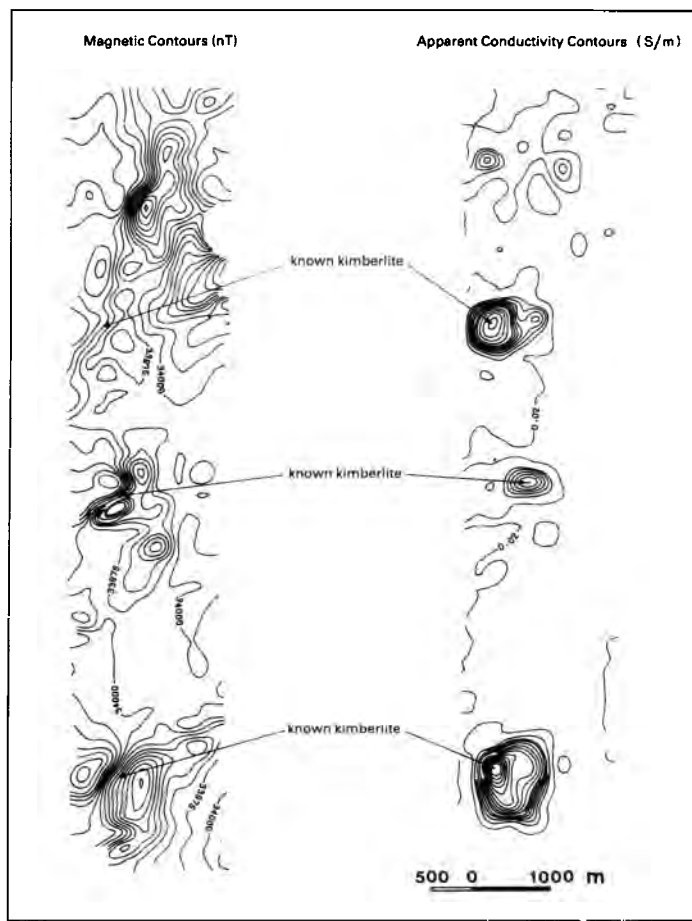


FIG. 43. Magnetic and apparent conductivity map of an area in Tanzania with three known kimberlite pipes. The maps were compiled from Tridem airborne geophysical data (after Johnson and Seigel, 1986).

aquifers. Their yield is usually modest ( $0.5$  to  $5 \text{ m}^3/\text{hr}$ ), but such aquifers may be the only source of water in the semiarid regions of Sahel and the adjacent savannahs. Palacky et al. (1981) and de Jong et al. (1981) published case histories from Burkina Faso, where horizontal-loop EM, VLF, and resistivity techniques were applied successfully in the search for groundwater. Some aid programs had as their aim the detection of small aquifers near existing villages, others were conceived to outline areas with abundant groundwater where new settlements could be established.

Figure 44 is an example of a survey in an area underlain by granite and gneiss near Rapanama, 50 km east of Ouagadougou, the capital of Burkina Faso. The weathered layer is about 10 m thick. Its average resistivity ( $70 \Omega \cdot \text{m}$ ) has been determined by numerous resistivity soundings. Apparent resistivity along the profiles is about  $1000 \Omega \cdot \text{m}$ , but decreases to less than  $500 \Omega \cdot \text{m}$  over fracture zones, where the weathered layer thickens. Such zones can also be detected by VLF surveys, on which lineaments are characterized by crossovers anomalies.

Resistivity and EM responses are different over volcano-sedimentary sequences. Figure 45 illustrates resistivity and horizontal-loop EM survey over an amphibolite sequence. Even though the weathered layer is not much thicker than over granite, it is significantly more conductive. A resistivity range of 5 to  $15 \Omega \cdot \text{m}$  was determined by resistivity soundings over amphibolite in Burkina Faso and also in neighboring Mali (Engalenc, 1978). The conductive layer thickens in zones of tectonic weakness, causing a clearly identifiable minimum on

resistivity profiling data and trough-like anomalies on horizontal-loop EM data. On Figures 44 and 45, the location of water wells and their yield is given. An extensive drilling program confirmed the accuracy of interpretation of geophysical data, particularly the determination of the saprolite thickness and the location of fracture zones.

### Geothermal exploration

In the 1970s, a considerable effort in the USA and other countries was expended in geothermal exploration (Keller, 1978). Effective use of electric and EM methods (including telurics and audiromagnetotellurics—AMT) was made possible by increased porosity, high fluid temperature, and the presence of conductive clays formed by hydrothermal alteration. The high salinity of brines was also a very important factor. An area studied in great detail with a variety of geophysics techniques is Roosevelt Hot Springs (Ward et al., 1978). This KGRA (Known Geothermal Resource Area) is located near the eastern margin of the Basin and Range province, 19 km northeast of Milford, Utah, USA. Igneous activity occurred repeat-

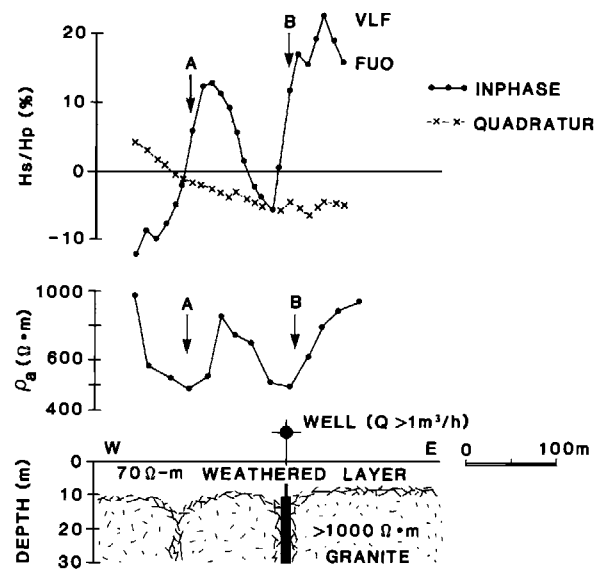


FIG. 44. Results of VLF surveys, resistivity profiling, and the corresponding geologic and resistivity section from soundings depicting fracture zones and weathered layer, Rapadama, Burkina Faso (after Palacky et al., 1981).

edly in the area during the last 30 Ma. The last major events comprise two rhyolite flows (about 0.8 Ma old, 3 km long and 80 m thick) and 10 rhyolite domes (300 m to 1 km in diameter and 250 m in height, dated 0.6–0.5 Ma). A few kilometers distant hot spring deposits consist of horizontally bedded siliceous sinter.

Hydrothermally altered Tertiary granites and alluvia have been investigated by means of shallow drill holes in the Roosevelt Hot Springs area. Clays show a distinct zonation: alunite, which predominates the near surface (2–9 m), is followed by kaolinite (9–18 m), and montmorillonite (20–35 m). With the exception of alunite, the zonation is strikingly similar to the distribution of clays found in a weathering profile. Hydrothermal alteration is closely associated with deep fractures. Clay minerals, primarily montmorillonite, occur to a depth of 500 m. The deeper alteration assemblage (500 m to 2 km) consists of chlorite, K-mica, K-feldspar, calcite, and pyrite (Ward et al., 1978).

Tripp et al. (1978) carried out extensive resistivity and EM surveys (including MT and AMT) in the Roosevelt Hot Springs area. A map of apparent resistivity contours obtained

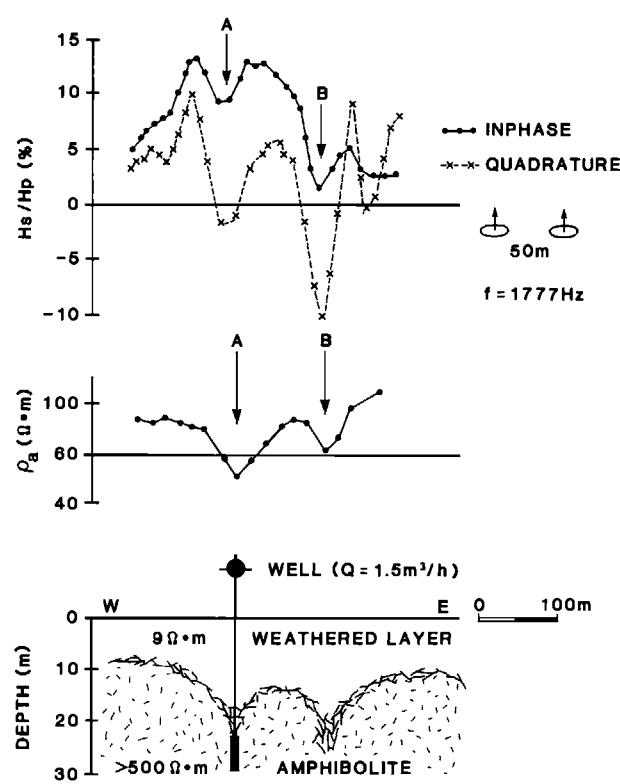


FIG. 45. Results of horizontal-loop EM surveys, resistivity profiling, and the corresponding geologic and resistivity section from soundings depicting fracture zones and weathered layer, Mankarga, Burkina Faso (after de Jong et al., 1981).

with a dipole-dipole array (100 m separation) is shown in Figure 46. The Hot Springs are enclosed by contours of low resistivity (about  $15 \Omega \cdot \text{m}$ ). The Early Steam Well and all subsequently drilled productive wells are also in areas of low resistivity. An east-west pseudo-geologic section, which was compiled in Tripp et al. (1978) on the basis of resistivity data, is depicted in Figure 47. The major components are two fracture zones of low resistivity ( $5 \Omega \cdot \text{m}$ ), where highly conductive brine-saturated clays (mostly montmorillonite) occur. Water-saturated clays of the altered zone are also conductive ( $12 \Omega \cdot \text{m}$ ). Their high conductivity was explained by brine leakage from a geothermal vent. Relatively high resistivity ( $300 \Omega \cdot \text{m}$ ) was interpreted for unaltered granite (in reality, the true resistivity is probably higher). The

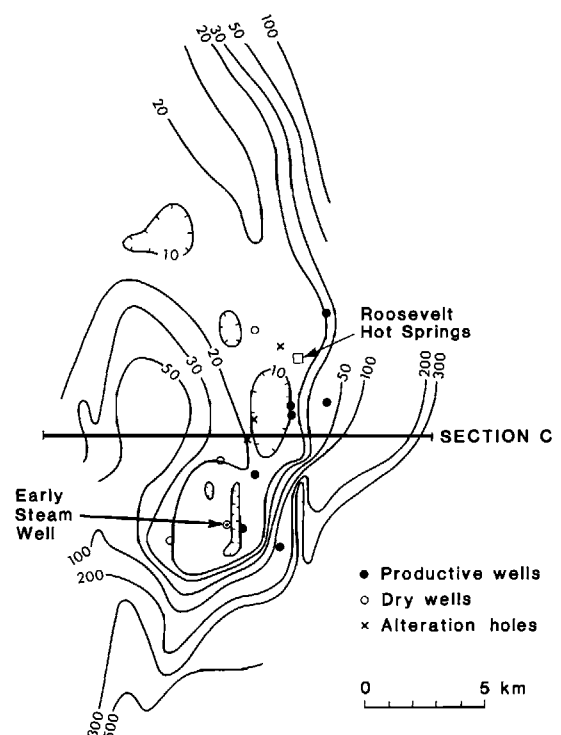


FIG. 46. Apparent resistivity map of the Roosevelt Hot Springs area, Utah, USA, compiled from dipole-dipole surveys (after Ward et al., 1978).

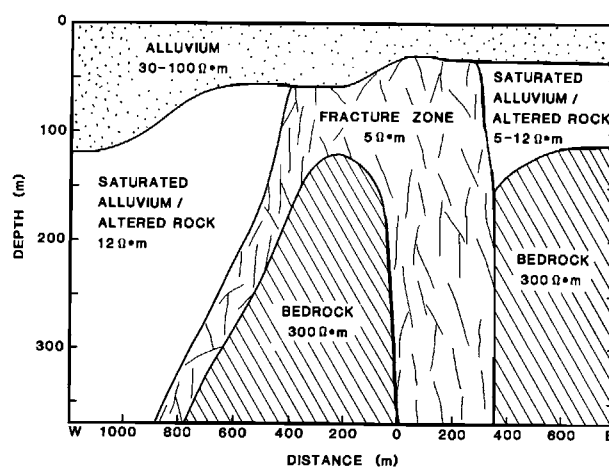


FIG. 47. Geologic interpretation of Section C (Figure 46) based on dipole-dipole resistivity surveys, Roosevelt Hot Springs, Utah, USA (after Tripp et al., 1978).

near surface alluvium had a resistivity varying from 30 to  $100 \Omega \cdot \text{m}$ .

Resistivity techniques were also used in Harthill (1978) to investigate geothermal fields in the Imperial Valley, California. Hoover et al. (1978) used AMT surveys in 40 geothermal areas in western USA and Alaska. More recently, Hoover and Pierce (1986) described the use of AEM systems in mapping of hydrothermal systems in Nevada and California. Figure 48 shows a resistivity map obtained with the Dighem helicopter AEM system operating at 900 Hz in Lassen National Park, California. In the map, four areas with resistivities less than  $1000 \Omega \cdot \text{m}$  are visible. Three of the areas have hot springs, and near the hot springs resistivity drops to  $30 \Omega \cdot \text{m}$ . The map clearly defines structures with which thermal activity is associated. A good correlation was found between the results of helicopter EM and AMT surveys.

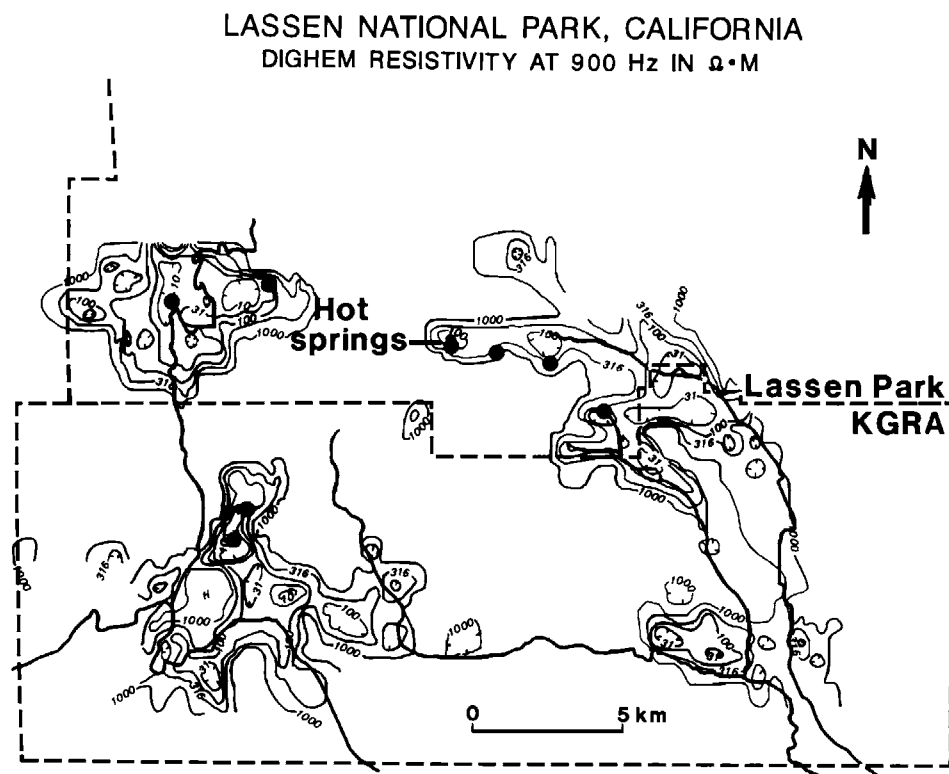


FIG. 48. Apparent resistivity map of Lassen National Park geothermal area, California, USA, compiled from horizontal-coplanar helicopter AEM data at 900 Hz (Dighem II). Only resistivities below  $1000 \Omega \cdot \text{m}$  were contoured (after Hoover and Pierce, 1986).

## Unconsolidated Sediments and Sedimentary Rocks

Resistivity of unconsolidated sediments and sedimentary rocks varies from 0.5 to over 100 000  $\Omega \cdot \text{m}$ , mostly as a function of their water and clay content. Because of their porosity unconsolidated sediments are more conductive than sedimentary rocks (Table 5). Among the former, sand and gravel can be resistive, if their water saturation is low or their pore fluid resistive. Argillite, shale, and slate, which are formed by consolidation of clay-rich substances, are moderately conductive. Conglomerate, sandstone, greywacke, dolomite, and limestone are generally resistive (average resistivity 1 000  $\Omega \cdot \text{m}$ ). Lignite and coal span virtually the whole range (1–200 000  $\Omega \cdot \text{m}$ ).

EM methods have been used in determining the thickness of unconsolidated sediments. In sedimentary basins, high-power EM sounding and magnetotelluric (MT) techniques have been used, even though on a rather limited scale. Most of the information on in-situ resistivities originates from well-logging. Frequent alternation of sandstone and shale, which is typical of many sedimentary areas, is difficult to resolve from the surface by EM techniques, but is the kind of information required in oil prospecting. In this section unconsolidated sediments, which are frequently of glacial or glaciolacustrine origin, will be treated first. A world map (Figure 49) depicts localities where the case histories mentioned here originated.

### Unconsolidated sediments in glaciated terrains

Extensive Quaternary glaciation of the northern parts of Europe, Asia, and North America resulted in deposition of a wide variety of unconsolidated sediments. Nonsorted, nonstratified

Table 5. Resistivities of sedimentary rocks

Unconsolidated	Range ( $\Omega \cdot \text{m}$ )
Clay	5–150
Gravel	480–900
Loam	20–160
Loess	25–40
Marl	12–70
Sand (valley)	360–1 500
Sand (dunes)	6 200–7 700
Glacial silt	13–20
Consolidated	
Argillite	74–840
Conglomerate	2 000–13 000
Dolomite	700–2 500
Greywacke	400–1 200
Limestone	350–6 000
Sandstone	1 000–4 000
Shale	20–2 000
Slate	340–1 600
Coal	1–200 000

Source: Angenheister (1982)

glacial sediments are termed tills. Because of their heterogenous composition (gravel, sand, clay), their resistivity can vary substantially, but usually stays within 50 to 2 000  $\Omega \cdot \text{m}$ . Because till filled topographic depressions first, its thickness can vary substantially even over short distances. Drumlins, eskers, and kames are accumulations of gravel and sand which can reach a height of 50 m. Drumlins are unstratified, and their long axis parallels the former flow of the glacier. A kames is a low, steep-sided hill of stratified drift formed in contact with glacier ice. An esker shows rude stratification and has the general direction of the drainage. Figure 50 is a sketch of glacial deposition. Extensive clay layers formed in the lakes after glaciers retreated. Soil layers developed in many areas during the present interglacial period. A sequence of tills and glaciolacustrine clays can be repeated several times reflecting various glacial periods.

Local accumulations of gravel may be used as a source of construction material. Resistivity and EM surveys have been used for their detection (Culley, 1973). In southern and central Saskatchewan, Canada, gravel deposits are usually covered by 0.3 to 3 m thick layer of unsorted tills. While in-situ resistivities of till range from 20 to 100  $\Omega \cdot \text{m}$ , those of gravel are in excess of 1 000  $\Omega \cdot \text{m}$ . Gravels are underlain by conductive glacial silt and till.

Palacky and Jagodits (1975) described interpretation of E-Phase® airborne resistivity surveys near Wadena, Saskatchewan (260 km east of Saskatoon). The AEM system, which is measuring the electric field at frequencies in the 15 kHz to 1 MHz range, has been used for detection of resistive inhomogeneities. Figure 51 depicts apparent resistivities calculated from the AEM data at 3 frequencies (VLF—15 to 25 kHz, LF—200 to 400 kHz, BCB—500 to 1 000 kHz), two resistivity logs obtained by their interpretation, and 5 drilling logs. Resistivities of 40, 1 000, and 10  $\Omega \cdot \text{m}$  were assumed as being typical of overburden till, gravel, and basal silt, respectively. The results of shallow auger drilling agree fairly well with the thicknesses interpreted from the AEM data. Figure 52 is a map of a portion of the surveyed area near Wadena. The profile of Figure 51 is line 47, which crosses an extensive area of

®Registered trademark of Barringer Research Ltd.

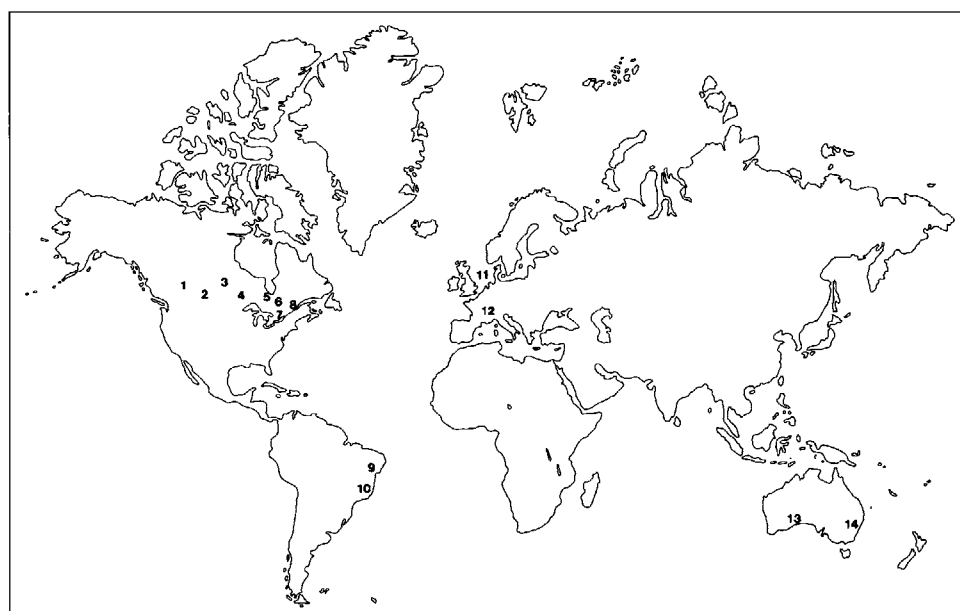


FIG. 49. Location of sites described in the section Unconsolidated Sediments and Sedimentary rocks (*Canada*: (1) Edmonton, Alberta, (2) Wadena, Saskatchewan, (3) Whiteshell, Manitoba, (4) Atikokan, Ontario, (5) Onakawana, Ontario, (6) Val Gagné, Ontario, (7) Kitchener, Ontario, (8) Alfred and Hawkesbury, Ontario; *Brazil*: (9) Cocolobó, Bahia, (10) Canavieiras, Bahia; *Europe*: (11) North Sea, (12) Sennecey, France; *Australia*: (13) Esperance, Western Australia, (14) Sydney Basin, New South Wales).

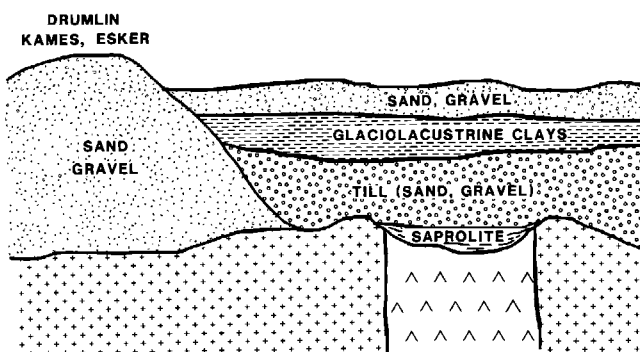


FIG. 50. Schematic geologic section of glacial sediments and basement. Glaciolacustrine clays and saprolite are conductive.

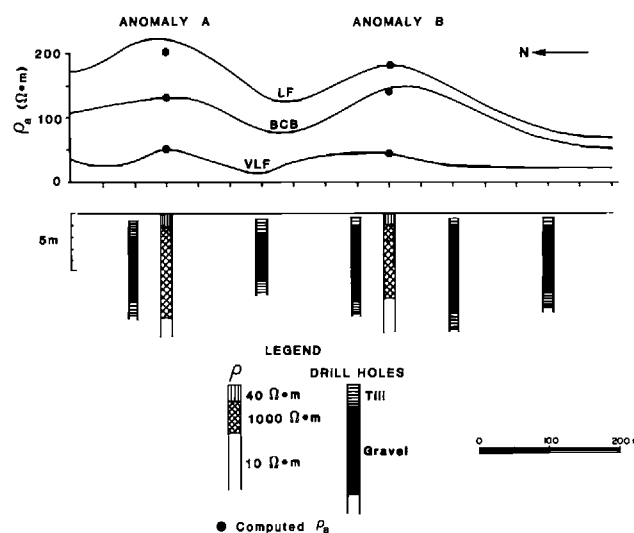


FIG. 51. Apparent resistivity profiles calculated from E-Phase AEM data at 3 frequencies (VLF – 18.6 kHz, LF – 368 kHz, BCB-600 kHz), line 47, survey near Wadena, Saskatchewan, Canada. The vertical columns depict logs of drill holes and results of quantitative interpretation of anomalies A and B (after Palacky and Jagodits, 1975).

high apparent resistivity (over 100  $\Omega \cdot m$ ). The map was compiled from the medium-frequency data (368 kHz). The LF transmitter was about 50 km west of the survey area. There were several other isolated spots of high apparent resistivity, but generally the area was moderately conductive (less than 50  $\Omega \cdot m$ ).

After retreat of glaciers, lakes were commonly formed in which predominantly clayey glaciolacustrine sediments were deposited. In Canada, highly conductive clay layers resulted from sedimentation in the ancient Lake Agassiz in Manitoba, Lake Champlain near Ottawa, Lake Ojibwe-Barlow in Ontario-Québec, and many other localities. Prior to the introduction of wide-band EM systems, such conductive clay sediments seriously hampered exploration for massive sulfides in the highly prospective Abitibi greenstone belt. Geochemical till sampling is a useful tool of base and precious metal exploration, but its success depends on accurate identification of ancient valleys. Under favorable conditions EM methods can be used for bedrock topography mapping.

AEM methods have been successfully applied to detect buried valleys near Matheson, Ontario, Canada (Pitcher et al., 1984). An area of 3 550 km<sup>2</sup> was covered using the Input

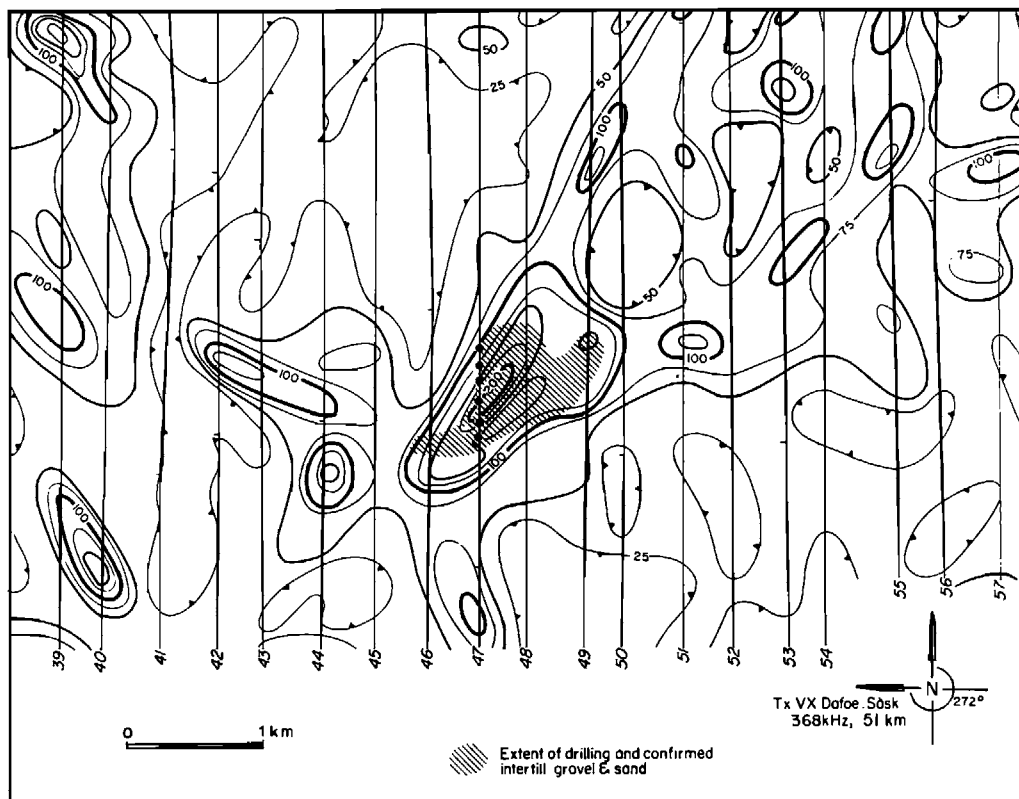


FIG. 52. Apparent resistivity map compiled from E-Phase AEM data at 368 kHz, survey near Wadena, Saskatchewan. Shaded area outlines the extent of a gravel deposit (after Palacky and Jagodits, 1975).

AEM system on a 200 m spaced, north-south line grid. The BRIM (Black River-Matheson) area stretches between Shillington (40 km east of Timmins) and the Québec border. The glacial sequence comprises eskers, kames, deltas, and ice-retreat glaciolacustrine sediments, including sequences of varved and massive silty clays. Detailed follow-up work has been carried out over Input anomalies which were attributed to thickening of glaciolacustrine clays (Barlow and Krentz, 1984). In test areas the conductivity of clays was found to be remarkably constant (mean  $37.2 \pm 3.5$  mS/m). Assuming constant conductivity values, Pitcher (1985) was able to calculate the thickness of the clay cover. His determinations were largely confirmed by drilling.

Geophysicists from the Geological Survey of Canada carried out a number of resistivity soundings near Val Gagné, Ontario in an area which has been designated as an AEM test site. Figure 53 depicts a resistivity section which was obtained by computer inversion of sounding data. In agreement with observations made by Barlow and Krentz (1984), the resistivity of clays was found fairly uniform (between 27 and 40  $\Omega \cdot \text{m}$ ). The clay thickness varied from 15 to 30 m in the area under investigation but increased to 30–50 m in buried

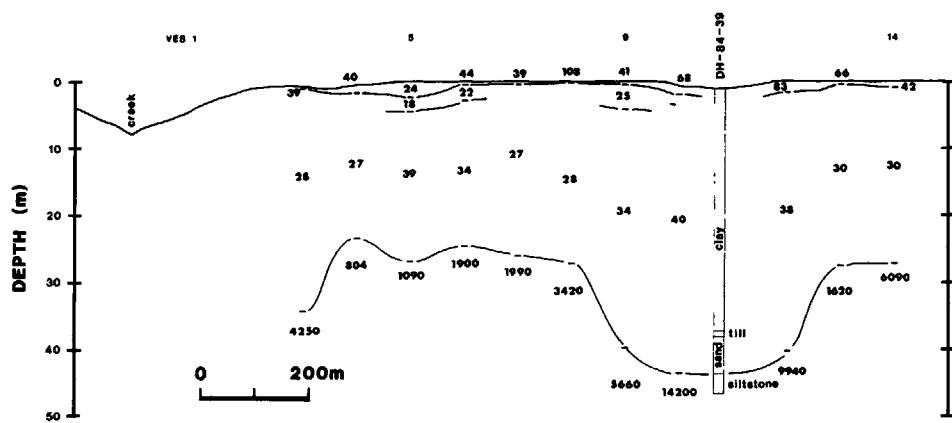


FIG. 53. Resistivity section at the Val Gagné test site, Ontario, Canada, obtained by interpretation of sounding data. As the log of drill hole DH-84-39 indicates, the conductive layer is formed by glaciolacustrine clays. Resistivity values in  $\Omega \cdot \text{m}$ .

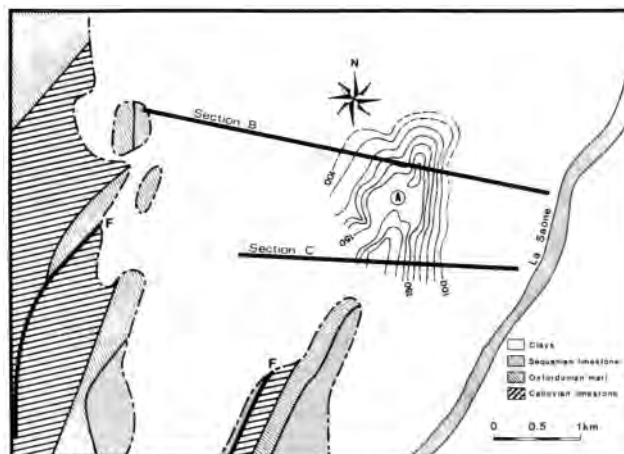


FIG. 54. Geologic map of the Sennecey test site, France. Contours indicate the elevation of the limestone horst above the mean sea level (The mean elevation of the area is 200 m). F – faults, A – horst (after Deletie and Lakshmanan, 1986).

valleys. As the log of the drill hole DH-84-39 shows, tills and sand were found at the valley bottom. Because of a limited till thickness, the clay-till interface could not be identified on this resistivity profile. Drilling confirmed a clay thickness of 36 m and depth to bedrock of 44 m.

Several attempts have been made in Canada to map conductive clays from the air and to investigate in-situ electrical properties of glacial sediments. Sinha (1980) performed 62 resistivity soundings near Alfred, Ontario, 65 km east of Ottawa. The near-surface layer consists of soil and sand of variable thickness (from zero to 25 m) and resistivity (from 20 to  $50 \Omega \cdot \text{m}$ ). This layer is underlain by highly conductive Champlain clays of Quaternary age, whose thickness varies from zero to 100 m. The resistivities determined by soundings were fairly consistent, between 1 and  $4 \Omega \cdot \text{m}$ , about one order of magnitude less than the previ-

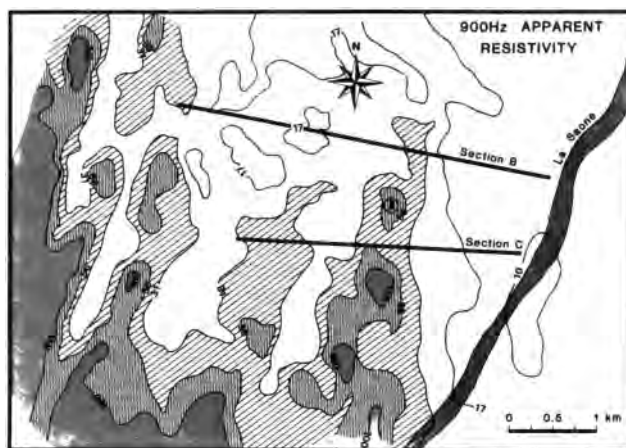


FIG. 55. Apparent resistivity map of the Sennecey test site, France, compiled from horizontal co-planar helicopter AEM data at 900 Hz (after Deletie and Lakshmanan, 1986).

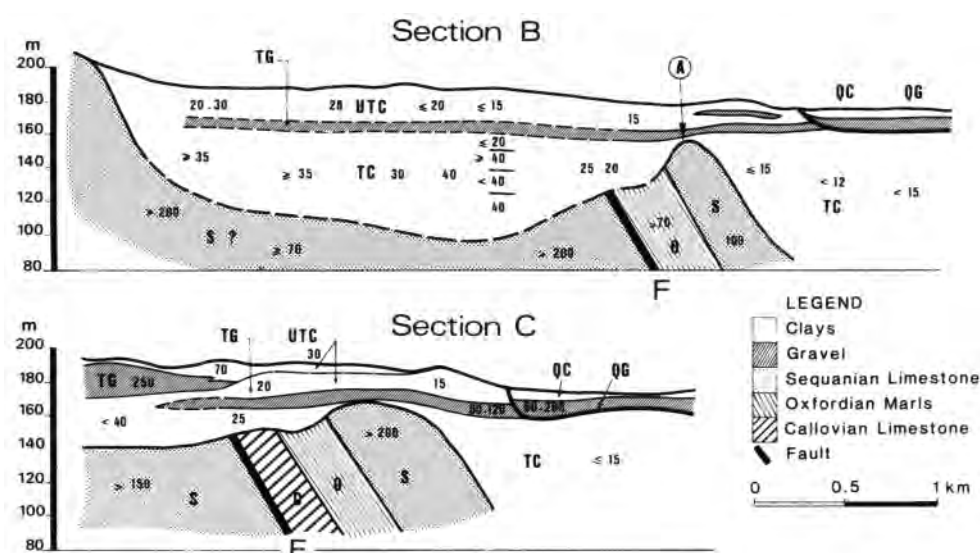


FIG. 56. Geologic sections B and C across the Sennecey test site, France. Letters indicate age of the clays (QC, Quaternary; UTC, Upper Tertiary; TG, Tertiary). F – fault, A – horst. Numbers indicate resistivities (in  $\Omega \cdot m$ ) interpreted from sounding data (after Deletie and Lakshmanan, 1986).

ously described Abitibi clays. Paleozoic limestone, shale, and sandstone, which underlie the clays, were found resistive. The Alfred/Hawkesbury area was used for the first tests of airborne resistivity mapping (Dyck et al., 1974, Seigel and Pitcher, 1978). Apparent conductivities of clays estimated from the Tridem AEM data range between 200 and 1 000 mS/m (corresponding to resistivities of 1–5  $\Omega \cdot m$ ), showing excellent agreement with the ground resistivity data. Input AEM surveys indicate 500 mS/m as the average clay conductivity.

AEM methods have been used by the Atomic Energy of Canada Ltd. (AECL) to map the thickness of glacial sediments and to identify lineaments as a part of the nuclear fuel waste management program. Results have been described in Paterson and Reford (1986) from the East Bull Lake research area near Massey, Ontario, and in Soonawala and Hayles (1986) from the Atikokan, Ontario, and Whiteshell, Manitoba, research areas.

### Nonglacial unconsolidated sediments

Mapping of the thickness and composition of unconsolidated sediments has an important application in geotechnical studies and groundwater exploration. Deletie and Lakshmanan (1986) described the use of resistivity soundings and AEM methods in site investigation for nuclear power plants in France. The Sennecey site is located in the Saône valley, about 90 km south of Dijon. Jurassic limestone and marl outcrop in the Burgundy Hills (west on the geologic map in Figure 54) and in a north-northeast to south-southwest striking horst, which plunges to the north. The horst was mapped as an area of high apparent resistivity by soundings along profiles B and C (as indicated in Figure 54). It was also clearly detected by helicopter AEM surveys (Dighem) carried out with a horizontal coplanar coil configuration. The apparent resistivity map (Figure 55) was compiled from the 900 Hz data. Moderately high resistivity values (over  $31 \Omega \cdot m$ ) were obtained over the horst, the Burgundy Hills, and in the southern part of the survey area. Conductive response was recorded over Quaternary and Tertiary clays, which were deposited by the Saône River.

Figure 56 depicts geologic sections B and C, which were compiled from the results of 50 holes drilled in the test area. Quaternary clay (QC) and Quaternary gravel (QG) outcrop near the Saône River (eastern portions in Sections B and C). Along most of the profiles, upper Tertiary clay (UTC) outcrops. Resistivities (also shown in Figure 56) were compiled from interpreted resistivity soundings. The UTC clay layer, which is approximately 20 m thick, is conductive (between 15 and  $30 \Omega \cdot m$ ). It is underlain by a 6 to 8 m thick resistive gravel layer ( $60$  to  $120 \Omega \cdot m$ ). The depressions in ancient topography were filled by Tertiary clay, which reaches a thickness of 60 m between the horst and the Burgundy Hills. Mesozoic basement appears much deeper east of the horst where the thickness of highly conductive clay (resistivity less than  $15 \Omega \cdot m$ ) is greater than 100 m. Both limestone and marl were found resistive (more than  $150 \Omega \cdot m$ ). The case history demonstrates the usefulness of AEM methods in qualitatively mapping bedrock topography. A complicating factor is the heterogeneity of unconsolidated sediments, which consist of clay and gravel.

Another example of mapping unconsolidated sediments by resistivity soundings is from Canavieiras, in the southern part of the Brazilian state of Bahia. Quaternary clay and sand were deposited in this coastal area at the top of Tertiary conglomerates. Leite (1975) described an application of geophysical methods to groundwater prospecting of coastal aquifers. Several shallow holes (from 30 to 60 m) were drilled at sites previously investigated by resistivity and seismic measurements (Figure 57). The water table in the area is shallow (less than 8 m), and the yield of wells is highly variable—over  $40 m^3/hr$  in the easternmost hole, but only  $2 m^3/hr$  in the westernmost hole, the two holes in the center having intermediate yields. Resistivity profiles did not show any variation that could be related to the change in water yield. Only one hole reached the resistive Tertiary conglomerate. The Quaternary clay layer, whose thickness varies between 20 and 40 m, is highly conductive (resistivities between 3 and  $10 \Omega \cdot m$ ). There is a resistivity interface between wet and dry sand, with a change from several thousand  $\Omega \cdot m$  to 100 to  $200 \Omega \cdot m$ . The example indicates that the water table in unconsolidated sand is detectable by resistivity and EM methods. EM techniques have had limited use in such applications, due to the traditional preference given by hydrologists to galvanic resistivity methods.

### Sedimentary rocks

Most resistivity determinations in sedimentary basins come from well-logging operations, usually performed in the course of oil and gas exploration, and less frequently from groundwater prospecting. Hydrogeologic studies using resistivity soundings and borehole measurements were carried out by Lima (1979) near Cocorobó, in the Mesozoic Tucano Basin, which extends northward from Salvador, the capital of the Brazilian state of Bahia. The results are interesting as they show the electric response of a weathered layer developed at the top of Mesozoic shale (Itaparica Formation). The 10 m thick saprolite layer has an even lower resistivity than the fairly conductive shale (both under  $20 \Omega \cdot m$ ). While shales are always characterized by low resistivities in the log (Figure 58), sandstones are moderately resistive (around  $300 \Omega \cdot m$ ). Sediments with intermediate clay content (shaly sandstone) have resis-

tivities between 100 and  $150 \Omega \cdot \text{m}$ . The results were obtained with a 162.5 cm normal logging tool (one current and one potential electrode in the hole). Resistivities clearly depend on lithology and are not affected by depth. Resistivity soundings were performed over outcrops of the three formations encountered in the hole (Itaparica Shale, Sergi Sandstone, and Aliança Shale). Both shale formations had similar resistivities, between 5 and  $20 \Omega \cdot \text{m}$ , which agreed with well-logging data. Sandstone, on the other hand, appeared more resistive on the sounding data (in excess of  $1200 \Omega \cdot \text{m}$ ) than in logging (around  $300 \Omega \cdot \text{m}$ ). No EM surveys were carried out.

Well-logging techniques used by the oil and gas industry are highly sophisticated and it is beyond the scope of this paper to even briefly describe this discipline of exploration geophysics. Only an example of oil-related resistivity well-logging will be given. Suau and Spurlin (1982) described interpretation of micaceous sandstone sequences in the North Sea. The goal of oil related well-logging is to determine lithology, to calculate porosity and water saturation, and to estimate the clay content. Global® is a new technique of computer-processed log interpretation used for describing lithology in terms of mineral content: clay, kaolinite, feldspar, mica, and sand. The geological sequence in Figure 59 consists of sandstone, shale, and shaly sandstone. Shale is characterized by a high clay content, sandstone consists mostly of sand. The two rock types also can be distinguished by their electric properties, shale is conductive (about  $5 \Omega \cdot \text{m}$ ) and sandstone is moderately resistive ( $50$ – $100 \Omega \cdot \text{m}$ ). The water-saturation log shows that clay-rich sediments are 100 percent saturated (the lower two shale layers). There is a clear correlation between resistivity, water saturation, and clay content. The shaly sandstone with a medium clay content is only 60 percent water saturated and is more resistive ( $15 \Omega \cdot \text{m}$ ) than shale. Accurate porosity estimation is essential in determining the potential of oil-bearing reservoirs.

During the last 20 years, deep time-domain EM soundings have been successfully used in mineral and hydrocarbon exploration in the USSR, and more recently also in the USA (Kaufman and Keller, 1983).

Strack (1984) described the results of a time-domain EM sounding experiment in the Sydney Basin, Australia. Data were interpreted to a depth of 2.5 km. From the surface, the first kilometer consisted of sandstone and shale of Triassic age. The average resistivity of the sediment rocks was  $32 \Omega \cdot \text{m}$  with a standard deviation of  $10 \Omega \cdot \text{m}$ . Despite the frequent alternation of conductive shales and resistive sandstones, this unit appeared fairly homogeneous on EM sounding data. The second layer, which could be clearly identified from EM measurements, is the 200 m thick Late Permian Illawara Coal Measures Group. This group,

® Trademark of Schlumberger.

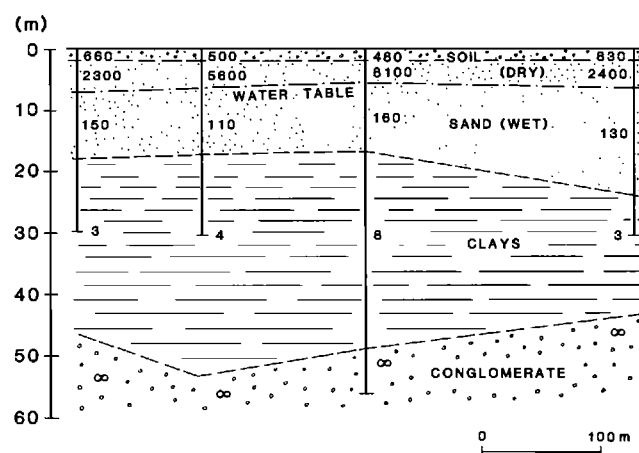


FIG. 57. Geologic and resistivity section of an aquifer at Canavieiras, Bahia, Brazil. Lithologic and hydrologic information from drilling. Resistivities (in  $\Omega \cdot \text{m}$ ) were obtained by interpretation of soundings (after Leite, 1975).

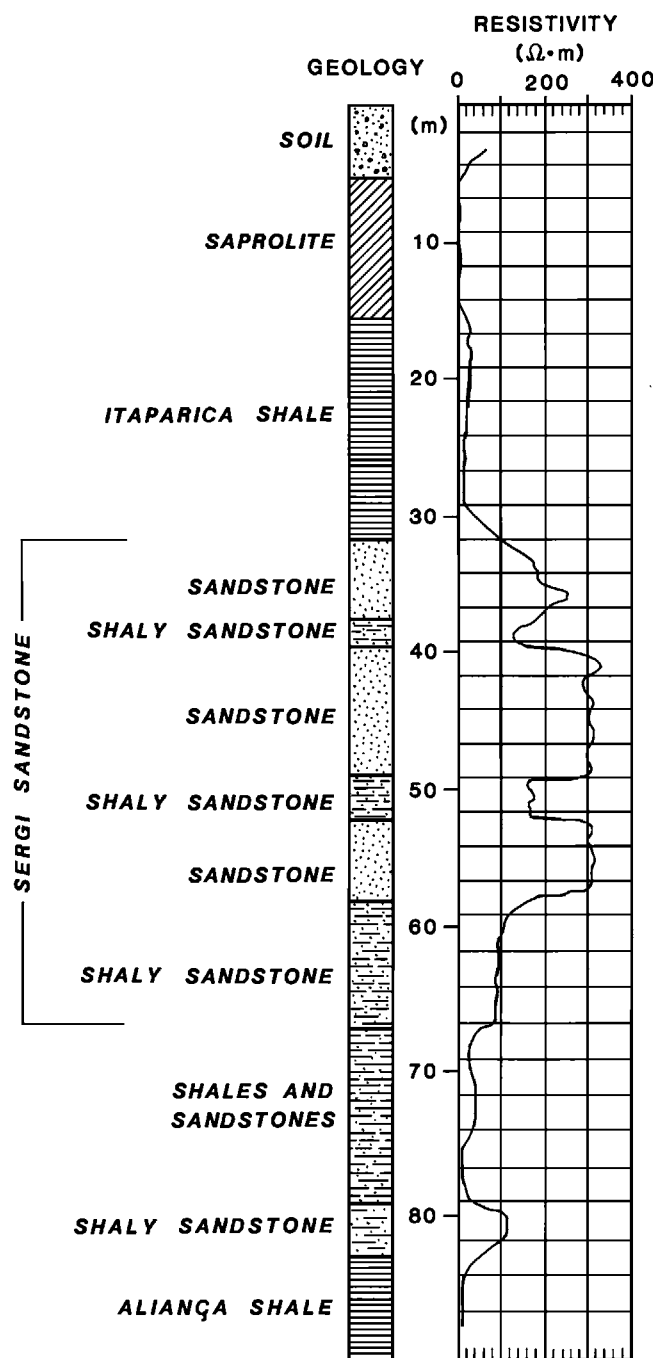


FIG. 58. Geologic and resistivity log of a drill hole at Cocomobó, Bahia, Brazil. The resistivity log was obtained with a 3-electrode array ( $AM = MN = 162.5$  cm), after Lima (1979).

named after its coal seam, is conductive (resistivity  $1.6 \Omega \cdot m$ ), probably because of the presence of carbonaceous shale. The underlying Shoalhaven group, which is of Permian age, consists of 200 m of sandstone and shale. An inversion of EM soundings indicated resistivity of  $53 \pm 3 \Omega \cdot m$ . The basement (Greta Coal Measures) could not be reliably resolved by EM soundings, but it appears conductive ( $2.5 \Omega \cdot m$ ). Conclusively, the method was successful in identifying the major geologic units. The typical sedimentary sequence consisting of shale and sandstone could not be resolved in its components (considering the scale of the system, this was not expected) and it appeared to have a resistivity value, which was about an average

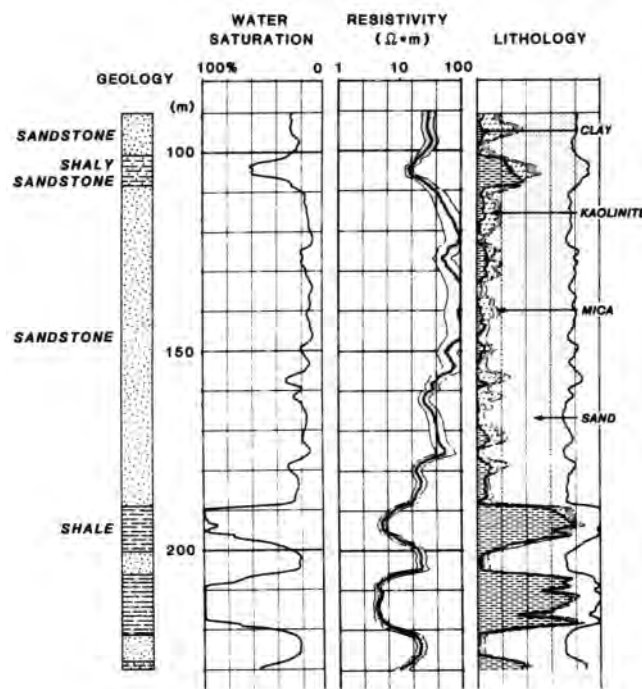


FIG. 59. Geologic, resistivity, and water saturation log of a portion of an oil well in the North Sea (after Suau and Spurlin, 1982). Global ® lithology log was obtained by computer data processing.

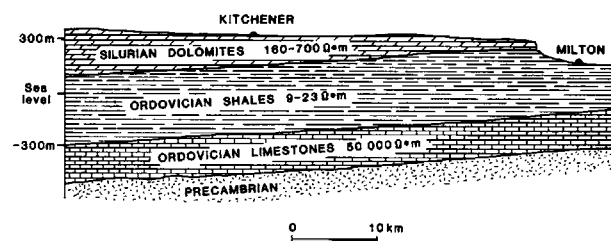


FIG. 60. Geologic section Kitchener-Milton in Southern Ontario, Canada. Resistivity values were obtained by interpretation of EM soundings (after Sinha et al., 1985).

of shale ( $10 \Omega \cdot m$ ) and sandstone ( $100 \Omega \cdot m$ ).

Sinha et al. (1985) used time-domain EM methods to investigate sedimentary formations in southern Ontario, Canada. Figure 60 depicts the geologic section Kitchener-Milton, along which 7 EM soundings have been carried out. Formations of Ordovician age (Queenston shale, Meaford-Dundas siltstone, Blue Mountain shale) appear conductive as a group but cannot be identified separately. Their resistivities ( $9$ – $23 \Omega \cdot m$ ) fall within the range observed over shale elsewhere. The shale formations are overlain by resistive Silurian dolomite ( $160$ – $700 \Omega \cdot m$ ) and underlain by even more resistive Ordovician limestone. The value of  $50\,000 \Omega \cdot m$  was obtained only at one location near Milton, where the thickness of the conductive shale is less than  $300 \text{ m}$ . At other sounding sites, the conductive Queenston shale was the last formation that could be reliably identified. The Precambrian basement, whose depth is known from drilling, could not be detected. As in the previous example from Australia, EM soundings were successful in identifying the major stratigraphic units, but could not be used for mapping of rock types, which vary within the individual units.

### **Coal and lignite prospecting**

The use of AEM systems in prospecting for lignite deposits has been described in Seigel and Pitcher (1978) and Whiting (1983), but in both cases the detection was largely indirect. The first case history is from Onakawana, which lies  $100 \text{ km}$  south of Moosonee, Ontario, Canada. A Quaternary clay layer filled the depression in which lignite was previously deposited. Both clay and lignite are conductive (resistivities  $30$  to  $50 \Omega \cdot m$ ) and thus could be identified in an area covered mostly by Quaternary till of medium apparent resistivity ( $100 \Omega \cdot m$ ).

The second case history (Whiting, 1983) describes the use of Input AEM in outlining depressions in Precambrian basement, in which lignite was deposited during the Tertiary. The deposits are located  $45 \text{ km}$  north of Esperance, Western Australia. The surficial clay layer has a resistivity of only  $0.5 \Omega \cdot m$  and a thickness varying from  $10$  to  $60 \text{ m}$ , depending on the Precambrian topography. Lignite, which is found at the bottom of paleovalleys, is less conductive than clay, but no accurate resistivity determinations were made.

In both cases the AEM methods located depressions filled with conductive, unconsolidated clay at the top and lignite at the bottom. Laboratory studies of resistivities made by various researchers indicated a range of  $9$  to  $200 \Omega \cdot m$  for lignite,  $160$  to  $150\,000 \Omega \cdot m$  for coal, and  $1$  to  $200\,000 \Omega \cdot m$  for anthracite (Angenheister, 1982). While the resistivities of lignite are low to medium, those of hard coal span almost the whole range of values found in rocks. Depending on the coal type and its geologic setting, a coal deposit may constitute a conductive or a resistive target. Generally, the highest resistivity values were obtained in a laboratory and are not necessarily representative of true in-situ conditions.

Sartorelli et al. (1985) described the use of various ground and borehole geophysical techniques in coal prospecting in Alberta, Canada. Coal seams are within sandstone, siltstone, and shale of Cretaceous-Tertiary age. A typical resistivity log is shown in Figure 61. Barren sedimentary rocks have resistivities below  $20 \Omega \cdot m$ , and coal seams can be identified by their high resistivity (over  $200 \Omega \cdot m$ ). Unfortunately, no detailed lithologic description of the barren section was made. Resistivity soundings and profiling were used to map the depth and thickness of the coal seam, which appeared as one resistive layer ( $200 \Omega \cdot m$ ) about  $15 \text{ m}$  thick (Figure 62). The coal seams are embedded in fairly conductive shales and sandstones with resistivities of  $8$  to  $20 \Omega \cdot m$ . Interpretation of geophysical data was confirmed by drilling.

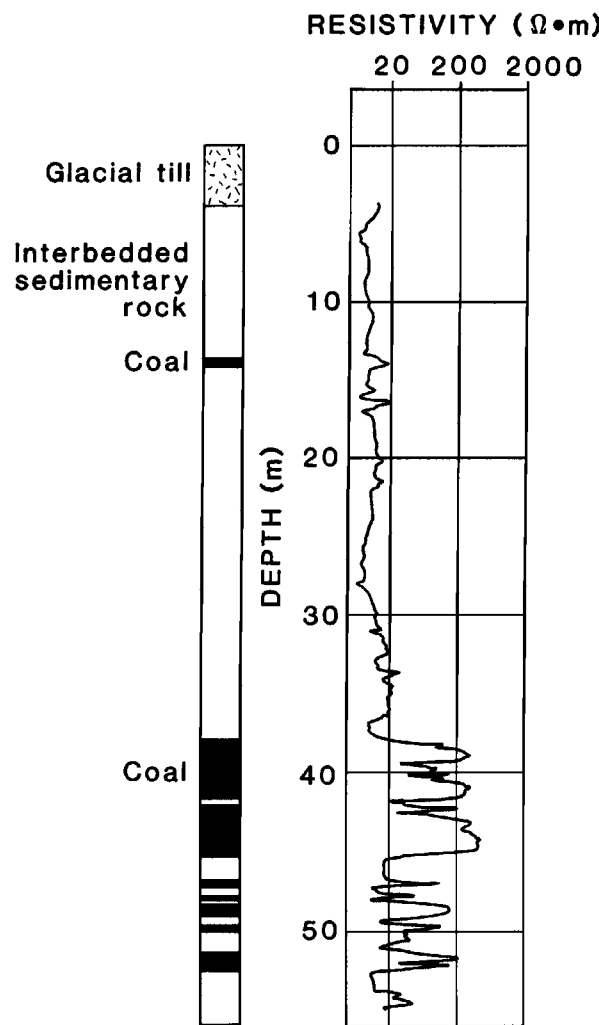


FIG. 61. Geologic and resistivity log of a sedimentary formation with coal seams near Edmonton, Alberta, Canada (after Sartorelli et al., 1985).

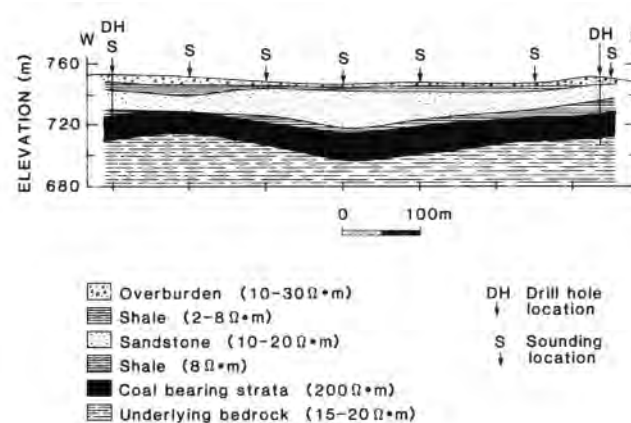


FIG. 62. Geologic section based on resistivity sounding data—coal seams near Edmonton, Alberta (after Sartorelli et al., 1985).

## Seawater, Aquifers, and Permafrost

Conductivity of many earth materials depends on their water content. Clays are conductive when watersaturated, but resistive when dry. In sedimentary environments, conductivity of most rocks is a function of their porosity and pore fluid conductivity. Fresh water by itself is only moderately conductive, and EM methods can only be used for detection of aquifers if the host rock distinguishes itself from the neighboring lithologic units. In many regions, conductive saprolites formed over certain rock types are water-saturated. Also lineaments can constitute locally important aquifers.

This section focuses on situations in which conductivity of water or water-saturated earth materials is a function of chemical composition and physical state of water, and not of its host. Such situations have a practical importance in bathymetric charting and in mapping of saltwater-freshwater interface, chemical pollution, and permafrost. Figure 63 is a map showing the location of case history sites described in this section.

### Bathymetric charting

Bathymetric charting of shallow oceans (shallow-water bathymetry), a new application for AEM surveys, has become feasible after the development of accurate multiparameter systems in which the instrument drift can be controlled. Experimental AEM surveys have been described in Zollinger et al. (1987) and Won and Smits (1986). Resistivity of sea water depends on its salinity and temperature. At 15°C, the resistivity decreases from 1.38 to 0.21  $\Omega \cdot \text{m}$  when NaCl concentration increases from 0.5 to 4 percent. Seawater with an average NaCl content of 3.5 weight percent has resistivity of 0.34  $\Omega \cdot \text{m}$  at 0°C temperature, but only 0.19

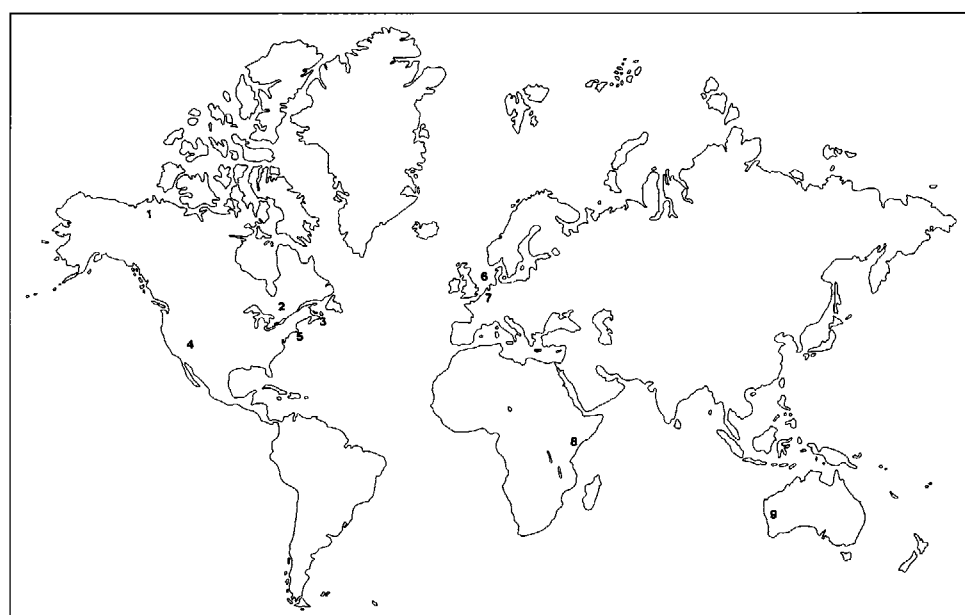


FIG. 63. Location of sites described in the section Seawater, Aquifers and Permafrost (*Canada*: (1) Mackenzie Delta, North West Territories, (2) Ottawa, Ontario, (3) Cape Breton Island, Nova Scotia; *USA*: (4) Las Vegas, Nevada, (5) Cape Cod, Massachusetts; *Europe*: (6) Spiekeroog, Germany; (7) Utrecht, The Netherlands, *Africa*: (8) Mombasa, Kenya; *Australia*: (9) Perenjori Basin, Western Australia).

$\Omega \cdot \text{m}$  at 25°C (Angenheister, 1982). Salinity of seawater varies from sea to sea—the Baltic has a low NaCl content, the Red Sea very high, but most major oceans are 3.5 weight percent.

In carrying out AEM bathymetric surveys, it is usually assumed that salinity and temperature are constant over a given area. This assumption is not valid in areas with a large influx of fresh water (deltas, estuaries), where significant variations in salinity occur over a short distance. Errors due to temperature changes can be expected in shallow beach and deltaic areas or over coral reefs, where water can be up to 10°C warmer than in an open sea. Another complication may arise if the sea bottom is formed by conductive sediments whose resistivity cannot be accurately determined in situ. A conductive layer of poorly known resistivity and thickness will have to be considered in inversion of AEM survey data. If the sea is covered by ice, an additional resistive layer at the top will have to be introduced. The problems related to inversion of data obtained in such complex conditions were treated in Holladay et al. (1986).

Zollinger et al. (1987) described the results of an Input AEM survey carried out along a line 27 km long off Cape Breton Island, Nova Scotia, Canada. The bottom sediments in the test area are resistive and the resistivity of seawater was assumed to be constant ( $0.25 \Omega \cdot \text{m}$ ). The depth of seawater, which remains the only unknown, was determined by computer matching of decay curves to a two-layer nomogram. Figure 64 shows the bottom profile obtained from AEM data flown at 210 m height (solid line) and from Coast Guard bathymetric charts (dots). The agreement is good, generally better than 2 m, except near kilometer 12 (the Lennox Passage), where a shipping channel is filled with unconsolidated sediments. There, the approach based on the assumption of resistive sea bottom breaks down.

Won and Smits (1986) described the use of a helicopter AEM system for bathymetric charting in Cape Cod Bay, Massachusetts, USA. The system was equipped with two horizontal coplanar coil pairs operating at 385 and 7 200 Hz. An average bird flight height of 40 to 50 m above sea surface was maintained. Thirteen segment profiles totaling 200 line km were surveyed. Spot shipborne measurements of seawater resistivity made at a 3 m depth

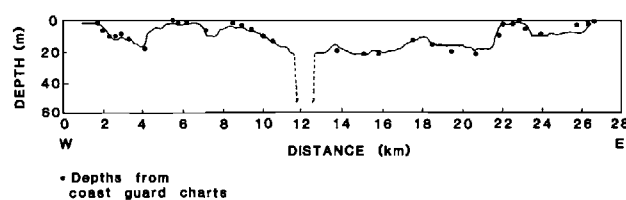


FIG. 64. Bathymetric profile computed from Input AEM data (solid line) and determined from Coast Guard charts (dots). The line was surveyed off Cape Breton Island, Nova Scotia, Canada (after Zollinger et al., 1987).

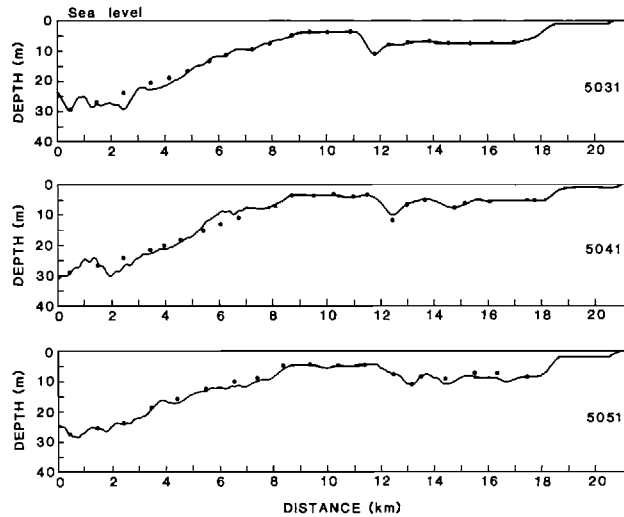


FIG. 65. Three bathymetric profiles computed from Dighem III helicopter AEM data (two horizontal coplanar coil pairs operated at 385 and 7200 Hz)—solid line—and from acoustic soundings (dots). The north-northwest south southeast lines, which are approximately 500 m apart, were surveyed in the Cape Cod Bay, Massachusetts, USA (after Won and Smits, 1986).

gave values between 0.24 and 0.25  $\Omega \cdot \text{m}$ . Bottom profiles were obtained by inversion of the AEM data (Figure 65). The data (solid line) are in good agreement with acoustic soundings (dots) for shallow areas, but deteriorate for depths over 20 m, when the resolution capabilities of the AEM system become limited. Won and Smith express hope that with improvements in instrumentation and interpretation the technique would be capable of bathymetric charting to a depth of 100 m. The physical limitation remains the penetration of EM waves, which is a function of the frequency of the system and the resistivity of the medium.

#### Mapping of freshwater-saltwater interface

Resistivity soundings have been used for decades in coastal areas to determine the position of the freshwater-saltwater interface. Some of the early work was reported in Flathe (1970). The interface may be vertical (a gradual increase in the salinity of aquifer near the coast) or horizontal (a freshwater lens overlying a saltwater lens). Both situations are common in coastal areas and both can be successfully mapped either by resistivity or EM surveys. The use of time-domain EM soundings in groundwater prospecting was recently summarized in Fitterman and Stewart (1986), a tutorial paper.

A good example illustrating the detection of a freshwater lens was published in Sengpiel (1983). The small island of Spiekeroog in Northern Germany was surveyed on the ground using resistivity soundings and from the air using a helicopter AEM system. The island is formed by sand with occasional clay intercalations. The resistivity of the freshwater-filled

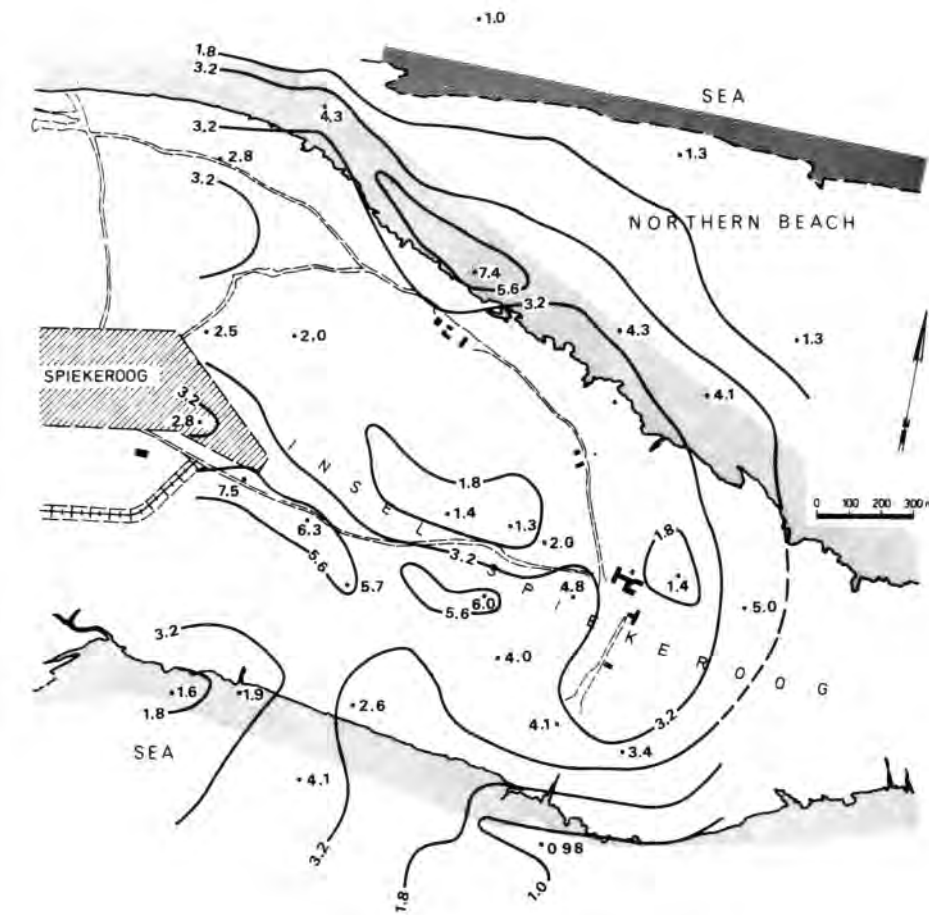


FIG. 66. Apparent resistivity map (in  $\Omega \cdot \text{m}$ ) of Spiekeroog Island, Germany, compiled from helicopter AEM data: horizontal coplanar coils at 900 Hz, line spacing 100 m (after Sengpiel, 1986).

sand is  $100$  to  $500 \Omega \cdot \text{m}$ , the saltwater-filled sand  $1$  to  $1.5 \Omega \cdot \text{m}$ , and the clay layers  $10$  to  $20 \Omega \cdot \text{m}$ . The apparent resistivity map (Figure 66) was calculated from AEM data (100 m line spacing, coplanar horizontal coils, frequency 900 Hz) using a homogeneous half-space model. The freshwater lens extends under the northern two thirds of the island—the northern interface follows roughly the coastline while the southern interface lies about 500 m inland. The apparent depth map (Figure 67), also compiled from the AEM data, maps the aquifer extent better. The apparent depth contours give interpreted depth to the conductive half-space, which is the surface of the seawater lens. Extensive depth soundings performed on the island confirmed the accuracy of the apparent depth map derived from AEM data.

The described AEM survey is not the first survey conducted for mapping of freshwater-saltwater interface. Baudoin et al. (1970) described application of the Input AEM system to such mapping near Arles in the Rhône delta, France. However, at that time interpretation of Input AEM data was only qualitative and numerous ground checks had to be performed in order to extract useful information.

Johnson and Seigel (1986) gave an example of aquifer mapping from Mombasa, Kenya. The apparent resistivity map (Figure 68) was compiled from Tridem AEM data at 520 Hz. The flight line spacing was 250 m. The coastal limestone reef containing seawater coincides with an area of low resistivity (between 3 and  $10 \Omega \cdot \text{m}$ ). The neighboring freshwater aquifer formed by sandstone has an average resistivity of  $25 \Omega \cdot \text{m}$ . The transition to the less permeable shale is marked by a prominent decrease in resistivity (less than  $12 \Omega \cdot \text{m}$ ).

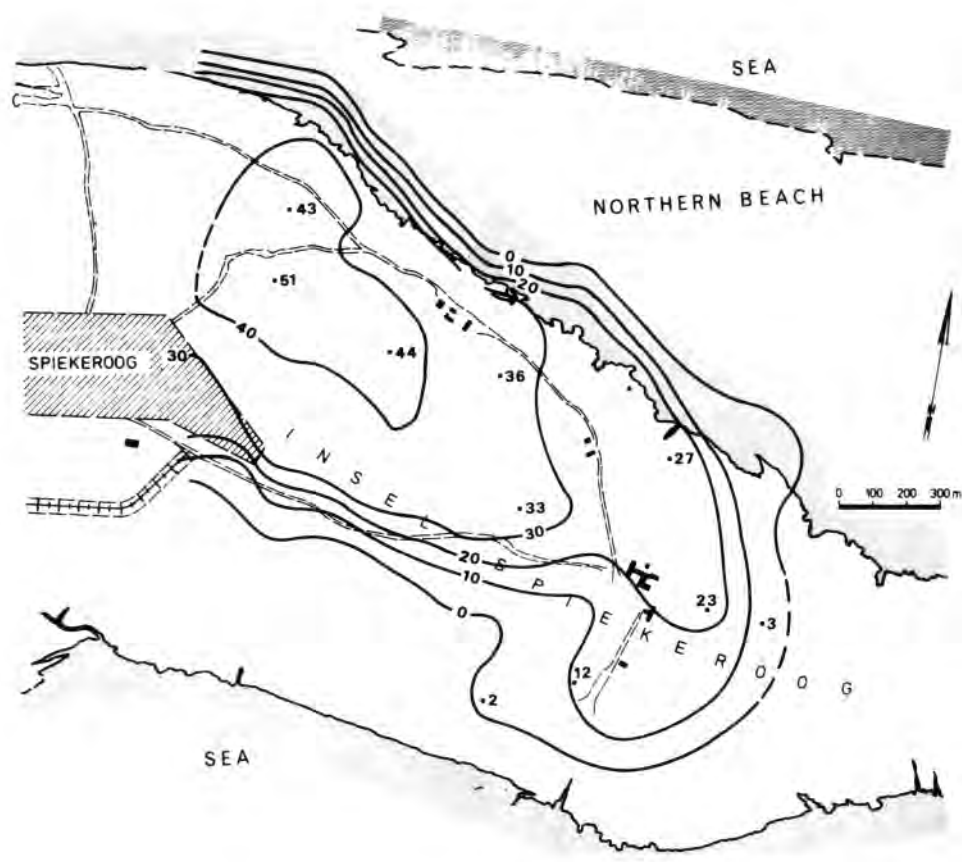


FIG. 67. Map of apparent depth (in meters) to the conductive layer (saltwater aquifer), which outlines the extent and thickness of a freshwater lens. The contour map was compiled from helicopter AEM data. Spiekeroog Island, Germany (after Sengpiel, 1986).

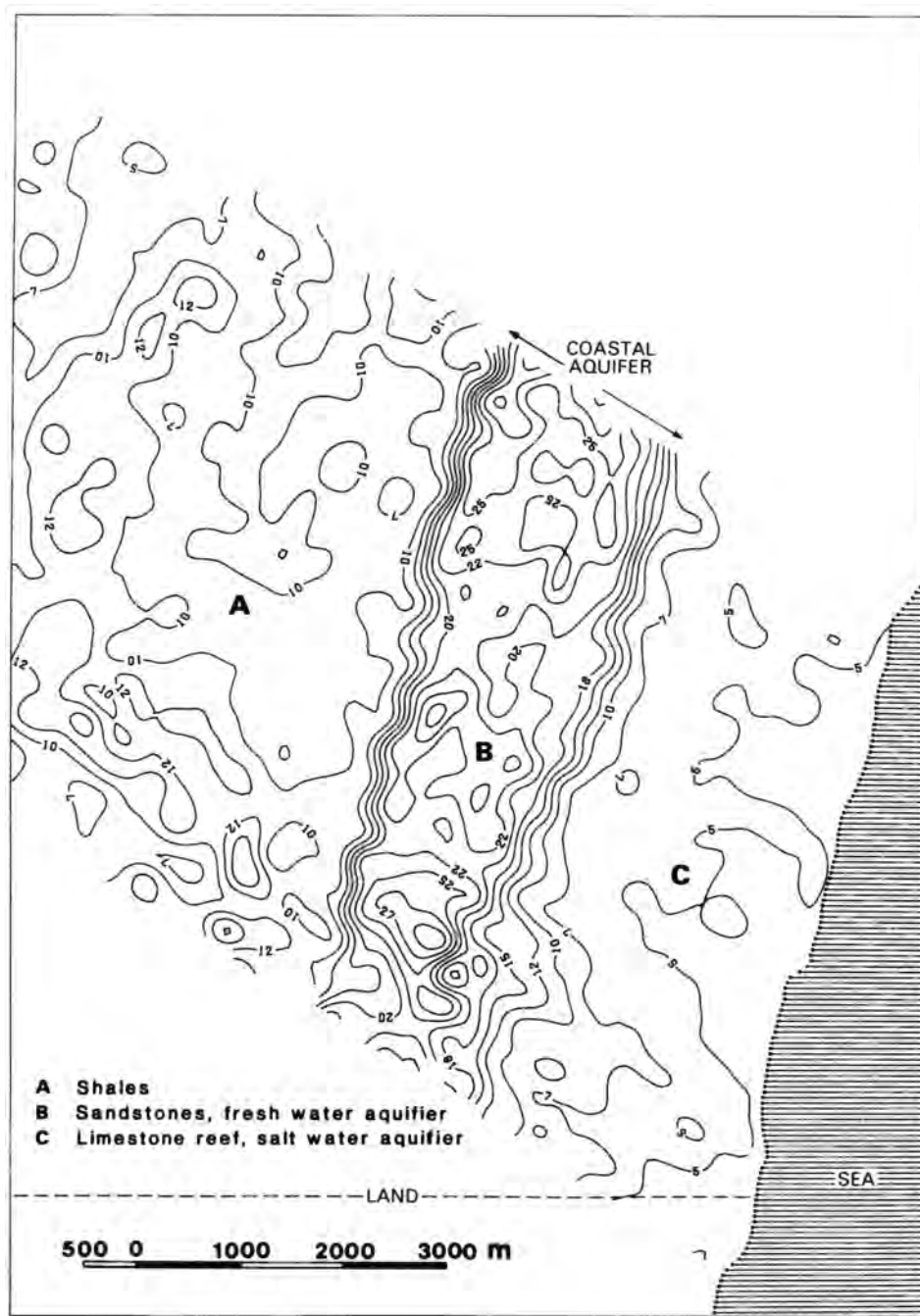


FIG. 68. Apparent resistivity map (in  $\Omega \cdot m$ ) of a coastal area near Mombasa, Kenya, which was compiled from Tri-diem AEM data (after Johnson and Seigel, 1986).

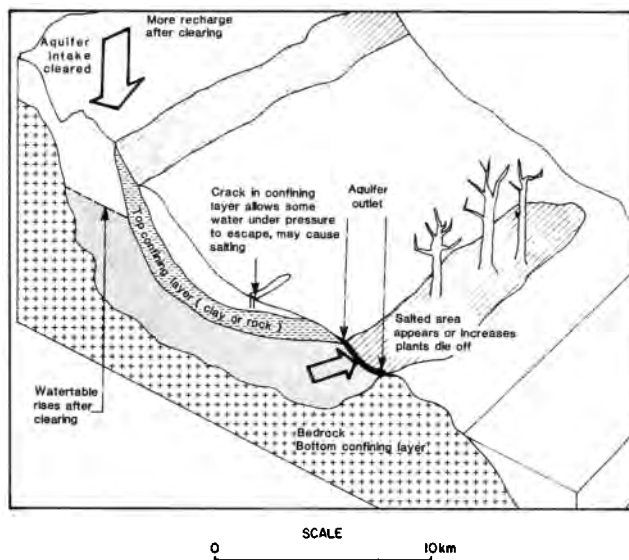


FIG. 69. Schematic diagram of salting or contamination of a confined aquifer (from Garland and Duff, 1984).

Saltwater aquifers are not restricted to coastal areas, they are common in many arid regions (e.g., Australia, Pakistan, the Middle East, parts of Africa, and northeastern Brazil). Salinization developing from a confined aquifer is illustrated in Figure 69. Such aquifer has a freshwater intake on high ground and a discharge area in a valley or in foothills. Because of rapid evaporation, the soil in the valley becomes saline. Irrigation in areas with high evaporation also leads to salinization. Resistivity and EM techniques can be used for mapping affected areas. Butt (1985) and O'Connell and Nader (1986) described mapping of salinization in the East Perenjori catchment area in Western Australia. The soil map of the Perenjori valley is shown in Figure 70. A build-up of saline water occurs in the center of the valley, where soil consists of sandy loam. Salt pans form near the valley outlet. An apparent resistivity map (Figure 71) was compiled from the results of an Input AEM survey, which was flown with a line spacing of 1.5 km (flight lines east-west). Low resistivity anomalies (less than  $20 \Omega \cdot m$ ) coincide with the area affected by salinization. Extremely low resistivity values (less than  $0.5 \Omega \cdot m$ ) were measured over salt pans. Apparent resistivities were obtained by computer fitting of the measured decay curve to a homogeneous half-space nomogram.

The case histories illustrate three common situations in groundwater prospecting: (1) Freshwater lens at the top of a saltwater aquifer in a coastal area with both aquifers having the same lithology (Spiekeroog), (2) Lithologically dependent interface freshwater-saltwater (Mombasa), (3) Salt pans and near-surface saline layers in arid areas (East Perenjori).

#### Mapping of chemical pollution plumes

Resistivity of water can be decreased by addition of chemical substances other than NaCl. Chemical pollution of aquifers is becoming an increasingly serious problem worldwide. Mapping of conductive pollution plumes can be accomplished rapidly and inexpensively by EM and resistivity techniques. Only a few test surveys have been carried out; they were in The Netherlands, Canada, and the USA.

Ritsema (1984) investigated electric properties of unconsolidated sediments in the vicinity of a waste disposal site near Utrecht, The Netherlands. Resistivity soundings were carried out at 5 and 10 m intervals along lines away from the site (Figure 72). The results identified several distinct horizons. From the top to bottom, clean sand, polluted sand, impermeable clay layer, clean sand, polluted sand, and saline water. While clean sand has a relatively high resistivity (between 18 and  $45 \Omega \cdot m$ ), sand containing chemicals is more conductive

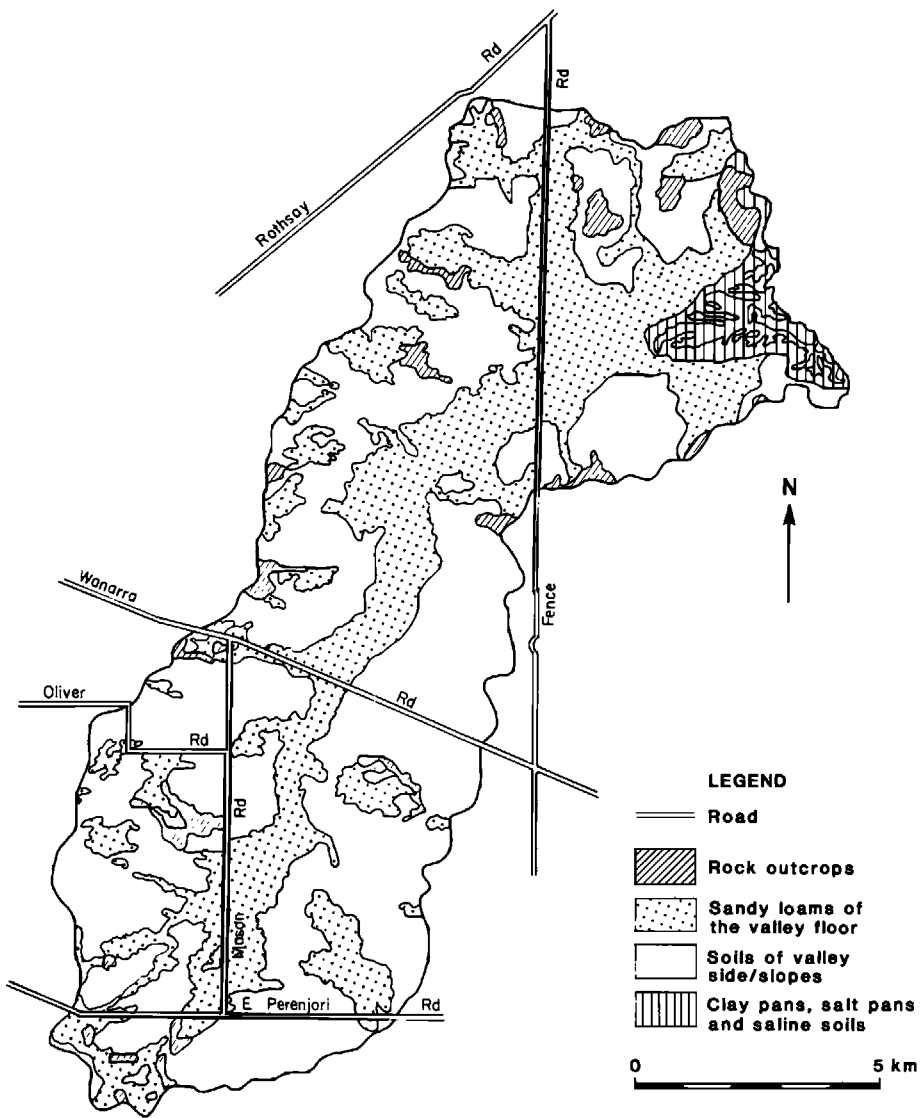


FIG. 70. Soil map of the East Perenjori catchment area, Western Australia (after O'Connel and Nader, 1986).

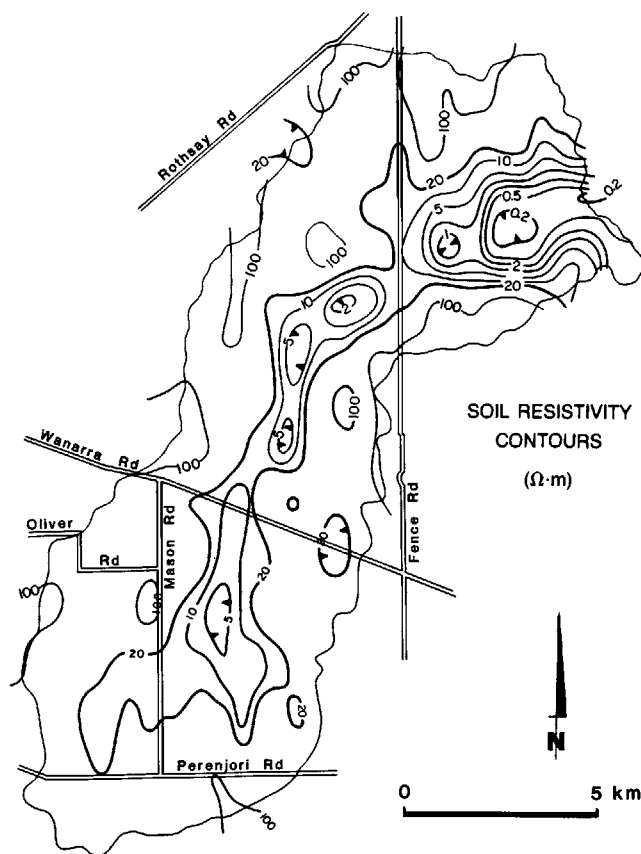


FIG. 71. Apparent resistivity map (in  $\Omega \cdot m$ ) of the East Perenjori area, Western Australia, compiled from Input AEM data (after Butt, 1985).

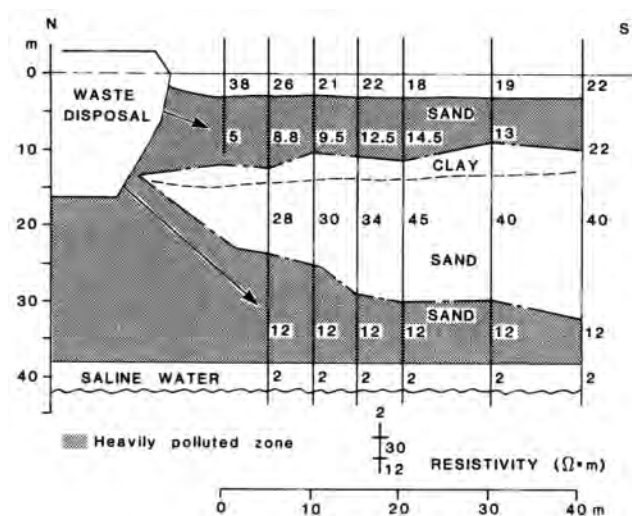


FIG. 72. Resistivity section of an area adjacent to a waste disposal site near Utrecht, The Netherlands (after Ritsema, 1984).

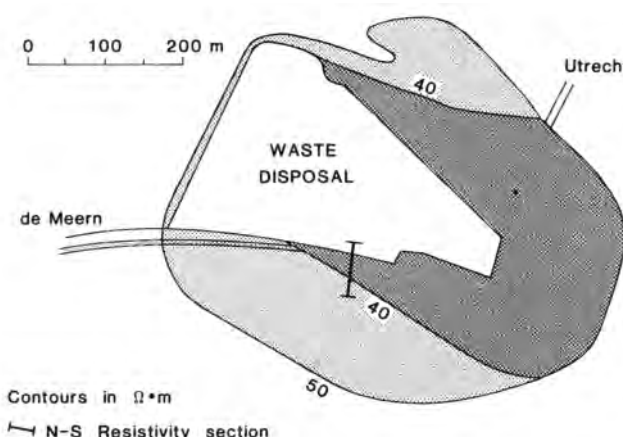


FIG. 73. Map of inductively measured apparent resistivity over a waste disposal site near Utrecht, The Netherlands. The location of the resistivity section of Figure 72 is also indicated (after Ritsema, 1984).

(between 5 and  $14.5 \Omega \cdot \text{m}$ ). Polluted water is concentrated in the lower portion of the two freshwater aquifers, which are separated by a 2 to 3 m thick clay layer. Saline water, which underlies most of Holland, is highly conductive (about  $2 \Omega \cdot \text{m}$ ). An EM instrument measuring conductivity at high induction numbers (Geonics EM-34) was also used to outline the direction of seepage from the waste disposal site (Figure 73). The coil selection was made to minimize the effect of the conductive saline aquifer on EM data.

Evan and Schweitzer (1984) described the mapping of a leachate plume spreading from a 30-year-old landfill. The plume threatened to pollute the nearby shallow unconfined aquifer, which served as a drinking water supply for a large city. The increased conductivity of the plume was due to the presence of sodium, potassium, magnesium, and chloride solutions. Resistivity and EM surveys were used to periodically monitor the plume migration (up to 0.5 m/day). The plume was found to have an apparent resistivity less than  $60 \Omega \cdot \text{m}$ . Zonge et al. (1985) used complex resistivity measurements to detect a chloride plume near Las Vegas, Nevada, USA. Chloride solutions originating from an industrial complex contaminated alluvial sands and gravels, which serve as a drinking water reservoir. Low apparent resistivity values (less than  $5 \Omega \cdot \text{m}$ ) coincide with the known extent of the contamination plume.

Stephens and Graham (1985) mapped conductivity at the Gloucester Landfill Site, 10 km south of Ottawa, Ontario, Canada. From a special waste site containing chemicals, which is located in unconsolidated sediments, two plumes spread: a shallow one in the near surface (less than 10 m deep) sand layer and a deeper one in the 15 to 30 m deep sand and gravel layer. The plumes are separated by an impermeable clay layer. The lower plume is confined at the base by a limestone layer. Three conductivity measuring EM instruments were used in the survey. Values over  $10 \text{ mS/m}$  (equivalent to resistivities below  $100 \Omega \cdot \text{m}$ ) coincide with the extent of the pollution plume. Borehole measurements were used to determine resistivity in situ. The plume was found to migrate faster in the lower semiconfined aquifer. Several local EM anomalies unrelated to the pollution plumes were caused by metallic objects in the landfill area. Increased conductivity was also observed along all roads which are salted in winter. The general heterogeneity of man-made materials deposited at landfill sites may cause difficulties in positive identification of anomalies due to chemical pollution plumes.

From the point of view of EM detection, the characteristics of pollution plumes are summarized as follows: (a) limited depth extent, typically less than 50 m, (b) high variability in the resistivity of plumes at individual sites due to diversity of dumped chemicals, (c) presence of other conductive inhomogeneities at landfill sites, and (d) rapid migration of pollution plumes (up to 0.5 m/day).

### Permafrost

While the three previously described applications of EM methods depend on the change of chemical composition of water, this last application depends on the change of its physical state. When frozen, resistivity of water and water-saturated earth materials increases substantially. Resistivities of polar glacier ice range from 20 000 to 200 000  $\Omega \cdot \text{m}$ . The range represents typical values obtained by resistivity soundings in the Canadian Arctic, Greenland, and Antarctica. Similarly determined resistivities for temperate glaciers in the Alps and Canada are on average 3 orders of magnitude higher—10 to  $100 \times 10^6 \Omega \cdot \text{m}$  (Angenheister, 1982).

Figure 74 illustrates the change in resistivity as a function of temperature for water-saturated unconsolidated sediments and a biotite granite sample (after Hoekstra et al., 1975). Because of the presence of unfrozen water at temperatures down to  $-15^\circ\text{C}$ , the increase in resistivity with decreasing temperature is gradual. Even frozen, clays remain more conductive than other unconsolidated sediments. The top permafrost layer (active layer), which is 0.5 to 3 m thick, thaws in summer, thus becoming about 10 times more conductive than in winter.

Resistivity of frozen ground depends also on the volume of ice in sediments, which may vary from 30 to 100 percent. The data shown in Figure 75 were obtained in situ by carrying out resistivity measurements on the walls of a tunnel excavated in Fairbanks silt at Fox, Alaska. The rock temperature during the survey was  $-2.9^\circ\text{C} \pm 0.2^\circ\text{C}$ . The results indicate that the resistivity of silt may vary by 2 orders of magnitude depending on ice content.

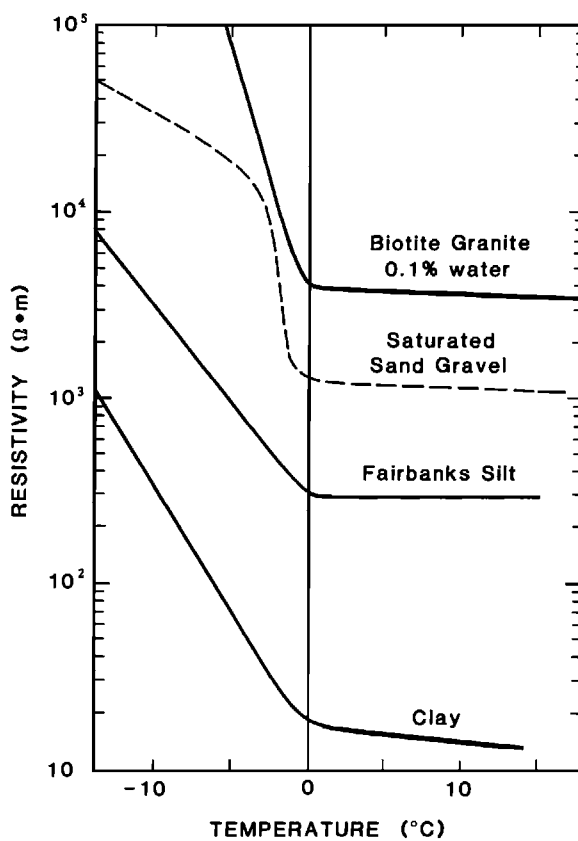


FIG. 74. Resistivity of water-saturated earth materials as a function of temperature (after Hoekstra et al., 1975).

Because of its compact texture, clay shows a much smaller increase in resistivity (about 1.2) with change from unfrozen to frozen state (Hoekstra et al., 1975). In summary then, the resistivity of permafrost depends on the underlying lithology, its ice content, and the temperature of the frozen ground. Electrical properties of permafrost were described in detail in Olhoeft (1975).

A typical resistivity section of permafrost obtained in the Canadian Arctic (Mackenzie Delta, North West Territories) is shown in Figure 76. Resistivity and depth values were obtained by interpretation of time-domain EM soundings and confirmed by resistivity well-logging (Rozenberg et al., 1985). The most resistive layer, which is 80 to 200 m thick, occurs in the near surface. The lowermost boundary is thought to form the lower limit of permafrost, but most likely the boundary is not sharp and the transition from frozen to unfrozen ground is gradual. Intermediate zones reflect a resistivity decrease due to gradually increasing temperature (compare with Figure 74).

An interesting experiment investigating the formation of permafrost was conducted at Ilisarvik, 60 km west of Tuktoyaktuk, Mackenzie Delta, North West Territories, Canada. The ground beneath lakes and rivers is usually unfrozen because of the thermal influence of water. A lake, 300 by 600 m by 4.7 m deep, was drained in order to study the resulting process of permafrost formation. Geologic and geophysical surveys were carried out before the drainage, which took place in August 1978, and for several years afterward (Sinha and Stephens, 1983). Drilling and temperature logging indicated that the upper 37 m of sediments were

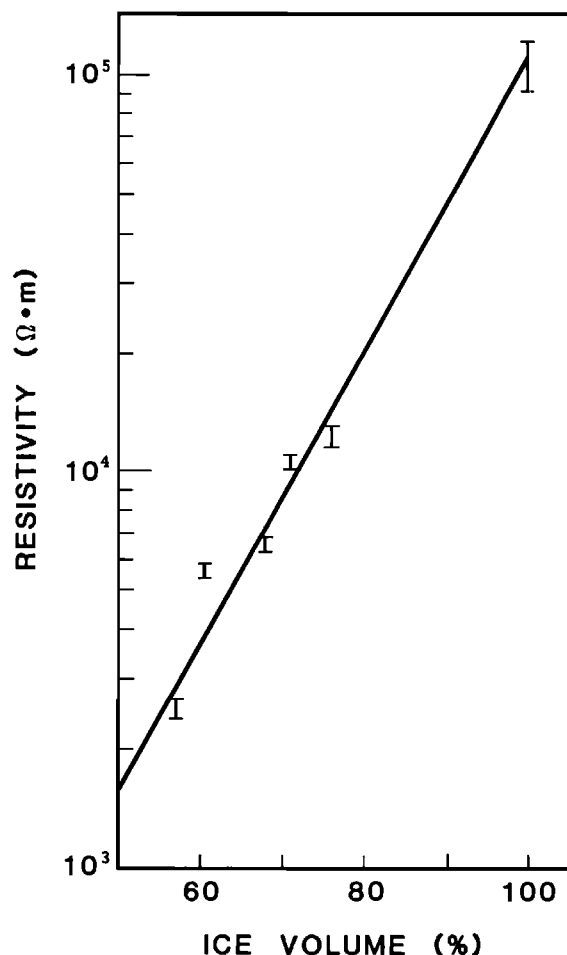


FIG. 75. In-situ resistivity of silt at  $-2.90^{\circ}\text{C} \pm 0.2^{\circ}\text{C}$  as a function of ice volume (in percent), from Fox, Alaska (after Hoekstra et al., 1975).

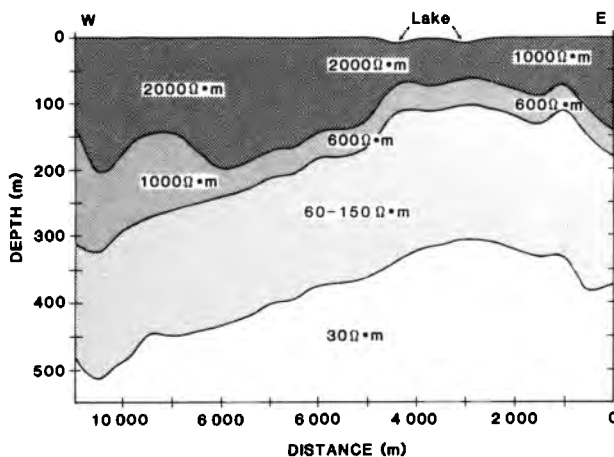


FIG. 76. Resistivity section of a permafrost layer from interpreted sounding data, Mackenzie Delta, North West Territories, Canada (after Rozenberg et al., 1985).

initially unfrozen. They consisted of 5 m of organic material and 32 m of sand with thin clay layers. Resistivity soundings carried out on the frozen lake before the drainage showed a moderately conductive layer at the top (thickness 15 m, resistivity  $35 \Omega \cdot \text{m}$ ). The frozen ground was highly resistive (over  $1000 \Omega \cdot \text{m}$ , depth 35 m from soundings). The medium layer had a low resistivity ( $5 \Omega \cdot \text{m}$ ). Measurements carried out in September 1980 revealed that the ground became frozen and resistive to a depth of 16 m. The following spring (April 1981) the ground had frozen to a depth of 28 m. Ground EM surveys conducted at that time (Sinha and Stephens, 1983) detected a clear conductivity anomaly in the center of the drained lake (about  $60 \text{ mS/m}$ ). Interpretation of the data indicated that a conductive (unfrozen) layer still existed between the frozen surface and the upper limit of permafrost. The contrast between frozen and unfrozen ground seems always sufficient to be detectable by both resistivity and EM techniques.

Geophysical methods have been extensively used in permafrost studies in Canada, USA, and USSR. The three countries maintain close scientific contacts in permafrost research and periodically organize international conferences on the subject. The applicability of various geophysical techniques to permafrost mapping was reviewed in Scott et al. (1978).

## Conclusions

The application of EM surveys can be greatly expanded beyond the traditional prospecting for massive sulfide orebodies. The most logical novel application is geologic mapping, particularly in regions devoid of outcrops. Systematic coverage by multiparameter airborne geophysical surveys would provide an excellent data base for subsequent ground geologic reconnaissance and mineral prospecting. The data would also be of value in groundwater exploration and regional planning (including new settlements in virgin areas, large-scale engineering projects).

Some of the more specialized new applications, such as shallow-water bathymetry, detection of pollution plumes, or permafrost studies, also hold great promise. The most significant obstacle to the development of new applications is the lack of communication channels between the geophysical community and nontraditional users.

## Acknowledgments

I acknowledge discussions on the subject I had during the last 10 years with a number of my friends and former colleagues: Peter Elliott, Bruce Harley, and Nigel Hungerford of Billiton, Australia, Melbourne, Australia (on electric properties of massive sulfide deposits, particularly during mine visits they organized to Broken Hill, Elura, Woodlawn, Que River, Rosebery, and Kambalda), Kiyoshi Kadokura and Florivaldo Sena of DOCEGEO, Rio de Janeiro, Brazil (with whom I commenced investigating electric properties of weathered layers), Olivar Lima at the Federal University of Bahia, Salvador, Brazil (on groundwater exploration in the Brazilian Northeast), Frits Dirks and Sieb de Jong of IWACO, Ouagadougou, Burkina Faso (on groundwater exploration in Western Africa), Roger Barlow and Doug Pitcher of the Ontario Geological Survey, Toronto, Canada (on geophysical mapping of glacial sediments), and with my former students at the State University of Utrecht, The Netherlands, Sjef Meekes and Ipo Ritsema (who shared with me the frequent hardships of field work in Burkina Faso). When I wrote this paper in 1986 I had numerous stimulating discussions with Gordon Bernius, Len Collett, Jim Franklin, John Katubbe, Pat Killeen, Allen Miller, Jonathan Mwenifumbo, Keith Richardson, and Larry Stephens at the Geological Survey of Canada, Ottawa. Last but not least I express my gratitude to Susan Davis who drafted most of the figures, and Muriel Wilson who typed the manuscript.

## References

- Acworth, R. I., and Griffiths, D. M., 1985, Simple data processing of tripotential apparent resistivity measurements as an aid to the interpretation of subsurface structure: *Geophys. Prosp.*, **33**, 861–887.
- Adams, R. L., and Schmidt, B. L., 1980, Geology of the Elura Zn-Pb-Ag deposit: *Bull. Austral. Soc. Expl. Geophys.*, **11**, 143–146.
- Agostini, A., Wootton, T. C., and Cifali, G., 1981, Ground magnetic surveys at Woodlawn, in R. J. Whiteley, Ed., *Geophysical case study of the Woodlawn orebody*, N.S.W., Australia: Pergamon Press, 475–483.
- Angenheister, G., Ed., 1982, *Physical properties of rocks*, in *Landolt-Börnstein, New series: 1b*, Springer-Verlag.
- Archie, G. E., 1942, The electrical resistivity log as an aid in determining some reservoir characteristics: *Trans. Am. Inst. Min. Metallurg., Petr. Eng.*, **146**, 54–62.
- Barlow, R. B., and Krentz, D. H., 1984, Electromagnetic depth soundings of Quaternary sequences in parts of Walker and Taylor Townships, Black River-Matheson (BRIM) Area, District of Cochrane, in J. Wood, O. L. White, R. B. Barlow, and A. C. Colvine, Eds., Summary of field work and other activities 1984: Ontario Geol. Surv. Misc. Paper 119, 133–138.
- Baudoin, P., Durozoy, G., and Utard, M., 1970, Étude par prospection électromagnétique aérienne d'un contact eau douce-eau salée dans le delta du Rhône, in L. W. Morley, Ed., *Mining and ground-water geophysics 1967*: *Geol. Surv. Can. Econ. Geol. Rept.* 26, 626–637.
- Birkett, N. E., 1981, Report on geophysical field work conducted at Kangaroo Hills, North Queensland: B.Sc. thesis, Univ. of New England.
- Boldy, J., 1979, Exploration discoveries, Noranda district, Quebec, in P. J. Hood, Ed., *Geophysics and geochemistry in the search for metallic ores*: *Geol. Surv. Can. Econ. Geol. Rept.* **31**, 593–603.
- Brant, A. A., Dolan, W. N., and Elliott, C. L., 1966, Coplanar and coaxial EM tests in Bathurst area, New Brunswick, Canada, 1956, in *Mining Geophysics I: Soc. Explor. Geophys.*, 130–141.
- Buselli, G., McCracken, K. G., and Thorburn, M., 1986, Transient electromagnetic response of the Teutonic Bore orebody: *Geophysics*, **51**, 957–963.
- Butt, C. R. M., 1982, History and characteristics of weathering in Australia, in R. E. Smith, Ed., *Geochemical exploration in deeply weathered terrain*: Comm. Sci. Ind. Res. Org., Inst. Energy and Earth Resour., 9–18.
- Butt, G. R., 1985, Case histories showing various applications of a combined Input-magnetometer-spectrometer airborne geophysical system in Australia: *Explor. Geophys.*, **16**, 180–183.
- Cameron, E. M., Ed. 1983, Uranium exploration in Athabasca Basin, Saskatchewan, Canada: *Geol. Surv. Can. Paper 82-11*, 310.
- Collett, L. S., 1986, Development of the airborne electromagnetic technique, in G. J. Palacky, Ed., *Airborne resistivity mapping*: *Geol. Surv. Can. Paper 86-22*, 9–18.
- Culley, R. W., 1973, Use of airborne resistivity for gravel location: *Can. Inst. Min. Metallurg. Bull.*, **66**(733), 70–74.
- DeJong, S. J., Dirks, F. J. H., Kikietta, A., Palacky, G. J., and Ritsema, I. L., 1981, Experiments de méthodes électromagnétiques appliquées à la recherche des eaux souterraines en terrain de socle cristallin en Haute Volta: *Bull. Comité interafricain d'études hydrauliques (C.I.E.H.)*, série hydrogéologie, **44**, 17–26.
- Deletie, P., and Lakshmanan, J., 1986, Airborne resistivity surveying applied to nuclear power plant site investigation in France, in G. J. Palacky, Ed., *Airborne resistivity mapping*: *Geol. Surv. Can. Paper 86-22*, 145–152.

- Dowsett, J. S., 1970, Geophysical exploration methods for nickel, in L. W. Morley, Ed., Mining and groundwater geophysics 1967: Geol. Surv. Can. Econ. Geol. Rept. 26, 310–321.
- Dyck, A. V., Becker A., and Collett, L. S., 1974, Surficial conductivity mapping with the airborne Input system: Can. Inst. Min. Metallurg. Bull., **67**(744), 104–109.
- , 1975, Input AEM results from Project Pioneer, Manitoba: Can. J. Earth Sci., **12**, 971–981.
- Eadie, E. T., Silic, J., and Jack, D. J., 1985, The application of geophysics to the discovery of the Hellyer ore deposit, Tasmania: Explor. Geophys., **16**, 207–209.
- Eckstrand, O. R., 1984, Magmatic nickel, copper, platinum group elements, in O. R. Eckstrand, Ed., Canadian mineral deposit types: A geological synopsis: Geol. Surv. Can. Econ. Geol. Rept. 36, 39–42.
- Elliott, P. J., and Staltari, G., 1985, The Mt. Keith South nickel sulphide deposits—a TEM case study: Explor. Geophys., **16**, 210–216.
- Emerson, D. W., Ed., 1980, The geophysics of the Elura orebody, Cobar, New South Wales: Bull. Austral. Soc. Expl. Geophys., **11**, 143–347.
- Engalenc, M., 1978, Méthode d'étude et de recherche de l'eau souterraine des roches cristallines de l'Afrique de l'ouest: Bull. Comité interafricain d'études hydrauliques (C.I.E.H.), série hydrogéologie, **41**.
- Evans, R. B., and Schweitzer, G. E., 1984, Assessing hazardous waste problems: Environ. Sci. Technol., **18**(11), 330A–338A.
- Fitterman, D. V., and Stewart, M. T., 1986, Transient electromagnetic sounding for groundwater: Geophysics, **51**, 995–1005.
- Flathe, H., 1970, Interpretation of geoelectrical resistivity measurements for solving hydrogeological problems, in L. W. Morley, Ed., Mining and groundwater geophysics 1967: Geol. Surv. Can. Econ. Geol. Rept. 26, 580–597.
- Fox, J., 1984, Besshi-type volcanogenic sulphide deposits—a review: Can. Inst. Min. Metallurg. Bull., **77**(864), 57–68.
- Fouques, J. P., Fowler, M., Knipping, H. P., and Schimann, K., 1986, Le gisement d'uranium de Cigar Lake: découverte et caractéristiques générales: Can. Inst. Min. Metallurg. Bull., **79**(886), 70–82.
- Francheteau, J., Needham, H. D., Choukroune, P., Juteau, T., Seguret, M., Ballard, R. D., Fox, P. J., Normark, W. R., Carranza, A., Cordoba, D., Guerro, J., Rangin, C., Bougault, H., Cambon, P., and Hekinian, R., 1979, Massive deep-sea sulfide ore deposits discovered on the East Pacific Rise: Nature, **277**, 523–528.
- Franklin, J. M., Lydon, J. W., and Sangster, D. F., 1981, Volcanic-associated massive sulphide deposits, in B. J. Skinner, Ed., Economic Geology: 75th Anniversary Vol., 1905–1980, 485–627.
- Fraser, D. C., 1973, Magnetite ore tonnage estimates from an aerial electromagnetic survey: Geoexplor., **11**, 97–105.
- , 1981, Response of the Woodlawn orebody to the Dighem II system, in R. J. Whiteley, Ed., Geophysical case study of the Woodlawn orebody, N.S.W., Australia: Pergamon Press, 137–146.
- Fritz, F. P., and Sheehan, G. M., 1984, The geophysical signature of the Teutonic Bore Cu-Zn-Ag massive sulphide deposit, Western Australia: Explor. Geophys., **15**, 127–142.
- Garland, K., and Duff, J. S., 1984, Saltland in Victoria: Victoria Irrigation Res. and Promotion Org.
- Gaucher, E., 1983, Estimation of sulphide content of a potential orebody from surface observations and its role in optimising exploration programmes, in A. A. Fitch, Ed., Developments in geophysical exploration methods: Applied Sci. Publ. Ltd., 1–37.
- Gerryts, E., 1970, Diamond prospecting by geophysical methods—a review of current practice, in L. W. Morley, Ed., Mining and groundwater geophysics 1967: Geol. Surv. Can. Econ. Geol. Rept. 26, 439–446.
- Ghosh, M. K., 1972, Interpretation of airborne EM measurements based on thin sheet models: Res. Appl. Geophys. 4, Univ. of Toronto.
- Goldich, S. S., 1938, A study in rock weathering: J. Geol., **46**, 17–23.
- Grant, F. S., and West, G. F., 1965, Interpretation theory in applied geophysics: McGraw-Hill Co.
- Greig, E. W., 1970, The application of geophysical methods in the exploration for bauxite deposits, in L. W. Morley, Ed., Mining and groundwater geophysics 1967: Geol. Surv. Can. Econ. Geol. Rept. 26, 470–475.
- Gross, G. A., 1984, Iron-rich sedimentary strata, in O. R. Eckstrand, Ed., Canadian mineral deposit types: A geological synopsis: Geol. Surv. Can. Econ. Geol. Rept. 36, 16–19.
- Gunn, P. J., and Chisholm, J., 1984, Non-conductive volcanogenic massive sulphide mineralization in the Pilbara area of Western Australia: Explor. Geophys., **15**, 143–153.
- Gustafson, L. B., and Williams, N., 1981, Sediment-hosted stratiform deposits of copper, lead, and zinc in B. J. Skinner, Ed., Economic Geology, 75th Anniversary Vol., 1905–1980; 139–178.
- Harthill, N., 1978, A quadripole resistivity survey of the Imperial Valley, California: Geophysics, **43**, 1485–1500.
- Hoekstra, P., Tellmann, P. V., and Delaney, A., 1975 Ground and airborne resistivity surveys of permafrost near Fairbanks, Alaska: Geophysics, **40**, 641–656.
- Holladay, J. S., Valleau, N., and Morrison, E., 1986, Application of multifrequency helicopter EM surveys to mapping of sea-ice thickness and shallow-water bathymetry, in G. J. Palacky, Ed., Airborne resistivity mapping: Geol. Surv. Can. Paper 86-22, 91–98.
- Hone, I. G., 1980, Geoelectric properties of the Elura prospect, Cobar, N.S.W.: Bull. Austral. Soc. Explor. Geophys., **11**, 178–183.
- Hoover, D. B., Long, C. L., and Senterfit, R. M., 1978, Some results from audiomagnetotelluric investigations in geothermal area: Geophysics, **43**, 1501–1514.

- Hoover, D. B., and Pierce, H. A., 1986, Airborne EM mapping of geothermal systems in the Basin and Range and Cascade provinces, in G. J. Palacky, Ed., Airborne resistivity mapping: Geol. Surv. Can. Paper 86-22, 139-144.
- Irvine, R. J., Hartley, J. S., and Mourot, A., 1985, The geophysical characteristics of the Thalanga volcanogenic sulphide deposit, Queensland: Explor. Geophys., **16**, 231-234.
- Jagodits, F. L., Betz, J. E., Krause, B. R., Saracoglu, N., and Wallis, R. H., 1986, Ground geophysical surveys over the McClean uranium deposits, northern Saskatchewan: Can. Inst. Min. Metallurg. Bull., **79**(886), 35-50.
- Johnson, I. M., and Seigel, H. O., 1986, Tridem resistivity mapping for natural resources development, in G. J. Palacky, Ed., Airborne resistivity mapping: Geol. Surv. Can. Paper 86-22, 125-129.
- Kamara, A. Y. S., 1981, Review: Geophysical methods for kimberlite prospecting: Austral. Soc. Expl., Geophys. Bull., **12**, 43-51.
- Kanehira, K., 1970, Conformable copper-pyrite deposits in the Iimori Mining district, in T. Tatsumi, Ed., Volcanism and ore genesis: Tokyo Univ. Press, 93-104.
- Kaufman, A. A., and Keller, G. V., 1983, Frequency and transient soundings: Elsevier.
- Keller, G. V., Ed. 1978, Special geothermal section—Introduction: Geophysics, **43**, 1449-1542.
- \_\_\_\_\_, 1988, Rock and mineral properties: This volume.
- Kilényi, E., and Szabó, Z., 1985, History and present state of the art of geophysics in Hungary: First Break, **3**, No. 5, 9-23.
- Killeen, P. G., 1986, A system of deep test holes and calibration facilities for developing and testing new borehole geophysical techniques, in P. G. Killeen, Ed., Borehole geophysics for mining and geotechnical applications: Geol. Surv. Can. Paper 85-27, 29-46.
- Konings, M. H., and DeCarle, R. J., 1985, Helicopter Input in British Columbia: Presented at Ann. Mtg. Can. Inst. Min. Metallurg.
- Lefebvre, D. L., Dion, D. J., and Keating P., 1986, La couverture en levé électromagnétique aéroporté de la province de Québec, in G. J. Palacky, Ed., Airborne resistivity mapping: Geol. Surv. Can. Paper 86-22, 169-173.
- Leite, J. L., 1975, Estudo geofísico dos aquíferos costeiros nas áreas de Canavieiras e Belmonte, Bahia: M.Sc. thesis, Federal Univ. of Bahia.
- Lima, O. A. L., 1979, Estudo de utilização de reservatórios subterrâneos naturais para armazenamento de água numa área experimental na região semi-árida do Nordeste Brasileiro: Ph.D. thesis, Federal Univ. of Bahia.
- Lydon, J. W., Franklin, J. M., and Sangster, D. F., 1984, Volcanic-associated massive sulphide, in O. R. Eckstrand, Ed., Canadian mineral deposit types: A geological synopsis: Geol. Surv. Can. Econ. Geol. Rept. 36, 33-34.
- Lydon, J. W., and Sangster, D. F., 1984, Sediment-hosted sulphide, in O. R. Eckstrand, Ed., Canadian mineral deposit types: A geological synopsis: Geol. Surv. Can. Econ. Geol. Rept. 36, 35.
- Macnae, J. C., 1979, Kimberlites and exploration geophysics, Geophysics, **44**, 1395-1416.
- Makowiecki, L. Z., King, A. J., and Cratchley, C. R., 1965, A comparison of three airborne electromagnetic methods of mineral prospecting—Results of test surveys in East Africa: Geol. Surv. Can. Paper 65-6, 63-83.
- Malone, E. J., 1981, Geology, geochemistry and setting of the Woodlawn deposit, in R. J. Whiteley, Ed., Geophysical case study of the Woodlawn orebody, N.S.W., Australia: Pergamon Press, 49-75.
- Malone, E. J., and Whiteley, R. J., 1981, Regional mineralization and geophysics of the Eastern Lachlan Fold Belt, in R. J. Whiteley, Ed., Geophysical case study of the Woodlawn orebody, N.S.W., Australia: Pergamon Press, 23-47.
- McCracken, K. G., Hohmann, G. W., and Oristaglio, M. L., 1980, Why time domain?: Bull. Austral. Soc. Explor. Geophys., **11**, 318-321.
- McNeill, J. D., 1980, Electrical conductivity of soils and rocks: Geonics Ltd., 22.
- Miller, L. J., and Gair, H. S., 1975, Mons Cupri copper-lead-zinc-silver deposit, in C. L. Knight, Ed., Economic geology of Australia and Papua New Guinea, v.1., Metals: Austral. Inst. Min. Metallurg., 195-202.
- O'Connell, M. D., and Nader, G. L., 1986, Conductive layer mapping by computer processing of airborne electromagnetic measurements, in G. J. Palacky, Ed., Airborne resistivity mapping: Geol. Surv. Can. Paper 86-22, 111-124.
- Olhoeft, G. R., 1975, The electrical properties of permafrost: Ph.D. thesis, Univ. of Toronto.
- Ollier, C. D., 1969, Weathering: American Elsevier.
- Palacky, G. J., 1975, Interpretation of Input AEM measurements in areas of conductive overburden: Geophysics, **40**, 490-502.
- \_\_\_\_\_, 1976, Use of decay patterns for the classification of anomalies in time-domain AEM measurements: Geophysics, **41**, 1031-1041.
- \_\_\_\_\_, 1978, Selection of a suitable model for quantitative interpretation of towed-bird AEM measurements: Geophysics, **43**, 576-587.
- \_\_\_\_\_, 1981, The airborne electromagnetic method as a tool of geological mapping: Geophys. Prosp., **29**, 60-88.
- \_\_\_\_\_, 1983, Tutorial: Research, applications, and publications in electrical and electromagnetic methods: Geophys. Prosp., **31**, 861-872.
- \_\_\_\_\_, 1986, Geological background to resistivity mapping, in G. J. Palacky, Ed., Airborne resistivity mapping: Geol. Surv. Can. Paper 86-22, 19-27.
- \_\_\_\_\_, 1987, Clay mapping using electromagnetic methods: First Break **5**, 295-306.
- Palacky, G. J., and Jagodits, F. L., 1975, Computer data processing and quantitative interpretation of airborne resistivity surveys: Geophysics, **40**, 818-830.

- Palacky, G. J., and Kadekaru, K., 1979, Effect of tropical weathering on electrical and electromagnetic measurements: *Geophysics*, **44**, 69–88.
- Palacky, G. J., Ritsema, I. L., and de Jong, S. J., 1981, Electromagnetic prospecting for groundwater in Precambrian terrains in the Republic of Upper Volta: *Geophys. Prosp.*, **29**, 932–955.
- Palacky, G. J., and Sena, F. O., 1979, Conductor identification in tropical terrains—Case histories from the Itapicuru greenstone belt, Bahia, Brazil: *Geophysics*, **44**, 1941–1962.
- Palacky, G. J., and West, G. F., 1973, Quantitative interpretation of Input AEM measurements: *Geophysics*, **38**, 1145–1158.
- Paterson, N. R., 1966, Mattagami Lake Mines—A discovery by geophysics, in *Mining Geophysics I*, Soc. Explor. Geophys., 185–196.
- \_\_\_\_\_, 1970, Exploration for massive sulphides in the Canadian Shield, in L. W. Morley, *Mining and groundwater geophysics 1967*: *Geol. Surv. Can. Econ. Geol. Rept.* 26, 275–289.
- Paterson, N. R., and Reford, S. W., 1986, Inversion of airborne electromagnetic data for overburden mapping and groundwater exploration, in G. J. Palacky, Ed., *Airborne resistivity mapping*: *Geol. Surv. Can. Paper* 86-22, 39–48.
- Pederson, R. N., 1981, Input results over Woodlawn, in R. J. Whiteley, Ed., *Geophysical case study of the Woodlawn orebody*, N.S.W., Australia: Pergamon Press, 123–136.
- Pelton, W. R., Ward, S. H., Mallof, P. G., Sill, W. R., and Nelson, P. H., 1978, Mineral discrimination and removal of inductive coupling with multifrequency IP: *Geophysics*, **43**, 588–609.
- Peltoniemi, M., 1982, Characteristics and results of an airborne electromagnetic method of geophysical surveying: *Geol. Surv. Finland Bull.* 321.
- Peredery, W. V., 1982, Geology and nickel sulphide deposits of the Thompson belt in Manitoba, in R. W. Hutchinson, C. D. Spence and J. M. Franklin, Eds., *Geol. Assoc. Can., Spec. Paper* 25, 165–209.
- Peric, M., 1981, Exploration of Burundi nickeliferous laterites by electrical methods: *Geophys. Prosp.*, **29**, 274–287.
- Pitcher, D. H., 1985, A correlation of airborne and ground electromagnetics with sonic drilling results in the Black River-Matheson (BRIM) area, District of Cochrane, in J. Wood, O. L. White, R. B. Barlow, and A. C. Colvine, Eds., *Summary of field work and other activities 1985*: Ontario Geol. Surv. Misc. Paper 126, 334–340.
- Pitcher, D. H., Barlow, R. B., and McNeill, J. D., 1984, Mapping the overburden in the Black River-Matheson (BRIM) area, District of Cochrane, employing an airborne time-domain system, in J. Wood, O. L. White, R. B. Barlow, and A. C. Colvine, Eds., *Summary of field work and other activities 1984*: Ontario Geol. Surv. Misc. Paper 119, 299–307.
- Poddar, M., and Rathor, B. S., 1983, VLF survey of the weathered layer in southern India: *Geophys. Prosp.*, **31**, 524–537.
- Podolsky, G., 1966, An evaluation of an airborne electromagnetic anomaly in northwestern Quebec, in *Mining Geophysics I*, Soc. Explor. Geophys., 197–205.
- Potter, R. R., 1985, New Brunswick's mineral industry—past, present and future: *Can. Inst. Min. Metallurg. Direct.*, 81–108.
- Questor Surveys, 1984, Input—Case histories and interpretation: privately published sales literature.
- Reed, L. E., 1981, The airborne electromagnetic discovery of the Detour zinc-copper-silver deposit, northwestern Québec: *Geophysics*, **46**, 1278–1290.
- Ritsema, I. L., 1984, Toepassing van geofysische meetmethoden bij milieoonderzoek (Bodem- en grondwaterverontreiniging): Dienst Grondwaterverkenning TNO, Delft, 1–18.
- Rozenberg, G., Henderson, J., and MacDonald, J. C., 1985, The use of transient electromagnetic data on permafrost distribution for CDP static correction: *Exp. Abstr. 55th Ann. Mtg., Soc. Expl. Geophys.*, Washington, 16.
- Ruzicka, V., and LeCheminant, G. M., 1986, Developments in uranium geology in Canada, 1985, in *Current Research, Part A: Geol. Surv. Can. Paper* 86-1A, 531–540.
- Salt, D. J., 1966, Tests of drill hole methods of geophysical prospecting on the property of Lake Dufault Mines Limited, Dufresnay Township, Quebec, in *Mining Geophysics I*, Soc. Explor. Geophys., 206–226.
- Sangster, D. F., 1984, Mississippi Valley lead-zinc, in O. R. Eckstrand, ed., *Canadian mineral deposit types: A geological synopsis*: *Geol. Surv. Can. Econ. Geol. Rept.* 36, 25.
- Saracoglu, N., Wallis, R. H., Brumner, J. J., and Golightly, J. P., 1983, The McClean uranium deposits, northern Saskatchewan—Discovery: *Can. Inst. Min. Metallurg. Bull.*, 76(852), 63–79.
- Sartorelli, A. N., Henderson, J. P., Rozenberg, G. S., and Pesowski, M., 1985, An overview of the uses of surface geophysical methods in Western Canadian Prairies coal mining areas: *Exp. Abstr. 55th Ann. Mtg., Soc. Expl. Geophys.*, Washington, 9–10.
- Scott, W. J., Sellmann, P. V., and Hunter, J. A., 1978, Geophysics in the study of permafrost: *Proc. 3rd. Int. Conf. on Permafrost*, Edmonton, 93–115.
- Seguin, M. K., 1975, Quantitative interpretation of a combined EM and magnetic heliported survey for the search of economic magnetic taconite: *Geophys. Prosp.*, **23**, 471–491.
- Seigel, H. O., 1966, Three recent Irish discovery case histories using pulse-type induced polarization, in *Mining Geophysics I*, 341–349.
- Seigel, H. O., and Pitcher, D. H., 1978, Mapping earth conductivities using a multifrequency airborne EM system: *Geophysics*, **43**, 563–575.
- Seigel, H. O., Winkler, H. A., and Boniwell, J. B., 1957, Discovery of the Mobrun Copper Ltd. sulphide deposit, Noranda mining district, Quebec, in J. P. de Wet, Ed., *Methods and case histories in mining geophysics: 6th Comm. Min. Metallurg. Congr.*, 237–245.
- Sengpiel, K. P., 1983, Resistivity/depth mapping with airborne electromagnetic survey data: *Geophysics*, **48**, 181–196.

- \_\_\_\_\_, 1986, Groundwater prospecting by multifrequency airborne electromagnetic techniques, in G. J. Palacky, Ed., Airborne resistivity mapping: Geol. Surv. Can. Paper 86-22, 131–138.
- Sibbald, T. I. I., 1983, Geology of the crystalline basement, NEA/IAEA Athabasca test area, in E. M. Cameron, Ed., Uranium exploration in Athabasca Basin, Saskatchewan, Canada: Geol. Surv. Can. Paper 82-11, 1–14.
- Sinha, A. K., 1980, Overburden characteristics in the Alfred-Hawkesbury area, Ontario, obtained by d.c. electrical soundings, in Current Research, Part C: Geol. Surv. Can. Paper 80-1C, 1–12.
- Sinha, A. K., Gresham, D. C., and Stephens, L. E., 1985, Deep electromagnetic mapping of sedimentary formations in southern Ontario, in Current Research, Part B: Geol. Surv. Can. Paper 85-1B, 199–207.
- Sinha, A. K., and Stephens, L. E., 1983, Permafrost mapping over a drained lake by electromagnetic induction methods, in Current Research, Part A: Geol. Surv. Can. Paper 83-1A, 213–220.
- Soonawala, N. M., and Hayles, J. G., 1986, Airborne electromagnetic methods in the concept assessment phase of the Canadian Nuclear Fuel Waste Management Program, in G. J. Palacky, Ed., Airborne resistivity mapping: Geol. Surv. Can. Paper 86-22, 153–158.
- Staltari, G., and Rutter, H., 1980, The Elura Dighem II survey: Bull. Austral. Soc. Explor. Geophys., 11, 240–244.
- Staples, P., 1984, Detection of massive sulphides beneath conductive overburden using the Geonics EM-37: Explor. Geophys., 15, 33–36.
- Stephens, L. E., and Graham, B. W., 1985, An electromagnetic survey over the Gloucester Landfill Site for the detection of contaminated groundwater, in Current Research, Part A: Geol. Surv. Can. Paper 85-1A, 431–440.
- Strack, K. M., 1984, The deep transient electromagnetic sounding technique: First field test in Australia: Explor. Geophys., 15, 251–259.
- Sua, J., and Spurlin, J., 1982, Interpretation of micaceous sandstones in the North Sea: Proc. Soc. Prof. Well Log Analysts, 23rd Ann. Mtg., 1–32.
- Telford, W. M., and Becker, A., 1979, Exploration case histories of the Iso and New Inscos orebodies, in P. J. Hood, Ed., Geophysics and geochemistry in the search for metallic ores: Geol. Surv. Can. Econ. Geol. Rept. 31, 605–629.
- Templeton, R. J., 1981, Gravity surveys at Woodlawn, in R. J. Whiteley, Ed., Geophysical case study of the Woodlawn orebody, N.S.W., Australia: Pergamon Press, 485–494.
- Tripp, A. C., Ward, S. H., Sill, W. R., Swift, Jr., C. M., and Petrick, W. R., 1978, Electromagnetic and Schlumberger resistivity soundings in the Roosevelt Hot Springs KGRA: Geophysics, 43, 1450–1469.
- Tyne, E. D., 1981, Drill hole resistivity and induced polarization logging at Woodlawn, in R. J. Whiteley, Ed., Geophysical case study of the Woodlawn orebody, N.S.W., Australia: Pergamon Press, 531–555.
- Tyne, E. D., Idnurm, M., and Malone, E. J., 1981, The physical properties of the Woodlawn orebody, and surrounding rocks, in R. J. Whiteley, Ed., Geophysical case study of the Woodlawn orebody, N.S.W., Australia: Pergamon Press, 99–111.
- Veillette, J. J., and Nixon, F. M., 1982, Saprolite in the Big Bald Mountain area, New Brunswick, in Current Research, Part B: Geol. Surv. Can. Paper 82-1B, 63–70.
- Verma, R. K., and Bandyopadhyay, T. K., 1983, Use of resistivity method in geological mapping—Case histories from Raniganj Coalfield, India: Geophys. Prosp., 31, 490–507.
- Wallis, R. H., Saracoglu, N., Brummer, J. J., and Golightly, J. P., 1984, Geology of the McClean uranium deposits, Northern Saskatchewan: Can. Inst. Min. Metallurg. Bull., 77(864), 57–68.
- Ward, S. H., 1957, The role of geophysics in exploration in New Brunswick, in J. P. de Wet, Ed., Methods and case histories in mining geophysics: 6th Comm. Min. Metallurg. Congr., 221–226.
- \_\_\_\_\_, 1966, The search for massive sulphides—Introduction, in Mining Geophysics I, 117–129.
- Ward, S. H. and Hohmann, W. G., 1988, Electromagnetic theory for geophysical applications: This volume.
- Ward, S. H., Parry, W. T., Nash, W. P., Sill, W. R., Cook, K. L., Smith, R. B., Chapman, D. S., Brown, F. H., Whelan, J. A., and Bowman, J. R., 1978, A summary of the geology, geochemistry, and geophysics of Roosevelt Hot Springs thermal area, Utah: Geophysics, 43, 1515–1542.
- Webster, S. S., and Skey, E. H., 1979, Geophysical and geochemical case history of the Que River deposit, Tasmania, Australia, in P. J. Hood, Ed., Geophysics and geochemistry in the search for metallic ores: Geol. Surv. Can. Econ. Geol. Rept. 31, 697–720.
- Whiteley, R. J., Ed., 1981, Geophysical case study of the Woodlawn orebody, New South Wales, Australia: Pergamon Press.
- Whiting, T. H., 1983, Surficial conductivity mapping with Input AEM system and its application to coal exploration: presented at 4th Int. Coal Explor. Symp., Sydney.
- Won, I. J., and Smits, K., 1986, Application of the airborne electromagnetic method for bathymetric charting in shallow oceans, in G. J. Palacky, Ed., Airborne resistivity mapping: Geol. Surv. Can. Paper 86-22, 99–104.
- Zollinger, R., Morrison, H. F., Lazenby, P. G., and Becker, A., 1987, Airborne electromagnetic bathymetry: Geophysics, 52, 1127–1137.
- Zonge, K. L., Figgins, S. J., and Hughes, L. J., 1985, Use of electrical geophysics to detect sources of groundwater contamination: Exp. Abst. 55th Ann. Mtg., Soc. Explor. Geophys., Washington, 147–149.



---

---

**4**

**Electromagnetic Theory  
for Geophysical Applications**

---

---



---

---

**4**

---

---

## **Electromagnetic Theory for Geophysical Applications**

***Stanley H. Ward\****

***and***

***Gerald W. Hohmann\****

### **Section 1 Fundamental Electromagnetism**

To comprehend the bases and the interpretational techniques of electrical prospecting methods, requires first a knowledge of the tools of electromagnetic theory. The ability to solve a boundary-value problem in electromagnetic theory then becomes the objective. All electromagnetic phenomena are governed by the empirical Maxwell's equations; we must start with them. Maxwell's equations are uncoupled first-order linear differential equations but can be coupled by the empirical constitutive relations which reduce the number of basic vector field functions from five to two. Care must be taken in selecting the form of the constitutive relations pertinent to the earth. In particular, for most earth problems, we assume isotropy, homogeneity, linearity, and temperature-time-pressure independence of the electrical parameters of local regions of the earth. A more complicated earth model is formed by juxtaposition of several such regions.

A concept fundamental in electricity and magnetism is that of magnetic and electric polarization. We introduce the polarization vector in a symmetrical sense which demands recognition of, at least, the theoretical existence of magnetic current density and magnetic monopoles, as well as electric current density and electric monopoles. Maxwell's equations are generalized and made more symmetric in the process with a conceptual advantage afforded when we come to deal with scalar and vector potentials. Total vector polarization functions, consisting of the algebraic sums of induced and source parts, frequently facilitate description of a physical problem.

Many boundary-value problems can be solved in terms of the vector electric and magnetic-field intensity functions. In an earth composed of several juxtaposed homogeneous isotropic linear regions, a solution of a wave equation is postulated for each region. These solutions must be matched at every boundary according to prescribed boundary conditions on two vector field functions or potentials. The wave equation used for each region is derived directly

\*Department of Geology and Geophysics, University of Utah.

from Maxwell's equations and really represents a compact form of these equations. If the wave equation is homogeneous, no sources are present in that region. If the wave equation is inhomogeneous, sources exist in that region.

Often a boundary-value problem is difficult to solve in terms of vector field functions and is easier to solve in terms of vector and/or scalar potential functions from which the vector field functions may be derived. Several different sets of potential functions appear in the literature; we use the Schelkunoff potentials because of their symmetry and because of the ease of relating them to the TE and TM modes of excitation. Any electromagnetic field, in a homogeneous, source-free region, may be decomposed into a part for which the electric field is transverse to some axis (TE mode) and a part for which the magnetic field is transverse to this same axis (TM mode). Mode decomposition simplifies the solution of boundary-value problems.

The development of a series of boundary conditions on vector field and vector plus scalar potential functions results from straight-forward application of the integral forms of Maxwell's equations. The symmetry of a boundary-value problem dictates the approach to its solution so, not surprisingly, we stress symmetry when formulating boundary conditions.

An extensive catalog of boundary conditions concludes the development which started with Maxwell's equations. SI units and an  $e^{i\omega t}$  time dependence are used to conform to the styles of most of the literature which applied geophysicists now read. This choice of harmonic time dependence corresponds to the Fourier transform pair

$$F(\omega) = \int_{-\infty}^{\infty} f(t)e^{-i\omega t} dt, \quad (1.1)$$

and

$$f(t) = \frac{1}{2\pi} \int_{-\infty}^{\infty} F(\omega)e^{i\omega t} d\omega. \quad (1.2)$$

Thus upper case letters are used for functions expressed in the frequency domain, while lower case letters are used for functions expressed in the time domain. The chosen transform pair then permits us to utilize much of the transform applications of the engineering literature. In addition our ingoing and outgoing wave functions follow those of Harrington (1961). To us, our choice was to follow the physics approach of Stratton (1941) as used in Mining Geophysics Vol. II or to adapt the more flexible approach of Harrington (1961). Our recent academic experience indicates the latter is preferable and hence we chose it. 

### Maxwell's equations in the time domain

An electromagnetic field may be defined as the domain of the four vector functions,  $\mathbf{e}$ ,  $\mathbf{b}$ ,  $\mathbf{d}$ ,  $\mathbf{h}$  where

- $\mathbf{e}$  is the electric field intensity in (V/m),
- $\mathbf{b}$  is the magnetic induction in (Wb/m<sup>2</sup> or Tesla).
- $\mathbf{d}$  is the dielectric displacement in C/m<sup>2</sup>,

and

- $\mathbf{h}$  is the magnetic field intensity in A/m.

Experimental evidence dictates that all electromagnetic phenomena obey Maxwell's equations described in the time domain as

$$\nabla \times \mathbf{e} + \frac{\partial \mathbf{b}}{\partial t} = 0, \quad (1.3)$$

$$\nabla \times \mathbf{h} - \frac{\partial \mathbf{d}}{\partial t} = \mathbf{j}, \quad (1.4)$$

$$\nabla \cdot \mathbf{b} = 0, \quad (1.5)$$

and

$$\nabla \cdot \mathbf{d} = \rho. \quad (1.6)$$

in which  $\mathbf{j}$  is electric current density in  $\text{A}/\text{m}^2$ , and  $\rho$  is electric charge density in  $\text{c}/\text{m}^3$ .

For homogeneous earth materials of conductivity  $10^{-4} \text{ S}/\text{m}$  or greater, free charge  $\rho_e$  dissipates in less than  $10^{-6} \text{ s}$  (Stratton, 1941, p. 15). Thus for geophysical prospecting, in which frequencies less than  $10^5 \text{ Hz}$  are employed,  $\partial \rho_e / \partial t \sim 0$ , and by taking the divergence of equation (1.4) we obtain

$$\nabla \cdot \mathbf{j} = 0. \quad (1.7)$$

Equation (1.7) does not apply to inhomogeneous regions; at the interface between two different media a surface charge accumulates as subsequently described.

Equations (1.3) through (1.6), the conventional forms of Maxwell's equations, are based on the experiments, for example, of Faraday and Ampere. Thus they are empirical but they do describe most macroscopic electromagnetic phenomena. They may be made symmetric, as shown subsequently, by adding a magnetic current source term on the right-hand side of equation (1.3) and the time derivative of a magnetic charge source on the right-hand side of equation (1.5). Considerable facility is afforded the solution of certain boundary-value problems by such a generalization.

### The constitutive relations

Equations (1.3) through (1.6), are uncoupled differential equations of the five vector functions,  $\mathbf{e}$ ,  $\mathbf{b}$ ,  $\mathbf{h}$ ,  $\mathbf{d}$ , and  $\mathbf{j}$ . These equations are coupled through the frequency-domain constitutive relations

$$\mathbf{D} = \epsilon(\omega, \mathbf{E}, \mathbf{r}, t, T, P, \dots) \cdot \mathbf{E}, \quad (1.8)$$

$$\mathbf{B} = \mu(\omega, \mathbf{H}, \mathbf{r}, t, T, P, \dots) \cdot \mathbf{H}, \quad (1.9)$$

and

$$\mathbf{J} = \sigma(\omega, \mathbf{E}, \mathbf{r}, t, T, P, \dots) \cdot \mathbf{E}, \quad (1.10)$$

in which the tensors,  $\epsilon$ ,  $\mu$ ,  $\sigma$  describe, respectively, the dielectric permittivity, the magnetic permeability, and the electric conductivity as functions of angular frequency  $\omega$ , electric field strength  $\mathbf{E}$  or magnetic induction  $\mathbf{B}$ , position  $\mathbf{r}$ , time  $t$ , temperature  $T$ , and pressure  $P$ . Each of these three tensors is complex in the general case, permitting the phases of  $\mathbf{D}$  and  $\mathbf{E}$ , of  $\mathbf{H}$  and  $\mathbf{B}$ , and of  $\mathbf{J}$  and  $\mathbf{E}$  to be different. In most elementary electromagnetic earth problems the following assumptions are made in order to simplify analysis:

- (1) all media are linear, isotropic, homogeneous, and possess electrical properties which are independent of time, temperature, or pressure, and
- (2) the magnetic permeability  $\mu$  is assumed to be that of free space, i.e.,  $\mu = \mu_0$ .

Neither of these assumptions is made in some applications; exceptions follow.

- (1) Attempts to exploit the subtle nonlinearities in  $\sigma$  and  $\mu$  have been made but they have not yet resulted in significant new methods.
- (2) Anisotropic media are included in some simple electromagnetic boundary-value problems to aid in interpretation of data.
- (3) Inhomogeneous media entering into electromagnetic boundary-value problems are treated as one-dimensionally inhomogeneous (plane-layered), two-dimensionally inhomogeneous (infinite cylinders of arbitrary cross-section), or three-dimensionally inhomogeneous. The latter case, which is the most general, has only recently become amenable to solution.
- (4) In geothermal exploration, attempts have been made to determine temperature from measurements of electric conductivity, but these attempts have not generally been successful because conductivity is much more affected by pore water salinity, for example, than by temperature.
- (5) In deep crustal studies the effects of temperature and pressure must be considered.
- (6) The time dependence of electric conductivity due to varying moisture content in surface soils cannot be ignored in some shallow geotechnical investigations.

For the purpose of subsequent discussion, the following three constitutive relations suffice:

$$\mathbf{D} = [\epsilon'(\omega) - i\epsilon''(\omega)]\mathbf{E} = \epsilon\mathbf{E}, \quad (1.11)$$

$$\mathbf{J} = [\sigma'(\omega) + i\sigma''(\omega)]\mathbf{E} = \sigma\mathbf{E}, \quad (1.12)$$

and

$$\mathbf{B} = \mu\mathbf{H}, \quad (1.13)$$

in which dielectric permittivity  $\epsilon$  and electric conductivity  $\sigma$  are complex functions of angular frequency, while magnetic permeability  $\mu$  is assumed to be independent of frequency and is real. For some applications, such as in studying the superparamagnetic effect (Buselli, 1982), the imaginary part of  $\mu$  is important.

### Maxwell's equations in the frequency domain

If we effect a one-dimensional (1-D) Fourier transformation of equations (1.3) and (1.4), and utilize the constitutive relations (1.11), (1.12), and (1.13), we obtain Maxwell's equations in the frequency domain

$$\nabla \times \mathbf{E} + i\mu\omega\mathbf{H} = 0, \quad (1.14)$$

and

$$\nabla \times \mathbf{H} - (\sigma + i\epsilon\omega)\mathbf{E} = 0. \quad (1.15)$$

Introducing the impedivity  $\hat{z} = i\mu\omega$  and the admittivity  $\hat{y} = \sigma + i\epsilon\omega$  (Harrington, 1961), equations (1.14) and (1.15) are written

$$\nabla \times \mathbf{E} + \hat{z}\mathbf{H} = 0, \quad (1.16)$$

and

$$\nabla \times \mathbf{H} - \hat{y}\mathbf{E} = 0. \quad (1.17)$$

### The wave equations

Upon taking the curl of each, equations (1.3) and (1.4) become

$$\nabla \times (\nabla \times \mathbf{e}) + \nabla \times \left( \frac{\partial \mathbf{b}}{\partial t} \right) = 0, \quad (1.18)$$

and

$$\nabla \times (\nabla \times \mathbf{h}) - \nabla \times \left( \frac{\partial \mathbf{d}}{\partial t} \right) = \nabla \times \mathbf{j}. \quad (1.19)$$

The constitutive relations in the time domain, restricted to nondispersive cases where  $\mu$ ,  $\epsilon$ , and  $\sigma$  are independent of time, are

$$\mathbf{d} = \epsilon \mathbf{e},$$

$$\mathbf{b} = \mu \mathbf{h},$$

and

$$\mathbf{j} = \sigma \mathbf{e}.$$

These may now be substituted in equation (1.18) and (1.19) to yield

$$\nabla \times \nabla \times \mathbf{e} + \nabla \times \left[ \frac{\partial}{\partial t} (\mu \mathbf{h}) \right] = 0, \quad (1.20)$$

and

$$\nabla \times \nabla \times \mathbf{h} - \nabla \times \left[ \frac{\partial}{\partial t} (\epsilon \mathbf{e}) \right] = \nabla \times (\sigma \mathbf{e}). \quad (1.21)$$

Then equations (1.20) and (1.21) reduce to

$$\nabla \times \nabla \times \mathbf{e} + \mu \nabla \times \frac{\partial \mathbf{h}}{\partial t} = 0, \quad (1.22)$$

and

$$\nabla \times \nabla \times \mathbf{h} - \epsilon \nabla \times \frac{\partial \mathbf{e}}{\partial t} = \sigma \nabla \times \mathbf{e}. \quad (1.23)$$

Provided the vector functions  $\mathbf{h}$  and  $\mathbf{e}$  are piecewise continuous and possess continuous first and second derivatives, then the operators  $\nabla \times$  and  $\partial/\partial t$  may be interchanged so that equations (1.22) and (1.23) become

$$\nabla \times \nabla \times \mathbf{e} + \mu \frac{\partial}{\partial t} (\nabla \times \mathbf{h}) = 0, \quad (1.24)$$

and

$$\nabla \times \nabla \times \mathbf{h} - \epsilon \frac{\partial}{\partial t} (\nabla \times \mathbf{e}) = \sigma \nabla \times \mathbf{e}. \quad (1.25)$$

The quantities  $\nabla \times \mathbf{h}$  and  $\nabla \times \mathbf{e}$  are, of course, given in equations (1.4) and (1.3), respectively, so that equations (1.24) and (1.25) are readily converted to

$$\nabla \times \nabla \times \mathbf{e} + \mu\epsilon \frac{\partial^2 \mathbf{e}}{\partial t^2} + \mu\sigma \frac{\partial \mathbf{e}}{\partial t} = 0, \quad (1.26)$$

and

$$\nabla \times \nabla \times \mathbf{h} + \mu\epsilon \frac{\partial^2 \mathbf{h}}{\partial t^2} + \mu\sigma \frac{\partial \mathbf{h}}{\partial t} = 0. \quad (1.27)$$

The vector identity

$$\nabla \times \nabla \times \mathbf{a} \equiv \nabla \nabla \cdot \mathbf{a} - \nabla^2 \mathbf{a}, \quad (1.28)$$

permits us to expand the first term in each of equations (1.26) and (1.27). Taking cognizance of the fact that  $\nabla \cdot \mathbf{e} = 0$  and  $\nabla \cdot \mathbf{h} = 0$ , for homogeneous regions, then equations (1.26) and (1.27) become

$$\nabla^2 \mathbf{e} - \mu\epsilon \frac{\partial^2 \mathbf{e}}{\partial t^2} - \mu\sigma \frac{\partial \mathbf{e}}{\partial t} = 0, \quad (1.29)$$

and

$$\nabla^2 \mathbf{h} - \mu\epsilon \frac{\partial^2 \mathbf{h}}{\partial t^2} - \mu\sigma \frac{\partial \mathbf{h}}{\partial t} = 0. \quad (1.30)$$

These are wave equations for the electric and magnetic fields, stated in the time domain. Fourier transformation of equations (1.29) and (1.30) with respect to time leads to

$$\nabla^2 \mathbf{E} + (\mu\epsilon\omega^2 - i\mu\sigma\omega)\mathbf{E} = 0, \quad (1.31)$$

and

$$\nabla^2 \mathbf{H} + (\mu\epsilon\omega^2 - i\mu\sigma\omega)\mathbf{H} = 0, \quad (1.32)$$

or

$$\nabla^2 \mathbf{E} + k^2 \mathbf{E} = 0, \quad (1.33)$$

and

$$\nabla^2 \mathbf{H} + k^2 \mathbf{H} = 0, \quad (1.34)$$

in which

$$k^2 = \mu\epsilon\omega^2 - i\mu\sigma\omega = -\hat{z}\hat{y}. \quad (1.35)$$

Equations (1.31) through (1.35) are the wave equations in the frequency domain, or more commonly, the Helmholtz equations in  $\mathbf{E}$  and  $\mathbf{H}$ . While  $\mu$ ,  $\epsilon$ , and  $\sigma$  were constant with respect to time in obtaining equations (1.22) and (1.23), in this case they can be functions of frequency. In equations (1.31) and (1.32),  $\mu\epsilon\omega^2 \ll \mu\sigma\omega$  for earth materials at frequencies less than  $10^5$  Hz; displacement currents are much smaller than conduction currents. Thus equations (1.29) through (1.32) may be rewritten as

$$\nabla^2 \mathbf{e} - \mu\sigma \frac{\partial \mathbf{e}}{\partial t} = 0, \quad (1.36)$$

$$\nabla^2 \mathbf{h} - \mu\sigma \frac{\partial \mathbf{h}}{\partial t} = 0, \quad (1.37)$$

$$\nabla^2 \mathbf{E} - i\mu\sigma\omega \mathbf{E} = 0, \quad (1.38)$$

and

$$\nabla^2 \mathbf{H} - i\mu\sigma\omega \mathbf{H} = 0. \quad (1.39)$$

Under this circumstance, the wave number is given by

$$k = (-i\mu\sigma\omega)^{1/2}. \quad (1.40)$$

Equations (1.36) through (1.39) represent diffusion equations. It is important to recognize that diffusion equations apply for real earth materials and lead to the attendant lack of resolution of electromagnetic prospecting methods. Their 1-D versions are

$$\frac{\partial^2 \mathbf{e}}{\partial z^2} - \mu\sigma \frac{\partial \mathbf{e}}{\partial t} = 0, \quad (1.41)$$

$$\frac{\partial^2 \mathbf{h}}{\partial z^2} - \mu\sigma \frac{\partial \mathbf{h}}{\partial t} = 0, \quad (1.42)$$

$$\frac{\partial^2 \mathbf{E}}{\partial z^2} - i\mu\sigma\omega \mathbf{E} = 0, \quad (1.43)$$

and

$$\frac{\partial^2 \mathbf{H}}{\partial z^2} - i\mu\sigma\omega \mathbf{H} = 0. \quad (1.44)$$

**Solutions of the Wave Equations.**—Equations (1.41) through (1.44) are second-order linear differential equations; two basic solutions are of interest. First, for a sinusoidal time dependence  $e^{i\omega t}$

$$\mathbf{e} = \mathbf{e}_0^+ e^{-i(kz - \omega t)} + \mathbf{e}_0^- e^{i(kz + \omega t)}, \quad (1.45)$$

and

$$\mathbf{h} = \mathbf{h}_0^+ e^{-i(kz - \omega t)} + \mathbf{h}_0^- e^{i(kz + \omega t)}. \quad (1.46)$$

Since  $k$  is complex, it is written

$$k = \alpha - i\beta \quad (1.47)$$

in which  $\alpha$  and  $\beta$  are both real. The quantities  $\alpha$  and  $\beta$  are given, in general, by (Stratton, 1941)

$$\alpha = \omega \left\{ \frac{\mu \epsilon}{2} \left[ \left( 1 + \frac{\sigma^2}{\epsilon^2 \omega^2} \right)^{1/2} + 1 \right] \right\}^{1/2}, \quad (1.48)$$

and

$$\beta = \omega \left\{ \frac{\mu \epsilon}{2} \left[ \left( 1 + \frac{\sigma^2}{\epsilon^2 \omega^2} \right)^{1/2} - 1 \right] \right\}^{1/2}. \quad (1.49)$$

When conduction currents dominate over displacement currents, as is customary in electrical prospecting,  $\alpha$  and  $\beta$  are identical real quantities defined by

$$\alpha = \beta = \left( \frac{\omega \mu \sigma}{2} \right)^{1/2}. \quad (1.50)$$

Then the solutions of equations (1.45) and (1.46) that decay in the positive  $z$  direction may be written

$$\mathbf{e} = \mathbf{e}_0^+ e^{-i\alpha z} \hat{e}^{-\beta z} e^{i\omega t}, \quad (1.51)$$

and

$$\mathbf{h} = \mathbf{h}_0^+ e^{-i\alpha z} e^{-\beta z} e^{i\omega t}. \quad (1.52)$$

From equations (1.51) and (1.52) we may draw the following conclusions.

- (1) Since  $\beta$  is real,  $e^{-\beta z}$  gets smaller as  $z$  gets larger. Hence it represents attenuation. An electromagnetic wave will be reduced in amplitude by a factor of  $1/e$  at a distance, within a medium, described by the skin depth  $\delta$ , where

$$\delta = \left( \frac{2}{\omega \mu \sigma} \right)^{1/2} = 503 \left( \frac{1}{f \sigma} \right)^{1/2}, \quad (1.53)$$

- (2)  $e^{-i\alpha z} = \cos(\alpha z) - i \sin(\alpha z)$  states that the wave varies sinusoidally with  $z$ . (1.54)

- (3)  $e^{i\omega t} = \cos(\omega t) + i \sin(\omega t)$  states that the wave varies sinusoidally with  $t$ . (1.55)

- (4) Over a plane fixed in space,  $\mathbf{e}$  and  $\mathbf{h}$  vary with time as in Figure 1.1(a).  
(5) If the wave propagates in the  $z$  direction,  $\mathbf{e}$  and  $\mathbf{h}$  will vary sinusoidally with  $z$  as in Figure 1.1(b).

How do we know that the wave propagates? The arguments follow.

- (1)  $\partial/\partial x = \partial/\partial y = 0$  states that  $e_x$  and  $h_y$  have constant magnitudes over a plane perpendicular to the  $z$  axis. This is a uniform plane wave as in Figure 1.1(c).
- (2) Planes at different distances along  $z$  will have their own magnitudes. At (1) and (3) in Figure 1.1b above,  $e_x$  and  $h_y$  are maximum. At (2) in the same figure,  $e_x$  and  $h_y$  are zero.
- (3) In any plane,  $\mathbf{e}$  or  $\mathbf{h}$  will exhibit the same phase, i.e. at each point over the plane,  $\mathbf{e}$  or  $\mathbf{h}$  will reach its positive peak, zero crossing, or negative peak at identical times. Any such plane is referred to, therefore, as a plane of constant phase.
- (4) The peaks of the  $\mathbf{e}$  or  $\mathbf{h}$  field which occur at  $t = 0, z = 0$ , will occur downstream at  $t = t_1, z = z_1$ . That is, a plane of constant phase will propagate in the  $z$  direction, if we set  $\partial/\partial x = \partial/\partial y = 0$  as appropriate to a uniform plane wave.
- (5) A plane of constant phase is described by

$$\mathbf{e} = \mathbf{e}_0^+ e^{-i(\alpha z - \omega t)} = \mathbf{e}_0^+ e^{-ic}, \quad (1.56)$$

where  $c$  is the phase, i.e. description of the amplitude of the sine wave as a function of  $z$  and  $t$ .

If we set

$$\alpha z - \omega t = c, \quad \text{then} \quad (1.57)$$

$$\frac{dz}{dt} = \frac{\omega}{\alpha} = V_{ph}, \quad (1.58)$$

which is a positive phase velocity.

Similarly for

$$\mathbf{h} = \mathbf{h}_0^- e^{i(\alpha z + \omega t)} = \mathbf{h}_0^- e^{ic}, \quad (1.59)$$

$$\frac{dz}{dt} = -\frac{\omega}{\alpha} = V_{ph}, \quad (1.60)$$

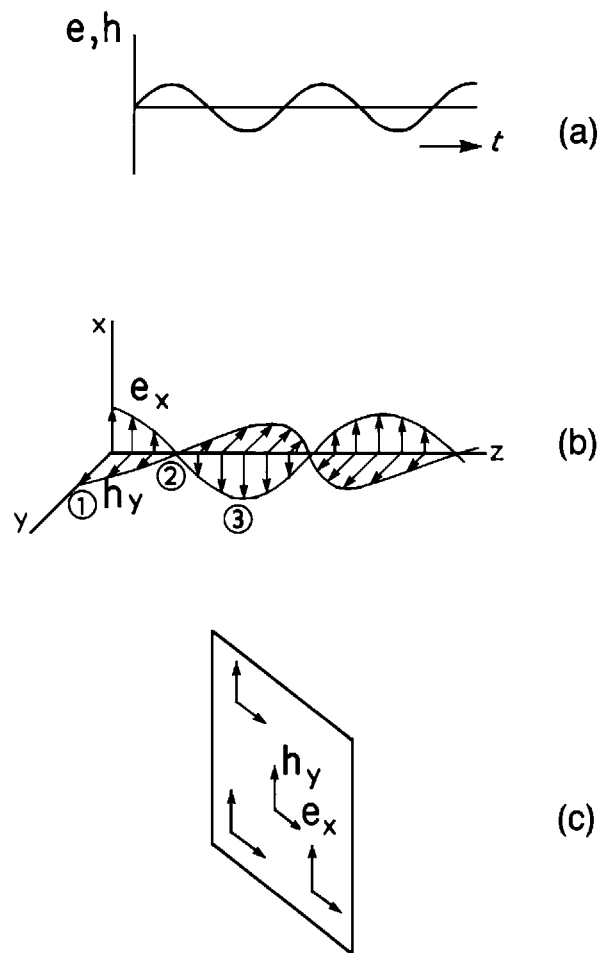


FIG. 1.1. (a) The sinusoidal behavior of  $e$  and  $h$  as functions of time. (b) The sinusoidal behavior of  $e_x$  and  $h_y$  as functions of propagation distance  $z$ . (c) Illustration of behavior of  $e_x$  and  $h_y$  in a uniform plane wave.

which is a negative phase velocity. This explains why we used  $\mathbf{e}_0^+$  and  $\mathbf{e}_0^-$  as the amplitudes of the positively and negatively traveling waves.

A medium is described as dispersive if the phase velocity is a function of frequency, i.e.,  $V_{ph} = V_{ph}(\omega)$ . This is generally the case in electromagnetic problems in geophysics. Similarly the wave number  $(\mu\epsilon\omega^2 - i\mu\sigma\omega)^{1/2}$  is a function of  $\omega$ , i.e.,  $k = k(\omega)$ ; and this relationship may be inverted to find  $\omega$  as a function of  $k$ , i.e.,  $\omega = \omega(k)$ . The expressions  $k = k(\omega)$  and  $\omega = \omega(k)$  are the more general expressions of dispersion. Note that when displacement currents are neglected, corresponding to  $\partial\rho_e/\partial t = 0$  or to the quasi-static approximation  $V_{ph} \sim (2\omega/\mu\sigma)^{1/2}$ , from equation (1.60) it follows that common earth materials are dispersive even if  $\mu$  and  $\sigma$  are independent of frequency.

The second basic set of solutions of equations (1.41) and (1.42) is for impulsive electric and magnetic fields at  $z = 0$ . If displacement currents are neglected, the solutions, which can be derived by inverse Fourier transformation of equations (1.45) and (1.46), are similar to that for the scalar Green's function given in equation (2.28). Because transient solutions have practical importance mainly for finite sources, we postpone the derivation until Section 2. By analogy with equation (2.28) the positive solutions of equations (1.41) and (1.42) for impulsive electric or magnetic fields in the  $z = 0$  plane are

$$\begin{pmatrix} \mathbf{e} \\ \mathbf{h} \end{pmatrix} = \begin{pmatrix} \mathbf{e}_0^+ \\ \mathbf{h}_0^+ \end{pmatrix} \frac{(\mu\sigma)^{1/2}z}{2\pi^{1/2}t^{3/2}} e^{-\mu\sigma z^2/4t}. \quad (1.61)$$

The behavior of the field as a function of time for a particular distance  $z$  is illustrated in Figure 1.2a. Basically, the field exhibits a peak with a long tail, with the peak occurring at

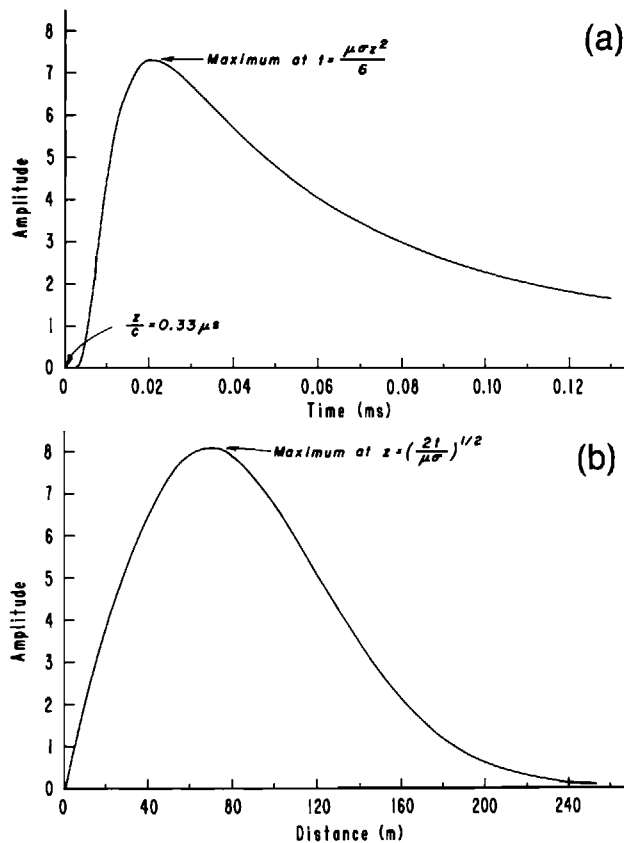


FIG. 1.2. (a) Electric or magnetic field as a function of time 100 m from a 1-D impulse in the field in a 0.01 S/m whole space. In free space the field would be an impulse at  $t = j z/c = 3.3 \times 10^{-4}$  ms. (b) Electric or magnetic field at  $t = 0.03$  ms as a function of distance from an impulse in the field.

$$t_{\max} = \frac{\mu\sigma z^2}{6}, \quad (1.62)$$

which can be derived by setting the time derivative of equation (1.61) to zero.

Figure 1.2b shows the field as a function of distance  $z$  for a fixed time. Setting the derivative of equation (1.61) with respect to  $z$  to zero reveals that for a fixed time the field reaches a maximum at a distance

$$z_{\max} = \left( \frac{2t}{\mu\sigma} \right)^{1/2}, \quad (1.63)$$

where  $z_{\max}$  is the penetration depth. The maximum travels with a velocity

$$V = \frac{dz_{\max}}{dt} = \frac{1}{(2\mu\sigma t)^{1/2}}. \quad (1.64)$$

Note the similarity between the penetration depth, which is proportional to  $t^{1/2}$  and the skin depth, which is proportional to  $1/\omega^{1/2}$ .

Nabighian (this volume) finds a similar temporal behavior for the diffusing electric field due to a step-function magnetic field at  $z = 0$ . His expression can be derived by integrating equation (1.61) with respect to time to obtain the magnetic field and applying Maxwell's equations to find the corresponding electric field.

### Dispersive electrical parameters

The total current density  $\nabla \times \mathbf{H}$  of equation (1.15) is made up of a part  $\sigma\mathbf{E}$ , the conduction current, which is in-phase with the electric field intensity for real  $\sigma$ , and a part  $i\epsilon\omega\mathbf{E}$ , the displacement current, which is in quadrature with the electric field intensity for real  $\epsilon$ . When both  $\sigma$  and  $\epsilon$  are complex, the association of conduction current with in-phase and displacement current with quadrature is no longer possible. Thus for general earth media we usually write

$$k = \{-i\mu\omega[\sigma'(\omega) + i\sigma''(\omega)]\}^{1/2},$$

or

$$k = \{-i\mu\omega|\sigma(\omega)|e^{i\phi(\omega)}\}^{1/2}, \quad (1.65)$$

in which real and imaginary parts of dielectric permittivity have become absorbed into imaginary and real parts, respectively, of electrical conductivity. The latter form is used for normal earth materials, where  $|\sigma(\omega)|$  is the amplitude and  $\phi(\omega)$  is the phase of conductivity.

The relative dielectric permittivity is defined as the dimensionless quantity

$$K_e = \epsilon/\epsilon_0, \quad (1.66)$$

and the relative magnetic permeability as the dimensionless quantity

$$K_m = \mu/\mu_0, \quad (1.67)$$

where  $\epsilon_0$  has the free-space value  $8.854 \times 10^{-12}$  F/m, while  $\mu_0$  has the free-space value  $4\pi \times 10^{-7}$  H/m.

In dealing with dry earth materials we sometimes prefer to describe a material by a relative dielectric permittivity,  $K_e$ , and a loss tangent,  $\tan \delta$ . The loss tangent is derived by absorbing the real and imaginary parts of electrical conductivity into imaginary and real parts, respectively, of dielectric permittivity. Thus for dielectric description

$$k^2 = \mu\epsilon\omega^2 \left[ 1 - i \frac{\sigma}{\epsilon\omega} \right] = \mu\epsilon\omega^2 [1 - i \tan \delta], \quad (1.68)$$

in which  $\tan \delta = \sigma/\epsilon\omega$  is the ratio of conduction, i.e., real, to displacement, i.e., quadrature, currents if both  $\sigma$  and  $\epsilon$  are real. If  $\sigma$  and  $\epsilon$  are both complex, then  $\tan \delta$  should be defined as the ratio of total real current to total quadrature current:

$$\tan \delta = \frac{\sigma' + \epsilon''\omega}{\sigma'' + \epsilon'\omega}. \quad (1.69)$$

Equation (1.69) becomes  $\tan \delta = \sigma'/\sigma''$ , at zero frequency, and  $\tan \delta = \epsilon''/\epsilon'$  at infinite frequency. At frequencies less than  $10^5$  Hz and for normal earth materials,  $\tan \delta$  is usually much greater than unity so it is customary to state that conduction currents predominate over displacement currents. If both  $\sigma$  and  $\epsilon$  are complex, no such simple interpretation can be made.

From equation (1.69),

$$\tan \delta \approx \frac{\epsilon''}{\epsilon'}, \quad (1.70)$$

for lossy dielectric media at high frequencies such that  $\epsilon''\omega \gg \sigma'$  and  $\epsilon'\omega \gg \sigma''$ . The radar sounding of ice or dry soils could readily utilize this approximation. When this occurs, electric and magnetic fields are given by equations (1.51) and (1.52), with

$$\alpha = \omega \left\{ \frac{\mu\epsilon}{2} [(1 + \tan^2 \delta)^{1/2} + 1] \right\}^{1/2}, \quad (1.71)$$

and

$$\beta = \omega \left\{ \frac{\mu\epsilon}{2} [(1 + \tan^2 \delta)^{1/2} - 1] \right\}^{1/2}. \quad (1.72)$$

If  $\epsilon$  is complex then  $\alpha$  and  $\beta$  are complex; propagation and attenuation must then be considered carefully in terms of  $\alpha = \alpha' + i\alpha''$  and  $\beta = \beta' + i\beta''$ .

### Polarization vectors

We introduce the polarization vectors  $\mathbf{p}$  and  $\mathbf{m}$  via the defining relations

$$\mathbf{p} \equiv \mathbf{d} - \epsilon_0 \mathbf{e}, \quad (1.73)$$

and

$$\mathbf{m} \equiv \frac{1}{\mu_0} \mathbf{b} - \mathbf{h}. \quad (1.74)$$

These vectors do not exist in free space, obviously, and therefore pertain to induced electric polarization,  $\mathbf{p}$ , and to induced magnetic polarization,  $\mathbf{m}$  of matter.

In isotropic linear earth media, induced  $\mathbf{p}$  is parallel to and proportional to  $\mathbf{e}$  while induced  $\mathbf{m}$  is parallel to and proportional to  $\mathbf{h}$ . Thus it is customary to introduce the dielectric susceptibility  $\chi_e$ , and the magnetic susceptibility  $\chi_m$ , via the defining equations for induced polarizations

$$\mathbf{p} \equiv \chi_e \epsilon_0 \mathbf{e}, \quad (1.75)$$

and

$$\mathbf{m} \equiv \chi_m \mathbf{h}. \quad (1.76)$$

Comparison of equation (1.75) with equation (1.73) and equation (1.76) with equation (1.74) yields the following relationships,

$$\chi_e = K_e - 1, \quad (1.77)$$

and

$$\chi_m = K_m - 1. \quad (1.78)$$

From equations (1.77) and (1.78)

$$\epsilon = \epsilon_0(1 + \chi_e), \quad (1.79)$$

and

$$\mu = \mu_0(1 + \chi_m). \quad (1.80)$$

It has been customary to express the susceptibilities of rocks in the cgs system, and therefore as  $k = \mu^c - 1/4\pi$  where  $\mu^c$  is the cgs permeability and  $k$  is the cgs susceptibility. Upon comparison of this expression with equation (1.80) we observe that  $\chi_m = 4\pi k$  and that  $\mu^c = K_m$ .

The total observed polarization vectors  $\mathbf{p}$  and  $\mathbf{m}$  are composed of source ( $S$ ) and induced ( $I$ ) parts given by

$$\mathbf{p} = \mathbf{p}^I + \mathbf{p}^S, \quad (1.81)$$

and

$$\mathbf{m} = \mathbf{m}^I + \mathbf{m}^S \quad (1.82)$$

Thus we may cast equations (1.73) and (1.74) in the forms

$$\mathbf{d} = [\epsilon_0 \mathbf{e} + \mathbf{p}^I] + \mathbf{p}^S = [\epsilon_0(1 + \chi_e) \mathbf{e}] + \mathbf{p}^S = \epsilon \mathbf{e} + \mathbf{p}^S, \quad (1.83)$$

and

$$\mathbf{b} = [\mu_0(\mathbf{h} + \mathbf{m}^I)] + \mu_0 \mathbf{m}^S = [\mu_0(1 + \chi_m) \mathbf{h}] + \mu_0 \mathbf{m}^S = \mu \mathbf{h} + \mu_0 \mathbf{m}^S. \quad (1.84)$$

Equations (1.83) and (1.84) enable us to eliminate  $\mathbf{d}$  and  $\mathbf{b}$  in Maxwell's equations (1.3) through (1.6) as follows

$$\nabla \times \mathbf{e} + \mu \frac{\partial \mathbf{h}}{\partial t} + \mu_0 \frac{\partial \mathbf{m}^S}{\partial t} = 0, \quad (1.85)$$

$$\nabla \times \mathbf{h} - \epsilon \frac{\partial \mathbf{e}}{\partial t} - \frac{\partial \mathbf{p}^S}{\partial t} = \mathbf{j}_e \quad (1.86)$$

$$K_m \nabla \cdot \mathbf{h} + \nabla \cdot \mathbf{m}^S = 0, \quad (1.87)$$

and

$$\epsilon \nabla \cdot \mathbf{e} + \nabla \cdot \mathbf{p}^s = \rho_e, \quad (1.88)$$

in situations where  $\mu$  and  $\epsilon$  are not dispersive and do not vary with position.

If in equation (1.86)  $\mathbf{j}_e$  is treated solely as an induced current density, then the electric source current density is described by

$$\mathbf{j}_e^s = \frac{\partial \mathbf{p}^s}{\partial t} = i\omega \mathbf{P}^s. \quad (1.89)$$

Also, the source contribution to charge density is, from equation (1.88)

$$\rho^s = \nabla \cdot \mathbf{p}^s. \quad (1.90)$$

In the frequency domain,  $\mathbf{J}_e^s = i\omega \mathbf{P}^s$  is the electric source current density, while  $\mathbf{J}_m^s = i\mu_0 \omega \mathbf{M}^s$  is the magnetic source current density.

### Schelkunoff potentials

Maxwell's equations in the frequency domain, equations (1.16) and (1.17), are homogeneous equations that apply in source-free regions. In regions containing sources they must be replaced by the inhomogeneous equations

$$\nabla \times \mathbf{E} + i\omega \mathbf{H} = -\mathbf{J}_m^s = -i\mu_0 \omega \mathbf{M}^s, \quad (1.91)$$

and

$$\nabla \times \mathbf{H} - i\omega \mathbf{E} = \mathbf{J}_e^s = i\omega \mathbf{P}^s, \quad (1.92)$$

in which  $\mathbf{J}_m^s$  is a magnetic current and  $\mathbf{J}_e^s$  is an electric current. For the purposes of this discussion the quantity  $\mathbf{J}_m^s$ , while a useful artifice, demands magnetic monopoles if an equation of continuity for magnetic charge

$$\nabla \cdot \mathbf{j}_m + \frac{\partial \rho_m}{\partial t} = 0 \quad (1.93)$$

is to apply.

Equations (1.91) and (1.92) can be solved readily for infinite homogeneous regions provided  $\mathbf{J}_m^s$  and  $\mathbf{J}_e^s$  can be described explicitly, as shown in Section 2. A device used to obtain solutions is that of expressing  $\mathbf{E}$  and  $\mathbf{H}$  in terms of potentials, i.e., functions from which  $\mathbf{E}$  and  $\mathbf{H}$  may be derived by differentiation. The equations in potentials sometimes are easier to solve than the equations in fields.

A very convenient set of potentials used to solve wave equations in a space composed of homogeneous regions is that due to Schelkunoff (1943). The following development introduces and defines this set.

We attribute extant electric and magnetic fields, in each homogeneous region, to a superposition of sources of electric type and of magnetic type. Thus, let

$$\mathbf{E} = \mathbf{E}_m + \mathbf{E}_e, \quad (1.94)$$

and

$$\mathbf{H} = \mathbf{H}_m + \mathbf{H}_e. \quad (1.95)$$

The electromagnetic field defined by the pairs of vector functions  $\mathbf{E}_m$ ,  $\mathbf{H}_m$  and  $\mathbf{E}_e$ ,  $\mathbf{H}_e$  shall be written  $[\mathbf{E}_m, \mathbf{H}_m]$  and  $[\mathbf{E}_e, \mathbf{H}_e]$  subsequently. For  $[\mathbf{E}_m, \mathbf{H}_m]$  we assume that  $\mathbf{J}_e^S$  is zero, while for  $[\mathbf{E}_e, \mathbf{H}_e]$  we assume that  $\mathbf{J}_m^S$  is zero. Accordingly,  $[\mathbf{E}_m, \mathbf{H}_m]$  are solutions of

$$\nabla \times \mathbf{E}_m = -\mathbf{J}_m^S - \hat{z}\mathbf{H}_m, \quad (1.96)$$

and

$$\nabla \times \mathbf{H}_m = \hat{y}\mathbf{E}_m. \quad (1.97)$$

On the other hand,  $[\mathbf{E}_e, \mathbf{H}_e]$  are solutions of

$$\nabla \times \mathbf{E}_e = -\hat{z}\mathbf{H}_e, \quad (1.98)$$

and

$$\nabla \times \mathbf{H}_e = \mathbf{J}_e^S + \hat{y}\mathbf{E}_e. \quad (1.99)$$

The field  $[\mathbf{E}_e, \mathbf{H}_e]$  is thus produced by electric currents while the field  $[\mathbf{E}_m, \mathbf{H}_m]$  is produced by magnetic currents. The total field  $[\mathbf{E}, \mathbf{H}] = [\mathbf{E}_e, \mathbf{H}_e] + [\mathbf{E}_m, \mathbf{H}_m]$  then will satisfy equations (1.91) and (1.92).

Taking the divergence of equations (1.96), (1.97), (1.98), and (1.99) yields

$$\nabla \cdot \mathbf{H}_m = -\frac{\nabla \cdot \mathbf{J}_m^S}{\hat{z}}, \quad (1.100)$$

$$\nabla \cdot \mathbf{E}_m = 0, \quad (1.101)$$

$$\nabla \cdot \mathbf{H}_e = 0, \quad (1.102)$$

and

$$\nabla \cdot \mathbf{E}_e = -\frac{\nabla \cdot \mathbf{J}_e^S}{\hat{y}}. \quad (1.103)$$

Singularities in the source functions  $\mathbf{J}_m^S$  and  $\mathbf{J}_e^S$  must be considered carefully if the differentiations in equations (1.100) and (1.103) are to be effected; we shall study this problem as we proceed.

Equations (1.101) and (1.102) suggest that  $\mathbf{E}_m$  and  $\mathbf{H}_e$  may be represented as the curls of two vector functions, i.e.

$$\mathbf{E}_m \equiv -\nabla \times \mathbf{F}, \quad (1.104)$$

and

$$\mathbf{H}_e \equiv \nabla \times \mathbf{A}, \quad (1.105)$$

where the signs of the equalities are arbitrary.

If we now substitute equations (1.104) and (1.105) into equations (1.97) and (1.98), respectively, we obtain

$$\mathbf{H}_m = -\hat{y}\mathbf{F} - \nabla U, \quad (1.106)$$

and

$$\mathbf{E}_e = -\hat{z}\mathbf{A} - \nabla V, \quad (1.107)$$

where  $U$  and  $V$  are two arbitrary scalar functions that are introduced because the equality of the curls of two vectors does not demand that the vectors be identical.

Equation (1.96) becomes, with the aid of equations (1.104) and (1.106)

$$\nabla \times \nabla \times \mathbf{F} = \mathbf{J}_m^S - \hat{y}\hat{z}\mathbf{F} - \hat{z}\nabla U, \quad (1.108)$$

while equation (1.99) becomes, with the aid of equations (1.105) and (1.107),

$$\nabla \times \nabla \times \mathbf{A} = \mathbf{J}_e^S - \hat{y}\hat{z}\mathbf{A} - \hat{y}\nabla V. \quad (1.109)$$

Expansion of the left-hand sides of equations (1.108) and (1.109) using (1.28) results in

$$\nabla \nabla \cdot \mathbf{F} - \nabla^2 \mathbf{F} = \mathbf{J}_m^S - \hat{y}\hat{z}\mathbf{F} - \hat{z}\nabla U, \quad (1.110)$$

and

$$\nabla \nabla \cdot \mathbf{A} - \nabla^2 \mathbf{A} = \mathbf{J}_e^S - \hat{y}\hat{z}\mathbf{A} - \hat{y}\nabla V. \quad (1.111)$$

Insofar as the scalars  $U$  and  $V$  are arbitrary, we may arbitrarily impose restrictions on them. It is convenient to impose the Lorentz conditions

$$\nabla \cdot \mathbf{F} = -\hat{z}U, \quad (1.112)$$

and

$$\nabla \cdot \mathbf{A} = -\hat{y}V. \quad (1.113)$$

These conditions facilitate expressing equations (1.110) and (1.111) solely in terms of  $\mathbf{F}$  and  $\mathbf{A}$  respectively as

$$\nabla^2 \mathbf{F} + k^2 \mathbf{F} = -\mathbf{J}_m^S, \quad (1.114)$$

and

$$\nabla^2 \mathbf{A} + k^2 \mathbf{A} = -\mathbf{J}_e^S. \quad (1.115)$$

Equations (1.114) and (1.115) are the inhomogeneous Helmholtz equations in  $\mathbf{F}$  and  $\mathbf{A}$ , respectively, which are applicable to homogeneous regions containing sources  $\mathbf{J}_m^S$  or  $\mathbf{J}_e^S$ . Note that the vector potentials are in the same directions as their sources, which is why these equations are easier to solve than those for the fields. We may obtain the Helmholtz equations for  $U$  and  $V$  by taking the divergences of equations (1.114) and (1.115) and then utilizing the Lorentz conditions, equations (1.112) and (1.113) and the equations of continuity

$$\nabla \cdot \mathbf{j}_e + \frac{\partial \rho_e}{\partial t} = 0, \quad (1.116)$$

and

$$\nabla \cdot \mathbf{j}_m + \frac{\partial \rho_m}{\partial t} = 0. \quad (1.117)$$

The results are the two equations

$$\nabla^2 U + k^2 U = -\frac{1}{\mu} \rho_m^s, \quad (1.118)$$

and

$$\nabla^2 V + k^2 V = \frac{-i\omega}{\hat{\gamma}} \rho_e^s. \quad (1.119)$$

The total electric and magnetic fields due to both  $\mathbf{J}_m^s$  and  $\mathbf{J}_e^s$  are obtained by summing equation (1.104) with equation (1.107) and equation (1.105) with equation (1.106), yielding

$$\mathbf{E} = -\hat{z}\mathbf{A} - \nabla V - \nabla \times \mathbf{F} = -\hat{z}\mathbf{A} + \frac{1}{\hat{\gamma}} \nabla(\nabla \cdot \mathbf{A}) - \nabla \times \mathbf{F}, \quad (1.120)$$

and

$$\mathbf{H} = -\hat{y}\mathbf{F} - \nabla U + \nabla \times \mathbf{A} = -\hat{y}\mathbf{F} + \frac{1}{\hat{z}} \nabla(\nabla \cdot \mathbf{F}) + \nabla \times \mathbf{A}. \quad (1.121)$$

If only one source is present at a time, equations (1.120) and (1.121) become the sets:

For electric sources                  For magnetic sources

$$\mathbf{E}_e = -\hat{z}\mathbf{A} + \frac{1}{\hat{\gamma}} \nabla(\nabla \cdot \mathbf{A}), \quad \mathbf{E}_m = -\nabla \times \mathbf{F}, \quad (1.122)$$

and

$$\mathbf{H}_e = \nabla \times \mathbf{A}. \quad \mathbf{H}_m = -\hat{y}\mathbf{F} + \frac{1}{\hat{z}} \nabla(\nabla \cdot \mathbf{F}). \quad (1.123)$$

For regions devoid of sources, the inhomogeneous equations (1.114), (1.115), (1.118), and (1.119) reduce to their homogeneous counterparts.

$$\nabla^2 \mathbf{F} + k^2 \mathbf{F} = 0, \quad (1.124)$$

$$\nabla^2 \mathbf{A} + k^2 \mathbf{A} = 0, \quad (1.125)$$

$$\nabla^2 U + k^2 U = 0, \quad (1.126)$$

and

$$\nabla^2 V + k^2 V = 0. \quad (1.127)$$

In many problems in electromagnetic theory we define  $\mathbf{F}$  and  $\mathbf{A}$  to have but a single component each, say in the  $z$ -direction. Then

$$\mathbf{A} = A_z \mathbf{u}_z \quad \text{and} \quad \mathbf{F} = F_z \mathbf{u}_z, \quad (1.128)$$

where  $\mathbf{u}_z$  is a unit vector in the  $z$ -direction, and  $A_z$  and  $F_z$  are scalar functions of  $x$ ,  $y$ ,  $z$ . When equations (1.128) are substituted into equations (1.122) and (1.123) the electric and magnetic field components may be expressed as the sets:

TM <sub>z</sub>	TE <sub>z</sub>
$E_x = \frac{1}{\hat{y}} \frac{\partial^2 A_z}{\partial x \partial z},$	$E_x = -\frac{\partial F_z}{\partial y},$
$E_y = \frac{1}{\hat{y}} \frac{\partial^2 A_z}{\partial y \partial z},$	$E_y = \frac{\partial F_z}{\partial x},$
$E_z = \frac{1}{\hat{y}} \left( \frac{\partial^2}{\partial z^2} + k^2 \right) A_z,$	and $E_z = 0,$

(1.129)

TM <sub>z</sub>	TE <sub>z</sub>
$H_x = \frac{\partial A_z}{\partial y},$	$H_x = \frac{1}{\hat{z}} \frac{\partial^2 F_z}{\partial x \partial z},$
$H_y = -\frac{\partial A_z}{\partial x},$	$H_y = \frac{1}{\hat{z}} \frac{\partial^2 F_z}{\partial y \partial z},$
$H_z = 0,$	and $H_z = \frac{1}{\hat{z}} \left( \frac{\partial^2}{\partial z^2} + k^2 \right) F_z.$

(1.130)

In equations (1.129) and (1.130) the subscripts *e* and *m* have been dropped from the field intensities for convenience in notation. The left-hand set of equations (1.129) and (1.130) is a field for which  $H_z$  is zero; this set then describes a field which is transverse magnetic to *z* (TM<sub>z</sub> mode). The right-hand set of equations (1.129) and (1.130) is a field for which  $E_z$  is zero; this set then describes a field which is transverse electric to *z* (TE<sub>z</sub> mode). An arbitrary field in a homogeneous source-free region can be expressed as the sum of TM<sub>z</sub> and TE<sub>z</sub> modes.

We might have chosen the *x* or the *y* direction, rather than the *z* direction, for the single components of **A** and **F**. Thus we could have TE<sub>x</sub>, TM<sub>x</sub>, TE<sub>y</sub> and TM<sub>y</sub> modes. If either expression "TE mode" or "TM mode" is used for cartesian coordinates, it shall be understood that the mode reference axis is *z*.

### Boundary conditions

Electromagnetic problems arising in the physics of the solid earth generally deal with the resultant current, field intensity, or potential in response to an impressed or primary field. The primary field gives rise to a secondary distribution of charges and currents and, hence, to a secondary field. The resultant field is the sum of the primary and secondary fields. Each of the fields must satisfy Maxwell's equations, or equations derived therefrom, plus appropriate conditions to be applied at boundaries between the homogeneous regions involved in the problem, e.g., at the air-earth interface. The problems we meet most frequently, therefore, are referred to as boundary-value problems. We state all of the ones commonly used here for ease in reference.

Boundary conditions are readily derived from the integral forms of Maxwell's equations (e.g. Stratton, 1941, p. 34). We merely state them here, although the detailed derivations are given in Appendix A.1.2.

**Normal B.**—The normal component  $B_n$  of **B** is continuous across an interface separating medium 1 from medium 2. This is written

$$B_{n_1} = B_{n_2}. \quad (1.131)$$

**Normal D.**—The normal component  $D_n$  of  $\mathbf{D}$  is discontinuous at an interface due to the accumulation of a surface-charge density  $\rho_s$ , i.e.,

$$D_{n_2} - D_{n_1} = \rho_s. \quad (1.132)$$

**Tangential E.**—The tangential component  $E_t$  of  $\mathbf{E}$  is continuous across an interface, i.e.

$$E_{t_1} = E_{t_2}. \quad (1.133)$$

**Tangential H.**—The tangential component  $H_t$  of  $\mathbf{H}$  is continuous across an interface if there is no surface current, i.e.

$$H_{t_1} = H_{t_2}. \quad (1.134)$$

**Current Density J.**—The normal component  $J_n$  of  $\mathbf{J}$  is continuous across an interface, i.e.,

$$J_{n_1} = J_{n_2}. \quad (1.135)$$

Strictly speaking, this result applies only to direct current but it is totally satisfactory for earth materials up to  $10^5$  Hz wherein displacement currents may be neglected.

**Scalar Potentials.**—The scalar potentials, appropriate to static fields,  $V$  and  $U$  defined by

$$\mathbf{E} = -\nabla V, \quad (1.136)$$

and

$$\mathbf{H} = -\nabla U, \quad (1.137)$$

are continuous across an interface, i.e.

$$V_1 = V_2, \quad (1.138)$$

and

$$U_1 = U_2. \quad (1.139)$$

We note from the above that of the quantities considered, only one is normally discontinuous across an interface. It is essential to explore the nature of this discontinuity at an interface separating media of different conductivities. Equation (1.132) may be rewritten as

$$E_{n_2} - E_{n_1} = \rho_s / \epsilon_0, \quad (1.140)$$

while equation (1.135) may be rewritten as

$$E_{n_1} = \frac{\sigma_2}{\sigma_1} E_{n_2}. \quad (1.141)$$

Combining equations (1.140) and (1.141) results in

$$\rho_s = \epsilon_0 \left( \frac{\sigma_1 - \sigma_2}{\sigma_1} \right) E_{n_2} = \epsilon_0 \frac{\sigma_1 - \sigma_2}{\sigma_1 + \sigma_2} (E_{n_1} + E_{n_2}), \quad (1.142)$$

indicating that a surface charge  $\rho_s$  occurs at the boundary between media of different con-

ductivities  $\sigma_1$  and  $\sigma_2$ . Although the surface charge density is small because  $\epsilon_0 = 8.854 \times 10^{-12} \text{ F/m}$ , its electric field  $\mathbf{E}$  is not necessarily small as we can deduce from the expression

$$\mathbf{E} = -\nabla V = -\nabla \int_s \frac{\rho_s}{4\pi \epsilon_0 |\mathbf{r}|} ds \quad (1.143)$$

in which  $ds$  is an element of the surface over which the charge occurs. In the case of two adjacent plane boundaries separating a region of conductivity  $\sigma_2$  from a background of conductivity  $\sigma_1$  the charge accumulation is as depicted in Figure 1.3 for the case  $\sigma_2 > \sigma_1$ .

Kaufman (1985) presented a comprehensive discussion of the distribution of electric charges in a conducting medium. He showed that equation (1.142) holds for time-varying fields, in which case  $E$  is the instantaneous value of the electric field.

**Schelkunoff Vector Potentials.**—The boundary conditions for Schelkunoff potentials recognize the need for one component of potential along a source direction, and along the direction of change in electrical properties. This principle is recognized in dealing with boundary conditions appropriate for various symmetries.

### 1. Schelkunoff vector potential $\mathbf{F}$ .

(a) *Single axis of symmetry, boundary surface normal to z* (e.g., magnetic dipole perpendicular to a layered earth). The fields arising in magnetic sources are, from equation (1.122) and (1.123),

$$\mathbf{E}_m = -\nabla \times \mathbf{F}, \quad (1.144)$$

and

$$\mathbf{H}_m = -\hat{y}\mathbf{F} + \frac{1}{z}\nabla(\nabla \cdot \mathbf{F}). \quad (1.145)$$

For this degree of symmetry, but a single component of  $\mathbf{F}$ ,  $F_z$ , is required. Then the components of  $\mathbf{E}_m$  and  $\mathbf{H}_m$  tangential to the boundary surface, in cylindrical coordinates, are

$$\mathbf{E}'_m = -\frac{1}{\rho} \frac{\partial F_z}{\partial \theta} \mathbf{u}_\rho + \frac{\partial F_z}{\partial \rho} \mathbf{u}_\theta, \quad (1.146)$$

and

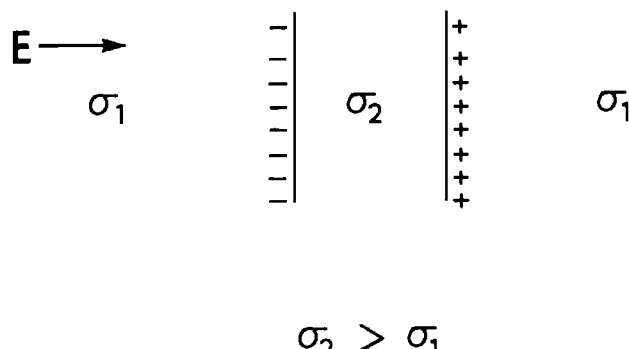


FIG. 1.3. Charge distribution on two adjacent interfaces, between media of different conductivities when a uniform electric field  $\mathbf{E}$  is applied.

$$\mathbf{H}_m^t = \frac{1}{\hat{z}} \left[ \frac{\partial^2 F_z}{\partial \rho \partial z} \mathbf{u}_\rho + \frac{1}{\rho} \frac{\partial^2 F_z}{\partial \theta \partial z} \mathbf{u}_\theta \right], \quad (1.147)$$

in which  $\mathbf{u}_\rho$ ,  $\mathbf{u}_\theta$ , and  $\mathbf{u}_z$  are unit vectors in the  $\rho$ ,  $\theta$ , and  $z$  directions, respectively.

Since the problem has symmetry about  $z$ , then  $\partial/\partial\theta = 0$ , permitting equation (1.146) and (1.147) to be written

$$\mathbf{E}_m^t = \frac{\partial F_z}{\partial \rho} \mathbf{u}_\theta, \quad (1.148)$$

and

$$\mathbf{H}_m^t = \frac{1}{\hat{z}} \frac{\partial^2 F_z}{\partial \rho \partial z} \mathbf{u}_\rho. \quad (1.149)$$

The boundary conditions of continuity of tangential  $\mathbf{E}$  and tangential  $\mathbf{H}$ , when expressed in terms of vector potentials, become, respectively,

$$\frac{\partial F_{z1}}{\partial \rho} = \frac{\partial F_{z2}}{\partial \rho}, \quad (1.150)$$

and

$$\frac{1}{\hat{z}_1} \frac{\partial^2 F_{z1}}{\partial \rho \partial z} = \frac{1}{\hat{z}_2} \frac{\partial^2 F_{z2}}{\partial \rho \partial z}, \quad (1.151)$$

evaluated at the boundary  $z = h$  which separates medium 1 from medium 2.

The conditions expressed in equations (1.150) and (1.151) hold for all  $\rho$  and hence can be integrated with respect to  $\rho$ . The functions  $F_{z1}$  and  $F_{z2}$ , if well-behaved, must vanish as  $\rho \rightarrow \infty$  so that the constants of integration must be zero. Thus the boundary conditions of equations (1.150) and (1.151) reduce to

$$F_{z1} = F_{z2}, \quad (1.152)$$

and

$$\frac{1}{\mu_1} \frac{\partial F_{z1}}{\partial z} = \frac{1}{\mu_2} \frac{\partial F_{z2}}{\partial z}, \quad (1.153)$$

at  $z = h$ .

Equation (1.152) is a statement of the continuity of the normal component of the vector potential. Because of the Lorentz condition

$$U = -\frac{1}{\hat{z}} \nabla \cdot \mathbf{F}, \quad (1.154)$$

it follows that equation (1.151) is equivalent to the statement of continuity of scalar potential.

(b) *Single axis of symmetry, cylindrical boundary surface* (e.g., infinite cylinder in uniform inducing magnetic field).—The bounding surfaces in problems with this symmetry are cylinders centered on the  $z$  axis. If the fields are independent of  $z$  and  $\theta$ , which is often the case in this class of problems, then  $\partial/\partial z = \partial/\partial\theta = 0$ . The tangential components of  $\mathbf{E}$  and  $\mathbf{H}$  are

$$\mathbf{E}'_m = \frac{\partial F_z}{\partial \rho} \mathbf{u}_\theta, \quad (1.155)$$

and

$$\mathbf{H}'_m = -\hat{y}F_z \mathbf{u}_z, \quad (1.156)$$

in which only an  $F_z$  component has been assumed.

The boundary conditions of continuity of tangential  $\mathbf{E}$  and tangential  $\mathbf{H}$ , when expressed in terms of vector potentials, now become

$$\frac{\partial F_{z1}}{\partial \rho} = \frac{\partial F_{z2}}{\partial \rho}, \quad (1.157)$$

and

$$\hat{y}_1 F_{z1} = \hat{y}_2 F_{z2} \quad (1.158)$$

at  $\rho = R$ .

(c) *Single axis of symmetry, spherical boundary surface* (e.g., sphere in uniform magnetic inducing field).—The bounding surfaces in problems with this symmetry are spheres centered at the origin. If the potentials are symmetric about  $z$ , a common occurrence, then  $\partial/\partial\phi = 0$ . These problems are then in mixed cylindrical and spherical geometry. Sommerfeld (1952, p. 150) shows that for  $\mathbf{F} = F_z \mathbf{u}_z$  we can write

$$\nabla_r \nabla \cdot \mathbf{F} = \cos \theta \frac{\partial^2 F_z}{\partial r^2}, \quad (1.159)$$

$$\nabla_\theta \nabla \cdot \mathbf{F} = -\frac{\sin \theta}{r} \frac{\partial F_z}{\partial r}, \quad (1.160)$$

and

$$\nabla_\phi \nabla \cdot \mathbf{F} = 0, \quad (1.161)$$

where  $\theta$  is the angle between  $r$  and  $z$ .

The tangential component of  $\mathbf{H}$  is obtained from equation (1.123), with the aid of equation (1.161), as

$$H_\theta = \hat{y} \sin \theta F_z - \frac{1}{z} \frac{\sin \theta}{r} \frac{\partial F_z}{\partial r}. \quad (1.162)$$

The boundary condition for tangential  $\mathbf{H}$  then becomes

$$\hat{y}_1 F_{z1} - \frac{1}{z_1} \frac{1}{r} \frac{\partial F_{z1}}{\partial r} = \hat{y}_2 F_{z2} - \frac{1}{z_2} \frac{1}{r} \frac{\partial F_{z2}}{\partial r} \quad (1.163)$$

at  $r = R$ .

Continuity of tangential  $\mathbf{E}$  is not so readily utilized due to the necessity of evaluating  $\nabla \times \mathbf{F}$ , of equation (1.122), in this mixed geometry. We may avoid this problem by invoking continuity of normal  $\mathbf{B}$ . If we multiply equation (1.123) by  $\mu_1$  and use equation (1.159) to evaluate equation (1.123), we readily derive the continuity of normal  $\mathbf{B}$  as

$$\mu_1 \left( \hat{y}_1 F_{z1} - \frac{1}{\hat{z}_1} \frac{\partial^2 F_{z1}}{\partial r^2} \right) = \mu_2 \left( \hat{y}_2 F_{z2} - \frac{1}{\hat{z}_2} \frac{\partial^2 F_{z2}}{\partial r^2} \right),$$

or

$$\frac{\partial^2 F_{z1}}{\partial r^2} + k_1^2 F_{z1} = \frac{\partial^2 F_{z2}}{\partial r^2} + k_2^2 F_{z2} \quad (1.164)$$

at  $r = R$ .

As we shall see, any two complementary boundary conditions are sufficient to solve a boundary-value problem in electromagnetic theory. The use of the word complementary shall become obvious as we address specific boundary-value problems.

(d) *Two orthogonal axes of symmetry, rectangular coordinates* (e.g., horizontal magnetic dipole).—If the problem under consideration involves two components of  $\mathbf{F}$ , say  $F_x$  and  $F_z$ , then the field components are written in cartesian coordinates as

$$E_x = \frac{\partial F_z}{\partial y}, \quad H_x = -\hat{y}F_x + \frac{1}{\hat{z}} \frac{\partial}{\partial x} \left( \frac{\partial F_x}{\partial x} + \frac{\partial F_z}{\partial z} \right),$$

$$E_y = \frac{\partial F_z}{\partial x} - \frac{\partial F_x}{\partial z}, \quad H_y = \frac{1}{\hat{z}} \frac{\partial}{\partial y} \left( \frac{\partial F_x}{\partial x} + \frac{\partial F_z}{\partial z} \right),$$

and

$$E_z = \frac{\partial F_x}{\partial y}, \quad H_z = -\hat{y}F_z + \frac{1}{\hat{z}} \frac{\partial}{\partial z} \left( \frac{\partial F_x}{\partial x} + \frac{\partial F_z}{\partial z} \right). \quad (1.165)$$

At a boundary  $z = h$  between two media we then derive from equations (1.165) the boundary conditions:

from  $H_x$ ,

$$\hat{y}_1 F_{x1} - \frac{1}{\hat{z}_1} \frac{\partial}{\partial x} \left( \frac{\partial F_{x1}}{\partial x} + \frac{\partial F_{z1}}{\partial z} \right) = \hat{y}_2 F_{x2} - \frac{1}{\hat{z}_2} \frac{\partial}{\partial x} \left( \frac{\partial F_{x2}}{\partial x} + \frac{\partial F_{z2}}{\partial z} \right),$$

$$(1.166)$$

from  $H_y$ ,

$$\frac{1}{\hat{z}_1} \frac{\partial}{\partial y} \left( \frac{\partial F_{x1}}{\partial x} + \frac{\partial F_{z1}}{\partial z} \right) = \frac{1}{\hat{z}_2} \frac{\partial}{\partial y} \left( \frac{\partial F_{x2}}{\partial x} + \frac{\partial F_{z2}}{\partial z} \right), \quad (1.167)$$

from  $E_x$ ,

$$\frac{\partial F_{z1}}{\partial y} = \frac{\partial F_{z2}}{\partial y}, \quad (1.168)$$

and from  $E_y$ ,

$$\frac{\partial F_{z1}}{\partial x} - \frac{\partial F_{x1}}{\partial z} = \frac{\partial F_{z2}}{\partial x} - \frac{\partial F_{x2}}{\partial z}. \quad (1.169)$$

The relations (1.166) through (1.169) hold for all  $x$  and  $y$  and can therefore be integrated with respect to  $x$  or  $y$ . The functions and their derivatives, if well-behaved, must vanish as  $x \rightarrow \infty$  and  $y \rightarrow \infty$  so that the constants of integration must be zero. Thus the boundary conditions (1.167) and (1.168) at  $z = h$  reduce to

from  $H_y$ ,

$$\frac{1}{\hat{z}_1} \left( \frac{\partial F_{x1}}{\partial x} + \frac{\partial F_{z1}}{\partial z} \right) = \frac{1}{\hat{z}_2} \left( \frac{\partial F_{x2}}{\partial x} + \frac{\partial F_{z2}}{\partial z} \right), \quad (1.170)$$

and from  $E_x$ ,

$$F_{z1} = F_{z2}, \quad (1.171)$$

which may then be utilized to reduce equations (1.163) and (1.169), respectively, to

from  $H_x$ ,

$$\hat{y}_1 F_{x1} = \hat{y}_2 F_{x2}, \quad (1.172)$$

and from  $E_y$ ,

$$\frac{\partial F_{x1}}{\partial z} = \frac{\partial F_{x2}}{\partial z}. \quad (1.173)$$

Equations (1.170) through (1.173) are the boundary conditions on  $F_x$  and  $F_z$ . Of these equations (1.170) and (1.171) are a complementary set being derived from  $H_y$  and  $E_x$  while equations (1.172) and (1.173) are also a complementary set being derived from  $H_x$  and  $E_y$ . Clearly, if only  $F_z$  is present, then the boundary conditions reduce to

$$\frac{1}{\mu_1} \frac{\partial F_{z1}}{\partial z} = \frac{1}{\mu_2} \frac{\partial F_{z2}}{\partial z}, \quad (1.174)$$

and

$$F_{z1} = F_{z2}, \quad (1.175)$$

which agree with equations (1.152) and (1.153) as they should.

## 2. Schelkunoff vector potential A.

(a) *Single axis of symmetry, boundary surface normal to z* (e.g., electric dipole perpendicular to a layered earth).—The fields arising in electric sources are, from equations (1.122) and (1.123),

$$\mathbf{E}_e = \frac{1}{\hat{y}} \nabla \nabla \cdot \mathbf{A} - \hat{z} \mathbf{A}, \quad (1.176)$$

and

$$\mathbf{H}_e = \nabla \times \mathbf{A}. \quad (1.177)$$

If  $\mathbf{A}$  has but a single component  $A_z$ , and if cylindrical symmetry ( $\partial/\partial\theta = 0$ ) is invoked, the components of  $\mathbf{E}_e$  and  $\mathbf{H}_e$ , tangential to  $z$ , become

$$\mathbf{E}'_e = \frac{1}{\hat{y}} \frac{\partial^2 A_z}{\partial \rho \partial z} \mathbf{u}_\rho, \quad (1.178)$$

and

$$\mathbf{H}'_e = -\frac{\partial A_z}{\partial \rho} \mathbf{u}_\theta. \quad (1.179)$$

Then, the boundary conditions of continuity of tangential  $\mathbf{E}$  and  $\mathbf{H}$  become, respectively,

$$\frac{1}{\hat{y}_1} \frac{\partial^2 A_{z1}}{\partial \rho \partial z} = \frac{1}{\hat{y}_2} \frac{\partial^2 A_{z2}}{\partial \rho \partial z}, \quad (1.180)$$

and

$$\frac{\partial A_{z1}}{\partial \rho} = \frac{\partial A_{z2}}{\partial \rho} \quad (1.181)$$

at  $z = h$ .

Integrating equations (1.180) and (1.181) with respect to  $\rho$ , and using the condition at infinity results in

$$\frac{1}{\hat{y}_1} \frac{\partial A_{z1}}{\partial z} = \frac{1}{\hat{y}_2} \frac{\partial A_{z2}}{\partial z}, \quad (1.182)$$

and

$$A_{z1} = A_{z2} \quad (1.183)$$

at  $z = h$ .

One may readily note that the boundary conditions (1.181) and (1.183) are identical to equations (1.152) and (1.153) except that  $A_z$  replaces  $F_z$  and  $\hat{y}$  replaces  $\hat{z}$ .

(b) **Single axis of symmetry, cylindrical boundary surface** (e.g., cylinder in uniform electric field).—For fields with radial symmetry and no  $z$  dependence, i.e.,  $\partial/\partial z = \partial/\partial\theta = 0$ , the tangential components of  $\mathbf{E}$  and  $\mathbf{H}$  are derived from equations (1.122) and (1.123) using  $A_z$  only. Thus

$$\mathbf{E}'_e = -\hat{z} A_z \mathbf{u}_z, \quad (1.184)$$

and

$$\mathbf{H}'_e = -\frac{\partial A_z}{\partial \rho} \mathbf{u}_\theta. \quad (1.185)$$

The boundary conditions for tangential  $\mathbf{E}$  and  $\mathbf{H}$  become, respectively,

$$\hat{z}_1 A_{z1} = \hat{z}_2 A_{z2}, \quad (1.186)$$

and

$$\frac{\partial}{\partial \rho} A_{z1} = \frac{\partial}{\partial \rho} A_{z2} \quad (1.187)$$

at  $\rho = R$ .

Equations (1.186) and (1.187) are the same as equations (1.158) and (1.157) except for interchange of  $F_z$  and  $A_z$  and  $\hat{y}$  with  $\hat{z}$ .

(c) **Single axis of symmetry, spherical boundary surface** (e.g., sphere in uniform electric field).—We proceed to obtain the boundary conditions on  $A_z$  in the same manner as we previously did for  $F_z$  except for interchanging  $H_m$  and  $E_e$ ,  $\mathbf{F}$  and  $\mathbf{A}$ , and  $\hat{y}$  and  $\hat{z}$  in equations (1.164) and (1.163). Thus the continuity of tangential  $\mathbf{E}$  becomes

$$\hat{z}_1 A_{z1} - \frac{1}{\hat{y}_1} \frac{1}{r} \frac{\partial A_{z1}}{\partial r} = \hat{z}_2 A_{z2} - \frac{1}{\hat{y}_2} \frac{1}{r} \frac{\partial A_{z2}}{\partial r} \quad (1.188)$$

at  $r = R$ .

Again the evaluation of the curl in this mixed geometry is awkward so we obtain the second boundary condition on  $A_z$  from continuity of normal *total* current

$$\hat{y}_1 E_{r1} = \hat{y}_2 E_{r2} \quad (1.189)$$

at  $r = R$ ,

and

$$\hat{y}_1 \left( -\hat{z}_1 A_{z1} + \frac{1}{y_1} \frac{\partial^2 A_{z1}}{\partial r^2} \right) = \hat{y}_2 \left( -\hat{z}_2 A_{z2} + \frac{1}{y_2} \frac{\partial^2 A_{z2}}{\partial r^2} \right), \quad (1.190)$$

or

$$k_1^2 A_{z1} + \frac{\partial^2 A_{z1}}{\partial r^2} = k_2^2 A_{z2} + \frac{\partial^2 A_{z2}}{\partial r^2}. \quad (1.191)$$

(d) **Two orthogonal axes of symmetry, rectangular coordinates** (e.g., horizontal electric dipole over layered earth).—When the problem under consideration involves two components of  $\mathbf{A}$ , say  $A_x$  and  $A_z$ , then the field components are written in cartesian coordinates as

$$E_x = -\hat{z} A_x + \frac{1}{\hat{y}} \frac{\partial}{\partial x} \left( \frac{\partial A_x}{\partial x} + \frac{\partial A_z}{\partial z} \right), \quad H_x = \frac{\partial A_z}{\partial y}, \quad (1.192)$$

$$E_y = \frac{1}{\hat{y}} \frac{\partial}{\partial y} \left( \frac{\partial A_x}{\partial x} + \frac{\partial A_z}{\partial z} \right), \quad H_y = \frac{\partial A_x}{\partial z} - \frac{\partial A_z}{\partial x}, \quad (1.193)$$

$$E_z = -\hat{z} A_z + \frac{1}{\hat{y}} \frac{\partial}{\partial z} \left( \frac{\partial A_x}{\partial x} + \frac{\partial A_z}{\partial z} \right), \quad H_z = -\frac{\partial A_x}{\partial y}. \quad (1.193a)$$

These components are obtained from equations (1.122) and (1.123). At a boundary  $z = h$  between two media we then derive from equation (1.193) the boundary conditions:

from  $E_x$

$$-\hat{z}_1 A_{x1} + \frac{1}{\hat{y}_1} \frac{\partial}{\partial x} \left( \frac{\partial A_{x1}}{\partial x} + \frac{\partial A_{z1}}{\partial z} \right) = -\hat{z}_2 A_{x2} + \frac{1}{\hat{y}_2} \frac{\partial}{\partial x} \left( \frac{\partial A_{x2}}{\partial x} + \frac{\partial A_{z2}}{\partial z} \right), \quad (1.194)$$

from  $E_y$

$$\frac{1}{\hat{y}_1} \frac{\partial}{\partial \hat{y}} \left( \frac{\partial A_{x1}}{\partial x} + \frac{\partial A_{z1}}{\partial z} \right) = \frac{1}{\hat{y}_2} \frac{\partial}{\partial y} \left( \frac{\partial A_{x2}}{\partial x} + \frac{\partial A_{z2}}{\partial z} \right), \quad (1.195)$$

from  $H_x$

$$\frac{\partial A_{z1}}{\partial y} = \frac{\partial A_{z2}}{\partial y}, \quad (1.196)$$

and from  $H_y$

$$\frac{\partial A_{x1}}{\partial z} - \frac{\partial A_{z1}}{\partial x} = \frac{\partial A_{x2}}{\partial z} - \frac{\partial A_{z2}}{\partial x}, \quad (1.197)$$

all at  $z = h$ .

These last four equations are the same as equations (1.166) through (1.169) provided interchanges are made between  $F_x$  and  $A_x$ ,  $F_z$  and  $A_z$ , plus  $\hat{z}$  and  $\hat{y}$ . Thus we reduce equations (1.194) through (1.197) in the same manner we did equations (1.166) through (1.169) to obtain,

$$\frac{1}{\hat{y}_1} \left( \frac{\partial A_{x1}}{\partial x} + \frac{\partial A_{z1}}{\partial z} \right) = \frac{1}{\hat{y}_2} \left( \frac{\partial A_{x2}}{\partial x} + \frac{\partial A_{z2}}{\partial z} \right), \quad (1.198)$$

$$A_{z1} = A_{z2}, \quad (1.199)$$

$$\hat{z}_1 A_{x1} = \hat{z}_2 A_{x2}, \quad (1.200)$$

and

$$\frac{\partial A_{x1}}{\partial z} = \frac{\partial A_{x2}}{\partial z}, \quad (1.201)$$

at  $z = h$ .

Of these, equations (1.198) and (1.199) are a complementary set as are equations (1.200) and (1.201), each complementary set being derived from an orthogonal  $[E, H]$  pair.

**Static Fields.**—From equations (1.106) and (1.107) the static fields are

$$\mathbf{E} = -\nabla V, \quad (1.202)$$

and

$$\mathbf{H} = -\nabla U, \quad (1.203)$$

the latter for nonconducting media. Thus we may rewrite

$$(\mathbf{B}_1 - \mathbf{B}_2) \cdot \mathbf{n} = 0, \quad (1.204)$$

$$(\mathbf{D}_1 - \mathbf{D}_2) \cdot \mathbf{n} = \rho_s, \quad (1.205)$$

$$\mathbf{n} \times (\mathbf{E}_1 - \mathbf{E}_2) = 0, \quad (1.206)$$

$$\mathbf{n} \times (\mathbf{H}_1 - \mathbf{H}_2) = 0, \quad (1.207)$$

and

$$(\mathbf{J}_1 - \mathbf{J}_2) \cdot \mathbf{n} = 0, \quad (1.208)$$

as

$$\mu_1 \left( \frac{\partial U}{\partial n} \right)^1 - \mu_2 \left( \frac{\partial U}{\partial n} \right)_2 = 0, \quad (1.209)$$

$$\epsilon_1 \left( \frac{\partial V}{\partial n} \right)^1 - \epsilon_2 \left( \frac{\partial V}{\partial n} \right)_2 = -\rho_s, \quad (1.210)$$

$$\left( \frac{\partial V}{\partial t} \right)^1 - \left( \frac{\partial V}{\partial t} \right)_2 = 0, \quad (1.211)$$

$$\left( \frac{\partial U}{\partial t} \right)^1 - \left( \frac{\partial U}{\partial t} \right)_2 = 0, \quad (1.212)$$

and

$$\sigma_1 \left( \frac{\partial V}{\partial n} \right)^1 - \sigma_2 \left( \frac{\partial V}{\partial n} \right)_2 = 0, \quad (1.213)$$

where  $\partial/\partial n$  and  $\partial/\partial t$  are, respectively, the normal and tangential derivatives.

In the absence of sources,  $V$  and  $U$  must be continuous across a boundary, for the work required to carry a small electric charge or magnetic pole from infinity to either of two adjacent points located on opposite sites of the boundary must be the same. Hence the boundary conditions on potential become

$$V_1 = V_2, \quad (1.214)$$

and

$$U_1 = U_2. \quad (1.215)$$

## Appendix 1.1 Expressions for Operators in Three Coordinate Systems

Because of the number of vector operations used in a typical electromagnetic boundary-value problem, a need exists for quick reference to expressions for several operators in cartesian, cylindrical, and spherical coordinates. The required expressions for the scalar function  $\psi$  and the vector function  $\mathbf{A}$  follow.

### Vector operators

**Cartesian Coordinates.**—If  $\mathbf{u}_x$ ,  $\mathbf{u}_y$ , and  $\mathbf{u}_z$  are the unit vectors in the  $x$ ,  $y$ , and  $z$  directions, respectively, then

$$\nabla\psi = \frac{\partial\psi}{\partial x}\mathbf{u}_x + \frac{\partial\psi}{\partial y}\mathbf{u}_y + \frac{\partial\psi}{\partial z}\mathbf{u}_z, \quad (\text{A1.1.1})$$

$$\nabla \cdot \mathbf{A} = \frac{\partial A_x}{\partial x} + \frac{\partial A_y}{\partial y} + \frac{\partial A_z}{\partial z}, \quad (\text{A1.1.2})$$

$$\nabla \mathbf{x} \mathbf{A} = \left( \frac{\partial A_z}{\partial y} - \frac{\partial A_y}{\partial z} \right) \mathbf{u}_x + \left( \frac{\partial A_x}{\partial z} - \frac{\partial A_z}{\partial x} \right) \mathbf{u}_y + \left( \frac{\partial A_y}{\partial x} - \frac{\partial A_x}{\partial y} \right) \mathbf{u}_z, \quad (\text{A1.1.3})$$

and

$$\nabla^2\psi = \frac{\partial^2\psi}{\partial x^2} + \frac{\partial^2\psi}{\partial y^2} + \frac{\partial^2\psi}{\partial z^2}. \quad (\text{A1.1.4})$$

**Cylindrical Coordinates.**—If  $\mathbf{u}_\rho$ ,  $\mathbf{u}_\theta$ , and  $\mathbf{u}_z$  are the unit vectors in the  $\rho$ ,  $\theta$ , and  $z$  directions, respectively, then

$$\nabla\psi = \frac{\partial\psi}{\partial\rho}\mathbf{u}_\rho + \frac{1}{\rho}\frac{\partial\psi}{\partial\theta}\mathbf{u}_\theta + \frac{\partial\psi}{\partial z}\mathbf{u}_z, \quad (\text{A1.1.5})$$

$$\nabla \cdot \mathbf{A} = \frac{1}{\rho}\frac{\partial}{\partial\rho}(\rho A_\rho) + \frac{1}{\rho}\frac{\partial A_\theta}{\partial\theta} + \frac{\partial A_z}{\partial z}, \quad (\text{A1.1.6})$$

$$\nabla \mathbf{x} \mathbf{A} = \frac{1}{\rho} \left[ \frac{\partial A_z}{\partial\theta} - \frac{\partial A_\theta}{\partial z} \right] \mathbf{u}_\rho + \left[ \frac{\partial A_\rho}{\partial z} - \frac{\partial A_z}{\partial\rho} \right] \mathbf{u}_\theta + \frac{1}{\rho} \left[ \frac{\partial}{\partial\rho}(\rho A_\theta) - \frac{\partial A_\rho}{\partial\theta} \right] \mathbf{u}_z, \quad (\text{A1.1.7})$$

and

$$\nabla^2\psi = \frac{1}{\rho}\frac{\partial}{\partial\rho} \left( \rho \frac{\partial\psi}{\partial\rho} \right) + \frac{1}{\rho^2}\frac{\partial^2\psi}{\partial\theta^2} + \frac{\partial^2\psi}{\partial z^2}. \quad (\text{A1.1.8})$$

**Spherical Coordinates.**—If  $\mathbf{u}_r$ ,  $\mathbf{u}_\theta$ , and  $\mathbf{u}_\phi$  are the unit vectors in the  $r$ ,  $\theta$ , and  $\phi$  directions, respectively, then

$$\nabla\psi = \frac{\partial\psi}{\partial r}\mathbf{u}_r + \frac{1}{r}\frac{\partial\psi}{\partial\theta}\mathbf{u}_\theta + \frac{1}{r\sin\theta}\frac{\partial\psi}{\partial\phi}\mathbf{u}_\phi, \quad (\text{A1.1.9})$$

$$\nabla \cdot \mathbf{A} = \frac{1}{r^2}\frac{\partial}{\partial r}(r^2 A_r) + \frac{1}{r\sin\theta}\frac{\partial}{\partial\theta}(\sin\theta A_\theta) + \frac{1}{r\sin\theta}\frac{\partial A_\phi}{\partial\phi}, \quad (\text{A1.1.10})$$

$$\begin{aligned} \nabla \mathbf{x} \mathbf{A} = & \frac{1}{r\sin\theta} \left[ \frac{\partial}{\partial\theta}(\sin\theta A_\phi) - \frac{\partial A_\theta}{\partial\phi} \right] \mathbf{u}_r + \frac{1}{r} \left[ \frac{1}{\sin\theta}\frac{\partial A_r}{\partial\phi} - \frac{\partial}{\partial r}(r A_\phi) \right] \mathbf{u}_\theta \\ & + \frac{1}{r} \left[ \frac{\partial}{\partial r}(r A_\theta) - \frac{\partial A_r}{\partial\theta} \right] \mathbf{u}_\phi, \end{aligned} \quad (\text{A1.1.11})$$

and

$$\nabla^2\psi = \frac{1}{r^2}\frac{\partial}{\partial r} \left( r^2 \frac{\partial\psi}{\partial r} \right) + \frac{1}{r^2\sin\theta}\frac{\partial}{\partial\theta} \left( \sin\theta \frac{\partial\psi}{\partial\theta} \right) + \frac{1}{r^2\sin^2\theta}\frac{\partial^2\psi}{\partial\phi^2}. \quad (\text{A1.1.12})$$

### Maxwell's equations

#### Cartesian Coordinates.—

$$\frac{\partial E_z}{\partial y} - \frac{\partial E_y}{\partial z} = -\hat{z} H_x \quad \frac{\partial H_z}{\partial y} - \frac{\partial H_y}{\partial z} = \hat{y} E_x \quad (\text{A1.1.13})$$

$$\frac{\partial E_x}{\partial z} - \frac{\partial E_z}{\partial x} = -\hat{z} H_y \quad \frac{\partial H_x}{\partial z} - \frac{\partial H_z}{\partial x} = \hat{y} E_y \quad (\text{A1.1.14})$$

$$\frac{\partial E_y}{\partial x} - \frac{\partial E_x}{\partial y} = -\hat{z} H_z \quad \frac{\partial H_y}{\partial x} - \frac{\partial H_x}{\partial y} = \hat{y} E_z \quad (\text{A1.1.15})$$

#### Cylindrical Coordinates.—

$$\frac{\partial E_z}{\partial \theta} - \rho \frac{\partial E_\theta}{\partial z} = -\hat{z}\rho H_\rho \quad \frac{\partial H_z}{\partial \theta} - \rho \frac{\partial H_\theta}{\partial z} = \hat{y}\rho E_\rho \quad (\text{A1.1.16})$$

$$\frac{\partial E_\rho}{\partial z} - \frac{\partial E_z}{\partial \rho} = -\hat{z}H_\theta \quad \frac{\partial H_\rho}{\partial z} - \frac{\partial H_z}{\partial \rho} = \hat{y}E_\theta \quad (\text{A1.1.17})$$

$$\frac{\partial}{\partial \rho} (\rho E_\theta) - \frac{\partial E_\rho}{\partial \theta} = -\hat{z}H_z \quad \frac{\partial}{\partial \rho} (\rho H_\theta) - \frac{\partial H_\rho}{\partial \theta} = \hat{y}\rho E_z \quad (\text{A1.1.18})$$

#### Spherical Coordinates.—

$$\frac{\partial}{\partial \theta} (\sin \theta E_\phi) = -\hat{z}r \sin \theta H_r \quad \frac{\partial}{\partial \theta} (\sin \theta H_\phi) = \hat{y}r \sin \theta E_r \quad (\text{A1.1.19})$$

$$\frac{\partial}{\partial r} (r E_\phi) = \hat{z}r H_\theta \quad \frac{\partial}{\partial r} (r H_\phi) = -\hat{y}r E_\phi \quad (\text{A1.1.20})$$

$$\frac{\partial}{\partial r} (r E_\theta) - \frac{\partial E_r}{\partial \theta} = -\hat{z}r H_\phi \quad \frac{\partial}{\partial r} (r H_\theta) - \frac{\partial H_r}{\partial \theta} = \hat{y}r E_\phi \quad (\text{A1.1.21})$$

#### Mode decomposition

In equations (1.129) and (1.130) are the expressions for the components of electric and magnetic fields for the TM<sub>z</sub> and TE<sub>z</sub> modes. The TM<sub>z</sub> mode requires only a single component  $A_z$  of the vector potential associated with electric sources while the TE<sub>z</sub> mode requires only a single component  $F_z$  of the vector potential associated with magnetic sources. Expressions (1.129) and (1.130) are repeated for completeness since we then give similar expressions in cylindrical and spherical coordinates.

#### Cartesian Coordinates.—

(TM <sub>z</sub> )	(TE <sub>z</sub> )
--------------------	--------------------

$$E_x = \frac{1}{\hat{y}} \frac{\partial^2 A_z}{\partial x \partial z} \quad E_x = -\frac{\partial F_z}{\partial y}$$

$$E_y = \frac{1}{\hat{y}} \frac{\partial^2 A_z}{\partial y \partial z} \quad E_y = \frac{\partial F_z}{\partial x}$$

$$\begin{aligned}
 E_z &= \frac{1}{\hat{y}} \left( \frac{\partial^2}{\partial z^2} + k^2 \right) A_z & E_z &= 0 \\
 H_x &= \frac{\partial A_z}{\partial y} & H_x &= \frac{1}{\hat{z}} \frac{\partial^2 F_z}{\partial x \partial x} \\
 H_y &= \frac{\partial A_z}{\partial x} & H_y &= \frac{1}{\hat{z}} \frac{\partial^2 F_z}{\partial y \partial z} \\
 H_z &= 0 & H_z &= \frac{1}{\hat{z}} \left( \frac{\partial^2}{\partial z^2} + k^2 \right) F_z \quad (\text{A1.1.22})
 \end{aligned}$$

### Cylindrical Coordinates.—

$$\begin{aligned}
 &(\text{TM}_z) & &(\text{TE}_z) \\
 E_\rho &= \frac{1}{\hat{y}} \frac{\partial^2 A_z}{\partial \rho \partial z} & E_\rho &= -\frac{1}{\rho} \frac{\partial F_z}{\partial \theta} \\
 E_\theta &= \frac{1}{\hat{y}\rho} \frac{\partial^2 A_z}{\partial \theta \partial z} & E_\theta &= \frac{\partial F_z}{\partial \rho} \\
 E_z &= \frac{1}{\hat{y}} \left( \frac{\partial^2}{\partial z^2} + k^2 \right) A_z & E_z &= 0 \\
 H_\rho &= \frac{1}{\rho} \frac{\partial A_z}{\partial \theta} & H_\rho &= \frac{1}{\hat{z}} \frac{\partial^2 F_z}{\partial \rho \partial z} \\
 H_\theta &= -\frac{\partial A_z}{\partial \rho} & H_\theta &= \frac{1}{\hat{z}\rho} \frac{\partial^2 F_z}{\partial \theta \partial z} \\
 H_z &= 0 & H_z &= \frac{1}{\hat{z}} \left( \frac{\partial^2}{\partial z^2} + k^2 \right) F_z \quad (\text{A1.1.23})
 \end{aligned}$$

### Spherical Coordinates.—

$$\begin{aligned}
 &(\text{TM}_r) & &(\text{TE}_r) \\
 E_r &= \frac{1}{\hat{y}} \left( \frac{\partial^2}{\partial r^2} + k^2 \right) A_r & E_r &= 0 \\
 E_\theta &= \frac{1}{\hat{y}r} \frac{\partial^2 A_r}{\partial r \partial \theta} & E_\theta &= \frac{-1}{r \sin \theta} \frac{\partial F_r}{\partial \phi} \\
 E_\phi &= \frac{1}{\hat{y}r \sin \theta} \frac{\partial^2 A_r}{\partial r \partial \phi} & E_\phi &= \frac{1}{r} \frac{\partial F_r}{\partial \theta} \\
 H_r &= 0 & H_r &= \frac{1}{\hat{z}} \left( \frac{\partial^2}{\partial r^2} + k^2 \right) F_r
 \end{aligned}$$

$$\begin{aligned} H_\theta &= \frac{1}{r \sin \theta} \frac{\partial A_r}{\partial \phi} & H_\theta &= \frac{1}{\hat{z} r} \frac{\partial^2 F_r}{\partial r \partial \theta} \\ H_\phi &= -\frac{1}{r} \frac{\partial A_r}{\partial \theta} & H_\phi &= \frac{1}{\hat{z} r \sin \theta} \frac{\partial^2 F_r}{\partial r \partial \phi} \end{aligned} \quad (\text{A1.1.24})$$

## Appendix 1.2 Boundary Conditions

### The integral forms of Maxwell's equations

In differential form, Faraday's law is written as Maxwell's first equation

$$\nabla \times \mathbf{E} + \frac{\partial \mathbf{B}}{\partial t} = 0, \quad (\text{A1.2.1})$$

and Ampere's law is written as Maxwell's second equation,

$$\nabla \times \mathbf{H} - \frac{\partial \mathbf{D}}{\partial t} = \mathbf{J}. \quad (\text{A1.2.2})$$

To equations (A1.2.1) and (A1.2.2) we may apply Stokes' theorem (Reitz and Milford, 1960, p. 16) which assures that the normal component of the curl of a vector, integrated over a surface, is equal to the contour integral of the tangential component of the vector, i.e., we find

$$\int_S (\nabla \times \mathbf{A}) \cdot \mathbf{n} ds = \oint_c \mathbf{A} \cdot d\mathbf{l} \quad (\text{A1.2.3})$$

in which  $\mathbf{n}$  is a unit vector normal to the area element  $ds$  of the surface  $S$  and  $d\mathbf{l}$  is a vector element of length along the contour. Equations (A1.2.1) and (A1.2.2) then may be written in integral form, using (A1.2.3) as:

$$\oint_c \mathbf{E} \cdot d\mathbf{l} = -\frac{\partial}{\partial t} \int_S \mathbf{B} \cdot \mathbf{n} ds, \quad (\text{A1.2.4})$$

and

$$\oint_c \mathbf{H} \cdot d\mathbf{l} = I + \frac{\partial}{\partial t} \int_S \mathbf{D} \cdot \mathbf{n} ds, \quad (\text{A1.2.5})$$

in which we define the *current*  $I$  by

$$I = \int_S \mathbf{J} \cdot \mathbf{n} ds \quad (\text{A1.2.6})$$

These are the integral forms of Faraday's and Ampere's laws, respectively. The time derivative is placed before the integral sign in equations (A1.2.4) with the understanding that the surface  $S$  does not vary with time.

The third and fourth Maxwell equations may be converted to integral form with the aid of the divergence, or Gauss, theorem,

$$\int_V \nabla \cdot \mathbf{A} dv = \int_S \mathbf{A} \cdot \mathbf{n} ds \quad (\text{A1.2.7})$$

where  $S$  denotes a closed surface enclosing the volume  $V$  and  $\mathbf{n}$  is a unit outward normal. Thus,

$$\nabla \cdot \mathbf{B} = 0 \quad (\text{A1.2.8})$$

becomes

$$\oint_S \mathbf{B} \cdot \mathbf{n} ds = 0, \quad (\text{A1.2.9})$$

and

$$\nabla \cdot \mathbf{D} = \rho \quad (\text{A1.2.10})$$

becomes

$$\oint_S \mathbf{D} \cdot \mathbf{n} ds = \int_V \rho dv = q \quad (\text{A1.2.11})$$

where  $q$  is the total charge in the volume. The equation of continuity

$$\nabla \cdot \mathbf{J} + \frac{\partial \rho}{\partial t} = 0 \quad (\text{A1.2.12})$$

similarly is

$$I = \oint_S \mathbf{J} \cdot \mathbf{n} ds = -\frac{\partial}{\partial t} \int_V \rho dv = -\frac{\partial q}{\partial t}, \quad (\text{A1.2.13})$$

or the total current out through a closed surface  $S$  is equal to the time rate of depletion of charge within the volume  $V$  bounded by the surface  $S$ .

The integral forms of Maxwell's equations are particularly useful in the derivation of *boundary conditions*.

### Boundary conditions

Electromagnetic problems arising in the physics of the solid earth generally deal with the resultant current, field intensity, or potential in response to an impressed or primary field. The primary field gives rise to a secondary distribution of charges and currents and, hence, to a secondary field. The resultant field is the sum of the primary and secondary fields. Each of the fields must satisfy Maxwell's equations, or equations derived therefrom, plus appropriate conditions to be applied at boundaries between the homogeneous regions involved in the problem, for instance, at the air-earth interface. The problems most frequently met, therefore, are referred to as boundary-value problems. Let us consider now the manner in which these boundary conditions are established.

**Normal B.**—First we consider the continuity of the normal component of magnetic induction  $\mathbf{B}$ . Two media of differing electrical properties are in contact as illustrated in Figure

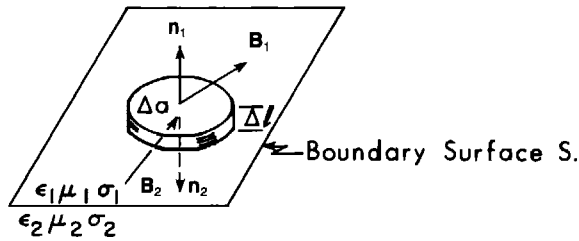


FIG. A1.2.1. Normal  $\mathbf{B}$  continuous. Pillbox enclosing surface between two media in contact. Media (1) and (2) of constant  $\epsilon_1\mu_1\sigma_1$  and  $\epsilon_2\mu_2\sigma_2$ , respectively. Magnetic induction in (1) and (2) are  $\mathbf{B}_1$  and  $\mathbf{B}_2$ , respectively, while  $\mathbf{n}_1$  and  $\mathbf{n}_2$  are outward directed normals to top and bottom surfaces of the pillbox.

A1.2.1. We wish to determine the behavior of the fields at the boundary  $S$  between the media described by the sets of physical parameters  $\epsilon_1\mu_1\sigma_1$  and  $\epsilon_2\mu_2\sigma_2$ . For this purpose we construct a small *pillbox* of height  $\Delta l$  and area  $\Delta a$  in which the surface is enclosed, i.e., its upper surface is in medium 1 while its lower surface is in medium 2. We now may evaluate the integral (A1.2.9) over the walls and ends of the *pillbox*. If the ends,  $\Delta a$ , are made sufficiently small we may assume that  $\mathbf{B}$  has a constant value  $\mathbf{B}_1$  over the end in the upper medium and a constant value  $\mathbf{B}_2$  over the end in the lower medium. We may then approximate equation (A1.2.9) by

$$(\mathbf{B}_1 \cdot \mathbf{n}_1 + \mathbf{B}_2 \cdot \mathbf{n}_2)\Delta a + \text{contributions from the walls} = 0. \quad (\text{A1.2.14})$$

Since the contribution of the walls to the surface integral is directly proportional to  $\Delta l$ , we may neglect it as  $\Delta l \rightarrow 0$ , provided  $\Delta a$  remains finite. Then equation (A1.2.14) becomes

$$\mathbf{B}_1 \cdot \mathbf{n}_1 + \mathbf{B}_2 \cdot \mathbf{n}_2 = 0. \quad (\text{A1.2.15})$$

The normals  $\mathbf{n}_1$  and  $\mathbf{n}_2$  are directed outward and hence we may write

$$\mathbf{n}_1 = \mathbf{n} = -\mathbf{n}_2 \quad (\text{A1.2.16})$$

and (A1.2.15) becomes

$$(\mathbf{B}_1 - \mathbf{B}_2) \cdot \mathbf{n} = 0. \quad (\text{A1.2.17})$$

Equation (A1.2.17) states that the normal component  $B_n$  of  $\mathbf{B}$  is continuous across an interface, i.e.,  $B_{n_1} = B_{n_2}$ .

**Normal  $\mathbf{D}$ .**—The vector  $\mathbf{D}$  may be considered similarly. The charge density given by the integral (A1.2.11) may be approximated by

$$\int_V \rho dv = \rho \Delta l \Delta a. \quad (\text{A1.2.18})$$

It is convenient now to replace the product  $\rho \Delta l$  by a surface charge density  $\rho_s$ , defined as the charge per unit area. Thus we find from equation (A1.2.11) that

$$(\mathbf{D}_1 \cdot \mathbf{n}_1 + \mathbf{D}_2 \cdot \mathbf{n}_2)\Delta a = \rho_s \Delta a, \quad (\text{A1.2.19})$$

or

$$(\mathbf{D}_1 - \mathbf{D}_2) \cdot \mathbf{n} = \rho_s. \quad (\text{A1.2.20})$$

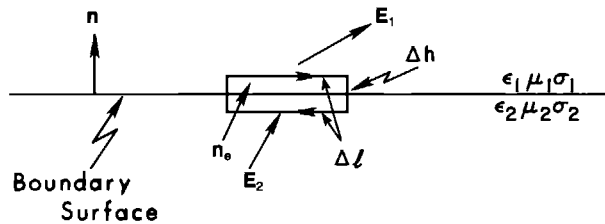


FIG. A1.2.2. Tangential  $\mathbf{E}$  continuous. Closed contour of integration spans surface between media in contact, constants  $\epsilon_1\mu_1\sigma_1$  and  $\epsilon_2\mu_2\sigma_2$ . Electric vectors  $\mathbf{E}_1$  and  $\mathbf{E}_2$  in media (1) and (2), respectively.

Equation (A1.2.20) informs us that the normal component  $D_n$  of the vector  $\mathbf{D}$  is discontinuous at an interface due to the accumulation of a surface charge density  $\rho_s$ .

**Tangential  $\mathbf{E}$ .**—Equation (A1.2.4) is the starting point for the development. Let us choose the contour as shown in Figure A1.2.2.

Thus we may write

$$-\int_S \frac{\partial \mathbf{B}}{\partial t} \cdot \mathbf{n}_e da = \oint_c \mathbf{E} \cdot d\mathbf{l} = \mathbf{E}_1 \cdot \Delta\mathbf{l} + \mathbf{E}_2 \cdot (-\Delta\mathbf{l}) + (\text{contributions from the ends}), \quad (\text{A1.2.21})$$

where  $\mathbf{E}_1 \cdot \Delta\mathbf{l}$  and  $\mathbf{E}_2 \cdot \Delta\mathbf{l}$  are the tangential components of  $\mathbf{E}$  in the media (1) and (2). Equation (A1.2.21) yields, when the left-hand side (L.H.S.) is similarly approximated,

$$-\frac{\partial \mathbf{B}}{\partial t} \cdot \mathbf{n}_e \Delta h \Delta l = (\mathbf{E}_1 - \mathbf{E}_2) \cdot \Delta\mathbf{l}. \quad (\text{A1.2.22})$$

In the limit, as the height  $\Delta h \rightarrow 0$ , L.H.S.  $\rightarrow 0$ , so that across the boundary surface, the tangential component  $E_t$  of  $\mathbf{E}$  is continuous, i.e.  $E_{t_1} = E_{t_2}$ . The vector  $\mathbf{n} \times \mathbf{E}$ , where  $\mathbf{n}$  is the unit normal to the boundary surface, will immediately give a tangential component, as reference to Figure A1.2.2 will attest. Hence, we often find this boundary condition written in the form.

$$\mathbf{n} \times (\mathbf{E}_1 - \mathbf{E}_2) = 0. \quad (\text{A1.2.23})$$

**Tangential  $\mathbf{H}$ .**—The procedure for this development is the same as for tangential  $\mathbf{E}$ .

The contour for integration of  $\mathbf{H}$  is the same as that shown in Figure A1.2.2. Then, by using just the components of  $\mathbf{H}$  tangential to the boundary surface and by proceeding to the limit of a contour of negligible height  $\Delta h$ , we are able to rewrite equation (A1.2.5) as

$$\mathbf{n} \times (\mathbf{H}_1 - \mathbf{H}_2) = \lim_{\Delta h \rightarrow 0} \left( \frac{\partial \mathbf{D}}{\partial t} + \mathbf{J} \right) \Delta h. \quad (\text{A1.2.24})$$

The first term on the right of equation (A1.2.24) vanishes as  $\Delta h \rightarrow 0$  because  $\mathbf{D}$  and its derivatives are bounded (by assumption). For a finite current density  $\mathbf{J}$ , the second term also vanishes. There may be a surface current

$$\mathbf{J}^s \equiv \lim_{\substack{\Delta h \rightarrow 0 \\ \mathbf{J} \rightarrow \infty}} \mathbf{J} \Delta h, \quad (\text{A1.2.25})$$

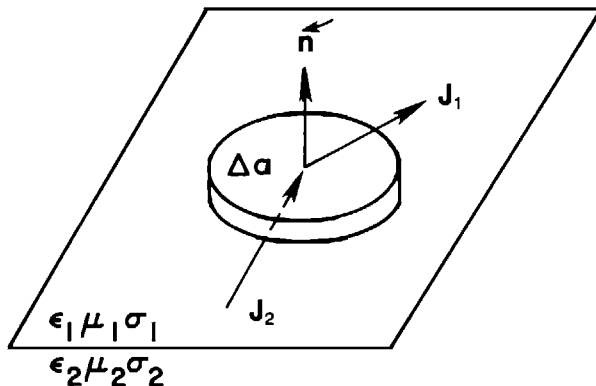


FIG. A1.2.3. Normal  $J$  continuous. Pillbox enclosing surface between two media in contact, constants  $\epsilon_1 \mu_1 \sigma_1$  and  $\epsilon_2 \mu_2 \sigma_2$ . Current densities are  $J_1$  in (1) and  $J_2$  in (2).

so that the boundary condition on tangential  $\mathbf{H}$  becomes

$$\mathbf{n} \times (\mathbf{H}_1 - \mathbf{H}_2) = \mathbf{J}_s \text{ (a surface current exists).} \quad (\text{A1.2.26})$$

If the conductivities of the two media are finite then  $E \equiv \mathbf{J}/\sigma$  must be finite and no surface current  $\mathbf{J}_s$  can exist, so that the boundary condition becomes

$$\mathbf{n} \times (\mathbf{H}_1 - \mathbf{H}_2) = 0 \text{ (for finite conductivity).} \quad (\text{A1.2.27})$$

When the conductivity  $\sigma$  is assumed to be infinite,  $\mathbf{J}$  could also be infinite and not violate our basic assumption that  $\mathbf{E}$ , as well as the other three field vectors, is bounded. Under these conditions we should employ the boundary condition (A1.2.26).

**Current Density  $\mathbf{J}$ -dc.**—The currents entering and leaving a *pillbox* spanning two conductive media, as in Figure A1.2.3, consist partly of tangential and partly of normal components.

As the *pillbox* height is collapsed to zero, the normal component, i.e. the current crossing the interface, may be computed either as

$$I = \mathbf{J}_1 \cdot \mathbf{n} \Delta a,$$

or as

$$I = \mathbf{J}_2 \cdot \mathbf{n} \Delta a.$$

Thus, the normal component  $\mathbf{J}_n$  of  $\mathbf{J}$  must be continuous across an interface

$$(\mathbf{J}_1 - \mathbf{J}_2) \cdot \mathbf{n} = 0,$$

or

$$J_{n_1} = J_{n_2}.$$

This is equivalent to  $\nabla_n \cdot \mathbf{J} = (\mathbf{J}_1 - \mathbf{J}_2) \cdot \mathbf{n} = 0$ .

**Current Density  $\hat{\gamma} \mathbf{E}$ -ac.**—When dealing with alternating fields at a plane boundary, the current which is continuous across the interface is the total current  $\hat{\gamma} \mathbf{E}$  and the boundary condition becomes

$$\hat{\gamma}_1 E_{n1} = \hat{\gamma}_2 E_{n2}.$$

This form realizes that

$$\nabla_n \cdot \mathbf{J} = (\mathbf{J}_1 - \mathbf{J}_2) \cdot \mathbf{n} \neq 0$$

since  $\nabla \cdot \mathbf{J} + \partial \rho / \partial t = 0$  for ac phenomena.

## Section 2 Sources in Unbounded Media

The theoretical response of an EM source in a whole space is of direct practical importance in geophysics for analysis of borehole methods, where the effect of the earth-air interface is negligible. However, it also is an important source of general insight and a first step in formulating analytical and numerical solutions for cases where conductivity boundaries exist. Formulations in cartesian coordinates are the most useful in applied geophysics, because the surface of the earth can be taken to be flat.

### Scalar Green's function

A key concept is that of the Green's function, which is the response of a unit point source at the origin. In the general case, the Green's function must account for the effects of conductivity boundaries and hence is derived by solving a boundary value problem. However, derivation of the Green's function is much simpler in the case of a whole space, where the only boundary condition is that the fields go to zero at infinity. In that case the Green's function can be found by solving the appropriate differential equation using a transform technique.

We begin by defining the triple spatial Fourier transform pair (Baños, 1966):

$$\tilde{\mathbf{A}}(k_x, k_y, k_z) = \int_{-\infty}^{\infty} \int_{-\infty}^{\infty} \int_{-\infty}^{\infty} \mathbf{A}(x, y, z) e^{-i[k_x x + k_y y + k_z z]} dx dy dz, \quad (2.1)$$

$$\mathbf{A}(x, y, z) = \frac{1}{8\pi^3} \int_{-\infty}^{\infty} \int_{-\infty}^{\infty} \int_{-\infty}^{\infty} \tilde{\mathbf{A}}(k_x, k_y, k_z) e^{i[k_x x + k_y y + k_z z]} dk_x dk_y dk_z. \quad (2.2)$$

Taking the transform of equation (1.115) and using the derivative property of the Fourier transform results in the algebraic equation

$$(-k_x^2 - k_y^2 - k_z^2 + k^2) \tilde{\mathbf{A}} = -\tilde{\mathbf{J}},$$

or

$$\tilde{\mathbf{A}} = \tilde{G} \tilde{\mathbf{J}}, \quad (2.3)$$

where

$$\tilde{G} = \frac{1}{k_x^2 + k_y^2 + k_z^2 - k^2}. \quad (2.4)$$

is the Fourier transform of the Green's function.

Because equation (2.3) is a product in the Fourier transform domain, it is a convolution in the space domain, given by

$$\mathbf{A}(x, y, z) = \int_{-\infty}^{\infty} \int_{-\infty}^{\infty} \int_{-\infty}^{\infty} G(x - x', y - y', z - z') \mathbf{J}(x', y', z') dx' dy' dz', \quad (2.5)$$

where  $G$  is the 3-D scalar EM Green's function. If  $G$  is known,  $\mathbf{A}$  can be computed for any

source distribution  $\mathbf{J}$  using equation (2.5). Thus the Green's function plays a role analogous to that of the impulse response in linear system theory.

Note that the Green's function satisfies the scalar differential equation

$$\nabla^2 G + k^2 G = -\delta(x)\delta(y)\delta(z), \quad (2.6)$$

which can be shown by transforming equation (2.6) and solving for  $\tilde{G}$  to obtain expression (2.4). It is, thus, the response of a point source at the origin. To find  $G$ , evaluate the inverse transform of equation (2.4), considering first integration with respect to  $z$ :

$$\tilde{G}(k_x, k_y, z) = \frac{1}{2\pi} \int_{-\infty}^{\infty} \frac{e^{ik_z z}}{k_z^2 + k_x^2 + k_y^2 - k^2} dk_z. \quad (2.7)$$

From Erdelyi (1954),

$$\tilde{G}(k_x, k_y, z) = \frac{e^{-uz}}{2u}, \quad (2.8)$$

with

$$u = (k_x^2 + k_y^2 - k^2)^{1/2}.$$

Next we need to evaluate the inverse 2-D Fourier transform

$$G(x, y, z) = \frac{1}{8\pi^2} \int_{-\infty}^{\infty} \int_{-\infty}^{\infty} \frac{1}{u} e^{-uz} e^{i(k_x x + k_y y)} dk_x dk_y. \quad (2.9)$$

For a circularly symmetric integrand such as that of equation (2.9), we can convert the double Fourier transform to a Hankel transform using the relation (Baños, 1966)

$$\int_{-\infty}^{\infty} \int_{-\infty}^{\infty} F(k_x^2 + k_y^2) e^{i(k_x x + k_y y)} dk_x dk_y = 2\pi \int_0^{\infty} F(\lambda) \lambda J_0(\lambda \rho) d\lambda, \quad (2.10)$$

with

$$\lambda^2 = k_x^2 + k_y^2,$$

and

$$\rho^2 = x^2 + y^2,$$

and where  $J_0$  is the Bessel function of order 0.

Equation (2.10) is derived by making the substitutions

$$k_x = \lambda \cos \psi,$$

$$k_y = \lambda \sin \psi,$$

$$x = \rho \cos \phi,$$

and

$$y = \rho \sin \phi,$$

and converting to an integral in cylindrical coordinates to obtain

$$\int_{-\infty}^{\infty} \int_{-\infty}^{\infty} F(k_x^2 + k_y^2) e^{i(k_x x + k_y y)} dk_x dk_y = \int_0^{\infty} F(\lambda) \int_0^{2\pi} e^{i\lambda \rho \cos(\psi - \phi)} d\psi \lambda d\lambda.$$

By using the integral representation (Watson, 1944),

$$\int_0^{2\pi} e^{i\lambda \rho \cos(\psi - \phi)} d\psi = 2\pi J_0(\lambda \rho), \quad (2.11)$$

for the Bessel function of order zero we obtain the relation (2.10).

Thus expression (2.9) becomes

$$G(\rho, z) = \frac{1}{4\pi} \int_0^{\infty} \frac{\lambda}{u} e^{-u|z|} J_0(\lambda \rho) d\lambda, \quad (2.12)$$

with

$$u = (\lambda^2 - k^2)^{1/2}.$$

From tables of Hankel transforms in Erdelyi (1954), we find that the whole-space Green's function is given by

$$G(r) = \frac{e^{-ikr}}{4\pi r} \quad (2.13)$$

with

$$r = |\mathbf{r}| = (x^2 + y^2 + z^2)^{1/2}.$$

Thus, for a source current in a volume  $v$ , from equation (2.5),

$$\mathbf{A}(x, y, z) = \int_v \frac{e^{-ik[(x-x')^2 + (y-y')^2 + (z-z')^2]^{1/2}}}{4\pi[(x-x')^2 + (y-y')^2 + (z-z')^2]^{1/2}} \mathbf{J}(x', y', z') dx' dy' dz', \quad (2.14)$$

or, in more concise notation

$$\mathbf{A}(\mathbf{r}) = \int_v \frac{e^{-ik|\mathbf{r}-\mathbf{r}'|}}{4\pi|\mathbf{r}-\mathbf{r}'|} \mathbf{J}(\mathbf{r}') dv'. \quad (2.15)$$

### Time-Domain Green's function

To find the Green's function in the time domain, perform the inverse Fourier transform with respect to frequency, defined by

$$g(r) = \frac{1}{8\pi^2 r} \int_{-\infty}^{\infty} e^{-ir(\omega^2 \mu \epsilon - \omega \mu \sigma)^{1/2}} e^{i\omega r} d\omega, \quad (2.16)$$

which is the response of an impulsive source at the origin of coordinates, at  $t = 0$ .

**Nonconductive Case.**—For some applications in geophysics, we may be interested in the field of a source in free space, in which case the conductivity is zero. Then equation (2.16) becomes

$$g(r) = \frac{1}{8\pi^2 r} \int_{-\infty}^{\infty} e^{i\omega[t \pm r(\mu\varepsilon)^{1/2}]} d\omega. \quad (2.17)$$

Using the relation (Jackson, 1975)

$$\delta(t \pm t') = \frac{1}{2\pi} \int_{-\infty}^{\infty} e^{i\omega(t \pm t')} d\omega, \quad (2.18)$$

results in

$$g(r) = \frac{1}{4\pi r} \delta(t - r/c), \quad (2.19)$$

where  $c = 1/(\mu\varepsilon)^{1/2}$  is the velocity of light ( $3.0 \times 10^8$  m/s in vacuum). We have chosen the negative sign in equation (2.19), because, due to causality,  $g$  must be zero for  $t < 0$ .

To find the vector potential, we substitute equation (2.19) into the time-domain version of equation (2.5),

$$\mathbf{a}(\mathbf{r},t) = \int_{-\infty}^{\infty} \int_{-\infty}^{\infty} \int_{-\infty}^{\infty} \int_{-\infty}^{\infty} g(\mathbf{r} - \mathbf{r}', t - t') \mathbf{j}(\mathbf{r}', t') dt' dx' dy' dz', \quad (2.20)$$

to obtain

$$\mathbf{a}(\mathbf{r},t) = \int_v \int_{-\infty}^{\infty} \frac{\delta\left(t - t' - \frac{R}{c}\right)}{4\pi R} \mathbf{j}(\mathbf{r}', t') dt' dv', \quad (2.21)$$

with  $R = |\mathbf{r} - \mathbf{r}'|$ .

Because the delta function is an even function, we can write

$$\mathbf{a}(\mathbf{r},t) = \int_v \int_{-\infty}^{\infty} \frac{\delta\left[t' - \left(t - \frac{R}{c}\right)\right]}{4\pi R} \mathbf{j}(\mathbf{r}', t') dt' dv', \quad (2.22)$$

which, by the sifting property of the delta function, becomes

$$\mathbf{a}(\mathbf{r},t) = \frac{1}{4\pi} \int_v \frac{1}{R} \mathbf{j}\left(\mathbf{r}', t - \frac{R}{c}\right) dv', \quad (2.23)$$

where the current in the integrand is evaluated at an earlier (retarded) time

$$t - \frac{R}{c}.$$

**General Case.**—The transient Green's function for the general case can be derived by writing equation (2.13) as a Laplace transform through the substitution  $s = i\omega$ :

$$G(r,s) = \frac{e^{-(\mu\varepsilon s^2 + \mu\sigma s)^{1/2}r}}{4\pi r},$$

or

$$G(r,s) = \frac{e^{-(s^2 + \sigma s/\epsilon)^{1/2}\alpha}}{4\pi r}, \quad (2.24)$$

with  $\alpha = r/c$ . Following Bhattacharyya (1957), we rewrite equation (2.24) as

$$G(r,s) = -\frac{1}{4\pi r} \frac{\partial}{\partial \alpha} \left[ \frac{e^{-(s^2 + \sigma s/\epsilon)^{1/2}\alpha}}{\left( s^2 + \frac{\sigma}{\epsilon} s \right)^{1/2}} \right].$$

From tables of Laplace transforms in Abramowitz and Stegun (1964) we find that

$$g(r,t) = -\frac{1}{4\pi r} \frac{\partial}{\partial \alpha} \left\{ e^{-\sigma t/2\epsilon} I_0 \left[ \frac{\sigma}{2\epsilon} (t^2 - \alpha^2)^{1/2} \right] u(t - \alpha) \right\}, \quad (2.25)$$

where  $u$  is the unit step function, and  $I_0$  is the modified Bessel function of the first kind of order zero.

Using the relation

$$I'_0(z) = I_1(z),$$

we can rewrite equation (2.25) as

$$g(r,t) = \frac{1}{4\pi r} \left\{ e^{-\alpha(r/c)} \delta\left(t - \frac{r}{c}\right) + \frac{a \frac{r}{c} e^{-at}}{\left(t^2 - \frac{r^2}{c^2}\right)^{1/2}} I_1 \left[ a \left(t^2 - \frac{r^2}{c^2}\right)^{1/2} \right] u\left(t - \frac{r}{c}\right) \right\}, \quad (2.26)$$

with  $a = \sigma/2\epsilon$ , which is the expression given in Wait (1958) and in Kaufman and Keller (1983).

**Quasistatic Case.**—Due to attenuation in the earth, geophysical EM surveys usually must utilize low frequencies or late times, in which case displacement currents can be neglected. Then equation (2.24) becomes

$$G(r,s) = \frac{e^{-(\mu\sigma s)^{1/2}r}}{4\pi r}. \quad (2.27)$$

From Abramowitz and Stegun (1964) the inverse Laplace transform of equation (2.27) is

$$g(r,t) = \frac{(\mu\sigma)^{1/2}}{8\pi^{3/2} t^{3/2}} e^{-\mu\sigma r^2/4t} u(t). \quad (2.28)$$

Figure 2.1 is a plot of  $g(r,t)$  versus time at a distance of 100 m in a 0.01 S/m whole space. In free space the Green's function would be an impulse at  $t = r/c$  as shown by the arrow, as specified by equation (2.19). The effect of the conductive whole-space is to delay and broaden the impulse. Values of the Green's function calculated using the exact expression in equation (2.26) are virtually identical to those computed using the quasistatic expression in Figure 2.1 for  $t \geq 3 \mu\text{s}$ . At 2  $\mu\text{s}$  the exact value is only 9 percent less than the quasistatic value shown. Note that the maximum, found by differentiating equation (2.28) and setting the result to zero, occurs at  $t = r^2 \mu_0 \sigma / 6 = 0.021 \text{ ms}$ . At late times the Green's function exhibits a  $t^{-3/2}$  time dependence, which shows up as a linear decrease at an angle of 56.3

degrees on the log-log plot of Figure 2.1.

Substituting equation (2.28), the convolution in equation (2.20) becomes

$$\mathbf{a}(\mathbf{r}, t) = \frac{(\mu\sigma)^{1/2}}{8\pi^{3/2}} \int_v \int_0^t \frac{1}{(t-t')^{3/2}} e^{-\mu\sigma|\mathbf{r}-\mathbf{r}'|^2/4(t-t')} \mathbf{j}(\mathbf{r}', t') dt' dv', \quad (2.29)$$

or, equivalently,

$$\mathbf{a}(\mathbf{r}, t) = \frac{(\mu\sigma)^{1/2}}{8\pi^{3/2}} \int_v \int_0^t \frac{1}{(t')^{3/2}} ce^{-\mu\sigma|\mathbf{r}-\mathbf{r}'|^2/4t'} \mathbf{j}(\mathbf{r}', t-t') dt' dv'. \quad (2.30)$$

### Point source of direct current

Although we are concerned primarily with electromagnetic fields produced by alternating current, it is useful to discuss briefly the solution for the electric field due to a point source of direct current. At zero frequency equation (1.119) for the scalar potential becomes

$$\nabla^2 V = -\frac{1}{\sigma} \nabla \cdot \mathbf{J}. \quad (2.31)$$

Now the total current flowing through a closed surface surrounding an electrode at the origin is given by

$$\int_s \mathbf{J} \cdot d\mathbf{s} = I.$$

Thus, by the divergence theorem

$$\int_v \nabla \cdot \mathbf{J} dv = I.$$

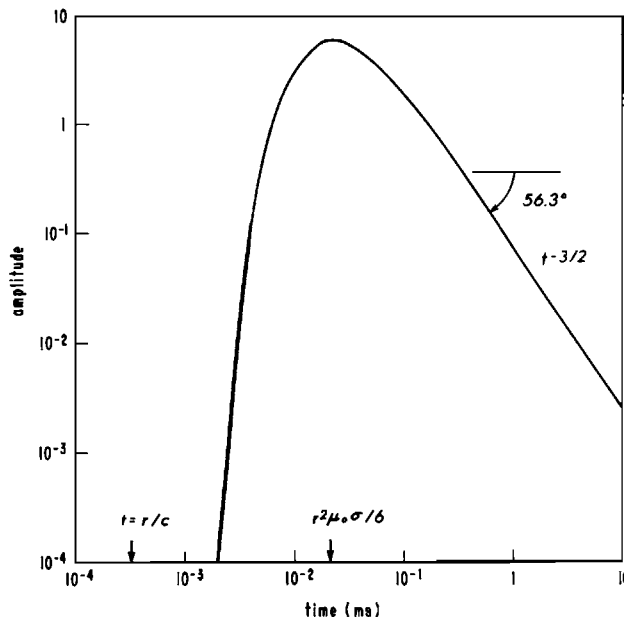


FIG. 2.1. Scalar EM Green's function in the time domain;  $r = 100$  m,  $\sigma = 0.01$  S/m.

Hence, treating  $\nabla \cdot \mathbf{J}$  as a generalized function,

$$\nabla \cdot \mathbf{J} = I \delta(x)\delta(y)\delta(z). \quad (2.32)$$

After substituting relation (2.32), equation (2.31) becomes

$$\nabla^2 V = -\frac{I}{\sigma} \delta(x)\delta(y)\delta(z). \quad (2.33)$$

By analogy with the solution of equation (2.6), with  $k = 0$ ,

$$V(r) = \frac{I}{4\pi\sigma r}. \quad (2.34)$$

Then the electric field of a point source is given by

$$\mathbf{E} = -\nabla V = \frac{I}{4\pi\sigma r^3} (x\mathbf{u}_x + y\mathbf{u}_y + z\mathbf{u}_z). \quad (2.35)$$

### Harmonic electric dipole

The current density in an  $x$ -directed electric dipole (a small current element of length  $\Delta s$ ) at the origin can be represented by (Baños, 1966)

$$\mathbf{J}(\mathbf{r}) = \mathbf{u}_x I \Delta s \left[ \frac{u\left(x + \frac{\Delta s}{2}\right) - u\left(x - \frac{\Delta s}{2}\right)}{\Delta s} \right] \delta(y)\delta(z). \quad (2.36)$$

Letting  $\Delta s \rightarrow ds$ ,

$$\mathbf{J}(\mathbf{r}) = \mathbf{u}_x I ds \delta(x)\delta(y)\delta(z), \quad (2.37)$$

because

$$u'(x) = \delta(x),$$

i.e., the derivative of the unit step function is the delta function.

Inserting expression (2.37) in equation (2.14), we obtain the vector potential of an electric dipole:

$$\mathbf{A}(\mathbf{r}) = \frac{I ds}{4\pi r} e^{-ikr} \mathbf{u}_x. \quad (2.38)$$

Note that the vector potential everywhere is oriented in the same direction as the source dipole. From equations (1.122), the electric field is given by

$$\mathbf{E} = \frac{I ds}{4\pi\sigma} \left[ \mathbf{u}_x \left( k^2 + \frac{\partial^2}{\partial x^2} \right) + \mathbf{u}_y \frac{\partial^2}{\partial x \partial y} + \mathbf{u}_z \frac{\partial^2}{\partial x \partial z} \right] \frac{e^{-ikr}}{r}, \quad (2.39)$$

which becomes

$$\mathbf{E} = \frac{I ds}{4\pi\sigma r^3} e^{-ikr} \left[ \left( \frac{x^2}{r^2} \mathbf{u}_x + \frac{xy}{r^2} \mathbf{u}_y + \frac{xz}{r^2} \mathbf{u}_z \right) (-k^2 r^2 + 3ikr + 3) + (k^2 r^2 - ikr - 1) \mathbf{u}_x \right]. \quad (2.40)$$

From equations (1.123), the magnetic field is given by

$$\mathbf{H} = \frac{I ds}{4\pi} \left[ \mathbf{u}_y \frac{\partial}{\partial z} - \mathbf{u}_z \frac{\partial}{\partial y} \right] \frac{e^{-ikr}}{r}, \quad (2.41)$$

which becomes

$$\mathbf{H} = \frac{I ds}{4\pi r^2} (ikr + 1) e^{-ikr} \left( -\frac{z}{r} \mathbf{u}_y + \frac{y}{r} \mathbf{u}_z \right). \quad (2.42)$$

In many practical cases the fields of a current-carrying wire grounded at its ends cannot be approximated as due to an electric dipole. For the dipole approximation to apply, the observation point should be at least five to ten wire-lengths from the center of the wire. At closer points, expressions (2.40) and (2.42) must be integrated along the wire. Analytic expressions for the fields of a finite-length wire in a homogeneous medium are given in Inan, et al. (1985), which also illustrates the behavior of the electric and magnetic fields with plots.

### Transient electric dipole

Since we have developed expressions for the fields (system functions) in the frequency domain, it is easier to find the inverse (time) Fourier transforms of equations (2.40) and (2.42), rather than begin the derivation with equation (2.29). However, we will ignore displacement currents and consider the practical case of a step function current  $I u(t)$ . The step response  $f(t)$  is given by the integral of the impulse response  $h(t)$ , which, for a causal system is

$$f(t) = \int_0^t h(\tau) d\tau \quad t \geq 0. \quad (2.43)$$

In geophysical applications, however, we usually measure the response  $f_-(t)$  of a negative step  $u(-t) = 1 - u(t)$ ; i.e., we measure the decay of the field after a constant current is turned off. Then

$$f_-(t) = \int_t^\infty h(\tau) d\tau = \int_0^\infty h(\tau) d\tau - \int_0^t h(\tau) d\tau \quad t \geq 0,$$

or

$$f_-(t) = f(\infty) - f(t) \quad t \geq 0. \quad (2.44)$$

Thus the derivative of  $f_-(t)$  with respect to time is  $-h(t)$ , the negative of the impulse response.

In transient problems it often is more convenient to use the Laplace transform rather than the Fourier transform. Thus, if the system function is denoted as  $H(\omega)$ , and if the substitution  $s = i\omega$  is made, the step response is given by

$$f(t) = \mathcal{L}^{-1} \left[ \frac{H(s)}{s} \right], \quad (2.45)$$

where  $\mathcal{L}^{-1}$  denotes the inverse Laplace transform. We will determine  $f(t)$ ; then the decay of the field after a constant current is shut off is given by equation (2.44).

To find the step response, we need the inverse Laplace transforms of three expressions, for which we use tables in Abramowitz and Stegun (1964). Defining a function

$$\theta = \left( \frac{\mu\sigma}{4t} \right)^{1/2}, \quad (2.46)$$

which is analogous to  $k$  in the frequency domain, we have the following inverse Laplace transforms:

$$\mathcal{L}^{-1} \left( \frac{k^2 r^2}{s} e^{-ikr} \right) = -\frac{4}{\pi^{1/2}} \theta^3 r^3 e^{-\theta^2 r^2}, \quad (2.47)$$

$$\mathcal{L}^{-1} \left( \frac{ikr}{s} e^{-ikr} \right) = \frac{2}{\pi^{1/2}} \theta r e^{-\theta^2 r^2}, \quad (2.48)$$

and

$$\mathcal{L}^{-1} \left( \frac{1}{s} e^{-ikr} \right) = \operatorname{erfc}(\theta r), \quad (2.49)$$

where

$$\operatorname{erfc}(\theta r) = 1 - \operatorname{erf}(\theta r) = 1 - \frac{2}{\pi^{1/2}} \int_0^{\theta r} e^{-v^2} dv$$

is the complementary error function. Thus from the expressions (2.40) and (2.42) the electric and magnetic fields after the current in an electric dipole is turned on abruptly are given by

$$\begin{aligned} \mathbf{e} &= \frac{Ids}{4\pi\sigma r^3} \left\{ \left[ \left( \frac{4}{\pi^{1/2}} \theta^3 r^3 + \frac{6}{\pi^{1/2}} \theta r \right) e^{-\theta^2 r^2} + 3 \operatorname{erfc}(\theta r) \right] \right. \\ &\quad \times \left. \left[ \frac{x^2}{r^2} \mathbf{u}_x + \frac{xy}{r^2} \mathbf{u}_y + \frac{xz}{r^2} \mathbf{u}_z \right] - \left[ \left( \frac{4}{\pi^{1/2}} \theta^3 r^3 + \frac{2}{\pi^{1/2}} \theta r \right) e^{-\theta^2 r^2} + \operatorname{erfc}(\theta r) \right] \mathbf{u}_x \right\} \end{aligned} \quad (2.50)$$

and

$$\mathbf{h} = \frac{Ids}{4\pi r^2} \left[ \frac{2}{\pi^{1/2}} \theta r e^{-\theta^2 r^2} + \operatorname{erfc}(\theta r) \right] \left[ -\frac{z}{r} \mathbf{u}_y - \frac{y}{r} \mathbf{u}_z \right], \quad (2.51)$$

which agree with the expressions given in Wait (1958).

However, in geophysical applications we usually measure the emf induced in a coil, which is proportional to the time derivative of the magnetic field. Thus, taking the time derivative of equation (2.51), we obtain

$$\frac{\partial \mathbf{h}}{\partial t} = \frac{Ids\theta^3 r}{2\pi^{3/2} t} e^{-\theta^2 r^2} \left( -\frac{z}{r} \mathbf{u}_y - \frac{y}{r} \mathbf{u}_z \right); \quad (2.52)$$

which is a simpler expression than equation (2.51) for the magnetic field. Note that at late times  $\partial \mathbf{h} / \partial t$  falls off as  $t^{-5/2}$ , which is characteristic of a dipole source. Because the source is a step current, equation (2.52) is the magnetic-field impulse response.

### Harmonic magnetic dipole

A small loop of current  $I$  at the origin and in the  $y$ - $z$  plane can be represented by an infinitesimal magnetic dipole with moment

$$\mathbf{m} = IS$$

where  $S$  is the area of the loop. The magnetization vector is given by

$$\mathbf{M} = m \mathbf{u}_x \delta(x)\delta(y)\delta(z). \quad (2.53)$$

Thus, the differential equation for  $\mathbf{F}$ , from equation (1.114), is

$$\nabla^2 \mathbf{F} + k^2 \mathbf{F} = -i\omega\mu\mathbf{M}, \quad (2.54)$$

so that, by analogy with equation (2.38)

$$\mathbf{F}(\mathbf{r}) = \frac{i\omega\mu m}{4\pi r} e^{-ikr} \mathbf{u}_x. \quad (2.55)$$

From the expression (1.122), by analogy with the expression (2.42), the electric field of a magnetic dipole is given by

$$\mathbf{E} = \frac{i\omega\mu m}{4\pi r^2} (ikr + 1) e^{-ikr} \left( \frac{z}{r} \mathbf{u}_y - \frac{y}{r} \mathbf{u}_z \right). \quad (2.56)$$

From the expression (1.123), by analogy with the expression (2.40), the magnetic field is given by

$$\mathbf{H} = \frac{m}{4\pi r^3} e^{-ikr} \left[ \left( \frac{x^2}{r^2} \mathbf{u}_x + \frac{xy}{r^2} \mathbf{u}_y + \frac{xz}{r^2} \mathbf{u}_z \right) (-k^2 r^2 + 3ikr + 3) + (k^2 r^2 - ikr - 1) \mathbf{u}_x \right]. \quad (2.57)$$

For illustration, Figures 2.2 and 2.3 show the real and imaginary parts of the magnetic

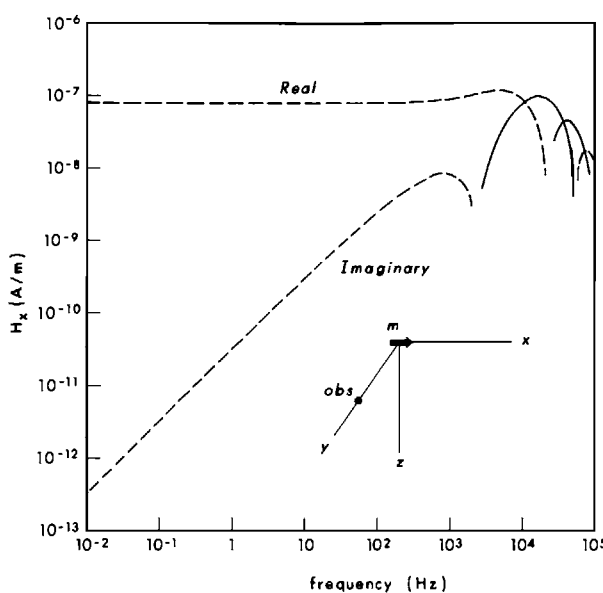


FIG. 2.2. Frequency-domain magnetic field 100 m from a magnetic dipole with moment 1 A-m<sup>2</sup> in a 0.01 S/m whole space. Observation point in equatorial plane of dipole. Solid line positive, dashed line negative.

field in the equatorial plane and along the axis, respectively, of a magnetic dipole. The field is plotted as a function of frequency at a distance of 100 m in a whole space with conductivity 0.01 S/m. Note that the real part of the field at low frequencies along the axis in Figure 2.3 is twice that in the equatorial plane in Figure 2.2. At low frequencies the imaginary parts exhibit a linear dependence on frequency, while at high frequencies both real and imaginary parts become oscillatory.

### Transient magnetic dipole

We derive the step response of a magnetic dipole by analogy with the inverse Laplace transforms of equations (2.40) and (2.42), which are for an electric dipole. Note, however, that the factor  $i\omega$  in equation (2.56) implies time differentiation. Hence, by analogy with equation (2.52),

$$\mathbf{e} = \frac{\mu m \theta^3 r}{2\pi^{3/2} t} e^{-\theta^2 r^2} \left( -\frac{z}{r} \mathbf{u}_y + \frac{y}{r} \mathbf{u}_z \right). \quad (2.58)$$

By analogy with equations (2.40) and (2.50), which give the electric field of an electric dipole, the magnetic field of a magnetic dipole with step excitation is, from equation (2.57),

$$\begin{aligned} \mathbf{h} = \frac{m}{4\pi r^3} & \left\{ \left[ \left( \frac{4}{\pi^{1/2}} \theta^3 r^3 + \frac{6}{\pi^{1/2}} \theta r \right) e^{-\theta^2 r^2} + 3 \operatorname{erfc}(\theta r) \right] \times \left[ \frac{x^2}{r^2} \mathbf{u}_x + \frac{xy}{r^2} \mathbf{u}_y + \frac{xz}{r^2} \mathbf{u}_z \right] \right. \\ & \left. - \left[ \left( \frac{4}{\pi^{1/2}} \theta^3 r^3 + \frac{2}{\pi^{1/2}} \theta r \right) e^{-\theta^2 r^2} + \operatorname{erfc}(\theta r) \right] \mathbf{u}_x \right\}. \end{aligned} \quad (2.59)$$

Equations (2.58) and (2.59) agree with the expressions given in Wait (1958).

Again, a more useful function for geophysical purposes is the time derivative of the magnetic field. After some algebra, the time derivative is given by

$$\frac{\partial \mathbf{h}}{\partial t} = \frac{m \theta^3}{\pi^{3/2} t} e^{-\theta^2 r^2} \left[ \theta^2 r^2 \left( \frac{x^2}{r^2} \mathbf{u}_x + \frac{xy}{r^2} \mathbf{u}_y + \frac{xz}{r^2} \mathbf{u}_z \right) + (1 - \theta^2 r^2) \mathbf{u}_x \right]. \quad (2.60)$$

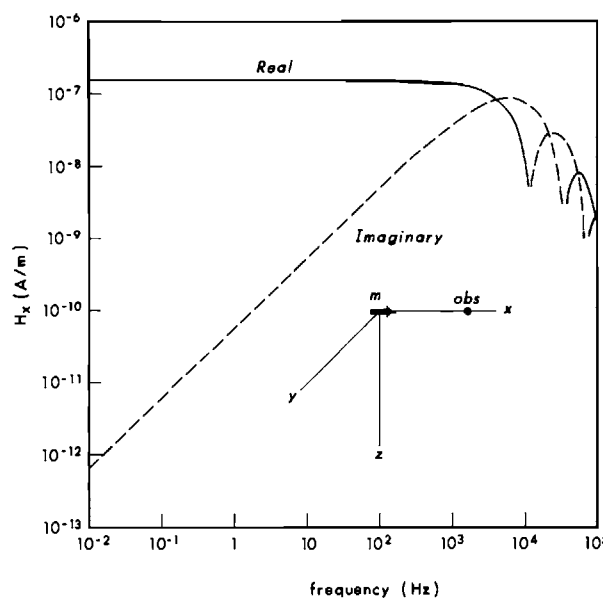


FIG. 2.3. Same as Figure 2.2 except observation point along axis of dipole.

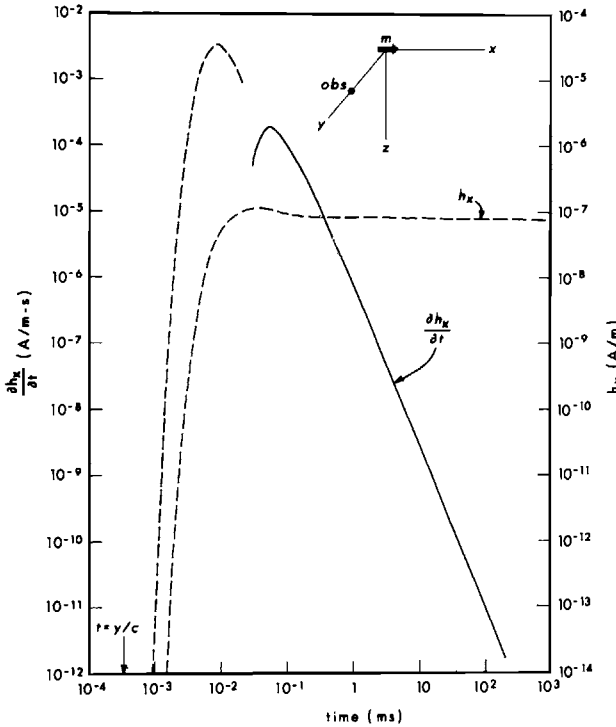


FIG. 2.4. Transient magnetic field 100 m from a magnetic dipole with step-function moment of 1 A-m<sup>2</sup> in a 0.01 S/m whole space. Observation point in equatorial plane of dipole.

Figures 2.4 and 2.5 show the equatorial and axial transient magnetic fields of a magnetic dipole with step-function moment, for the same configuration as that of the harmonic fields in Figures 2.2 and 2.3. As in Figure 2.1 for the scalar Green's function, the propagation time in free space ( $y/c$  or  $x/c$ ) is shown by an arrow. At late time the magnetic field approaches a constant,  $1/4\pi r^3$  or  $1/2\pi r^3$ , while the time derivative of the magnetic field decays with a time dependence of  $t^{-5/2}$ .

#### Harmonic line source

The current density for a two-dimensional (2-D) line source of electric current can be described by the distribution

$$\mathbf{J}(\mathbf{r}) = I \delta(x)\delta(z)\mathbf{u}_y, \quad (2.61)$$

where the line source is in the  $y$  direction and intersects the  $x - z$  plane at the origin.

Instead of substituting the expression (2.61) into equation (2.14) and integrating, let us first derive a 2-D Green's function  $G_2$ . If there is no variation in the  $y$  direction, equation (2.6) becomes

$$\nabla^2 G_2 + k^2 G_2 = -\delta(x)\delta(z), \quad (2.62)$$

so that equation (2.9) becomes a one-dimensional (1-D) Fourier transform

$$G_2(x, z) = \frac{1}{4\pi} \int_{-\infty}^{\infty} \frac{1}{(k_x^2 - k^2)^{1/2}} e^{-(k_x^2 - k^2)^{1/2}|z|} e^{ik_x x} dk_x. \quad (2.63)$$

From Erdelyi (1954, v. 1, 17)

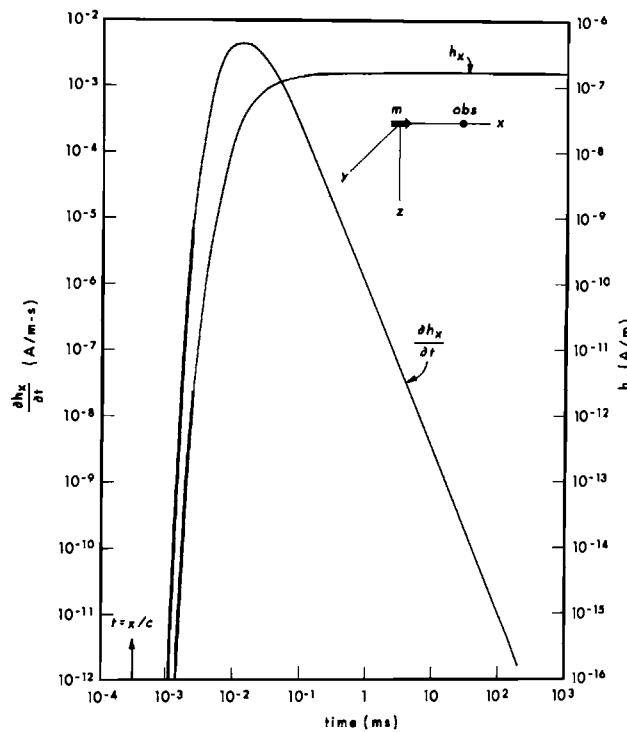


FIG. 2.5. Same as Figure 2.4 except observation point along axis of dipole. Solid line positive, dashed line negative.

$$G_2(x,z) = \frac{1}{2\pi} K_0[ik(x^2 + z^2)^{1/2}], \quad (2.64)$$

where  $K_0$  is the modified Bessel function of the second kind of order zero.

Because the line source is at the origin, the vector potential is given by substituting equation (2.61) into the 2-D version of equation (2.5) to obtain

$$\mathbf{A}(x,z) = \int_{-\infty}^{\infty} \int_{-\infty}^{\infty} \frac{I}{2\pi} K_0[ik[(x-x')^2 + (z-z')^2]^{1/2}] \delta(x') \delta(z') dx' dz' \mathbf{u}_y,$$

which results in

$$\mathbf{A}(x,z) = \frac{I}{2\pi} K_0[ik(x^2 + z^2)^{1/2}] \mathbf{u}_y. \quad (2.65)$$

Because the divergence of  $\mathbf{A}$  is zero, the electric field has only a  $y$  component, given from equation (1.122) by

$$E_y = -\frac{i\omega\mu J}{2\pi} K_0(i k \rho), \quad (2.66)$$

where

$$\rho = (x^2 + z^2)^{1/2}.$$

From equation (1.16), using the relation

$$K'_0(\alpha) = -K_1(\alpha),$$

the magnetic field is given by

$$\mathbf{H} = \frac{ikI}{2\pi} K_1(ik\rho) \left( \frac{z}{\rho} \mathbf{u}_x - \frac{x}{\rho} \mathbf{u}_z \right). \quad (2.67)$$

### Transient line source

Substituting  $s = i\omega$  in equation (2.66), neglecting displacement currents, and dividing by  $s$  so that the source is a step current,

$$e_y = -\frac{\mu I}{2\pi} \mathcal{L}^{-1}\{K_0[s^{1/2}(\mu\sigma)^{1/2}\rho]\}.$$

From a table of inverse Laplace transforms in Abramowitz and Stegun (1964),

$$e_y = -\frac{\mu I}{4\pi t} e^{-\theta^2\rho^2}, \quad (2.68)$$

where, as before,  $\theta^2 = \mu\sigma/4t$ .

From equation (2.67) the transient magnetic field due to a step current source is

$$\mathbf{h} = \frac{(\mu\sigma)^{1/2}I}{2\pi} \mathcal{L}^{-1}\left\{\frac{1}{s^{1/2}} K_1[s^{1/2}(\mu\sigma)^{1/2}\rho]\right\} \left( \frac{z}{\rho} \mathbf{u}_x - \frac{x}{\rho} \mathbf{u}_z \right).$$

From Abramowitz and Stegun (1964),

$$\mathbf{h} = \frac{I}{2\pi\rho} e^{-\theta^2\rho^2} \left( \frac{z}{\rho} \mathbf{u}_x - \frac{x}{\rho} \mathbf{u}_z \right). \quad (2.69)$$

Finally, the time derivative of the magnetic field is given by

$$\frac{\partial \mathbf{h}}{\partial t} = \frac{I\theta^2\rho}{2\pi t} e^{-\theta^2\rho^2} \left( \frac{z}{\rho} \mathbf{u}_x - \frac{x}{\rho} \mathbf{u}_z \right). \quad (2.70)$$

### Tensor Green's functions

Because the vector potential is in the same direction as its source current, the Green's function defined in expression (2.13) is a scalar. However, by applying the expression (1.122) to equation (2.15), we can define a convolution integral for calculating the electric field due to current in a volume  $v$ . In the frequency domain

$$\mathbf{E}(\mathbf{r}) = \int_v \mathbf{G}(\mathbf{r}, \mathbf{r}') \mathbf{J}(\mathbf{r}') dv'. \quad (2.71)$$

Because the electric field at a point  $\mathbf{r}$  is not in the same direction as its source current at  $\mathbf{r}'$ , the Green's function is a tensor, given by

$$\mathbf{G}(\mathbf{r}, \mathbf{r}') = \left[ -i\omega\mu\mathbf{I} + \frac{1}{\sigma} \nabla\nabla \right] G(R), \quad (2.72)$$

where  $\mathbf{I}$  is the identity tensor, and where  $R = |\mathbf{r} - \mathbf{r}'|$ .

As shown by VanBladel (1961), to include the case where  $\mathbf{r}$  is in  $v$ , the tensor Green's function must be written as a generalized function

$$\mathbf{G}(\mathbf{r}, \mathbf{r}') = \left[ -i\omega\mu G(R) - \frac{1}{3\sigma} \delta(\mathbf{r} - \mathbf{r}') \right] \mathbf{I} + \frac{1}{\sigma} \text{PV} [\nabla \nabla G(R)], \quad (2.73)$$

where PV denotes principal value integration.

For the case of  $\mathbf{r}$  outside  $v$ , we can derive  $\mathbf{G}$  easily by generalizing equation (2.40), which was derived for an  $x$ -directed electric dipole of moment  $I ds$  at the origin. Thus

$$\mathbf{G}(\mathbf{r}, \mathbf{r}') = \frac{e^{-ikR}}{4\pi\sigma R^3} \begin{bmatrix} \frac{(x-x')^2}{R^2} \beta_1 + \beta_2 & \frac{(x-x')(y-y')}{R^2} \beta_1 \frac{(x-x')(z-z')}{R^2} \beta_1 \\ \frac{(x-x')(y-y')}{R^2} \beta_1 \frac{(y-y')^2}{R^2} \beta_1 + \beta_2 & \frac{(y-y')(z-z')}{R^2} \beta_1 \\ \frac{(x-x')(z-z')}{R^2} \beta_1 \frac{(y-y')(z-z')}{R^2} \beta_1 & \frac{(z-z')^2}{R^2} \beta_1 + \beta_2 \end{bmatrix} \quad (2.74)$$

with

$$R = [(x-x')^2 + (y-y')^2 + (z-z')^2]^{1/2},$$

$$\beta_1 = -k^2 R^2 + 3 ikR + 3,$$

and

$$\beta_2 = k^2 R^2 - ikR - 1.$$

If we let

$$\mathbf{G} = \begin{bmatrix} G_{xx} & G_{xy} & G_{xz} \\ G_{yx} & G_{yy} & G_{yz} \\ G_{zx} & G_{zy} & G_{zz} \end{bmatrix} \quad (2.75)$$

where, e.g.,  $G_{xy}$  is the  $x$ -component of electric field due to a  $y$ -directed current element, then the reciprocity theorem takes the form (Harrington, 1961).

$$G_{ij}(\mathbf{r}, \mathbf{r}') = G_{ij}(\mathbf{r}', \mathbf{r}). \quad (2.76)$$

In other words, if both the transmitter/receiver positions and the transmitter/receiver components are interchanged, the measurement will be the same. This reciprocity relation is valid for linear, isotropic, homogeneous, or inhomogeneous media.

We also can derive a tensor Green's function for calculating the magnetic field due to an arbitrary current distribution using the integral

$$\mathbf{H}(\mathbf{r}) = \int_v \mathbf{G}_H(\mathbf{r}, \mathbf{r}') \mathbf{J}(\mathbf{r}') dv'. \quad (2.77)$$

Generalizing equation (2.42),

$$\mathbf{G}_H(\mathbf{r}, \mathbf{r}') = \frac{(ikR + 1)e^{-ikR}}{4\pi R^3} \begin{bmatrix} 0 & z - z' & y' - y \\ z' - z & 0 & x - x' \\ y - y' & x' - x & 0 \end{bmatrix}. \quad (2.78)$$

The time-domain convolution corresponding to equation (2.71) is

$$\mathbf{e}(\mathbf{r}, t) = \int_v \int_{-\infty}^t \mathbf{g}(\mathbf{r}, \mathbf{r}', t - t') \mathbf{j}(\mathbf{r}', t') dt' dv', \quad (2.79)$$

where the time-domain tensor Green's function  $\mathbf{g}$  is given by the time-domain version of equation (2.72):

$$\mathbf{g}(\mathbf{r}, \mathbf{r}', t) = \left( -\mu \mathbf{I} \frac{\partial}{\partial t} + \frac{1}{\sigma} \nabla \nabla \right) g(R, t). \quad (2.80)$$

The scalar Green's function  $g$  is given by equation (2.28), which can be rewritten as

$$g(R, t) = \frac{(\mu\sigma)^{1/2}}{8(\pi t)^{3/2}} e^{-\theta^2 R^2} u(t), \quad (2.81)$$

with  $\theta^2 = \mu\sigma/4t$  and  $R^2 = (x - x')^2 + (y - y')^2 + (z - z')^2$ . For the first term in equation (2.80)

$$-\mu \frac{\partial g}{\partial t} = -\frac{\mu\theta}{4\pi^{3/2} t^2} (\theta^2 R^2 - 3/2) e^{-\theta^2 R^2} u(t). \quad (2.82)$$

The  $\nabla \nabla$  operator in equation (2.80) results in two types of terms:

$$\frac{1}{\sigma} \frac{\partial^2 g}{\partial x^2} = \frac{\mu\theta}{8\pi^{3/2} t^2} [2\theta^2(x - x')^2 - 1] e^{-\theta^2 R^2} u(t), \quad (2.83)$$

and

$$\frac{1}{\sigma} \frac{\partial^2 g}{\partial x \partial y} = \frac{\mu\theta}{4\pi^{3/2} t^2} [\theta^2(x - x')(y - y')] e^{-\theta^2 R^2} u(t). \quad (2.84)$$

Thus, using equations (2.80), (2.82) and  $x, y, z$  permutations of equations (2.83) and (2.84), we obtain

$$\mathbf{g}(\mathbf{r}, \mathbf{r}', t) = \frac{\mu\theta^3 e^{-\theta^2 R^2}}{4\pi^{3/2} t^2} \begin{bmatrix} \left[ (x - x')^2 - R^2 + \frac{1}{\theta^2} \right] & (x - x')(y - y') & (x - x')(z - z') \\ (x - x')(y - y') & \left[ (y - y')^2 - R^2 + \frac{1}{\theta^2} \right] & (y - y')(z - z') \\ (x - x')(z - z') & (y - y')(z - z') & (z - z')^2 - R^2 + \frac{1}{\theta^2} \end{bmatrix} u(t). \quad (2.85)$$

Either by inverse transformation of equation (2.78) or by using equation (2.52) and similar expressions for  $y$ - and  $z$ -directed impulsive electric dipoles, we obtain the time-domain tensor Green's function for magnetic field as

$$\mathbf{g}_h(\mathbf{r}, \mathbf{r}', t') = \frac{\theta^3 e^{-\theta^2 R^2}}{2\pi^{3/2} t} \begin{bmatrix} 0 & z - z' & y' - y \\ z' - z & 0 & x - x' \\ y - y' & x' - x & 0 \end{bmatrix} u(t). \quad (2.86)$$

### Section 3 Reflection and Refraction of Plane Waves

Electromagnetic waves are reflected and refracted at a plane interface separating media of different electrical parameters. The reflection and refraction at an interface of plane waves are governed by Snell's laws and the Fresnel equations.

Following Stratton (1941) we develop both Snell's laws and the Fresnel equations from first principles. The concepts of wave impedance and impedance at a plane interface are then introduced. There follows consideration of the notion of total reflection for dielectric media and a brief exposition on the Brewster angle at which this occurs. These concepts are important in electromagnetic studies of dielectrics such as ice. The plane-layered impedance of an  $n$ -layered isotropic earth, essential to 1-D interpretation of magnetotelluric (MT) and audiagnetotelluric (AMT) data, is developed in detail.

#### Snell's laws

At the outset we shall treat reflection of a uniform, linearly polarized, homogeneous, plane wave. Referring to Figure 3.1, two media of electrical parameters,  $\sigma_1 \mu_1 \epsilon_1$  and  $\sigma_2 \mu_2 \epsilon_2$  are in contact at an infinite plane surface  $S$ . A uniform, homogeneous, plane wave is propagated in the incident direction denoted by the vector wave number  $\mathbf{k}_i$  or by the angle of incidence  $\theta_i$ . The vector  $\mathbf{k}_i$  is confined to the  $x$ - $z$  plane. The wave is reflected in the direction denoted by  $\mathbf{k}_r$  or by the angle  $\theta_r$ ; it is also transmitted into the second medium in the direction denoted by  $\mathbf{k}_t$  or  $\theta_t$ . For a uniform, homogeneous, plane wave,  $\mathbf{E}$ ,  $\mathbf{H}$ , and the direction of propagation are orthogonal to one another such that  $\mathbf{E} \times \mathbf{H} = \mathbf{k}$ .

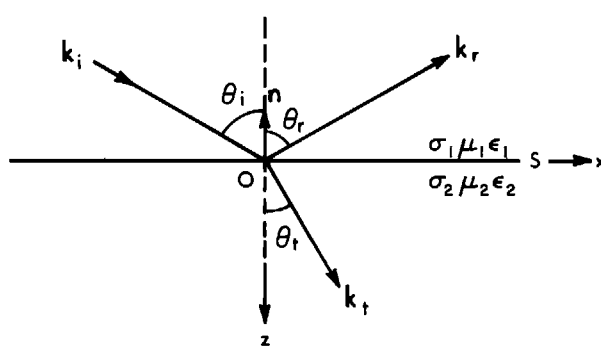


FIG. 3.1. Incident  $\mathbf{k}_i$ , reflected  $\mathbf{k}_r$ , and transmitted  $\mathbf{k}_t$  wave vectors at a plane interface  $S$ . The angles of incidence, reflection, and transmission are  $\theta_i$ ,  $\theta_r$ , and  $\theta_t$ , respectively. The unit normal to the surface  $S$ , separating the medium  $\sigma_1 \mu_1 \epsilon_1$  from the medium  $\sigma_2 \mu_2 \epsilon_2$  is denoted by  $\mathbf{n}$ .

The outward-drawn unit vector  $\mathbf{n}$  in Figure 3.1 is normal to the plane  $S$ . If  $\mathbf{r}$  is a position vector drawn from the origin  $O$  to any point in either medium (1) or medium (2), then for any point in the plane  $S$ ,

$$\mathbf{n} \cdot \mathbf{r} = 0. \quad (3.1)$$

The electric and magnetic vectors of the incident wave are given by

$${}^i\mathbf{E} = \mathbf{E}_i e^{-i(k_i x + k_x z)} = \mathbf{E}_i e^{-i\mathbf{k}_i \cdot \mathbf{r}}, \quad (3.2)$$

and

$${}^i\mathbf{H} = \frac{\mathbf{k}_i \times {}^i\mathbf{E}}{\omega \mu_1} \quad (3.3)$$

where  $\mathbf{E}_i$  is the complex amplitude of the incident wave. The plane defined by the pair of vectors  $\mathbf{n}$  and  $\mathbf{k}_i$  is called the plane of incidence.

Similarly the reflected and transmitted waves are written

$${}^r\mathbf{E} = \mathbf{E}_r e^{-i\mathbf{k}_r \cdot \mathbf{r}}, \quad (3.4)$$

$${}^r\mathbf{H} = \frac{\mathbf{k}_r \times {}^r\mathbf{E}}{\omega \mu_1}, \quad (3.5)$$

and

$${}^t\mathbf{E} = \mathbf{E}_t e^{-i\mathbf{k}_t \cdot \mathbf{r}}, \quad (3.6)$$

$${}^t\mathbf{H} = \frac{\mathbf{k}_t \times {}^t\mathbf{E}}{\omega \mu_2}. \quad (3.7)$$

We have designated the incident wave as a uniform plane wave and shall assume that the reflected and transmitted waves are likewise uniform and plane. Then the amplitudes  $\mathbf{E}_i$ ,  $\mathbf{E}_r$ , and  $\mathbf{E}_t$  are each independent of coordinate position on a plane of constant phase. We may find relations between the three directions by invoking the boundary conditions calling for continuity of tangential  $\mathbf{E}$  and tangential  $\mathbf{H}$  at the surface  $S$  ( $z = 0$ ). Continuity of tangential  $\mathbf{E}$  is stated by

$$\underline{\mathbf{n}} \times ({}^i\mathbf{E} + {}^r\mathbf{E}) = \underline{\mathbf{n}} \times {}^t\mathbf{E}, \quad (3.8)$$

or

$$\mathbf{E}_i e^{-i(\mathbf{k}_i \cdot \mathbf{r} - \omega t)} + \mathbf{E}_r e^{-i(\mathbf{k}_r \cdot \mathbf{r} - \omega t)} = \mathbf{E}_t e^{-i(\mathbf{k}_t \cdot \mathbf{r} - \omega t)}. \quad (3.9)$$

The only way that this equation can be satisfied is for the arguments of the exponential terms to be equal, i.e.,

$$\mathbf{k}_i \cdot \mathbf{r} = \mathbf{k}_r \cdot \mathbf{r} = \mathbf{k}_t \cdot \mathbf{r}. \quad (3.10)$$

At this point the expansion

$$\mathbf{A} \times (\mathbf{B} \times \mathbf{C}) = (\mathbf{A} \cdot \mathbf{C})\mathbf{B} - (\mathbf{A} \cdot \mathbf{B})\mathbf{C} \quad (3.11)$$

is used to obtain, on the surface  $S$ ,

$$\mathbf{n} \times (\mathbf{n} \times \mathbf{r}) = (\mathbf{n} \cdot \mathbf{r})\mathbf{n} - \mathbf{r} = -\mathbf{r}. \quad (3.12)$$

Note that  $\mathbf{n} \cdot \mathbf{r} = 0$  according to equation (3.1). Equation (3.12) is substituted in equation (3.10) to yield

$$\mathbf{k}_i \cdot \mathbf{n} \times (\mathbf{n} \times \mathbf{r}) = \mathbf{k}_r \cdot \mathbf{n} \times (\mathbf{n} \times \mathbf{r}), \quad (3.13)$$

and

$$\mathbf{k}_i \cdot \mathbf{n} \times (\mathbf{n} \times \mathbf{r}) = \mathbf{k}_r \cdot \mathbf{n} \times (\mathbf{n} \times \mathbf{r}). \quad (3.14)$$

Using the vector identity

$$\mathbf{A} \cdot \mathbf{B} \times \mathbf{C} = \mathbf{A} \times \mathbf{B} \cdot \mathbf{C}, \quad (3.15)$$

equations (3.13) and (3.14) become

$$(\mathbf{k}_i \times \mathbf{n} - \mathbf{k}_r \times \mathbf{n}) \cdot \mathbf{n} \times \mathbf{r} = 0, \quad (3.16)$$

and

$$(\mathbf{k}_i \times \mathbf{n} - \mathbf{k}_r \times \mathbf{n}) \cdot \mathbf{n} \times \mathbf{r} = 0. \quad (3.17)$$

If the vectors in these last two expressions are replaced by

$$(\mathbf{k}_i \times \mathbf{n} - \mathbf{k}_r \times \mathbf{n}) = \mathbf{A}, \quad (3.18)$$

$$\mathbf{n} \times \mathbf{r} = \mathbf{B} \quad (3.19)$$

and

$$(\mathbf{k}_i \times \mathbf{n} - \mathbf{k}_r \times \mathbf{n}) = \mathbf{C}, \quad (3.20)$$

then equations (3.16) and (3.17) become

$$\mathbf{A} \cdot \mathbf{B} = 0, \quad (3.21)$$

and

$$\mathbf{C} \cdot \mathbf{B} = 0. \quad (3.22)$$

Equation (3.21) demands that  $\mathbf{A}$  be perpendicular to  $S$  since  $\mathbf{B}$  is contained in  $S$ , by equation (3.19). However,  $\mathbf{A}$  is defined by two cross-products, each of which contains  $\mathbf{n}$ ; hence  $\mathbf{A}$  must be parallel to  $S$  according to the condition (3.18). The only way for these two conditions to be met is that  $\mathbf{A} = 0$ . Similarly we may establish that  $\mathbf{C} = 0$ . Thus

$$\mathbf{k}_i \times \mathbf{n} = \mathbf{k}_r \times \mathbf{n}, \quad (3.23)$$

and

$$\mathbf{k}_i \times \mathbf{n} = \mathbf{k}_r \times \mathbf{n}. \quad (3.24)$$

The magnitudes of  $\mathbf{k}_i$  and  $\mathbf{k}_r$  must be equal since the vector wave numbers lie in the common medium (1). The vectors represented by the left- and right-hand sides of equation (3.23) are parallel to each other and perpendicular to  $\mathbf{k}_i$ ,  $\mathbf{k}_r$ , and  $\mathbf{n}$ . Similarly the left- and right-hand

sides of equation (3.24) are parallel, and each is perpendicular to  $\mathbf{k}_i$ ,  $\mathbf{k}_r$ , and  $\mathbf{n}$ . Thus  $\mathbf{k}_i$ ,  $\mathbf{k}_r$ , and  $\mathbf{n}$  are coplanar. The planes of constant phase of both transmitted and reflected waves are normal to the plane of incidence.

With reference to Figure 3.1, we find that the magnitude of the left-hand side of equation (3.23) is

$$k_i \sin(\pi - \theta_i) = k_i \sin \theta_i, \quad (3.25)$$

and that the magnitude of the right-hand side of equation (3.23) is

$$k_r \sin \theta_r. \quad (3.26)$$

We conclude that

$$\sin \theta_i = \sin \theta_r \quad (3.27)$$

since  $k_i = k_r$ . Thus the angle of incidence  $\theta_i$  is equal to the angle of reflection  $\theta_r$ . From equation (3.24),

$$k_i \sin \theta_i = k_t \sin \theta_t$$

or

$$k_1 \sin \theta_i = k_2 \sin \theta_t, \quad (3.28)$$

where  $k_1$  and  $k_2$  are the complex scalar wave numbers in medium (1) and medium (2), respectively. Equations (3.27) and (3.28) are Snell's Laws of reflection and refraction.

### Fresnel's equations

Having obtained Snell's Laws, which specify angular relationships, we now turn to the Fresnel equations which interrelate the amplitudes of the vector fields. As before, we consider reflection and refraction of uniform plane waves at an interface  $S$  as depicted in Figure 3.1.

From the continuity of tangential  $\mathbf{E}$  considering that the arguments of the exponential terms of incident, reflected, and transmitted waves are identical at the surface  $S$  (equation 3.10),

$$\mathbf{n} \times (\mathbf{E}_i + \mathbf{E}_r) = \mathbf{n} \times \mathbf{E}_t, \quad (3.29)$$

while from the continuity of tangential  $\mathbf{H}$ ,

$$\mathbf{n} \times (\mathbf{H}_i + \mathbf{H}_r) = \mathbf{n} \times \mathbf{H}_t. \quad (3.30)$$

Substituting equations (3.3), (3.5), and (3.7) in equation (3.30) results in,

$$\mathbf{n} \times (\mathbf{k}_i \times \mathbf{E}_i + \mathbf{k}_r \times \mathbf{E}_r) \frac{1}{\mu_1} = \mathbf{n} \times (\mathbf{k}_t \times \mathbf{E}_t) \frac{1}{\mu_2}. \quad (3.31)$$

The three terms of equation (3.31) may be expanded by use of the expansion (3.11) to yield

$$\mathbf{n} \times (\mathbf{k}_i \times \mathbf{E}_i) = (\mathbf{n} \cdot \mathbf{E}_i) \mathbf{k}_i - (\mathbf{n} \cdot \mathbf{k}_i) \mathbf{E}_i, \quad (3.32)$$

$$\mathbf{n} \times (\mathbf{k}_r \times \mathbf{E}_r) = (\mathbf{n} \cdot \mathbf{E}_r) \mathbf{k}_r - (\mathbf{n} \cdot \mathbf{k}_r) \mathbf{E}_r, \quad (3.33)$$

and

$$\mathbf{n} \times (\mathbf{k}_t \times \mathbf{E}_t) = (\mathbf{n} \cdot \mathbf{E}_t) \mathbf{k}_t - (\mathbf{n} \cdot \mathbf{k}_t) \mathbf{E}_t. \quad (3.34)$$

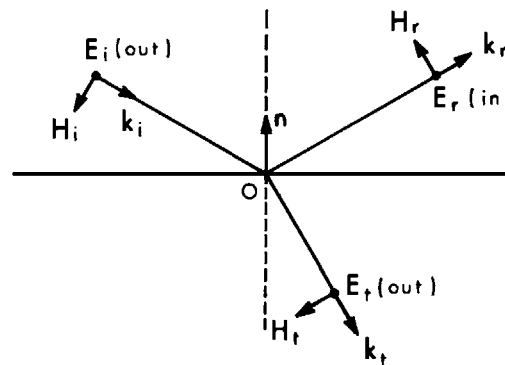


FIG. 3.2. The relative orientations of the  $\mathbf{E}$ ,  $\mathbf{H}$ , and  $\mathbf{k}$  vectors for reflection at a plane interface when  $\mathbf{E}$  is normal to the plane of incidence.

The orientation of the incident vector  $\mathbf{E}_i$  is arbitrary, but it can be resolved into a component normal to the plane of incidence and a component in the plane of incidence. These two cases shall be discussed separately.

**$\mathbf{E}_i$  Normal to the Plane of Incidence.**—Since the plane of incidence contains  $\mathbf{k}_i$ ,  $\mathbf{k}_r$ ,  $\mathbf{k}_t$ , and  $\mathbf{n}$ , and since  $\mathbf{E}_i$  is normal to this plane, as shown in Figure 3.2 then

$$\mathbf{n} \cdot \mathbf{E}_i = \mathbf{k}_i \cdot \mathbf{E}_i = 0. \quad (3.35)$$

For isotropic media,  $\mathbf{E}_t$  and  $\mathbf{E}_r$  are similarly normal to the plane of incidence, or

$$\mathbf{n} \cdot \mathbf{E}_t = \mathbf{n} \cdot \mathbf{E}_r = 0. \quad (3.36)$$

We have thus evaluated as zero, the first term in the right-hand side of each of equations (3.32), (3.33), and (3.34). The second terms may be evaluated directly from Figure 3.2 as

$$\mathbf{n} \cdot \mathbf{k}_i = k_i \cos(\pi - \theta_i) = -k_i \cos \theta_i, \quad (3.37)$$

$$\mathbf{n} \cdot \mathbf{k}_r = k_r \cos \theta_r, \quad (3.38)$$

and

$$\mathbf{n} \cdot \mathbf{k}_t = k_t \cos(\pi - \theta_t) = -k_t \cos \theta_t. \quad (3.39)$$

These relations may be substituted in equations (3.32), (3.33), and (3.34), and in turn in equation (3.31) to yield

$$\cos \theta_i \mathbf{E}_i - \cos \theta_r \mathbf{E}_r = \frac{\mu_1 k_2}{\mu_2 k_1} \cos \theta_t \mathbf{E}_t, \quad (3.40)$$

in which we have set  $|\mathbf{k}_i| = |\mathbf{k}_r|$ . This is the first of two equations relating  $\mathbf{E}_i$ ,  $\mathbf{E}_r$ , and  $\mathbf{E}_t$ . To obtain the second equation, take the cross-product of  $\mathbf{n}$  with equation (3.29) to yield

$$\mathbf{n} \times (\mathbf{n} \times \mathbf{E}_i) + \mathbf{n} \times (\mathbf{n} \times \mathbf{E}_r) = \mathbf{n} \times (\mathbf{n} \times \mathbf{E}_t). \quad (3.41)$$

Expanding this equation via the expansion (3.11), i.e.,

$$(\mathbf{n} \cdot \mathbf{E}_i)\mathbf{n} - (\mathbf{n} \cdot \mathbf{n})\mathbf{E}_i + (\mathbf{n} \cdot \mathbf{E}_r)\mathbf{n} - (\mathbf{n} \cdot \mathbf{n})\mathbf{E}_r = (\mathbf{n} \cdot \mathbf{E}_t)\mathbf{n} - (\mathbf{n} \cdot \mathbf{n})\mathbf{E}_t, \quad (3.42)$$

and using the equalities (3.35) and (3.36),

$$\mathbf{E}_i + \mathbf{E}_r = \mathbf{E}_t. \quad (3.43)$$

We may now solve equations (3.40) and (3.43) simultaneously for  $\mathbf{E}_r$  and  $\mathbf{E}_t$  in terms of the incident electric field intensity  $\mathbf{E}_i$ ; the procedure leads to

$$\mathbf{E}_r = \frac{\mu_2 k_1 \cos \theta_i - \mu_1 k_2 \cos \theta_t}{\mu_2 k_1 \cos \theta_r - \mu_1 k_2 \cos \theta_t} \mathbf{E}_i, \quad (3.44)$$

and

$$\mathbf{E}_t = \frac{\mu_2 k_1 (\cos \theta_r + \cos \theta_i)}{\mu_2 k_1 \cos \theta_r + \mu_1 k_2 \cos \theta_t} \mathbf{E}_i. \quad (3.45)$$

Equations (3.44) and (3.45) are the basic defining equations for  $\mathbf{E}_r$  and  $\mathbf{E}_t$ . Caution must be exercised in using them if  $\theta_t$  is complex as we shall discuss subsequently. However, they need to be cast in a form suited to application by eliminating all angles other than the specified angle  $\theta_i$ . To do this, compute from Snell's second law (3.28)

$$\cos^2 \theta_t = 1 - \sin^2 \theta_t = 1 - \left( \frac{k_1}{k_2} \right)^2 \sin^2 \theta_i, \quad (3.46)$$

and from Snell's first law (3.27)

$$\cos \theta_r = \cos \theta_i. \quad (3.47)$$

When the expressions (3.46) and (3.47) are substituted in equations (3.44) and (3.45) there results

$$\mathbf{E}_r = \frac{\mu_2 k_1 \cos \theta_i - \mu_1 (k_2^2 - k_1^2 \sin^2 \theta_i)^{1/2}}{\mu_2 k_1 \cos \theta_i + \mu_1 (k_2^2 - k_1^2 \sin^2 \theta_i)^{1/2}} \mathbf{E}_i, \quad (3.48)$$

and

$$\mathbf{E}_t = \frac{2\mu_2 k_1 \cos \theta_i}{\mu_2 k_1 \cos \theta_i + \mu_1 (k_2^2 - k_1^2 \sin^2 \theta_i)^{1/2}} \mathbf{E}_i. \quad (3.49)$$

The transmitted and reflected waves will, in general, not be of the same phase as the incident wave. For the important case of normal incidence, i.e.,  $\theta_i = 0$ , then equations (3.48) and (3.49) become

$$\mathbf{E}_r = \frac{\mu_2 k_1 - \mu_1 k_2}{\mu_2 k_1 + \mu_1 k_2} \mathbf{E}_i, \quad (3.50)$$

and

$$\mathbf{E}_t = \frac{2\mu_2 k_1}{\mu_2 k_1 + \mu_1 k_2} \mathbf{E}_i. \quad (3.51)$$

The ratio of the reflected to the incident electric fields is termed the amplitude reflection coefficient  $r_\perp$  for  $\mathbf{E}_i$  perpendicular to the plane of incidence. Thus from equation (3.48)

$$r_{\perp} \equiv \frac{E_r}{E_i} = \frac{\mu_2 k_1 \cos \theta_i - \mu_1 (k_2^2 - k_1^2 \sin^2 \theta_i)^{1/2}}{\mu_2 k_1 \cos \theta_i + \mu_1 (k_2^2 - k_1^2 \sin^2 \theta_i)^{1/2}}. \quad (3.52)$$

Substituting

$$u_1 = k_1 \cos \theta_i, \quad (3.53)$$

and

$$u_2 = (k_2^2 - k_1^2 \sin^2 \theta_i)^{1/2}, \quad (3.54)$$

then  $r_{\perp}$  may be written

$$r_{\perp} = \frac{\mu_2 u_1 - \mu_1 u_2}{\mu_2 u_1 + \mu_1 u_2}. \quad (3.55)$$

At an interface between medium  $m$  and medium  $n$ , the formula (3.55) becomes

$$r_{\perp} = \frac{\mu_n u_m - \mu_m u_n}{\mu_n u_m + \mu_m u_n}, \quad (3.56)$$

where the wave originates in medium  $m$  and is reflected from medium  $n$ . The symbol  $r_{\perp}$  may be replaced by  $r_{TE}$  to indicate that the reflection coefficient applies to waves transverse electric to  $z$ .

**E<sub>i</sub> in the Plane of Incidence.**—The magnetic vector must be normal to the plane of incidence for this case so that

$$\mathbf{n} \cdot \mathbf{H}_i = \mathbf{n} \cdot \mathbf{H}_r = \mathbf{n} \cdot \mathbf{H}_t = 0, \quad (3.57)$$

where we have assumed that the arguments of the exponents in the wave functions must be identical at the interface. This observation will be used in the subsequent development which proceeds as follows. Taking the cross-product of the identity (3.3) with  $\mathbf{k}_i$ ,

$$\omega \mu_1 \mathbf{k}_i \times \mathbf{H}_i = \mathbf{k}_i \times (\mathbf{k}_i \times \mathbf{E}_i) = (\mathbf{k}_i \cdot \mathbf{E}_i) \mathbf{k}_i - (\mathbf{k}_i \cdot \mathbf{k}_i) \mathbf{E}_i. \quad (3.58)$$

Clearly, since  $\mathbf{E}_i$ ,  $\mathbf{H}_i$ , and  $\mathbf{k}_i$  are an orthogonal set,

$$\mathbf{k}_i \cdot \mathbf{E}_i = 0, \quad (3.59)$$

and equation (3.58) becomes

$$\mathbf{E}_i = - \frac{\omega \mu_1}{k_1} \mathbf{n}_i \times \mathbf{H}_i, \quad (3.60)$$

where  $\mathbf{n}_i$  is a unit vector in the  $\mathbf{k}_i$  direction. Similarly

$$\mathbf{E}_r = - \frac{\omega \mu_1}{k_1} \mathbf{n}_r \times \mathbf{H}_r, \quad (3.61)$$

and

$$\mathbf{E}_t = - \frac{\omega \mu_2}{k_2} \mathbf{n}_t \times \mathbf{H}_t. \quad (3.62)$$

The boundary condition for tangential  $\mathbf{H}$  is,

$$\mathbf{n} \times (\mathbf{H}_i + \mathbf{H}_r) = \mathbf{n} \times \mathbf{H}_t. \quad (3.63)$$

The boundary condition for tangential  $\mathbf{E}$ , obtained by inserting the expressions (3.60), (3.61), and (3.62) in equation (3.29) is

$$\mathbf{n} \times \frac{\omega\mu_1}{k_1} (\mathbf{n}_i \times \mathbf{H}_i) + \frac{\omega\mu_1}{k_1} (\mathbf{n}_r \times \mathbf{H}_r) = \mathbf{n} \times \frac{\omega\mu_2}{k_2} (\mathbf{n}_t \times \mathbf{H}_t). \quad (3.64)$$

Equation (3.64) may be simplified via the expansions

$$\mathbf{n} \times (\mathbf{n}_i \times \mathbf{H}_i) = (\mathbf{n} \cdot \mathbf{H}_i)\mathbf{n}_i - (\mathbf{n} \cdot \mathbf{n}_i)\mathbf{H}_i = \cos \theta_i \mathbf{H}_i, \quad (3.65)$$

$$\mathbf{n} \times (\mathbf{n}_r \times \mathbf{H}_r) = (\mathbf{n} \cdot \mathbf{H}_r)\mathbf{n}_r - (\mathbf{n} \cdot \mathbf{n}_r)\mathbf{H}_r = -\cos \theta_r \mathbf{H}_r, \quad (3.66)$$

and

$$\mathbf{n} \times (\mathbf{n}_t \times \mathbf{H}_t) = (\mathbf{n} \cdot \mathbf{H}_t)\mathbf{n}_t - (\mathbf{n} \cdot \mathbf{n}_t)\mathbf{H}_t = \cos \theta_t \mathbf{H}_t. \quad (3.67)$$

Hence

$$\cos \theta_i \mathbf{H}_i - \cos \theta_r \mathbf{H}_r = \frac{\mu_2 k_1}{\mu_1 k_2} \cos \theta_t \mathbf{H}_t. \quad (3.68)$$

Taking the cross-product of equation (3.63) with  $\mathbf{n}$ ,

$$\mathbf{n} \times (\mathbf{n} \times \mathbf{H}_i) + \mathbf{n} \times (\mathbf{n} \times \mathbf{H}_r) = \mathbf{n} \times (\mathbf{n} \times \mathbf{H}_t), \quad (3.69)$$

or

$$(\mathbf{n} \cdot \mathbf{H}_i)\mathbf{n} - (\mathbf{n} \cdot \mathbf{n})\mathbf{H}_i + (\mathbf{n} \cdot \mathbf{H}_r)\mathbf{n} - (\mathbf{n} \cdot \mathbf{n})\mathbf{H}_r = (\mathbf{n} \cdot \mathbf{H}_t)\mathbf{n} - (\mathbf{n} \cdot \mathbf{n})\mathbf{H}_t. \quad (3.70)$$

In view of the orthogonality of  $\mathbf{n}$  and the magnetic field vectors according to the identities (3.57), equation (3.70) reduces to

$$\mathbf{H}_i + \mathbf{H}_r = \mathbf{H}_t. \quad (3.71)$$

Equations (3.68) and (3.71) may now be combined to yield

$$\mathbf{H}_r = \frac{\mu_1 k_2 \cos \theta_i - \mu_2 k_1 \cos \theta_t}{\mu_2 k_2 \cos \theta_r + \mu_1 k_1 \cos \theta_t} \mathbf{H}_i, \quad (3.72)$$

and

$$\mathbf{H}_t = \frac{(\cos \theta_i + \cos \theta_r)\mu_1 k_2}{\mu_2 k_1 \cos \theta_t + \mu_1 k_2 \cos \theta_r} \mathbf{H}_i. \quad (3.73)$$

We may eliminate the angles of reflection and refraction from these last two equations by using the definitions (3.46) and (3.47). The result is

$$\mathbf{H}_r = \frac{\mu_1 k_2^2 \cos \theta_i - \mu_2 k_1 (k_2^2 - k_1^2 \sin^2 \theta_i)^{1/2}}{\mu_1 k_2^2 \cos \theta_i + \mu_2 k_1 (k_2^2 - k_1^2 \sin^2 \theta_i)^{1/2}} \mathbf{H}_i, \quad (3.74)$$

and

$$\mathbf{H}_r = \frac{2 \cos \theta_i \mu_1 k_2^2}{\mu_2 k_1 (k_2^2 - k_1^2 \sin^2 \theta_i)^{1/2} + \mu_1 k_2^2 \cos \theta_i} \mathbf{H}_i. \quad (3.75)$$

By analysis of equation (3.74) we can deduce that the ratio  $H_r/H_i$  is positive for  $k_2 > k_1$ . Hence the reflection coefficient  $r_{\parallel}$ , for the electric vector parallel to the plane of incidence, can be written

$$r_{\parallel} = \frac{\mu_2 k_1 (k_2^2 - k_1^2 \sin^2 \theta_i)^{1/2} - \mu_1 k_2^2 \cos \theta_i}{\mu_2 k_1 (k_2^2 - k_1^2 \sin^2 \theta_i)^{1/2} + \mu_1 k_2^2 \cos \theta_i}, \quad (3.76)$$

or

$$r_{\parallel} = \frac{\mu_2 u_2 k_1^2 - \mu_1 u_1 k_2^2}{\mu_2 u_2 k_1^2 + \mu_1 u_1 k_2^2}, \quad (3.77)$$

and in general

$$r_{\parallel} = \frac{\mu_n u_n k_m^2 - \mu_m u_m k_n^2}{\mu_n u_n k_m^2 + \mu_m u_m k_n^2}, \quad (3.78)$$

where the wave originates in the medium  $m$  and is reflected from medium  $n$ . The symbol  $r_{\parallel}$  may be replaced by  $r_{TM}$  to indicate that the reflection coefficient is for waves transverse magnetic to  $z$ .

**Normal Incidence.**—When incidence is normal, i.e.,  $\theta_i = 0$ , then the expressions (3.52) and (3.76) reduce to

$$r = \frac{\mu_2 k_1 - \mu_1 k_2}{\mu_2 k_1 + \mu_1 k_2}, \quad (3.79)$$

or

$$r = \frac{\mu_n k_m - \mu_m k_n}{\mu_n k_m + \mu_m k_n} \quad (3.80)$$

for the general interface between medium  $m$  and medium  $n$ . The  $r_{\perp}$  and  $r_{\parallel}$  reflection coefficients are then equal.

**Reflection and Wave Impedance.**—Sometimes it is convenient to write the reflection coefficient in terms of the plane wave impedance  $Z$  which is defined as the ratio of the amplitudes of the orthogonal electric and magnetic field pairs,

$$Z = \frac{\omega \mu}{k} = \frac{E_x}{H_y} = -\frac{E_y}{H_x} \quad (3.81)$$

for waves traveling in the positive  $z$  direction. For waves traveling in the negative  $z$  direction, the signs in the definitions (3.81) are reversed.

The reflection coefficients then can be written

$$r_{\perp} = \frac{Z_n \cos \theta_i - Z_m \left[ 1 - \left( \frac{k_m}{k_n} \right)^2 \sin^2 \theta_i \right]^{1/2}}{Z_n \cos \theta_i + Z_m \left[ 1 - \left( \frac{k_m}{k_n} \right)^2 \sin^2 \theta_i \right]^{1/2}}, \quad (3.82)$$

and

$$r_{\parallel} = \frac{Z_n \left[ 1 - \left( \frac{k_m}{k_n} \right)^2 \sin^2 \theta_i \right]^{1/2} - Z_m \cos \theta_i}{Z_n \left[ 1 - \left( \frac{k_m}{k_n} \right)^2 \sin^2 \theta_i \right]^{1/2} + Z_m \cos \theta_i}. \quad (3.83)$$

For normal incidence these expressions are identical and equal to

$$r_{mn} = \frac{Z_n - Z_m}{Z_n + Z_m}. \quad (3.84)$$

The reflection coefficients discussed in this section are the amplitude reflection coefficients, as distinguished from the power reflection coefficients

$$R_{mn} \equiv |r_{mn}|^2. \quad (3.85)$$

**Total Reflection for Dielectric Media.**—For a perfect dielectric, the conductivity is zero and the permeability is essentially that of free space, i.e.,  $\mu_i = \mu_0$ .

Snell's law of refraction, equation (3.28), then reduces to

$$\frac{\sin \theta_i}{\sin \theta_t} = \frac{k_2}{k_1} = \left( \frac{\epsilon_2}{\epsilon_1} \right)^{1/2} = n_{12}, \quad (3.86)$$

where  $n_{12}$  is the relative index of refraction. If  $\epsilon_2 > \epsilon_1$  then  $n_{12} > 1$ . Under this circumstance, for any angle of incidence  $\theta_i$ , there is a real angle of transmission  $\theta_t$ . On the other hand, if  $\epsilon_2 < \epsilon_1$ , then  $\theta_t$  is real only when  $n_{12} \sin \theta_t \leq 1$ . Total reflection occurs when  $n_{12} \sin \theta_t > 1$ .

**The Brewster Angle for Perfect Dielectrics.**—From equation (3.52), the reflection coefficient for perfect dielectrics can be written

$$\begin{aligned} r_{\perp} &= \frac{(\epsilon_1)^{1/2} \cos \theta_i - (\epsilon_2)^{1/2} \cos \theta_t}{(\epsilon_1)^{1/2} \cos \theta_i + (\epsilon_2)^{1/2} \cos \theta_t} \\ &= \frac{\cos \theta_i - \left( \frac{\epsilon_2}{\epsilon_1} \right)^{1/2} \cos \theta_t}{\cos \theta_i + \left( \frac{\epsilon_2}{\epsilon_1} \right)^{1/2} \cos \theta_t}, \end{aligned} \quad (3.87)$$

by Snell's first law. Then from the relation (3.28)

$$\left( \frac{\epsilon_2}{\epsilon_1} \right)^{1/2} = \frac{\sin \theta_i}{\sin \theta_t}. \quad (3.88)$$

With the expression (3.88), equation (3.87) becomes

$$r_{\perp} = \frac{\cos \theta_i \sin \theta_t - \sin \theta_i \cos \theta_t}{\cos \theta_i \sin \theta_t + \sin \theta_i \cos \theta_t} = \frac{\sin(\theta_t - \theta_i)}{\sin(\theta_t + \theta_i)}. \quad (3.89)$$

Similarly, from equation (3.76) for a perfect dielectric

$$r_{\parallel} = \frac{\tan(\theta_i - \theta_t)}{\tan(\theta_i + \theta_t)},$$

and

$$R_{\parallel} = \frac{\tan^2(\theta_i - \theta_t)}{\tan^2(\theta_i + \theta_t)}$$

If  $(\theta_i + \theta_t) \rightarrow \pi/2$ , then  $\tan(\theta_i + \theta_t) \rightarrow \infty$ , and  $r_{\parallel} \rightarrow 0$ . The reflected and refracted waves are then normal to one another, and

$$\sin \theta_t = \sin(\pi/2 - \theta_i) = \cos \theta_i, \quad (3.90)$$

so that the expression (3.88) becomes

$$\tan \theta_i = \left( \frac{\epsilon_2}{\epsilon_1} \right)^{1/2} = n_{12}. \quad (3.91)$$

The angle that this equation satisfies is known as the Brewster angle.

For reflection from a conductive surface, there will be a minimum in  $R_{\parallel}$ , analogous to the Brewster angle, for some particular angle of incidence. No such minimum occurs in  $R_{\perp}$  (Stratton, 1941, p. 508). Figure 3.3 illustrates these features.

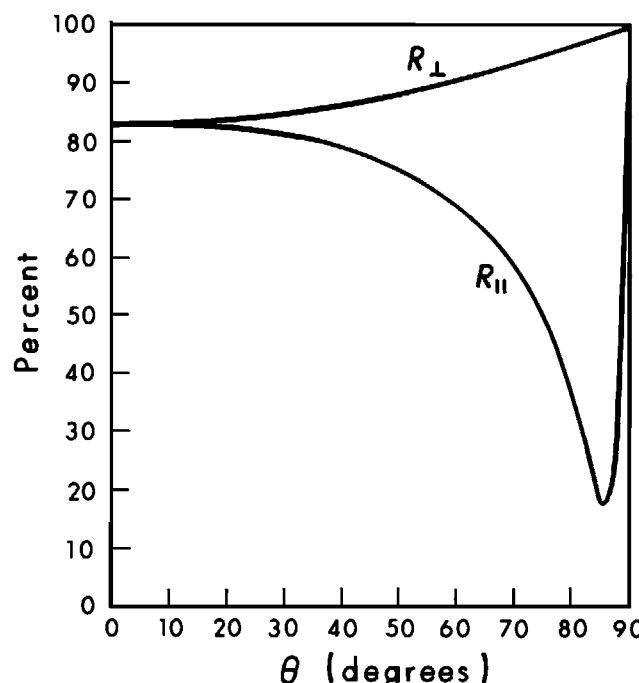


FIG. 3.3. The power reflection coefficients  $R_{\parallel}$  and  $R_{\perp}$  versus angle of incidence for plane waves at an air-sea interface. The conductivity and dielectric permittivity of sea water are taken to be 3 S/m, and  $\epsilon = \epsilon_0$ , respectively. The frequency is  $6 \times 10^5$  Hz (after Stratton, 1941).

### The plane-wave impedance of an $n$ -layered isotropic earth

**Normal Incidence.**—We wish to consider normal incidence of a uniform, homogeneous, plane wave upon a  $n$ -layered isotropic model of the earth. The plane wave propagates in the positive  $z$ , or downward, direction. The earth model is illustrated in Figure 3.4.

In any layer we may write the electric and magnetic fields in terms of an outgoing wave and a reflected wave. For normal incidence of a uniform plane wave upon a plane-layered nonpermeable isotropic earth, the fields in the  $i^{\text{th}}$  layer are

$$E_{yi} = {}^+E_i e^{-ik_i(z-z_i)} + {}^-E_i e^{ik_i(z-z_i)}, \quad (3.92)$$

and

$$H_{xi} = -\frac{k_i}{\omega\mu_0} [{}^+E_i e^{-ik_i(z-z_i)} - {}^-E_i e^{ik_i(z-z_i)}], \quad (3.93)$$

where

- $k_i$  is the complex wave number in the  $i^{\text{th}}$  layer,
- $\mu_0$  is the permeability of free space,
- $\omega$  is the angular frequency,
- $z_i$  is the vertical distance to the bottom of the  $i^{\text{th}}$  layer,
- $z$  is any vertical distance within a layer at which the field is measured,
- ${}^+E_i$  is the amplitude of the positive traveling electric wave in the  $i^{\text{th}}$  layer,

and

- ${}^-E_i$  is the amplitude of the negative traveling electric wave in the  $i^{\text{th}}$  layer.

Selection of  $E_y$  and  $H_x$  implies that the electric vector is normal to the plane of incidence.

Over the plane  $z = z_i$

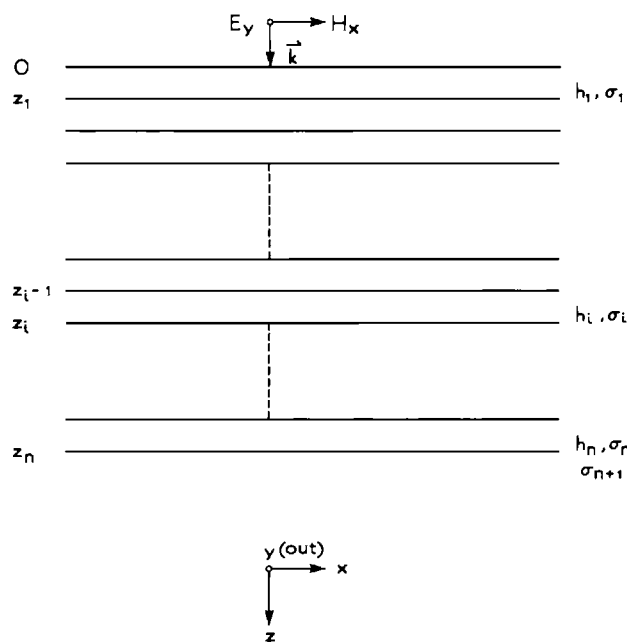


FIG. 3.4. A plane-layered earth upon which is normally incident a plane electromagnetic wave.  $E_y$ ,  $H_x$ , and  $\vec{k}$  are a right-handed orthogonal set.  $\sigma_i$  and  $h_i$  are the conductivity and thickness, respectively, of the  $i^{\text{th}}$  layer;  $z_i$  is the depth to the bottom of the  $i^{\text{th}}$  layer.

$$E_{yi} = {}^+E_i + {}^-E_i, \quad (3.94)$$

and

$$H_{xi} = \frac{1}{Z_i} ({}^-E_i - {}^+E_i), \quad (3.95)$$

in which

$$Z_i = \frac{\omega\mu_0}{k_i} \quad (3.96)$$

is the intrinsic impedance of the  $i^{\text{th}}$  layer.

Equations (3.94) and (3.95) yield

$${}^+E_i = \frac{1}{2} (E_{yi} - Z_i H_{xi}) \quad (3.97)$$

and

$${}^-E_i = \frac{1}{2} (E_{yi} + Z_i H_{xi}). \quad (3.98)$$

At  $z = z_{i-1}$ , continuity of tangential electric and magnetic fields demands that

$$H_{xi} = H_{x(i-1)}, \quad (3.99)$$

and

$$E_{yi} = E_{y(i-1)}. \quad (3.100)$$

Therefore

$$E_{y(i-1)} = {}^+E_i e^{-ik_i(z_{i-1}-z_i)} + {}^-E_i e^{ik_i(z_{i-1}-z_i)}, \quad (3.101)$$

and

$$H_{x(i-1)} = -\frac{1}{Z_i} [{}^+E_i e^{-ik_i(z_{i-1}-z_i)} - {}^-E_i e^{ik_i(z_{i-1}-z_i)}]. \quad (3.102)$$

Now if we let

$$z_i - z_{i-1} = h_i, \quad (3.103)$$

and substitute the expressions (3.97) and (3.98) in equations (3.101) and (3.102),

$$E_{y(i-1)} = E_{yi} \cosh(ik_i h_i) - Z_i H_{xi} \sinh(ik_i h_i), \quad (3.104)$$

and

$$H_{x(i-1)} = H_{xi} \cosh(ik_i h_i) - \frac{1}{Z_i} E_{yi} \sinh(ik_i h_i), \quad (3.105)$$

where use has been made of the identities

$$\cosh x = \frac{e^x + e^{-x}}{2}, \quad (3.106)$$

and

$$\sinh x = \frac{e^x - e^{-x}}{2}. \quad (3.107)$$

Equations (3.104) and (3.105) can be written in matrix form as

$$\begin{bmatrix} E_{y(i-1)} \\ H_{x(i-1)} \end{bmatrix} = \begin{bmatrix} \cosh(ik_i h_i) & -Z_i \sinh(ik_i h_i) \\ -\frac{1}{Z_i} \sinh(ik_i h_i) & \cosh(ik_i h_i) \end{bmatrix} \begin{bmatrix} E_{yi} \\ H_{xi} \end{bmatrix}, \quad (3.108)$$

or

$$\begin{bmatrix} E_{y(i-1)} \\ H_{x(i-1)} \end{bmatrix} = \mathbf{T}_i \begin{bmatrix} E_{yi} \\ H_{xi} \end{bmatrix}. \quad (3.109)$$

The matrix  $\mathbf{T}_i$  is referred to as the transfer matrix of the  $i^{\text{th}}$  layer. For  $n$  layers we can find a succession of  $\mathbf{T}_i$  from  $\mathbf{T}_1$  through  $\mathbf{T}_n$ , each transfer matrix permitting us to write the fields in one layer in terms of the fields in the next layer. Thus, we can readily find the matrix relationship between the fields in the  $(i-1)^{\text{th}}$  layer and those in the infinite medium terminating the  $n^{\text{th}}$  layer.

$$\begin{bmatrix} E_{y(i-1)} \\ H_{x(i-1)} \end{bmatrix} = \prod_{i=1}^n \mathbf{T}_i \begin{bmatrix} E_{y(n+1)} \\ H_{x(n+1)} \end{bmatrix}. \quad (3.110)$$

The product  $\prod \mathbf{T}_i$  of  $n$  matrices is itself a matrix  $\mathbf{S}$  so that equation (3.110) can be written

$$\begin{bmatrix} E_{y(i-1)} \\ H_{x(i-1)} \end{bmatrix} = \mathbf{S} \begin{bmatrix} E_{y(n+1)} \\ H_{x(n+1)} \end{bmatrix}, \quad (3.111)$$

in which

$$\mathbf{S} = \begin{bmatrix} \alpha_{11} & \alpha_{12} \\ \alpha_{21} & \alpha_{22} \end{bmatrix}. \quad (3.112)$$

Then the impedance  $\hat{Z}_{i-1}$  looking into the  $n$ -layered medium, from the surface of the  $i^{\text{th}}$  layer is

$$\hat{Z}_{i-1} = -\frac{E_{y(i-1)}}{H_{x(i-1)}} = -\frac{\alpha_{11}E_{y(n+1)} + \alpha_{12}H_{x(n+1)}}{\alpha_{21}E_{y(n+1)} + \alpha_{22}H_{x(n+1)}} \quad (3.113)$$

$$= \frac{\alpha_{11}Z_{n+1} - \alpha_{12}}{\alpha_{22} - \alpha_{21}Z_{n+1}}, \quad (3.114)$$

where the substitution  $Z_{n+1} = -E_{y(n+1)}/H_{x(n+1)}$  has been made.

For an earth model consisting of one layer overlying an infinite half-space (this model is usually referred to as a two-layered earth) the impedance can be found by making the substitutions for  $\alpha_{ij}$  from equation (3.108), i.e.,

$$\alpha_{11} = \cosh(ik_1 h_1), \quad (3.115)$$

$$\alpha_{12} = -Z_1 \sinh(ik_1 h_1), \quad (3.116)$$

$$\alpha_{21} = -\frac{1}{Z_1} \sinh(ik_1 h_1), \quad (3.117)$$

and

$$\alpha_{22} = \cosh(ik_1 h_1). \quad (3.118)$$

Thus from equation (3.114) the surface impedance

$$\hat{Z}_t = -\frac{E_{y1}}{H_{x1}}, \quad (3.119)$$

which is defined in terms of the electric and magnetic fields measured at the surface of the earth, becomes

$$\hat{Z}_1 = Z_1 \frac{Z_2 + Z_1 \tanh(ik_1 h_1)}{Z_1 + Z_2 \tanh(ik_1 h_1)}. \quad (3.120)$$

The expression (3.120) is the impedance at the surface of the two-layered earth. Here  $Z_1$  and  $Z_2$  are the intrinsic impedances of layers 1 and 2, defined by (3.96).

For a homogeneous earth, set  $h_1 = \infty$  in the expression (3.120). Then  $\tanh(ik_1 h_1) = 1$ , and the surface impedance  $\hat{Z}_1$  becomes  $Z_1$ , the impedance of the half-space.

For an  $n$ -layered earth model, begin with the impedance  $\hat{Z}_n$  at the top of the first layer above the basal half-space. By analogy with equation (3.120),

$$\hat{Z}_n = Z_n \frac{\hat{Z}_{n+1} + Z_n \tanh(ik_n h_n)}{Z_n + \hat{Z}_{n+1} \tanh(ik_n h_n)}. \quad (3.121)$$

Once this impedance is computed it may be used as the terminating impedance of an equivalent homogeneous half-space. Then the impedance at the top of the  $(n-1)^{\text{th}}$  layer is given by

$$\hat{Z}_{n-1} = Z_{n-1} \frac{\hat{Z}_n + Z_{n-1} \tanh(ik_{n-1} h_{n-1})}{Z_{n-1} + \hat{Z}_n \tanh(ik_{n-1} h_{n-1})}, \quad (3.122)$$

and so on up to the surface where

$$\hat{Z}_1 = Z_1 \frac{\hat{Z}_2 + Z_1 \tanh(ik_1 h_1)}{Z_1 + \hat{Z}_2 \tanh(ik_1 h_1)}. \quad (3.123)$$

We have used the notation  $\hat{Z}_i$  to denote the impedance at the top of the  $i^{\text{th}}$  layer and the notation  $Z_i$  to denote the characteristic impedance of the  $i^{\text{th}}$  layer.

For normal incidence of a plane wave, the reflection coefficient for free space overlying a homogeneous earth is, from the definition (3.84)

$$r_{01} = \frac{Z_1 - Z_0}{Z_1 + Z_0}. \quad (3.124)$$

If the impedance looking into the interface is  $\hat{Z}_1$ , rather than  $Z_1$ , then the reflection coefficient will be

$$r_{0a} = \frac{\hat{Z}_1 - Z_0}{\hat{Z}_1 + Z_0}, \quad (3.125)$$

in which  $r_{0a}$  is the reflection coefficient for an equivalent, or apparent, half-space.

**Oblique Incidence.**—The previous development may be generalized to accommodate an arbitrary angle of incidence (Wait, 1953c). The earth model is illustrated in Figure 3.5; a uniform plane wave is incident at an angle  $\theta_i$  on a stratified earth composed of  $n$  layers overlying a basal half-space. The electric vector may be normal to the plane of incidence, as illustrated in Figure 3.5, or it may be in the plane of incidence. The two pertinent reflection coefficients for a homogeneous earth, from the expressions (3.82) and (3.83), are

$$r_{\perp} = r_{TE} = \frac{Z_1 \cos \theta_i - Z_0 \left[ 1 - \left( \frac{k_0}{k_1} \right)^2 \sin^2 \theta_i \right]^{1/2}}{Z_1 \cos \theta_i + Z_0 \left[ 1 - \left( \frac{k_0}{k_1} \right)^2 \sin^2 \theta_i \right]^{1/2}} \quad (3.126)$$

for  $\mathbf{E}$  normal to the plane of incidence, and

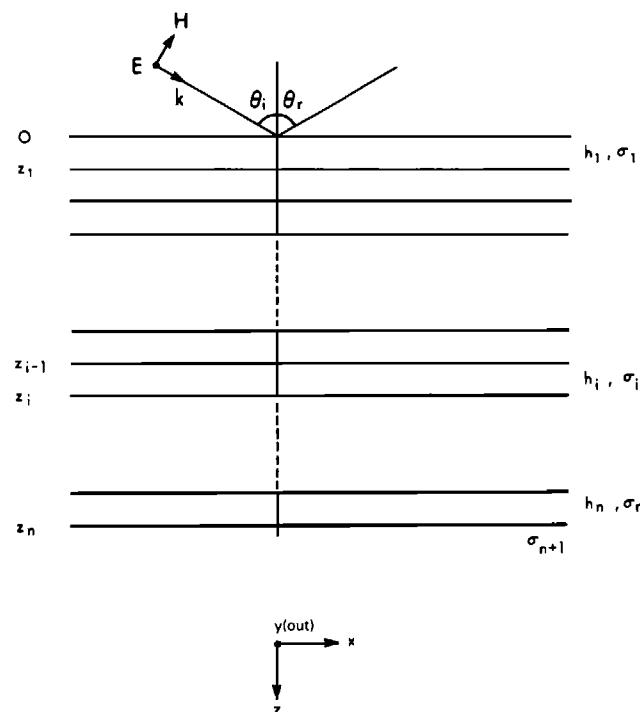


FIG. 3.5. A plane-layered earth upon which is obliquely incident a plane electromagnetic wave.  $\mathbf{E}$ ,  $\mathbf{H}$ , and  $\mathbf{k}$  are a right-handed orthogonal set. The layer parameters are as for Figure 3.3.

$$r_{\parallel} = r_{TM} = \frac{Z_1 \left[ 1 - \left( \frac{k_0}{k_1} \right)^2 \sin^2 \theta_i \right]^{1/2} - Z_0 \cos \theta_i}{Z_1 \left[ 1 - \left( \frac{k_0}{k_1} \right)^2 \sin^2 \theta_i \right]^{1/2} + Z_0 \cos \theta_i} \quad (3.127)$$

for  $\mathbf{E}$  in the plane of incidence.

Substituting the expressions (3.53) and (3.54), equations (3.126) and (3.127) can be written

$$r_{TE} = \frac{u_0 - u_1}{u_0 + u_1}, \quad (3.128)$$

and

$$r_{TM} = \frac{u_1 k_0^2 - u_0 k_1^2}{u_1 k_0^2 + u_0 k_1^2}, \quad (3.129)$$

in which we have set the permeability of the earth to that of free space.

Let us now find the impedances of the layered earth for the TE and TM modes, treating the former first. Since reflection takes place solely in the  $z$  direction, the total electric field in the free space above the layered earth can be written

$$E_{y0} = k_0 [{}^+ E_{y0} e^{-iu_0 z} + {}^- E_{y0} e^{iu_0 z}] e^{-i\lambda x}. \quad (3.130)$$

For equation (3.130) to be a solution of the Helmholtz equation

$$[\nabla^2 + k_0^2] E_{y0} = 0, \quad (3.131)$$

requires that

$$-u_0^2 - \lambda^2 + k_0^2 = 0, \quad (3.132)$$

as found by direct substitution of the solution (3.130) in equation (3.131). The incident electric field may also be written

$${}^i E_{y0} = E_{y0} e^{-ik_0 \cdot \mathbf{r}}. \quad (3.133)$$

The term  $\mathbf{k}_0 \cdot \mathbf{r}$  can be expanded as

$$\mathbf{k}_0 \cdot \mathbf{r} = k_0 x \sin \theta_i + k_0 z \cos \theta_i. \quad (3.134)$$

Hence the solution (3.133) becomes

$${}^i E_{y0} = E_{y0} e^{-ik_0(x \sin \theta_i + z \cos \theta_i)}. \quad (3.135)$$

Equating the first term in equation (3.130) with equation (3.135) results in

$$u_0 = k_0 \cos \theta_i, \quad (3.136)$$

and

$$\lambda = k_0 \sin \theta_i. \quad (3.137)$$

As far as reflections are concerned we may ignore  $e^{-i\lambda x}$  in (3.130) since  $e^{-i\lambda x}$  can only represent propagation parallel to interfaces. Hence, we may at once write down the impedance of an  $n$  layered earth to an obliquely incident wave as

$$\hat{Z}_1 = Z_1 \frac{\hat{Z}_2 + Z_1 \tanh(iu_1 h_1)}{Z_1 + \hat{Z}_2 \tanh(iu_1 h_1)}. \quad (3.138)$$

However, the  $Z_i$  are now defined as  $Z_i = \omega \mu_i / u_i$ .

For the case of  $\mathbf{E}$  in the plane of incidence, the starting point is the solution to the Helmholtz equation for magnetic field

$$\mathbf{H}_{y0} = [{}^+H_{y0}e^{-iu_0 z} + {}^-H_{y0}e^{iu_0 z}]e^{-i\lambda x}. \quad (3.139)$$

In a development parallel to the previous case the impedance becomes

$$\hat{Z}_1 = -Z_1 \frac{\hat{Z}_2 + Z_1 \tanh(iu_1 h_1)}{Z_1 + \hat{Z}_2 \tanh(iu_1 h_1)}, \quad (3.140)$$

which is entirely consistent with the impedances

$$Z = \frac{E_x}{H_y} = -\frac{E_y}{H_x}$$

given in equation (3.81). Again, the  $Z_i$  are defined as  $Z_i = \omega \mu_i / u_i$ .

The quantity  $u_1$  is an equivalent wave number defined by

$$u_1 = k_1 \cos \theta_1. \quad (3.141)$$

From Snell's law of refraction, equation (3.28),

$$k_0 \sin \theta_0 = k_1 \sin \theta_1. \quad (3.142)$$

If displacement currents are neglected in the air,  $k_0 \sim 0$ , and  $\cos \theta_1 = (1 - k_0^2/k_1^2 \sin^2 \theta_1)^{1/2} = 1$ , so that  $u_1 = k_1$ . This quasi-static approximation, so called because the Helmholtz equation in air reduces to Laplace's equation, is valid in most geophysical applications when frequencies less than  $10^5$  Hz are employed. Under this approximation, homogeneous, uniform plane waves always travel vertically in the earth ( $\cos \theta_1 \sim 0$ ) regardless of the real angle of incidence. Planes of constant phase then correspond with planes of constant amplitude so that inhomogeneous uniform plane waves described in Stratton (1941, p. 500–504) are not of interest. While Ward (1967) included them in his earlier discourse, we have purposely omitted them here since we are primarily concerned with the quasi-static approximation. The measured impedance at the earth's surface is just that of a normally incident plane wave, making the MT method possible.

In practice, however, the earth is not horizontally homogeneous, in which case the electric field in one direction reflects variations parallel to, as well as perpendicular to, its direction. Then the impedance must be defined as a tensor

$$\mathbf{Z} = \begin{bmatrix} Z_{xx} & Z_{xy} \\ Z_{yx} & Z_{yy} \end{bmatrix}, \quad (3.143)$$

so that

$$\mathbf{E} = \mathbf{Z} \cdot \mathbf{H}. \quad (3.144)$$

### Magnetotelluric formulation for a 1-D earth

Orthogonal horizontal electric and magnetic field pairs  $[E_x, H_y]$  or  $[E_y, H_x]$  are measured at the surface of the earth in the MT method. These quantities are simply related to the electromagnetic impedance  $Z$ , of a plane wave, as in equation (3.81) by

$$Z = \frac{\omega\mu_0}{k} = \frac{E_x}{H_y} = -\frac{E_y}{H_x}. \quad (3.145)$$

When displacement currents are neglected, which is justifiable for earth materials at the frequencies employed in MT surveys, then the impedance (3.145) is rewritten as

$$Z = \frac{\omega\mu_0}{\sqrt{-i\mu_0\sigma\omega}} = \sqrt{i} \sqrt{\omega\mu_0\rho} = \sqrt{\omega\mu_0\rho} e^{i\pi/4} \quad (3.146)$$

The impedance phase is  $45^\circ$  with  $E_x$  leading  $H_y$  by this amount. The resistivity of the half-space is then given as

$$\rho = \frac{1}{\omega\mu_0} |Z|^2 = 0.2T \left| \frac{E_x}{B_y} \right|^2 \quad (3.147)$$

where  $E_x$  is in mV/km,  $B_y$  is in nT, and the period  $T$  is in seconds. (Historically,  $H$  has been used in this expression, but for SI units,  $B$  is correct.)

When the earth is layered, as in Figures 3.4 and 3.5, the plane wave impedance is given

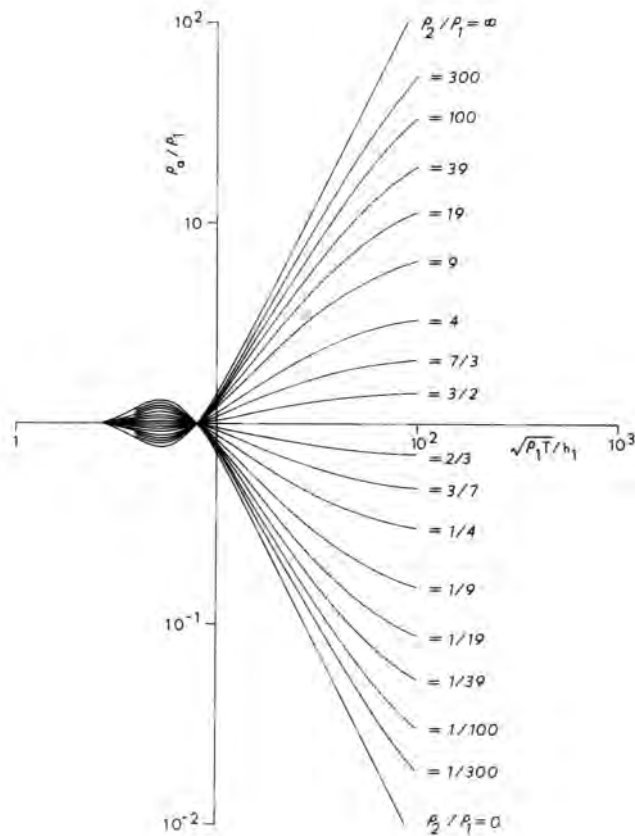


FIG. 3.6. Two-layer curves for the MT apparent resistivity  $\rho_a$  plotted versus  $\sqrt{T\rho_1}/h_1$  where  $\rho_1$  and  $h_1$  are the resistivity and thickness, respectively, of first layer.  $T$  is period in seconds (after Patella, 1976).

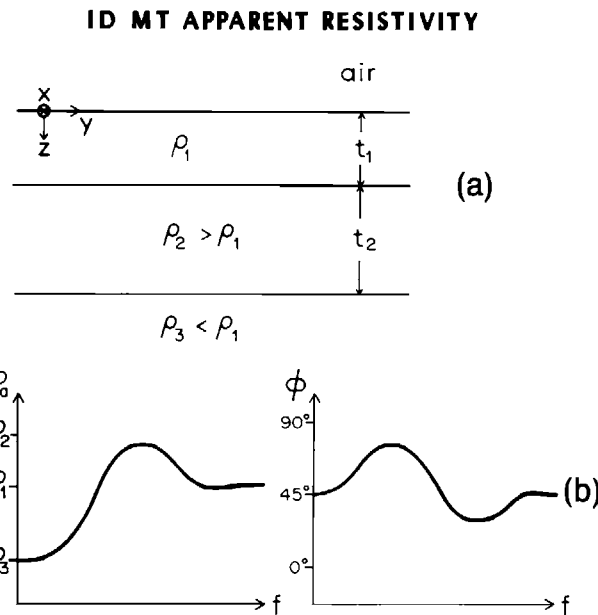


FIG. 3.7. Typical model and schematic representations of apparent resistivity and impedance phase for a 1-D earth.

by the recursive formulas 3.121 through 3.123. From equation 3.123 we write the impedance phase  $\phi$  and the apparent resistivity  $\rho_a$  as

$$\hat{Z}_1 = |\hat{Z}_1| e^{i\phi} \quad (3.148)$$

$$\rho_a = \frac{1}{\omega \mu_0} |\hat{Z}_1|^2. \quad (3.149)$$

The apparent resistivity  $\rho_a$  is plotted versus  $(\rho_1 T)^{1/2}/h_1$  in Figure 3.6 for a range of two-layered earths (after Patella, 1976). Boehl et al. (1977) showed that one can predict the phase from the apparent resistivity approximately by

$$\phi \sim 45^\circ \pm 45^\circ \frac{\partial \ln \rho_a}{\partial \ln \omega}. \quad (3.150)$$

Equation (3.150) is based on the assumption that the resistivity and impedance phase are related through a Hilbert transform for a 1-D earth (Kunetz, 1972). Figure 3.7 schematically illustrates this relationship for a three-layered earth (after Ward and Wannamaker, 1983).

## Section 4

### Finite Sources over a Layered Half-Space

The solution for the EM field of a finite source such as a magnetic dipole in the presence of a homogeneous or layered earth can be represented as a superposition of plane-wave solutions with varying, complex angles of incidence. As in Section 3, the problem is simplified if the solution is developed in terms of TE and TM modes, where “transverse” again means normal to the  $z$  (vertical) direction.

Because changes in physical properties coincide with coordinate surfaces (planes of constant  $z$ ) we can solve the boundary-value problem by converting the partial differential equation to an ordinary differential equation in  $z$ . This conversion takes the form of a Hankel or 2-D Fourier transform since the coordinate surfaces are infinite in extent in the  $x$  and  $y$  directions. The solution in Fourier transform space can be derived using the plane-wave impedance formulas for a layered earth developed in Section 3. Then the final solution, obtained by inverse Fourier or Hankel transformation, is a superposition of plane waves with continuously varying, complex angles of incidence.

The general solution of a boundary-value problem is the sum of the particular solution of the inhomogeneous differential equation and the complementary solution of the homogeneous equation. In Section 4 we first derive the complementary solution using TM and TE potentials. The complementary solution, which applies to any source, is given in terms of undetermined coefficients in  $k_x$ ,  $k_y$  space. Then we find and add the particular solutions for a vertical magnetic dipole, a large horizontal loop, a horizontal magnetic dipole, a horizontal electric dipole, a long grounded wire carrying current, and a line source of current. The coefficients in the complementary solution are determined using reflection coefficients. Solutions are developed in the cartesian coordinate system, first in the frequency domain, and then in the time domain. We emphasize formulations for computation by numerical integration, derive many analytical solutions for a homogeneous earth, and conclude Section 4 with a discussion of numerical techniques. For additional insight, we recommend the book by Kaufman and Keller (1983), which includes many useful asymptotic approximations. Analytic expressions for a homogeneous earth are tabulated in Kraichman (1970). Finally, Wait (1982) is an important reference for additional theory, especially for the case of anisotropic conductivity, which we do not consider.

#### Complementary solution

As Harrington (1961) points out, in a source-free region we do not need to consider the vector potentials  $\mathbf{A}$  as due to electric sources and  $\mathbf{F}$  as due to magnetic sources. Because of the relations

$$\mathbf{H} = \nabla \times \mathbf{A}, \quad (4.1)$$

and

$$\mathbf{E} = -\nabla \times \mathbf{F}, \quad (4.2)$$

we can define TM and TE vector potentials as follows:

$$\mathbf{A} = A \mathbf{u}_z \quad (\text{TM}), \quad (4.3)$$

and

$$\mathbf{F} = F \mathbf{u}_z \quad (\text{TE}). \quad (4.4)$$

Thus, from equations (1.114) and (1.115), the scalar potentials  $A$  and  $F$  satisfy the following equations:

$$\nabla^2 A + k^2 A = 0, \quad (4.5)$$

and

$$\nabla^2 F + k^2 F = 0. \quad (4.6)$$

To convert equations (4.5) and (4.6) to ordinary differential equations, transform them using the following double Fourier transform pair:

$$\tilde{F}(k_x, k_y, z) = \int_{-\infty}^{\infty} \int_{-\infty}^{\infty} F(x, y, z) e^{-i(k_x x + k_y y)} dx dy, \quad (4.7)$$

and

$$F(x, y, z) = \frac{1}{4\pi^2} \int_{-\infty}^{\infty} \int_{-\infty}^{\infty} \tilde{F}(k_x, k_y, z) e^{i(k_x x + k_y y)} dk_x dk_y. \quad (4.8)$$

Then

$$\frac{d^2 \tilde{A}}{dz^2} - u^2 \tilde{A} = 0, \quad (4.9)$$

and

$$\frac{d^2 \tilde{F}}{dz^2} - u^2 \tilde{F} = 0, \quad (4.10)$$

with

$$u^2 = k_x^2 + k_y^2 - k^2. \quad (4.11)$$

The solutions of equations (4.9) and (4.10), which are similar to the plane wave solutions of Section 3, are

$$\tilde{A}(k_x, k_y, z) = A^+(k_x, k_y) e^{-uz} + A^-(k_x, k_y) e^{uz}, \quad (4.12)$$

and

$$\tilde{F}(k_x, k_y, z) = F^+(k_x, k_y) e^{-uz} + F^-(k_x, k_y) e^{uz}, \quad (4.13)$$

where superscripts “+” and “-” refer to downward and upward decaying solutions, respectively.

For an  $N$ -layered earth, we set up solutions in the different regions as shown in Figure 4.1, where

$$u_n = (k_x^2 + k_y^2 - k_n^2)^{1/2}, \quad (4.14)$$

with  $k_n$  the wave number of the  $n$ th layer. Note that above the surface of the earth we can use only solutions that decay upward, and in the substratum (layer  $N$ ) we can use only solutions that decay downward. The solution in the  $n$ th layer is given in terms of the constants  $A_n^+$ ,  $A_n^-$ ,  $F_n^+$ , and  $F_n^-$ , which remain to be determined by incorporating the particular solution and applying boundary conditions.

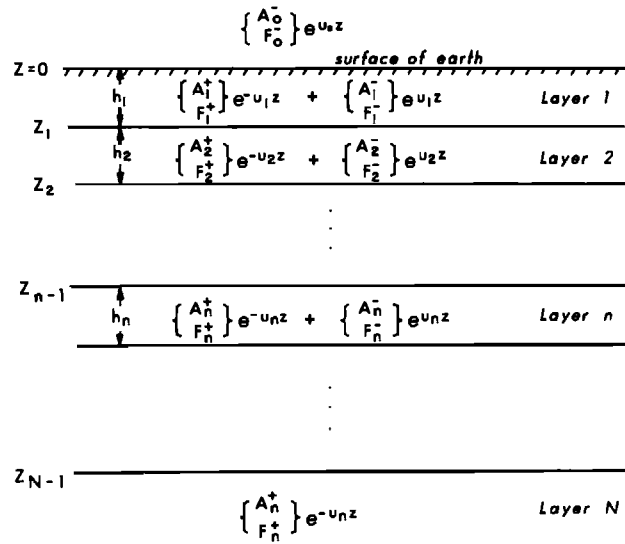


FIG. 4.1. Solutions for Fourier transformed TM and TE potentials ( $\tilde{A}$  and  $\tilde{F}$ , respectively) in an  $N$ -layered earth.

### General solution

In a layer containing the source we must add the particular solution of the inhomogeneous differential equations to the complementary solution. Consider a point source at  $z = -h$ , above the earth. If the source is decomposed into TM and TE modes (as we will do later for each source considered), we see from expression (2.8) for the Green's function that the particular solutions in the air can be written

$$A_p(k_x, k_y) e^{-u_0|z+h|} \quad (\text{TM}), \quad (4.15)$$

and

$$F_p(k_x, k_y) e^{-u_0|z+h|} \quad (\text{TE}), \quad (4.16)$$

which decay both above and below the source. Here  $A_p$  and  $F_p$  depend on the particular source.

In this chapter we only consider solutions at the surface of the earth. Other applications, such as finding the fields above the earth or evaluating the fields due to sources in the earth, follow easily using the same technique.

By analogy with the plane-wave solutions of Section 3 and of Wait (1962), considering  $A_p$  and  $F_p$  to be the amplitudes of the incident field, we can write the coefficients  $A_0^-$  and  $F_0^-$ , which are all we need to determine, as

$$A_0^- = r_{\text{TM}} A_p e^{-u_0 h} \quad (4.17)$$

and

$$F_0^- = r_{\text{TE}} F_p e^{-u_0 h}, \quad (4.18)$$

where  $r_{\text{TM}}$  and  $r_{\text{TE}}$  are reflection coefficients, given by

$$r_{\text{TE}} = \frac{Y_0 - \hat{Y}_1}{Y_0 + \hat{Y}_1} \quad (4.19)$$

and

$$r_{\text{TM}} = \frac{Z_0 - \hat{Z}_1}{Z_0 + \hat{Z}_1}, \quad (4.20)$$

with

$$Y_0 = \frac{u_0}{\hat{z}_0} \text{ (intrinsic admittance of free space)}, \quad (4.21)$$

$$Z_0 = \frac{u_0}{\hat{y}_0} \text{ (intrinsic impedance of free space)}, \quad (4.22)$$

where

$$\hat{z}_0 = i\omega\mu_0,$$

and

$$\hat{y}_0 = i\omega\epsilon_0,$$

and with

$$\hat{Y}_1 = \frac{H_y^{\text{TE}}}{E_x^{\text{TE}}} = -\frac{H_x^{\text{TE}}}{E_y^{\text{TE}}} \text{ (surface admittance at } z=0), \quad (4.23)$$

and

$$\hat{Z}_1 = \frac{E_x^{\text{TM}}}{H_y^{\text{TM}}} = -\frac{E_y^{\text{TM}}}{H_x^{\text{TM}}} \text{ (surface impedance at } z=0). \quad (4.24)$$

For  $N$  layers as in Figure 4.1 the surface admittance and impedance are given by

$$\hat{Y}_1 = Y_1 \frac{\hat{Y}_2 + Y_1 \tanh(u_1 h_1)}{Y_1 + \hat{Y}_2 \tanh(u_1 h_1)}, \quad (4.25)$$

$$\hat{Y}_n = Y_n \frac{\hat{Y}_{n+1} + Y_n \tanh(u_n h_n)}{Y_n + \hat{Y}_{n+1} \tanh(u_n h_n)},$$

$$\hat{Y}_N = Y_N,$$

$$\hat{Z}_1 = Z_1 \frac{\hat{Z}_2 + Z_1 \tanh(u_1 h_1)}{Z_1 + \hat{Z}_2 \tanh(u_1 h_1)}, \quad (4.26)$$

$$\hat{Z}_n = Z_n \frac{\hat{Z}_{n+1} + Z_n \tanh(u_n h_n)}{Z_n + \hat{Z}_{n+1} \tanh(u_n h_n)},$$

$$\hat{Z}_N = Z_N,$$

with

$$Y_n = \frac{u_n}{\hat{z}_n}, \quad (4.27)$$

$$Z_n = \frac{u_n}{\hat{y}_n}, \quad (4.28)$$

$$u_n = (k_x^2 + k_y^2 - k_n^2)^{1/2}, \quad (4.29)$$

and

$$k_n^2 = -\hat{z}_n \hat{y}_n = \omega^2 \mu_n \epsilon_n - i\omega \mu_n \sigma_n. \quad (4.30)$$

Thus  $\hat{Y}_1$  and  $\hat{Z}_1$  can be determined recursively by starting at the deepest layer and iterating upward. For calculation it may be desirable to formulate the equation in terms of negative exponentials instead of tanh functions for greater numerical stability.

In order to gain insight regarding the TE and TM fields, let us consider the reflection coefficients for a nonmagnetic homogeneous half-space. From equations (4.19) and (4.20)

$$r_{TE} = \frac{Y_0 - Y_1}{Y_0 + Y_1} = \frac{u_0 - u_1}{u_0 + u_1}, \quad (4.31)$$

and

$$r_{TM} = \frac{Z_0 - Z_1}{Z_0 + Z_1} = \frac{\frac{u_0 - \hat{y}_0}{\hat{y}_1} u_1}{\frac{u_0 + \hat{y}_0}{\hat{y}_1} u_1}. \quad (4.32)$$

For the low frequencies of interest in most geophysical applications,  $k_0$  and  $\hat{y}_0$  are very small, so that

$$r_{TE} \approx \frac{\lambda - u_1}{\lambda + u_1}, \quad (4.33)$$

and

$$r_{TM} \approx 1, \quad (4.34)$$

where

$$\lambda = (k_x^2 + k_y^2)^{1/2}.$$

Thus, for the TM mode, the tangential magnetic field at the surface of the earth is double the primary field, while the tangential electric field is zero: the earth appears to be a perfect conductor. For a source that generates only a TM mode, e.g., a vertical electric dipole, the resultant fields will not be sensitive to conductivity changes in the earth.

The derivation to this point is general, applying to any source. Before specializing to a particular source, let us illustrate the essential form of the general solution. Combining the particular and complementary (also called primary and secondary) solutions between the source and the earth, we obtain in transform space,

$$\tilde{A} = A_p e^{-u_0 h} (e^{-u_0 z} + r_{TM} e^{u_0 z}) \quad (4.35)$$

and

$$\tilde{F} = F_p e^{-u_0 h} (e^{-u_0 z} + r_{\text{TE}} e^{u_0 z}). \quad (4.36)$$

Finally, the potentials as a function of  $x$  and  $y$  are given by inverse Fourier transformation as

$$A = \frac{1}{4\pi^2} \int_{-\infty}^{\infty} \int_{-\infty}^{\infty} A_p e^{-u_0 h} (e^{-u_0 z} + r_{\text{TE}} e^{u_0 z}) e^{i(k_x x + k_y y)} dk_x dk_y \quad (4.37)$$

and

$$F = \frac{1}{4\pi^2} \int_{-\infty}^{\infty} \int_{-\infty}^{\infty} F_p e^{-u_0 h} (e^{-u_0 z} + r_{\text{TE}} e^{u_0 z}) e^{i(k_x x + k_y y)} dk_x dk_y \quad (4.38)$$

Comparing the term  $k_x x + k_y y$  in equations (4.37) and (4.38) with  $\lambda$  in equations (3.130), (3.137), and (3.139), we see that our solution is in the form of a superposition of plane waves with continuously varying angle of incidence. However, because  $k_x$  and  $k_y$  vary from  $-\infty$  to  $\infty$ , the angles are complex.

### Vertical magnetic dipole

**Layered Earth.**—The particular solution (primary field) for a vertical magnetic dipole of moment  $m u_z$  at  $z = -h$  above the surface of the earth satisfies from equation (1.114) the differential equation,

$$\nabla^2 F + k_0^2 F = -\hat{z}_0 m \delta(x) \delta(y) \delta(z + h), \quad (4.39)$$

since the dipole is  $z$ -directed. By analogy with the solution for the scalar 3-D Green's function in equation (2.6) and (2.8), we have, between the dipole and the earth

$$\tilde{F} = \frac{\hat{z}_0 m}{2u_0} e^{-u_0 h} e^{-u_0 z}. \quad (4.40)$$

Due to the symmetry of the problem, currents flow only horizontally. Hence, there is no vertical component of electric field, and the EM field of a vertical magnetic dipole above a horizontally layered earth is a TE field. From equation (4.40), we see that  $F_p$  in equation (4.36) is given by

$$F_p = \frac{\hat{z}_0 m}{2u_0}. \quad (4.41)$$

Substituting equation (4.41) into equation (4.38) we have the following expression for the potential between the dipole and the earth:

$$F(x, y, z) = \frac{\hat{z}_0 m}{8\pi^2} \int_{-\infty}^{\infty} \int_{-\infty}^{\infty} [e^{-u_0(z+h)} + r_{\text{TE}} e^{u_0(z-h)}] \frac{1}{u_0} e^{i(k_x x + k_y y)} dk_x dk_y. \quad (4.42)$$

Because the integral is a function of  $k_x^2 + k_y^2$ , we can convert to a Hankel transform using equation (2.10). Then

$$F(\rho, z) = \frac{\hat{z}_0 m}{4\pi} \int_0^{\infty} [e^{-u_0(z+h)} + r_{\text{TE}} e^{u_0(z-h)}] \frac{\lambda}{u_0} J_0(\lambda\rho) d\lambda, \quad (4.43)$$

where, now,

$$u_n = (\lambda^2 - k_n^2)^{1/2},$$

and

$$\rho = (x^2 + y^2)^{1/2}.$$

Due to symmetry, there will be only a  $\phi$  component of electric field. To evaluate it use equation (1.129) and the relations

$$E_\phi = -\frac{y}{\rho} E_x + \frac{x}{\rho} E_y,$$

and

$$\frac{\partial J_0(\lambda\rho)}{\partial x} = -\lambda \frac{x}{\rho} J_1(\lambda\rho).$$

Thus

$$E_\phi = -\frac{\hat{z}_0 m}{4\pi} \int_0^\infty [e^{-u_0(z+h)} + r_{TE} e^{u_0(z-h)}] \frac{\lambda^2}{u_0} J_1(\lambda\rho) d\lambda. \quad (4.44)$$

The horizontal magnetic field has only a radial component, given by

$$H_\rho = \frac{x}{\rho} H_x + \frac{y}{\rho} H_y.$$

Hence, from equation (1.130)

$$H_\rho = \frac{m}{4\pi} \int_0^\infty [e^{-u_0(z+h)} - r_{TE} e^{u_0(z-h)}] \lambda^2 J_1(\lambda\rho) d\lambda. \quad (4.45)$$

Finally, using equation (1.130) and applying the relation

$$\frac{\partial^2}{\partial z^2} + k_0^2 = u_0^2 + k_0^2 = \lambda^2,$$

inside the integrand of equation (4.43), the vertical magnetic field is given by

$$H_z = \frac{m}{4\pi} \int_0^\infty [e^{-u_0(z+h)} + r_{TE} e^{u_0(z-h)}] \frac{\lambda^3}{u_0} J_0(\lambda\rho) d\lambda. \quad (4.46)$$

Equations (4.44), (4.45), and (4.46) are general expressions for the EM field components above the earth's surface. In the general case, they can be evaluated only by numerical integration, using techniques discussed later in this chapter. If the source or the receiver is on the surface of the earth, simply set  $h$  or  $z$  to zero.

The reflection coefficient can be simplified if, as is usually the case, we can take the magnetic permeability of the earth to be that of free space. Then  $\mu_n = \mu_0$ , and

$$r_{TE} = \frac{\lambda - \hat{\mu}_1}{\lambda + \hat{\mu}_1}, \quad (4.47)$$

with

$$\hat{u}_1 = u_1 \frac{\hat{u}_2 + u_1 \tanh(u_1 h_1)}{u_1 + \hat{u}_2 \tanh(u_1 h_1)},$$

$$\hat{u}_n = u_n \frac{\hat{u}_{n+1} + u_n \tanh(u_n h_n)}{u_n + \hat{u}_{n+1} \tanh(u_n h_n)},$$

and

$$\hat{u}_N = u_N.$$

Knight and Raiche (1982) found that formulating equation (4.47) in terms of  $\exp(-2u_i h_i)$  instead of  $\tanh(u_i h_i)$  is more stable numerically.

**Homogeneous Earth.**—Only for the case of the source and receiver on the surface of a homogeneous earth under the quasi-static approximation ( $k_0 \approx 0$ ) can we derive analytic expressions for the fields. The quasi-static approximation is valid when distances are much less than a wavelength in free space, and hence is applicable in most cases of geophysical interest. Setting  $k_0 = 0$  and letting  $u = u_1$  and  $k = k_1$  for notational simplicity,

$$r_{\text{TE}} = \frac{\lambda - u}{\lambda + u}, \quad (4.48)$$

so that, from equations (4.44), (4.45), and (4.46), with  $z$  and  $h$  set to zero,

$$E_\phi = -\frac{\hat{z}_0 m}{2\pi} \int_0^\infty \frac{\lambda^2}{\lambda + u} J_1(\lambda\rho) d\lambda, \quad (4.49)$$

$$H_\rho = \frac{m}{2\pi} \int_0^\infty \frac{\lambda^2 u}{\lambda + u} J_1(\lambda\rho) d\lambda, \quad (4.50)$$

and

$$H_z = \frac{m}{2\pi} \int_0^\infty \frac{\lambda^3}{\lambda + u} J_0(\lambda\rho) d\lambda. \quad (4.51)$$

To evaluate the expression for the electric field, rewrite it as

$$E_\phi = \frac{\hat{z}_0 m}{2\pi} \frac{\partial}{\partial \rho} \int_0^\infty \frac{\lambda}{\lambda + u} J_0(\lambda\rho) d\lambda. \quad (4.52)$$

Since  $\lambda^2 - u^2 = k^2$ , multiplying the numerator and denominator of the integrand by  $\lambda - u$  yields

$$E_\phi = \frac{\hat{z}_0 m}{2\pi k^2} \frac{\partial}{\partial \rho} \left[ \int_0^\infty \lambda^2 J_0(\lambda\rho) d\lambda - \int_0^\infty \lambda u J_0(\lambda\rho) d\lambda \right].$$

Using the Lipschitz integral,

$$\int_0^\infty e^{-\lambda z} J_0(\lambda\rho) d\lambda = \frac{1}{r}, \quad (4.53)$$

with  $r = (\rho^2 + z^2)^{1/2}$ , and the Sommerfield integral from equations (2.12) and (2.13)

$$\int_0^\infty \frac{\lambda}{u} e^{-uz} J_0(\lambda\rho) d\lambda = \frac{e^{-ikr}}{r}, \quad (4.54)$$

we obtain

$$E_\phi = -\frac{m}{2\pi\sigma} \frac{\partial}{\partial\rho} \left[ \frac{\partial^2}{\partial z^2} \left( \frac{1}{r} \right) - \frac{\partial^2}{\partial z^2} \left( \frac{e^{-ikr}}{r} \right) \right]_{z=0}$$

Finally,

$$E_\phi = \frac{-m}{2\pi\sigma\rho^4} [3 - (3 + 3ik\rho - k^2\rho^2)e^{-ik\rho}]. \quad (4.55)$$

We can derive  $H_z$  from  $E_\phi$  using Faraday's law, equation (1.16), in cylindrical coordinates. Thus

$$H_z = -\frac{1}{\hat{z}_0} \frac{1}{\rho} \frac{\partial}{\partial\rho} (\rho E_\phi),$$

and

$$H_z = \frac{m}{2\pi k^2 \rho^5} [9 - (9 + 9ik\rho - 4k^2\rho^2 - ik^3\rho^3)e^{-ik\rho}]. \quad (4.56)$$

The behavior of the vertical magnetic field as a function of frequency is illustrated in Figure 4.2. The real and imaginary components of the field are shown at a position 100 m from a vertical magnetic dipole of unit moment at the surface of a homogeneous half-space. At low frequencies the real part of the field approaches its free-space value of  $-7.96 \times 10^{-8}$  A/m, while the imaginary part goes to zero and varies linearly with frequency. Both components

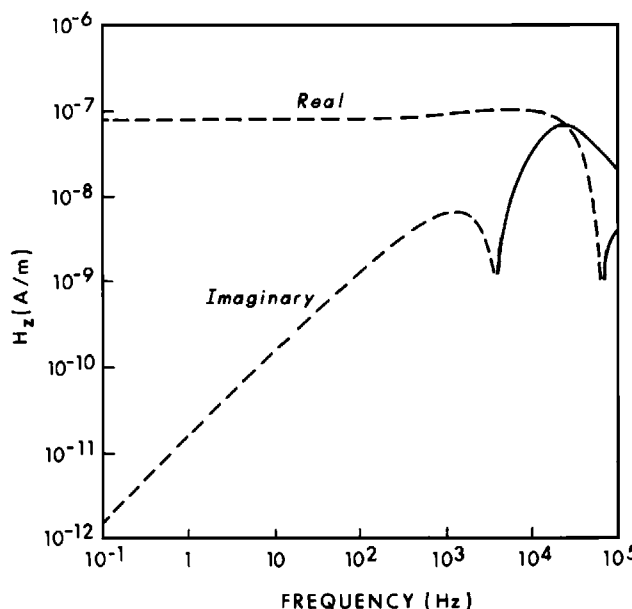


FIG. 4.2. Vertical magnetic field as a function of frequency 100 m from a vertical magnetic dipole at the surface of a  $100 \Omega \cdot \text{m}$  homogeneous earth.

change sign at high frequencies.

Because the radial component of the primary (free-space) magnetic field is zero in the plane of the loop, we only need to consider the secondary field, which, from equation (4.45), can be written

$$H_p = \frac{m}{4\pi} \frac{\partial}{\partial p} \int_0^\infty \frac{\lambda - u}{\lambda + u} \lambda J_0(\lambda p) d\lambda \quad (4.57)$$

or, after multiplying the numerator and denominator of the integrand by  $\lambda + u$ ,

$$H_p = \frac{mk^2}{4\pi} \frac{\partial}{\partial p} \int_0^\infty \frac{\lambda}{(\lambda + u)^2} J_0(\lambda p) d\lambda. \quad (4.58)$$

Following Kaufman and Keller (1983), we rewrite equation (4.58) as

$$H_p = \frac{mk^2}{16\pi} \frac{\partial}{\partial p} \left[ \int_0^\infty \frac{1}{u} J_0(\lambda p) d\lambda - \int_0^\infty \left( \frac{u - \lambda}{u + \lambda} \right)^2 \frac{1}{u} J_0(\lambda p) d\lambda \right].$$

If we multiply the numerator and denominator of the second integral by  $(u + \lambda)^2$ , we can evaluate both integrals using Erdelyi (1954, v. 2, p. 8, no. 16) to obtain

$$H_p = \frac{mk^2}{16\pi} \frac{\partial}{\partial p} \left[ I_0\left(\frac{ikp}{2}\right) K_0\left(\frac{ikp}{2}\right) - I_2\left(\frac{ikp}{2}\right) K_2\left(\frac{ikp}{2}\right) \right].$$

Finally

$$H_p = \frac{-mk^2}{4\pi p} \left[ I_1\left(\frac{ikp}{2}\right) K_1\left(\frac{ikp}{2}\right) - I_2\left(\frac{ikp}{2}\right) K_2\left(\frac{ikp}{2}\right) \right], \quad (4.59)$$

which is a simplified form of the expression given in Wait (1955).

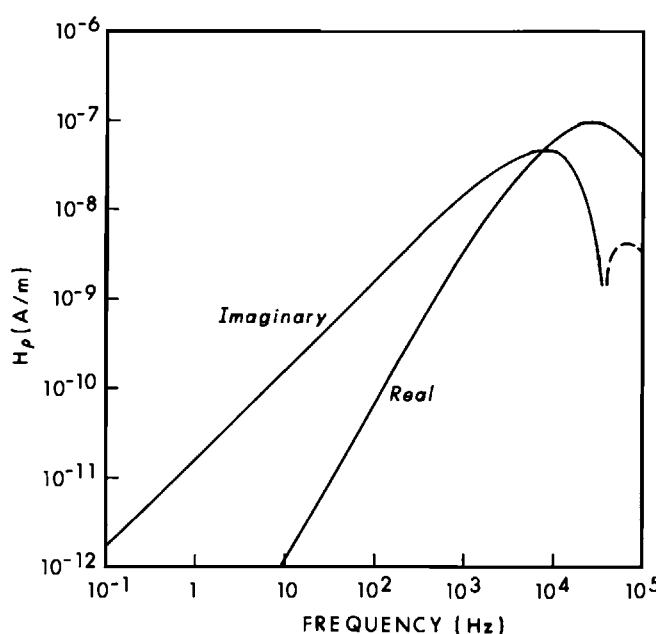


FIG. 4.3. Horizontal magnetic field as a function of frequency 100 m from a vertical magnetic dipole at the surface of a  $100 \Omega \cdot \text{m}$  homogeneous earth.

Figure 4.3 shows the horizontal magnetic field for the same model as that of Figure 4.2. Both the real and imaginary components are zero at zero frequency. At low frequencies the imaginary component varies linearly with frequency, while the real component increases as  $f^2$ . The peak value of the real component is just slightly higher than the low-frequency asymptote of the vertical magnetic field shown in Figure 4.2.

**Transient Response.**—Inverse Fourier transformation of equations (4.44), (4.45), and (4.46) divided by  $i\omega$  yields the step response of the earth for a vertical magnetic dipole. However, as explained in Section 2, in the case of the magnetic field we are usually interested in the impulse response, the derivative of the step response, which is given by transforming equations (4.45) and (4.46) directly. In general the transient fields can only be computed numerically; techniques are discussed later.

Analytic expressions can be derived, however, for the case of the dipole and receiver at the surface of the earth. To transform from the frequency domain to the time domain, substitute  $s = i\omega$ , so that

$$ik\rho = \alpha s^{1/2},$$

$$k^2 \rho^2 = -\alpha^2 s,$$

and

$$ik^3 \rho^3 = -\alpha^3 s^{3/2},$$

with

$$\alpha = (\mu\sigma)^{1/2} \rho.$$

Then, from equation (4.55) the electric field step response is given by

$$e_\phi = \mathcal{L}^{-1}\left\{\frac{E_\phi}{s}\right\} = \mathcal{L}^{-1}\left\{\frac{-m}{2\pi\sigma\rho^4} \left[ \frac{3}{s} - \left( \frac{3}{s} + \frac{3\alpha}{s^{1/2}} + \alpha^2 \right) e^{-\alpha s^{1/2}} \right] \right\}.$$

Abramowitz and Stegun (1964) give the following inverse Laplace transforms valid for  $t > 0$ :

$$\mathcal{L}^{-1}\left\{\frac{1}{s}\right\} = 1, \quad (4.60)$$

$$\mathcal{L}^{-1}\left\{\frac{1}{s} e^{-\alpha s^{1/2}}\right\} = \text{erfc}\left(\frac{\alpha}{2t^{1/2}}\right), \quad (4.61)$$

$$\mathcal{L}^{-1}\left\{\frac{1}{s^{1/2}} e^{-\alpha s^{1/2}}\right\} = \frac{1}{(\pi t)^{1/2}} e^{-\alpha^2/4t}, \quad (4.62)$$

and

$$\mathcal{L}^{-1}\left\{e^{-\alpha s^{1/2}}\right\} = \frac{\alpha}{2\pi^{1/2} t^{3/2}} e^{-\alpha^2/4t}, \quad (4.63)$$

Thus

$$e_\phi = -\frac{m}{2\pi\sigma\rho^4} \left[ 3 \operatorname{erf}(\theta\rho) - \frac{2}{\pi^{1/2}} \theta\rho(3 + 2\theta^2\rho^2)e^{-\theta^2\rho^2} \right], \quad (4.64)$$

with

$$\theta = \left( \frac{\mu_0\sigma}{4t} \right)^{1/2},$$

an expression given, e.g., in Wait (1960b).

From equation (4.56), the vertical magnetic field step response is given by

$$h_z = -\frac{m}{2\pi\mu_0\sigma\rho^5} \mathcal{L}^{-1} \left\{ \frac{9}{s^2} - \left( \frac{9}{s^2} + \frac{9\alpha}{s^{3/2}} + \frac{4\alpha^2}{s} + \frac{\alpha^3}{s^{1/2}} \right) e^{-\alpha s^{1/2}} \right\}. \quad (4.65)$$

To evaluate this expression we need the following additional inverse Laplace transforms from Abramowitz and Stegun (1964):

$$\mathcal{L}^{-1} \left\{ \frac{1}{s^2} \right\} = t, \quad (4.66)$$

$$\mathcal{L}^{-1} \left\{ \frac{1}{s^{3/2}} e^{-\alpha s^{1/2}} \right\} = 2 \frac{t^{1/2}}{\pi^{1/2}} e^{-\theta^2\rho^2} - \alpha \operatorname{erfc}(\theta\rho), \quad (4.67)$$

and from Erdelyi (1954):

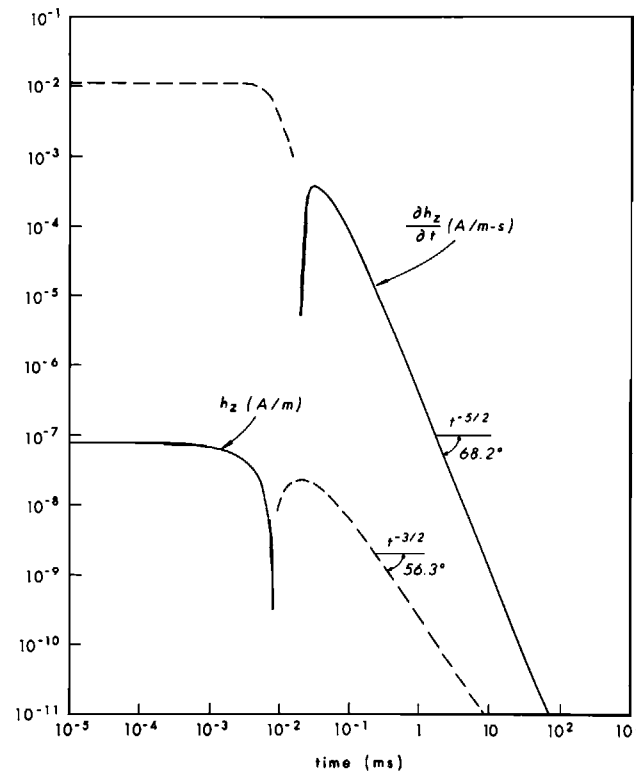


FIG. 4.4. Vertical magnetic field and its time derivative 100 m from a vertical magnetic dipole that is terminated abruptly. Source and receiver at surface of a  $100 \Omega \cdot \text{m}$  homogeneous earth. Solid lines positive, dashed lines negative.

$$\mathcal{L}^{-1}\left\{\frac{1}{s^2}e^{-\alpha s^{1/2}}\right\} = t(1 + 2\theta^2 p^2) \operatorname{erfc}(\theta p) - \frac{2t}{\pi^{1/2}} \theta p e^{-\theta^2 p^2} \quad (4.68)$$

After some algebra we obtain

$$h_z = -\frac{m}{4\pi p^3} \left[ \frac{9}{2\theta^2 p^2} \operatorname{erf}(\theta p) + \operatorname{erfc}(\theta p) - \frac{1}{\pi^{1/2}} \left( \frac{9}{\theta p} + 4\theta p \right) e^{-\theta^2 p^2} \right], \quad (4.69)$$

which agrees with the expression given in Kaufman and Keller (1983).

Applying equation (2.44) to equation (4.69), we find that the decay of the vertical magnetic field after a constant vertical magnetic dipole is terminated abruptly is given by

$$h_z = \frac{m}{4\pi p^3} \left[ \frac{9}{2\theta^2 p^2} \operatorname{erf}(\theta p) - \operatorname{erf}(\theta p) - \frac{1}{\pi^{1/2}} \left( \frac{9}{\theta p} + 4\theta p \right) e^{-\theta^2 p^2} \right], \quad (4.69a)$$

The time derivative of the vertical magnetic field (the magnetic field impulse response), given by equation (4.65) multiplied by  $s$ , is

$$\frac{\partial h_z}{\partial t} = -\frac{m}{2\pi\mu_0\sigma p^5} \left[ 9 \operatorname{erf}(\theta p) - \frac{2\theta p}{\pi^{1/2}} (9 + 6\theta^2 p^2 + 4\theta^4 p^4) e^{-\theta^2 p^2} \right]. \quad (4.70)$$

an expression given in Kaufman and Keller (1983).

To illustrate the behavior of the magnetic field in the time domain, Figure 4.4 shows the vertical magnetic field and its time derivative, calculated using equations (4.69a) and (4.70), respectively. The transmitter is a vertical magnetic dipole of unit moment that is terminated abruptly. Hence for a realistic moment of  $1\,000\text{ A-m}^2$ , the magnetic field before the transmitter is turned off is about  $10^{-4}\text{ A/m}$ , corresponding to a magnetic induction  $B$  of about  $0.1\text{ nT}$ .

Immediately upon termination of the dipole, a circular current is induced directly below the dipole in such a way that it prevents the magnetic field from shutting off immediately. As shown in Nabighian (1979), the decaying magnetic field at subsequent times is due to a system of circular currents in the earth, the maximum of which diffuses outward and downward from the dipole. As shown by Figure 4.4, the vertical magnetic field changes sign near the time that the current maximum passes beneath the observation point, and the time-derivative of the magnetic field changes sign at a slightly later time. Nabighian showed that the magnetic field can be represented approximately as due to an expanding circular line of current, commonly called a “smoke ring.”

From equations (4.69a) and (4.70), the late-time asymptotic forms for the step and impulse response are, respectively,

$$h_z \approx \frac{m}{30} \left( \frac{\sigma\mu_0}{\pi} \right)^{3/2} t^{-3/2}, \quad (4.70a)$$

and

$$\frac{\partial h_z}{\partial t} \approx \frac{-m}{20} \left( \frac{\sigma\mu_0}{\pi} \right)^{3/2} t^{-5/2}. \quad (4.70b)$$

These late-time decays show up as linear relations on the log-log plot of Figure 4.4, with angles of 56.3 degrees and 68.2 degrees, as shown. Measuring these angles provides a quick check on measured or computed responses, because any layered earth must exhibit the same decay at late-times.

To derive an expression for the step response of the horizontal magnetic field, we substitute  $s = i\omega$  in equation (4.59) and divide by  $s$  to obtain

$$\frac{H_p}{s} = \frac{m\mu_0\sigma}{4\pi\rho} \left[ I_1\left(\frac{\alpha}{2}s^{1/2}\right)K_1\left(\frac{\alpha}{2}s^{1/2}\right) - I_2\left(\frac{\alpha}{2}s^{1/2}\right)K_2\left(\frac{\alpha}{2}s^{1/2}\right) \right],$$

with  $\alpha = (\mu\sigma)^{1/2}\rho$ .

Erdelyi (1954, p. 284, no. 56) gives the following Laplace transform pair:

$$\mathcal{L}^{-1}\{K_\nu(a^{1/2}s^{1/2} + b^{1/2}s^{1/2})I_\nu(a^{1/2}s^{1/2} - b^{1/2}s^{1/2})\} = \frac{1}{2t} e^{-(a+b)/2t} I_\nu\left(\frac{a-b}{2t}\right). \quad (4.71)$$

Taking the limit as  $b \rightarrow 0$  in the expression for  $h_p$ , and changing sign so that it applies to a step turn-off, we obtain

$$h_p = \frac{-m\theta^2}{2\pi\rho} e^{-\theta^2\rho^2/2} \left[ I_1\left(\frac{\theta^2\rho^2}{2}\right) - I_2\left(\frac{\theta^2\rho^2}{2}\right) \right], \quad (4.72)$$

which agrees with the expression given in Kaufman and Keller (1983). Using small-argument approximations yields, for late times,

$$h_p \approx -\frac{m\rho\mu_0^2\sigma^2}{128\pi t^2}. \quad (4.73)$$

The time derivative of the magnetic field is given by

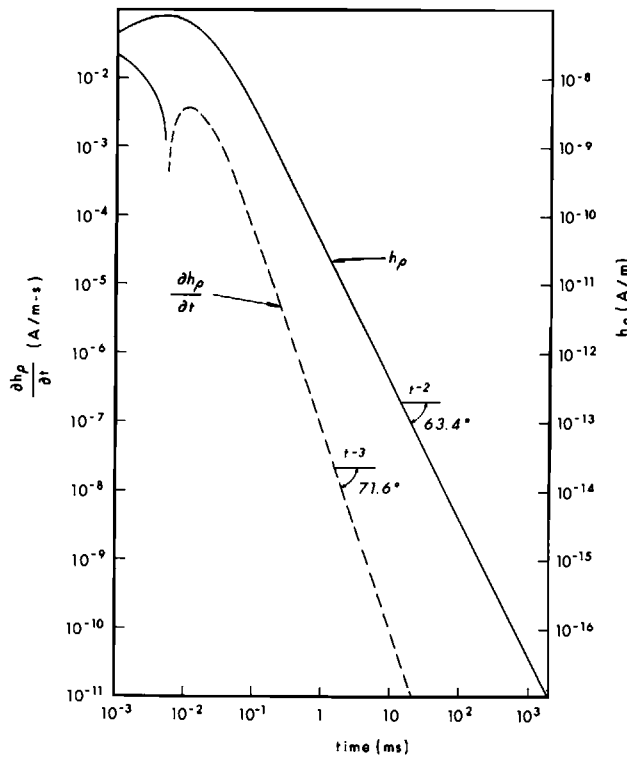


FIG. 4.5. Horizontal magnetic field and its time derivative 100 m from a vertical magnetic dipole that is terminated abruptly. Source and receiver at surface of a  $100 \Omega \cdot \text{m}$  homogeneous earth. Solid lines positive, dashed lines negative.

$$\frac{\partial h_p}{\partial t} = \frac{m\theta^2}{2\pi p t} e^{-\theta^2 p^2/2} \left[ (1 + \theta^2 p^2) I_0\left(\frac{\theta^2 p^2}{2}\right) - \left(2 + \theta^2 p^2 + \frac{4}{\theta^2 p^2}\right) I_1\left(\frac{\theta^2 p^2}{2}\right) \right] \quad (4.74)$$

which again agrees with the expression given in Kaufman and Keller (1983), except for a factor of two. Values computed using equation (4.74) agree with results computed by numerical integration. The late-time asymptote is

$$\frac{\partial h_p}{\partial t} \approx \frac{mp\mu_0^2\sigma^2}{64\pi t^3}. \quad (4.75)$$

Figure 4.5 shows the horizontal magnetic field and its time derivative calculated using expressions (4.72) and (4.74), respectively, for the same configuration as that of Figure 4.4. Note the peak in the horizontal field over the diffusing current maximum at the same time as the crossover in the vertical field in Figure 4.4. The late-time decays, from equations (4.73) and (4.75), exhibit  $t^{-2}$  and  $t^{-3}$  dependences, corresponding to angles of 63.4 degrees and 71.6 degrees, respectively.

### Large horizontal loop

One of the most widely used EM sources is a large loop lying on the surface of the earth; measurements are made inside or outside the loop. Usually the source loop is square or rectangular, as shown in Figure 4.6a.

**Rectangular Loop.**—Let us consider the element of dipole moment

$$dm = I dx' dy' \quad (4.76)$$

shown in Figure 4.6a, where  $I$  is the current in the loop. Substituting  $dm$  for  $m$  in equation (4.42) and integrating over the loop,

$$F(x, y, z) = \frac{\hat{z}_0 I}{8\pi^2} \int_{-\infty}^{\infty} \int_{-\infty}^{\infty} \tilde{F}(k_x, k_y, z) \int_{-L}^{L} \int_{-W}^{W} e^{i[k_x(x-x')+k_y(y-y')]} dx' dy' dk_x dk_y,$$

or

$$F(x, y, z) = \frac{\hat{z}_0 I L W}{2\pi^2} \int_{-\infty}^{\infty} \int_{-\infty}^{\infty} \tilde{F}(k_x, k_y, z) \text{sinc}(k_x W) \text{sinc}(k_y L) e^{i(k_x x + k_y y)} dk_x dk_y, \quad (4.77)$$

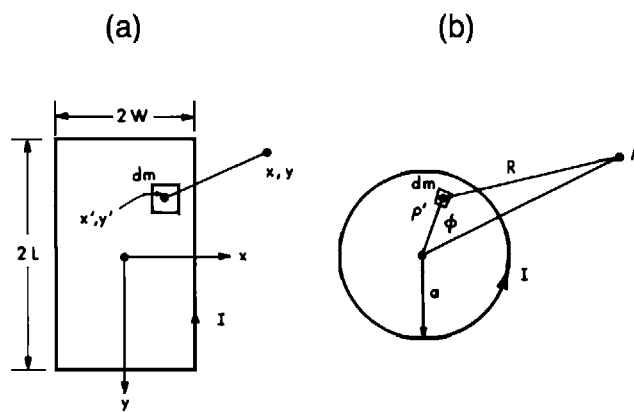


FIG. 4.6. Plan views of (a) rectangular loop and (b) circular loop at the surface of the earth.

with

$$\hat{F}(k_x, k_y, z) = \frac{1}{u_0} [e^{u_0(z+h)} + r_{\text{TE}} e^{u_0(z-h)}],$$

and where

$$\text{sinc}(x) = \sin(x)/x$$

is the sinc function.

The integrand of equation (4.77) is not a circularly symmetric function, so that the 2-D Fourier transform cannot be written as a Hankel transform. However, the field components  $E_x$ ,  $E_y$ ,  $H_x$ ,  $H_y$ , and  $H_z$  can be written as 2-D Fourier transforms using equations (1.122), (1.123), and (4.77), and the integrals can be evaluated numerically using a 2-D FFT (Fast Fourier Transform) algorithm.

Alternatively, one can substitute  $dm$  from equation (4.76) for  $m$  in equations (4.44), (4.45), and (4.46) and integrate numerically over the loop. Another possibility is to integrate numerically around the loop using the TE expression for a horizontal electric dipole, with grounding terms excluded, which is developed later in this chapter. Poddar (1982) used this latter technique to compute the response of a rectangular loop on a layered earth.

**Circular Loop.**—Let us now consider the circular transmitting loop illustrated in Figure 4.6b, because the integration over the loop can be carried out analytically. A circular loop is a good approximation to a square loop of the same area if the receiver is located at the center of the loop or some distance away outside the loop.

The TE potential is given by substituting

$$dm = I\rho' d\phi dp' \quad (4.78)$$

in equation (4.43) and integrating over the loop. Using the notation defined in Figure 4.6b,

$$F(\rho, z) = \frac{\hat{z}_0 I}{4\pi} \int_0^\infty \lambda \hat{F}(\lambda, z) \int_0^a \int_0^{2\pi} J_0(\lambda R) \rho' d\phi dp' d\lambda, \quad (4.79)$$

with

$$\hat{F}(\lambda, z) = \frac{1}{u_0} [e^{-u_0(z+h)} + r_{\text{TE}} e^{u_0(z-h)}]. \quad (4.80)$$

Substituting the following addition theorem (Watson, 1944, p. 36):

$$J_0(\lambda R) = \sum_{m=-\infty}^{\infty} J_m(\lambda \rho) J_m(\lambda \rho') \cos m\phi \quad (4.81)$$

in equation (4.79) and interchanging order of integration and summation yields

$$F(\rho, z) = \frac{\hat{z}_0 I}{4\pi} \int_0^\infty \lambda \hat{F}(\lambda, z) \sum_{m=-\infty}^{\infty} J_m(\lambda \rho) \int_0^a \int_0^{2\pi} J_m(\lambda \rho') \rho' \cos m\phi d\phi dp' d\lambda.$$

The inner integral is nonzero only for  $m = 0$ , so that

$$F(\rho, z) = \frac{\hat{z}_0 I}{2} \int_0^\infty \lambda \hat{F}(\lambda, z) J_0(\lambda \rho) \int_0^a J_0(\lambda \rho') \rho' dp' d\lambda. \quad (4.82)$$

Using the relation (Dwight, 1961)

$$\int x^n J_{n-1}(x) dx = x^n J_n(x), \quad (4.83)$$

we obtain

$$F(\rho, z) = \frac{\hat{z}_0 I a}{2} \int_0^\infty \tilde{F}(\lambda, z) J_1(\lambda a) J_0(\lambda \rho) d\lambda. \quad (4.84)$$

Applying the small-argument approximation,

$$J_1(\lambda a) \approx \frac{\lambda a}{2}, \quad (4.85)$$

we see that for  $a \ll \rho$  the expression (4.84) reduces to expression (4.43) with  $m = \pi a^2 I$ . Hence, for distances which are large compared with the radius, the field of a small loop is approximately that of a magnetic dipole.

From a derivation similar to that used for equations (4.44), (4.45), and (4.46),

$$E_\phi = -\frac{\hat{z}_0 I a}{2} \int_0^\infty [e^{-u_0(z+h)} + r_{TE} e^{u_0(z-h)}] \frac{\lambda}{u_0} J_1(\lambda a) J_1(\lambda \rho) d\lambda, \quad (4.86)$$

$$H_\rho = \frac{I a}{2} \int_0^\infty [e^{-u_0(z+h)} - r_{TE} e^{u_0(z-h)}] \lambda J_1(\lambda a) J_1(\lambda \rho) d\lambda, \quad (4.87)$$

and

$$H_z = \frac{I a}{2} \int_0^\infty [e^{-u_0(z+h)} + r_{TE} e^{u_0(z-h)}] \frac{\lambda^2}{u_0} J_1(\lambda a) J_0(\lambda \rho) d\lambda. \quad (4.88)$$

Computational considerations for these integrals are discussed in Ryu et al. (1970). In the quasi-static range  $u_0$  can be set to  $\lambda$ .

For the case of the source and receiver on the surface of a homogeneous earth, substitute  $r_{TE}$  from equation (4.48), and set  $z$  and  $h$  to zero to obtain

$$E_\phi = -\hat{z}_0 I a \int_0^\infty \frac{\lambda}{\lambda + u} J_1(\lambda a) J_1(\lambda \rho) d\lambda, \quad (4.89)$$

$$H_\rho = I a \int_0^\infty \frac{\lambda u}{\lambda + u} J_1(\lambda a) J_1(\lambda \rho) d\lambda, \quad (4.90)$$

and

$$H_z = I a \int_0^\infty \frac{\lambda^2}{\lambda + u} J_1(\lambda a) J_0(\lambda \rho) d\lambda. \quad (4.91)$$

Unlike the case of a magnetic dipole, no analytic expressions exist for a large loop, except for the vertical field at the center of the loop.

**Measurements Inside the Loop.**—For EM sounding applications one often measures only the vertical component of the magnetic field at the center of the loop, in order to reduce the effects of lateral inhomogeneities (Patra, 1970). The response for this *central-loop* configuration is given by setting  $\rho$  to zero in equation (4.88) to obtain

$$H_z = \frac{Ia}{2} \int_0^\infty [e^{-u_0(z+h)} + r_{TE} e^{u_0(z-h)}] \frac{\lambda^2}{u_0} J_1(\lambda a) d\lambda. \quad (4.92)$$

If the source and receiver are at the surface of a homogeneous earth, we have from equation (4.91)

$$H_z = Ia \int_0^\infty \frac{\lambda^2}{\lambda + u} J_1(\lambda a) d\lambda. \quad (4.93)$$

By analogy with the derivation of the electric field in equation (4.55) from equation (4.49), the integral (4.93) can be evaluated to give

$$H_z = -\frac{I}{k^2 a^3} [3 - (3 + 3ika - k^2 a^2)e^{-ika}], \quad (4.94)$$

an expression given in Kaufman (1979) for the magnetic field at the center of a circular loop. Note that at zero frequency equation (4.94) reduces to  $I/2a$ , which is the field at the center of a loop carrying a direct current.

Figure 4.7 illustrates the vertical magnetic field at the center of a loop with radius 50 m lying on a homogeneous half-space of resistivity  $100 \Omega \cdot \text{m}$ . The real and imaginary parts of the field, calculated using equation (4.94), are shown as functions of frequency.

Because the current in the loop is 1A the real part of the field approaches  $10^{-2} \text{ A/m}$  at low frequencies, corresponding to a magnetic induction  $B$  of about 10 nT. The imaginary part of the field approaches zero at low frequencies, and varies linearly with frequency.

In the *coincident-loop* configuration, one measures the voltage induced in a large loop that is essentially coincident with the transmitting loop. The response is thus the time derivative of the magnetic flux through the loop, or, in the frequency domain, from equation (4.88)

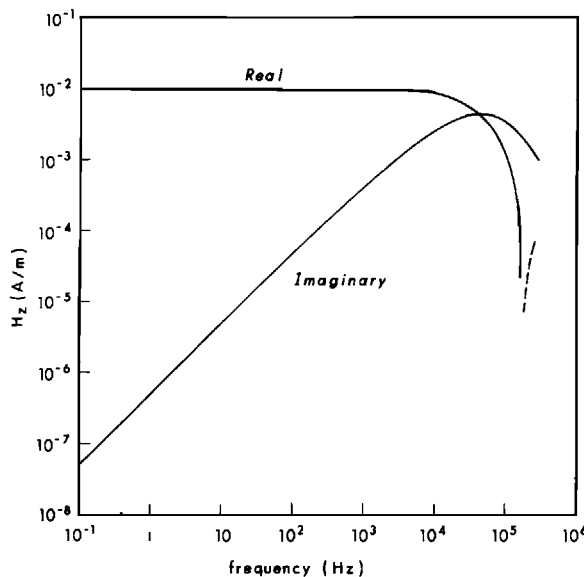


FIG. 4.7. Vertical magnetic field as a function of frequency at the center of a circular loop on a  $100 \Omega \cdot \text{m}$  homogeneous earth. The loop has a radius of 50 m and carries a current of 1A.

$$V = -i\omega\mu_0 \int_0^a \int_0^{2\pi} H_z(p, z) p d\phi dp.$$

From the relation (4.83) and the expression (4.88), in the general case,

$$V = -i\omega\mu_0\pi a^2 I \int_0^\infty [e^{u_0(z+h)} + r_{TE}e^{u_0(z-h)}] \lambda [J_1(\lambda a)]^2 d\lambda. \quad (4.95)$$

For the coincident-loop configuration at the surface of a homogeneous earth, from equation (4.91)

$$V = -i\omega\mu_0 2\pi a^2 I \int_0^\infty \frac{\lambda}{\lambda + u} [J_1(\lambda a)]^2 d\lambda. \quad (4.96)$$

**Transient Response.**—As in the case of a dipole, the transient fields of a large loop can only be computed numerically for general layered models. Impulse responses are given by inverse Fourier transformation of the frequency-domain expressions given above. Computation of the step response requires a prior division by  $i\omega$ .

No analytic expressions have yet been published for the general case of a source and receiver at the surface of a homogeneous earth, due to the complexity caused by the product of Bessel functions in equations (4.89), (4.90), and (4.91). However, it is easy to derive an analytic expression for the transient response of the central-loop configuration by inverse Laplace transformation of the expression (4.94). By analogy with the derivation of  $e_\phi$  in equation (4.64) from  $E_\phi$  in equation (4.55), we see that the time derivative of the negative step response is given by

$$\frac{\partial h_z}{\partial t} = -\frac{I}{\mu_0\sigma a^3} \left[ 3 \operatorname{erf}(\theta a) - \frac{2}{\pi^{1/2}} \theta a (3 + 2\theta^2 a^2) e^{-\theta^2 a^2} \right]; \quad (4.97)$$

an expression given, e.g., in Kaufman (1979).

Raab and Frishknecht (1983) give a procedure for calculating apparent resistivity for the central-loop configuration based on equation (4.97). Transient voltages are transformed to curves of apparent resistivity versus time, which are more meaningful and which aid in defining an initial guess for inversion.

The magnetic field step response at the center of the loop is evaluated by inverse Laplace transformation of equation (4.94) divided by  $s$ , employing the transform pairs used to derive equation (4.69). Applying the relation (2.44), between the positive and negative step responses, the magnetic field at the center of the loop after the current is shut off is given by

$$h_z = \frac{I}{2a} \left[ \frac{3}{\sqrt{\pi}\theta a} e^{-\theta^2 a^2} + \left( 1 - \frac{3}{2\theta^2 a^2} \right) \operatorname{erf}(\theta a) \right], \quad (4.98)$$

which agrees with the expression given in Kaufman (1979) except for the sign of the second term. The term  $I/2a$  is the magnetic field that would be present in free space before the current is shut off; multiplying by the term within the square brackets gives the decaying magnetic field due to currents flowing in the conductive earth. Differentiating equation (4.98) yields equation (4.97).

Figure 4.8 illustrates the decaying magnetic field and its time derivative at the center of a loop after a 1A current is turned off. The model is that of Figure 4.7: a loop of radius 50 m lying on a  $100 \Omega \cdot \text{m}$  half-space. Before the current is shut off, the magnetic field at the center of the loop, given by the ratio of the current to the diameter of the loop is 0.01 A/m, corresponding to a magnetic induction of about 10 nT.

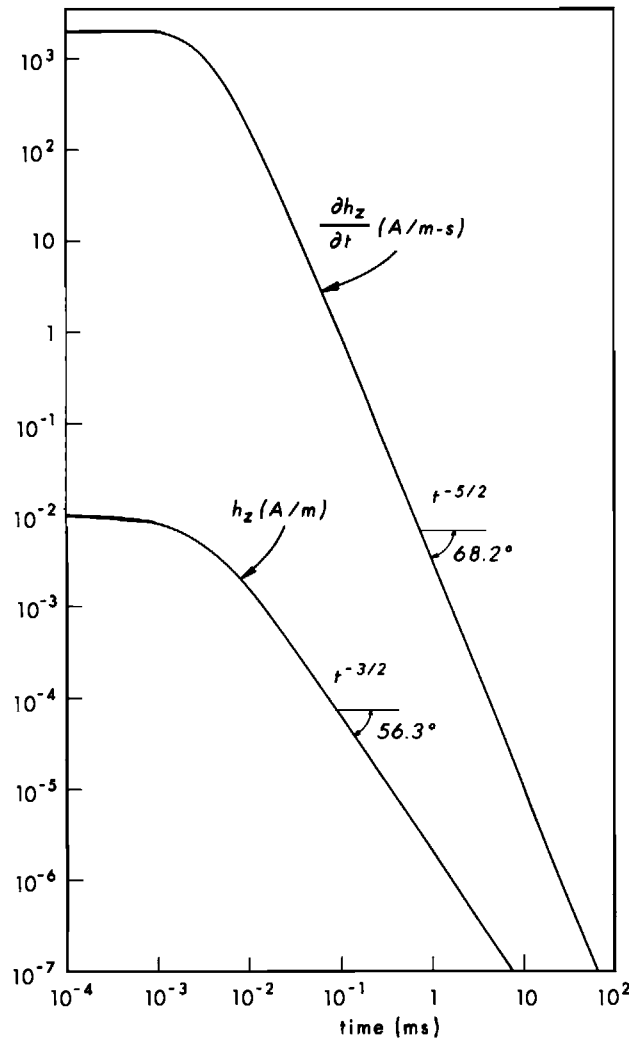


FIG. 4.8. Vertical magnetic field and its time derivative at the center of a circular loop of radius 50 m on a  $100 \Omega \cdot \text{m}$  homogeneous earth. A 1A current in the loop is turned off abruptly at zero time.

As shown in Nabighian (1979) the transient magnetic field is due to a system of circular currents that flow in the same direction as the transmitting current. With time, the maximum of this current system moves outward and downward. Nabighian showed that the magnetic field can be viewed as approximately due to a circular current filament. This “smoke ring” moves downward with velocity  $2/(\pi\sigma\mu_0 t)^{1/2}$ , and its radius is given by  $(4.37t/\sigma\mu_0)^{1/2}$ . Outside the loop, the vertical magnetic field changes sign when the smoke ring passes approximately beneath the observation point. However, as shown by Figure 4.8, both the magnetic field and its time derivative maintain the same sign at the center of the loop.

At late times (small  $\theta$  in equations (4.97) and (4.98)),

$$h_z \approx \frac{I\sigma^{3/2}\mu_0^{3/2}a^2}{30\pi^{1/2}} t^{-3/2}, \quad (4.98a)$$

and

$$\frac{\partial h_z}{\partial t} \approx \frac{-I\sigma^{3/2}\mu_0^{3/2}a^2}{20\pi^{1/2}} t^{-5/2}. \quad (4.98b)$$

Hence, as in the case of a magnetic dipole source, the vertical magnetic field and its time derivative exhibit  $t^{-3/2}$  and  $t^{-5/2}$  decays, respectively.

The transient response of the coincident-loop configuration for step excitation is given by inverse Laplace transformation of equation (4.96) divided by  $s = i\omega$ . Thus

$$v = -2\pi\mu_0 a^2 I \int_0^\infty \mathcal{L}^{-1} \left\{ \frac{1}{\lambda + u} \right\} \lambda [J_1(\lambda a)]^2 d\lambda. \quad (4.99)$$

The term in brackets can be written

$$\frac{1}{\lambda + u} = \frac{\lambda - u}{k^2} = \frac{\lambda}{\mu_0 \sigma s} - \frac{\left( s + \frac{\lambda^2}{\mu_0 \sigma} \right)^{1/2}}{(\mu_0 \sigma)^{1/2} s}.$$

The inverse Laplace transform of  $1/s$  is the unit step function, while the inverse Laplace transform of the second term is given in Erdelyi (1954, v. 1, p. 235, no. 22). Combining them,

$$v = -2\pi\mu_0 a^2 I \int_0^\infty \left\{ \frac{\lambda^2}{\mu_0 \sigma} \operatorname{erfc} \left[ \frac{\lambda t^{1/2}}{(\mu_0 \sigma)^{1/2}} \right] - \frac{\lambda}{(\pi\mu_0 \sigma t)^{1/2}} e^{-\lambda^2 t / \mu_0 \sigma} \right\} [J_1(\lambda a)]^2 d\lambda, \quad (4.100)$$

which is the expression given in Lee and Lewis (1974).

In general, equation (4.100) can only be evaluated numerically. However, Raiche and Spies (1981) expand the squared Bessel function using equation (9.1.14) in Abramowitz and Stegun (1964) and integrate term-by-term to obtain the following expression for the coincident-loop response of a homogeneous earth:

$$v = \frac{2Ia\mu_0\pi^{1/2}}{t} (\theta a)^3 \sum_{m=0}^{\infty} \frac{(-1)^m (2m+2)! (\theta a)^{2m}}{m! (m+1)! (m+2)! (2m+5)}. \quad (4.101)$$

Raiche and Spies (1981) and Raab and Frishknecht (1983) discuss the calculation of apparent resistivity for the coincident loop configuration based on equation (4.101).

### Horizontal magnetic dipole

In this section we derive the cartesian components of the magnetic fields about a horizontal,  $x$ -directed magnetic dipole above or on the surface of the earth. The fields for a  $y$ -directed dipole can be derived by a simple permutation of coordinates. In applications, a horizontal magnetic dipole represents a vertical transmitting loop if fields are measured at a distance of at least five loop radii. Due to the difficulty in producing a large dipole moment with such a source, the applications of this solution are mainly in the frequency domain, and especially in airborne EM.

**Layered Earth.**—By analogy with the solution for a vertical magnetic dipole in equation (4.40), the vector potential for the particular solution between the horizontal dipole and the earth is given by

$$\tilde{\mathbf{F}} = \frac{\hat{z}_0 m}{2u_0} e^{-u_0(z+h)} \mathbf{u}_x. \quad (4.102)$$

In this case, however, there is both a vertical electric field (from the relations 1.122)

$$\tilde{E}_z^p = \frac{\partial \tilde{F}_x}{\partial y} = ik_y \frac{\hat{z}_0 m}{2u_0} e^{-u_0(z+h)}, \quad (4.103)$$

and a vertical magnetic field (from the relations 1.123)

$$\tilde{H}_z^p = \frac{1}{\hat{z}_0} \frac{\partial^2 \tilde{F}_x}{\partial x \partial z} = -ik_x \frac{m}{2} e^{-u_0(z+h)}. \quad (4.104)$$

Now that we have expressions for the vertical fields, we have no further need for the vector potential of a magnetic dipole in equation (4.102).

Thus the EM field has both TE and TM components, which can be treated separately if we break the primary field (particular solution) into its TE and TM components. Because only the TM mode has a vertical electric field, the TM coefficient  $A_p$  in equation (4.35) is obtained by equating  $\tilde{E}_z^p$  in equation (4.103) with  $E_z$  in equation (1.129), which yields

$$A_p = -\frac{k_0^2 m}{2u_0} \frac{ik_y}{k_x^2 + k_y^2}. \quad (4.105)$$

Because only the TE mode has a vertical magnetic field, we find the TE coefficient  $F_p$  in equation (4.36), by equating  $\tilde{H}_z^p$  in equation (4.104) with  $H_z$  in equation (1.130) to obtain

$$F_p = -\frac{\hat{z}_0 m}{2} \frac{ik_x}{k_x^2 + k_y^2}. \quad (4.106)$$

Substituting the expression (4.105) into equation (4.37) and the expression (4.106) into equation (4.38), we have the following expressions for the TM and TE potentials between the dipole and the earth:

$$A(x, y, z) = -\frac{k_0^2 m}{8\pi^2} \int_{-\infty}^{\infty} \int_{-\infty}^{\infty} [e^{-u_0(z+h)} + r_{TM} e^{u_0(z-h)}] \frac{ik_y}{u_0(k_x^2 + k_y^2)} e^{i(k_x x + k_y y)} dk_x dk_y, \quad (4.107)$$

and

$$F(x, y, z) = -\frac{\hat{z}_0 m}{8\pi^2} \int_{-\infty}^{\infty} \int_{-\infty}^{\infty} [e^{-u_0(z+h)} + r_{TE} e^{u_0(z-h)}] \frac{ik_x}{k_x^2 + k_y^2} e^{i(k_x x + k_y y)} dk_x dk_y. \quad (4.108)$$

Converting from Fourier to Hankel transforms using equation (2.10),

$$A(\rho, z) = -\frac{k_0^2 m}{4\pi} \frac{\partial}{\partial y} \int_0^{\infty} [e^{-u_0(z+h)} + r_{TM} e^{u_0(z-h)}] \frac{1}{\lambda u_0} J_0(\lambda \rho) d\lambda, \quad (4.109)$$

and

$$F(\rho, z) = -\frac{\hat{z}_0 m}{4\pi} \frac{\partial}{\partial x} \int_0^{\infty} [e^{-u_0(z+h)} + r_{TE} e^{u_0(z-h)}] \frac{1}{\lambda} J_0(\lambda \rho) d\lambda. \quad (4.110)$$

The electric and magnetic fields can be derived from equations (4.109) and (4.110) using the formulas (1.129) and (1.130). The complete expressions are given in Dey and Ward

(1970). However, for a horizontal magnetic dipole source, usually only the magnetic fields are of interest in geophysical applications. Furthermore, distances usually are much greater than a wavelength in free space so that we can apply the quasi static approximation ( $k_0 \approx 0$ ). Thus we can neglect the TM mode.

Then, taking the derivatives of equation (4.110) specified by the formulas (1.130), we obtain

$$H_x = \frac{m}{4\pi} \frac{\partial^2}{\partial x^2} \int_0^\infty [e^{-\lambda(z+h)} - r_{TE} e^{\lambda(z-h)}] J_0(\lambda p) d\lambda, \quad (4.111)$$

$$H_y = \frac{m}{4\pi} \frac{\partial^2}{\partial x \partial y} \int_0^\infty [e^{-\lambda(z+h)} - r_{TE} e^{\lambda(z-h)}] J_0(\lambda p) d\lambda, \quad (4.112)$$

and

$$H_z = \frac{m}{4\pi} \frac{\partial}{\partial x} \int_0^\infty [e^{-\lambda(z+h)} + r_{TE} e^{\lambda(z-h)}] \lambda J_0(\lambda p) d\lambda, \quad (4.113)$$

with  $r_{TE}$  given by the expression (4.19).

Hence, for the low frequencies of interest in most geophysical applications, the magnetic field response of the earth is due only to currents flowing horizontally, even in this case of a horizontal magnetic dipole source.

Interchanging order of differentiation and integration and noting that

$$\frac{\partial}{\partial x} = \frac{x}{p} \frac{\partial}{\partial p}, \quad (4.114)$$

$$\frac{\partial^2}{\partial x^2} = \left( \frac{1}{p} - \frac{x^2}{p^3} \right) \frac{\partial}{\partial p} + \frac{x^2}{p^2} \frac{\partial^2}{\partial p^2}, \quad (4.115)$$

$$\frac{\partial^2}{\partial x \partial y} = -\frac{xy}{p^3} \frac{\partial}{\partial p} + \frac{xy}{p^2} \frac{\partial^2}{\partial p^2}, \quad (4.116)$$

$$\frac{\partial J_0(\lambda p)}{\partial p} = -\lambda J_1(\lambda p), \quad (4.117)$$

and

$$\frac{\partial^2 J_0(\lambda p)}{\partial p^2} = \frac{\lambda}{p} J_1(\lambda p) - \lambda^2 J_0(\lambda p), \quad (4.118)$$

then

$$\begin{aligned} H_x &= -\frac{m}{4\pi} \left( \frac{1}{p} - \frac{2x^2}{p^3} \right) \int_0^\infty [e^{-\lambda(z+h)} - r_{TE} e^{\lambda(z-h)}] \lambda J_1(\lambda p) d\lambda \\ &\quad - \frac{m}{4\pi} \frac{x^2}{p^2} \int_0^\infty [e^{-\lambda(z+h)} - r_{TE} e^{\lambda(z-h)}] \lambda^2 J_0(\lambda p) d\lambda, \\ H_y &= \frac{m}{2\pi} \frac{xy}{p^3} \int_0^\infty [e^{-\lambda(z+h)} - r_{TE} e^{\lambda(z-h)}] \lambda J_1(\lambda p) d\lambda \end{aligned} \quad (4.119)$$

$$-\frac{m}{4\pi} \frac{xy}{\rho^2} \int_0^\infty [e^{-\lambda(z+h)} - r_{TE} e^{\lambda(z-h)}] \lambda^2 J_0(\lambda\rho) d\lambda, \quad (4.120)$$

and

$$H_z = \frac{m}{4\pi} \frac{x}{\rho} \int_0^\infty [e^{-\lambda(z+h)} + r_{TE} e^{\lambda(z-h)}] \lambda^2 J_1(\lambda\rho) d\lambda. \quad (4.121)$$

These expressions are equivalent to those given in Dey and Ward (1970), allowing for the facts that they use  $m = 4\pi$ , and in their coordinate system the positive  $z$  direction is upward.

Comparing equation (4.121) with equation (4.45), which gives the radial component of the magnetic field of a vertical magnetic dipole, we see that these expressions satisfy the reciprocity relation, as required. Note that the sign of the first term in each expression must be changed if the receiver position is above the transmitter position. The reciprocity relation, simply stated, is

$$H_{ij}(\mathbf{r}, \mathbf{r}') = H_{ji}(\mathbf{r}', \mathbf{r}),$$

where the first subscript denotes the magnetic field component at the first spatial position, and the second subscript denotes the magnetic dipole component at the second spatial position.

**Homogeneous Earth.**—As in the case of a vertical magnetic dipole, we can derive analytic expressions for the fields only when the transmitter and receiver are on the surface of a homogeneous earth. The derivation for the horizontal fields is easiest if we return to equations (4.111) and (4.112), set  $z$  and  $h$  to zero, and write them in the forms

$$H_x = -\frac{m}{4\pi} \frac{\partial}{\partial x} \left( \frac{x}{\rho} \Phi \right), \quad (4.122)$$

and

$$H_y = -\frac{m}{4\pi} \frac{\partial}{\partial y} \left( \frac{x}{\rho} \Phi \right), \quad (4.123)$$

with

$$\Phi = 2 \int_0^\infty \frac{\lambda u}{\lambda + u} J_1(\lambda\rho) d\lambda. \quad (4.124)$$

Multiplying the numerator and denominator of the integrand by  $\lambda - u$ ,

$$\Phi = \frac{2}{k^2} \int_0^\infty (\lambda - u) \lambda u J_1(\lambda\rho) d\lambda,$$

or

$$\Phi = \Phi_1 + \Phi_2 + \Phi_3,$$

with

$$\Phi_1 = \frac{2}{k^2} \int_0^\infty \lambda^2 u J_1(\lambda\rho) d\lambda,$$

$$\Phi_2 = -\frac{2}{k^2} \int_0^\infty \lambda^3 J_1(\lambda p) d\lambda,$$

and

$$\Phi_3 = 2 \int_0^\infty \lambda J_1(\lambda p) d\lambda.$$

Differentiating the Sommerfeld integral (equation 4.54) once with respect to  $p$  and twice with respect to  $z$  and setting  $z$  to zero,

$$\Phi_1 = \frac{2}{k^2 p^4} (k^2 p^2 - 3ikp - 3)e^{-ikp}.$$

Differentiating the Lipschitz integral (equation 4.53) once with respect to  $p$  and setting  $z$  to zero yields an expression for  $\Phi_3$ , while further differentiating twice with respect to  $z$  before setting  $z$  to zero provides a simple expression for  $\Phi_2$ . Thus

$$\Phi_2 = \frac{6}{k^2 p^4},$$

and

$$\Phi_3 = \frac{2}{p^2}.$$

Finally,

$$\Phi = \frac{2}{k^2 p^4} [3 + k^2 p^2 - (3 + 3ikp - k^2 p^2)e^{-ikp}]. \quad (4.125)$$

Substituting for  $\Phi$  in equations (4.122) and (4.123), we can write the horizontal magnetic fields in the following forms:

$$H_x = -\frac{m}{4\pi p^3} \left[ y^2 \Phi + x^2 p \frac{\partial \Phi}{\partial p} \right], \quad (4.126)$$

and

$$H_y = \frac{m}{4\pi p^3} \left[ xy \Phi - xyp \frac{\partial \Phi}{\partial p} \right], \quad (4.127)$$

with

$$\frac{\partial \Phi}{\partial p} = \frac{2}{k^2 p^5} [-2k^2 p^2 - 12 + (-ik^3 p^3 - 5k^2 p^2 + 12ikp + 12)e^{-ikp}]. \quad (4.128)$$

The primary vertical magnetic field is zero in the plane of the dipole. Thus we only need to evaluate the secondary field, which, from expression (4.121) can be written

$$H_z = -\frac{m}{4\pi} \frac{x}{p} \frac{\partial}{\partial p} \int_0^\infty \frac{\lambda - u}{\lambda + u} \lambda J_0(\lambda p) d\lambda.$$

Except for the sign change required by reciprocity and the factor  $x/\rho$ , this expression is the same as expression (4.57) for the radial component of magnetic field due to a horizontal magnetic dipole. Equation (4.57) is for the radial magnetic field at  $\rho$  due to a vertical magnetic dipole at the origin, which, by reciprocity, is the same as the vertical magnetic field at the origin due to a radial magnetic dipole at  $\rho$ . In the present case, however, we are evaluating the vertical magnetic field at distance  $x$  from a horizontal magnetic dipole at the origin. Hence, from the expression (4.59)

$$H_z = \frac{mk^2x}{4\pi\rho^2} \left[ I_1\left(\frac{ik\rho}{2}\right)K_1\left(\frac{ik\rho}{2}\right) - I_2\left(\frac{ik\rho}{2}\right)K_2\left(\frac{ik\rho}{2}\right) \right]. \quad (4.129)$$

**Mutual Impedance of Loops.**—Particularly useful forms result from evaluating these expressions for  $H_x$  and  $H_z$  on the  $x$  and  $y$  axes. Wait (1955) and Frishknecht (1967) put them in the form of mutual impedance ratios  $Z/Z_0$ , where  $Z$  is the mutual impedance of small loops at the surface of the earth, and  $Z_0$  is the mutual impedance of the same loops in free space. These ratios are obtained by dividing our expressions for  $H_x$  and  $H_z$  by the fields that would be measured in free space. For coplanar loops the free space field is  $-m/4\pi\rho^3$ , while for coaxial loops it is  $m/2\pi\rho^3$ .

Some particular cases are the following:

(a) vertical coplanar loops (from equation 4.126 with  $x = 0$ ):

$$Z/Z_0 = \frac{2}{k^2\rho^2} [3 + k^2\rho^2 - (3 + 3ik\rho - k^2\rho^2)e^{-ik\rho}] \quad (4.130)$$

(b) horizontal coplanar loops (from equation 4.56):

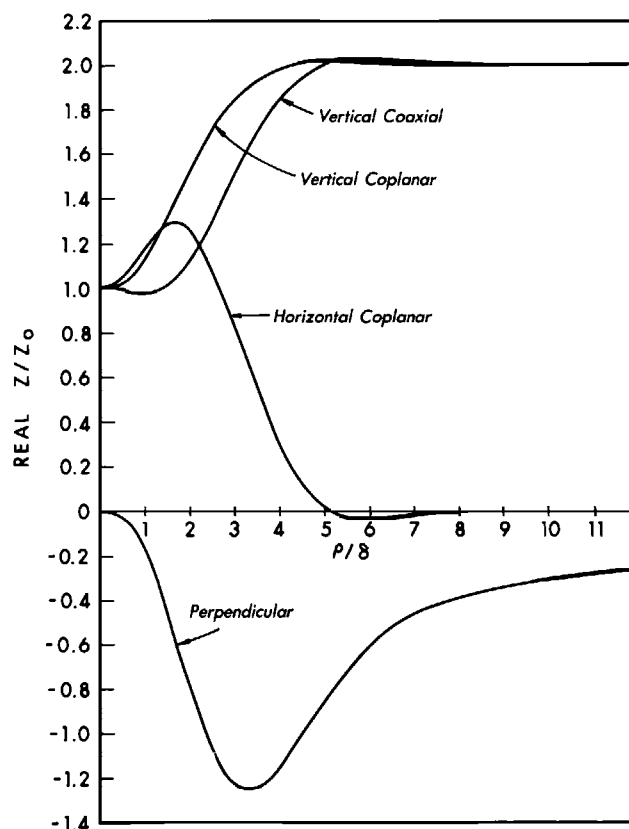


FIG. 4.9. Real part of mutual impedance for various loop configurations over a homogeneous earth as a function of loop separation in skin depths.

$$Z/Z_0 = \frac{2}{k^2 p^2} [-9 + (9 + 9ikp - 4k^2 p^2 - ik^3 p^3)e^{-ikp}] \quad (4.131)$$

(c) vertical coaxial loops (from equation 4.126 with  $y = 0$ ):

$$Z/Z_0 = \frac{1}{k^2 p^2} [12 + 2k^2 p^2 - (12 + 12ikp - 5k^2 p^2 - ik^3 p^3)e^{-ikp}] \quad (4.132)$$

(d) perpendicular loops (vertical transmitting loop with horizontal receiving loop along axis of transmitting loop; from equation (4.129) with  $x = p$  and  $Z_0 = m/2\pi p^3$ ):

$$Z/Z_0 = \frac{k^2 p^2}{2} \left[ I_1\left(\frac{ikp}{2}\right) K_1\left(\frac{ikp}{2}\right) - I_2\left(\frac{ikp}{2}\right) K_2\left(\frac{ikp}{2}\right) \right]. \quad (4.133)$$

Wait (1955) shows plots of the amplitudes of these and other mutual impedance ratios for a homogeneous earth, while Frishknecht (1967) gives extensive tables of mutual impedance ratios for homogeneous and two-layer earths. Figures 4.9 and 4.10 show the real and imaginary mutual impedances, respectively, for four loop configurations over a homogeneous earth calculated using expressions (4.130)–(4.133). The curves are plotted as a function of the ratio  $p/\delta$ , i.e. the loop separation in skin depths. Except for perpendicular loops, the in-phase components approach 1 at low frequencies and either 0 or 2 at high frequencies. The in-phase component for perpendicular loops and all of the out-of-phase components go to zero at both low and high frequencies, with either a positive or negative peak at intermediate frequencies.

Knowledge of various mutual impedance ratios for small loops also is important in airborne EM applications. In that case, however, even for a homogeneous earth they can be computed only by numerically integrating equations (4.46), (4.119), and (4.121). Such cases are included in Frishknecht's tables.

### Horizontal electric dipole

A source consisting of a short grounded wire can be treated as an electric dipole if the distance to an observation point is much greater than (at least 5 times) the dipole length. In most geophysical applications, however, measurements are made closer to the wire, in which

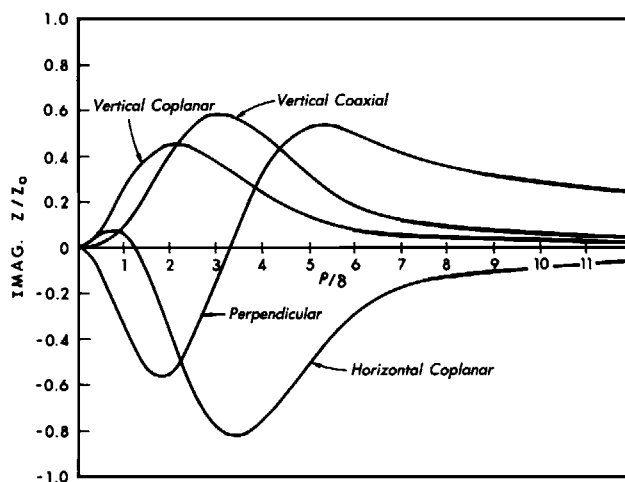


FIG. 4.10. Imaginary part of mutual impedance for various loop configurations over a homogeneous earth as a function of loop separation in skin depths.

case the source must be treated as a superposition of electric dipoles. Because the EM field of a vertical electric dipole is a TM field and hence is insensitive to conductivity changes in the earth at low frequencies, we consider only a horizontal electric dipole.

**Layered Earth.**—By analogy with equations (2.8), (2.13), and (2.38), the 2-D Fourier transform of the particular solution for the vector potential of an  $x$ -directed electric dipole is

$$\bar{\mathbf{A}} = \frac{Ids}{2u_0} e^{-u_0(z+h)} \mathbf{u}_x,$$

where  $I$  is the current in the dipole, and  $ds$  is its length. The dipole is located on the  $z$  axis at point  $z = -h$  above the earth's surface, and the vector potential is evaluated between the dipole and the earth.

From the field expressions (1.122) and (1.123) it is apparent that the dipole produces both a vertical electric field

$$\tilde{E}_z^p = \frac{1}{\hat{y}_0} \frac{\partial^2 \tilde{A}_x}{\partial x \partial z} = -\frac{Ids}{2\hat{y}_0} ik_x e^{-u_0(z+h)} \quad (4.134)$$

and a vertical magnetic field

$$\tilde{H}_z^p = -\frac{\partial \tilde{A}_x}{\partial y} = -\frac{Ids}{2} \frac{ik_y}{u_0} e^{-u_0(z+h)}. \quad (4.135)$$

Hence, as in the case of a horizontal magnetic dipole, the EM field has both TE and TM components. The TE and TM fields can be treated separately by breaking the primary field into its TE and TM components.

Because only the TM mode has a vertical electric field, the TM coefficient  $A_p$  in equation (4.35) is obtained by equating  $\tilde{E}_z^p$  in equation (4.134) with  $E_z$  in the field expressions (1.129) for Cartesian coordinates. Thus

$$A_p = -\frac{Ids}{2} \frac{ik_x}{k_x^2 + k_y^2}. \quad (4.136)$$

Because only the TE mode has a vertical magnetic field, we find the TE coefficient  $F_p$  in equation (4.36), by equating  $\tilde{H}_z^p$  in equation (4.135) with  $H_z$  in the field expressions (1.130) to obtain

$$F_p = -\frac{\hat{z}_0 Ids}{2u_0} \frac{ik_y}{k_x^2 + k_y^2}. \quad (4.137)$$

Substituting these expressions into equations (4.37) and (4.38), as in the case of similar expressions for a horizontal magnetic dipole, yields the following expressions for the TM and TE potentials between the dipole and the earth:

$$A(x, y, z) = -\frac{Ids}{8\pi^2} \int_{-\infty}^{\infty} \int_{-\infty}^{\infty} [e^{-u_0(z+h)} + r_{TM} e^{u_0(z-h)}] \frac{ik_x}{k_x^2 + k_y^2} e^{i(k_x x + k_y y)} dk_x dk_y \quad (4.138)$$

and

$$F(x, y, z) = -\frac{\hat{z}_0 Ids}{8\pi^2} \int_{-\infty}^{\infty} \int_{-\infty}^{\infty} [e^{-u_0(z+h)} + r_{TE} e^{u_0(z-h)}] \frac{ik_y}{u_0(k_x^2 + k_y^2)} e^{i(k_x x + k_y y)} dk_x dk_y. \quad (4.139)$$

To derive the electric fields, apply the expressions (1.129) to equations (4.138) and (4.139). Only the horizontal electric fields are of interest and only for the case of a dipole at the

earth's surface ( $h = 0$ ). Thus the  $x$ -component of the electric field above the earth (or on the earth's surface if  $z = 0$ ) is given by

$$E_x = -\frac{Ids}{8\pi^2 \hat{y}_0} \int_{-\infty}^{\infty} \int_{-\infty}^{\infty} [1 - r_{TM}] e^{u_0 z} \frac{u_0 k_x^2}{k_x^2 + k_y^2} e^{i(k_x x + k_y y)} dk_x dk_y \\ - \frac{\hat{z}_0 Ids}{8\pi^2} \int_{-\infty}^{\infty} \int_{-\infty}^{\infty} [1 + r_{TE}] e^{u_0 z} \frac{k_y^2}{u_0 (k_x^2 + k_y^2)} e^{i(k_x x + k_y y)} dk_x dk_y. \quad (4.140)$$

To simplify subsequent development for a long grounded wire, it is important to separate the solution into terms with charge and current sources. This separation is effected by making the substitution

$$\frac{k_y^2}{k_x^2 + k_y^2} = 1 - \frac{k_x^2}{k_x^2 + k_y^2}.$$

Thus

$$E_x = -\frac{Ids}{8\pi^2} \int_{-\infty}^{\infty} \int_{-\infty}^{\infty} \left[ \frac{u_0}{\hat{y}_0} - \frac{\hat{z}_0}{u_0} - \frac{\hat{z}_0}{u_0} r_{TE} - \frac{u_0}{\hat{y}_0} r_{TM} \right] e^{u_0 z} \frac{k_x^2}{k_x^2 + k_y^2} e^{i(k_x x + k_y y)} dk_x dk_y \\ - \frac{\hat{z}_0 Ids}{8\pi^2} \int_{-\infty}^{\infty} \int_{-\infty}^{\infty} [1 + r_{TE}] e^{u_0 z} \frac{1}{u_0} e^{i(k_x x + k_y y)} dk_x dk_y. \quad (4.141)$$

Converting from Fourier to Hankel transforms using equation (2.10) and setting  $z$  to zero so that the field is evaluated at the surface of the earth.

$$E_x = \frac{Ids}{4\pi} \frac{\partial^2}{\partial x^2} \int_0^{\infty} \left[ (1 - r_{TM}) \frac{u_0}{\hat{y}_0} - (1 + r_{TE}) \frac{\hat{z}_0}{u_0} \right] \frac{1}{\lambda} J_0(\lambda \rho) d\lambda \\ - \frac{\hat{z}_0 Ids}{4\pi} \int_0^{\infty} (1 + r_{TE}) \frac{\lambda}{u_0} J_0(\lambda \rho) d\lambda, \quad (4.142)$$

or

$$E_x = -\frac{Ids}{4\pi} \frac{\partial}{\partial x} \frac{x}{\rho} \int_0^{\infty} \left[ (1 - r_{TM}) \frac{u_0}{\hat{y}_0} - (1 + r_{TE}) \frac{\hat{z}_0}{u_0} \right] J_1(\lambda \rho) d\lambda \\ - \frac{\hat{z}_0 Ids}{4\pi} \int_0^{\infty} (1 + r_{TE}) \frac{\lambda}{u_0} J_0(\lambda \rho) d\lambda. \quad (4.143)$$

We leave the solution in this form, because in the important case of a long grounded wire the  $x$ -derivative in the first term disappears when the solution is integrated over the wire. Then the remainder of the first term, with a change in sign, is evaluated for each grounding point.

From a similar derivation

$$E_y = -\frac{Ids}{4\pi} \frac{\partial}{\partial x} \frac{y}{\rho} \int_0^{\infty} \left[ (1 - r_{TM}) \frac{u_0}{\hat{y}_0} - (1 + r_{TE}) \frac{\hat{z}_0}{u_0} \right] J_1(\lambda \rho) d\lambda. \quad (4.144)$$

The magnetic field components are found by applying the expressions (1.130) to equations

(4.138) and (4.139). Thus, for a horizontal electric dipole at the earth's surface, the  $x$ -component of magnetic field on or above the earth's surface is

$$H_x = \frac{Ids}{8\pi^2} \int_{-\infty}^{\infty} \int_{-\infty}^{\infty} (1 + r_{TM}) e^{u_0 z} \frac{k_x k_y}{k_x^2 + k_y^2} e^{i(k_x x + k_y y)} dk_x dk_y - \frac{Ids}{8\pi^2} \int_{-\infty}^{\infty} \int_{-\infty}^{\infty} (1 - r_{TE}) e^{u_0 z} \frac{k_x k_y}{k_x^2 + k_y^2} e^{i(k_x x + k_y y)} dk_x dk_y. \quad (4.145)$$

Combining the integrals in expression (4.145), converting to a Hankel transform using equation (2.10), and retaining the  $z$  dependence so that the solution applies to semiairborne applications,

$$H_x = -\frac{Ids}{4\pi} \frac{\partial^2}{\partial x \partial y} \int_0^{\infty} (r_{TM} + r_{TE}) e^{u_0 z} \frac{1}{\lambda} J_0(\lambda \rho) d\lambda. \quad (4.146)$$

Note that there is no primary  $H_x$ , as expected for an  $x$ -directed electric dipole in a whole space.

Applying the  $y$  derivative to the Bessel function yields

$$H_x = \frac{Ids}{4\pi} \frac{\partial}{\partial x} \frac{y}{\rho} \int_0^{\infty} (r_{TM} + r_{TE}) e^{u_0 z} J_1(\lambda \rho) d\lambda. \quad (4.147)$$

The remaining derivative will be cancelled when the expression is integrated over a grounded wire oriented in the  $x$  direction.

The  $y$ -component is given by

$$H_y = -\frac{Ids}{8\pi^2} \int_{-\infty}^{\infty} \int_{-\infty}^{\infty} (1 + r_{TM}) e^{u_0 z} \frac{k_x^2}{k_x^2 + k_y^2} e^{i(k_x x + k_y y)} dk_x dk_y - \frac{Ids}{8\pi^2} \int_{-\infty}^{\infty} \int_{-\infty}^{\infty} (1 - r_{TE}) e^{u_0 z} \frac{k_y^2}{k_x^2 + k_y^2} e^{i(k_x x + k_y y)} dk_x dk_y. \quad (4.148)$$

Following a derivation similar to that for equation (4.141),

$$H_y = -\frac{Ids}{8\pi^2} \int_{-\infty}^{\infty} \int_{-\infty}^{\infty} (r_{TM} + r_{TE}) e^{u_0 z} \frac{k_x^2}{k_x^2 + k_y^2} e^{i(k_x x + k_y y)} dk_x dk_y - \frac{Ids}{8\pi^2} \int_{-\infty}^{\infty} \int_{-\infty}^{\infty} (1 - r_{TE}) e^{u_0 z} e^{i(k_x x + k_y y)} dk_x dk_y, \quad (4.149)$$

or, in terms of Hankel transforms,

$$H_y = -\frac{Ids}{4\pi} \frac{\partial}{\partial x} \frac{x}{\rho} \int_0^{\infty} (r_{TM} + r_{TE}) e^{u_0 z} J_1(\lambda \rho) d\lambda - \frac{Ids}{4\pi} \int_0^{\infty} (1 - r_{TE}) e^{u_0 z} \lambda J_0(\lambda \rho) d\lambda. \quad (4.150)$$

Finally, the vertical magnetic field, which depends only on the TE potential  $F$ , is given by

$$H_z = -\frac{Ids}{8\pi^2} \int_{-\infty}^{\infty} \int_{-\infty}^{\infty} (1 + r_{TE}) e^{u_0 z} \frac{ik_y}{u_0} e^{i(k_x x + k_y y)} dk_x dk_y, \quad (4.151)$$

or, as a Hankel transform

$$H_z = \frac{Ids}{4\pi} \frac{y}{\rho} \int_0^{\infty} (1 + r_{TE}) e^{u_0 z} \frac{\lambda^2}{u_0} J_1(\lambda\rho) d\lambda. \quad (4.152)$$

**Homogeneous Earth, Frequency Domain.**—As usual in finite-source problems the only case for which analytic solutions can be derived readily is that where the transmitter and receiver are on the surface of the earth, and the frequency is low enough that the quasi-static approximation applies. When  $r_{TM}$  and  $r_{TE}$  from the definitions (4.31) and (4.32) are substituted in the expressions (4.142) and (4.144) for  $E_x$  and  $E_y$ , respectively, the integrands simplify considerably, because

$$(1 - r_{TM}) \frac{u_0}{\hat{y}_0} = 2 \left[ \frac{u_1/\hat{y}_1}{u_0/\hat{y}_0 + u_1/\hat{y}_1} \right] \frac{u_0}{\hat{y}_0} \approx 2 \frac{u_1}{\hat{y}_1},$$

and

$$2 \frac{u_1}{\hat{y}_1} - (1 + r_{TE}) \frac{\hat{z}_0}{u_0} = \frac{2}{\hat{y}_1} \left( u_1 + \frac{k_1^2}{u_0 + u_1} \right) = \frac{2\lambda}{\hat{y}_1}.$$

Thus, using the Lipschitz integral, we can write  $E_x$  and  $E_y$  in the notation of Sunde (1968) as

$$E_x = Ids \left[ -P(\rho) + \frac{\partial^2 Q(\rho)}{\partial x^2} \right], \quad (4.153)$$

and

$$E_y = Ids \frac{\partial^2 Q(\rho)}{\partial x \partial y}, \quad (4.154)$$

with

$$Q(\rho) = \frac{1}{2\pi\sigma\rho}, \quad (4.155)$$

and

$$P(\rho) = \frac{i\omega\mu_0}{2\pi} \int_0^{\infty} \frac{\lambda}{\lambda + u} J_0(\lambda\rho) d\lambda. \quad (4.156)$$

Here  $\sigma$  is the conductivity of the half-space,  $\rho$  denotes radial distance ( $\rho^2 = x^2 + y^2$ ), and we have set  $u = u_1$  for notational simplicity.

We already have found a closed form expression for the integral (4.156), which is known as the Foster integral, when we evaluated the integral (4.52). Thus

$$P(\rho) = \frac{1}{2\pi\sigma\rho^3} [1 - (ik\rho + 1)e^{-ik\rho}]. \quad (4.157)$$

Equations (4.153) and (4.154) apply to a general layered earth, but in that case  $P$  and  $Q$  are the much more complicated expressions defined implicitly in equations (4.143) and (4.144). Only for a homogeneous earth is the grounding term  $Q$  independent of frequency.

Equation (4.153) for the electric field parallel to the dipole can be reduced to

$$E_x = \frac{Ids}{2\pi\sigma\rho^3} \left[ -2 + (ik\rho + 1)e^{-ik\rho} + \frac{3x^2}{\rho^2} \right], \quad (4.158)$$

or, equivalently,

$$E_x = \frac{Ids}{2\pi\sigma\rho^3} \left[ 1 + (ik\rho + 1)e^{-ik\rho} - \frac{3y^2}{\rho^2} \right]. \quad (4.159)$$

Substituting the quasi-static approximations (4.33) and (4.34) for  $r_{TE}$  and  $r_{TM}$  in equation (4.146) and setting  $z$  to zero yields an expression for the  $x$  component of magnetic field at the surface of the earth:

$$H_x = -\frac{Ids}{4\pi} \frac{\partial^2}{\partial x \partial y} \int_0^\infty \frac{2}{\lambda + u} J_0(\lambda\rho) d\lambda. \quad (4.160)$$

Kaufman and Keller (1983) rewrite expression (4.160) as

$$H_x = -\frac{Ids}{4\pi} \frac{\partial^2}{\partial x \partial y} \left\{ \int_0^\infty \frac{1}{u} J_0(\lambda\rho) d\lambda + \int_0^\infty \frac{1}{u} \frac{u-\lambda}{u+\lambda} J_0(\lambda\rho) d\lambda \right\}, \quad (4.161)$$

Then they apply the identity

$$\int_0^\infty \frac{1}{u} \left( \frac{u-\lambda}{u+\lambda} \right)^n J_0(\lambda\rho) d\lambda = I_n \left( \frac{ik\rho}{2} \right) K_n \left( \frac{ik\rho}{2} \right), \quad (4.162)$$

which can be derived from Erdelyi (1954, v. 2, p. 8, no. 17) and the fact that  $I_n$  and  $K_n$  are even functions. Thus

$$H_x = -\frac{Ids}{4\pi} \frac{\partial^2}{\partial x \partial y} \left[ I_0 \left( \frac{ik\rho}{2} \right) K_0 \left( \frac{ik\rho}{2} \right) + I_1 \left( \frac{ik\rho}{2} \right) K_1 \left( \frac{ik\rho}{2} \right) \right]. \quad (4.163)$$

Applying the recurrence relations (Watson, 1944):

$$I'_0(z) = I_1(z),$$

$$K'_0(z) = -K_1(z),$$

$$I'_1(z) = I_0(z) - \frac{1}{z} I_1(z), \quad (4.164)$$

and

$$K'_1(z) = -K_0(z) - \frac{1}{z} K_1(z),$$

then

$$H_x = \frac{Ids}{2\pi} \frac{\partial}{\partial x} \left[ \frac{y}{\rho^2} I_1\left(\frac{ik\rho}{2}\right) K_1\left(\frac{ik\rho}{2}\right) \right]. \quad (4.165)$$

Carrying out the  $x$  derivative yields

$$H_x = \frac{Ids}{4\pi} \frac{xy}{\rho^4} \left\{ ik\rho \left[ I_0\left(\frac{ik\rho}{2}\right) K_1\left(\frac{ik\rho}{2}\right) - I_1\left(\frac{ik\rho}{2}\right) K_0\left(\frac{ik\rho}{2}\right) \right] - 8I_1\left(\frac{ik\rho}{2}\right) K_1\left(\frac{ik\rho}{2}\right) \right\}, \quad (4.166)$$

which agrees with the expression given in Kaufman and Keller (1983).

To find the  $y$ -component of magnetic field at the surface of the earth, substitute the approximations (4.33) and (4.34) for  $r_{TE}$  and  $r_{TM}$  in equation (4.150) to obtain

$$H_y = \frac{Ids}{4\pi} \frac{\partial^2}{\partial x^2} \int_0^\infty \frac{2}{\lambda + u} J_0(\lambda\rho) d\lambda - \frac{Ids}{4\pi} \int_0^\infty \frac{2\lambda u}{\lambda + u} J_0(\lambda\rho) d\lambda. \quad (4.167)$$

We already have evaluated the first integral in deriving equation (4.163). Again following Kaufman and Keller (1983), write the second integral as

$$\int_0^\infty \frac{2\lambda u}{\lambda + u} J_0(\lambda\rho) d\lambda = \int_0^\infty \lambda J_0(\lambda\rho) d\lambda - \frac{k^2}{4} \int_0^\infty \frac{1}{u} \left[ 1 - \left( \frac{u - \lambda}{u + \lambda} \right)^2 \right] J_0(\lambda\rho) d\lambda. \quad (4.168)$$

From the relation

$$\int_0^\infty \lambda J_0(\lambda\rho) d\lambda = 0 \quad (4.169)$$

and the identity (4.162), we find

$$H_y = -\frac{Ids}{2\pi} \frac{\partial}{\partial x} \left[ \frac{x}{\rho^2} I_1\left(\frac{ik\rho}{2}\right) K_1\left(\frac{ik\rho}{2}\right) \right] + \frac{Ids k^2}{16\pi} \left[ I_0\left(\frac{ik\rho}{2}\right) K_0\left(\frac{ik\rho}{2}\right) - I_2\left(\frac{ik\rho}{2}\right) K_2\left(\frac{ik\rho}{2}\right) \right]. \quad (4.170)$$

After taking the  $x$ -derivative and combining terms

$$H_y = -\frac{Ids}{4\pi\rho^2} \left\{ 6I_1K_1 + ik\rho(I_1K_0 - I_0K_1) + \frac{x^2}{\rho^2} [ik\rho(I_0K_1 - I_1K_0) - 8I_1K_1] \right\}, \quad (4.171)$$

where the argument of the modified Bessel functions is  $ik\rho/2$  as above. Equation (4.171) agrees with the expression given in Kaufman and Keller (1983) except that their expression has a 2 instead of an 8 in the last term.

Finally, the quasi-static vertical magnetic field is given by setting  $k_0$  and  $z$  to zero in equation (4.152) to obtain

$$H_z = \frac{Ids}{2\pi} \frac{y}{\rho} \int_0^\infty \frac{\lambda^2}{\lambda + u} J_1(\lambda\rho) d\lambda. \quad (4.172)$$

We encountered this integral previously in equation (4.49), the expression for the electric field of a vertical magnetic dipole. Thus, from equation (4.55),

$$H_z = -\frac{Ids}{2\pi k^2 \rho^5} [3 - (3 + 3ik\rho - k^2 \rho^2)e^{-ik\rho}]. \quad (4.173)$$

Note that reciprocity is satisfied: the vertical magnetic field broadside to the electric dipole ( $\rho = y$ ) is the same as the electric field due to a vertical magnetic dipole if the substitution  $Ids = -i\omega\mu_0 m$  is made. It is important also to note that there are no grounding terms (due to  $x$ -derivatives) in the expression for the vertical magnetic field.

**Homogeneous Earth, Time Domain.**—As in the case of a magnetic dipole, the response due to a step function current is obtained by substituting  $s = i\omega$  in the frequency domain expression, dividing by  $s$ , and deriving the inverse Laplace transform. Thus, from expressions (4.153) and (4.154),

$$e_x = Ids \left[ -p(\rho) + \frac{\partial^2 q(\rho)}{\partial x^2} \right], \quad (4.174)$$

and

$$e_y = Ids \frac{\partial^2 q(\rho)}{\partial x \partial y}, \quad (4.175)$$

with

$$q(\rho) = \frac{1}{2\pi\sigma\rho} u(t), \quad (4.176)$$

and

$$p(\rho) = \frac{1}{2\pi\sigma\rho^3} \left[ \text{erf}(\theta\rho) - \frac{2}{\pi^{1/2}} \theta\rho e^{-\theta^2\rho^2} \right], \quad (4.177)$$

where, as usual,  $\theta^2 = \mu\sigma/4t$ . Equation (4.177) can be derived by substituting  $s = i\omega$  in equation (4.157), dividing by  $s$ , and applying the Laplace transform pairs given in equations (4.60), (4.61), and (4.62).

The  $h_x$  impulse response (time derivative of the step response) can be derived from equation (4.165) using equation (4.71). Thus, for a step current,

$$\frac{\partial h_x}{\partial t} = \frac{Ids}{4\pi t} \frac{\partial}{\partial x} \left[ \frac{y}{\rho^2} e^{-\theta^2\rho^2/2} I_1\left(\frac{\theta^2\rho^2}{2}\right) \right]. \quad (4.178)$$

After taking the  $x$ -derivative,

$$\frac{\partial h_x}{\partial t} = -\frac{Idsxy}{4\pi t^4} e^{-\theta^2\rho^2/2} \left[ (\theta^2\rho^2 + 4)I_1\left(\frac{\theta^2\rho^2}{2}\right) - \theta^2\rho^2 I_0\left(\frac{\theta^2\rho^2}{2}\right) \right], \quad (4.179)$$

which is similar to expressions given in Kaufman and Keller (1983) and in Weir (1980).

In a similar manner, from equation (4.170),

$$\begin{aligned} \frac{\partial h_y}{\partial t} = & \frac{Ids}{4\pi t} \frac{\partial}{\partial x} \left[ \frac{x}{\rho^2} e^{-\theta^2\rho^2/2} I_1\left(\frac{\theta^2\rho^2}{2}\right) \right] + \frac{Ids\mu\sigma}{32\pi} \frac{\partial}{\partial t} \left[ \frac{1}{t} e^{-\theta^2\rho^2/2} I_0\left(\frac{\theta^2\rho^2}{2}\right) \right. \\ & \left. - \frac{1}{t} e^{-\theta^2\rho^2/2} I_2\left(\frac{\theta^2\rho^2}{2}\right) \right]. \end{aligned} \quad (4.180)$$

After taking the time derivative and applying the recurrence relation  $I_2(\alpha) = I_0(\alpha) - 2I_1(\alpha)/\alpha$ ,

$$\frac{\partial h_y}{\partial t} = \frac{Ids}{4\pi t} \frac{\partial}{\partial x} \left[ \frac{x}{\rho^2} e^{-\theta^2 \rho^2/2} I_1\left(\frac{\theta^2 \rho^2}{2}\right) \right] - \frac{Ids\theta^2}{4\pi t} e^{-\theta^2 \rho^2/2} \left[ I_0\left(\frac{\theta^2 \rho^2}{2}\right) - \left(1 + \frac{2}{\theta^2 \rho^2}\right) I_1\left(\frac{\theta^2 \rho^2}{2}\right) \right]. \quad (4.181)$$

Carrying out the  $x$ -derivative yields

$$\begin{aligned} \frac{\partial h_y}{\partial t} = & \frac{Ids\theta^2}{\mu_0 \sigma \pi \rho^2} e^{-\theta^2 \rho^2/2} \left\{ 3I_1\left(\frac{\theta^2 \rho^2}{2}\right) + \theta^2 \rho^2 \left[ I_1\left(\frac{\theta^2 \rho^2}{2}\right) - I_0\left(\frac{\theta^2 \rho^2}{2}\right) \right] \right. \\ & \left. - \frac{x^2}{\rho^2} \left[ (\theta^2 \rho^2 + 4)I_1\left(\frac{\theta^2 \rho^2}{2}\right) - \theta^2 \rho^2 I_0\left(\frac{\theta^2 \rho^2}{2}\right) \right] \right\}, \end{aligned} \quad (4.182)$$

which agrees with the expression given in Kaufman and Keller (1983).

By analogy with the derivation of the electric field of a vertical magnetic dipole given in equation (4.64), inverse Laplace transformation of equation (4.173) yields

$$\frac{\partial h_z}{\partial t} = \frac{Ids}{2\pi\sigma\mu_0} \frac{y}{\rho^5} \left[ 3 \operatorname{erf}(\theta\rho) - \frac{2}{\pi^{1/2}} \theta\rho(3 + 2\theta^2\rho^2)e^{-\theta^2\rho^2} \right], \quad (4.183)$$

an expression given in Kaufman and Keller (1983) and in Weir (1980).

### Long grounded wire

In most geophysical applications, to overcome natural field noise one must use a long grounded wire source that cannot be approximated as an electric dipole. The EM field components are given by integrating the dipole expressions along the wire, which is the reason we have retained the derivatives with respect to  $x$  in the dipole fields. In those expressions  $ds$  is replaced by  $dx'$  and  $\partial/\partial x$  by  $-\partial/\partial x'$ . We assume that the wire is centered at the origin and extends from  $-L$  to  $L$  along the  $x$ -axis.

**Layered Earth.**—From equations (4.143) and (4.144), the electric fields at the surface of a layered earth are given by

$$E_x = -I \left[ \int_{-L}^L P(R) dx' + \frac{\partial Q(R)}{\partial x} \Big|_{R_1}^{R_2} \right], \quad (4.184)$$

and

$$E_y = -I \frac{\partial Q(R)}{\partial y} \Big|_{R_1}^{R_2}, \quad (4.185)$$

with

$$P(R) = \frac{\hat{z}_0 I}{4\pi} \int_0^\infty (1 + r_{TE}) \frac{\lambda}{u_0} J_0(\lambda R) d\lambda, \quad (4.186)$$

$$\frac{\partial Q(R)}{\partial x} = -\frac{I}{4\pi R} \frac{x}{R} \int_0^\infty \left[ (1 - r_{TM}) \frac{u_0}{\hat{y}_0} - (1 + r_{TE}) \frac{\hat{z}_0}{u_0} \right] J_1(\lambda R) d\lambda, \quad (4.187)$$

$$R = [(x - x')^2 + y^2]^{1/2},$$

$$R_1 = [(x + L)^2 + y^2]^{1/2},$$

and

$$R_2 = [(x - L)^2 + y^2]^{1/2},$$

and where  $\partial Q/\partial y$  is given by equation (4.187) with  $x$  replaced by  $y$ .

From equation (4.147), at or above the surface of the earth,

$$H_x = -\frac{I}{4\pi} \frac{y}{R} \int_0^\infty (r_{TM} + r_{TE}) e^{\mu_0 z} J_1(\lambda R) d\lambda |_{R_1}^{R_2}. \quad (4.188)$$

From equation (4.150)

$$H_y = -\frac{I}{4\pi} \frac{x}{R} \int_0^\infty (r_{TM} + r_{TE}) e^{\mu_0 z} J_1(\lambda R) d\lambda |_{R_1}^{R_2} - \frac{I}{4\pi} \int_{-L}^L \int_0^\infty (1 - r_{TE}) e^{\mu_0 z} \lambda J_0(\lambda R) d\lambda dx'. \quad (4.189)$$

From equation (4.152)

$$H_z = \frac{I}{4\pi} \int_{-L}^L \frac{y}{R} \int_0^\infty (1 + r_{TE}) e^{\mu_0 z} \frac{\lambda^2}{\mu_0} J_1(\lambda R) d\lambda dx'. \quad (4.190)$$

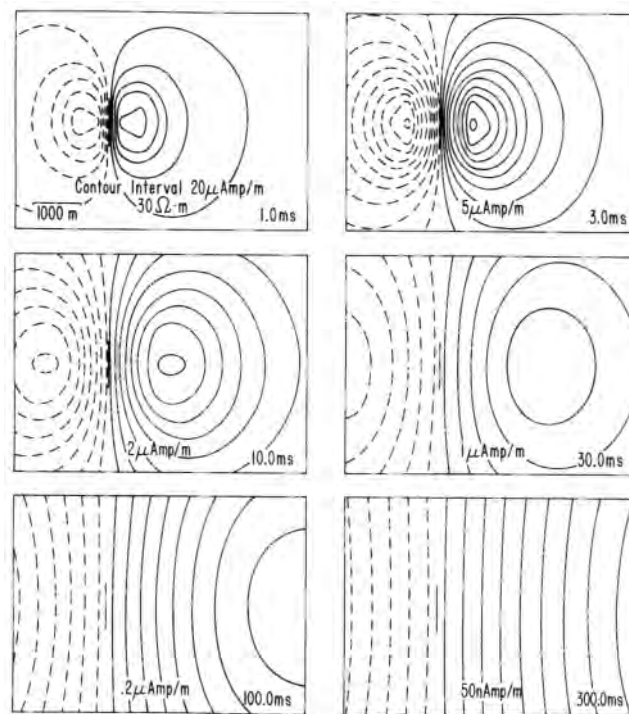


FIG. 4.11. Plan view showing vertical magnetic field contours around a 1 km, grounded-wire transmitter on a  $30 \Omega \cdot m$  homogeneous half-space from 1 to 300 ms after the current is turned off. Solid contours positive, dashed contours negative.

These expressions for the electric and magnetic fields are separated into terms involving the grounding points (those containing  $R_1$  and  $R_2$ ) and terms involving an integration over the wire. Note that the expressions for  $E_y$  and  $H_x$  involve only grounding terms, while that for  $H_z$  contains no grounding terms. Kauahikaua (1978) discusses the numerical evaluation of the fields.

The expressions are especially useful in this form if they are to be used for evaluating the fields due to a large rectangular loop. In that case the grounding terms cancel, and the fields can be calculated by integrating the other terms numerically. If, on the other hand, the complete dipole expressions are integrated around the loop, round-off errors can lead to erroneous values.

**Homogeneous Earth.**—The fields for a homogeneous earth are given by a similar integration of the analytic expressions derived above for an electric dipole. The terms involving  $x$ -derivatives again are evaluated at the grounding points. In general, the integrations along the wire can only be evaluated numerically, but Nabighian and Oristaglio (1984) derived the following analytic expression for the time derivative of the vertical magnetic field on the equatorial axis of (broadside to) the wire:

$$\frac{\partial h_z}{\partial t} = \frac{2I}{\pi\mu_0\sigma y^3} \left\{ (1 + \theta^2 y^2) e^{-\theta^2 y^2} \operatorname{erf}(\theta L) - \frac{L}{R} \left( 1 + \frac{y^2}{2R^2} \right) \operatorname{erf}(\theta R) + \frac{\theta Ly^2}{\sqrt{\pi}R^2} e^{-\theta^2 R^2} \right\} \quad (4.191)$$

with  $R = (y^2 + L^2)^{1/2}$ .

To illustrate the behavior of the transient magnetic field, Figures 4.11 and 4.12 show contours of  $h_z$  and  $h_y$ , respectively, at the surface of a homogeneous earth. The source is a 1 km grounded wire carrying 1A of current, and the transient fields are shown at six times after the current is turned off.

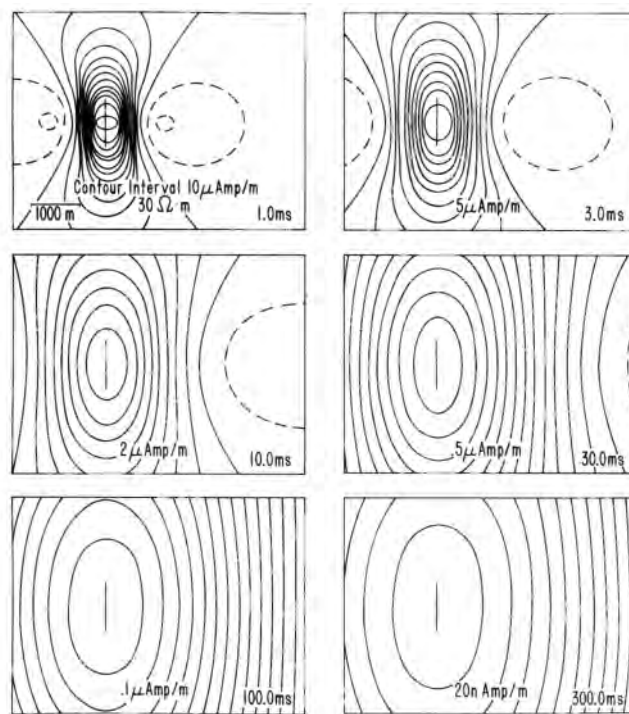


FIG. 4.12. Plan view showing contours of  $h_y$  (horizontal component, perpendicular to wire) for same model as that of Figure 4.11. Solid contours positive, dashed contours negative.

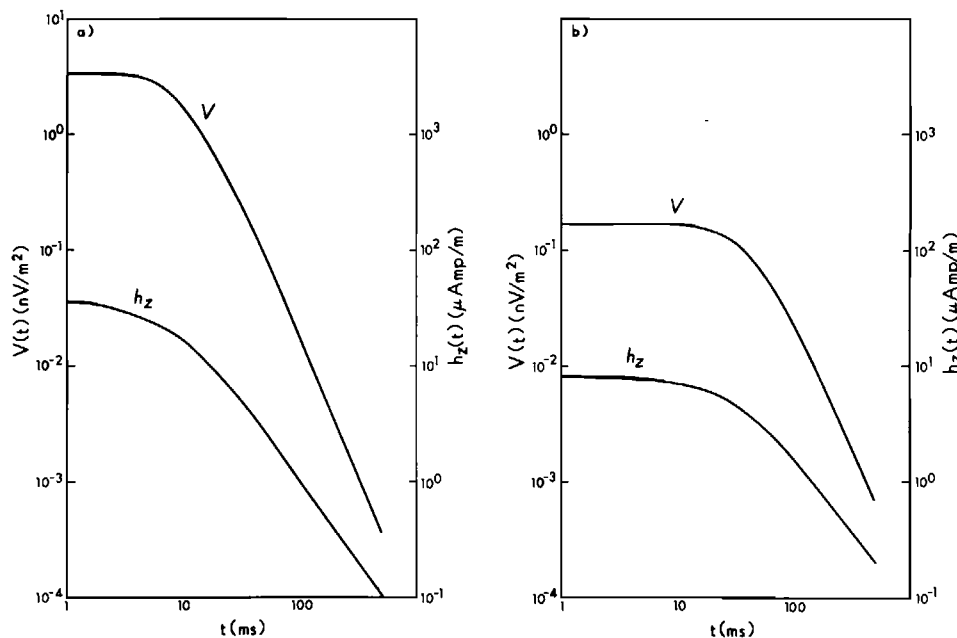


FIG. 4.13. Vertical magnetic field and voltage transients  
(a) 1.4 km and (b) 3 km from the wire for the model of  
Figures 4.11 and 4.12.

As shown in Gunderson et al. (1986), when the transmitter is turned off, currents immediately flow in the earth to preserve the magnetic field, in accordance with Lenz's law. Initially these currents are concentrated near the wire, with a broad zone of return currents deep in the earth. Then the current maximum broadens and moves downward below the wire. Hence the vertical magnetic field in Figure 4.11 is characterized by a positive peak to the right of the transmitter and a negative peak to the left. As the current maximum diffuses downward, the corresponding maximum and minimum of the vertical magnetic field move away from the wire. The horizontal magnetic field shows a peak over the wire; the peak broadens but remains over the wire as time progresses.

Figure 4.13 shows the decay of the vertical magnetic field and the voltage induced in a horizontal coil (proportional to the time-derivative of the vertical magnetic field) for the model of Figures 4.11 and 4.12. Transients are shown at positions 1.4 km and 3 km from the wire along the perpendicular bisector of the wire. As in the case of a loop source, at late times the vertical magnetic field and its time derivative exhibit  $t^{-3/2}$  and  $t^{-5/2}$  decays, respectively.

**Mutual Impedance of Grounded Wires.**—So far, we have been considering the electric and magnetic fields at points near a grounded wire centered at the origin and extending from  $-L$  to  $+L$  along the  $x$  axis. However, in many geophysical applications, such as in induced polarization (IP) exploration, the voltage (integral of the electric field) is measured between two widely separated electrodes.

Consider the configuration shown in plan view in Figure 4.14. The current electrodes are located at  $\mathbf{r}_1$  and  $\mathbf{r}_2$  along the  $x$  axis, while the measuring electrodes are located at points denoted  $\mathbf{r}_3$  and  $\mathbf{r}_4$ . A line joining the measuring electrodes intersects the  $x$  axis at angle  $\alpha$ . Hence, the electric field component  $E_s$  along the receiver line is given by

$$E_s = E_x \cos \alpha + E_y \sin \alpha,$$

so that the voltage across the element as shown in Figure 4.14 is

$$dV = (E_x \cos \alpha + E_y \sin \alpha) ds.$$

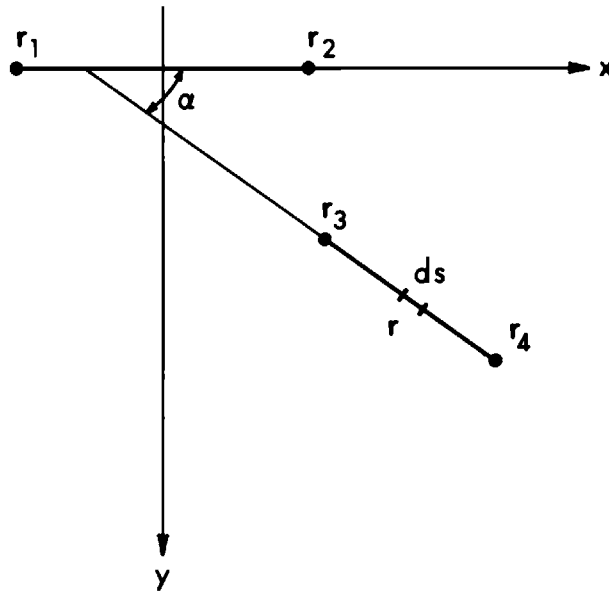


FIG. 4.14. Configuration for calculating the mutual impedance between grounded wires. Plan view.

Substituting from equations (4.184) and (4.185), the electric field along a line joining the measuring electrodes is given by

$$E_s(\mathbf{r}) = -I \int_{\mathbf{r}_1}^{\mathbf{r}_2} P(R) \cos \alpha dx' - I \left[ \frac{\partial Q(R)}{\partial x} \cos \alpha + \frac{\partial Q(R)}{\partial y} \sin \alpha \right] \Big|_{R_1}^{R_2}, \quad (4.192)$$

where  $R_1 = |\mathbf{r} - \mathbf{r}_1|$  and  $R_2 = |\mathbf{r} - \mathbf{r}_2|$ .

Integrating equation (4.192) between the measuring electrodes yields the measured voltage

$$V = -I \left[ \int_{\mathbf{r}_3}^{\mathbf{r}_4} \int_{\mathbf{r}_1}^{\mathbf{r}_2} P(R) \cos \alpha dx' ds + Q(R_{42}) - Q(R_{41}) - Q(R_{32}) + Q(R_{31}) \right], \quad (4.193)$$

where  $R_{41} = |\mathbf{r}_4 - \mathbf{r}_1|$ , etc. Equation (4.193) often is written in terms of the mutual impedance  $Z = V/I$ .

Note that for the case of perpendicular transmitting and receiving wires, the integral in equation (4.193) disappears and  $V$  is given by just the grounding terms. If the earth is homogeneous,  $Q$  and  $P$  are given by equations (4.155) and (4.157), respectively. Only for a homogeneous earth under the quasi-static approximation are the grounding terms independent of frequency.

For a general layered earth,  $P$  is given by equation (4.186), while, from equation (4.187)

$$Q(R) = \frac{I}{4\pi} \int_0^\infty \left[ (1 - r_{TM}) \frac{u_0}{\hat{y}_0} - (1 + r_{TE}) \frac{\hat{z}_0}{u_0} \right] \frac{1}{\lambda} J_0(\lambda R) d\lambda. \quad (4.194)$$

Both expressions (4.186) and (4.194) agree with the corresponding expressions given in Dey and Morrison (1973).

Both Dey and Morrison (1973) and Hohmann (1973) discuss the computation of voltage (4.193) for the dipole-dipole electrode array, in which the transmitting and receiving electrodes are colinear.

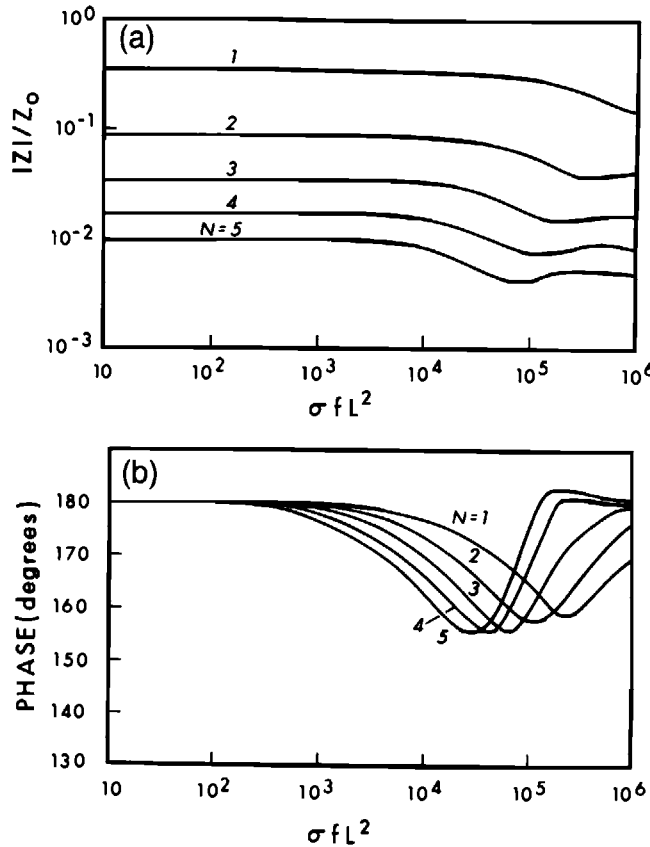


FIG. 4.15. Normalized mutual impedance for the co-linear dipole-dipole electrode configuration on a homogeneous half-space: (a) amplitude, (b) phase. Adapted from Dey and Morrison (1973).

Figure 4.15, adapted from Dey and Morrison (1973), shows the amplitude and phase of the mutual impedance for the colinear, dipole-dipole electrode array, which is often used in resistivity and induced polarization surveys. The mutual impedance is normalized by  $Z_0 = I/2\pi\sigma L$ , where  $\sigma$  is the conductivity of the half-space, and  $L$  is the distance between the transmitting electrodes and between the receiving electrodes. Results are plotted as a function of the dimensionless parameter  $\sigma f L^2$ , and are shown for five values of  $N$ , the number of dipoles lengths between the transmitter and receiver. Analysis of numerical results such as those in Figure 4.15 provides important insight regarding the unwanted EM coupling component in induced polarization surveys.

#### Line source of current

**Layered Earth.**—Consider an infinite line of electric current in the  $y$  direction, located at  $(0, 0, -h)$  above the earth in Figure 4.1. Such a source is used to simulate a long grounded wire or one side of a large rectangular loop.

Obviously, a line source over a layered earth gives rise to a TE field only, because there is no vertical electric field. Hence, the coefficient for the response of the earth in the wave number domain is given by expression (4.18), which is

$$F_0^- = r_{TE} F_p e^{-u_0 h}. \quad (4.195)$$

Because the field does not vary in the  $y$  direction, one can set  $k_y = 0$ , so that

$$u_0 = (k_x^2 - k_0^2)^{1/2}.$$

To derive an expression for the primary TE potential, denote the impressed current as

$$\mathbf{J} = I\delta(x)\delta(z+h)\mathbf{u}_y. \quad (4.196)$$

Thus the primary vector potential has only a  $y$  component, which from equation (1.115) satisfies the differential equation

$$\nabla^2 A_y + k_0^2 A_y = -I\delta(x)\delta(z+h). \quad (4.197)$$

Multiplying both sides of equation (4.197) by  $-\hat{z}_0$  and using the field expressions (1.122) with  $\nabla \cdot \mathbf{A} = \partial A_y / \partial y = 0$ , we obtain a differential equation for the primary electric field

$$\nabla^2 E_y^p + k_0^2 E_y^p = \hat{z}_0 I \delta(x) \delta(z+h). \quad (4.198)$$

By analogy with the solution for the scalar Green's function in equations (2.6) and (2.8) with  $k_y = 0$ ,

$$\tilde{E}_y^p(k_x, z) = -\frac{\hat{z}_0 I}{2u_0} e^{-u_0 h} e^{-u_0 z}, \quad (4.199)$$

which is the primary electric field between the line source and the earth. If the primary field is represented in terms of a TE potential  $F_p$ , then from equations (1.129) and (4.36)

$$\tilde{E}_y^p = ik_x F_p e^{-u_0 h} e^{-u_0 z}. \quad (4.200)$$

Comparing with equation (4.199) shows that

$$F_p = -\frac{\hat{z}_0 I}{2ik_x u_0}. \quad (4.201)$$

Substituting expression (4.201) into equation (4.38) with the  $k_y$  transform eliminated results in the following equation for the TE potential between the line source and the earth:

$$F(x, z) = -\frac{\hat{z}_0 I}{4\pi} \int_{-\infty}^{\infty} [e^{-u_0(z+h)} + r_{TE} e^{u_0(z-h)}] \frac{1}{ik_x u_0} e^{ik_x x} dk_x. \quad (4.202)$$

In geophysical applications the line source is on the surface of the earth. Thus we set  $h = 0$ , requiring a change in the sign of the exponent in the first term so that the primary field decays upward. Since the integrand is an odd function of  $k_x$ ,

$$F = -\frac{\hat{z}_0 I}{2\pi} \int_0^{\infty} (1 + r_{TE}) e^{u_0 z} \frac{1}{k_x u_0} \sin(k_x x) dk_x. \quad (4.203)$$

Applying the electric field expression (1.129),

$$E_y = -\frac{\hat{z}_0 I}{2\pi} \int_0^{\infty} (1 + r_{TE}) e^{u_0 z} \frac{1}{u_0} \cos(k_x x) dk_x. \quad (4.204)$$

Applying the magnetic field expressions (1.130) yields the two components of magnetic field for a line source in the  $y$  direction:

$$H_x = -\frac{I}{2\pi} \int_0^{\infty} (1 + r_{TE}) e^{u_0 z} \cos(k_x x) dk_x, \quad (4.205)$$

and

$$H_z = -\frac{I}{2\pi} \int_0^\infty (1 + r_{TE}) e^{u_0 z} \frac{k_x}{u_0} \sin(k_x x) dk_x. \quad (4.206)$$

In general the TE reflection coefficient is given by equation (4.19). Usually, though, the magnetic permeability of the earth can be taken as that of free space, in which case  $r_{TE}$  is given by equation (4.47). In either case,  $\lambda$  becomes  $k_x$ , because the fields are constant in the  $y$  direction. For notational convenience and to correspond to the published literature, we substitute  $\lambda$  for  $k_x$  in the following sections.

**Homogeneous Earth, Frequency Domain.**—For a nonmagnetic, homogeneous half-space

$$r_{TE} = \frac{u_0 - u_1}{u_0 + u_1}, \quad (4.207)$$

so that

$$E_y = -\frac{\hat{z}_0 I}{\pi} \int_0^\infty \frac{1}{u_0 + u_1} e^{u_0 z} \cos(\lambda x) d\lambda, \quad (4.208)$$

$$H_x = -\frac{I}{\pi} \int_0^\infty \frac{u_0}{u_0 + u_1} e^{u_0 z} \cos(\lambda x) d\lambda, \quad (4.209)$$

$$H_z = -\frac{I}{\pi} \int_0^\infty \frac{\lambda}{u_0 + u_1} e^{u_0 z} \sin(\lambda x) d\lambda. \quad (4.210)$$

Following Wait (1953b, 1962), after setting  $z$  to zero and multiplying the numerator and denominator of (4.208) by  $u_0 - u_1$ , we obtain

$$E_y = -\frac{\hat{z}_0 I}{\pi(k_1^2 - k_0^2)} \left\{ \int_0^\infty u_0 \cos(\lambda x) d\lambda - \int_0^\infty u_1 \cos(\lambda x) d\lambda \right\}. \quad (4.211)$$

Watson (1944) gives the following integral representation for the modified Bessel function of the second kind of order zero:

$$K_0(ikx) = \int_0^\infty \frac{\cos(\lambda x)}{(\lambda^2 - k^2)^{1/2}} d\lambda. \quad (4.212)$$

Hence we can write

$$\left[ \frac{\partial^2}{\partial x^2} + k^2 \right] K_0(ikx) = \left[ \frac{\partial^2}{\partial x^2} + k^2 \right] \int_0^\infty \frac{\cos(\lambda x)}{(\lambda^2 - k^2)^{1/2}} d\lambda,$$

or

$$\frac{ik}{x} K_1(ikx) = - \int_0^\infty (\lambda^2 - k^2)^{1/2} \cos(\lambda x) d\lambda. \quad (4.213)$$

Applying the identity (4.213) to equation (4.211),

$$E_y = \frac{i\omega\mu_0 I}{\pi(k_1^2 - k_0^2)x^2} [ik_0xK_1(ik_0x) - ik_1xK_1(ik_1x)]. \quad (4.214)$$

From Faraday's law, equation (1.14)

$$H_z = -\frac{1}{i\omega\mu_0} \frac{\partial E_y}{\partial x}.$$

Thus

$$H_z = \frac{I}{\pi(k_1^2 - k_0^2)x^3} [2ik_0xK_1(ik_0x) - k_0^2x^2K_0(ik_0x) - 2ik_1xK_1(ik_1x) + k_1^2x^2K_0(ik_1x)]. \quad (4.215)$$

To obtain simpler quasistatic expressions valid at low frequencies and near the line source, apply the small-argument approximations (Abramowitz and Stegun, 1964)

$$\alpha K_0(\alpha) \approx 0$$

and

$$K_1(\alpha) \approx \frac{1}{\alpha},$$

to obtain

$$E_y = -\frac{I}{\pi\alpha x^2} [1 - ikxK_1(ikx)], \quad (4.216)$$

and

$$H_z = \frac{I}{\pi k^2 x^3} [2 - 2ikxK_1(ikx) + k^2 x^2 K_0(ikx)], \quad (4.217)$$

where for notational simplicity, we have let  $k = k_1$ .

Wait (1953b) derived the following expressions for the horizontal magnetic field at quasi-static frequencies:

$$H_x = \frac{I}{2} \frac{\partial}{\partial x} \left\{ \frac{1}{ikx} [I_1(ikx) - L_1(ikx)] \right\}, \quad (4.218)$$

where  $L_1$  is the modified Struve function (Abramowitz and Stegun, 1964). For small values of  $|kx|$ ,

$$H_x \approx \frac{I}{2\pi x} \left( \frac{ikx}{\sqrt{2}} \right). \quad (4.219)$$

If  $|kx|$  is not small, it is easier to compute  $H_x$  by numerical integration of expression (4.209).

In most of the frequency-domain figures in this chapter, real and imaginary magnetic fields are shown as functions of frequency in order to illustrate actual values for practical cases. However in this section we illustrate alternative, more general plots.

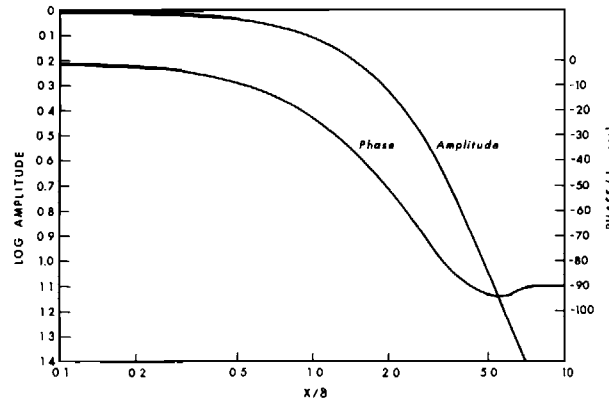


FIG. 4.16. Normalized vertical magnetic field due to a line source on a homogeneous half-space.

Figure 4.16 shows the amplitude and phase of the normalized vertical magnetic field of a line source at the surface of the earth, calculated by numerical integration of expression (4.210). Normalization is by the magnetic field of a line source in free space:  $H_0 = -I/2\pi x$ . The numerical integration technique is described in Hohmann (1971). The response is plotted as function of  $x/\delta$ , the distance from the line source normalized by a skin depth in the earth, i.e.,  $(\omega\mu_0\sigma/2)^{1/2}x$ . At a distance of about 5 skin depths the vertical magnetic field is about a tenth of its free-space value. The phase decreases from 0 to  $-90$  degrees in the range shown, with a slight undershoot at around 5 skin depths.

Similar curves for the horizontal magnetic field are shown in Figure 4.17. Again the field is normalized by  $H_0 = -I/2\pi x$ . In this case the amplitude shows a peak near two skin depths from the line source, and the phase varies from 45 degrees near the source or at low frequencies to  $-45$  degrees far from the source or at high frequencies.

**Homogeneous Earth, Time Domain.**—Two important analytic solutions have been developed for the electric field in the earth due to a line source of current at the surface. The first, due to Wait (1971) is for the electric field impulse response, or, equivalently, the time derivative of the electric field due to a step current.

Equation (4.208) gives the electric field in the air. Since the field is continuous across the earth-air interface, the electric field in the earth is given by

$$E_y(\omega) = -\frac{i\omega\mu_0 I(\omega)}{\pi} \int_0^\infty \frac{e^{-u_1 z}}{\lambda + u_1} \cos(\lambda x) d\lambda, \quad (4.220)$$

which can be rewritten as

$$E_y(\omega) = \frac{I(\omega)}{\pi\sigma} \int_0^\infty (\lambda - u_1) e^{-u_1 z} \cos(\lambda x) d\lambda. \quad (4.221)$$

If the current is an impulse at  $t = 0$ , then  $I(\omega) = I$ , and inverse Fourier transformation of the frequency-domain expression (4.221) yields the impulse response, which is the same as the derivative of the step response. Assuming a step function current and converting the inverse Fourier transform to an inverse Laplace transform with the substitution  $s = i\omega$ ,

$$\frac{\partial e_y(t)}{\partial t} = \frac{I}{\pi\sigma} \int_0^\infty \left[ \frac{\partial}{\partial z} + \lambda \right] \mathcal{L}^{-1}\{e^{-(\mu_0\sigma)^{1/2}z(s + \lambda^2/\mu_0\sigma)^{1/2}}\} \cos(\lambda x) d\lambda. \quad (4.222)$$

From equation (4.63)

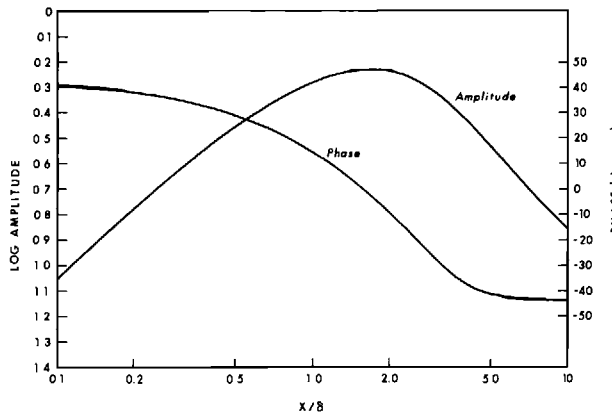


FIG. 4.17. Normalized horizontal magnetic field due to a line source on a homogeneous half-space.

$$\mathcal{L}^{-1}\{e^{-(\mu_0\sigma)^{1/2}zs^{1/2}}\} = \frac{(\mu_0\sigma)^{1/2}z}{2\pi^{1/2}t^{3/2}} e^{-\mu_0\sigma z^2/4t}.$$

Using the shift property of Laplace transforms and the usual substitution  $\theta = (\mu_0\sigma/4t)^{1/2}$

$$\frac{\partial e_y}{\partial t} = \frac{I}{\pi\sigma} \int_0^\infty \left[ \frac{\partial}{\partial z} + \lambda \right] \frac{\theta z}{\pi^{1/2}t} e^{-\theta^2 z^2} e^{-\lambda^2/4\theta^2} \cos(\lambda x) d\lambda. \quad (4.223)$$

From Gradshteyn and Ryzhik (1965),

$$\int_0^\infty e^{-\lambda^2/4\theta^2} \cos(\lambda x) d\lambda = \pi^{1/2} \theta e^{-\theta^2 x^2}, \quad (4.224)$$

and

$$\begin{aligned} \int_0^\infty \lambda e^{-\lambda^2/4\theta^2} \cos(\lambda x) d\lambda &= \frac{\partial}{\partial x} \int_0^\infty e^{-\lambda^2/4\theta^2} \sin(\lambda x) d\lambda \\ &= \frac{\partial}{\partial x} \left[ 2\theta^2 x e^{-\theta^2 x^2} {}_1F_1\left(\frac{1}{2}; \frac{3}{2}; -\theta^2 x^2\right) \right] \\ &= \frac{\partial}{\partial x} [2\theta F(\theta x)] \\ &= 2\theta^2(1 - 2\theta x)F(\theta x), \end{aligned} \quad (4.225)$$

where  ${}_1F_1$  is the confluent hypergeometric function, and

$$F(u) = e^{-u^2} \int_0^u e^{v^2} dv \quad (4.226)$$

is Dawson's integral (Abramowitz and Stegun, 1964).

Finally,

$$\frac{\partial e_y}{\partial t} = \frac{\mu_0 I}{4\pi t^2} e^{-\theta^2 z^2} \left\{ (1 - 2\theta^2 z^2) e^{-\theta^2 x^2} + \frac{2\theta z}{\pi^{1/2}} [1 - 2\theta x F(\theta x)] \right\}. \quad (4.227)$$

In a similar but more complicated derivation, Lewis and Lee (1981) and Oristaglio (1982) find the following expression for the electric field due to a negative step current, i.e., the field after a constant current is shut off:

$$e_y = \frac{I}{\pi \sigma r^2} \left\{ 2\theta^2 z^2 e^{-\theta^2 r^2} + \frac{x^2 - z^2}{r^2} (\operatorname{erfc}(\theta z) - e^{-\theta^2 r^2}) - \frac{2}{\pi^{1/2}} \theta z e^{-\theta^2 z^2} \left[ 1 - 2\theta x \left( 1 + \frac{1}{\theta^2 r^2} \right) F(\theta x) \right] \right\}, \quad (4.228)$$

where  $r^2 = x^2 + z^2$ .

At the surface of the earth where  $z = 0$ , these equations simplify to

$$\frac{\partial e_y}{\partial t} = \frac{\mu_0 I}{4\pi t^2} e^{-\theta^2 x^2}, \quad (4.229)$$

and

$$e_y = \frac{I}{\pi \sigma x^2} (1 - e^{-\theta^2 x^2}). \quad (4.230)$$

Applying Faraday's law, equation (1.3), we obtain the time derivatives of the magnetic field components at the surface of the earth after a constant current is turned off:

$$\frac{\partial h_z}{\partial t} = \frac{I}{2\pi\theta^2 x^3 t} [1 - (1 + \theta^2 x^2) e^{-\theta^2 x^2}], \quad (4.231)$$

or, in series form,

$$\frac{\partial h_z}{\partial t} = \frac{I}{2\pi\sigma x t} \sum_{n=1}^{\infty} \frac{(-1)^{n+1} n}{(n+1)!} (\theta x)^{2n},$$

and

$$\frac{\partial h_x}{\partial t} = \frac{I}{\pi^{3/2} x t} \left[ \left( 1 + \frac{1}{\theta^2 x^2} \right) F(\theta x) - \frac{1}{\theta x} \right],$$

or

$$\frac{\partial h_x}{\partial t} = \frac{I}{\pi^{3/2} x t} \sum_{n=0}^{\infty} \frac{(-1)^n (2n+1)(n+1)!}{(2n+3)!} (2\theta x)^{2n+1}, \quad (4.232)$$

expressions given in Oristaglio and Hohmann (1984). The series forms are easier to compute for values of  $\theta x$  less than one.

Retaining only the first term in each series, we obtain the following late-time expressions:

$$\frac{\partial h_z}{\partial t} \approx \frac{\mu_0 \sigma I x}{16\pi t^2}, \quad (4.233)$$

and

$$\frac{\partial h_x}{\partial t} \approx \frac{(\mu_0\sigma)^{1/2} I}{6\pi^{3/2} t^{3/2}}. \quad (4.233a)$$

Figure 4.18 shows the vertical and horizontal magnetic field impulse responses, calculated using expressions (4.231) and (4.232), respectively, 100 m from a line source on a  $100 \Omega \cdot \text{m}$  half-space. In this case the responses cannot be expressed in terms of a dimensionless quantity as in the frequency-domain plots of Figures 4.16 and 4.17. As shown by Oristaglio (1982), the magnetic field after current termination is due to currents in the earth flowing in the same direction as that in the line source. The current maximum is directly beneath the line source and moves downward with time, with a velocity given approximately by  $v = 4/9(\pi\sigma\mu_0 t)^{1/2}$ .

Finally, integrating equations (4.231) and (4.232) yields the following expressions for the magnetic field step response:

$$h_z = -\frac{I}{2\pi x} \left[ 1 + \frac{1}{\theta^2 x^2} (e^{-\theta^2 x^2} - 1) \right], \quad (4.233b)$$

$$h_x = \frac{I}{\pi^{3/2} x} \left[ \frac{F(\theta x)}{\theta^2 x^2} - \frac{1}{\theta x} \right]. \quad (4.233c)$$

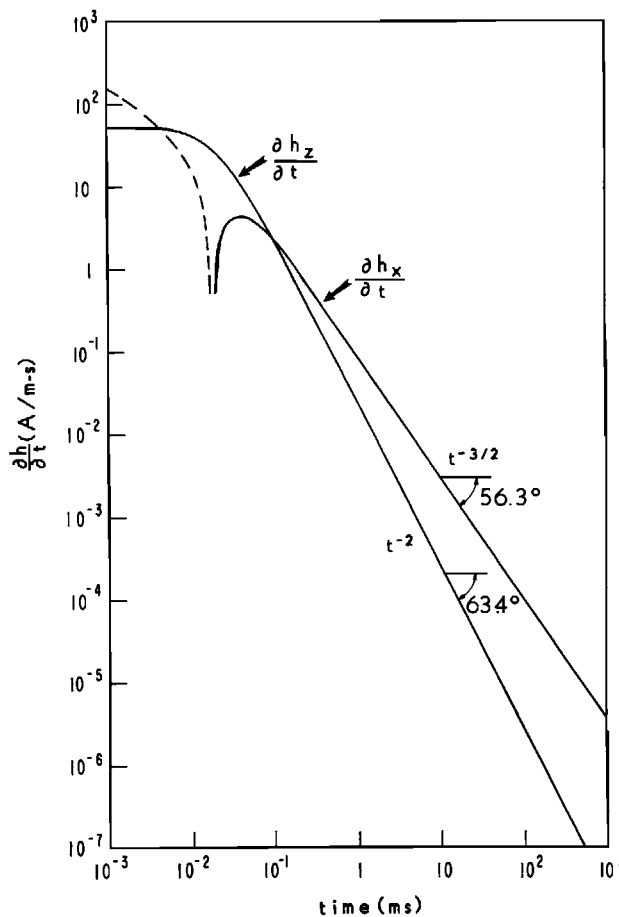


FIG. 4.18. Time derivatives of vertical and horizontal magnetic fields 100 m from a line source of current that is terminated abruptly. Source and receiver at surface of  $100 \Omega \cdot \text{m}$  half-space. Solid lines positive, dashed lines negative.

### Computations

**Analytic Expressions.**—Many of the analytic expressions for electric and magnetic fields at the surface of a homogeneous earth contain special functions such as modified Bessel functions or error functions. Computing these special functions accurately throughout the necessary argument range is difficult, particularly because they often are subtracted in the expressions for fields. Often it is easier to compute the corresponding integral, which is in the form of a Hankel or Fourier transform, by numerical integration.

Series expressions generally are not useful for computing special functions throughout the argument range of interest, so we have not included them in this volume. In general, it is better to use polynomial approximations, such as those given in Abramowitz and Stegun (1964), or to evaluate integral representations numerically. For the quasi-static case in the frequency domain, the arguments of the frequently occurring modified Bessel functions  $I_n$  and  $K_n$  are complex with a phase of  $\pi/4$ . Therefore these functions can be expressed in terms of Kelvin functions of a real argument (i.e.,  $\text{ber}_n$ ,  $\text{bei}_n$ ,  $\text{ker}_n$ ,  $\text{kei}_n$ ), resulting in a more numerically stable form, provided double-precision arithmetic is used.

One of the main uses of the analytic expression is in deriving asymptotic formulas as discussed, for example, in Kaufman and Keller (1983). Although we emphasize computing exact values of fields in this volume, these asymptotic relations are extremely important for developing insight.

**Numerical Integration.**—The integrals to be evaluated in the expressions for electric and magnetic fields over a layered half-space are of the form

$$f(r) = \int_0^{\infty} F(\lambda)Z(\lambda r)d\lambda. \quad (4.234)$$

Here  $Z$  denotes a Bessel function of order 0 or 1 for a dipole source, or a sine or cosine in the case of a line source. Two properties that make such integrals difficult to compute are the infinite range and the oscillatory nature of  $Z$ . Further, in some cases it may be necessary to subtract a term that can be integrated analytically, such as a homogeneous-half-space or whole-space expression, from  $F(\lambda)$  so that the integrand decreases with  $\lambda$  (e.g., see Frishknecht, 1967).

A general and accurate technique for numerical evaluation of the integral (4.234) is to compute it as the sum of an alternating decreasing series of integrals between zeros of the circular or Bessel function. The technique is described in Frishknecht (1967), who computed extensive tables of mutual impedances for magnetic dipoles.

Usually the first term in the series (and additional terms if  $r$  is large) should be integrated with an algorithm that computes enough points to obtain a specified accuracy. In most cases, in order to save computer time, the remaining terms can be computed using an 8-point Gaussian quadrature routine, although Frishknecht used 16-point Gaussian quadrature. In the case of a Hankel transform, the Bessel function should be computed using a polynomial approximation. To reduce computer time, values of  $Z$  can be drawn from a precomputed table, since they are always needed for the same arguments.

Normally 20 terms in the series are sufficient. In cases where the series does not decay sufficiently by the twentieth term, Euler's transformation (Abramowitz and Stegun, 1964) or a continued fraction expansion (Chave, 1983; Anderson, 1984b) is applied to force the series to converge.

**Digital Filtering.**—Because values of the integral (4.234) often are required for many values of  $r$ , the standard method of computing the integral is to convert the integral to a convolution, as described originally by Ghosh (1971) and as developed further by Anderson (1975, 1979, 1982, 1984a), among others. Substitute

$$r = e^x,$$

$$\lambda = e^{-y},$$

and multiply by  $e^x$  to obtain

$$e^x f(e^x) = \int_{-\infty}^{\infty} F(e^{-y}) [e^{x-y} Z(e^{x-y})] dy, \quad (4.235)$$

which is in the form of a convolution integral for evaluating the output of a linear, shift-invariant system. In simpler notation,

$$g(x) = \int_{-\infty}^{\infty} k(y) h(x - y) dy, \quad (4.236)$$

where

$$g(x) = e^x f(e^x)$$

is the output,

$$k(y) = F(e^{-y})$$

is the input (kernel of the integral),  
and

$$h(x - y) = e^{x-y} Z(e^{x-y})$$

is the shifted impulse response of the linear system, which can be viewed as a filter.

Equation (4.236) can be approximated by the discrete convolution

$$g[j] = \sum_i k[i] h[j - i], \quad (4.237)$$

or, because convolution is commutative,

$$g[j] = \sum_{i=N_1}^{N_2} k[j - i] h[i]. \quad (4.238)$$

Here  $h[i]$  are predetermined filter weights representing an approximation to  $h(x)$  for purposes of numerical integration;  $N_1$  and  $N_2$  are determined by adaptive convolution (Anderson, 1982, 1984a). Computational efficiency is achieved by storing values of  $k[n]$  so that they do not have to be recomputed when the convolution sum is evaluated for many values of  $j$ , a procedure called “lagged convolution” by Anderson (1975, 1982). Further computational efficiency is obtained when integrals with similar or related kernels are to be computed, such as in evaluating multiple EM components or tensor Green’s functions (Anderson, 1984a and b).

The key to successful approximation of the integral in equation (4.236) lies in defining appropriate filter weights  $h[n]$ . Upon Fourier transformation, equation (4.236) becomes

$$G(\omega) = K(\omega)H(\omega). \quad (4.239)$$

Thus, for a kernel for which the integral can be evaluated analytically, the system function of the filter is given by

$$H(\omega) = G(\omega)/K(\omega). \quad (4.240)$$

In designing general-purpose filters, Anderson (1979) found empirically that accuracy is improved and the length and magnitude of the filter tails are reduced by selecting input-

output functions with rapid decay characteristics. He recommends the Gaussian pairs defined by the following integrals (Gradshteyn and Ryzhik, 1965):

$$\int_0^\infty \lambda^{n+1} e^{-a\lambda^2} J_n(\lambda r) d\lambda = r^n \exp\left(-\frac{r^2}{4a}\right) / (2a)^{n+1}, \quad (4.241)$$

$$\int_0^\infty \lambda e^{-a^2\lambda^2} \sin(\lambda r) d\lambda = \pi^{1/2} r \exp\left(-\frac{r^2}{4a^2}\right) / 4a^3, \quad (4.242)$$

and

$$\int_0^\infty e^{-a^2\lambda^2} \cos(\lambda r) d\lambda = \pi^{1/2} \exp\left(-\frac{r^2}{4a^2}\right) / 2a. \quad (4.243)$$

The steps in filter design, then, as detailed in Anderson (1979), are to digitize the input-output functions, compute their discrete Fourier transforms, and then divide as specified by equation (4.240) to get the frequency response of the filter. Division by zero is avoided by selecting a suitable initial sampling point. Finally, the filter is truncated at the Nyquist frequency, and the filter weights are calculated by inverse discrete Fourier transformation.

## Section 5

### Boundary-Value Problems in Cylindrical Coordinates

Data from electrical methods frequently is interpreted via two-dimensional (2-D) models where the length of a subsurface inhomogeneity is considered infinite in the strike direction. The basic 2-D model is an infinite circular cylinder, but this model is readily generalized to cylinders of arbitrary cross-sections. The basic solutions of electrical boundary-value problems in cylindrical coordinates thus are introduced. To illustrate application of these solutions we solve, in detail, the problems of (a) a conducting cylinder in a uniform transverse electrostatic field and by inference a permeable cylinder in a uniform transverse magnetostatic field, and (b) a conducting permeable cylinder in a uniform alternating *magnetic* field. Full details of the development of these solutions are provided so the reader can assimilate the methodologies used. When we turn to a conducting cylinder in a uniform alternating *electromagnetic* field, we eliminate the detail and assume the reader prefers a discussion restricted to the basic elements of the solution. Adequate references are given from which the reader can ferret out the details. The same abbreviated approach is used in presenting the solution of the problem of a conducting cylinder in the field of a line source. Different approaches to these problems and much insight regarding applications are presented in Kaufman and Keller (1985).

#### Basic solutions

In many geophysical boundary-value problems, the symmetry is such that solutions in cylindrical coordinates are desirable. The frequency-domain Helmholtz equation in cylindrical coordinates, in terms of the wave function  $\psi$ , is

$$\left[ \frac{1}{\rho} \frac{\partial}{\partial \rho} \left( \rho \frac{\partial}{\partial \rho} \right) + \frac{1}{\rho^2} \frac{\partial^2}{\partial \theta^2} + \frac{\partial^2}{\partial z^2} + k^2 \right] \psi(\rho, \theta, z) = 0. \quad (5.1)$$

If we now Fourier transform equation (5.1) from  $[\rho, \theta, z, \omega]$  to  $[\rho, \nu, h, \omega]$  space using the Fourier transform pair

$$\psi(\rho, \theta, z) = \frac{1}{4\pi^2} \int_{-\infty}^{\infty} \int_{-\infty}^{\infty} \psi(\rho, \nu, h) e^{i\nu\theta} e^{ihz} d\nu dh, \quad (5.2)$$

and

$$\tilde{\psi}(\rho, \nu, h) = \int_{-\infty}^{\infty} \int_{-\infty}^{\infty} \psi(\rho, \theta, z) e^{-i\nu\theta} e^{-ihz} d\theta dz, \quad (5.3)$$

we obtain

$$\left[ \rho \frac{d}{d\rho} \left( \rho \frac{d}{d\rho} \right) + (k^2 - h^2)\rho^2 - \nu^2 \right] \tilde{\psi}(\rho, \nu, h, \omega) = 0. \quad (5.4)$$

This is Bessel's equation. The solutions of Bessel's equation that are finite on the axis  $\rho = 0$  are known as Bessel functions of order  $\nu$  and are denoted by  $J_\nu[(k^2 - h^2)^{1/2}\rho]$ . However, if we remove the restriction of finite value on the axis  $\rho = 0$ , then we usually give the solutions the name cylinder functions and denote them by  $Z_\nu[(k^2 - h^2)^{1/2}\rho]$ . Since Bessel's equation is a second-order linear differential equation, it must have two linearly independent solutions.

Upon making the change of variable  $x = (k^2 - h^2)^{1/2}\rho$ , Bessel's equation (5.4) becomes

$$\left[ x^2 \frac{d^2}{dx^2} + x \frac{d}{dx} + (x^2 - \nu^2) \right] \tilde{\psi}(\rho, \nu, h, \omega) = 0 \quad (5.5)$$

the general solution of which is

$$\tilde{\psi}(\rho, \nu, h, \omega) = C_1 J_\nu(x) + C_2 N_\nu(x). \quad (5.6)$$

In solution (5.6),  $C_1$  and  $C_2$  are arbitrary constants, the function  $J_\nu(x)$  is called the Bessel function of order  $\nu$  of the first kind, and the function  $N_\nu(x)$  is called the Bessel function of order  $\nu$  of the second kind, or Neumann function. These functions, which are tabulated (Jahnke and Emde, 1945), behave somewhat like trigonometric functions of damped amplitude and are generated from

$$J_\nu(x) = \left( \frac{x}{2} \right)^\nu \sum_{k=0}^{\infty} \frac{1}{k!} \frac{(-x^2/4)^k}{\Gamma(\nu + k + 1)}, \quad (5.7)$$

and

$$N_\nu(x) \sin \nu\pi = J_\nu(x) \cos \nu\pi - J_{\nu+1}(x). \quad (5.8)$$

where  $\Gamma(x)$  is the gamma function (a generalization of the factorial).

Other linear combinations of Bessel functions which are frequently used are the Hankel functions of the first and second kind

$$H_\nu^{(1)}(x) = J_\nu(x) + iN_\nu(x), \quad (5.9)$$

and

$$H_\nu^{(2)}(x) = J_\nu(x) - iN_\nu(x). \quad (5.10)$$

When  $x = iu$  is purely imaginary, modified Bessel functions of the first and second kind can be defined, respectively, as

$$I_\nu(u) = i^\nu J_\nu(-iu), \quad (5.11)$$

and

$$K_\nu(u) = \frac{\pi}{2} (-i)^{\nu+1} H_\nu^{(2)}(-iu). \quad (5.12)$$

The properties of all of the above functions are discussed in detail in Watson (1944). Those properties which are of particular interest here are summarized in Appendix 5.1.

We learn from the large-argument expressions in Appendix 5.1 that, except for an attenuation of  $1/\sqrt{x}$ , the following analogies may be made.

$$J_\nu(x) \text{ is analogous to } \cos x, \quad (5.13)$$

$$N_\nu(x) \text{ is analogous to } \sin x, \quad (5.14)$$

$$H_\nu^{(1)}(x) \text{ is analogous to } e^{ix}, \quad (5.15)$$

$$H_\nu^{(2)}(x) \text{ is analogous to } e^{-ix}, \quad (5.16)$$

$$I_\nu(x) \text{ is analogous to } e^{Re(x)}, \quad (5.17)$$

and that

$$K_\nu(x) \text{ is analogous to } e^{-Re(x)}. \quad (5.18)$$

Useful references for pictorial and tabular representation of all cylindrical functions are given in Jahnke and Emde (1945) and Abramowitz and Stegun (1964). The function  $J_\nu(x)$  is the only cylinder function which is finite at the origin and at infinity. If  $x$  is complex, then either  $H_\nu^{(1)}(x)$  or  $H_\nu^{(2)}(x)$  is finite at infinity.

The above discussion suggests that solution (5.6) can be written as

$$\tilde{\psi}(\rho, \nu, h, \omega) = C_1 Z_\nu^{(1)}(x) + C_2 Z_\nu^{(2)}(x), \quad (5.19)$$

where  $Z_\nu^{(1)}(x)$  and  $Z_\nu^{(2)}(x)$  are appropriate cylinder functions. With this solution obtained for the triple Fourier transformed wave equation (5.5), we may inverse Fourier transform solution (5.19) to obtain a solution to equation (5.1) as

$$\psi(\rho, \theta, z, t) = \frac{1}{8\pi^3} \int_{-\infty}^{\infty} \int_{-\infty}^{\infty} \int_{-\infty}^{\infty} [C_1 Z_\nu^{(1)}(x) + C_2 Z_\nu^{(2)}(x)] e^{iv\theta} e^{ihz} e^{i\omega t} dv dh d\omega. \quad (5.20)$$

Of course, each spectral component described by  $\nu, h, \omega$  is also a solution. Further,  $\nu, h$ , and  $\omega$ , in general, might take on both positive and negative values. Hence, an elementary solution of equation (5.5) may be expected to assume the form

$$\psi(\rho, \theta, z, t) = [C_1 Z_\nu^{(1)}(x) + C_2 Z_\nu^{(2)}(x)][C_3 e^{iv\theta} + C_4 e^{-iv\theta}][C_5 e^{ihz} + C_6 e^{-ihz}]e^{i\omega t}. \quad (5.21)$$

In solving many problems, we conveniently let the wave number in the  $z$  direction,  $h$ , be fixed, and always require that the wave potential  $\psi$  be a single-valued function of  $\theta$ . The latter constraint demands that  $\nu$  take only integral values. Reflecting these considerations, we rewrite solution (5.21) as

$$\psi(\rho, \theta, z, t) = \sum_{m=1}^{\infty} [C_{1m} Z_m^{(1)}(x) + C_{2m} Z_m^{(2)}(x)][C_{3m} e^{im\theta} + C_{4m} e^{-im\theta}][C_5 e^{ihz} + C_6 e^{-ihz}]e^{i\omega t}. \quad (5.22)$$

Within a homogeneous isotropic domain, every electromagnetic field can be represented by linear combinations of elementary wave functions such as depicted by solution (5.22). Each elementary wave is characterized by the parameters  $m$ ,  $h$ , and  $k$ . When  $m = 0$ , the field is symmetric about the  $z$  axis. When  $h = 0$ , there is no variation in the  $z$  direction; the propagation is then strictly radial, and the field is said to be 2-D.

For problems in electrostatics and magnetostatics,  $\omega$ , and therefore  $k$ , is zero. Further, for those problems in which there is no  $z$  dependence,  $h = 0$ , so that Bessel's equation (5.4) reduces to

$$\left[ \rho^2 \frac{d^2}{d\rho^2} + \rho \frac{d}{d\rho} - m^2 \right] \tilde{\psi}(\rho, m, 0, 0) = 0. \quad (5.23)$$

The solutions of equation (5.23) are

$$\psi = \sum_{m=1}^{\infty} [C_{1m}\rho^m + C_{2m}\rho^{-m}][C_{3m} \cos m\theta + C_{4m} \sin m\theta]; \quad m \neq 0 \quad (5.24)$$

and

$$\psi = [C_1 \ln \rho + C_2]; \quad m = 0, \quad (5.25)$$

where the quantity  $[C_{3m}e^{im\theta} + C_{4m}e^{-im\theta}]$  has been written in terms of  $\cos m\theta$  and  $\sin m\theta$ . If  $m = 0$ , then the field or potential is symmetric about the  $z$  axis and the problem must involve monopolar line sources, since dipolar and higher order line sources are not symmetric about the  $z$  axis.

### A conducting cylinder in a uniform transverse electrostatic field

Consider the case where a uniform electrostatic field is directed perpendicular to the axis of a conducting cylinder of infinite length embedded in a conducting medium as in Figure 5.1. Because the cylinder is infinite in length, and the field is uniform, there is no  $y$  dependence in the solution. Hence we may write the solution, in terms of the scalar electric potential, from equation (5.24) as

$$V = \sum_{m=1}^{\infty} [C_{1m}\rho^m + C_{2m}\rho^{-m}][C_{3m} \cos m\theta + C_{4m} \sin m\theta]. \quad (5.26)$$

The applied potential outside the cylinder may be calculated from the applied electric-field intensity  $E_0$  as

$$V = -E_0x = -E_0\rho \cos \theta. \quad (5.27)$$

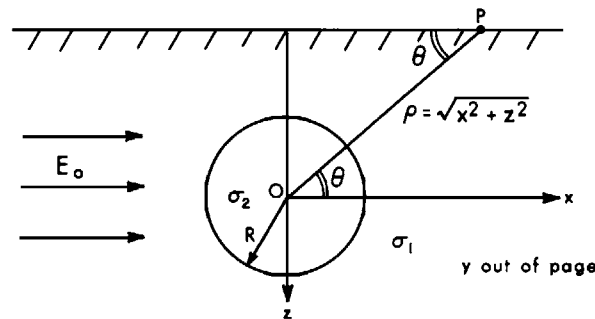


FIG. 5.1. A conducting cylinder in a uniform transverse electrostatic field  $E_0$ . The conductivities of the cylinder and the enclosing medium are  $\sigma_2$  and  $\sigma_1$ , respectively. The point of observation is  $P(x, y, z)$  while the radius of the cylinder is  $R$ .

The condition at infinity demands that no terms in  $\rho^m$  appear in the solution; therefore  $C_{1m}$  is zero. Further, the potential must be symmetric about the  $x$  axis and, hence, no terms involving  $\sin m\theta$  can appear. Thus  $C_{4m}$  must be zero and the potential exterior to the cylinder,  $V_e$ , must be of the form

$$V_e = -E_0 \cos \theta + \sum_{m=1}^{\infty} A_m^e \rho^{-m} \cos m\theta, \quad (5.28)$$

where the constant  $A_m^e$  is given by  $A_m^e = C_{2m}C_{3m}$ .

Inside the cylinder, solutions involving  $\rho^{-m}$  must be excluded if the potential is to remain finite at the origin. Hence we have the interior potential  $V_i$  given by

$$V_i = \sum_{m=1}^{\infty} [A_m^i \cos m\theta + B_m^i \sin m\theta] \rho^m, \quad (5.29)$$

in which

$$A_m^i = C_{1m}C_{3m} \text{ and } B_m^i = C_{2m}C_{4m}.$$

However, if we are to match this interior solution with the exterior solution then, clearly, the  $\sin m\theta$  dependency must disappear, resulting in a zero value for  $B_m^i$ .

At the boundary  $\rho = R$  we apply the boundary conditions of continuous potential and continuous normal current-density, respectively, to yield

$$V_e = V_i|_{\rho=R} \quad (5.30)$$

and

$$\sigma_1 \frac{\partial V_e}{\partial \rho} = \sigma_2 \frac{\partial V_i}{\partial \rho} \Big|_{\rho=R} \quad (5.31)$$

The boundary condition (5.30) reveals that  $m$  must assume the value unity, because the inducing field is restricted to  $m = 1$  according to expression (5.28). Then from boundary condition (5.31), upon utilizing expressions (5.28) and (5.29),

$$-E_o R + \frac{A_1^e}{R} = A_1^i R, \quad (5.32)$$

and

$$B_1^i = 0. \quad (5.33)$$

From boundary condition (5.31),

$$-\sigma_1 E_o - \frac{\sigma_1 A_1^e}{R^2} = \sigma_2 A_1^i. \quad (5.34)$$

Equations (5.32) and (5.34) may be combined to yield

$$A_1^i = -\frac{2\sigma_1 E_o}{\sigma_1 + \sigma_2}, \quad (5.35)$$

and

$$A_1^e = E_o R^2 \left( \frac{\sigma_2 - \sigma_1}{\sigma_2 + \sigma_1} \right). \quad (5.36)$$

Expression (5.36) may be inserted in equation (5.28) to give

$$V_e = -E_o \rho \cos \theta + E_o \frac{R^2}{\rho} \left( \frac{\sigma_2 - \sigma_1}{\sigma_2 + \sigma_1} \right) \cos \theta = V_e^n + V_e^s. \quad (5.37)$$

The second term in this last expression represents the anomalous or secondary potential, while the first term represents the normal or primary potential. The anomalous potential decreases as the first power of the distance from the center of the cylinder and increases as the square of the radius of the cylinder.

The variation of the physical property factor (PPF)

$$\text{PPF} = \frac{\sigma_2 - \sigma_1}{\sigma_2 + \sigma_1} \quad (5.38)$$

as a function of the conductivity contrast  $\sigma_2/\sigma_1$  appears in Figure 5.2. Its magnitude rises asymptotically to a saturation level of unity as the ratio  $\sigma_2/\sigma_1$  increases. As much as 82 percent of the peak value is reached for a  $\sigma_2/\sigma_1$  ratio of 10 and any further increase in conductivity contrast adds little to the magnitude of the anomaly.

The secondary electric field intensity is then

$$\mathbf{E}^s = -\nabla V_e^s = E_o R^2 \left( \frac{\sigma_2 - \sigma_1}{\sigma_2 + \sigma_1} \right) \left[ \frac{(x^2 - z^2)\mathbf{u}_x + 2xz\mathbf{u}_z}{\rho^4} \right]. \quad (5.39)$$

This is the field of a line of dipoles and decreases as the inverse second power of the radial distance from the center of the cylinder. The anomaly in the electric field intensity, given by the electric field in equation (5.39) has been computed for a particular model and appears in Figure 5.3; a central negative peak is flanked by small positives.

#### A permeable cylinder in a uniform transverse magnetostatic field

By using an entirely parallel development to that just presented, we can establish that the anomalous magnetic field intensity due to a magnetically permeable cylinder in a uniform inducing magnetic field normal to its axis is

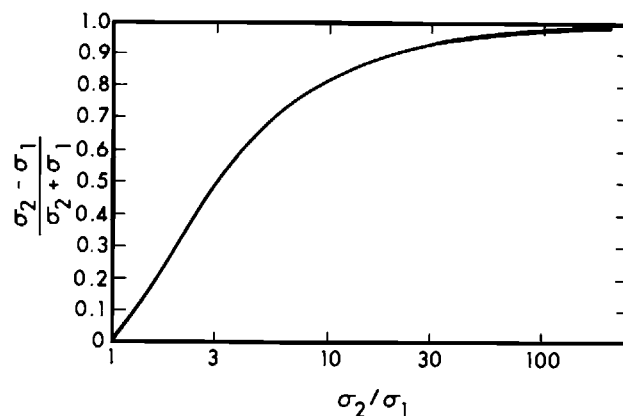


FIG. 5.2. The physical property factor  $\text{PPF} = (\sigma_2 - \sigma_1)/(\sigma_2 + \sigma_1)$  versus  $\sigma_2/\sigma_1$  for a buried cylinder in an electrostatic field.

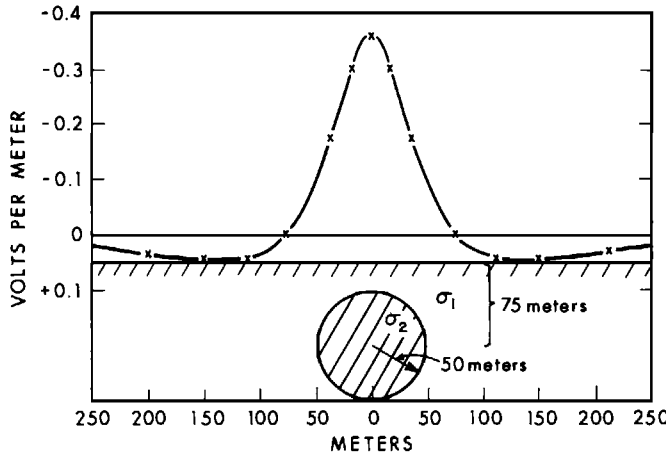


FIG. 5.3.. The anomaly in electric field, in  $V/m$ , versus the distance transverse to a cylinder of radius 50 m at a depth 75 m, where  $\sigma_2/\sigma_1 = 10$ , and  $E_0 = 1 V/m$ .

$$\mathbf{H}^a = H_o R^2 \left( \frac{\mu_2 - \mu_1}{\mu_2 + \mu_1} \right) \left[ \frac{(x^2 - z^2)\mathbf{u}_x + 2xz\mathbf{u}_z}{\rho^4} \right]. \quad (5.40)$$

#### A conducting permeable cylinder in a uniform alternating magnetic field

The cylinder exhibits constants  $\epsilon_2$ ,  $\mu_2$  and  $\sigma_2$  while the surrounding medium exhibits free-space constants  $\epsilon_o$ ,  $\mu_o$  and  $\sigma_o$ . According to Figure 5.4, a uniform alternating magnetic field  $H = H_o e^{i\omega t}$  is incident upon the cylinder; the direction of the field relative to the axis of the cylinder is arbitrary. We treat the problem from the viewpoint that the inducing field is either parallel to or perpendicular to the axis of the cylinder following Meyer (1963). The general solution of the problem can then be obtained by a superposition of these two special solutions. The cylinder is infinite in length and hence the problem can be described as 2-D. Since the problem is 2-D and since the incident wave is uniform, there can be no  $y$  dependence in the solutions we seek. For the component of alternating magnetic field in the  $x$ -direction, we introduce the Schelkunoff potential  $\mathbf{A}$ ; the secondary magnetic fields are then attributed to effective electric sources in the cylinder. For the component of alternating magnetic field in the  $y$ -direction, we introduce the Schelkunoff potential  $\mathbf{F}$ ; the secondary magnetic fields are then attributed to effective magnetic sources in the cylinder. This convenient device yields:

For electric sources      For magnetic sources

$$\nabla \times \mathbf{E} = \hat{z}\mathbf{H}, \quad \nabla \times \mathbf{H} = \hat{y}\mathbf{E},$$

$$\nabla \cdot \mathbf{H} = 0 \quad \nabla \cdot \mathbf{E} = 0,$$

$$\mathbf{H} = \nabla \times \mathbf{A}, \quad \mathbf{E} = -\nabla \times \mathbf{F},$$

$$\mathbf{E} = -\hat{z}\mathbf{A} + 1/\hat{y}\nabla\nabla \cdot \quad \mathbf{H} = -\hat{y}\mathbf{F} + 1/\hat{z}\nabla\nabla \cdot$$

$$\mathbf{A}, \quad \mathbf{F},$$

and                          and

$$[\nabla^2 + k^2]\mathbf{A} = 0. \quad [\nabla^2 + k^2]\mathbf{F} = 0.$$

We treat first a magnetic field transverse to  $y$ , corresponding to the use of the  $\mathbf{A}$  potential.

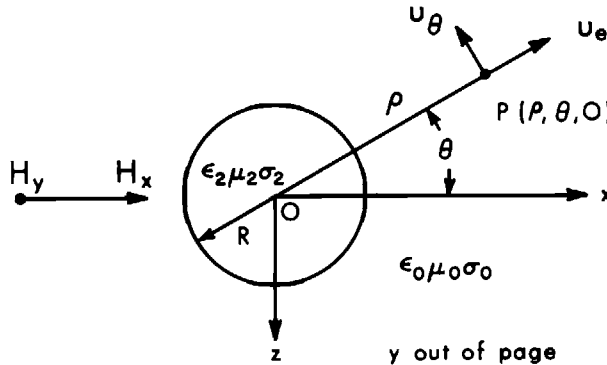


FIG. 5.4. A conducting permeable cylinder in a uniform alternating magnetic field  $H_0 e^{i\omega t}$ . The parameters of the cylinder and the surroundings are  $\sigma_2 \mu_2 \epsilon_2$ ,  $\sigma_0 \mu_0 \epsilon_0$ , respectively. The radius of the cylinder is  $R$  while the point of observation is  $P(\rho, \theta, 0)$ .

**Transverse Inducing Field.**—Expansion of the  $\mathbf{H} = \nabla \times \mathbf{A}$  in cylindrical coordinates yields

$$H_\rho = \frac{1}{\rho} \left[ \frac{\partial A_y}{\partial \theta} - \frac{\partial A_\theta}{\partial y} \right], \quad (5.41)$$

$$H_\theta = \left[ \frac{\partial A_\rho}{\partial y} - \frac{\partial A_y}{\partial \rho} \right], \quad (5.42)$$

and

$$H_y = \frac{1}{\rho} \left[ \frac{\partial}{\partial \rho} (\rho A_\theta) - \frac{\partial A_\rho}{\partial \theta} \right]. \quad (5.43)$$

Since the cylinder is infinite and the field is transverse to its axis,  $\partial/\partial y = 0$  and  $H_y = 0$ . Under these conditions equations (5.41) through (5.43) reduce to

$$H_\rho = \frac{1}{\rho} \frac{\partial A_y}{\partial \theta}, \quad (5.44)$$

$$H_\theta = - \frac{\partial A_y}{\partial \rho}, \quad (5.45)$$

and

$$H_y = 0. \quad (5.46)$$

There thus results only a  $y$  component of  $\mathbf{A}$ .

For the field to be uniform across the cylinder, the radius of the cylinder must be much less than a wave length in the external medium. We express this condition as

$$R \ll \lambda_0.$$

or as

$$\frac{R}{\lambda_0} \sim |k_0 R| \ll 1; \quad k_0 = \frac{2\pi}{\lambda_0}. \quad (5.47)$$

If displacement currents are ignored, wave number  $k_2$  becomes

$$k_2 = (-i\mu_2\sigma_2\omega)^{1/2}, \quad (5.48)$$

while wave number  $k_0$  is given as

$$k_0 \sim 0, \quad (5.49)$$

since both displacement and conduction currents are negligible in free space. The wave equation external to the cylinder then reduces to Laplace's equation

$$\nabla^2 A_y^e = 0. \quad (5.50)$$

Internal to the cylinder the potential must obey the Helmholtz equation

$$[\nabla^2 + k_2^2] A_y^i = 0. \quad (5.51)$$

The solutions of equations (5.50) and (5.51) are, respectively,

$$A_y^e = \sum_{m=1}^{\infty} [C_{1m}^e \cos m\theta + C_{2m}^e \sin m\theta][\rho^{-m}]; \quad \rho > R, \quad (5.52)$$

and

$$A_y^i = \sum_{m=1}^{\infty} [C_{1m}^i \cos m\theta + C_{2m}^i \sin m\theta][J_m(k_2\rho)]; \quad \rho < R. \quad (5.53)$$

These forms come directly from equations (5.24) and (5.22), respectively, upon imposition of the requirements of well-behaved functions at the origin and at infinity.

The primary field outside the cylinder is  $H_x = H_0 e^{i\omega t}$ , and its radial component is  $H_\rho = H_0 \cos \theta e^{i\omega t}$ . Thus the applied potential, derived from expression (5.44), is

$$A_y^p = H_0 \rho \sin \theta e^{i\omega t}. \quad (5.54)$$

Equation (5.54) immediately informs us that the order  $m$  in solutions (5.52) and (5.53) must be unity, and that  $C_{1m} = 0$ , if we are to satisfy appropriate boundary conditions.

$$A_y^e = H_0 \rho \sin \theta + B_1^e \sin \theta \rho^{-1}, \quad (5.55)$$

and

$$A_y^i = B_1^i \sin \theta J_1(k_2 \rho), \quad (5.56)$$

where we made the replacements  $B_1^e = C_{21}^e$  and  $B_1^i = C_{21}^i$ .

The appropriate boundary conditions from expressions (1.186) and (1.187), repeated here in appropriate nomenclature, are

$$\hat{z}_0 A_y^e = \hat{z}_2 A_y^i \Big|_{\rho=R}, \quad (5.57)$$

and

$$\frac{\partial}{\partial \rho} \left( A_y^e \right) = \frac{\partial}{\partial \rho} \left( A_y^i \right) \Big|_{\rho=R}. \quad (5.58)$$

Inserting expressions (5.55) and (5.56) into equations (5.57) and (5.58), results in

$$\mu_0 H_0 R + \mu_0 B_1^e R^{-1} = \mu_2 B_1^i J_1(k_2 R), \quad (5.59)$$

and

$$H_0 - B_1^e R^{-2} = B_1^i \frac{d}{d\rho} [J_1(k_2 \rho)] \Big|_{\rho=R}. \quad (5.60)$$

The derivative in equation (5.60) is evaluated via the identity

$$\frac{d}{d\rho} [J_m(k\rho)] = k \left[ J_{m-1}(k\rho) - \frac{m}{k\rho} J_m(k\rho) \right]. \quad (5.61)$$

When the identity (5.61) is substituted in equation (5.60), we find

$$H_0 - B_1^e R^{-2} = B_1^i k_2 \left[ J_0(k_2 R) - \frac{1}{k_2 R} J_1(k_2 R) \right]. \quad (5.62)$$

Equations (5.59) and (5.62) may now be solved simultaneously for  $B_1^e$  and  $B_1^i$  by Cramer's rule. We are interested here solely in external potentials and fields and accordingly restrict our attention to  $B_1^e$ , which is given by

$$B_1^e = \frac{\begin{vmatrix} k_2 \left[ J_0(k_2 R) - \frac{1}{k_2 R} J_1(k_2 R) \right] & H_0 \\ \mu_2 J_1(k_2 R) & \mu_0 H_0 R \end{vmatrix}}{\begin{vmatrix} k_2 \left[ J_0(k_2 R) - \frac{1}{k_2 R} J_1(k_2 R) \right] & R^{-2} \\ \mu_2 J_1(k_2 R) & -\mu_0 R^{-1} \end{vmatrix}}. \quad (5.63)$$

Then  $B_1^e$ , after the substitution  $\alpha = k_2 R$ , is given by

$$B_1^e = -H_0 R^2 \frac{\mu_0 [\alpha J_0(\alpha) - J_1(\alpha)] - \mu_2 J_1(\alpha)}{\mu_0 [\alpha J_0(\alpha) - J_1(\alpha)] + \mu_2 J_1(\alpha)}. \quad (5.64)$$

Because  $\alpha$  is complex, so is  $B_1^e$ , which we write as

$$B_1^e = -H_0 R^2 [M - iN]. \quad (5.65)$$

Withdrawing of the negative sign is intentional to ensure that  $M$  and  $N$  are defined positively.

Referring to the asymptotes (A5.1) of Appendix 5.1, as

$$\alpha \rightarrow 0,$$

then

$$J_0(\alpha) \rightarrow 1,$$

$$J_1(\alpha) \rightarrow \frac{\alpha}{2},$$

and

$$\left[ \frac{\alpha J_0(\alpha)}{J_1(\alpha)} - 1 \right] \rightarrow 1.$$

Equation (5.64), when divided by  $J_1(\alpha)$  in numerator and denominator and allowing the arguments to tend to zero, yields

$$B_1^e = H_0 R^2 \frac{\mu_2 - \mu_1}{\mu_2 + \mu_1}, \quad (5.66)$$

which is the coefficient for the magnetostatic case.

When we substitute coefficient (5.64) in potential (5.55) we have the full expression for the external potential. We may then use expressions (5.44) and (5.45) to calculate components of the external magnetic fields as

$$H_\rho = H_0 \cos \theta e^{i\omega t} + H_0 \left( \frac{R}{\rho} \right)^2 \left\{ \frac{\mu_0[\alpha J_0(\alpha) - J_1(\alpha)] - \mu_2 J_1(\alpha)}{\mu_0[\alpha J_0(\alpha) - J_1(\alpha)] + \mu_2 J_1(\alpha)} \right\} \cos \theta e^{i\omega t} \quad (5.67)$$

and

$$H_\theta = -H_0 \sin \theta e^{i\omega t} + H_0 \left( \frac{R}{\rho} \right)^2 \left\{ \frac{\mu_0[\alpha J_0(\alpha) - J_1(\alpha)] - \mu_2 J_1(\alpha)}{\mu_0[\alpha J_0(\alpha) - J_1(\alpha)] + \mu_2 J_1(\alpha)} \right\} \sin \theta e^{i\omega t}. \quad (5.68)$$

The cartesian field components may be obtained from expressions

$$H_x = H_\rho \cos \theta - H_\theta \sin \theta,$$

and

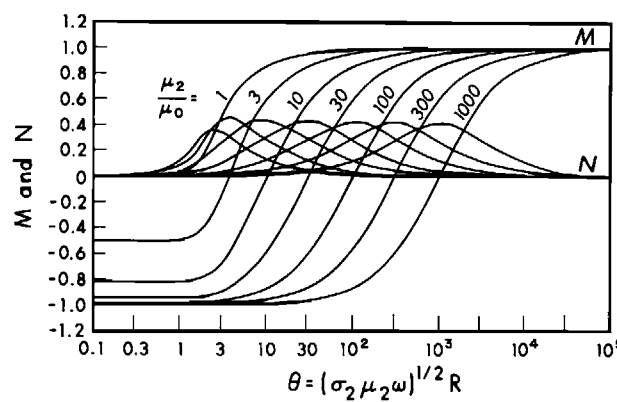


FIG. 5.5. The in-phase ( $M$ ) and out-of-phase ( $N$ ) components of the induced dipole moment of an infinite cylinder in a transverse uniform alternating magnetic field (after Ward, 1967).

$$H_z = H_0 \sin \theta + H_0 \cos \theta,$$

yielding equation

$$\begin{aligned} \mathbf{H} = H_x \mathbf{u}_x + H_z \mathbf{u}_z &= H_0 e^{i\omega t} \mathbf{u}_x + H_0 R^2 \frac{\mu_0 [\alpha J_0(\alpha) - J_1(\alpha)] - \mu_2 J_1(\alpha)}{\mu_0 [\alpha J_0(\alpha) - J_1(\alpha)] + \mu_2 J_1(\alpha)} \\ &\times \left[ \frac{(x^2 - z^2) \mathbf{u}_x + 2xz \mathbf{u}_z}{\rho^4} \right] e^{i\omega t}. \end{aligned} \quad (5.69)$$

The induced field is that of a line of dipoles oriented in the  $x$  direction.

The physical property factor  $M - iN$  is portrayed in Figure 5.5 as a function of the dimensionless induction number  $\theta$ , where the argument of the Bessel functions is given by

$$\alpha = k_2 R = (-i\sigma_2 \mu_2 \omega)^{1/2} R = (1 - i)\theta. \quad (5.70)$$

Note that the in-phase component  $M$  saturates at a value of unity, regardless of the permeability, as  $\theta \rightarrow \infty$ . For low values of induction number  $\theta$ , the value of  $M$  ranges from 0 to  $-1.0$ , depending upon the permeability. The quadrature component  $N$  rises from zero for  $\theta \rightarrow 0$  to a peak and then falls to zero as  $\theta \rightarrow \infty$ . The locations of the peak in the quadrature component or the zero crossing of the in-phase component are dependent upon the permeability.

**Concentric Cylinders in a Uniform Transverse Inducing Field.**—Three regions for which solutions must now be found are shown in Figure 5.6. The solution for the inner core appropriately involves  $J_1(k_2 R)$ . For the annulus surrounding the core, solutions that decay inward and outward are necessary. For an  $e^{i\omega t}$  time dependence the outgoing solution involves  $H_n^{(2)}(kp)$  while the ingoing solution involves  $H_n^{(1)}(kp)$  as may be deduced from a study of Table 5.1. Finally, the solution exterior to the cylinder is the solution of Laplace's equation, for the quasi-static case, and hence involves negative powers of  $\rho$ . Boundary conditions pertinent to the surfaces separating region 2 from region 1 and region 1 from region 0 are then applied to solve the problem. Negi and Raval (1969) provide details of the solution, while Negi (1962a) gives a solution for an inhomogeneous cylinder with conductivity given by  $\sigma_0(\rho/R)^p$ .

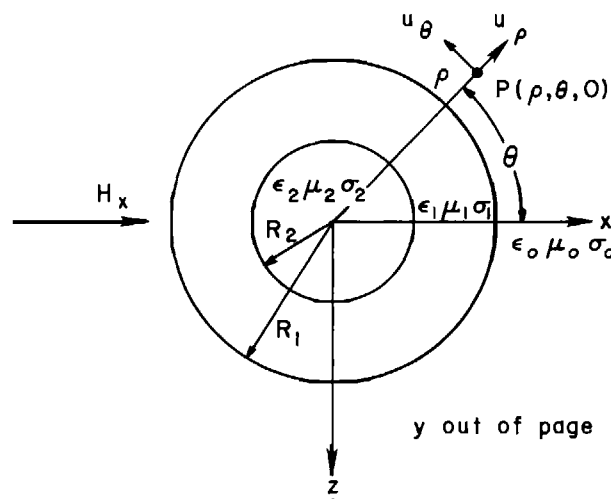


FIG. 5.6. Concentric cylinders in a uniform transverse inducing magnetic field. The inner core is of parameters  $\sigma_2 \mu_2 \epsilon_2$ , the concentric shell is of parameters  $\sigma_1 \mu_1 \epsilon_1$  while the exterior region is of parameters  $\sigma_0 \mu_0 \epsilon_0$ . The radius of the core is  $R_2$  while that of the shell is  $R_1$ . The point of observation is  $P_2(\rho, \theta, 0)$ .

**Longitudinal Inducing Field.**—This field will induce ring currents only in the cylinder. There will be only a  $y$  component of inducing field. Following equation (1.121) we write the magnetic field as

$$\mathbf{H} = -\hat{\mathbf{y}}\mathbf{F} + \frac{1}{\hat{\mathbf{z}}}\nabla(\nabla \cdot \mathbf{F}). \quad (5.71)$$

For a single component  $H_y$  and  $\partial/\partial y = 0$ , this reduces to

$$H_y = -\hat{\mathbf{y}}F_y. \quad (5.72)$$

The fields, when displacement currents are neglected, are given as:

$$H_\rho = 0, \quad E_\rho = 0,$$

$$H_\theta = 0, \quad E_\theta = \frac{\partial F_y}{\partial \rho},$$

$$H_y = -\sigma F_y, \quad E_y = 0, \quad (5.73)$$

and the Helmholtz equations are

$$\nabla^2 F_y^i + k_2^2 F_y^i = 0; \quad r \leq R, \quad (5.74)$$

and

$$\nabla^2 F_y^e = 0; \quad r > R. \quad (5.75)$$

Because  $\sigma_0 = 0$  there are no external magnetic fields.

**Conducting Permeable Cylinder in a Uniform Transient Magnetic Field.**—The equivalent time-domain problem was solved in Verma (1972). The anomalous part of equation (5.69) may be considered as a multiplication of  $H_0$  (the inducing field factor)  $R^2$  (the size factor)  $M - iN$  (the physical property factor), and the geometrical factor. The physical property factor of equation (5.69) is written

$$M - iN = \frac{\mu_0[\alpha J_0(\alpha) - J_1(\alpha)] - \mu_2 J_1(\alpha)}{\mu_0[\alpha J_0(\alpha) - J_1(\alpha)] + \mu_2 J_1(\alpha)}. \quad (5.76)$$

When there is no permeability contrast between the cylinder and its host, then response (5.76) may be rewritten, after numerator and denominator are divided by  $J_1(\alpha)$ , as

$$M - iN = 1 - \frac{2J_1(\alpha)}{\alpha J_0(\alpha)}. \quad (5.77)$$

Hence the magnitude of the magnetic field in the frequency domain may be written as

$$H = K \left[ 1 - \frac{2J_1(\alpha)}{\alpha J_0(\alpha)} \right] H_0, \quad (5.78)$$

where  $K$  depends on geometry, but is independent of frequency.

In the time domain, the magnetic field impulse response (time derivative of the step response) is given by the inverse Laplace transform

$$\frac{\partial h(t)}{\partial t} = \frac{K}{2\pi i} \int_{c-i\infty}^{c+i\infty} \left[ 1 - \frac{2J_1(\alpha)}{\alpha J_0(\alpha)} \right] H_0 e^{st} ds, \quad (5.79)$$

where we have substituted  $s = i\omega$ .

Verma (1972) produced a similar expression. When  $H_0$  is a step function, i.e.,

$$h_0(t) = h_0 u(t), \quad (5.80)$$

$$u(t) = 1; \quad t > 0 \quad (5.81)$$

$$u(t) = 0; \quad t < 0, \quad (5.82)$$

then

$$H_0(s) = H_0/s, \quad (5.83)$$

and we may follow Verma (1972) in writing a function

$$F(t) = \frac{h(t)}{KH_0}. \quad (5.84)$$

$F(t)$  is plotted versus  $\tau = t/\sigma_2 \mu_2 R^2$  in Figure 5.7.

### A conducting cylinder in a plane-wave electromagnetic field

We include this section to illustrate the approach used in high-frequency EM scattering problems.

**Wave Transformation.**—Harrington (1961, p. 230) points out that it may be convenient to express the elementary wave functions of one coordinate system as functions in another coordinate system. The electric field of a plane wave traveling in the positive  $x$ -direction

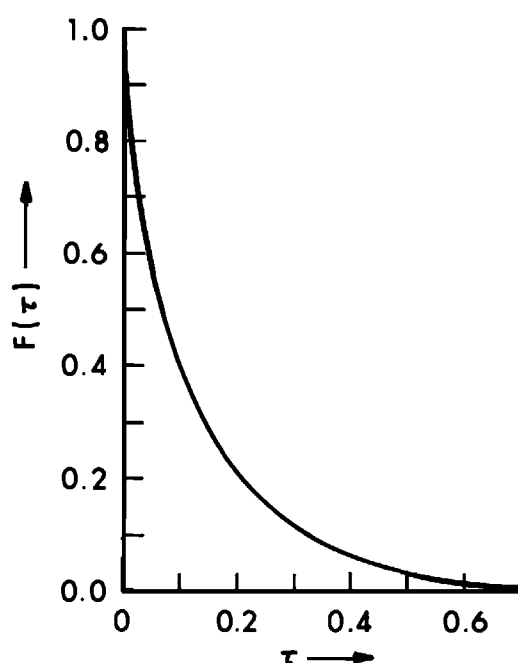


FIG. 5.7. The decay of the response  $F(t)$  as a function of normalized time  $\tau = t/\sigma_2 \mu_2 R^2$  for a conducting cylinder in a transverse uniform alternating magnetic field (after Verma, 1972).

may be written, following equation (3.2) as

$$\mathbf{E} = \mathbf{E}_0^+ e^{-ikx}, \quad (5.85)$$

where the exponential may be written as

$$e^{-ikx} = e^{-ikp\cos\theta}, \quad (5.86)$$

where conversion to a cylindrical coordinate system has been effected as per Figure 5.8. We assert next that expression (5.86) must be expressible in terms of Bessel functions, i.e.

$$e^{-ikp\cos\theta} = \sum_{n=-\infty}^{\infty} a_n J_n(kp)e^{in\theta}, \quad (5.87)$$

in which the  $a_n$  are constants. To evaluate the  $a_n$  multiply each side of equation (5.87) by  $e^{-im\theta}$  and integrate from 0 to  $2\pi$ , to obtain

$$\int_0^{2\pi} e^{-ikp\cos\theta} e^{-im\theta} d\theta = 2\pi a_m J_m(kp), \quad (5.88)$$

where the summation on the right-hand side is eliminated using the orthogonality condition for exponentials. The left-hand side of equation (5.88) is evaluated via equation 9.1.21 in Abramowitz and Stegun (1964), which, after substituting  $J_m(-z) = (-1)^m J_m(z)$  and recognizing that the integrand is an even function of  $\theta$ , states that

$$J_m(kp) = \frac{i^m}{2\pi} \int_0^{2\pi} e^{ikp\cos\theta} e^{-im\theta} d\theta. \quad (5.89)$$

Comparing the expressions (5.89) and (5.88) yields the values of the coefficients  $a_m$  as

$$a_m = i^{-m}. \quad (5.90)$$

Thus, returning to equation (5.87)

$$e^{-ikx} = e^{-ikp\cos\theta} = \sum_{n=-\infty}^{\infty} i^{-n} J_n(kp)e^{in\theta}. \quad (5.91)$$

Equation (5.91) is the wave transformation expressing the plane wave  $e^{-ikx}$  in terms of cylindrical wave functions.

**Electric Field Parallel to Axis of Cylinder.**—Harrington (1961, p. 232) discusses scat-

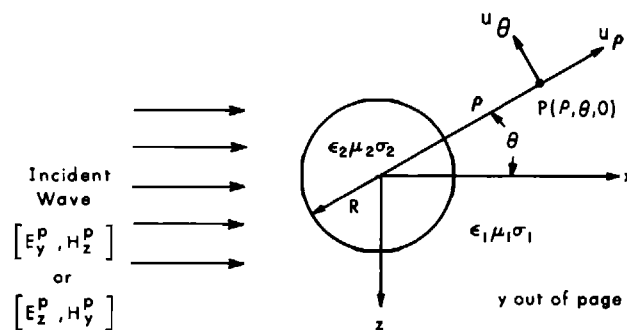


FIG. 5.8. A conducting cylinder in a plane-wave field.

Table 5-1. Properties of Solutions to Bessel's Equation ( $\gamma = 1.781$ )

$Z_n(k\rho)$	Alternative representations	Small-argument formulas ( $k\rho \rightarrow 0$ )	Large-argument formulas ( $k\rho \rightarrow \infty$ )	Zeros	Infinites	Physical interpretation
$H_n^{(1)}(k\rho)$	$J_n(k\rho) + iN_n(k\rho)$	$1 - i\frac{2}{\pi} \log\left(\frac{2}{\gamma k\rho}\right)$ $\frac{(k\rho)^n - i2^n(n-1)!}{2^n n! - \pi(k\rho)^n}$	$n=0$ $\sqrt{\frac{2i}{\pi k\rho}} e^{-n} e^{ik\rho}$ $n>0$	$k\rho \rightarrow i\infty$	$k\rho = 0$ $k\rho \rightarrow -i\infty$	$k$ real— <i>inward-traveling wave</i> $k$ imaginary— <i>evanescent field</i> $k$ complex— <i>attenuated traveling wave</i>
$H_n^{(2)}(k\rho)$	$J_n(k\rho) - iN_n(k\rho)$	$1 + i\frac{2}{\pi} \log\left(\frac{2}{\gamma k\rho}\right)$ $\frac{(k\rho)^n + i2^n(n-1)!}{2^n n! - \pi(k\rho)^n}$	$n=0$ $\sqrt{\frac{2i}{\pi k\rho}} e^{-n} e^{-ik\rho}$ $n>0$	$k\rho \rightarrow -i\infty$	$k\rho = 0$ $k\rho \rightarrow i\infty$	$k$ real— <i>outward-traveling wave</i> $k$ imaginary— <i>evanescent field</i> $k$ complex— <i>attenuated traveling wave</i>
$J_n(k\rho)$	$\frac{1}{2}[H_n^{(1)}(k\rho) + H_n^{(2)}(k\rho)]$	$1$ $n=0$ $\frac{(k\rho)^n}{2^n n!}$ $n>0$	$\sqrt{\frac{2}{\pi k\rho}} \cos\left(k\rho - \frac{n\pi}{2} - \frac{\pi}{4}\right)$	Infinite number along the real axis	$k\rho \rightarrow +i\infty$	$k$ real— <i>standing wave</i> $k$ imaginary— <i>two evanescent fields</i> $k$ complex— <i>localized standing wave</i>
$N_n(k\rho)$	$\frac{1}{2i}[H_n^{(1)}(k\rho) - H_n^{(2)}(k\rho)]$	$-i\frac{2}{\pi} \log\left(\frac{2}{\gamma k\rho}\right)$ $\frac{-2^n(n-1)!}{\pi(k\rho)^n}$	$n=0$ $\sqrt{\frac{2}{\pi k\rho}} \sin\left(k\rho - \frac{n\pi}{2} - \frac{\pi}{4}\right)$ $n>0$	Infinite number along the real axis	$k\rho = 0$ $k\rho \rightarrow \pm i\infty$	$k$ real— <i>standing wave</i> $k$ imaginary— <i>two evanescent fields</i> $k$ complex— <i>localized standing waves</i>

When  $k = -i\alpha$ , the functions  $I_n(-i k\rho) = I_n(i\alpha\rho) = I_n(i\alpha\rho)$  and  $K_n(-i k\rho) = K_n(i\alpha\rho) = K_n(i\alpha\rho) = \frac{2}{\pi} (-i)^{n+1} H_n^{(2)}(-i\alpha\rho)$  are used.

When  $k = 0$ , the Bessel functions are 1 and  $\log \rho, n=0$ , and  $\rho^n$  and  $\rho^{-n}, n \neq 0$ .

(after Harrington, 1961, p.203.)

tering of a plane wave from a perfectly conducting cylinder. Figure 5.8 illustrates the geometry of the problem. The incident or primary wave is transverse magnetic to the  $y$  axis; the primary electric field therefore may be written as

$$E_y^p = E_0 e^{-ikx} = E_0 e^{-ik\rho \cos \theta}. \quad (5.92)$$

The wave transformation (5.91) may now be utilized to write the incident electric field as

$$E_y^p = E_0 \sum_{n=-\infty}^{\infty} i^{-n} J_n(k\rho) e^{in\theta}. \quad (5.93)$$

The total field outside the conducting cylinder may be written as the sum of incident and scattered fields, i.e.

$$E_y = E_y^p + E_y^s. \quad (5.94)$$

As Harrington (1961, p. 233) shows, an outward-traveling wave is represented by a Hankel function of the second kind  $H_n^{(2)}$ , which is finite at infinity (Appendix 5.1, equation A5.18 and Table 5.1). Thus we write the scattered field  $E_y^s$  as

$$E_y^s = E_0 \sum_{n=-\infty}^{\infty} i^{-n} a_n H_n^{(2)}(k\rho) e^{in\theta}, \quad (5.95)$$

whereupon the total field becomes

$$E_y = E_0 \sum_{n=-\infty}^{\infty} i^{-n} [J_n(k\rho) + a_n H_n^{(2)}(k\rho)] e^{in\theta}. \quad (5.96)$$

At the boundary of the cylinder where  $\rho = R$ , we must have continuity of tangential electric field, i.e.,  $E_y = 0$  if the cylinder is a perfect conductor. Therefore, from equation (5.96) we obtain the coefficients  $a_n$  as

$$a_n = \frac{-J_n(kR)}{H_n^{(2)}(kR)}. \quad (5.97)$$

The magnetic fields then can be obtained from Maxwell's equations.

If the cylinder were not perfectly conducting, expressions for the interior fields would be written and the coefficients evaluated by equating interior and exterior  $E_y$  and  $H_\theta$  at the surface of the cylinder.

**Magnetic Field Parallel to the Axis of a Cylinder.**—We now write

$$H_y^p = H_0 e^{-ikx} = H_0 \sum_{n=-\infty}^{\infty} i^{-n} J_n(k\rho) e^{in\theta}. \quad (5.98)$$

Following Harrington (1961, p. 234) we write the sum of incident and scattered fields as

$$H_y = H_y^p + H_y^s. \quad (5.99)$$

The outward-traveling scattered field is given by

$$H_y^s = H_0 \sum_{n=-\infty}^{\infty} i^{-n} b_n H_n^{(2)}(k\rho) e^{in\theta}, \quad (5.100)$$

and the total field is given by

$$H_y = H_0 \sum_{n=-\infty}^{\infty} i^{-n} [J_n(k\rho) + b_n H_n^{(2)}(k\rho)] e^{in\theta}. \quad (5.101)$$

Now at the boundary of the cylinder where  $\rho = R$ , we must have continuity of tangential electric fields, i.e.,  $E_\theta = 0$  at  $\rho = R$  if the cylinder is a perfect conductor. From Maxwell's equations we write

$$E_\theta = -\frac{1}{\hat{y}} \frac{\partial H_y}{\partial \rho} = \frac{ik}{\epsilon\omega} H_0 \sum_{n=0}^{\infty} i^{-n} [J'_n(k\rho) + b_n H_n^{(2)}(k\rho)] e^{in\theta}. \quad (5.102)$$

The boundary condition  $E_\theta = 0$  at  $\rho = R$  is met if

$$b_n = -\frac{J'_n(kR)}{H_n^{(2)}(kR)}. \quad (5.103)$$

The magnetic fields are given by the expression (5.101) with the coefficient (5.103) substituted.

The solution for an incident wave of arbitrary polarization can be treated as a superposition of solutions (5.96) and (5.102).

D'Yakanov (1953), Hvozdara (1972), Ogunade and Dosso (1980) and others have treated the same problem but with allowance for finite conductivity of the space about the cylinder. By considering concentric cylinders with the outer one having a large radius, D'Yakanov (1953) approximates the case of a cylinder in a half-space.

#### A conducting cylinder in the field of a line source—frequency domain

The geometry of the problem is shown in Figure 5.9. A cylinder with radius  $R$  and electrical parameters  $\sigma_2$ ,  $\mu_2$ ,  $\epsilon_2$  is situated in a whole space with parameters  $\sigma_1$ ,  $\mu_1$ ,  $\epsilon_1$ . The cylinder is excited by an infinitely long line source of current located at  $\rho'$ ,  $\theta'$  and parallel to the axis of the cylinder, which coincides with the  $y$  axis.

From equation (2.66), the primary field of the line source is given by

$$E_y^p = \frac{-i\omega\mu_1 I}{2\pi} K_0(ik_1|\rho - \rho'|), \quad (5.104)$$

with

$$k_1^2 = \omega^2\mu_1\epsilon_1 - i\omega\mu_1\sigma_1.$$

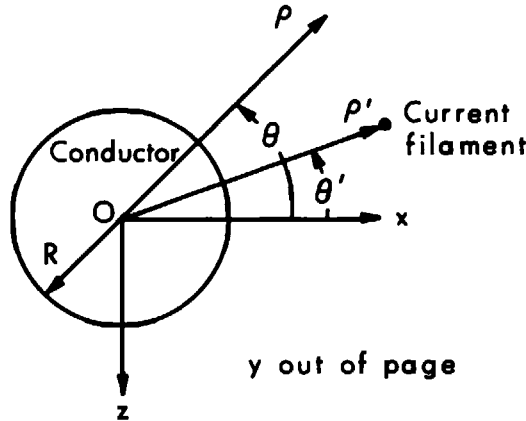


FIG. 5.9. A line source parallel to a conducting cylinder.

Using an addition theorem from Watson (1944), we separate the  $\rho$  and  $\rho'$  dependencies in equation (5.104) and write, for  $\rho < \rho'$ ,

$$E_y^p = \frac{-i\omega\mu_1 I}{2\pi} \sum_{n=0}^{\infty} \lambda_n K_n(ik_1\rho') I_n(ik_1\rho) \cos [n(\theta - \theta')], \quad (5.105)$$

where  $\lambda_0 = 1$  and  $\lambda_n = 2$  for  $n > 0$ .

Following Wait (1952), we write the electric field exterior to the cylinder as

$$E_y^e = \sum_{n=0}^{\infty} A_n K_n(ik_1\rho) \cos [n(\theta - \theta')] + E_y^p. \quad (5.106)$$

The electric field inside the cylinder is given by

$$E_y^i = \sum_{n=0}^{\infty} B_n I_n(ik_2\rho) \cos [n(\theta - \theta')]. \quad (5.107)$$

Equating tangential electric and magnetic fields ( $E_y$  and  $H_\rho$ ) at the surface of the cylinder results in the following two equations for  $A_n$  and  $B_n$ :

$$-\frac{-i\omega\mu_1 I}{2\pi} \lambda_n K_n(ik_1\rho') I_n(ik_1R) + A_n K_n(ik_1R) = B_n I_n(ik_2R), \quad (5.108)$$

and

$$\frac{-i\omega\mu_1 I}{2\pi} \lambda_n K_n(ik_1\rho') I'_n(ik_1R) + A_n K'_n(ik_1R) = B_n I'_n(ik_2R) \frac{\mu_1 k_2}{\mu_2 k_1}. \quad (5.109)$$

Solving for  $A_n$  and inserting in equation (5.106) yields an expression for the electric field outside the cylinder:

$$E_y^e = \frac{-i\omega\mu_1 I}{2\pi} \sum_{n=0}^{\infty} \lambda_n Q_n \frac{I_n(ik_1R)K_n(ik_1\rho')}{K_n(ik_1R)} K_n(ik_1\rho) \cos [n(\theta - \theta')] + E_y^p, \quad (5.110)$$

with

$$Q_n = \frac{\eta_2 \frac{I'_n(ik_1R)}{I_n(ik_1R)} - \eta_1 \frac{I'_n(ik_2R)}{I_n(ik_2R)}}{-\eta_2 \frac{K'_n(ik_1R)}{K_n(ik_1R)} + \eta_1 \frac{I'_n(ik_2R)}{I_n(ik_2R)}}, \quad (5.111)$$

with

$$\eta_1 = \left( \frac{i\omega\mu_1}{\sigma_1 + i\omega\varepsilon_1} \right)^{1/2},$$

and

$$\eta_2 = \left( \frac{i\omega\mu_2}{\sigma_2 + i\omega\varepsilon_2} \right)^{1/2}.$$

If the exterior medium is poorly conducting such that  $|ik_1R| \ll 1$ , we can use small argument approximations and recurrence relations to write, for  $n > 0$ ,

$$Q_n = \frac{n(k_m + 1)I_n(ik_2R) - ik_2RI_{n-1}(ik_2R)}{n(k_m - 1)I_n(ik_2R) + ik_2RI_{n-1}(ik_2R)}, \quad (5.112)$$

with  $k_m = \mu_2/\mu_1$ .

From Faraday's law, under the quasi-static approximation the magnetic field components outside the cylinder are given by

$$H_\rho^e = \frac{I}{2\pi\rho} \sum_{n=1}^{\infty} Q_n \left( \frac{R^2}{\rho' \rho} \right)^n \sin [n(\theta - \theta')] + H_\rho^p, \quad (5.113)$$

and

$$H_\theta^e = H_{\theta 0}^e + \frac{I}{2\pi\rho} \sum_{n=1}^{\infty} Q_n \left( \frac{R^2}{\rho' \rho} \right)^n \cos [n(\theta - \theta')] + H_\theta^p, \quad (5.114)$$

where

$$H_{\theta 0}^e = \frac{I}{2\pi\rho} Q_0 \ln (0.89 ik_1\rho') / \ln (0.89ik_1R), \quad (5.115)$$

with  $Q_n$  given by equation (5.111), and where  $H_\rho^p$  and  $H_\theta^p$  are the primary magnetic field components due to the line source.

Wait's (1952) expression for  $Q_n$  in equation (5.112) was wrong, and he did not include the  $n = 0$  term,  $H_{\theta 0}^e$ , in equation (5.114). Based on subsequent discussion in the literature [see, e.g., Wait (1973), Wait and Hill (1973), Singh (1977)] we have given the correct expressions. The term  $H_{\theta 0}^e$  is the axially symmetric component of the magnetic field, and Singh (1977) showed that it may be important. However, if the line source is far enough away so that the primary magnetic field is approximately uniform, this  $n = 0$  term becomes negligible, as shown by our previous solution for a uniform primary field.

If the magnetic field of the cylinder is the same as that of the exterior medium, we can use the relation

$$\frac{2n}{x} I_n(x) = I_{n-1}(x) - I_{n+1}(x) \quad (5.116)$$

to obtain

$$Q_n = -I_{n+1}(ik_2R)/I_{n-1}(ik_2R). \quad (5.117)$$

### A conducting cylinder in the field of a line source-time domain

Verma (1973) computed the transient field of a nonmagnetic cylinder due to a step-function current in a line source. However, following Wait (1952), he ignored the term  $H_{\theta 0}^e$  in expression (5.114). Subsequent discussion in the literature [e.g., Wait (1973), Singh (1977)] showed that the term may be important, even though Kaufman and Keller (1985) also ignore it.

However, Verma's results are correct for the  $e_y^s(t)$ , the electric field scattered by the cylinder and  $h_\rho^s(t)$ , the radial magnetic field scattered by the cylinder. It will be sufficient for our purposes to outline the derivation of  $h_\rho^s(t)$ .

The frequency dependence of the scattered field in expression (5.113) is in the factor  $Q_n$ , which for a nonmagnetic cylinder is given by equation (5.117). Hence the time dependence of the transient field due a step current turnoff is given by the inverse Laplace transform

$$q_n(t) = \frac{1}{2\pi i} \int_{c-i\infty}^{c+i\infty} \frac{I_{n+1}(\beta\sqrt{s})}{s I_{n-1}(\beta\sqrt{s})} e^{st} ds, \quad (5.118)$$

where we have replaced  $i\omega$  by  $s$ , divided by  $-s$ , and set  $\beta = R\sqrt{\mu_0\sigma_2}$ .

Using the calculus of residues, Verma (1973) derived the following expressions:

$$q_n(t) = 4n \sum_{m=1}^{\infty} \frac{1}{\lambda_{mn}^2} e^{-\lambda_{mn}^2 t/\beta^2}, \quad (5.119)$$

where the  $\lambda_{mn}$  are the roots of the equation

$$J_{n-1}(\lambda) = 0.$$

Thus, from equation (5.113), the decay of the radial magnetic field after a constant current in the line source is terminated at  $t = 0$  is given by

$$h_p^r(t) = \frac{I}{2\pi p} \sum_{n=1}^{\infty} q_n(t) \left( \frac{R^2}{p' p} \right)^n \sin [n(\theta - \theta')], \quad (5.120)$$

where  $q_n(t)$  is given by the infinite sum in equation (5.119). The time derivative of the radial magnetic field is given by equation (5.120) with  $q_n(t)$  replaced by

$$\frac{\partial q_n}{\partial t} = -\frac{4n}{\mu_0\sigma_2 R^2} \sum_{m=1}^{\infty} e^{-\lambda_{mn}^2 t/\beta^2}. \quad (5.121)$$

Kaufman and Keller (1985) present a detailed analysis of the transient response, except for ignoring the  $n = 0$  term in the expression for  $h_\theta^r(t)$ .

## Appendix 5.1 Properties of Cylinder Functions

Various solutions to Bessel's equation, the cylinder functions of integral order  $Z_m(x)$ , are defined by

$$J_m(x) = \left( \frac{x}{2} \right)^m \sum_{j=0}^{\infty} \frac{(-1)^j}{j! \Gamma(j+m+1)} \left( \frac{x}{2} \right)^{2j},$$

$$N_m(x) = \frac{J_m(x) \cos(m\pi) - J_{-m}(x)}{\sin m\pi},$$

$$H_m^{(1)}(x) = J_m(x) + iN_m(x),$$

$$H_m^{(2)}(x) = J_m(x) - iN_m(x),$$

$$I_m(x) = i^{-m} J_m(ix),$$

and

$$K_m(x) = \frac{\pi}{2} i^{m+1} H_m^{(1)}(ix).$$

The cylinder functions  $Z_m(x)$ , exhibit the following properties:

**Small argument asymptotes ( $x \rightarrow 0$ )**

$$J_m(x) \rightarrow \frac{1}{m!} \left(\frac{x}{2}\right)^m, \quad J_0(x) \rightarrow 1, \quad (\text{A5.1})$$

$$N_m(x) \rightarrow -\frac{(m-1)!}{\pi} \left(\frac{2}{x}\right)^m, \quad N_0(x) \rightarrow \frac{2}{\pi} \log\left(\frac{\gamma x}{2}\right), \quad (\text{A5.2})$$

$$H_m^{(1)}(x) \rightarrow \frac{x^m}{2^m m!} - \frac{i 2^m (m-1)!}{\pi x^m}, \quad H_0^{(1)}(x) \rightarrow 1 - i \frac{2}{\pi} \log\left(\frac{2}{\gamma x}\right), \quad (\text{A5.3})$$

$$H_m^{(2)}(x) \rightarrow \frac{x^m}{2^m m!} + \frac{i 2^m (m-1)!}{\pi x^m}, \quad H_0^{(2)}(x) \rightarrow 1 + i \frac{2}{\pi} \log\left(\frac{2}{\gamma x}\right), \quad (\text{A5.4})$$

$$I_m(x) \rightarrow \frac{1}{m!} \left(\frac{x^m}{2}\right), \quad (\text{A5.5})$$

and

$$K_m(x) \rightarrow \frac{\pi}{2} (-1)^{m+1} \frac{(-ix)^m}{2^m m!} + \frac{i 2^m (m-1)!}{\pi (-x)^m}. \quad (\text{A5.6})$$

**Large argument asymptotes ( $x \rightarrow \infty$ )**

The cylinder functions  $Z_m(x)$ , exhibit the following properties:

$$J_m(x) \rightarrow \sqrt{\frac{2}{\pi x}} \cos\left(x - \frac{\pi}{4} - \frac{m\pi}{2}\right), \quad (\text{A5.7})$$

$$N_m(x) \rightarrow \sqrt{\frac{2}{\pi x}} \sin\left(x - \frac{\pi}{4} - \frac{m\pi}{2}\right), \quad (\text{A5.8})$$

$$H_m^{(1)}(x) \rightarrow \sqrt{\frac{2}{\pi x}} e^{i(x-\pi/4-m\pi/2)}, \quad (\text{A5.9})$$

$$H_m^{(2)}(x) \rightarrow \sqrt{\frac{2}{\pi x}} e^{-i(x-\pi/4-m\pi/2)}, \quad (\text{A5.10})$$

$$I_m(x) \rightarrow \frac{e^x}{\sqrt{2\pi x}}, \quad (\text{A5.11})$$

and

$$K_m(x) \rightarrow \sqrt{\frac{\pi}{2x}} e^{-x}. \quad (\text{A5.12})$$

In the above,  $\log \gamma = 1.772$  is Euler's constant. When  $x = kr$  and  $k = 0$  we have the following degenerate forms of the cylinder functions

$$Z_0(or) \sim 1, \log \rho, \quad (\text{A5.13})$$

and

$$Z_m(or) \sim \rho^m, \rho^{-m}; \quad m \neq 0, \quad (\text{A5.14})$$

which are the solutions of Laplace's equation.

### Zeros of cylinder functions

The following zeros of the cylinder functions may be derived:

- (1)  $J_m(x)$  has an infinite number along the real  $x$  axis.
- (2)  $N_m(x)$  has an infinite number along the real  $x$  axis,
- (3)  $H_m^{(1)}(x)$  has a zero as  $x \rightarrow i\infty$ ,  
and
- (4)  $H_m^{(2)}(x)$  has a zero as  $x \rightarrow -i\infty$ .

### Singularities of cylinder functions

The following singularities of the cylinder functions are recognized:

$$(1) \quad J_m(x); \quad x \rightarrow i\infty, \quad (\text{A5.15})$$

$$(2) \quad N_m(x); \quad x = 0 \\ x \rightarrow \pm i\infty, \quad (\text{A5.16})$$

$$(3) \quad H_m^{(1)}(x); \quad x = 0 \\ x \rightarrow -i\infty, \quad (\text{A5.17})$$

and

$$(4) \quad H_m^{(2)}(x); \quad x = 0 \\ x \rightarrow i\infty. \quad (\text{A5.18})$$

### The recurrence formulas

Watson (1944, p. 16) notes that

$$J_{-m}(x) = (-1)^m J_m(x). \quad (\text{A5.19})$$

Using this relation and others, Watson (1944) establishes that

$$J_{m-1}(x) + J_{m+1}(x) = \frac{2m}{x} J_m(x), \quad (\text{A5.20})$$

and

$$J_{m-1}(x) - J_{m+1}(x) = 2J'_m(x), \quad (\text{A5.21})$$

where the prime denotes differentiation with respect to the argument  $x$ . If we add and subtract equations (A5.1.20) and (A5.1.21) we obtain the results

$$xJ'_m(x) + mJ^m(x) = xJ_{m-1}(x), \quad (\text{A5.22})$$

and

$$xJ'_m(x) - mJ_m(x) = -xJ_{m+1}(x). \quad (\text{A5.23})$$

Similarly we write

$$xN'_m(x) + mN_m(x) = xN_{m-1}(x), \quad (\text{A5.24})$$

$$xN'_m(x) - mM_m(x) = -xN_{m+1}(x), \quad (\text{A5.25})$$

$$x[H_m^{(1)}(x)]' + mH_m^{(1)} = xH_{m-1}^{(1)}(x), \quad (\text{A5.26})$$

$$x[H_m^{(1)}(x)]' - mH_m^{(1)}(x) = -xH_{m+1}^{(1)}(x), \quad (\text{A5.27})$$

$$x[H_m^{(2)}(x)]' + mH_m^{(2)}(x) = xH_{m-1}^{(2)}(x), \quad (\text{A5.28})$$

$$x[H_m^{(2)}(x)]' - mH_m^{(2)}(x) = -xH_{m+1}^{(2)}(x), \quad (\text{A5.29})$$

$$xI'_m(x) + mI_m(x) = xI_{m-1}(x), \quad (\text{A5.30})$$

$$xI'_m(x) - mI_m(x) = xI_{m+1}(x), \quad (\text{A5.31})$$

$$xK'_m(x) + mK_m(x) = -xK_{m-1}(x), \quad (\text{A5.32})$$

and

$$xK'_m(x) - mK_m(x) = -xK_{m+1}(x). \quad (\text{A5.33})$$

The higher-order derivatives of  $J_m$ ,  $N_m$ ,  $H_m^{(1)}$ ,  $H_m^{(2)}$ ,  $I_m$ , and  $K_m$  are obtained from the general formulas

$$\left(\frac{d}{dx}\right)^n [x^m J_m(x)] = x^{m-n} J_{m-n}(x), \quad (\text{A5.34})$$

$$\left(\frac{d}{dx}\right)^n [x^{-m} J_m(x)] = (-1)^n x^{-m-n} J_{m+n}(x), \quad (\text{A5.35})$$

$$\left(\frac{d}{dx}\right)^n [x^m H_m^{(1)}(x)] = x^{n-m} H_{m-n}^{(1)}(x), \quad (\text{A5.36})$$

$$\left(\frac{d}{dx}\right)^n \left[ \frac{H_m^{(1)}(x)}{x^m} \right] = (-1)^n \frac{H_{m+n}^{(1)}(x)}{x^{m+n}}, \quad (\text{A5.37})$$

$$\left(\frac{d}{xdx}\right)^n [x^m I_m(x)] = x^{m-n} I_{m-n}(x), \quad (\text{A5.38})$$

$$\left(\frac{d}{xdx}\right)^n \left[ \frac{I_m(x)}{x^m} \right] = \frac{I_{m+n}(x)}{x^{m+n}}, \quad (\text{A5.39})$$

$$\left(\frac{d}{xdx}\right)^n [x^m K_m(x)] = (-1)^n x^{m-n} K_{m-n}(x), \quad (\text{A5.40})$$

and

$$\left(\frac{d}{xdx}\right)^n \left[ \frac{K_m(x)}{x^m} \right] = (-1)^n \frac{K_{m+n}(x)}{x^{m+n}}. \quad (\text{A5.41})$$

Graphic illustration and tabulation of the cylinder functions is given in Jahnke and Emde (1945).

## Section 6

### Boundary-Value Problems in Spherical Coordinates

The simplest shape to consider for 3-D modeling of electrical geophysical data is a sphere in a whole space. Basic solutions of Laplace's equation and the wave equation in spherical coordinates are important and hence are described in reasonable detail. These solutions also permit us to solve the problems of (a) a conducting sphere in a uniform electrostatic or magnetostatic field and (b) a conducting permeable sphere in a uniform alternating magnetic field, and are presented in detail. As we did for the cylinder, we abbreviate our developments for the conducting sphere in a plane-wave field and for a conducting sphere in the field of a magnetic dipole, but refer the reader to pertinent referenced literature for details. We recommend that the reader consult Kaufman and Keller (1985) for different approaches to the problems and for additional insight. Although solutions for a sphere in a whole space have produced a great amount of insight, they are assuming less importance now that reliable numerical solutions have been developed for plates and prisms in a half-space.

#### Basic solutions

In spherical coordinates, the scalar Helmholtz equation is written

$$\left[ \frac{\partial}{\partial r} \left( r^2 \frac{\partial}{\partial r} \right) + \frac{1}{\sin \theta} \frac{\partial}{\partial \theta} \left( \sin \theta \frac{\partial}{\partial \theta} \right) + \frac{1}{\sin^2 \theta} \frac{\partial^2}{\partial \phi^2} + k^2 r^2 \right] \psi(r, \theta, \phi, \omega) = 0, \quad (6.1)$$

where  $\theta$  denotes the angle from the polar axis, and  $\phi$  is the azimuthal angle. This equation may be solved by separating the variables according to

$$\psi(r, \theta, \phi, \omega) = R(r) \cdot \Theta(\theta) \cdot \Phi(\phi) e^{i\omega t} = R(r)S(\theta, \phi)e^{i\omega t}. \quad (6.2)$$

The function  $S(\theta, \phi) = \Theta(\theta) \cdot \Phi(\phi)$  is called a surface harmonic. The function  $\Theta(\theta)$ , when  $\Phi$  is a constant, is called a zonal surface harmonic.

If we substitute the expression (6.2) in equation (6.1) and divide through by  $R(r)S(\theta, \phi)$ , we have

$$\frac{1}{R} \frac{\partial}{\partial r} \left( r^2 \frac{\partial R}{\partial r} \right) + \frac{1}{S \sin \theta} \frac{\partial}{\partial \theta} \left( \sin \theta \frac{\partial S}{\partial \theta} \right) + \frac{1}{S \sin^2 \theta} \frac{\partial^2 S}{\partial \phi^2} + k^2 r^2 = 0. \quad (6.3)$$

The first and last terms are functions of  $r$  only, and the other terms involve only  $\theta$  and  $\phi$ . Therefore, they must each be a constant, say  $p^2$ ,

$$\frac{1}{R} \frac{\partial}{\partial r} \left( r^2 \frac{\partial R}{\partial r} \right) + k^2 r^2 = p^2,$$

or

$$r^2 \frac{d^2 R}{dr^2} + 2r \frac{dR}{dr} + (k^2 r^2 - p^2)R = 0, \quad (6.4)$$

and

$$\frac{1}{S \sin \theta} \frac{\partial}{\partial \theta} \left( \sin \theta \frac{\partial S}{\partial \theta} \right) + \frac{1}{S \sin^2 \theta} \frac{\partial^2 S}{\partial \phi^2} = -p^2. \quad (6.5)$$

If in equation (6.4) we make the substitution  $R = (kr)^{-1/2}f(r)$  there results the equation

$$r^2 \frac{d^2 f}{dr^2} + r \frac{df}{dr} + [k^2 r^2 - (p^2 + 1/4)]f = 0, \quad (6.6)$$

which, upon placing  $p^2 = n(n + 1)$  becomes the Bessel equation of half-odd integral order

$$r^2 \frac{d^2 f}{dr^2} + r \frac{df}{dr} + [k^2 r^2 - (n + 1/2)^2]f = 0. \quad (6.7)$$

The cylindrical functions of half-odd integral order satisfy equation (6.7) so that for the original equation (6.4) we may write the solution

$$R = \frac{A}{\sqrt{kr}} Z_{n+1/2}(kr), \quad (6.8)$$

where  $A$  is an arbitrary constant. If  $k = 0$ , equation (6.4) has the solution

$$R = Ar^n + Br^{-n-1}, \quad (6.9)$$

which is the radial part of the solution of Laplace's equation and is applicable to electrostatic and magnetostatic problems. The complete solution of Laplace's equation in spherical coordinates may be written

$$\psi = (Ar^n + Br^{-n-1})S_n \quad (6.10)$$

where  $S_n$  is a solution of equation (6.5) with  $p^2 = n(n + 1)$ .

A very important special solution of equation (6.5) is the one in which the wave function  $\psi$  is independent of  $\phi$  so that  $\Phi$  is a constant and  $S_n$  is a function of  $\theta$  only. For this case

$$\frac{\partial^2 S_n}{\partial \phi^2} = 0, \quad (6.11)$$

and equation (6.5) reduces to

$$\frac{1}{\sin \theta} \frac{\partial}{\partial \theta} \left( \sin \theta \frac{\partial S_n}{\partial \theta} \right) + n(n+1)S_n = 0. \quad (6.12)$$

If we write  $x = \cos \theta$ , then equation (6.12) becomes

$$\frac{d}{dx} \left[ (1-x^2) \frac{dS_n}{dx} \right] + n(n+1)S_n = 0, \quad (6.13)$$

where the partial derivatives have been replaced since only one variable is now involved. This is the Legendre equation of degree  $n$ . If  $n$  is a positive integer, a solution of equation (6.13) is given by the Legendre polynomial

$$S_n = P_n(x) = P_n(\cos \theta). \quad (6.14)$$

Upon summing all such solutions and multiplying by expressions (6.8) or (6.9) we obtain the general solution of the wave equation (6.1) as

$$\psi = \sum_{n=0}^{\infty} \frac{A_n}{\sqrt{kr}} Z_{n+1/2}(kr) P_n(\cos \theta), \quad (6.15)$$

and

$$\psi = \sum_{n=0}^{\infty} \left( A_n r^n + \frac{B_n}{r^{n+1}} \right) P_n(\cos \theta) \quad (6.16)$$

as a general solution of Laplace's equation. The quantities  $A_n$  and  $B_n$  are arbitrary constants.

For the more general case where  $\psi$  is not independent of  $\phi$ , a further separation of variables must be completed. Thus, in equation (6.5) substitute  $S = \Theta\Phi$  and multiply through by  $\sin^2 \theta$  to obtain

$$\frac{\sin \theta}{\Theta} \frac{\partial}{\partial \theta} \left( \sin \theta \frac{\partial \Theta}{\partial \theta} \right) + \frac{1}{\Phi} \frac{\partial^2 \Phi}{\partial \phi^2} + n(n+1) \sin^2 \theta = 0. \quad (6.17)$$

Then let

$$\frac{1}{\Phi} \frac{\partial^2 \Phi}{\partial \phi^2} = -m^2 \quad (6.18)$$

a solution of which is

$$\Phi = e^{im\phi}. \quad (6.19)$$

There remains

$$\frac{\sin \theta}{\Theta} \frac{\partial}{\partial \theta} \left( \sin \theta \frac{\partial \Theta}{\partial \theta} \right) - m^2 + n(n+1) \sin^2 \theta = 0. \quad (6.20)$$

Substituting  $x = \cos \theta$  in equation (6.20) gives

$$(1 - x^2) \frac{d^2\Theta}{dx^2} - 2x \frac{d\Theta}{dx} + \left( n(n+1) - \frac{m^2}{1-x^2} \right) \Theta = 0 \quad (6.21)$$

This is the associated Legendre equation and is satisfied by

$$\Theta = (1 - x^2)^{m/2} \frac{d^m}{dx^m} P_n(x). \quad (6.22)$$

The function  $\Theta$  given in expression (6.22) is the associated Legendre function, and it is denoted by  $P_n^m(x)$ . We therefore have

$$P_n^m(x) = (1 - x^2)^{m/2} \frac{d^m}{dx^m} P_n(x). \quad (6.23)$$

A general solution of the Helmholtz equation in spherical coordinates is then

$$\psi = \sum_{n=0}^{\infty} \sum_{m=0}^n \frac{A_{nm}}{\sqrt{kr}} Z_{n+1/2}(kr) P_n^m(\cos \theta) e^{im\phi}, \quad (6.24)$$

and for Laplace's equation it is

$$\psi = \sum_{n=0}^{\infty} \sum_{m=0}^n \left( A_{nm} r^n + \frac{B_{nm}}{r^{n+1}} \right) P_n^m(\cos \theta) e^{im\phi}, \quad (6.25)$$

where  $A_{nm}$  and  $B_{nm}$  are arbitrary constants associated with each  $m,n$ .

A nomenclature commonly used for the cylindrical functions (6.8) is that of the spherical Bessel functions

$$\begin{aligned} z_n(\rho) &= \sqrt{\frac{\pi}{2\rho}} Z_{n+1/2}(\rho), & j_n(\rho) &= \sqrt{\frac{\pi}{2\rho}} J_{n+1/2}(\rho), \\ n_n(\rho) &= \sqrt{\frac{\pi}{2\rho}} N_{n+1/2}(\rho), & h_n^{(1)}(\rho) &= \sqrt{\frac{\pi}{2\rho}} H_{n+1/2}^{(1)}(\rho), \end{aligned}$$

and

$$h_n^{(2)}(\rho) = \sqrt{\frac{\pi}{2\rho}} H_{n+1/2}^{(2)}(\rho). \quad (6.26)$$

Some of the properties of these functions are given in Appendix 6.1.

#### Alternative solution of the Helmholtz equation in spherical coordinates

If an attempt is made to use mode decomposition in spherical coordinates, as in the expressions (A1.129 and A1.130), then care must be taken in formulating the solution of the wave equation. Let us write

$$\mathbf{F} = F_r \mathbf{u}_r, \quad (6.27)$$

and

$$\mathbf{A} = A_r \mathbf{u}_r. \quad (6.28)$$

The  $A_r$  and  $F_r$  are not solutions of the scalar Helmholtz equation, because  $\nabla^2 A_r \neq (\nabla^2 \mathbf{A})_r$  (Harrington, 1961, p. 267). We then need to know what equations  $A_r$  and  $F_r$  do satisfy. In order to find out we return to equations (1.108) and (1.109) and rewrite them here, for a source-free region, as

$$\nabla \times \nabla \times \mathbf{F} - k^2 \mathbf{F} = -\hat{z} \nabla U, \quad (6.29)$$

and

$$\nabla \times \nabla \times \mathbf{A} - k^2 \mathbf{A} = -\hat{y} \nabla V. \quad (6.30)$$

The  $\theta$  and  $\phi$  components of equation (6.30) are

$$\frac{\partial^2 A_r}{\partial r \partial \theta} = -\hat{y} \frac{\partial V}{\partial \theta}, \quad (6.31)$$

and

$$\frac{\partial^2 A_r}{\partial r \partial \phi} = -\hat{y} \frac{\partial V}{\partial \phi}. \quad (6.32)$$

The relation

$$-\hat{y}V = \frac{\partial A_r}{\partial r} \quad (6.33)$$

satisfies both of equations (6.31) and (6.32).

Then substitute the relation (6.33) into the  $r$ -component of the equation obtained from the expansion of equation (6.30) to yield

$$\frac{\partial^2 A_r}{\partial r^2} + \frac{1}{r^2 \sin \theta} \frac{\partial}{\partial \theta} \left( \sin \theta \frac{\partial A_r}{\partial \theta} \right) + \frac{1}{r^2 \sin^2 \theta} \frac{\partial^2 A_r}{\partial \phi^2} + k^2 A_r = 0. \quad (6.34)$$

The  $\nabla^2$  operator in spherical coordinates is given in equation (A1.1.12) from which we recognize that the first term in  $\nabla^2(A_r/r)$  would be

$$\frac{1}{r^2} \frac{\partial}{\partial r} \left( r^2 \frac{\partial A_r}{\partial r} \right) = \frac{1}{r} \frac{\partial^2 A_r}{\partial r^2}. \quad (6.35)$$

Hence dividing equation (6.34) by  $r$  yields

$$(\nabla^2 + k^2) \frac{A_r}{r} = 0, \quad (6.36)$$

so that  $A_r/r$  is a solution of the scalar Helmholtz equation. Similarly

$$(\nabla^2 + k^2) \frac{F_r}{r} = 0 \quad (6.37)$$

is the equation for  $F_r$ .

Thus solutions to equations (6.29) and (6.30) in spherical coordinates may be written

$$\mathbf{F} = \mathbf{r}\psi_f, \quad (6.38)$$

and

$$\mathbf{A} = \mathbf{r}\psi_a, \quad (6.39)$$

where  $\mathbf{r} = r\mathbf{u}_r$  is the radius vector from the origin and now  $\psi_a$  and  $\psi_f$  are solutions to the Helmholtz equation.

The superposed TE<sub>r</sub> and TM<sub>r</sub> fields are

$$\mathbf{E} = \mathbf{E}_m + \mathbf{E}_e, \quad (6.40)$$

and

$$\mathbf{H} = \mathbf{H}_m + \mathbf{H}_e, \quad (6.41)$$

from the expressions (1.104) and (1.105), where

$$\mathbf{E}_m = -\nabla \times \mathbf{F}, \quad (6.42)$$

and

$$\mathbf{H}_e = \nabla \times \mathbf{A}. \quad (6.43)$$

Ampere's law

$$\nabla \times \mathbf{H}_e = \hat{\mathbf{y}}\mathbf{E}_e, \quad (6.44)$$

may then be written

$$\nabla \times \nabla \times \mathbf{A} = \hat{\mathbf{y}}\mathbf{E}_e. \quad (6.45)$$

By adding the expression (6.42) and (6.45) we obtain the total electric field as

$$\mathbf{E} = -\nabla \times \mathbf{F} + \frac{1}{\hat{\mathbf{y}}}(\nabla \times \nabla \times \mathbf{A}). \quad (6.46)$$

Similarly

$$\mathbf{H} = \nabla \times \mathbf{A} + \frac{1}{\hat{\mathbf{z}}}(\nabla \times \nabla \times \mathbf{F}). \quad (6.47)$$

When the expressions (6.38) and (6.39) are substituted in equations (6.46) and (6.47) there results

$$\mathbf{E} = -\nabla \times \mathbf{r}\psi_f + \frac{1}{\hat{\mathbf{y}}}\nabla \times \nabla \times \mathbf{r}\psi_a, \quad (6.48)$$

and

$$\mathbf{H} = \nabla \times \mathbf{r}\psi_a + \frac{1}{\hat{\mathbf{z}}}\nabla \times \nabla \times \mathbf{r}\psi_f. \quad (6.49)$$

Because the  $\psi$ 's of equations (6.48) and (6.49) are always multiplied by  $r$ , it is desirable to introduce the Schelkunoff (1943) versions of the spherical cylinder functions. These are defined as

$$\hat{Z}_n(kr) = krz_n(kr) = \sqrt{\frac{\pi kr}{2}} Z_{n+1/2}(kr). \quad (6.50)$$

The differential equation that they satisfy (Harrington, 1961, p. 268) is

$$\left[ \frac{d^2}{dr^2} + k^2 - \frac{n(n+1)}{r^2} \right] \hat{Z}_n = 0, \quad (6.51)$$

which results from substituting for  $z_n$  in terms of  $\hat{Z}_n$  in equation (6.4) with  $p^2 = n(n+1)$ . The hat over  $Z_n$  follows conventional usage and is not to be confused with two previous uses of a hat.

### Integral solutions in spherical coordinates

In spherical coordinates, the Hankel transform pair is

$$f_m(r) = \left( \frac{2}{\pi} \right)^{1/2} \int_0^\infty F_m(\lambda) j_m(\lambda r) \lambda^2 d\lambda, \quad (6.52)$$

and

$$F_m(\lambda) = \left( \frac{2}{\pi} \right)^{1/2} \int_0^\infty f_m(r) j_m(\lambda r) r^2 dr. \quad (6.53)$$

Accordingly (Stratton, 1941, p. 412), the integral solution of the wave equation in spherical coordinates is

$$\psi(r, \theta, \phi, t) = e^{i\omega t} \sum_{n=0}^{\infty} \sum_{m=-\infty}^{\infty} \left( \frac{2}{\pi} \right)^{1/2} \int_0^\infty F_m(\lambda) j_m(\lambda r) \lambda^2 P_n^m(\cos \theta) e^{im\phi} d\lambda. \quad (6.54)$$

Stratton (1941) expands these and other ideas for solutions of problems with spherical symmetry.

### A conducting sphere in a uniform electrostatic field

A uniform electrostatic field immerses a conducting sphere as in Figure 6.1. The external conductivity is denoted by  $\sigma_1$ , while the internal conductivity is denoted by  $\sigma_2$ .

The external electric-field intensity may be deduced from the scalar potential  $V$  by

$$\mathbf{E}_e = -\nabla V_e, \quad (6.55)$$

according to equation (1.120), and the potential is described by the function  $\psi$  of the expression (6.25). The problem, as posed, is of direct interest in resistivity surveying for spherical ore lenses when an approximately uniform electrostatic field is established by an appropriate current electrode array. Note, however, that a sphere in a whole space is simulated, not a sphere in a half-space.

The uniform primary electrostatic field may be derived as the negative of the primary field potential as

$$E_0^P = -\frac{\partial V^P}{\partial x} \quad (6.56)$$

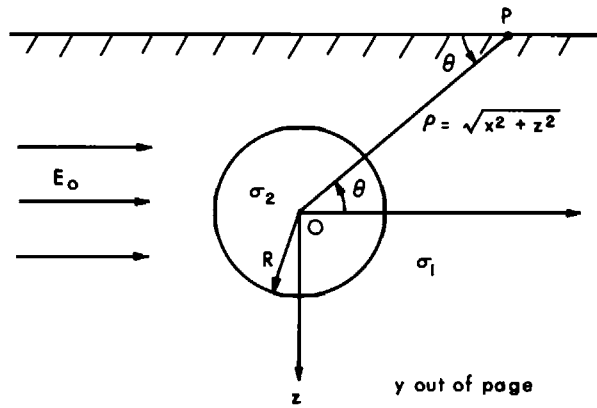


FIG. 6.1. A uniform electrostatic field  $E_0$  incident upon a conducting sphere of radius  $R$  and conductivity  $\sigma_2$  immersed in a whole space of conductivity  $\sigma_1$ .

Upon integration, with infinity as the zero potential reference, equation (6.56) yields

$$V^P = -E_0 x = -E_0 r \cos \theta = -E_0 r P_1(\cos \theta), \quad (6.57)$$

because the Legendre polynomial of order one is  $\cos \theta$ . The primary field, as described in Figure 6.1, is restricted to the  $x$  direction, and there is no component in the  $y$  direction. From the expression (6.57) we observe that  $V^P$  must have only an  $x$  dependence and it is therefore independent of the rotation angle  $\phi$  about the  $x$  axis. The  $\phi$  dependence in the general solution (6.25) is dropped by setting  $m$  to zero in the secondary potential expression. Further the primary potential is restricted to  $n = 1$  so that secondary potentials must be restricted similarly if boundary conditions are to be satisfied.

The solution for the anomalous or secondary potentials then reduces to

$$V^s = [A_1 r + B_1 r^{-2}] P_1(\cos \theta). \quad (6.58)$$

Versions of the solution (6.58) which assure finite values of the potential exterior and interior to the sphere, respectively, are

$$V_e^s = B_1 r^{-2} P_1(\cos \theta); \quad r > R, \quad (6.59)$$

and

$$V_i^s = A_1 r P_1(\cos \theta); \quad r \leq R. \quad (6.60)$$

The total external potential  $V_e = V^P + V_e^s$  is then

$$V_e = [-E_0 r + B_1 r^{-2}] P_1(\cos \theta). \quad (6.61)$$

On the surface of the sphere, according to the boundary conditions (1.213) and (1.214), both the normal current density and the potential must be continuous across the surface of the sphere. Hence we may insert the expressions (6.60) and (6.61) in equations (1.213) and (1.214) to yield, respectively,

$$-\sigma_2 A_1 = 2\sigma_1 B_1 R^{-3} + \sigma_1 E_0, \quad (6.62)$$

and

$$A_1 R = -E_0 R + B_1 R^{-2}. \quad (6.63)$$

Simultaneous solution of equations (6.62) and (6.63) yields

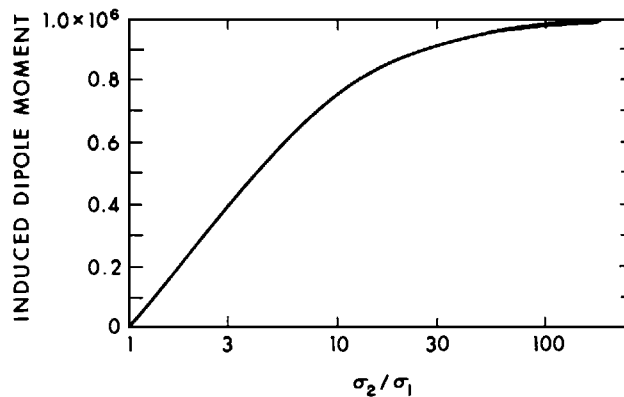


FIG. 6.2. Induced dipole moment  $P = (\sigma_2 - \sigma_1/\sigma_2 + 2\sigma_1) E_0 R^3$  versus  $\sigma_2/\sigma_1$  for a buried sphere in an electrostatic field.

$$A_1 = -\frac{3\sigma_1}{\sigma_2 + 2\sigma_1} E_0, \quad (6.64)$$

and

$$B_1 = E_0 R^3 \left[ \frac{\sigma_2 - \sigma_1}{\sigma_2 + 2\sigma_1} \right]. \quad (6.65)$$

Then the total exterior potential, from the expression (6.61) is

$$V_e = \left\{ -E_0 r + E_0 R^3 \left[ \frac{\sigma_2 - \sigma_1}{\sigma_2 + 2\sigma_1} \right] r^{-2} \right\} \cos \theta. \quad (6.66)$$

In geophysical prospecting it is customary to consider the anomalous field only and to measure potential gradients. The anomalous electric field is

$$\mathbf{E}^s = -\nabla V_e^s = \mathbf{E}_0 \mathbf{R}^3 \left( \frac{\sigma_2 - \sigma_1}{\sigma_2 - 2\sigma_1} \right) \left[ \frac{(2x^2 - y^2 - z^2)\mathbf{u}_x + 3xy\mathbf{u}_y + 3xz\mathbf{u}_z}{r^5} \right]. \quad (6.67)$$

The quantity

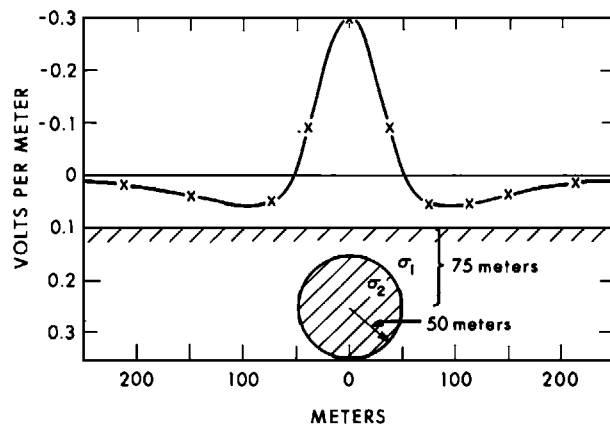


FIG. 6.3. Anomaly in electric field, in V/m, versus traverse distance across the center of a sphere of radius 50 m at a depth of 75 m,  $E_0 = 1$  V/m.

$$P = E_0 R^3 \frac{\sigma_2 - \sigma_1}{\sigma_2 + 2\sigma_1}, \quad (6.68)$$

which is the induced electric dipole moment of the sphere, is plotted in Figure 6.2.

The horizontal voltage gradient has been computed from the expression (6.67) for a section parallel to the  $x$  axis and through the center of a sphere with  $\sigma_2/\sigma_1 = 10$ ;  $R = 50$  m, and  $z = 75$  m; the profile appears in Figure 6.3.

### A permeable sphere in a uniform magnetostatic field

By an entirely parallel development to that immediately above, we can establish that the anomalous magnetic field intensity due to a magnetically permeable sphere in a uniform inducing magnetic field is

$$\mathbf{H}^s = -\nabla U = H_0 R^3 \left( \frac{\mu_2 - \mu_1}{\mu_2 + 2\mu_1} \right) \left[ \frac{(2x^2 - y^2 - z^2)\mathbf{u}_x + 3xy\mathbf{u}_y + 3xz\mathbf{u}_z}{r^5} \right]. \quad (6.69)$$

### A conducting permeable sphere in a uniform alternating magnetic field

A sphere with parameters  $\epsilon_2\mu_2\sigma_2$  is surrounded by a medium with parameters  $\epsilon_1\mu_1\sigma_1$  as in Figure 6.4. A uniform alternating magnetic field  $H = H_0 e^{i\omega t}$  is applied in the  $x$  direction. Assuming a uniform primary field implies that the radius is much less than a wavelength in the external medium, i.e.,  $|k_1 R| \ll 1$ .

Intuitively we know that the induced eddy currents will circulate in planes normal to the  $x$  axis if the electric fields are to be perpendicular to the magnetic fields. At a distance, the effective source will look like a magnetic dipole so that the vector potential  $\mathbf{F}$  should be selected. Given the symmetry of the problem, only an  $x$  component  $F_x$  of vector potential is required according to equations (1.159)–(1.161). From the expressions (1.123) we may write the magnetic fields as

$$H_x = \frac{1}{z} \left( \frac{\partial^2}{\partial x^2} + k^2 \right) F_x, \quad (6.70)$$

$$H_y = \frac{1}{z} \frac{\partial^2 F_x}{\partial y \partial x}, \quad (6.71)$$

and

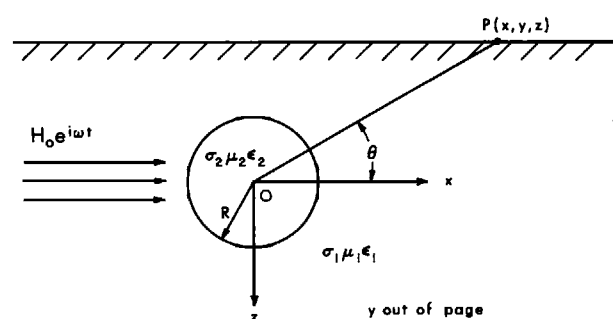


FIG. 6.4. A conducting permeable sphere in a uniform alternating magnetic field  $H_0 e^{i\omega t}$ . Constants of sphere and host are  $\sigma_2\mu_2\epsilon_2$ , and  $\sigma_1\mu_1\epsilon_1$ , respectively. The radius of the sphere is  $R$  and the point of observation is  $P(x, y, z)$ .

$$H_z = \frac{1}{\hat{z}} \frac{\partial^2 F_x}{\partial x \partial z}. \quad (6.72)$$

Hence, because the primary field is uniform, it may be expressed as

$$H_0 = -\hat{y} F_x^P. \quad (6.73)$$

If the primary field may be represented in terms of a single component of vector potential, then the secondary fields may be derived from a single component ensuring that the boundary conditions will be satisfied.

A general solution of the Helmholtz equation in spherical coordinates is given by the expansion (6.24) as

$$F_x = \sum_{n=0}^{\infty} \sum_{m=0}^n \frac{A_{nm}}{\sqrt{kr}} Z_{n+1/2}(kr) P_n^m(\cos \theta) e^{im\phi}. \quad (6.74)$$

As for the problem of the sphere in a uniform electrostatic field, there is no  $\phi$  dependence in the potential function so that we may set  $m = 0$ . The primary potential has a zeroeth-order  $\theta$  dependence according to equation (6.73), so that  $n = 0$ . Thus, we may write solutions for secondary potentials, interior and exterior to the sphere, as

$$F_{xs}^e = B_0 h_0^{(2)}(k_1 r); \quad r > R, \quad (6.75)$$

and

$$F_{xi}^i = A_0 j_0(k_2 r); \quad r \leq R. \quad (6.76)$$

The total external potential  $F_x^e = F_{xp}^e + F_{xs}^e$  is then

$$F_x^e = \left[ -\frac{1}{\hat{y}_1} H_0 + B_0 h_0^{(2)}(k_1 r) \right]. \quad (6.77)$$

Wait (1951a) developed a similar solution, except he used modified Bessel functions of argument  $ikr$  in place of our Bessel and Hankel functions.

On the surface of the sphere where  $r = R$ , according to the boundary conditions (1.163) and (1.164),

$$\hat{y}_1 F_x^e - \frac{1}{z_1} \frac{1}{r} \frac{\partial F_x^e}{\partial r} = \hat{y}_2 F_x^i - \frac{1}{z_2} \frac{1}{r} \frac{\partial F_x^i}{\partial r}, \quad (6.78)$$

and

$$\mu_1 \left( \hat{y}_1 F_x^e - \frac{1}{z_1} \frac{\partial^2 F_x^e}{\partial r^2} \right) = \mu_2 \left( \hat{y}_2 F_x^i - \frac{1}{z_2} \frac{\partial^2 F_x^i}{\partial r^2} \right). \quad (6.79)$$

For  $n = 0$ , the wave functions are

$$h_0^{(2)}(kr) = -\frac{e^{-ikr}}{ikr} \quad \text{and} \quad j_0(kr) = \frac{\sin(kr)}{kr} \quad (6.80)$$

according to Harrington (1961, p. 266), so that

$$F_x^i = A_0 j_0(k_2 r) = A_0 \frac{\sin(k_2 r)}{k_2 r}, \quad (6.81)$$

and

$$F_x^e = \left( -\frac{1}{j} H_0 + B_0 \frac{e^{-ik_1 r}}{ik_1 r} \right). \quad (6.82)$$

These two expressions may be inserted in equations (6.78) and (6.79) to yield two equations in the two unknowns  $A_0$  and  $B_0$ . Solving for  $B_0$ , we obtain

$$B_0 = H_0 R^3 \frac{2\mu_2[\sin \alpha - \alpha \cos \alpha] - \mu_1[\alpha \cos \alpha - \sin \alpha + \alpha^2 \sin \alpha]}{2\mu_2[\sin \alpha - \alpha \cos \alpha] + 2\mu_1[\alpha \cos \alpha - \sin \alpha + \alpha^2 \sin \alpha]} \quad (6.83)$$

in which  $\alpha = k_2 R$ . Substituting  $\gamma_2 = ik_2$  yields Wait's (1951a) solution, with the circular functions in equation (6.83) replaced by hyperbolic functions of argument  $\gamma_2 R$ .

Equation (6.83) can also be cast in the form

$$B_0 = H_0 R^3 (M - iN) \quad (6.84)$$

in which

$$M - iN = \left[ \frac{2\mu_2(\tan \alpha - \alpha) - \mu_1(\alpha - \tan \alpha + \alpha^2 \tan \alpha)}{2\mu_2(\tan \alpha - \alpha) - 2\mu_1(\alpha - \tan \alpha + \alpha^2 \tan \alpha)} \right]. \quad (6.85)$$

The field is given by

$$\mathbf{H} = H_0 R^3 (M - iN) \frac{(2x^2 - y^2 - z^2)\mathbf{u}_x + 3xy\mathbf{u}_y + 3xz\mathbf{u}_z}{r^5}, \quad (6.86)$$

which is the field of a dipole. The quantities  $M$  and  $N$  are plotted versus induction number in Figure 6.5.

**A Conducting Permeable Sphere in a Uniform Transient Magnetic Field.**—Wait (1951a) shows that the equivalent time-domain problem is readily solved if the permeability of the sphere is the same as that of the external medium. In that case, the expression (6.85) reduces to

$$M - iN = \frac{3}{2} \left[ \frac{1}{\alpha^2} - \frac{1}{3} - \frac{\cos \alpha}{\alpha \sin \alpha} \right]. \quad (6.87)$$

The steady-state amplitude of any component of the secondary magnetic field is then given by

$$H(\omega) = K \left( \frac{1}{\beta^2} + \frac{1}{3} - \frac{\cosh \beta}{\beta \sinh \beta} \right) H_0(\omega), \quad (6.88)$$

where  $\beta = ik_2 R$ , and  $K$  is a constant that depends on geometry.

The transient response is given by replacing  $i\omega$  with  $s$  and performing the inverse Laplace transformation

$$h(t) = \frac{K}{2\pi i} \int_{c-i\infty}^{c+i\infty} \left( \frac{1}{\beta^2} + \frac{1}{3} - \frac{\cosh \beta}{\beta \sinh \beta} \right) H_0 e^{st} ds. \quad (6.89)$$

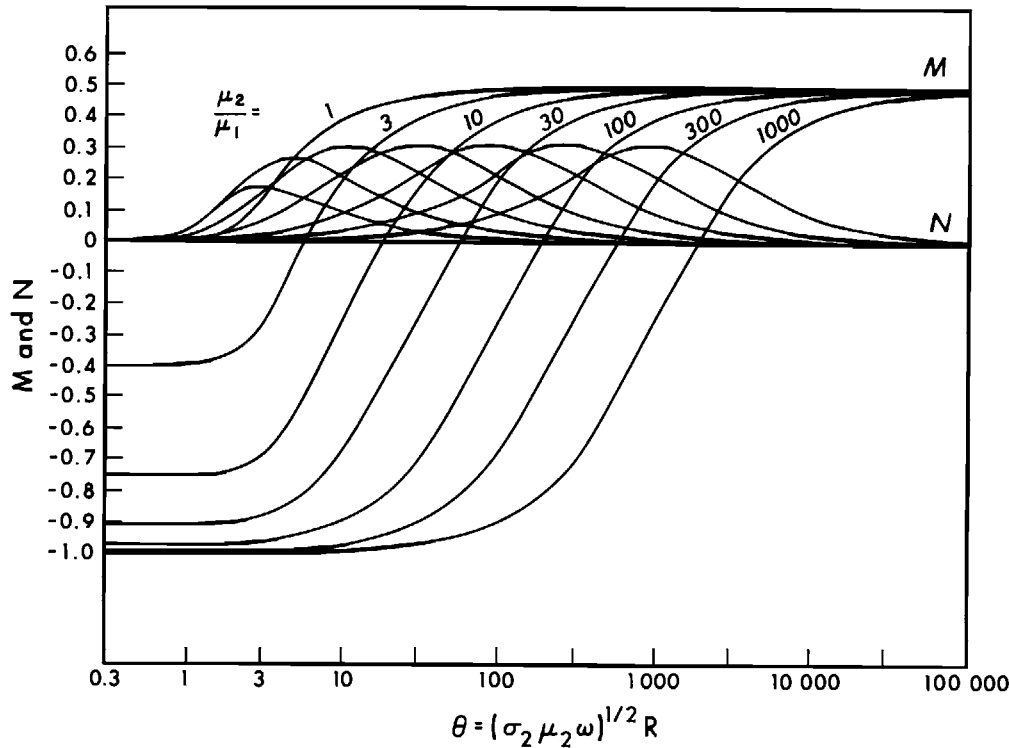


FIG. 6.5. In-phase ( $M$ ) and out-of-phase ( $N$ ) components of induced dipole moment, for a sphere in a uniform alternating magnetic field. Plotted versus induction number  $\theta = (\sigma_2 \mu_2 \omega)^{1/2} R$ .

Wait (1951a) considers the applied field  $h_0(t)$  to be a step function given by

$$h_0(t) = h_0 u(t), \quad (6.90)$$

where

$$u(t) = 1; \quad t > 0, \quad (6.91)$$

and

$$u(t) = 0; \quad t < 0, \quad (6.92)$$

so that

$$H_0(s) = H_0/s, \quad (6.93)$$

Wait (1951a) then evaluated the integral (6.89) to obtain the secondary field components outside the sphere as

$$h_z(t) = \frac{3}{2} R^3 h_0 F(t) \left( \frac{1}{r^3} - \frac{3z^2}{r^5} \right) u(t), \quad (6.94)$$

and

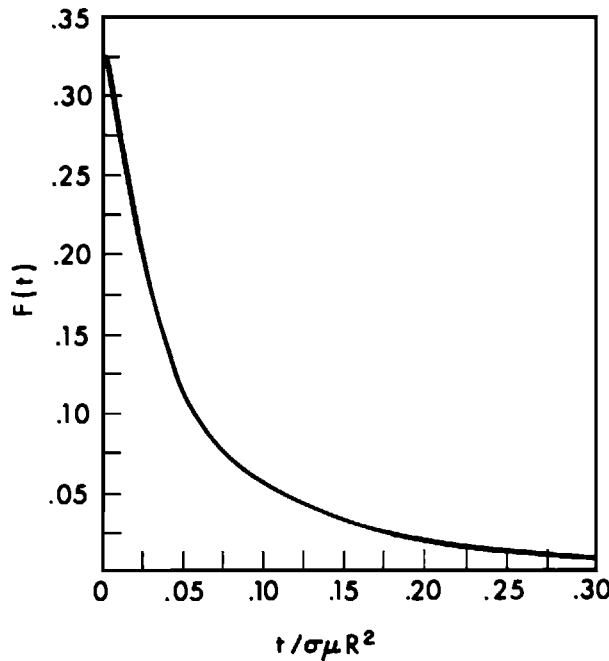


FIG. 6.6. Transient response of a sphere for a step function excitation (after Wait, 1951a).

$$h_p(t) = \frac{3}{2} R^3 h_0 F(t) \left( \frac{3zp}{r^5} \right) u(t), \quad (6.95)$$

in which

$$F(t) = \frac{h(t)}{K} = x^2 + \frac{1}{3} - 2\pi^{-1/2}x - \sum_{n=1}^{\infty} 2n \left[ \frac{x}{n} \operatorname{erf}'(n/x) - 2 \operatorname{erfc}(n/x) \right], \quad (6.96)$$

with

$$x = \frac{t^{1/2}}{(\sigma_2 \mu)^{1/2} R},$$

and where  $\operatorname{erf}'$  is the derivative of the error function, and  $\operatorname{erfc}$  is the complementary error function. A graph of  $F(t)$  versus  $t/\sigma_2 \mu R^2$  is given in Figure 6.6.

Wait and Spies (1969) give a dimensionless function characterizing the impulse response of a nonpermeable conducting sphere as

$$B(t) = \beta^2 h'(t) = 3 \left[ 1 + \frac{\delta(T)}{3} - \frac{1}{(\pi T)^{1/2}} - \frac{2}{(\pi T)^{1/2}} \sum_{m=1}^{\infty} e^{-m^2/T} \right] u(t), \quad (6.97)$$

where  $\beta = (\sigma \mu_0)^{1/2} R$ , and where  $T = t/\sigma \mu_0 R^2$  is the normalized time.

Similarly, Wait and Spies (1969) give the step-function response of a nonpermeable conducting sphere as

$$h(t) = A(t) = \left[ T + \frac{1}{3} - 2\left(\frac{T}{\pi}\right)^{1/2} - 2 \sum_{m=1}^{\infty} \left\{ T^{1/2} \operatorname{erf}'\left(\frac{m}{T^{1/2}}\right) - 2m \operatorname{erfc}\left(\frac{m}{T^{1/2}}\right) \right\} \right] u(T), \quad (6.98)$$

in which

$$\operatorname{erfc}(Z) = \frac{2}{\sqrt{\pi}} \int_z^{\infty} e^{-x^2} dx,$$

and

$$\operatorname{erf}'(Z) = \frac{2}{\sqrt{\pi}} e^{-Z^2}.$$

Expression (6.98) is equivalent to expression (6.96). The functions  $A(t)$  and  $B(t)$  are plotted in Figure 6.7 as functions of dimensionless time  $T$ .

Wait and Spies (1969) used contour integration to derive the step-function response of a conducting permeable sphere as

$$h(t) = A(t) = \left\{ 6K_m \sum_{n=1}^{\infty} \frac{e^{-\delta_n^2 T}}{(K_m + 2)(K_m - 1) + \delta_n^2} - 2 \left[ \frac{K_m - 1}{K_m + 2} \right] \right\} u(T), \quad (6.99)$$

where

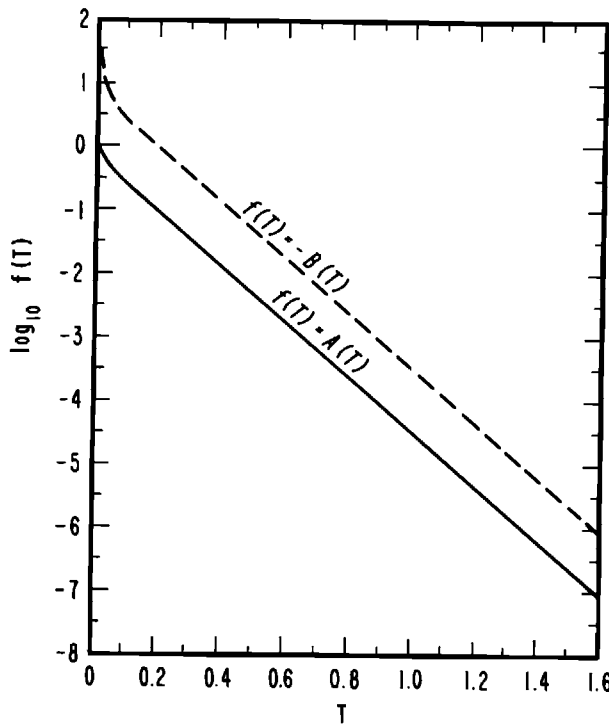


FIG. 6.7. The transient response of a nonpermeable conducting sphere for both impulse  $B(t)$  and step-function  $A(t)$  excitation of a uniform magnetic field plotted on a log-linear scale (after Wait and Spies, 1969).

$$T = t/\beta^2 = \frac{t}{\sigma\mu_2 R^2},$$

$$K_m = \frac{\mu_2}{\mu_0},$$

and the real  $\delta_n$  are given by

$$\tan \delta_n = \frac{(K_m - 1) \delta_n}{K_m - 1 + \delta_n^2}.$$

The function  $A(t)$  of equation (6.99) is plotted in Figure 6.8, for different values of  $K_m$ , versus dimensionless time  $T$ .

### A conducting sphere in a plane-wave field

**Wave Transformation.**—Harrington (1961, p. 289) gives a transformation of a plane wave  $e^{iz}$  in terms of spherical wave functions as

$$e^{iz} = e^{ir\cos\theta} = \sum_{n=0}^{\infty} a_n j_n(r) P_n(\cos\theta) \quad (6.100)$$

in which the wave is considered to be finite at the origin and independent of the angle  $\phi$  of rotation about  $z$ . To determine the coefficient  $a_n$  we multiply each side of equation (6.100) by  $P_q(\cos\theta) \sin\theta$  and integrate over  $\theta$  from 0 to  $\pi$ . Because of orthogonality (Harrington, 1961, p. 273), all terms except  $q = n$  vanish and hence

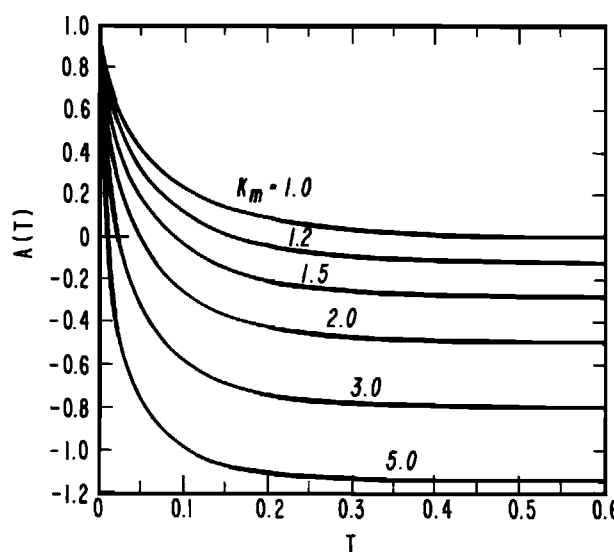


FIG. 6.8. The step-function response of a permeable conducting sphere for various values of permeability contrast  $K_m$  (after Wait and Spies, 1969).

$$\int_0^\pi e^{ir\cos\theta} P_n(\cos \theta) \sin \theta d\theta = \frac{2a_n}{2n+1} j_n(r). \quad (6.101)$$

The  $n$ th derivative of the left-hand side of equation (6.101) with respect to  $r$ , at  $r = 0$ , is

$$i^n \int_0^\pi \cos^n \theta P_n(\cos \theta) \sin \theta d\theta = \frac{i^n 2^{n+1} (n!)^2}{(2n+1)!} \quad (6.102)$$

while the same derivative of the right-hand side of equation (6.101) is

$$\frac{2^{n+1}}{(2n+1)} \frac{(n!)^2}{(2n+1)!} a_n. \quad (6.103)$$

Equating equation (6.102) and (6.103) results in

$$a_n = i^n (2n+1). \quad (6.104)$$

The expression (6.104) may now be substituted back in equation (6.100) to yield

$$e^{iz} = e^{ir\cos\theta} = \sum_{n=0}^{\infty} i^n (2n+1) j_n(r) P_n(\cos \theta), \quad (6.105)$$

which is the transformation expressing a plane wave in terms of spherical wave functions.

**Scattering by a Sphere.**—In Figure 6.9 a uniform plane wave is incident upon a conducting sphere. If the wave is propagated in the  $z$  direction with the incident or primary electric field  $E_x^p$  oriented in the  $x$  direction, then the corresponding magnetic field  $H_y^p$  will be oriented in the  $y$  direction. Under these circumstances

$$E_x^p = E_0 e^{-ikz} = E_0 e^{-ikr\cos\theta}, \quad (6.106)$$

and

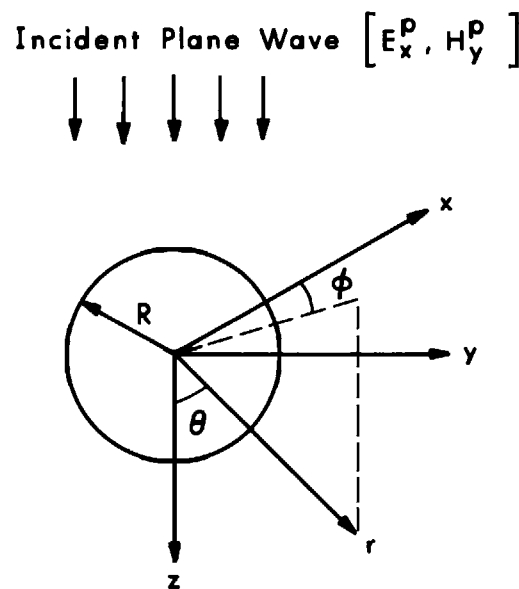


FIG. 6.9. Plane *electromagnetic* wave incident upon a conducting sphere (after Harrington, 1961).

$$H_y^p = \frac{E_0}{Z} e^{-ikz} = \frac{E_0}{Z} e^{-ikr\cos\theta}. \quad (6.107)$$

To facilitate application of boundary conditions we express this incident field in terms of TM, and TE, modes as in the expression (A1.1.24). The potential  $A_r$  can be obtained from  $E_r$ , and the potential  $F_r$  can be obtained from  $H_r$ . Thus we need to construct  $E_r$  and  $H_r$  from equations (6.106) and (6.107). By reference to Figure 6.9

$$\begin{aligned} E_r^p &= \cos \phi \sin \theta E_x^p \\ &= E_0 \cos \phi \sin \theta e^{-ikr\cos\theta} \\ &= E_0 \frac{\cos \phi}{ikr} \frac{\partial}{\partial \theta} (e^{-ikr\cos\theta}). \end{aligned} \quad (6.108)$$

Substituting the expression (6.105) into the expression (6.108) results in

$$E_r^p = \frac{E_0 \cos \phi}{ikr} \sum_{n=0}^{\infty} i^{-n} (2n+1) j_n(kr) \frac{\partial}{\partial \theta} P_n(\cos \theta). \quad (6.109)$$

From the relation between the Legendre and associated Legendre functions (Pipes, 1958, p. 372)

$$P_n^m(x) = (1 - x^2)^{m/2} \frac{d^m}{dx^m} P_n(x), \quad (6.110)$$

we conclude that

$$\frac{\partial P_n}{\partial \theta} = P_n^1. \quad (6.111)$$

Noting that for  $m > n$

$$P_n^m(x) = 0, \quad (6.112)$$

the  $n = 0$  term drops out, and expression (6.109) can be rewritten

$$\begin{aligned} E_r^p &= \frac{-iE_0 \cos \phi}{kr} \sum_{n=1}^{\infty} i^{-n} (2n+1) j_n(kr) P_n^1(\cos \theta) \\ &= \frac{-iE_0 \cos \phi}{(kr)^2} \sum_{n=1}^{\infty} i^{-n} (2n+1) \hat{J}_n(kr) P_n^1(\cos \theta) \end{aligned} \quad (6.113)$$

in which

$$\hat{J}_n(kr) = kr j_n(kr). \quad (6.114)$$

Given from the field expressions (A1.1.24) that

$$E_r = \frac{1}{j} \left( \frac{\partial^2}{\partial r^2} + k^2 \right) A_r \quad (6.115)$$

we observe from equation (6.51) that  $A_r$  in expression (6.115) must have the form

$$A_r^p = \frac{E_0}{\omega\mu} \cos \phi \sum_{n=1}^{\infty} a_n \hat{J}_n(kr) P_n^1(\cos \theta). \quad (6.116)$$

Applying expression (6.115) we find  $E_r^p$  as

$$E_r^p = \frac{-iE_0 \cos \phi}{(kr)^2} \sum_{n=1}^{\infty} a_n n(n+1) \hat{J}_n(kr) P_n^1(\cos \theta). \quad (6.117)$$

Comparing equations (6.117) and (6.113) we obtain the coefficients  $a_n$  as

$$a_n = \frac{-i^n(2n+1)}{n(n+1)}. \quad (6.118)$$

From a similar derivation,

$$F_r^p = \frac{E_0}{k} \sin \phi \sum_{n=1}^{\infty} a_n \hat{J}_n(kr) P_n^1(\cos \theta) \quad (6.119)$$

with the  $a_n$  again given by equation (6.118).

Since the incident fields are given as a superposition of TM<sub>r</sub> and TE<sub>r</sub> modes, the scattered fields will have the same form except that  $\hat{J}_n$  must be replaced by  $\hat{H}_n^{(2)}$ , appropriate to an outward traveling wave. Hence the scattered potentials may be written as

$$A_r^s = \frac{E_0}{\omega\mu} \cos \phi \sum_{n=1}^{\infty} b_n \hat{H}_n^{(2)}(kr) P_n^1(\cos \theta), \quad (6.120)$$

and

$$F_r^s = \frac{E_0}{k} \sin \phi \sum_{n=1}^{\infty} c_n \hat{H}_n^{(2)}(kr) P_n^1(\cos \theta). \quad (6.121)$$

The total potentials are the sums of incident and scattered potentials and hence are written

$$A_r = \frac{E_0}{\omega\mu} \cos \phi \sum_{n=1}^{\infty} [a_n \hat{J}_n(kr) + b_n \hat{H}_n^{(2)}(kr)] P_n^1(\cos \theta), \quad (6.122)$$

and

$$F_r = \frac{E_0}{k} \sin \phi \sum_{n=1}^{\infty} [a_n \hat{J}_n(kr) + c_n \hat{H}_n^{(2)}(kr)] P_n^1(\cos \theta). \quad (6.123)$$

The field components are obtained from the expressions (6.122) and (6.123) by use of equations (A1.1.24).

For a perfectly conducting sphere, the boundary conditions  $E_\theta = E_\phi = 0$  at  $r = R$  result in an evaluation of the unknown coefficients in the expressions (6.122) and (6.123) as

$$b_n = -a_n \frac{\hat{J}'_n(kR)}{\hat{H}'_n(kR)}, \quad (6.124)$$

and

$$c_n = -a_n \frac{\hat{J}_n(kR)}{\hat{H}_n^{(2)}(kR)}. \quad (6.125)$$

The ratio  $b_n/a_n = r_{TE}$ , is the TE<sub>r</sub> mode reflection coefficient while the ratio  $c_n/a_n = r_{TM}$ , is the TM<sub>r</sub> mode reflection coefficient.

Note that F and A can be expressed, as in equations (6.38) and (6.39) in terms of scalar functions  $\psi_f$  and  $\psi_a$ , respectively. Also note that  $A_r$  and  $F_r$  are not solutions of the scalar Helmholtz equation [see equations (6.36) and (6.37)] but that  $\psi_f$  and  $\psi_a$  are such solutions.

Fuller (1971) using a similar approach, obtained  $r_{TE}$ , for a three-layered sphere, and he showed that the response for a plane wave is the same as that for a uniform field under quasi-static assumptions. One of his results is shown in Figure 6.10. A conducting core of  $10^{-2}$  S/m is perfectly insulated from a conducting shell also of  $10^{-2}$  S/m. The core exhibits a peak response at about  $10^2$  Hz while the shell exhibits a peak response at about  $3 \times 10^4$  Hz. The effects of both core and shell are clearly seen in this illustration in which the induction numbers  $\sigma_c$  and  $\sigma_s$  for core and shell, respectively, are well separated at any given frequency. Negi (1962b, 1967) and Wait (1969) earlier studied the same problem.

From observation of equation A6.3 note that  $j_n(kr)$  should be used for the spherical core of Figure 6.10 while a superposition of  $h_n^{(1)}(k_i r) + h_n^{(2)}(k_i r)$  should be used for each of the shells surrounding the core.  $h_n^{(1)}(k_i r)$  corresponds to an inward traveling wave for an  $e^{i\omega t}$  time dependence while  $h_n^{(2)}(k_i r)$  corresponds to an outward traveling wave. Solutions exterior to the outer shell involve negative powers of  $r$  appropriate to solutions of Laplace's equation applicable in a nonconducting region. Appropriate boundary conditions at  $r = R_1, R_2, R_3$  permit evaluation of unknown coefficients and hence permit solving the problem. Fuller (1971) used a superposition of  $j_n(k_i r) + h_n^{(1)}(k_i r)$  for the shells. This approach is also satisfactory since,  $h_n^{(1)}(kr)$ , for zero order, can be expanded in terms of  $\sin(k_i r)$  plus  $\cos(k_i r)$ . However, the use of  $h_n^{(1)}(kr) + h_n^{(2)}(kr)$  is more appealing since it relates obviously to inward and outward propagating waves. Note that for the zeroeth order and an  $e^{i\omega t}$  time dependence, the phase velocity is positive for

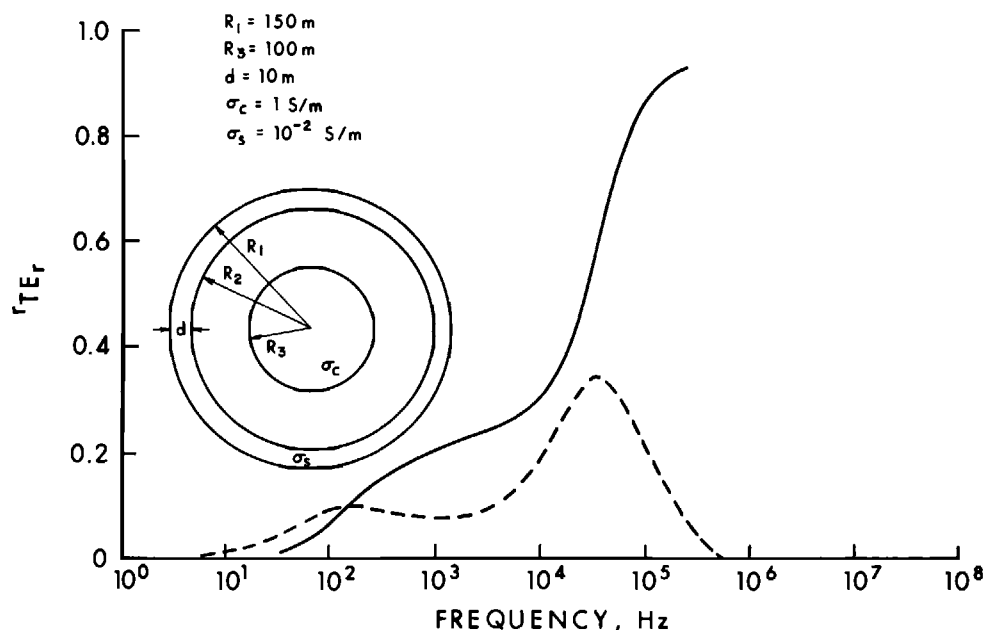


FIG. 6.10. The reflection coefficient  $r_{TE}$  (real solid and imaginary dashed) versus frequency for a three-layered sphere in a uniform alternating electromagnetic field. The parameters of the sphere are shown in the figure (after Fuller, 1971).

$$h_0^{(2)}(kr) e^{i\omega t} = -\frac{e^{i(\omega t - kr)}}{ikr}$$

whereas for an  $e^{-i\omega t}$  time dependence, the phase velocity is positive for

$$h_0^{(1)}(kr)e^{-i\omega t} = \frac{e^{-i(\omega t - kr)}}{ikr}.$$

### A conducting sphere in the field of an alternating magnetic dipole

The problem of a conducting sphere in the field of an alternating magnetic dipole has been studied by March (1953), Wait (1953a), Harrington (1961), and Grant and West (1965). March (1953) uses TE, and TM, modes as we have done above for a conducting sphere in a uniform alternating electromagnetic field, so we follow his approach.

In Figure 6.11 a dipole is located at a distance  $h$  above the center of a sphere of radius  $R$ , conductivity  $\sigma_2$ , magnetic permeability  $\mu_2$ , and dielectric permittivity  $\epsilon_2$ . The sphere is embedded in a medium of conductivity  $\sigma_1$ , magnetic permeability  $\mu_1$ , and dielectric permittivity  $\epsilon_1$ . The dipole may be oriented in either the radial or the transverse directions. The fields are expressed in terms of TM, and TE<sub>r</sub>, modes by the field expressions (6.48) and (6.49).

**The Transverse Magnetic Dipole.**—The primary potential at the observation point  $P(r, \theta, \phi)$  may be written

$$\mathbf{F} = \mathbf{m} \frac{e^{-ik_1\rho}}{\rho}, \quad (6.126)$$

where

$$\rho = (h^2 + r^2 - 2hr \cos \theta)^{1/2}. \quad (6.127)$$

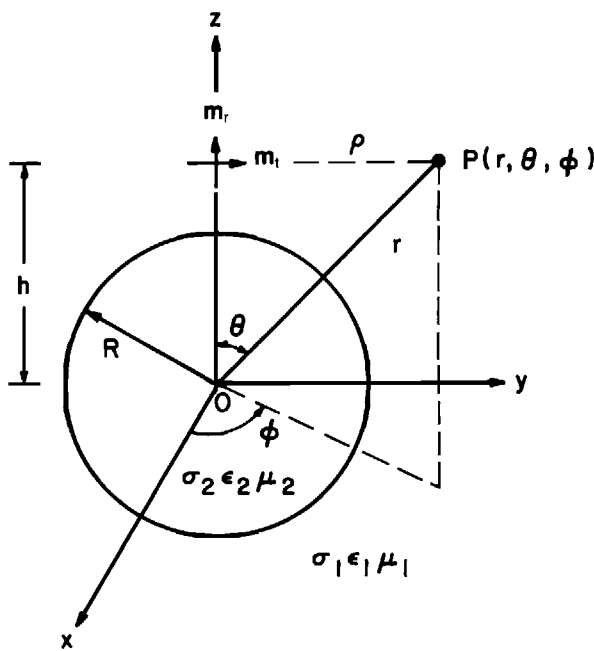


FIG. 6.11. A conducting sphere in the field of a magnetic dipole (after Harrington, 1961).

For the Green's function  $e^{-ik_1 p}/\rho$  we may use a wave transformation

$$\frac{e^{-ik_1 p}}{\rho} = \sum_{n=0}^{\infty} a_n \frac{\hat{J}_n(k_1 r)}{r} P_n(\cos \theta); \quad r < h. \quad (6.128)$$

and

$$\frac{e^{-ik_1 p}}{\rho} = \sum_{n=0}^{\infty} b_n \frac{\hat{H}_n^{(2)}(k_1 r)}{r} P_n(\cos \theta); \quad r > h, \quad (6.129)$$

where

$$a_n = -i(2n + 1) \frac{\hat{H}_n^{(2)}(k_1 h)}{(k_1 h)}, \quad (6.130)$$

and

$$b_n = -i(2n + 1) \frac{\hat{J}_n(k_1 h)}{(k_1 h)}. \quad (6.131)$$

The electric and magnetic fields due to the dipole may be obtained from the expressions (1.122) and (1.123) for a magnetic source. In order to compute the fields, we then need the components of  $\mathbf{F}$  in spherical coordinates. These components are obtained by multiplying equations (6.128) or (6.129) by  $\cos \phi \sin \theta$  for the  $r$  component, by  $\cos \phi \cos \theta$  for the  $\theta$  component, and by  $(-\sin \phi)$  for the  $\phi$  component as may be deduced from Figure 6.11. When equation (6.128) is substituted in  $\mathbf{E}_{TE} = -\nabla \times \mathbf{F}$  of expression (1.122) using the components of curl given by equation (A1.1.11) there results

$$E_r^p = -\sin \phi \sum_{n=1}^{\infty} a_n \frac{\hat{J}_n(k_1 r)}{r^2} P_n^1(\cos \theta); \quad r < h, \quad (6.132)$$

and

$$E_{\theta}^p = -\sin \phi \sum_{n=0}^{\infty} a_n \left[ \frac{\hat{J}_n(k_1 r)}{r^2} - k_1 \frac{\hat{J}'_n(k_1 r)}{r} \right] P_n(\cos \theta); \quad r < h. \quad (6.133)$$

To obtain the expression (6.132), use was made of the relation (6.111). In equation (6.133),  $\hat{J}'_n(k_1 r)$  means  $\partial/\partial r[\hat{J}_n(k_1 r)]$ . Equations (6.132) and (6.133) will be used to find the potentials  $A_r = r\psi_a = r\pi_a \hat{y}$  (TM<sub>r</sub>) and  $F_r = r\psi_f = r\pi_f \hat{z}$  (TE<sub>r</sub>) into which this primary field may be decomposed. The components of the two partial primary fields are given by the expressions (A1.1.24) and are here written, following March (1953), in terms of  $\pi_a$  and  $\pi_f$  as follows:

TM, mode

TE<sub>r</sub> mode

$$E_{mr} = \left( \frac{\partial^2}{\partial r^2} + k^2 \right) r \pi_a \quad E_{er} = 0$$

$$E_{m\theta} = \frac{1}{r} \frac{\partial^2(r\pi_a)}{\partial r \partial \theta} \quad E_{e\theta} = -\frac{\hat{z}}{r \sin \theta} \frac{\partial(r\pi_f)}{\partial \phi}$$

$$E_{m\phi} = \frac{1}{r \sin \theta} \frac{\partial^2(r\pi_a)}{\partial r \partial \phi} \quad E_{e\phi} = \frac{\hat{z}}{r} \frac{\partial(r\pi_f)}{\partial \theta}$$

$$\begin{aligned}
H_{mr} &= 0 & H_{er} &= \frac{\partial^2(r\pi_f)}{\partial r^2} + k^2 r^2 \pi_f \\
H_{m\theta} &= \frac{\hat{y}}{r \sin \theta} \frac{\partial(r\pi_a)}{\partial \phi} & H_{e\theta} &= \frac{1}{r} \frac{\partial^2(r\pi_f)}{\partial r \partial \theta} \\
H_{m\phi} &= -\frac{\hat{y}}{r} \frac{\partial(r\pi_a)}{\partial \theta} & H_{e\phi} &= \frac{1}{r \sin \theta} \frac{\partial^2(r\pi_f)}{\partial r \partial \phi}
\end{aligned} \tag{6.134}$$

Wait (1960a) refers to  $\pi_a$  and  $\pi_f$  as Debye functions.

According to expressions (6.134),  $E_{er}^p = 0$  so that  $E_{mr}^p$  is given by the expression (6.132). From the first of the expressions (6.134) we observe that  $E_{mr}^p$  is related to  $\pi_a$  by

$$E_{mr}^p = \left[ \frac{\partial^2}{\partial r^2} + k_1^2 \right] r \pi_a^p. \tag{6.135}$$

Then  $\pi_a$  should have a form similar to  $E_{mr}^p$  with one lower power of  $r$  in the denominator. Thus we try

$$\pi_a^p = \sin \phi \sum_{n=0}^{\infty} c_n \frac{\hat{J}_n(k_1 r)}{r} P_n^1(\cos \theta), \tag{6.136}$$

where the  $c_n$  are unknown coefficients. We may now calculate  $E_{mr}^p$  from the expression (6.136) and compare the result with the expression (6.132) to obtain  $c_n$  as

$$c_n = -\frac{\hat{z}_1 a_n}{n(n+1)}. \tag{6.137}$$

Hence

$$\pi_a^p = -\hat{z}_1 \sin \phi \sum_{n=1}^{\infty} \frac{a_n}{n(n+1)} \frac{\hat{J}_n(k_1 r)}{r} P_n^1(\cos \theta). \tag{6.138}$$

The potential  $\pi_f$  is now obtained by considering a component  $E_{er}^p$  of the second partial primary field. We write

$$E_{\theta}^p = E_{m\theta}^p + E_{e\theta}^p, \tag{6.139}$$

or

$$E_{e\theta}^p = E_{\theta}^p - E_{m\theta}^p. \tag{6.140}$$

Equation (6.134) provides that

$$E_{m\theta}^p = \frac{1}{r} \frac{\partial^2(r\pi_a)}{\partial r \partial \theta},$$

and we already have  $\pi_a$  from equation (6.138). Thus

$$E_{m\theta}^p = -\hat{z}_1 \sin \phi \sum_{n=1}^{\infty} \frac{k_1 a_n \hat{J}_n(k_1 r)}{n(n+1)r} \frac{dP_n^1(\cos \theta)}{d\theta}. \tag{6.141}$$

When equation (6.141) is subtracted from equation (6.133) there results

$$\begin{aligned} E_{e\theta}^p = \hat{z}_1 \sin \phi & \left\{ a_0 \left( \frac{\hat{J}_0(k_1 r)}{r^2} - k_1 \frac{\hat{J}'_0(k_1 r)}{r} \right) \right. \\ & + \sum_{n=1}^{\infty} a_n \left[ \left( \frac{\hat{J}_n(k_1 r)}{r^2} - \frac{k_1 \hat{J}'_n(k_1 r)}{r} \right) P_n(\cos \theta) + \frac{k_1 \hat{J}'_n(k_1 r)}{n(n+1)r} \frac{dP_n^1(\cos \theta)}{d\theta} \right] \left. \right\}. \end{aligned} \quad (6.142)$$

From the expressions (6.134)

$$E_{e\theta} = -\frac{\hat{z}_1}{r \sin \theta} \frac{\partial(r \pi_f)}{\partial \phi}. \quad (6.143)$$

By equating the expressions (6.142) and (6.143) we find

$$\begin{aligned} \pi_f^p = \cos \phi & \left\{ a_0 \left[ \frac{\hat{J}_0(k_1 r)}{r^2} - \frac{k_1 \hat{J}'_0(k_1 r)}{r} \right] \sin \theta \right. \\ & + \sum_{n=1}^{\infty} a_n \sin \theta \left[ \frac{\hat{J}_n(k_1 r)}{r^2} P_n(\cos \theta) + \frac{k_1 \hat{J}'_n(k_1 r)}{n(n+1)r} \right. \\ & \times \left. \left. \left( \frac{dP_n^1(\cos \theta)}{d\theta} - n(n+1)P_n(\cos \theta) \right) \right] \right\}. \end{aligned} \quad (6.144)$$

March (1953) simplifies the expression (6.144) to

$$\pi_f^p = -\frac{i \cos \phi}{h} \sum_{n=1}^{\infty} \frac{(2n+1)}{n(n+1)} \hat{H}_n^{(2)\prime}(k_1 r) \frac{\hat{J}_n(k_1 r)}{r} P_n^1(\cos \theta). \quad (6.145)$$

Equations (6.138) and (6.145) thus may be written

$$\pi_a^p = \sin \phi \sum_{n=1}^{\infty} \alpha_n \frac{\hat{J}_n(k_1 r)}{r} P_n^1(\cos \theta), \quad (6.146)$$

and

$$\pi_f^p = \cos \phi \sum_{n=1}^{\infty} \beta_n \frac{\hat{J}_n(k_1 r)}{r} P_n^1(\cos \theta), \quad (6.147)$$

where

$$\alpha_n = \frac{i \hat{z}_1 (2n+1) \hat{H}_n^{(2)}(k_1 h)}{n(n+1) k_1 h}, \quad (6.148)$$

and

$$\beta_n = \frac{-i (2n+1) \hat{H}_n^{(2)\prime}(k_1 h)}{n(n+1) h}. \quad (6.149)$$

The forms of the primary potentials  $\pi_a^p$  and  $\pi_f^p$  given in equations (6.146) and (6.147), respectively, suggest that we write the secondary potentials outside the sphere as

$$\pi_a^s = \sin \phi \sum_{n=1}^{\infty} a_{en} \frac{\hat{H}_n^{(2)}(k_1 r)}{r} P_n^1(\cos \theta), \quad (6.150)$$

and

$$\pi_f^s = \cos \phi \sum_{n=1}^{\infty} b_{en} \frac{\hat{H}_n^{(2)}(k_1 r)}{r} P_n^1(\cos \theta). \quad (6.151)$$

Similarly the total potentials inside the sphere are written

$$\pi_a^i = \sin \phi \sum_{n=1}^{\infty} a_{in} \frac{\hat{J}_n(k_2 r)}{r} P_n^1(\cos \theta), \quad (6.152)$$

and

$$\pi_f^i = \cos \phi \sum_{n=1}^{\infty} b_{in} \frac{\hat{J}_n(k_2 r)}{r} P_n^1(\cos \theta). \quad (6.153)$$

In the exterior medium,

$$\pi_f^e = \pi_f^p + \pi_f^s, \quad (6.154)$$

and  $\pi_f^p$  and  $\pi_f^s$  are, respectively, the primary and secondary Debye potentials.

The boundary conditions to be satisfied are the continuity of tangential  $E$  and the continuity of tangential  $H$  at the surface of the sphere where  $r = R$ . From the expressions (6.134) we may write, for continuity of  $E_{m\theta}$ ,

$$\frac{\partial^2(r\pi_a^e)}{\partial r \partial \theta} = \left. \frac{\partial^2(r\pi_a^i)}{\partial r \partial \theta} \right|_{r=R}. \quad (6.155)$$

This equation applies for all  $\theta$  and hence we may write, after integration with respect to  $\theta$  and after using equation (6.154)

$$\frac{\partial}{\partial r} (r\pi_a^p + r\pi_a^s) = \left. \frac{\partial}{\partial r} (r\pi_a^i) \right|_{r=R}. \quad (6.156)$$

The same result could have been obtained had we started with  $E_{m\phi}$  from the expressions (6.134). Similarly from continuity of either  $H_{e\theta}$  or  $H_{e\phi}$

$$\frac{\partial}{\partial r} (r\pi_f^p + r\pi_f^s) = \left. \frac{\partial}{\partial r} (r\pi_f^i) \right|_{r=R}. \quad (6.157)$$

Then from  $H_{m\theta}$  or  $H_{m\phi}$  and  $E_{e\theta}$  or  $E_{e\phi}$

$$\hat{y}_2(r\pi_a^p + r\pi_a^s) = \hat{y}_1(r\pi_a^i), \quad (6.158)$$

and

$$\hat{z}_2(r\pi_f^p + r\pi_f^s) = \hat{z}_1(r\pi_f^i) \Big|_{r=R}. \quad (6.159)$$

Equations (6.150) through (6.153) are four equations concerning the four unknown coefficients  $a_{en}$ ,  $b_{en}$ ,  $a_{in}$ , and  $b_{in}$ . Application of the four boundary conditions of equations (6.155) through (6.158) permits us to write, for the region exterior to the sphere,

$$a_{en} = -\frac{k_2 \hat{y}_1 \hat{J}_n(k_1 R) \hat{J}'_n(k_2 R) - k_1 \hat{y}_2 \hat{J}'_n(k_1 R) \hat{J}_n(k_2 R)}{k_2 \hat{y}_1 \hat{H}_n^{(2)}(k_1 R) \hat{J}'_n(k_2 R) - k_1 \hat{y}_2 \hat{H}_n^{(2)\prime}(k_1 R) \hat{J}_n(k_2 R)} \alpha_n, \quad (6.160)$$

and

$$b_{en} = -\frac{k_2 \hat{z}_1 \hat{J}_n(k_1 R) \hat{J}'_n(k_2 R) - k_1 \hat{z}_2 \hat{J}'_n(k_1 R) \hat{J}_n(k_2 R)}{k_2 \hat{z}_1 \hat{H}_n^{(2)}(k_1 R) \hat{J}'_n(k_2 R) - k_1 \hat{z}_2 \hat{H}_n^{(2)\prime}(k_1 R) \hat{J}_n(k_2 R)} \beta_n. \quad (6.161)$$

Equations (6.146), (6.147), and (6.150) through (6.153) are the potentials from which the fields may be calculated.

**The Radial Magnetic Dipole.**—As before, the primary field is derived from the potential (6.126). However, for this orientation of the dipole, the  $\phi$ -component of the potential vanishes. The  $r$  and  $\theta$ -components of  $\mathbf{F}_n$  are obtained by multiplying  $e^{-ik\rho}/\rho$  by  $\cos \theta$  and  $(-\sin \theta)$ , respectively. The symmetry of the field about the  $z$  axis, implying circulating currents confined to the  $x - y$  plane in the sphere, suggests that we now treat the sphere as a radiating dipole with its axis in the  $z$  direction. As we have seen in Section 1, this requires but a single component of potential  $F_r^p = r \pi_f^p z$ . Thus we write

$$\pi_a^p = 0, \quad (6.162)$$

and

$$\pi_f^p = C \frac{e^{-ik\rho}}{\rho}. \quad (6.163)$$

The electric field and magnetic field obtained from this latter expression by use of expressions (6.134) are then again to be compared with the fields expressed by equations (6.132) and (6.133). The result is that  $C = 1/h$ . Again  $e^{-ik\rho}/\rho$  may be expanded according to the transformation (6.128) to yield

$$\pi_f^p = \frac{1}{h} \sum_{n=0}^{\infty} a_n \frac{\hat{J}_n(kr)}{r} P_n(\cos \theta). \quad (6.164)$$

As before

$$\pi_f^e = \frac{1}{h} \sum_{n=0}^{\infty} c_{en} \frac{\hat{H}_n^{(2)}(k_1 r)}{r} P_n(\cos \theta), \quad (6.165)$$

and

$$\pi_f^i = \frac{1}{h} \sum_{n=0}^{\infty} c_{in} \frac{\hat{J}_n(k_2 r)}{r} P_n(\cos \theta). \quad (6.166)$$

Application of the boundary conditions then yields

$$c_{en} = -\frac{k_2 \hat{z}_1 \hat{J}_n(k_1 R) J'_n(k_2 R) - k_1 \hat{z}_2 \hat{J}'_n(k_1 R) \hat{J}_n(k_2 R)}{k_2 \hat{z}_1 \hat{H}_n^{(2)}(k_1 R) \hat{J}'_n(k_2 R) - k_1 \hat{z}_2 \hat{H}_n^{(2)\prime}(k_1 R) \hat{J}_n(k_2 R)} a_n. \quad (6.167)$$

Since we are interested only in the fields exterior to the sphere there is no need to evaluate  $c_{in}$ .

**Approximations.**—The following approximations are made in order to simplify the solutions obtained:

- (1)  $\mu_2 = \mu_1 = \mu_0$ ,
- (2) displacement currents may be neglected ( $\sigma_2 >> \varepsilon_2 \omega$ ),
- (3) the sphere has a radius much less than a wavelength so that  $|k_1 R| << 1$ ,
- (4) the dipole is located much less than a wavelength from the sphere so that  $|k_1 h| << 1$ , and
- (5) the observer is located much less than a wavelength from the sphere so that  $|k_1 r| << 1$ .

In the coefficient (6.161) the ratio  $b_{en}/\beta_n$  is essentially the ratio of secondary to primary potentials for the TE<sub>r</sub> mode for a transverse dipole. Similarly in the coefficient (6.167) the ratio  $c_{en}/a_n$  is essentially the ratio of secondary to primary potentials for the TE<sub>r</sub> mode for a radial dipole. Hence write  $r_{TE_r} = -c_{en}/a_n = b_{en}/\beta_n$  as the reflection coefficient

$$r_{TE_r} = \frac{(k_2 R) \mu_1 \frac{\hat{J}'_n(k_2 R)}{\hat{J}_n(k_2 R)} - (k_1 R) \mu_2 \frac{\hat{J}'_n(k_1 R)}{\hat{J}_n(k_1 R)}}{(k_2 R) \mu_1 \frac{\hat{J}'_n(k_2 R)}{\hat{J}_n(k_2 R)} - (k_1 R) \mu_2 \frac{\hat{H}_n^{(2)*}(k_1 R)}{\hat{H}_n^{(2)}(k_1 R)}}. \quad (6.168)$$

Wait (1953a, 1960a), shows that

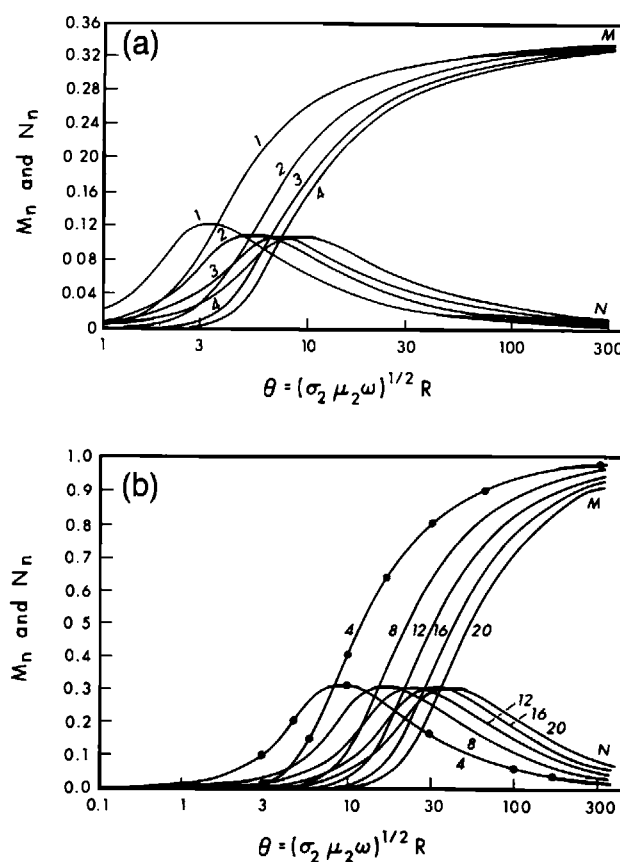


FIG. 6.12. The in-phase and quadrature multipole functions versus induction number  $\theta = (\sigma_2 \mu_2 \omega)^{1/2} R$ . (a) after Wait, 1953a and (b) after Lodha and West, 1976.

$$r_{TE,r} = \frac{\mu_1 \alpha \frac{\hat{I}'_n(\alpha)}{I_n(\alpha)} - \mu_2(n+1)}{\mu_1 \alpha \frac{\hat{I}'_n(\alpha)}{\hat{I}_2(\alpha)} + \mu_2 n} = M_n - iN_n, \quad (6.169)$$

where  $\alpha = k_2 R$ .

Wait (1953a) plotted  $M_n$  and  $N_n$  for the first four orders of  $n$ ; his results are shown in Figure 6.12a. Lodha and West (1976) extended these results to order  $n = 20$  (Figure 6.12b).

The ratio  $r_{TM,r} = a_{en}/\alpha_n$  in the coefficient (6.157) pertinent to the  $TM_r$  mode reduces to, for the approximation stated,

$$r_{TM,r} = \frac{\hat{J}_n(k_1 R)}{\hat{H}_n(k_1 R)} \frac{n+1}{n} \quad (6.170)$$

and is independent of  $\alpha = k_2 R$ .

**The Fields.**—The secondary magnetic field components may now be computed from the potentials via the expressions (6.134). Grant and West (1965, p. 515–519) give these components as follows:

Transverse dipole (receiver location  $r$  in same axial plane as dipole)

$$H_r^s = \frac{m}{4\pi} e^{i\omega t} \sum_{n=1}^{\infty} (M_n - iN_n) \frac{R^{2n+1}}{(rh)^{n+2}} n P_n^1(\cos \theta), \quad (6.171)$$

$$H_\theta^s = -\frac{m}{4\pi} e^{i\omega t} \sum_{n=1}^{\infty} (M_n - iN_n) \frac{R^{2n+1}}{(rh)^{n+2}} \left[ n^2 P_n(\cos \theta) - \frac{n}{n+1} \cos \theta P_n^1(\cos \theta) \right], \quad (6.172)$$

and

$$H_\phi^s = 0. \quad (6.173)$$

Radial dipole

$$H_r^s = -\frac{m}{4\pi} e^{i\omega t} \sum_{n=1}^{\infty} (M_n - iN_n) \frac{R^{2n+1}}{(rh)^{n+2}} n(n+1) P_n(\cos \theta), \quad (6.174)$$

$$H_\theta^s = -\frac{m}{4\pi} e^{i\omega t} \sum_{n=1}^{\infty} (M_n - iN_n) \frac{R^{2n+1}}{(rh)^{n+2}} n P_n^1(\cos \theta), \quad (6.175)$$

and

$$H_\phi^s = 0. \quad (6.176)$$

Lodha and West (1976) obtained the response of a vertical coaxial coil EM system to a conducting sphere in a whole space. An example of their results, applicable to a ground EM system traversed over the center of the sphere, is shown in Figure 6.13. Best and Shamma (1979) extended these calculations to make them applicable to a number of AEM systems and to traverses offset from the center of the sphere.

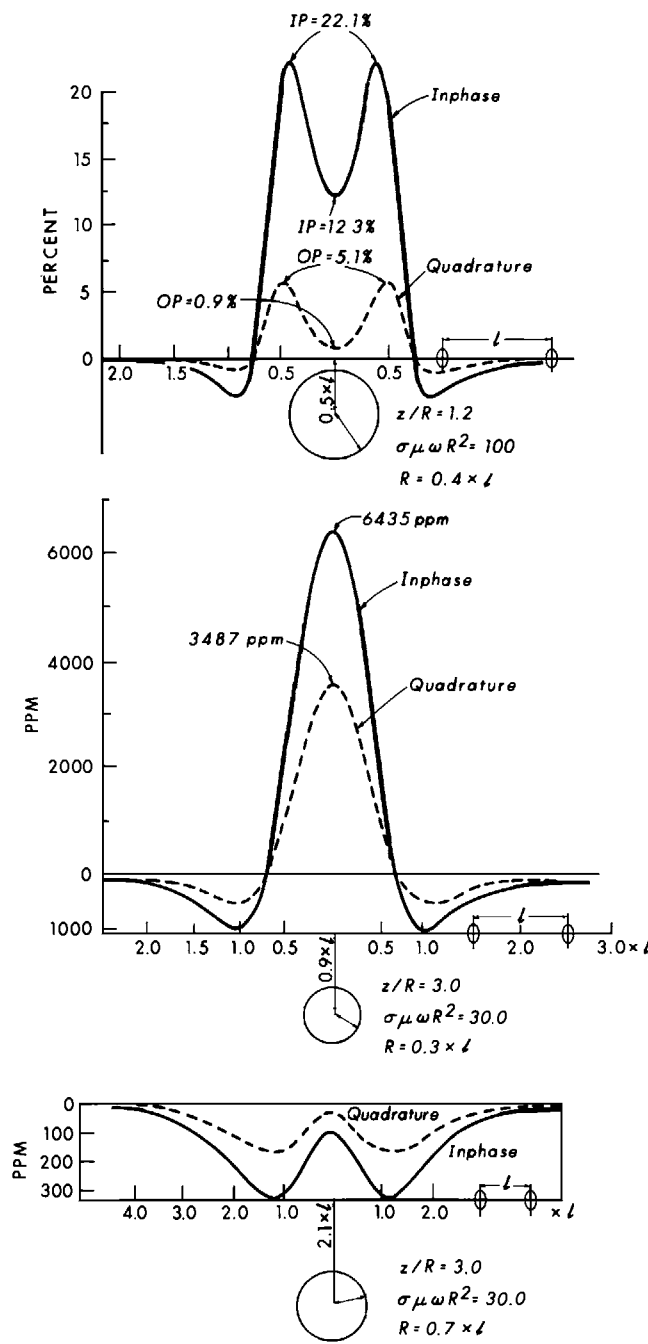


FIG. 6.13. In-phase and quadrature profiles for a vertical coaxial coil EM system traversed across the center of a sphere. The coil spacing is  $l$ , the depth to the center of the sphere is  $z$ , the radius of the sphere is  $R$ , and the induction number is  $\theta = \sigma\mu\omega R^2$ . For 6.13 (a)  $z = 0.5l$ ,  $z/R = 1.2$ , and  $\theta = 100$ . For 6.13 (b)  $z = 0.9l$ ,  $z/R = 3.0$ , and  $\theta = 30.0$ . For 6.13 (c)  $z = 2.1l$ ,  $z/R = 3.0$ , and  $\theta = 30.0$  (after Lodha and West, 1976).

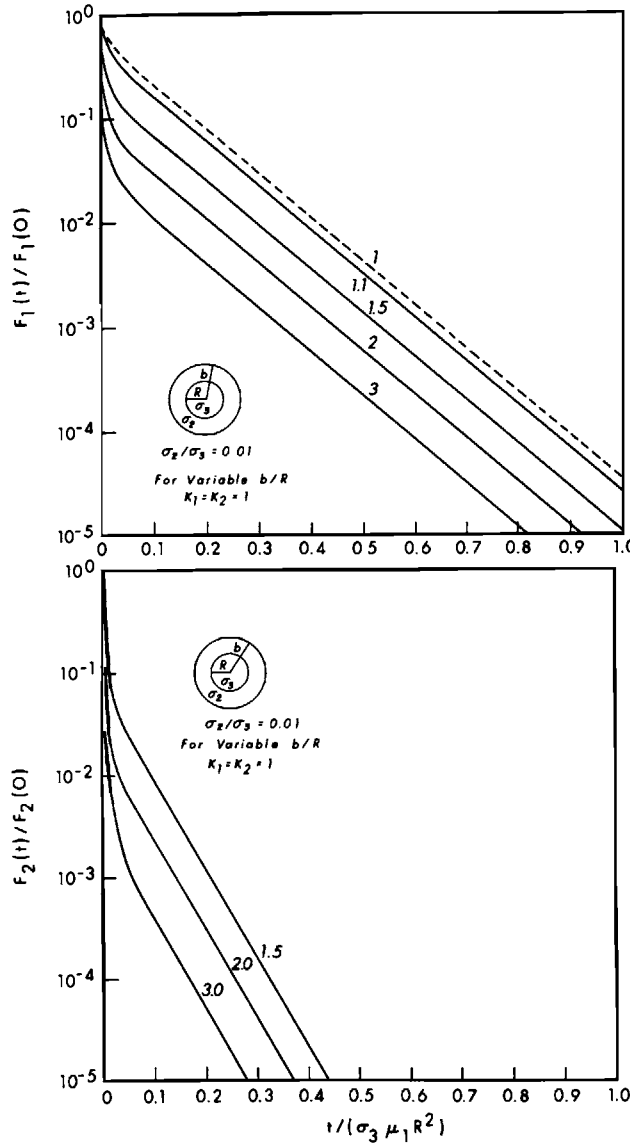


FIG. 6.14. Decay curves for variable  $b/R$  and  $\sigma_2/\sigma_3 = 0.01$ . Both  $F_1(t)/F_1(0)$  and  $F_2(t)/F_2(0)$  are presented (after Nabighian, 1971).

#### A conducting sphere in the field of a transient magnetic dipole.

Nabighian (1970) gives the secondary magnetic potential of a magnetic pole source at  $(0, 0, h)$  in Figure 6.11 as

$$u_0(t) = P \sum_{n=1}^{\infty} \frac{n}{n+1} \frac{R^{2n+1}}{h^{n+1} r^{n+1}} P_n(\cos \theta) F_n(t), \quad (6.177)$$

where

$$F_n(t) = 2(2n+1)K_m$$

$$\sum_{s=1,2,\dots} \frac{e^{i\omega_s t}}{nK_m(nK_m + 1) - \alpha_s^2 - n(n+1)}, \quad (6.178)$$

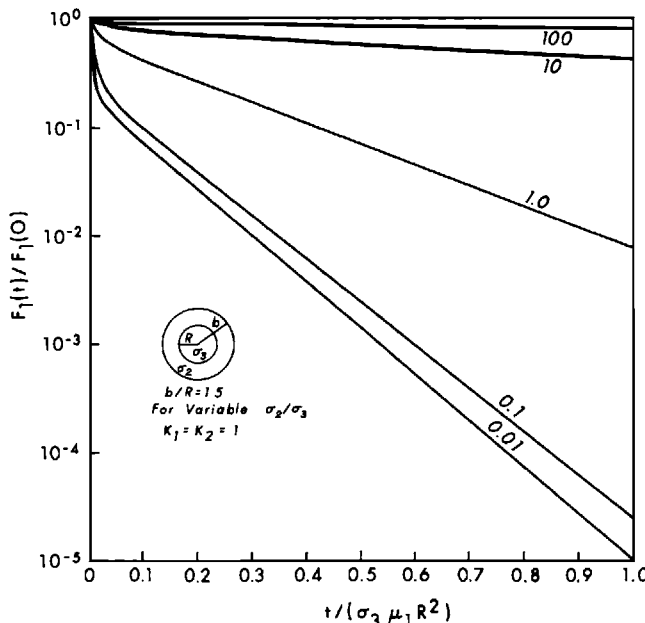


FIG. 6.15. Decay curves for  $b/R = 1.5$  and variable  $\sigma_2/\sigma_3$  for the function  $F_1(t)/F_1(0)$  (after Nabighian, 1971).

in which  $\omega_s$  and  $k_s$  are the frequencies and wave numbers of the fundamental modes of the sphere, and where  $\alpha_s = k_s R$  and  $K_m = \mu_2/\mu_1$ . Since the fields will have the same time variation as the potential, it is sufficient to study  $F_n(t)$ . Nabighian (1971) extends this formulation to a two-layer sphere. Figure 6.14 contains plots of the first and second terms of the expression (6.178), normalized by the values of these functions at  $t = 0$  for a two-layer sphere with no permeability contrast. Note that the normalized  $F_1(t)$  function dominates the normalized  $F_2(t)$  function throughout most of the normalized time interval displayed; all decay curves then approach a simple exponential.

As Nabighian (1971) states, "As long as the conductivity of the core is much larger than that of the shell, the decay curves, at large times, approach the effect due to the core alone. This is the basis for all transient EM methods." Figure 6.15, from Nabighian (1971) displays the normalized  $F_1(t)$  as a function of normalized time, with the ratio of shell conductivity to core conductivity varied. For a fixed shell thickness, the core can be detected if it has a conductivity higher than that of the shell. This observation is consistent with the results earlier quoted from Fuller (1971) for a layered sphere in a plane wave.

## Appendix 6.1 Spherical Cylinder Functions

We introduced the spherical Bessel functions in equation (6.26) as

$$z_n(x) = \left( \frac{\pi}{2x} \right)^{1/2} Z_{n+1/2}(x),$$

$$j_n(x) = \left( \frac{\pi}{2x} \right)^{1/2} J_{n+1/2}(x), \quad (\text{A6.1})$$

$$\begin{aligned} n_n(x) &= \left(\frac{\pi}{2x}\right)^{1/2} N_{n+1/2}(x), \\ h_n^{(1)}(x) &= \left(\frac{\pi}{2x}\right)^{1/2} H_{n+1/2}^{(1)}(x), \end{aligned} \quad (\text{A6.2})$$

and

$$h_n^{(2)}(x) = \left(\frac{\pi}{2x}\right)^{1/2} H_{n+1/2}^{(2)}(x).$$

### Derivation of the spherical Bessel functions

Jackson (1975) defined these functions and presented some of their properties. For example,

$$j_n(x) = (-x)^n \left(\frac{1}{x} \frac{d}{dx}\right)^n \left(\frac{\sin x}{x}\right), \quad (\text{A6.3})$$

$$n_n(x) = -(-x)^n \left(\frac{1}{x} \frac{d}{dx}\right)^n \left(\frac{\cos x}{x}\right), \quad (\text{A6.4})$$

$$h_n^{(1)}(x) = \left(\frac{\pi}{2x}\right)^{1/2} [J_{n+1/2}(x) + iN_{n+1/2}(x)],$$

and

$$h_n^{(2)}(x) = \left(\frac{\pi}{2x}\right)^{1/2} [J_{n+1/2}(x) - iN_{n+1/2}(x)].$$

Thus for the zeroeth order ( $n = 0$ ) the explicit forms of equations (A6.3) and (A6.4) are

$$\begin{aligned} j_0(x) &= \frac{\sin x}{x}, & n_0(x) &= -\frac{\cos x}{x}, \\ h_0^1(x) &= \frac{e^{ix}}{ix}, & h_0^2(x) &= -\frac{e^{-ix}}{ix}. \end{aligned} \quad (\text{A6.5})$$

### The Schelkunoff spherical Bessel functions

In definition (6.50) we introduced the functions

$$\hat{Z}_n(x) = x z_n(x) = \left(\frac{\pi x}{2}\right)^{1/2} Z_{n+1/2}(x). \quad (\text{A6.6})$$

Thus the properties of the  $\hat{Z}_n(x)$  can be deduced from those given for  $Z_m(x)$  in Appendix 5.1. Interestingly, for large arguments, the asymptotic expansions for  $Z_{n+1/2}$  become exact, leading to

$$\hat{J}_n(x) = C_n(x) \sin\left(x - \frac{n\pi}{2}\right) + D_n(x) \cos\left(x - \frac{n\pi}{2}\right), \quad (\text{A6.7})$$

$$\hat{N}_n(x) = D_n(x) \sin\left(x - \frac{n\pi}{2}\right) - C_n(x) \cos\left(x - \frac{n\pi}{2}\right), \quad (\text{A6.8})$$

$$\hat{H}_n^{(1)}(x) = i^{-n} [D_n(x) - iC_n(x)] e^{ix}, \quad (\text{A6.9})$$

and

$$\hat{H}_n^{(2)}(x) = i^n [D_n(x) + iC_n(x)] e^{-ix}, \quad (\text{A6.10})$$

where

$$C_n(x) = \sum_{m=0}^{2m \leq n} \frac{(-1)^m (n+2m)!}{(2m)!(n-2m)!(2x)^{2m}}, \quad (\text{A6.11})$$

and

$$D_n(x) = \sum_{m=0}^{2m \leq n-1} \frac{(-1)^m (n+2m+1)!}{(2m+1)!(n-2m-1)!(2x)^{2m+1}} \quad (\text{A6.12})$$

## Acknowledgments

Many people have influenced us or aided us in the preparation of this manuscript. Influence has evolved from our long use of the texts by Harrington (1961), Jackson (1975), and Stratton (1941); we are indebted to them for our underlying knowledge of electromagnetic theory.

Reviews of parts or all of this manuscript were gratefully received from W. L. Anderson, C. W. Beasley, H. M. Bibby, N. A. Butterworth, P. A. Eaton, M. F. Flis, F. C. Frischknecht, C. M. Furse, S. L. Howard, G. R. Jiracek, J. M. Johnston, M. N. Nabighian, G. R. Olhoeft, L. D. Pellerin, A. P. Raiche, and B. R. Spies. Their constructive criticism helped us immensely in making this mathematical excursion more palatable and of interest to a broader audience than we would have envisioned. While each reviewer has caught mistakes and omissions that we made in early drafts, responsibility for all remaining errors and omissions must lie solely with us.

We thank M. F. Flis for computing the dipole responses in Sections 2 and 4. The text has been typed with incredible care by Holly Baker through about ten drafts. Sandra Bromley and Paul Onstot prepared the illustrations to our, and hopefully your, satisfaction.

## References

- Abramowitz, M., and Stegun, I. A., 1964, Handbook of mathematical functions: Dover Publ., Inc.  
 Anderson, W. L., 1975, Improved digital filters for evaluating Fourier and Hankel transform integrals: Nat. Tech. Inf. Serv. Rep. PB-242-800.  
 —, 1979, Numerical integration of related Hankel transforms of orders 0 and 1 by adaptive digital filtering: Geophysics, **44**, 1287–1305.  
 —, 1982, Fast Hankel transforms using related and lagged convolutions: Assn. Comp. Mach. Trans. on Math. Software, **8**, 344–368.

- \_\_\_\_\_, 1984a, Computation of Green's tensor integrals for three-dimensional electromagnetic problems using fast Hankel transforms: *Geophysics*, **49**, 1754–1759.
- \_\_\_\_\_, 1984b, Discussion on: "Numerical integration of related Hankel transforms by quadrature and continued fraction expansion" with reply by author (A. D. Chave): *Geophysics*, **49**, 1811–1812.
- Baños, A., 1966, Dipole radiation in the presence of a conducting half-space: Pergamon Press, Inc.
- Best, M. E., and Shammas, B. R., 1979, A general solution for a spherical conductor in a magnetic dipole field: *Geophysics*, **44**, 781–800.
- Bhattacharyya, B. K., 1957, Propagation of an electric pulse through a homogeneous and isotropic medium: *Geophysics*, **22**, 905–921.
- Boehl, J. E., Bostick, F. X., Jr., and Smith, H. W., 1977, An application of the Hilbert transform to the magnetotelluric method: *Elec. Geophys. Res. Lab. Rep.*, Univ. of Texas at Austin.
- Busselli, G., 1982, The effect of near-surface superparamagnetic material on electromagnetic measurements: *Geophysics*, **47**, 1315–1324.
- Chave, A. D., 1983, Numerical integration of related Hankel transforms by quadrature and continued fraction expansion: *Geophysics*, **48**, 1671–1686.
- Dey, A., and Ward, S. H., 1970, Inductive sounding of a layered earth with a horizontal magnetic dipole: *Geophysics*, **35**, 660–703.
- Dey, A., and Morrison, H. F., 1973, Electromagnetic coupling in frequency and time-domain induced polarization surveys over a multilayered earth: *Geophysics*, **38**, 380–405.
- Dwight, H. B., 1961, Tables of integrals and other mathematical data: MacMillan Publ. Co., Inc.
- D'Yakanov, B. P., 1953, The diffraction of electromagnetic waves in a circular cylinder in a homogeneous half-space: *Izv. Acad. Sci. USSR, Geophys. Ser.*, 950–955.
- Erdelyi, A., Ed., 1954, Tables of integral transforms: McGraw-Hill Book Co.
- Frishknecht, F. C., 1967, Fields about an oscillating magnetic dipole over a two-layer earth: Colorado School of Mines Quart., **62**, no. 1.
- Fuller, B. D., 1971, Electromagnetic response of a conductive sphere surrounded by a conductive shell: *Geophysics*, **36**, 9–24.
- Ghosh, D. P., 1971, The application of linear filter theory to the direct interpretation of geoelectrical resistivity sounding measurements: *Geophys. Prosp.*, **19**, 192–217.
- Gradshteyn, I. S., and Ryzhik, I. M., 1965, Table of integrals, series, and products: Academic Press Inc.
- Grant, F. S., and West, G. F., 1965, Interpretation theory in applied geophysics: McGraw-Hill Book Co.
- Gunderson, B. M., Newman, G. A., and Hohmann, G. W., 1986, Three-dimensional transient electromagnetic responses for a grounded source: *Geophysics*, **51**, 2117–2130.
- Harrington, R. F., 1961, Time-harmonic electromagnetic fields: McGraw-Hill Book Co.
- Hohmann, G. W., 1971, Electromagnetic scattering by conductors in the earth near a line source of current: *Geophysics*, **36**, 101–131.
- \_\_\_\_\_, 1973, Electromagnetic coupling between grounded wires at the surface of a two-layer earth: *Geophysics*, **38**, 854–863.
- Hvozdara, M., 1972, Electromagnetic induction in a half-space with a cylindrical inhomogeneity: *Studia Geophys. et Geod.*, **16**, 240–261.
- Inan, A. S., Fraser-Smith, A. C., and Villard, O. G., 1985, ULF/ELF electromagnetic fields produced in a conducting medium of infinite extent by a linear current source of finite length: *Inst. Elect. and Electron. Eng., Trans. on Ant. and Prop.*, **AP-33**, 1363–1369.
- Jackson, J. D., 1975, Classical electrodynamics: John Wiley and Sons, Inc.
- Jahnke, E., and Emde, F., 1945, Tables of functions with formulae and curves, second edition: Dover Publ., Inc.
- Kauahikaua, J., 1978, Electromagnetic fields about a horizontal electric wire source of arbitrary length: *Geophysics*, **43**, 1019–1022.
- Kaufman, A. A., 1979, Harmonic and transient fields on the surface of a two-layer medium: *Geophysics*, **44**, 1208–1217.
- \_\_\_\_\_, 1985, Distribution of alternating electrical charges in a conducting medium: *Geophys. Prosp.*, **33**, 171–184.
- Kaufman, A. A., and Keller, G. V., 1983, Frequency and transient soundings: Elsevier Science Publ. Co., Inc.
- \_\_\_\_\_, 1985, Inductive mining prospecting Part 1: Theory: Elsevier Science Publ. Co., Inc.
- Knight, J. H., and Raiche, A. P., 1982, Transient electromagnetic calculations using the Gaver-Stehfest inverse Laplace transform method: *Geophysics*, **47**, 47–50.
- Kraichman, M. B., 1970, Handbook of electromagnetic propagation in conducting media: U.S. Govt. Printing Office.
- Kunetz, G., 1972, Processing and interpretation of magnetotelluric soundings: *Geophysics*, **37**, 1005–1021.
- Lee, T., and Lewis, R., 1974, Transient EM response of a large loop on a layered ground: *Geophys. Prosp.*, **22**, 430–444.
- Lewis, R., and Lee, T., 1981, The effect of host rock on transient electromagnetic fields: *Bull. Austral. Soc. Explor. Geophys.*, **12**, 5–12.
- Lodha, G. S., and West, G. F., 1976, Practical airborne EM (AEM) interpretation using a sphere model: *Geophysics*, **41**, 1157–1169.
- March, H. W., 1953, The field of a magnetic dipole in the presence of a conducting sphere: *Geophysics*, **16**, 671–684.
- Meyer, J., 1963, Elektromagnetische induktion in einem leitenden homogenen zylinder durch aussere magnetische und elektrische wechselfelder miteilungen aus dem: Max-Planck-Inst. für Aeronomie.
- Nabighian, M. N., 1970, Quasi-static transient response of a conducting permeable sphere in a dipolar field: *Geophysics*, **35**, 303–309.

- \_\_\_\_\_, 1971, Quasi-static transient response of a conducting permeable two-layer sphere in a dipolar field: *Geophysics*, **36**, 25–37.
- \_\_\_\_\_, 1979, Quasi-static transient response of a conducting half-space—An approximate representation: *Geophysics*, **44**, 1700–1705.
- Nabighian, M. N., and Oristaglio, M. L., 1984, On the approximation of finite loop sources by two-dimensional line sources: *Geophysics*, **49**, 1027–1029.
- Negi, J. G., 1962a, Inhomogeneous cylindrical ore body in presence of a time varying magnetic field: *Geophysics*, **27**, 386–392.
- \_\_\_\_\_, 1962b, Diffraction of electromagnetic waves by an inhomogeneous sphere: *Geophysics*, **27**, 480–492.
- \_\_\_\_\_, 1967, Electromagnetic screening due to a disseminated spherical zone over a conducting sphere: *Geophysics*, **32**, 69–87.
- Negi, J. G., and Raval, V., 1969, Negative electromagnetic screening by a cylindrical conducting cover: *Geophysics*, **34**, 944–957.
- Ogunade, S. O., and Dosso, H. W., 1980, The inductive response of a horizontal conducting cylinder buried in a uniform earth for a uniform inducing field: *Geophys. Prosp.*, **28**, 601–609.
- Oristaglio, M. L., 1982, Diffusion of electromagnetic fields into the earth from a line source of current: *Geophysics*, **47**, 1585–1592.
- Oristaglio, M. L., and Hohmann, G. W., 1984, Diffusion of electromagnetic fields in a two-dimensional earth: A finite-difference approach: *Geophysics*, **49**, 870–894.
- Patra, H. P., 1970, Central frequency sounding in shallow engineering and hydro-geological problems: *Geophys. Prosp.*, **18**, 236–254.
- Patella, D., 1976, Interpretation of magnetotelluric resistivity and phase soundings over horizontal layers: *Geophysics*, **41**, 96–105.
- Pipes, L. A., 1958, Applied mathematics for engineers and physicists: McGraw-Hill Book Co.
- Poddar, M., 1982, A rectangular loop source of current on a two-layered earth: *Geophys. Prosp.*, **30**, 101–114.
- Raab, P., and Frishknecht, F., 1983, Desktop computer processing of coincident and central loop time-domain electromagnetic data: U.S. Geol. Surv. Open File Rep. 83–240.
- Raiche, A. P., and Spies, B. P., 1981, Coincident loop transient electromagnetic master curves for interpretation of two-layer earths: *Geophysics*, **46**, 53–64.
- Reitz, J. R., and Milford, F. J., 1960, Foundations of electromagnetic theory: Addison-Wesley Publ. Co., Inc.
- Ryu, J., Morrison, H. F., and Ward, S. H., 1970, Electromagnetic fields about a loop source of current: *Geophysics*, **35**, 862–896.
- Schelkunoff, S. A., 1943, Electromagnetic waves: D. Van Nostrand Co., Inc.
- Singh, S. K., 1977, Discussion on “Time dependent electromagnetic fields of an infinite, conducting cylinder excited by a long current-carrying cable”: *Geophysics*, **42**, 661–662.
- Sommerfeld, A., 1952, Electrodynamics: Academic Press Inc.
- Stratton, J. A., 1941, Electromagnetic theory: McGraw-Hill Book Co.
- Sunde, E. D., 1968, Earth conduction effects in transmission systems: Dover Publ. Inc.
- VanBladel, J., 1961, Some remarks on Green’s dyadic for infinite space: *Inst. Radio Eng., Trans. Ant. and Prop.*, **9**, 563–566.
- Verma, S. K., 1972, Quasi-static time-domain electromagnetic response of a homogeneous conducting infinite cylinder: *Geophysics*, **37**, 92–97.
- \_\_\_\_\_, 1973, Time-dependent electromagnetic fields of an infinite, conducting cylinder excited by a long current-carrying cable: *Geophysics*, **38**, 369–379.
- Wait, J. R., 1951a, A conducting sphere in a time varying magnetic field: *Geophysics*, **16**, 666–672.
- \_\_\_\_\_, 1952, The cylindrical ore body in the presence of a cable carrying an oscillating current: *Geophysics*, **17**, 378–386.
- \_\_\_\_\_, 1953a, A conducting permeable sphere in the presence of a coil carrying an oscillating current: *Can. J. Phys.*, **31**, 670–678.
- \_\_\_\_\_, 1953b, The fields of a line source of current over a stratified conductor: *App. Sci. Res.*, **B3**, 279–292.
- \_\_\_\_\_, 1953c, Propagation of radio waves over a stratified ground: *Geophysics*, **18**, 416–422.
- \_\_\_\_\_, 1955, Mutual electromagnetic coupling of loops over a homogeneous ground: *Geophysics*, **20**, 630–637.
- \_\_\_\_\_, 1958, Propagation of electromagnetic pulses in a homogeneous conducting earth: *App. Sci. Res.*, **8**, 213–253.
- \_\_\_\_\_, 1960a, On the electromagnetic response of a conducting sphere to a dipole field: *Geophysics*, **25**, 649–658.
- \_\_\_\_\_, 1960b, Propagation of electromagnetic pulses in a homogeneous conducting earth: *Appl. Sci. Res., Section B*, **8**, 213–253.
- \_\_\_\_\_, 1962, Electromagnetic waves in stratified media: The MacMillan Co.
- \_\_\_\_\_, 1969, Electromagnetic induction in a solid conducting sphere enclosed by a thin conducting spherical shell: *Geophysics*, **34**, 753–759.
- \_\_\_\_\_, 1971, Transient excitation of the earth by a line source of current: *Proc. Inst. Elect. Electron. Eng.*, **59**, 1287–1288.
- \_\_\_\_\_, 1973, On electromagnetic induction in elongated ore bodies: *Geophysics*, **38**, 984–985.
- \_\_\_\_\_, 1982, Geo-electromagnetism: Academic Press Inc.
- Wait, J. R., and Spies, K. P., 1969, Quasi-static transient response of a conducting permeable sphere: *Geophysics*, **34**, 789–792.
- Wait, J. R., and Hill, D. A., 1973, Excitation of a homogeneous conductive cylinder of finite length by a prescribed axial current distribution: *Radio Sci.*, **8**, 1169–1176.

- Ward, S. H., 1967, The electromagnetic method: *in* Mining Geophysics, **2**, 228–372, Soc. Explor. Geophys.
- Ward, S. H., and Wannamaker, P. E., 1983, The MT/AMT electromagnetic method in geothermal exploration: United Nations Univ. Geothermal Training Programme, Iceland, Rep. 1983–5.
- Watson, G. N., 1944, A treatise on the theory of Bessel functions: Cambridge Univ. Press.
- Weir, G. J., 1980, Transient electromagnetic fields about an infinitesimally long grounded horizontal electric dipole on the surface of a uniform half-space: *Geophys. J. Roy. Astr. Soc.*, **61**, 41–56.



---

---

# 5

## Numerical Modeling for Electromagnetic Methods of Geophysics

---

---



---

---

---

5

---

---

## Numerical Modeling for Electromagnetic Methods of Geophysics

*Gerald W. Hohmann\**

With the development of accurate, flexible, and reliable digital field instruments, electrical methods of geophysics now are limited mainly by a lack of interpretation capability. Forward solutions for one-dimensional (1-D) (layered) models have been available for many years; they consist of Fourier or Bessel integrals, which can be easily evaluated numerically. Inverse solutions for 1-D models also have been used routinely for many years. However, calculating the response of a two-dimensional (2-D) or three-dimensional (3-D) model is much more difficult, except for certain simple geometries such as spheres or cylinders, where conductivity boundaries correspond to constant-coordinate surfaces. Advances in understanding and interpretation for electrical methods now depend on forward and inverse numerical solutions for arbitrary 2-D and 3-D models.

Numerical solutions are achieved by approximating the relevant differential or integral equation and solving a large matrix equation. Differential equation (DE) solutions, the easiest to implement, result in large banded matrices. Because the entire earth within the range of the particular EM system is modeled on a grid, DE methods are preferable for simulating complex geology, and they have been most successful in 2-D applications. Integral equation (IE) formulations involve more difficult mathematics, but the unknown fields only need to be found in anomalous regions. Thus IE solutions are less expensive for calculating the response of one or a few small bodies and hence are most useful for evaluating field techniques, designing surveys, and computing interpretation catalogs. IE methods have been more successful than DE methods for 3-D modeling.

Time-domain solutions have appeared only recently. They can be achieved by Fourier transforming frequency-domain results or by time-stepping directly in the time domain. Explicit DE solutions are particularly important, because inversion of large matrices is not required.

The numerous possibilities for theoretical and programming errors make it necessary to compare results computed by different methods before a numerical solution can be considered valid. Convergence and reciprocity are necessary self-checks for a valid numerical solution.

This chapter is not a comprehensive treatment of numerical methods in EM: the field is too broad and is changing too rapidly. Rather, the chapter is a guide to the current literature and a summary of the important numerical solutions developed to date. Therefore, I have organized the chapter by geological model instead of by mathematical technique.

\*Department of Geology and Geophysics, University of Utah, Salt Lake City, Utah, 84112

I begin the chapter with derivations of the relevant differential and integral equations. The mathematical foundations of numerical solutions of the equations are covered in many books, so I simply present a brief discussion of the fundamental unifying concept: the method of weighted residuals. Then finite element and integral equation solutions are discussed for a 2-D model and 2-D source in the frequency domain. For the same model, I summarize a time-domain, finite difference solution. Next, progress in solving the problem of a 2-D model excited by a 3-D source is discussed. The remainder of the chapter is devoted to the full 3-D problem, with emphasis on integral equation and hybrid techniques.

## Differential and Integral Equations

Figure 1 shows the most useful simple model, consisting of an overburden layer of conductivity  $\sigma_1$ , a host rock of conductivity  $\sigma_2$ , a 2-D or 3-D body of variable conductivity  $\sigma_b(r)$  imbedded in the host rock, and a basement of conductivity  $\sigma_3$ . Due to attenuation in the earth only low frequencies are of interest, so displacement currents can be ignored. Furthermore, the effects of conductivity changes usually dominate effects of magnetic permeability changes, so we set  $\mu = \mu_0$  everywhere. For IP modeling, conductivity is complex and varies with frequency.

As illustrated in Figure 1, the source of the EM field can be either an impressed electric current  $j_p$  (a large loop or grounded wire) or a magnetic dipole with moment per unit volume  $m_p$  formed by a small loop of current.

### Time-domain equations

If displacement currents are neglected, the coupled space and time dependence of the electric and magnetic fields is described by Maxwell's equations

$$\nabla \times \mathbf{e}(\mathbf{r}, t) = -\mu_0 \frac{\partial \mathbf{h}(\mathbf{r}, t)}{\partial t} - \mu_0 \frac{\partial \mathbf{m}_p}{\partial t}(\mathbf{r}, t), \quad (1)$$

and

$$\nabla \times \mathbf{h}(\mathbf{r}, t) = \sigma \mathbf{e}(\mathbf{r}, t) + \mathbf{j}_p(\mathbf{r}, t). \quad (2)$$

Here  $\mathbf{m}_p$  and  $\mathbf{j}_p$  are the primary (impressed) magnetic and electric currents, respectively.

Taking the curl of equation (1) and substituting equation (2) yields a vector diffusion equation for the electric field:

$$\nabla \times \nabla \times \mathbf{e} + \mu_0 \sigma \frac{\partial \mathbf{e}}{\partial t} = -\mu_0 \frac{\partial \mathbf{j}_p}{\partial t} - \mu_0 \nabla \times \frac{\partial \mathbf{m}_p}{\partial t}. \quad (3)$$

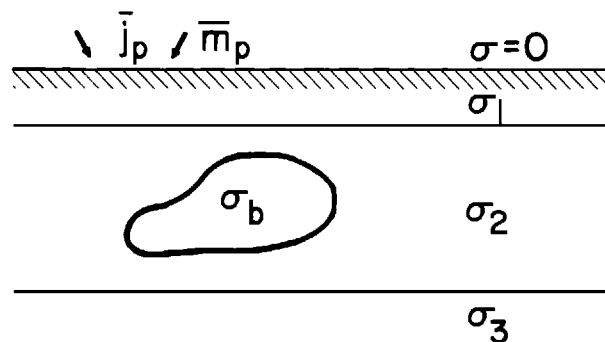


FIG. 1. General model for formulation of a numerical solution.

Similarly, taking the curl of equation (2) and substituting equation (1) yields a diffusion equation for the magnetic field:

$$\nabla \times \left( \frac{\nabla \times \mathbf{h}}{\sigma} \right) + \mu_0 \frac{\partial \mathbf{h}}{\partial t} = \nabla \times \left( \frac{\mathbf{j}_p}{\sigma} \right) - \mu_0 \frac{\partial \mathbf{m}_p}{\partial t}. \quad (4)$$

Equations (3) and (4) illustrate the important point that, due to attenuation in the earth, EM prospecting frequencies must be so low that we deal with a diffusion, rather than a wave, phenomenon. Hence, resolution of conductivity with the EM method is much less than resolution of velocity with the seismic method, which is governed by wave propagation.

Applying the vector identity

$$\nabla \times \nabla \times \mathbf{A} = -\nabla^2 \mathbf{A} + \nabla(\nabla \cdot \mathbf{A}),$$

equation (3) becomes

$$-\nabla^2 \mathbf{e} + \nabla(\nabla \cdot \mathbf{e}) + \mu_0 \sigma \frac{\partial \mathbf{e}}{\partial t} = -\mu_0 \frac{\partial \mathbf{j}_p}{\partial t} - \mu_0 \nabla \times \frac{\partial \mathbf{m}_p}{\partial t}. \quad (5)$$

Taking the divergence of equation (2) yields

$$\nabla \cdot (\sigma \mathbf{e}) = \sigma \nabla \cdot \mathbf{e} + \nabla \sigma \cdot \mathbf{e} = -\nabla \cdot \mathbf{j}_p.$$

Substituting for  $\nabla \cdot \mathbf{e}$  in equation (5) yields

$$\nabla^2 \mathbf{e} + \nabla \left( \mathbf{e} \cdot \frac{\nabla \sigma}{\sigma} \right) - \mu_0 \sigma \frac{\partial \mathbf{e}}{\partial t} = \mu_0 \frac{\partial \mathbf{j}_p}{\partial t} - \frac{1}{\sigma} \nabla(\nabla \cdot \mathbf{j}_p) + \mu_0 \nabla \times \frac{\partial \mathbf{m}_p}{\partial t}, \quad (6)$$

assuming that the source is in a region of homogeneous conductivity.

Using the identity

$$\nabla \times \phi \mathbf{A} = \phi \nabla \times \mathbf{A} - \mathbf{A} \times \nabla \phi,$$

equation (4) can be written

$$\frac{1}{\sigma} \nabla \times \nabla \times \mathbf{h} - (\nabla \times \mathbf{h}) \times \nabla \left( \frac{1}{\sigma} \right) + \mu_0 \frac{\partial \mathbf{h}}{\partial t} = \frac{1}{\sigma} \nabla \times \mathbf{j}_p - \mu_0 \frac{\partial \mathbf{m}_p}{\partial t},$$

or as

$$-\nabla^2 \mathbf{h} + \nabla(\nabla \cdot \mathbf{h}) - \sigma(\nabla \times \mathbf{h}) \times \nabla \left( \frac{1}{\sigma} \right) + \mu_0 \sigma \frac{\partial \mathbf{h}}{\partial t} = \nabla \times \mathbf{j}_p - \mu_0 \sigma \frac{\partial \mathbf{m}_p}{\partial t}.$$

The divergence of the magnetic field is nonzero only at a magnetic source; taking the divergence of equation (1) shows that

$$\nabla \cdot \mathbf{h} = -\nabla \cdot \mathbf{m}_p.$$

Thus

$$\nabla^2 \mathbf{h} + \sigma(\nabla \times \mathbf{h}) \times \nabla \left( \frac{1}{\sigma} \right) - \mu_0 \sigma \frac{\partial \mathbf{h}}{\partial t} = \mu_0 \sigma \frac{\partial \mathbf{m}_p}{\partial t} - \nabla(\nabla \cdot \mathbf{m}_p) - \nabla \times \mathbf{j}_p. \quad (7)$$

Equations (6) and (7), general equations for the total electric and magnetic fields valid at every point, apply to the time-invariant case if the time derivatives are set to zero. Either equation can be solved numerically by time stepping, and then the other field can be calculated using equation (1) or (2). If, for example, only the magnetic field is desired, it would be advantageous to solve for it directly, since numerical differentiation introduces errors.

The primary fields, which would apply everywhere if the body were absent, satisfy the equations

$$\nabla \mathbf{x} \mathbf{e}_p = -\mu_0 \frac{\partial \mathbf{h}_p}{\partial t} - \mu_0 \frac{\partial \mathbf{m}_p}{\partial t}, \quad (8)$$

and

$$\nabla \mathbf{x} \mathbf{h}_p = \sigma_* \mathbf{e}_p + \mathbf{j}_p, \quad (9)$$

where  $\sigma_*$  is the “normal” (layered-earth) conductivity with the body not present. These primary fields usually are in the form of integrals that can be evaluated numerically.

Subtracting equation (8) from equation (1) and equation (9) from equation (2) yields equations for the secondary fields:

$$\nabla \mathbf{x} \mathbf{e}_s = -\mu_0 \frac{\partial \mathbf{h}_s}{\partial t}, \quad (10)$$

and

$$\nabla \mathbf{x} \mathbf{h}_s = \sigma \mathbf{e}_s + \sigma_a \mathbf{e}_p, \quad (11a)$$

or

$$\nabla \mathbf{x} \mathbf{h}_s = \sigma_* \mathbf{e}_s + \mathbf{j}_s, \quad (11b)$$

where

$$\mathbf{j}_s = \sigma_a \mathbf{e}_p,$$

and where  $\sigma_a = \sigma - \sigma_*$  is the anomalous conductivity at a point. In Figure 1  $\sigma_a$  is nonzero only in the body, where it becomes  $\sigma_a = \sigma_b - \sigma_*$ . The quantity  $\mathbf{j}_s$  is the equivalent (scattering) current that replaces the body and is the source of the secondary field.

Comparing equations (10) and (11a) with equations (1) and (2), shows that the DE for  $\mathbf{e}_s$  is the same as that for  $\mathbf{e}$  in equation (6), with the magnetic source terms deleted and with  $\mathbf{j}_p$  replaced by  $\sigma_a \mathbf{e}_p$ , i.e.,

$$\nabla^2 \mathbf{e}_s + \nabla \left( \mathbf{e}_s \cdot \frac{\nabla \sigma}{\sigma} \right) - \mu_0 \sigma \frac{\partial \mathbf{e}_s}{\partial t} = \mu_0 \sigma_a \frac{\partial \mathbf{e}_p}{\partial t} - \nabla \left( \mathbf{e}_p \cdot \frac{\nabla \sigma_a}{\sigma} \right), \quad (12)$$

since  $\nabla \cdot \mathbf{e}_p$  is zero in the body, which is the only place  $\sigma_a$  is not zero.

Similarly, the secondary magnetic field is given by modifying equation (7) in the same way:

$$\nabla^2 \mathbf{h}_s + \sigma (\nabla \mathbf{x} \mathbf{h}_s) \mathbf{x} \nabla \left( \frac{1}{\sigma} \right) - \mu_0 \sigma \frac{\partial \mathbf{h}_s}{\partial t} = -\sigma \nabla \mathbf{x} \left( \frac{\sigma_a}{\sigma} \mathbf{e}_p \right) = -\sigma_a \nabla \mathbf{x} \mathbf{e}_p - \sigma \nabla \left( \frac{\sigma_a}{\sigma} \right) \mathbf{x} \mathbf{e}_p,$$

or

$$\nabla^2 \mathbf{h}_s + \nabla \mathbf{x} \mathbf{h}_s \mathbf{x} \nabla \left( \frac{1}{\sigma} \right) - \mu_0 \sigma \frac{\partial \mathbf{h}_s}{\partial t} = \mu_0 \sigma_a \frac{\partial \mathbf{h}_p}{\partial t} - \sigma \nabla \left( \frac{\sigma_a}{\sigma} \right) \mathbf{x} \mathbf{e}_p, \quad (13)$$

since  $\sigma_a$  is zero at the position of the impressed magnetic source.

Notice that the sources of the secondary electric field in equation (12) are currents and charges in the volume and on the surface of the body, respectively, where  $\sigma_a$  and  $\nabla \sigma_a$  are nonzero. The sources of the secondary magnetic field in equation (13) are volume and surface currents in and on the body. The reasons for solving equations (12) and (13) rather than the equations for total fields are that the secondary field equations require fine discretization only in the body, and the source is a smoother function of time.

### Frequency-domain equations

To obtain equations in the frequency domain, perform a Fourier transformation, using the pair

$$\mathbf{F}(\mathbf{r}, \omega) = \int_{-\infty}^{\infty} \mathbf{f}(\mathbf{r}, t) e^{-i\omega t} dt \quad (14a)$$

$$\mathbf{f}(\mathbf{r}, t) = \frac{1}{2\pi} \int_{-\infty}^{\infty} \mathbf{F}(\mathbf{r}, \omega) e^{i\omega t} d\omega, \quad (14b)$$

which amounts to assuming  $e^{i\omega t}$  time dependence. Then equation (6) becomes

$$\nabla^2 \mathbf{E} + \nabla \left( \mathbf{E} \cdot \frac{\nabla \sigma}{\sigma} \right) + k^2 \mathbf{E} = i\omega \mu_0 \mathbf{J}_p - \frac{1}{\sigma} \nabla (\nabla \cdot \mathbf{J}_p) + i\omega \mu_0 \nabla \mathbf{x} \mathbf{M}_p. \quad (15)$$

From equation (7)

$$\nabla^2 \mathbf{H} + \sigma (\nabla \mathbf{x} \mathbf{H}) \mathbf{x} \nabla \left( \frac{1}{\sigma} \right) + k^2 \mathbf{H} = i\omega \mu_0 \sigma \mathbf{M}_p - \nabla (\nabla \cdot \mathbf{M}_p) - \nabla \mathbf{x} \mathbf{J}_p. \quad (16)$$

From equation (12)

$$\nabla^2 \mathbf{E}_s + \nabla \left( \mathbf{E}_s \cdot \frac{\nabla \sigma}{\sigma} \right) + k^2 \mathbf{E}_s = -k_a^2 \mathbf{E}_p - \nabla \left( \mathbf{E}_p \cdot \frac{\nabla \sigma_a}{\sigma} \right). \quad (17)$$

From equation (13)

$$\nabla^2 \mathbf{H}_s + \sigma (\nabla \mathbf{x} \mathbf{H}_s) \mathbf{x} \nabla \left( \frac{1}{\sigma} \right) + k^2 \mathbf{H}_s = -k_a^2 \mathbf{H}_p - \sigma \nabla \left( \frac{\sigma_a}{\sigma} \right) \mathbf{x} \mathbf{E}_p. \quad (18)$$

In the above four equations

$$k^2 = -i\omega \mu_0 \sigma,$$

and

$$k_a^2 = -i\omega \mu_0 \sigma_a.$$

Equations (15) through (18) are the DE's to be solved for the total and secondary electric and magnetic fields in the frequency domain. In the case of total fields, away from sources the other component can be found using the frequency-domain versions of equations (1) and (2):

$$\nabla \times \mathbf{E} = -i\omega\mu_0 \mathbf{H}, \quad (19)$$

and

$$\nabla \times \mathbf{H} = \sigma \mathbf{E}. \quad (20)$$

For secondary field solutions the other component can be calculated using the frequency-domain versions of equations (10) and (11b):

$$\nabla \times \mathbf{E}_s = -i\omega\mu_0 \mathbf{H}_s, \quad (21)$$

and

$$\nabla \times \mathbf{H}_s = \sigma_* \mathbf{E}_s + \mathbf{J}_s. \quad (22)$$

To formulate an integral equation, treat  $\mathbf{J}_s$  in equation (22) as a source current. In a whole space the secondary electric field would be given by

$$\mathbf{E}_s = -i\omega\mu_0 \mathbf{A}_s - \nabla V_s, \quad (23)$$

where  $A_s$  and  $V_s$  are secondary vector and scalar potentials for the Lorentz gauge, given by

$$\mathbf{A}_s(\mathbf{r}) = \int_v \mathbf{J}_s(\mathbf{r}') G(\mathbf{r}, \mathbf{r}') dv', \quad (24)$$

and

$$V_s(\mathbf{r}) = -\frac{1}{\sigma_*} \int_v \nabla \cdot \mathbf{J}_s(\mathbf{r}') G(\mathbf{r}, \mathbf{r}') dv', \quad (25)$$

where  $G$  is the scalar EM Green's function

$$G(\mathbf{r}, \mathbf{r}') = \frac{e^{-ik_*|\mathbf{r}-\mathbf{r}'|}}{4\pi|\mathbf{r}-\mathbf{r}'|}, \quad (26)$$

with  $k_* = (-i\omega\mu_0\sigma_*)^{1/2}$ . For a body in a half-space, an additional term, given in Hohmann (1975) for a homogeneous earth and in Wannamaker, et al. (1984) for a layered earth, must be added to expression (23) to account for the layering.

By adding the primary field to the secondary field of expression (23) we get a singular Fredholm integral equation of the second kind for the total electric field, which can be written symbolically as

$$\mathbf{E}(\mathbf{r}) = \mathbf{E}_p(\mathbf{r}) + \int_v \mathbf{G}(\mathbf{r}, \mathbf{r}') \cdot \sigma_a(\mathbf{r}') \mathbf{E}(\mathbf{r}') dv', \quad (27)$$

where  $\mathbf{G}$  is a tensor Green's function.

Hence, the body has been replaced by a volume of scattering current  $\mathbf{J}_s = \sigma_a \mathbf{E}$ . The secondary field is due to currents and charges; the charges occur at discontinuities in the scattering current. The effects of other boundaries are included in the Green's function. At present integral equation solutions are restricted to bodies in layered earths, because easily computable Green's functions do not exist for boundaries that are not parallel, such as that of a dipping contact in a homogeneous or layered earth. However, as Raiche (1978) showed, the Green's functions for a dipping contact can be computed for borehole modeling, in which case the air-earth interface can be ignored.

The described volume integral equation formulation allows for varying conductivity in the body. For a homogeneous body it is possible to formulate a surface integral equation solution in terms of equivalent electric and magnetic surface currents (Won and Kuo, 1975a). However, numerical results based on surface integral equation solutions have been presented only for 2-D models (Won and Kuo, 1975b; Parry and Ward, 1971).

### Direct current equations

For resistivity and IP modeling we assume that the source is a direct current (dc). From expression (23), at zero frequency,

$$\mathbf{E}_s = -\nabla V_s. \quad (28)$$

By analogy

$$\mathbf{E} = -\nabla V, \quad (29)$$

and

$$\mathbf{E}_p = -\nabla V_p. \quad (30)$$

Substituting expression (29) in equation (15) at zero frequency yields

$$\nabla^2 V + \frac{1}{\sigma} \nabla V \cdot \nabla \sigma = \frac{1}{\sigma} \nabla \cdot \mathbf{J}_p, \quad (31)$$

which is a DE for the total potential. For the practical case of a point electrode,

$$\nabla \cdot \mathbf{J}_p = I \delta(x - x') \delta(y - y') \delta(z - z'),$$

which is based on the equivalence relation for generalized functions. Substituting expressions (28) and (30) in equation (17), we obtain the DE for the secondary potential

$$\nabla^2 V_s + \frac{1}{\sigma} \nabla V_s \cdot \nabla \sigma = -\frac{1}{\sigma} \nabla V_p \cdot \nabla \sigma_a. \quad (32)$$

To derive an integral equation for total potential substitute the relation

$$\nabla \cdot \mathbf{J}_s = -\nabla \cdot \sigma_a \nabla V = -\nabla \sigma_a \cdot \nabla V - \sigma_a \nabla^2 V$$

in the integral (25). From equation (31), since  $\nabla \cdot \mathbf{J}_p = 0$  and  $\nabla \sigma_a = \nabla \sigma$  inside the body,

$$\nabla \cdot \mathbf{J}_s = -\nabla \sigma \cdot \nabla V + \frac{\sigma_a}{\sigma} \nabla \sigma \cdot \nabla V,$$

or

$$\nabla \cdot \mathbf{J}_s = -\frac{\sigma_*}{\sigma} \nabla \sigma \cdot \nabla V.$$

Substituting this last expression in the integral (25) and adding the primary potential yields

$$V(\mathbf{r}) = V_p(\mathbf{r}) + \int_v \frac{\nabla' \sigma(\mathbf{r}') \cdot \nabla' V(\mathbf{r}')}{\sigma(\mathbf{r}')} G_0(\mathbf{r}, \mathbf{r}') d\mathbf{v}', \quad (33)$$

where, from the Green's function (26) with  $k_* = 0$ ,

$$G_0(\mathbf{r}, \mathbf{r}') = \frac{1}{4\pi(\mathbf{r} - \mathbf{r}')} + G_0^s(\mathbf{r}, \mathbf{r}'), \quad (34)$$

in which the second term accounts for the earth-air interface and any other layers.

For the practical case of a homogeneous body we write

$$\frac{\nabla\sigma}{\sigma} = \frac{\sigma_* - \sigma_b}{\sigma_* + \sigma_b} \mathbf{u}_n \delta_s, \\ \frac{2}{2}$$

where  $\delta_s$  is a surface delta function at the surface of the body, and  $\mathbf{u}_n$  is the outward-directed unit normal vector. Hence equation (33) simplifies to the surface integral

$$V(\mathbf{r}) = V_p(\mathbf{r}) + \int_s q(\mathbf{r}') G_0(\mathbf{r}, \mathbf{r}') ds', \quad (35)$$

with normalized charge density

$$q = -2 \frac{\sigma_b - \sigma_*}{\sigma_b + \sigma_*} \mathbf{u}_n \cdot \nabla V. \quad (36)$$

To obtain an integral equation for the charge density, take the normal derivative of equation (35) at a point  $\mathbf{r}$  on the surface of the body, resulting in

$$\mathbf{u}_n \cdot \nabla V(\mathbf{r}) = \mathbf{u}_n \cdot \nabla V_p(\mathbf{r}) + \int_s q(\mathbf{r}') \mathbf{u}_n \cdot \nabla G_0(\mathbf{r}, \mathbf{r}') ds'.$$

Substituting the expression (36) yields an integral equation for the normalized charge density on the surface of the body:

$$\frac{1}{2} \frac{\sigma_* + \sigma_b}{\sigma_* - \sigma_b} q(\mathbf{r}) = \frac{\partial V_p(\mathbf{r})}{\partial n} + \int_s q(\mathbf{r}') \frac{\partial G_0(\mathbf{r}, \mathbf{r}')}{\partial n} ds', \quad (37)$$

which is the equation derived in Snyder (1976).

Once the charge has been determined by solving equation (37) numerically, the potential can be calculated anywhere using equation (35). For a body in an otherwise homogeneous earth the Green's function assumes the particularly simple form

$$G_0(\mathbf{r}, \mathbf{r}') = \frac{1}{4\pi} \left( \frac{1}{R} + \frac{1}{R_s} \right), \quad (38)$$

with

$$R = [(x - x')^2 + (y - y')^2 + (z - z')]^{1/2},$$

and

$$R_s = [(x - x')^2 + (y - y')^2 + (z + z')]^{1/2}.$$

## Method of Weighted Residuals

All numerical solutions in the frequency domain and numerical solutions for the spatial dependence in the time domain can be placed in the context of the method of weighted residuals (MWR), also called the method of moments (Harrington, 1968). The spatial variation portion of any of the equations derived above can be written

$$Lf = s, \quad (39)$$

where  $L$  is a differential or integral operator,  $f$  is an unknown vector or scalar field, and  $s$  is a source term.

For example, in equation (17),

$$L = \nabla^2 + \nabla \left( \frac{\nabla \sigma}{\sigma} \cdot + k^2 \right),$$

$$f = \mathbf{E}_s$$

and

$$s = -k_a^2 \mathbf{E}_p - \nabla \left( \mathbf{E}_p \cdot \frac{\nabla \sigma_a}{\sigma} \right).$$

In equation (27)

$$L = \mathbf{I} - \int_v dv' \sigma_a(\mathbf{r}') \mathbf{G}(\mathbf{r}, \mathbf{r}'),$$

where  $\mathbf{I}$  is the identity tensor,

$$f = \mathbf{E},$$

and

$$s = \mathbf{E}_p.$$

Approximating  $f$  by an  $N$ -term sum of suitably chosen basis functions,

$$f(x) \approx \hat{f}(x) = \sum_{n=1}^N a_n f_n(x). \quad (40)$$

Substituting the approximation (40) in equation (39) yields

$$\sum_{n=1}^N a_n L f_n + \epsilon = s, \quad (41)$$

due to the linearity of the operator. Here  $\epsilon$  is the residual due to using  $\hat{f}$  instead of  $f$ .

The objective of MWR is to select the coefficients  $a_n$  such that the residual is forced to zero in some average sense. To that end define a set of  $N$  weighting functions  $w_m(x)$  and a suitable inner product, which is just an integral over some volume in the earth. Then take the inner product of equation (41) with each  $w_m$ :

$$\sum_{n=1}^N a_n \langle w_m, Lf_n \rangle + \langle w_m, \epsilon \rangle = \langle w_m, s \rangle, \\ m = 1, 2, \dots, N. \quad (42)$$

Setting the weighted residuals,  $\langle w_m, \epsilon \rangle$ , to zero for all  $m$  forces the error to be orthogonal to the weighting functions, and equation (42) becomes

$$\sum_{n=1}^N a_n \langle w_m, Lf_n \rangle = \langle w_m, s \rangle, \\ m = 1, 2, \dots, N, \quad (43)$$

which defines a matrix equation

$$\mathbf{Z}\mathbf{a} = \mathbf{s}, \quad (44)$$

where the matrix elements are given by

$$Z_{mn} = \langle w_m, Lf_n \rangle,$$

and the elements of the source vector are given by

$$s_m = \langle w_m, s \rangle,$$

to be solved for  $a$ , the vector of unknown coefficients. Then  $\hat{f}$ , the approximation for  $f$ , is given by expression (40).

The crux of the numerical problem, then, is to choose basis and weighting functions that approximate  $f$  well with a reasonable number of terms and that provide a stable solution for the particular operator. Another important practical consideration is that the matrix elements must be relatively easy to evaluate. Ordinarily subsectional basis functions (finite elements) are used, each of which is nonzero over only a small portion of the domain of  $L$ . Another common technique is to use delta weighting functions, which results in a point-matching (collocation) solution. In the Galerkin method the same functions are used for basis and weighting functions.

Pulse basis functions, resulting in a step approximation, and delta weighting functions have been used almost exclusively for IE solutions in geophysical EM problems. Finite-difference methods approximate the operator and use collocation, as discussed in Harrington (1968). Finite-element methods generally utilize the Galerkin technique with the same linear, subsection basis and weight functions.

## Two-Dimensional Model and Source

By far the simplest numerical modeling problem is that of a 2-D model excited by a 2-D source. The two sources of practical interest are: (1) a plane-wave natural field impinging on the surface of the earth as in the magnetotelluric (MT) method, and (2) a line source of time-varying current at the surface of the earth approximating a long grounded wire or one side of a large loop. There is no 2-D zero-frequency application in geophysics.

### Frequency-domain differential-equation methods

Solutions of 2-D frequency-domain EM problems were first developed around 1970, and a number of numerical techniques are discussed in the February, 1971 *Geophysics* Special

**Issue on Electromagnetic Scattering.** Jones and Price (1971) presented a finite-difference solution, and Swift (1971) discussed a network analogy formulation of a finite-difference solution. Coggon (1971) discussed a finite-element formulation using a variational approach, while Hohmann (1971) and Parry and Ward (1971) developed volume and surface integral equation solutions, respectively. Hohmann (1971) introduced the use of half-space Green's functions. In other literature Silvester and Haslam (1972) presented a finite-element solution based on the MWR approximation of the differential equation, rather than using a variational formulation, and Ward et al. (1973) reviewed the various 2-D formulations.

For the MT problem the EM field can be taken as the superposition of transverse electric (TE) and transverse magnetic (TM) modes, with components  $(E_y, H_x, H_z)$  and  $(H_y, E_x, E_z)$ , respectively. Here  $y$  is the strike (infinite) direction, and transverse refers to the  $z$  (vertical) direction, with  $z$  positive downward. The source of excitation is a plane wave, and there are no conductivity boundaries normal to  $E$  for the TE mode, so that the DE's of equations (15) and (16) for the total field become

$$\text{TE: } \frac{\partial^2 E_y}{\partial x^2} + \frac{\partial^2 E_y}{\partial z^2} + k^2 E_y = 0, \quad (45)$$

and

$$\text{TM: } \frac{\partial}{\partial x} \left( \frac{1}{\sigma} \frac{\partial H_y}{\partial x} \right) + \frac{\partial}{\partial z} \left( \frac{1}{\sigma} \frac{\partial H_y}{\partial z} \right) - i\omega\mu_0 H_y = 0. \quad (46)$$

The total electric field about a line source of current  $I$  at the surface of the earth is a TE field, described by

$$\frac{\partial^2 E_y}{\partial x^2} + \frac{\partial^2 E_y}{\partial z^2} + k^2 E_y = i\omega\mu_0 I \delta(x) \delta(z). \quad (47)$$

For both plane-wave and line-source excitation the secondary fields satisfy equations (17) and (18), which become

$$\text{TE: } \frac{\partial^2 E_y^s}{\partial x^2} + \frac{\partial^2 E_y^s}{\partial z^2} + k^2 E_y^s = -k_a^2 E_y^p, \quad (48)$$

and

$$\text{TM: } \frac{\partial}{\partial x} \left( \frac{1}{\sigma} \frac{\partial H_y^s}{\partial x} \right) + \frac{\partial}{\partial z} \left( \frac{1}{\sigma} \frac{\partial H_y^s}{\partial z} \right) - i\omega\mu_0 H_y^s = -\frac{1}{\sigma} k_a^2 H_y^p + E_z^p \frac{\partial \left( \frac{\sigma_a}{\sigma} \right)}{\partial x} - E_x^p \frac{\partial \left( \frac{\sigma_a}{\sigma} \right)}{\partial z}. \quad (49)$$

These are simple scalar DE's; finite-element and finite-difference solutions for them are reliable and useful. Note that the source of the secondary field in equation (48) is distributed throughout the cross-sections of anomalous regions, while the source for equation (49) occurs in the cross-sections and also on the boundaries. Once  $E_y$  or  $H_y$  is calculated, the other components can be obtained by approximating the derivatives in Maxwell's equations numerically.

From equation (20), for the TM mode

$$\frac{\partial H_y}{\partial x} = J_z.$$

Because the vertical current must be zero at the earth's surface, the magnetic field is constant there. Hence, the grid need not include the air, which simplifies the numerical problem. The air must be discretized for TE-mode problems, since the electric field is not constant at the earth's surface.

Rijo (1977) showed that, in the case of a simple homogeneous medium, the finite-difference method is equivalent to the finite-element method with linear basis functions. However, the two methods are not equivalent for inhomogeneous models. The finite-element method is advantageous for frequency-domain EM problems in geophysics, because it can handle abrupt and sloping conductivity interfaces and topography with greater ease. Thus, we discuss the finite-element method in this section and save the finite-difference discussion for the section on transient EM, where it provides the advantage of permitting an explicit method, which requires no matrix inversion.

### Finite-element technique

Early finite-element work, such as that of Coggon (1971), was based on variational formulations. However, it is equivalent, and simpler in concept, to solve the appropriate differential equation by the method of weighted residuals, as discussed in Silvester and Haslam (1972), Rijo (1977), and in Lapidus and Pinder (1982).

A typical finite-element mesh shown in Figure 2 is taken from Rijo (1977). Ideally the mesh should be fine near an inhomogeneity in the center of the mesh and coarse toward the top and bottom. However, the mesh in Figure 2 represents a compromise between ease of implementation and minimization of the number of nodes.

Let us represent the unknown 2-D function  $f$  by subsection basis functions  $f(x,z)$  which are nonzero only within the  $n$ th triangle in Figure 2 and which vary linearly. Figure 3 defines conventions for the  $n$ th triangle, in which

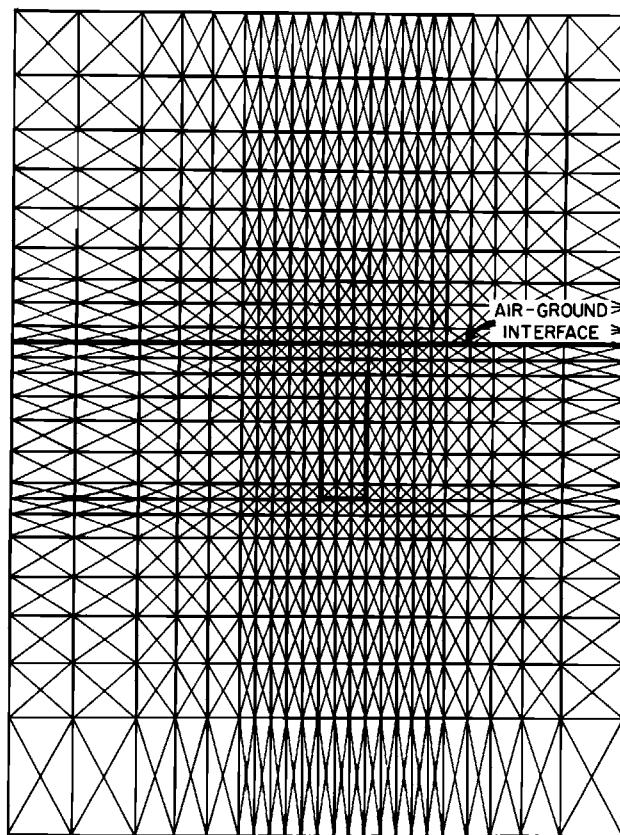


FIG. 2. Typical finite-element mesh.

$$f_n(x, z) = a_n + b_n x + c_n z. \quad (50)$$

The values of  $f$  at the three nodes of the  $n$ th element are

$$f_n^i = a_n + b_n x_i + c_n z_i,$$

$$f_n^j = a_n + b_n x_j + c_n z_j,$$

and

$$f_n^k = a_n + b_n x_k + c_n z_k.$$

Solving for  $a_n$ ,  $b_n$ , and  $c_n$  and inserting in equation (50), we obtain

$$f_n(x, z) = f_n^i g_n^i(x, z) + f_n^j g_n^j(x, z) + f_n^k g_n^k(x, z), \quad (51)$$

where the interpolation functions  $g_n^i$ ,  $g_n^j$ ,  $g_n^k$  are now the basis functions for the problem; they are often called shape functions. The unknowns now are  $f_n^i$ ,  $f_n^j$ , and  $f_n^k$ , the nodal values of  $f$ . The first basis function is given by

$$g_n^i(x, z) = -\frac{1}{2A_n} (\alpha_i + \beta_i x + \gamma_i z), \quad (52)$$

where  $A_n$  is the area of element  $n$ , and where

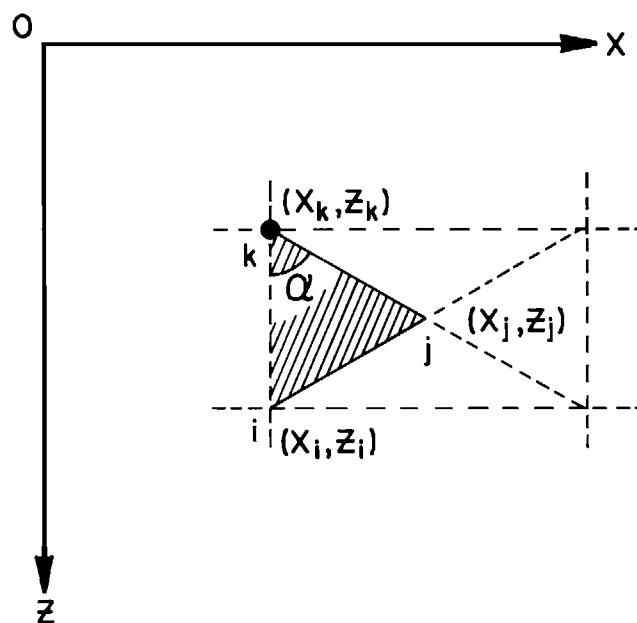


FIG. 3. Expanded view of the  $n$ th element in the finite element mesh of Figure 2. The dot represents an impressed source located at node  $k$ .

$$\alpha_i = x_j z_k - x_k z_j,$$

$$\beta_i = z_j - z_k,$$

and

$$\gamma_i = x_k - x_j.$$

The other two basis functions,  $g_n^j$  and  $g_n^k$ , are obtained through a cyclic permutation of the subscripts  $i$ ,  $j$ , and  $k$ . Note that  $g_n^i$  is zero at nodes  $j$  and  $k$ , while it is unity at node  $i$ .

Equation (51) can be written as the product

$$f_n = \mathbf{g}_n^T \mathbf{f}_n, \quad (53)$$

in which

$$\mathbf{g}_n^T = (g_n^i, g_n^j, g_n^k),$$

and

$$\mathbf{f}_n = (f_n^i, f_n^j, f_n^k)^T.$$

Finally, the approximation to the complete function  $f$  is given by

$$\hat{f}(x, z) = \sum_{n=1}^N f_n(x, z) = \sum_{n=1}^N \mathbf{g}_n^T(x, z) \mathbf{f}_n, \quad (54)$$

which is rewritten as a global finite-element expansion

$$\hat{f}(x, z) = \sum_{n=1}^M f_n h_n(x, z), \quad (54a)$$

where  $\{f_n\}_1^M$  are the  $M < N$  nodal values of  $f$ , and where  $h_n(x, z)$ , the global basis function for node  $n$ , is formed by summing the element basis functions for the triangular elements surrounding node  $n$ . The global basis functions are similar to the element basis functions:  $h_n$  is 1 at node  $n$ , zero at the other nodes, and varies linearly.

As shown in Rijo (1977) the 2-D differential equations of interest in geophysics, including equations (45) through (49) and the equations for dc problems to be derived later, can be written in the form of equation (39), with the operator given by

$$L = \frac{\partial}{\partial x} \left( \frac{1}{r} \frac{\partial}{\partial x} \right) + \frac{\partial}{\partial z} \left( \frac{1}{r} \frac{\partial}{\partial z} \right) + p. \quad (55)$$

If the electric field equations are rewritten to allow for varying magnetic permeability, then  $r = i\omega\mu$  and  $p = -\sigma$ . From equations (46) and (49), for magnetic field computations  $r$  and  $p$  are given by  $\sigma$  and  $-i\omega\mu$ , respectively.

In the usual Galerkin finite-element solution the weighting function is the same as the basis function:

$$w_m(x, z) = \mathbf{g}_m(x, z). \quad (56)$$

The inner product for the problem is

$$\langle s, t \rangle = \iint s(x, z) t(x, z) dx dz,$$

where the integral is over the entire cross-section of the mesh. Then equation (43) becomes

$$\sum_{n=1}^N \langle \mathbf{g}_m, L\mathbf{g}_n^T \rangle \mathbf{f}_n = \langle \mathbf{g}_m, \mathbf{s} \rangle, \quad (57)$$

where  $\mathbf{g}_n^T$  denotes a row vector (transpose of a column vector).

Because  $\mathbf{g}_m(x, z)$  is nonzero only in the  $m$ th element, equation (57) becomes the element equation

$$\langle \mathbf{g}_m, L\mathbf{g}_m^T \rangle \mathbf{f}_m = \langle \mathbf{g}_m, \mathbf{s} \rangle, \quad (57a)$$

or, written in integral form

$$\iint_m \mathbf{g}_m \left[ \frac{\partial}{\partial x} \frac{1}{r} \frac{\partial \mathbf{g}_m^T}{\partial x} + \frac{\partial}{\partial z} \left( \frac{1}{r} \frac{\partial \mathbf{g}_m^T}{\partial z} \right) \right] dx dz \mathbf{f}_m + \iint_m \mathbf{g}_m \mathbf{g}_m^T p dx dz \mathbf{f}_m = \iint_m \mathbf{g}_m s dx dz, \quad (58)$$

where the integral is over the area of the  $n$ th triangular element.

However, second derivatives of the linear basis functions  $\mathbf{g}_m$  in the first term in equation (58) produce delta functions, which are not in the domain of the operator. Hence, the domain of the operator must be extended (Harrington, 1968) to include linear basis functions, through integration by parts. Integrating the first term in equation (58) by parts with respect to  $x$  gives

$$\iint_m \mathbf{g}_m \frac{\partial}{\partial x} \left( \frac{1}{r} \frac{\partial \mathbf{g}_m^T}{\partial x} \right) dx dz = - \iint_m \frac{1}{r} \frac{\partial \mathbf{g}_m}{\partial x} \frac{\partial \mathbf{g}_m^T}{\partial x} dx dz + \oint_{\partial m} \frac{1}{r} \mathbf{g}_m \frac{\partial \mathbf{g}_m^T}{\partial x} n_x dl,$$

where the second integral on the right hand side is a line integral around the boundary  $\partial m$  of element  $m$ , and  $n_x$  is the  $x$  component of the unit normal to the boundary. Treating the term involving derivatives with respect to  $z$  in the same way,

$$\begin{aligned} \langle \mathbf{g}_m, L \mathbf{g}_m^T \rangle &= -\frac{1}{r_m} \iint_m \left( \frac{\partial \mathbf{g}_m}{\partial x} \frac{\partial \mathbf{g}_m^T}{\partial x} + \frac{\partial \mathbf{g}_m}{\partial z} \frac{\partial \mathbf{g}_m^T}{\partial z} \right) dx dz \\ &\quad + p_m \iint_m \mathbf{g}_m \mathbf{g}_m^T dx dz + \frac{1}{r_m} \oint_{\partial m} \mathbf{g}_m \frac{\partial \mathbf{g}_m^T}{\partial n} dl, \end{aligned} \quad (59)$$

where

$$\frac{\partial \mathbf{g}_m^T}{\partial n} = \frac{\partial \mathbf{g}_m^T}{\partial x} n_x + \frac{\partial \mathbf{g}_m^T}{\partial z} n_z$$

is the partial derivative of the element basis function in the direction normal to the boundary of element  $m$ . Note that we assumed  $r = r_m$  and  $p = p_m$  to be constant within element  $m$ .

The basis functions are continuous at the element boundaries, as are the terms

$$\frac{1}{r_m} \frac{\partial \mathbf{g}_m^T}{\partial n}$$

for each of our 2-D geophysical problems. Because each internal boundary is traversed twice, in opposite directions, the line integrals in equation (59) for adjacent elements add to zero. Either Dirichlet or Neumann boundary conditions are applied to evaluate the line integral for external mesh boundaries.

Ignoring any nonzero external boundary terms, we write equation (58) as an element matrix equation

$$(\mathbf{R}_m + \mathbf{P}_m) \mathbf{f}_m = \mathbf{s}_m, \quad (60)$$

in which

$$\begin{aligned} [\mathbf{R}_m]_{ij} &= -\frac{1}{r_m} \iint_m \left( \frac{\partial g_m^i}{\partial x} \frac{\partial g_m^j}{\partial x} + \frac{\partial g_m^i}{\partial z} \frac{\partial g_m^j}{\partial z} \right) dx dz, \\ [\mathbf{P}_m]_{ij} &= p_m \iint_m g_m^i g_m^j dx dz, \end{aligned}$$

and

$$s_m^i = \iint_m s g_m^i dx dz,$$

and where  $\mathbf{f}_m$  is the vector of three nodal values of  $f(x, z)$  to be determined.

Using the expression for  $g_m^i$  in equation (52) and the integral (Lapidus and Pinder, 1982)

$$\iint_m (g_m^i)^a (g_m^j)^b (g_m^k)^c dx dz = \frac{2 a! b! c! A_m}{(a + b + c + 2)!}, \quad (61)$$

where  $A_m$  is the area of the  $m$ th element, the matrices in equation (60) can be written

$$\mathbf{R}_m = -\frac{1}{4rA_m} \begin{bmatrix} \alpha_i^2 + \gamma_i^2 & \beta_i\beta_j + \gamma_i\gamma_j & \beta_i\beta_k + \gamma_i\gamma_k \\ \beta_j^2 + \gamma_j^2 & \beta_j\beta_k + \gamma_j\gamma_k & \beta_k^2 + \gamma_k^2 \\ \text{Symmetric} & & \end{bmatrix}, \quad (62)$$

and

$$\mathbf{P}_m = \frac{p A_m}{12} \begin{bmatrix} 2 & 1 & 1 \\ 1 & 2 & 1 \\ 1 & 1 & 2 \end{bmatrix}. \quad (63)$$

For MT problems the source is incorporated by imposing boundary values at the upper edge of the mesh; hence  $\mathbf{s}_m$  of equation (60) is zero. To illustrate the incorporation of the source in line-source problems or in the case of the secondary field equations, assume that the source is concentrated at node  $k$  in Figure 3 for the problem defined by equation (47). Now at node  $k$

$$g_m^i(x_k, z_k) = g_m^j(x_k, z_k) = 0,$$

and

$$g_m^k(x_k, z_k) = 1.$$

Therefore we write  $\mathbf{s}_m$  in equation (60) as

$$\mathbf{s}_m = \left( 0, 0, \frac{\alpha}{2\pi} I \right)^T, \quad (64)$$

since

$$s_m^k = \iint_m \frac{\alpha}{2\pi} I \delta(x)\delta(z) dx dz = \frac{\alpha}{2\pi} I. \quad (65)$$

Because the source is shared by more than one element, it is allocated to node  $k$  of element  $m$  according to the angle  $\alpha$  shown in Figure 3.

The next step is to assemble the  $N$  element equations (60) into a single matrix equation, known as the global finite-element matrix equation:

$$\mathbf{G} \mathbf{f} = \mathbf{s}, \quad (66)$$

where  $\mathbf{G}$  is an  $M \times M$ , symmetric, sparse, banded, diagonally dominant matrix, and  $\mathbf{f}$  is the vector of  $M$  unknown nodal values. The entries in  $\mathbf{G}$  corresponding to a particular nodal value contain information from each of the triangular elements that share the node. The source vector  $\mathbf{s}$  is obtained by assembling the  $\mathbf{s}_m$  in expression (64).

Dirichlet boundary conditions can be incorporated by partitioning equation (66) as follows:

$$\begin{bmatrix} \mathbf{G}_{ii} & \mathbf{G}_{ib} \\ \mathbf{G}_{bi} & \mathbf{G}_{bb} \end{bmatrix} \cdot \begin{bmatrix} \mathbf{f}_i \\ \mathbf{f}_b \end{bmatrix} = \begin{bmatrix} \mathbf{s}_i \\ \mathbf{s}_b \end{bmatrix}, \quad (67)$$

where subscript  $i$  refers to internal nodes, and subscript  $b$  refers to boundary nodes. Thus

$$\mathbf{G}_{ii} \mathbf{f}_i = \mathbf{s}_i - \mathbf{G}_{ib} \mathbf{f}_b, \quad (68)$$

which is a matrix equation to solve for  $\mathbf{f}_i$ , the vector of internal nodal values of  $f(x,y)$ . Now the right-hand side of the matrix equation includes the known boundary values. In the special case where the fields are set to zero at the boundary, the matrix reduces to

$$\mathbf{G}_{ii} \mathbf{f}_i = \mathbf{s}_i. \quad (69)$$

Usually the global matrix equation is solved by block Gaussian elimination. The matrix is divided into blocks along the diagonal and each block is factored in turn into upper and lower triangular matrices, so  $\mathbf{f}$  can be found by simple forward and back substitution. The factorization is particularly simple for a symmetric matrix.

If the other field values are desired, for example,  $H_x$  and  $H_z$  for a TE-mode problem, they can be obtained by difference approximations. Alternatively, we could fit the nodal values of  $f$  with splines and calculate derivatives analytically.

### Integral equation solution

For the TE mode (plane wave or line source) the volume integral equation (27) becomes

$$E_y(x,z) = E_y^p(x,z) + \int_s G(x,z; x',z') \sigma_a(x',z') E_y(x',z') dx' dz'. \quad (70)$$

The integration is over the cross-sections of anomalous bodies, and the Green's function is a scalar, given, e.g., for a homogeneous-half-space host (Hohmann, 1971) as .

$$G = G_p + G_s, \quad (71)$$

where

$$G_p(x,z; x',z') = -\frac{i\omega\mu_0}{2\pi} K_0\{ik_*[(x-x')^2 + (z-z')^2]^{1/2}\}, \quad (71a)$$

is the Green's function for a whole space. Here  $K_0$  is the modified Bessel function of the second kind of order zero. The second term in equation (71) accounts for the earth-air interface; it is given by

$$G_s(x,z; x',z') = \frac{-i\omega\mu_0}{2\pi} \int_0^\infty \frac{u_1 - \lambda}{u_1(u_1 + \lambda)} e^{-u_1(z+z')} \cos [\lambda(x-x')] d\lambda, \quad (71b)$$

which can only be evaluated numerically. Here  $u_1 = (\lambda^2 - k_*^2)^{1/2}$ . Note that equation (71a) is singular at  $x = x'$ ,  $z = z'$ , while equation (71b) is not.

Howard (1972) solved equation (70) for a body with circular cross-section using a mode-matching technique wherein the electric field is expanded in the natural modes of a cylinder.

For an inhomogeneity with rectangular cross-section equation (70) can be solved by dividing the area into  $N$  square cells of dimension  $\Delta$  as illustrated in Figure 4 and assuming that the electric field is constant in each cell (Hohmann, 1971). That is, the basis functions are 2-D pulse functions centered at the center of each cell, resulting in a step approximation to the electric field. Using delta weighting functions requires an expression for the electric field at the center of cell  $m$ , which is given by a summation over all of the cells:

$$E_m = E_m^p + \sum_{n=1}^N \sigma_{an} E_n \left[ \int_{x_n-\Delta/2}^{x_n+\Delta/2} \int_{z_n-\Delta/2}^{z_n+\Delta/2} G_p(x_m - x', z_m - z') dx' dz' \right. \\ \left. + \Delta^2 G_s(x_m - x_n, z_m + z_n) \right], \quad (72)$$

where we dropped the  $y$  subscript. Here  $E_m^p$  is the primary (half-space) field at the center of cell  $m$ , and the term involving the summation is the secondary field, which is due to the body. Note that  $G_s$  is taken to be constant over each cell. However, the integral over  $G_p$  is carried out, because it is singular and because it is more important than  $G_s$ .

The integral could be evaluated numerically, but, because the Green's function does not vary rapidly with distance, it is sufficient to approximate the square cell by a circular cell of the same area and integrate analytically (Hohmann, 1971). For the singular cell ( $m = n$ ) the integral becomes

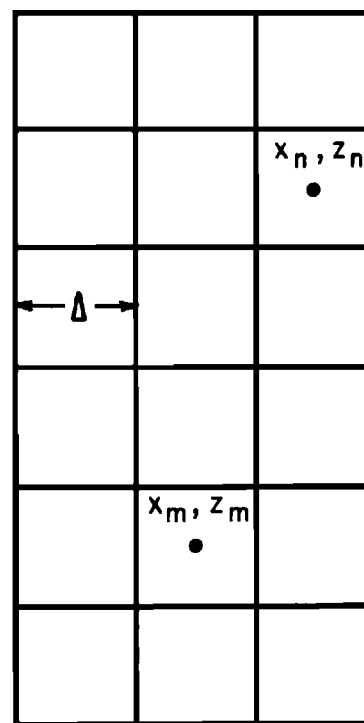


FIG. 4. Cross-section of a 2-D body divided into square cells for integral equation solution.

$$\int_{x_n-\Delta/2}^{x_n+\Delta/2} \int_{z_n-\Delta/2}^{z_n+\Delta/2} G_p dx' dz' \approx \frac{1}{\sigma_*} [ik_* a K_1(ik_* a) - 1], \quad (73)$$

where  $K_1$  is the modified Bessel function of the second kind of order one, and  $a$  is the radius of the equivalent circular cell, given by

$$a = \Delta/\pi^{1/2}.$$

The integral over nonsingular cells ( $m \neq n$ ) can be evaluated to give

$$\int_{x_n-\Delta/2}^{x_n+\Delta/2} \int_{z_n-\Delta/2}^{z_n+\Delta/2} G_p dx' dz' \approx \frac{-\omega \mu_0 a}{k_*} K_0(ik_* r) I_1(ik_* a), \quad (74)$$

where  $I_1$  is the modified Bessel function of the first kind of order 1, and

$$r = [(x_m - x_n)^2 + (z_m - z_n)^2]^{1/2}.$$

Then by writing equation (72) for  $m = 1, 2, \dots, N$ , we can formulate a matrix equation

$$\underline{\mathbf{Z}} \mathbf{E} = \mathbf{E}_p, \quad (75)$$

where  $\mathbf{E}$  and  $\mathbf{E}_p$  and  $N \times 1$  vectors of unknown total and known primary  $E_y$  fields, and where the elements of the impedance matrix  $\underline{\mathbf{Z}}$  are given by

$$z_{mn} = \delta_{mn} - \sigma_{an} G_{mn}, \quad (76)$$

where

$$\delta_{mn} = \begin{cases} 1 & \text{for } m = n \\ 0 & \text{for } m \neq n \end{cases}$$

and where  $G_{mn}$  is the term in the brackets in equation (72).

Once equation (75) is solved for the electric fields in the body, the electric fields outside the body are calculated by modifying equation (70) to

$$E_y(x, z) = E_y^p(x, z) + \Delta^2 \sum_{n=1}^N \sigma_{an} E_n G(x, z; x_n z_n). \quad (77)$$

Finally, the exterior magnetic fields are found by applying the relations

$$H_x = \frac{1}{i\omega \mu_0} \frac{\partial E_y}{\partial z}, \quad (78)$$

and

$$H_z = -\frac{1}{i\omega \mu_0} \frac{\partial E_y}{\partial x}, \quad (79)$$

to expression (77). Complete expressions for the primary and secondary fields at the surface of the earth are given in Hohmann (1971). The techniques described in Ward and Hohmann (this volume) can be used to modify the Green's functions to account for a layered-earth host.

The secondary parts of the Green's functions can be calculated very efficiently through bilinear interpolation on a 2-D table of precalculated values versus  $x - x'$  and  $z + z'$  at intervals of 0.1 skin depth. In general the matrix equation (75) is solved by LU decompo-

sition, i.e.,  $\mathbf{Z}$  is factored as

$$\mathbf{Z} = \mathbf{L}\mathbf{U}, \quad (80)$$

where  $\mathbf{L}$  and  $\mathbf{U}$  are lower and upper triangular matrices, respectively. Then if we set

$$\mathbf{U}\mathbf{E} = \mathbf{C},$$

we can solve

$$\mathbf{L}\mathbf{C} = \mathbf{E}_p$$

very simply by forward substitution, and, finally, we can solve

$$\mathbf{U}\mathbf{E} = \mathbf{C}$$

by back substitution. Factorization of  $\mathbf{Z}$  constitutes the main part of the computations, and the process is equivalent to Gauss elimination.

In the case of equal-sized cells and uniform conductivity in the body, the solution is particularly efficient, for then  $\mathbf{Z}$  can be factored as

$$\mathbf{Z} = \mathbf{L}\mathbf{L}^T \quad (81)$$

by Cholesky decomposition.

Accurate solutions are relatively easy to compute even for high contrasts in conductivity for 2-D problems, because the unknown electric field is continuous. Figure 5, for example,

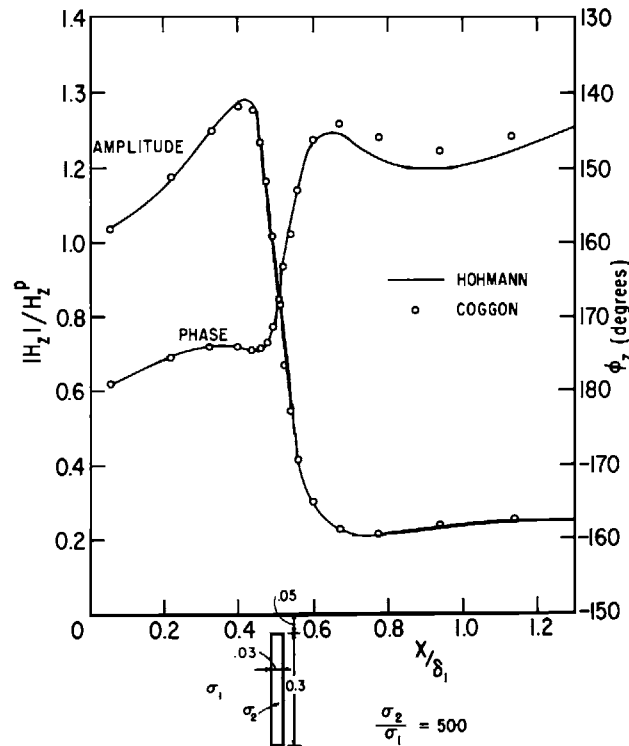


FIG. 5. Comparison between Hohmann's integral equation results and Coggon's finite-element results for a 2-D model with a line source. Shown are the amplitude and phase of the vertical magnetic field.

shows a comparison between finite-element results of Coggon (1971) and integral-equation results of Hohmann (1971) for the vertical magnetic field over a 2-D conductor excited by a line source of current. The agreement is excellent, indicating that both solutions are valid. Hohmann found that a cell size of 0.6 skin depths in the body produces accurate results with the integral-equation solution.

Recently Lee and Morrison (1985b) presented an efficient TM-mode integral-equation solution for a 2-D body in a half-space. The integral equation to be solved is

$$\mathbf{E}(x, z) = \mathbf{E}_p(x, z) + \int_s \mathbf{G}(x, z; x', z') \sigma_a(x', z') \mathbf{E}(x', z') dx' dz', \quad (82)$$

where the electric field has  $x$  and  $z$  components and where  $\mathbf{G}$  is a tensor Green's function of the form

$$\mathbf{G} = \begin{bmatrix} G_{xx} & G_{xz} \\ G_{zx} & G_{zz} \end{bmatrix}. \quad (83)$$

Although the integral equation is more complicated than in the case of the TE-mode, the TM-mode Green's function elements for a homogeneous half-space are analytic, requiring no numerical integration.

Differential-equation solutions are more useful than integral-equation solutions for 2-D problems, because they can model complex subsurface conductivity distributions without much additional cost. Figure 6 shows a model, obtained after many iterations, that produces an acceptable fit to MT data at the Roosevelt Hot Springs geothermal area in Utah (Wannamaker, 1983). The MT response of the model was calculated using a finite-element computer code (Rijo, 1977). One way of obtaining an initial guess for this type of interpretation is to carry out a 1-D inversion at each receiver site.

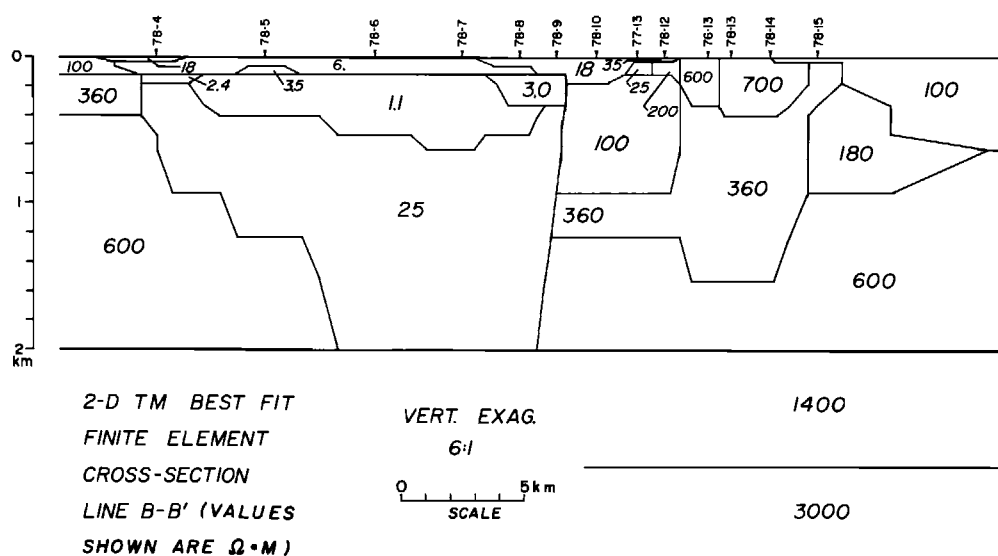


FIG. 6. Best-fitting finite element model for TM-mode MT data in southern Utah.

### Time-domain finite-difference solution

When a 2-D earth is excited by a line source of current, the total and secondary differential equations (5) and (12) become

$$\frac{\partial^2 e_y}{\partial x^2} + \frac{\partial^2 e_y}{\partial z^2} - \sigma \mu_0 \frac{\partial e_y}{\partial t} = \mu_0 \frac{\partial j_y^p}{\partial t}, \quad (84)$$

and

$$\frac{\partial^2 e_y^s}{\partial x^2} + \frac{\partial^2 e_y^s}{\partial z^2} - \sigma \mu_0 \frac{\partial e_y^s}{\partial t} = \mu_0 \sigma_a \frac{\partial e_y^p}{\partial t}. \quad (85)$$

These equations can be solved by time-stepping (marching in time) from given initial values. Implicit methods require a matrix inversion at each time step, while explicit methods do not: the field at a certain time is calculated from the known field at previous times.

Kuo and Cho (1980) published an explicit solution to the damped wave equation corresponding to equation (84), based on finite-element discretization in space and a finite-difference approximation in time. Goldman and Stoyer (1983) also formulated an implicit finite-difference transient solution to a similar, axisymmetric problem.

In this section we discuss an explicit finite-difference solution first presented in Oristaglio and Hohmann (1984). The solution is based on the Dufort-Frankel scheme (Dufort and Frankel, 1953), which is discussed in Lapidus and Pinder (1982). Oristaglio and Hohmann generalized the method to inhomogeneous 2-D models with irregular grids, and used an upward-continuation boundary condition at the earth's surface to avoid solving for fields in the air. This type of boundary condition only applies to an explicit time-domain solution. Variable grid spacing is necessary to permit a large enough grid that Dirichlet or Neumann boundary conditions can be imposed at the boundaries in the earth.

The solution of Oristaglio and Hohmann was based on equation (84), but it is much more efficient to solve equation (85) for the secondary field (Adhidjaja et al., 1985). Because the source for the secondary field is smoother than that for the primary field, larger time steps can be used. Moreover, fine spatial discretization is not required around the primary source.

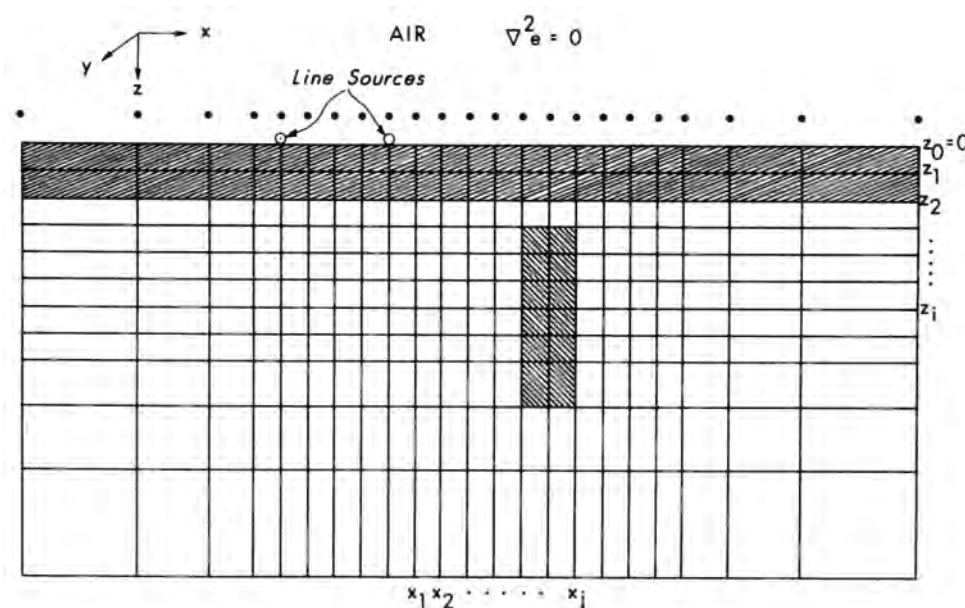


FIG. 7. Finite difference grid for 2-D time-stepping solution.

For models with an overburden layer, the overburden should be specified as the background or primary medium, with the primary fields on the right-hand side of equation (85) computed everywhere beneath.

The model geometry and the rectangular finite-difference grid are shown in Figure 7. Note that Laplace's equation applies in the air, which is the key to the upward-continuation boundary condition. Conductivity is assumed to be constant within each rectangular cell.

**Spatial Terms.**—A finite-difference approximation for the spatial derivatives in equations (84) or (85) on a variable, rectangular grid can be developed by the integration method. The resulting equations closely resemble those of the finite-element method.

For notational simplicity, we denote  $e_y^s$  or  $e_y^p$  simply by  $e$ . Figure 8 shows a typical node  $(i, j)$ , with coordinates  $x_i, z_i$  and electric field  $e_{i,j}$ , surrounded by its nearest neighbors. Ignoring the source term for now, integrating equations (84) or (85) over the rectangle  $ABCD$  (Figure 8) formed by joining the midpoints of the rectangles connecting the nodes, and applying Green's theorem, gives

$$\begin{aligned} \iint_{ABCD} \mu_0 \sigma \frac{\partial e}{\partial t} dx dz &= \iint_{ABCD} \left( \frac{\partial^2 e}{\partial x^2} + \frac{\partial^2 e}{\partial z^2} \right) dx dz \\ &= \int_{BC} \frac{\partial e}{\partial z} dx - \int_{AD} \frac{\partial e}{\partial z} dx + \int_{DC} \frac{\partial e}{\partial x} dz - \int_{AB} \frac{\partial e}{\partial x} dz. \quad (86) \end{aligned}$$

The integrals can be approximated as follows:

$$\begin{aligned} \iint_{ABCD} \mu_0 \sigma \frac{\partial e}{\partial t} dx dz &\approx \frac{\mu_0}{4} [\sigma_{i,j} \Delta z_i \Delta x_j + \sigma_{i+1,j} \Delta z_{i+1} \Delta x_j \\ &\quad + \sigma_{i,j+1} \Delta z_i \Delta x_{j+1} + \sigma_{i+1,j+1} \Delta z_{i+1} \Delta x_{j+1}] \frac{\partial e_{i,j}}{\partial t}, \\ \int_{BC} \frac{\partial e}{\partial z} dx &\approx \left( \frac{\Delta x_j + \Delta x_{j+1}}{2} \right) \left( \frac{e_{i+1,j} - e_{i,j}}{\Delta z_{i+1}} \right), \end{aligned}$$

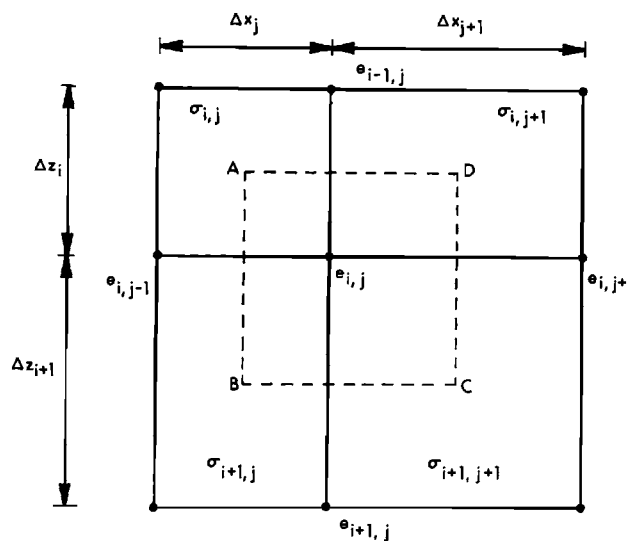


FIG. 8. Expanded view of node  $i, j$  and surrounding nodes in the grid of Figure 7.

$$\int_{AD} \frac{\partial e}{\partial z} dx \approx \left( \frac{\Delta x_j + \Delta x_{j+1}}{2} \right) \left( \frac{e_{i,j} - e_{i-1,j}}{\Delta z_i} \right),$$

$$\int_{DC} \frac{\partial e}{\partial x} dz \approx \left( \frac{\Delta z_i + \Delta z_{i+1}}{2} \right) \left( \frac{e_{i,j+1} - e_{i,j}}{\Delta x_{j+1}} \right),$$

and

$$\int_{AB} \frac{\partial e}{\partial x} dz \approx \left( \frac{\Delta z_i + \Delta z_{i+1}}{2} \right) \left( \frac{e_{i,j} - e_{i,j-1}}{\Delta x_j} \right).$$

Substituting this last expression into equation (86) and rearranging, we obtain

$$\begin{aligned} \mu_0 \bar{\sigma}_{ij} \frac{\partial e_{i,j}}{\partial t} &= \frac{1}{\Delta z_i \Delta z_{i+1}} \left[ \frac{2\Delta z_{i+1}}{\Delta z_i + \Delta z_{i+1}} e_{i-1,j} + \frac{2\Delta z_i}{\Delta z_i + \Delta z_{i+1}} e_{i+1,j} - 2e_{i,j} \right] \\ &+ \frac{1}{\Delta x_j \Delta x_{j+1}} \left[ \frac{2\Delta x_{j+1}}{\Delta x_j + \Delta x_{j+1}} e_{i,j-1} + \frac{2\Delta x_j}{\Delta x_j + \Delta x_{j+1}} e_{i,j+1} - 2e_{i,j} \right], \end{aligned} \quad (87)$$

where, as in Brewitt-Taylor and Weaver (1976),

$$\bar{\sigma}_{i,j} = \frac{\sigma_{i,j} \Delta z_i \Delta x_j + \sigma_{i+1,j} \Delta z_{i+1} \Delta x_j + \sigma_{i,j+1} \Delta z_i \Delta x_{j+1} + \sigma_{i+1,j+1} \Delta z_{i+1} \Delta x_{j+1}}{(\Delta z_i + \Delta z_{i+1}) + (\Delta x_j + \Delta x_{j+1})}$$

is the area-weighted average of the conductivities surrounding node  $(i,j)$ , while the right-hand side of equation (87) is just the standard five-point difference approximation to the Laplacian on an irregular grid.

**Time-stepping.**—The last step in discretizing the diffusion equation is to approximate the time-derivative. This topic has a vast literature. Richtmyer and Morton (1967), for example, describe 14 different schemes for just the 1-D diffusion equation. We discuss here some features of the time-stepping for geophysical EM applications. A more general treatment, including both 2-D and 3-D models, is given in Lapidus and Pinder (1982). Similar issues for time-stepping the elastic wave equation are discussed in Emerman et al. (1982).

Consider, first, a model with equal spacings  $\Delta x = \Delta z = \Delta$ , so that equation (87) becomes

$$\frac{\partial e_{i,j}^n}{\partial t} = \frac{e_{i+1,j}^n + e_{i-1,j}^n + e_{i,j+1}^n + e_{i,j-1}^n - 4e_{i,j}^n}{\mu \bar{\sigma}_{i,j} \Delta^2}, \quad (88)$$

where the superscript  $n$  denotes the electric field at time  $t = n\Delta t$ .

The simplest approximation to the time-derivative is a forward difference between times  $t = n\Delta t$  and  $t = (n + 1)\Delta t$ :

$$\frac{\partial e_{i,j}^n}{\partial t} \approx \frac{e_{i,j}^{n+1} - e_{i,j}^n}{\Delta t}, \quad (88a)$$

which is accurate to first order in  $\Delta t$ . Substituting this expression into equation (88) and solving for  $e_{i,j}^{n+1}$  gives the explicit Euler method for marching the diffusion equation in time:

$$e_{i,j}^{n+1} = (1 - 4r_{i,j})e_{i,j}^n + r_{i,j}(e_{i+1,j}^n + e_{i-1,j}^n + e_{i,j+1}^n + e_{i,j-1}^n), \quad (89)$$

where

$$r_{i,j} = \frac{\Delta t}{\mu \bar{\sigma}_{i,j} \Delta^2}$$

is a dimensionless quantity called the local mesh ratio.

For a homogeneous model, it is easy to show that the Euler method is stable if the mesh ratio is less than or equal to 1/4 (Oristaglio and Hohmann, 1984); when the mesh ratio exceeds 1/4, numerical errors grow exponentially and eventually dominate the solution. Inhomogeneous models are more difficult to analyze for stability, but keeping  $r_{i,j}$  less than or equal to 1/4 everywhere is usually a safe approach. Thus, the maximum time step for equation (89) is set by

$$\Delta t_{\max} = \frac{\mu \min(\bar{\sigma}_{i,j}) \Delta^2}{4}, \quad (90)$$

where  $\min(\bar{\sigma}_{i,j})$  is the lowest value of  $\bar{\sigma}_{i,j}$  in the model.

The problem with the Euler method is that most geophysical models contain both weak and strong conductors and thus have both fast and slow diffusion times. In a typical geoelectric section,  $\min(\bar{\sigma}_{i,j})$  corresponds to the conductivity of the host rock or half-space, which may be  $10^{-3}$  S/m. On a grid with 10 m spacing, equation (90) then gives a maximum time step of about 0.03  $\mu$ s. Orebodies, of course, respond on a much longer time scale. Computing the response of an orebody in a half-space would thus require an enormous number of steps with the Euler method.

There are many time-stepping schemes for the diffusion equation that are stable for any time step ("unconditionally stable") and are therefore more efficient than the Euler method. The most accurate are the implicit methods, such as the Crank-Nicolson, alternating direction, and backward-difference methods, which require matrix inversions at each time step (Lapidus and Pinder, 1982; Goldman and Stoyer, 1983). Even with implicit methods, however, large time steps give accurate results only at late times, after diffusion has smoothed the electric field and the slower response of the strong conductors dominates. If the early response of the model is of interest, as it is for many geophysical models, then a time step determined by equation (90) must be used at early times to track the rapid diffusion of the electric field through the weak conductors.

Oristaglio and Hohmann (1984) used the DuFort-Frankel method, the simplest of several methods for the diffusion equation that are explicit and unconditionally stable (Lapidus and Pinder, 1982). Consider, instead of equation (88a), the more accurate centered difference approximation

$$\frac{\partial e_{i,j}^n}{\partial t} \approx \frac{e_{i,j}^{n+1} - e_{i,j}^{n-1}}{2\Delta t}. \quad (91)$$

If, in addition to equation (91), we substitute

$$e_{i,j}^n \approx \frac{e_{i,j}^{n+1} + e_{i,j}^{n-1}}{2} \quad (92)$$

into equation (88), we achieve an unconditionally stable time-stepping algorithm. The classical DuFort-Frankel method for a regular grid is thus given by

$$\frac{e_{i,j}^{n+1} - e_{i,j}^{n-1}}{2\Delta t} = \frac{e_{i+1,j}^n + e_{i-1,j}^n + e_{i,j+1}^n + e_{i,j-1}^n - 2(e_{i,j}^{n+1} + e_{i,j}^{n-1})}{\mu \bar{\sigma}_{i,j} \Delta^2},$$

or, solving for  $e_{i,j}^{n+1}$ ,

$$e_{i,j}^{n+1} = \frac{1 - 4r_{i,j}}{1 + 4r_{i,j}} e_{i,j}^{n-1} + \frac{2r_{i,j}}{1 + 4r_{i,j}} (e_{i+1,j}^n + e_{i-1,j}^n + e_{i,j+1}^n + e_{i,j-1}^n). \quad (93)$$

Oristaglio and Hohmann (1984) show that the maximum practical time step for the DuFort-Frankel method is

$$\Delta t_{\max} = (\mu\sigma)^{1/2} \frac{\Delta}{2}. \quad (94)$$

In EM modeling, a reasonable choice for  $t$  is 0.1 ms, which is about when most transient EM systems begin recording. For  $\sigma = 10^{-3}$  S/m and  $\Delta = 10$ m, equation (94) gives a time step of 1.77  $\mu$ s, which is very small but about 50 times larger than the maximum step for the Euler method. The method can easily be generalized to an irregular grid by substituting equations (91) and (92) into equation (87). The result is similar to equation (94), if we define the following average grid spacings:

$$\overline{\Delta z_i} = \frac{\Delta z_{i+1} + \Delta z_i}{2},$$

and

$$\overline{\Delta x_j} = \frac{\Delta x_{j+1} + \Delta x_j}{2},$$

and the following local mesh ratios for diffusion in the  $x$  and  $z$  directions:

$$r_{i,j}^z = \frac{\Delta t}{\mu\bar{\sigma}_{i,j}\Delta z_i\Delta z_{i+1}},$$

and

$$r_{i,j}^x = \frac{\Delta t}{\mu\bar{\sigma}_{i,j}\Delta x_j\Delta x_{j+1}}.$$

The generalized DuFort-Frankel method is then given by

$$\begin{aligned} e_{i,j}^{n+1} &= \frac{1 - 4\bar{r}_{i,j}}{1 + 4\bar{r}_{i,j}} e_{i,j}^{n-1} + \frac{2\bar{r}_{i,j}^z}{1 + 4\bar{r}_{i,j}} \left[ \frac{\Delta z_i}{\overline{\Delta z_i}} e_{i+1,j}^n + \frac{\Delta z_{i+1}}{\overline{\Delta z_i}} e_{i-1,j}^n \right] \\ &\quad + \frac{2\bar{r}_{i,j}^x}{1 + 4\bar{r}_{i,j}} \left( \frac{\Delta x_j}{\overline{\Delta x_j}} e_{i,j+1}^n + \frac{\Delta x_{j+1}}{\overline{\Delta x_j}} e_{i,j-1}^n \right), \end{aligned} \quad (95)$$

where

$$\bar{r}_{i,j} = \frac{r_{i,j}^x + r_{i,j}^z}{2}$$

is the average of the mesh ratios in the  $x$  and  $z$  directions. Oristaglio and Hohmann's (1984) numerical experiments indicate that the generalized DuFort-Frankel method given by equation (95) is stable for any time step.

Note that the DuFort-Frankel difference equation can be applied to only half the grid points at any time level, because the central point in the finite-difference stencil (Figure 8) is defined only by the time average, equation (92). In two dimensions the method can be implemented as follows. At times  $n\Delta t$ , where  $n$  is an odd number, the difference equation (95) can be used to advance  $e_{i,j}^{n-1}$ , where  $(i+j)$  is odd, to the time level  $(n+1)$ . The new values can be used to advance  $e_{i,j}^n$ , where  $(i+j)$  is even, to the level  $(n+2)$ , and the cycle can then be repeated. This requires that the field be given initially on two time levels,  $n=0$  and  $n=1$ , but these values can easily be obtained by physical arguments, or by using the Euler method to advance the values at  $n=0$  (which are always required for the diffusion equation) by one time step.

**Boundary Conditions.**—Consider first the boundary condition in the air, where the electric field satisfies Laplace's equation under the quasi-static approximation, i.e.,

$$\frac{\partial^2 e}{\partial x^2} + \frac{\partial^2 e}{\partial z^2} = 0.$$

The electric field in the air  $e(x, z < 0, t)$  can thus be computed from its value at the earth-air interface  $e(x, z = 0, t)$  by upward continuation:

$$e(x, z < 0, t) = -\frac{z}{\pi} \int_{-\infty}^{\infty} dx' e(x', z = 0, t) / [(x - x')^2 + z^2], \quad (96)$$

or

$$e(x, z < 0, t) = \frac{1}{2\pi} \int_{-\infty}^{\infty} dk_x e^{|k_x|z + ik_x x} \hat{e}(k_x, z = 0, t), \quad (97)$$

where  $\hat{e}(k_x, z = 0, t)$  is the Fourier transform of the electric field at the earth-air interface, i.e.,

$$\hat{e}(k_x, z = 0, t) = \int_{-\infty}^{\infty} dx e^{ik_x x} e(x, z = 0, t).$$

The boundary condition can be approximated numerically in the following way. At the first time step, the electric field at  $z = 0$  is given by the initial conditions, and the integrals (96) or (97) can be used to compute the field a distance  $\Delta z$  above the interface. Once these values are found, the regular finite-difference equations can then be used to advance the field at  $z = 0$  to the next time level. This cycle can obviously be repeated for any number of steps; it corresponds to a standard approach for normal-derivative boundary conditions (Lapidus and Pinder, 1982). In Oristaglio and Hohmann's solution, the upward continuation is done using the Fast Fourier Transform. In addition, since they always use a graded grid, they first interpolate the electric field to a uniform spacing  $\Delta x$  with a cubic spline. The resulting upward continuation is very accurate, but it is probably less efficient than a direct approximation of equation (96).

Goldman and Stoyer (1983) used a similar method to handle the air layer in their axisymmetric models, but, since their finite-difference solution is implicit, it is necessary to solve an integral equation to incorporate the boundary condition. Upward continuation also is closely related to the asymptotic boundary conditions used for frequency-domain modeling in Zhdanov et al. (1982) and Weaver and Brewitt-Taylor (1978). In frequency-domain modeling, a direct upward continuation is impossible, since the field at the earth-air interface is not known until the problem has been completely solved.

No useful asymptotic boundary conditions have yet been found for truncating the grid in the earth; one attempt is discussed in Adhidjaja et al. (1985). It appears necessary to use a large graded grid and set the boundary fields or normal derivatives to the analytic solution for a half-space in the case of a total-field solution or to zero for a secondary-field solution.

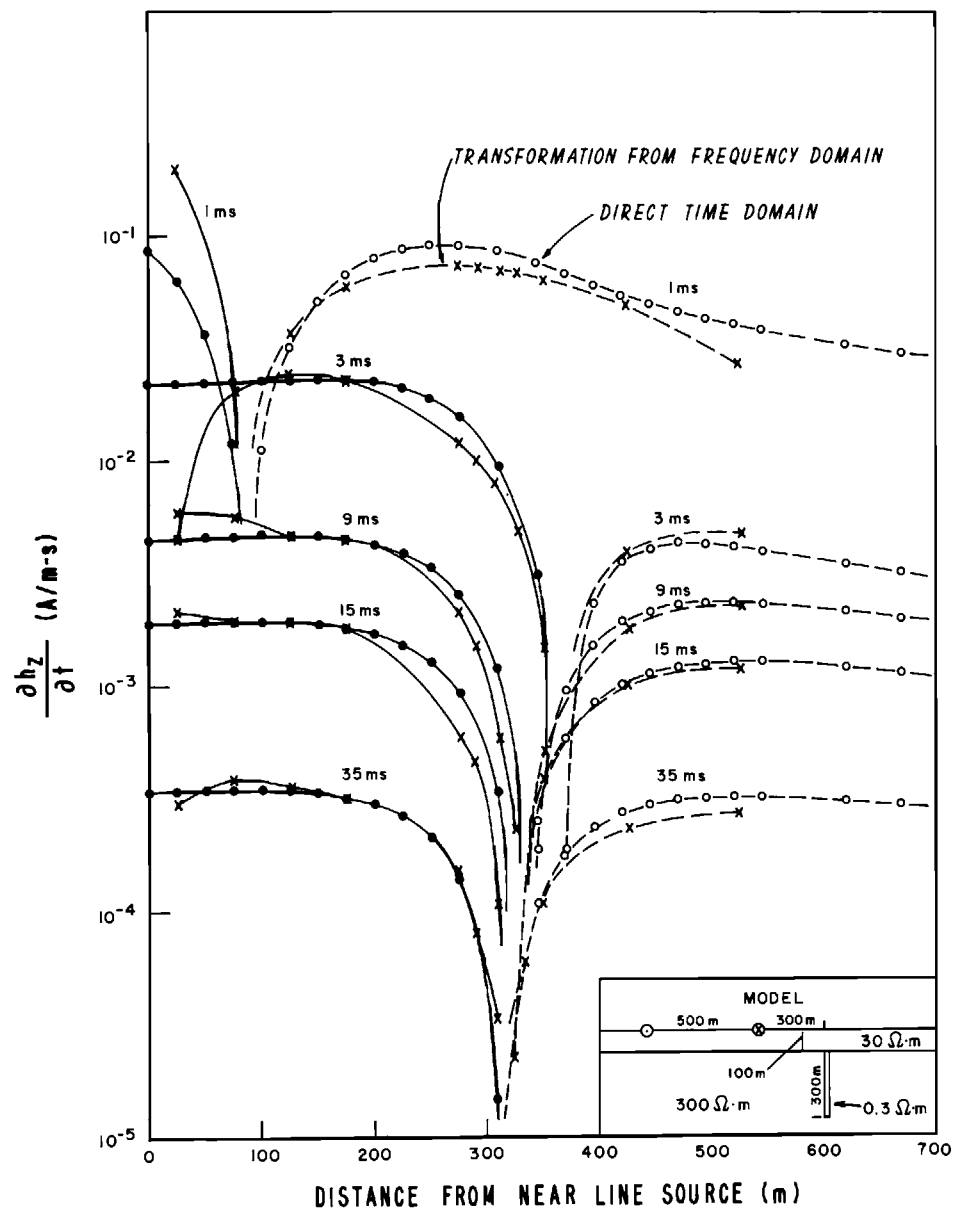


FIG. 9. Comparison between 2-D transient EM results computed with a finite difference, time-stepping solution and by inverse Fourier transforming frequency-domain finite-element results. Solid lines are positive, dashed lines negative.

Figure 9 shows a check between results computed with the time-stepping, finite difference solution and results computed by inverse Fourier transforming finite-element results by the method of Tripp (1982). The model is a good conductor beneath conductive overburden, with two line sources simulating a large fixed loop. Results are displayed as profiles at five times ranging from 1 ms to 35 ms. The agreement is quite good, except near the source, where the Fourier transformation is unstable.

The finite difference grid consisted of  $80 \times 40$  nodes; it was fine and uniform near the body and coarse and nonuniform toward the boundaries. A total of 2 000 iterations was required to compute the response to 35 ms. The time step was increased gradually every few hundred iterations, from an initial  $0.1 \mu\text{s}$ . Computation time was 80 minutes on a Univac 1100/61 computer, due to the need to compute primary fields everywhere beneath the over-

burden. If the surrounding half-space is homogeneous, similar results can be computed in about 40 minutes.

## Two-Dimensional Model: Three-Dimensional Source

With a 2-D model and a 3-D source, sometimes called 2 1/2-D or 2-D/3-D, conductivity does not vary in the strike ( $y$ ) direction, but the source is finite, as in the case of a loop or grounded wire. This problem is of great practical importance, because discretization is necessary only over a cross-section, rather than throughout a volume. The price paid for this reduction in matrix size is that many numerical solutions must be computed—one for each value of the Fourier transform variable.

### Zero-frequency solutions

Several numerical solutions have been developed for the galvanic 2-D/3-D problem, and they have been widely applied in data interpretation and in model catalog computation. DE solutions are the most useful, due to their capability for simulating complex resistivity distributions.

The key is to Fourier transform the governing equations with respect to  $y$ . Then denoting

$$\hat{V}(x, k_y, z) = \int_{-\infty}^{\infty} V(x, y, z) e^{-ik_y y} dy, \quad (98)$$

and using the derivative property of Fourier transforms, we obtain

$$\nabla \hat{V} = \frac{\partial \hat{V}}{\partial x} \mathbf{u}_x + ik_y \hat{V} \mathbf{u}_y + \frac{\partial \hat{V}}{\partial z} \mathbf{u}_z. \quad (99)$$

Because conductivity does not vary in the  $y$  direction, the differential equations for the total and secondary potentials (equations (31) and (32), respectively) can be written

$$\frac{\partial^2 \hat{V}}{\partial x^2} + \frac{\partial^2 \hat{V}}{\partial z^2} + \frac{1}{\sigma} \frac{\partial \sigma}{\partial x} \frac{\partial \hat{V}}{\partial x} + \frac{1}{\sigma} \frac{\partial \sigma}{\partial z} \frac{\partial \hat{V}}{\partial z} - k_y^2 \hat{V} = \frac{I}{\sigma} \delta(x - x') \delta(z - z'), \quad (100)$$

and

$$\frac{\partial^2 \hat{V}_s}{\partial x^2} + \frac{\partial^2 \hat{V}_s}{\partial z^2} + \frac{1}{\sigma} \frac{\partial \sigma}{\partial x} \frac{\partial \hat{V}_s}{\partial x} + \frac{1}{\sigma} \frac{\partial \sigma}{\partial z} \frac{\partial \hat{V}_s}{\partial z} - k_y^2 \hat{V}_s = -\frac{1}{\sigma} \frac{\partial \sigma}{\partial x} \frac{\partial \hat{V}_p}{\partial x} - \frac{1}{\sigma} \frac{\partial \sigma}{\partial z} \frac{\partial \hat{V}_p}{\partial z}. \quad (101)$$

For finite-element formulations, these equations can be put in the same general form as equations (39) and (55), with  $r = 1/\sigma$  and  $p = -\sigma k_y^2$ , and solved for each  $k_y$  value using the Galerkin technique described above. Usually about 7  $k_y$  values are utilized for dc problems. Then  $\hat{V}(k_y)$  is approximated with spline functions or exponentials, and the inverse transform is evaluated analytically.

Figure 10a, from Fox et al. (1980), illustrates the type of complex earth model that can be simulated with a finite-element algorithm for the dc case. These results are for the dipole-dipole array, wherein measurements are made with many transmitter-receiver positions and plotted at the intersections of 45-degree diagonals from the centers of transmitter and receiver wires. Values are shown in terms of apparent resistivity—the resistivity of a half-space that would give the same measurement. Topography is simulated by specifying air conductivities three or four orders of magnitude less than that of the earth. While FD and FE solutions have similar properties, the FE method is more amenable to modeling sloping topography.

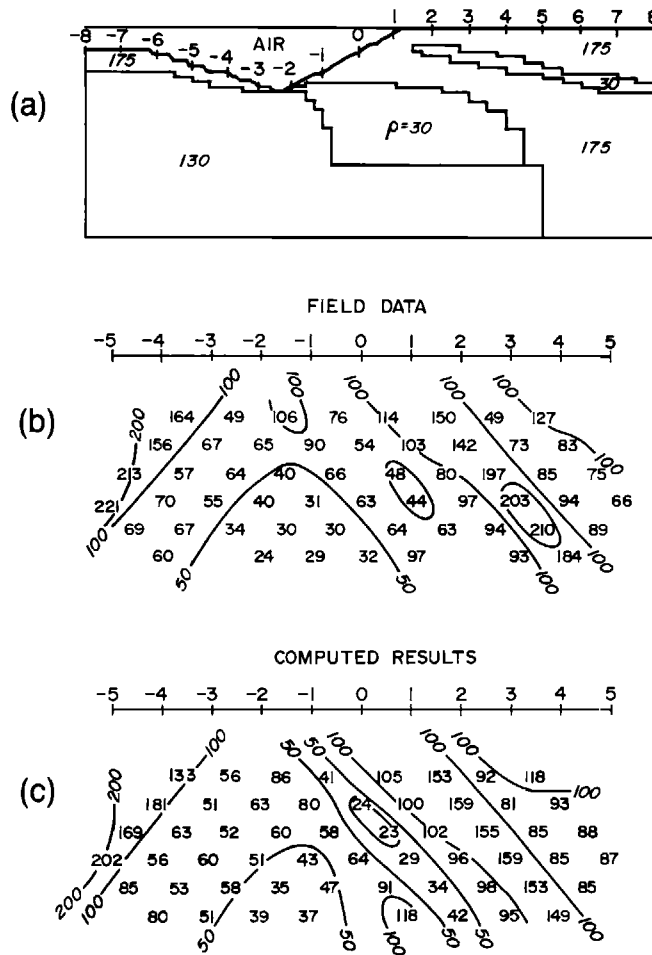


FIG. 10. Illustration of the use of a 2-D/3-D, zero-frequency solution to interpret resistivity data: (a) best-fitting model; (b) field data; (c) computed results for best-fitting model.

Figure 10b shows actual field data from an area with rugged terrain, while Figure 10c shows computed results for the model in Figure 10a. Resistivities of  $30 \Omega \cdot m$  represent conductive sulfide horizons. However, the major portion of the anomaly is due to topography.

Snyder (1976) described a dc integral equation solution for 2-D/3-D problems; the integral involved is a line integral around the cross-section of the 2-D body. He found that, due to the singular kernel, smooth surfaces are required.

### EM solutions

The EM problem for a 2-D earth excited by a 3-D source has not received the attention it deserves. At present this model represents the only way of interpreting controlled-source EM data in terms of a complex earth, due to the prohibitive amount of computer time and storage required for a complex 3-D model. Thus, again, DE solutions are the most useful.

Differential equations for the electric and magnetic fields as functions of  $x$ ,  $k_y$ , and  $z$  are obvious modifications of equations (15) through (18), using the relation (99) and the fact that conductivity does not vary in the  $y$  direction.

Lee (1978) and Lee and Morrison (1985a) present a finite-element solution for secondary electric field, with the primary field that of a vertical or horizontal magnetic dipole in free space. The advantage of using a free-space, rather than a half-space, primary field is that it is analytic. However, the unknown secondary field varies rapidly in the vicinity of the source, which is undesirable and does not happen for a half-space primary field.

Lee (1978) shows that the electric fields are well behaved as functions of  $k_y$ . His numerical values for a half-space agree with analytical results for a vertical magnetic dipole source, in which case there is no component of electric field normal to the earth-air interface. However, his check for a horizontal magnetic dipole source was not as good due to errors in computing numerical derivatives of the electric field. The finite-element scheme assumes continuity of fields, but the normal component of electric field has a sharp discontinuity at the earth's surface. Lee alleviates this problem within the mesh by invoking gradational, rather than sharp, boundaries. Unfortunately, since the effective skin depth changes with  $k_y$ , one mesh cannot be used for all 15 or so  $k_y$  values. Lee found good agreement between his results for a 2-D body excited by a vertical magnetic dipole and those of Pridmore et al. (1981) for a low-contrast 3-D body with the same cross-section.

Lee and Morrison (1985a) obtained good agreement with scale-model results for a horizontal magnetic dipole when they computed the magnetic field by integrating over scattering currents  $\mathbf{J}_s = \sigma_a \mathbf{E}$  using an equation similar to equation (27). However, this integral method of calculating the magnetic field is time consuming, and thus limits the model to small zones of anomalous conductivity and negates the flexibility of the FE method.

As shown in Stoyer and Greenfield (1976), another way to formulate the 2-D/3-D problem is in terms of two coupled second-order differential equations for  $E_y$  and  $H_y$ , the EM components in the strike direction. The advantages of this approach are that the number of unknowns is reduced from 3 to 2, and, more importantly, they are continuous. Thus the problems encountered by Lee at the earth-air interface are eliminated, and it is not necessary to set up gradational boundaries at conductivity discontinuities within the grid. Other components can be computed by numerical differentiation.

Because the source terms for the total field equations involve derivatives of spatial delta functions, it appears advantageous to solve for secondary fields. From Maxwell's equations (10) and (11a), transformed to the frequency domain, we find the following equations for the other field components in terms of  $\hat{E}_y$  and  $\hat{H}_y$ :

$$\hat{E}_x^s = \frac{1}{k_e^2} \left( -ik_y \frac{\partial \hat{E}_y^s}{\partial x} - i\omega\mu_0 \frac{\partial \hat{H}_y^s}{\partial z} + k_a^2 \hat{E}_x^p \right), \quad (102)$$

$$\hat{E}_z^s = \frac{1}{k_e^2} \left( -ik_y \frac{\partial \hat{E}_y^s}{\partial z} + i\omega\mu_0 \frac{\partial \hat{H}_y^s}{\partial x} + k_a^2 \hat{E}_z^p \right), \quad (103)$$

$$\hat{H}_x^s = \frac{1}{k_e^2} \left( -ik_y \frac{\partial \hat{H}_y^s}{\partial x} + \sigma \frac{\partial \hat{E}_y^s}{\partial z} + ik_y \sigma_a \hat{E}_z^p \right), \quad (104)$$

and

$$\hat{H}_z^s = \frac{1}{k_e^2} \left( -ik_y \frac{\partial \hat{H}_y^s}{\partial z} - \sigma \frac{\partial \hat{E}_y^s}{\partial x} - ik_y \sigma_a \hat{E}_x^p \right), \quad (105)$$

with

$$k_a^2 = -i\omega\mu_0\sigma_a,$$

and

$$k_e^2 = k_y^2 - k^2 = k_y^2 + i\omega\mu_0\sigma.$$

Substituting expressions (102) through (105) into the  $y$  components of Maxwell's equations, which are

$$\frac{\partial \hat{E}_x^s}{\partial z} - \frac{\partial \hat{E}_z^s}{\partial x} = -i\omega\mu\hat{H}_y^s, \quad (106a)$$

and

$$\frac{\partial \hat{H}_x^s}{\partial z} - \frac{\partial \hat{H}_z^s}{\partial x} = \sigma\hat{E}_y^s + \sigma_a\hat{E}_y^p, \quad (106b)$$

we obtain the following coupled differential equations to solve for  $\hat{E}_y^s$  and  $\hat{H}_y^s$ :

$$\begin{aligned} \frac{\partial}{\partial x} \left( \frac{\sigma}{k_e^2} \frac{\partial \hat{E}_y^s}{\partial x} \right) + \frac{\partial}{\partial z} \left( \frac{\sigma}{k_e^2} \frac{\partial \hat{E}_y^s}{\partial z} \right) + ik_y \left[ \frac{\partial \left( \frac{1}{k_e^2} \right)}{\partial x} \frac{\partial \hat{H}_y^s}{\partial z} - \frac{\partial \left( \frac{1}{k_e^2} \right)}{\partial z} \frac{\partial \hat{H}_y^s}{\partial x} \right] - \sigma\hat{E}_y^s = \sigma_a\hat{E}_y^p \\ - ik_y \left[ \frac{\partial}{\partial x} \left( \frac{\sigma_a}{k_e^2} \hat{E}_x^p \right) + \frac{\partial}{\partial z} \left( \frac{\sigma_a}{k_e^2} E_z^p \right) \right], \end{aligned} \quad (107)$$

and

$$\begin{aligned} \frac{\partial}{\partial x} \left( \frac{1}{k_e^2} \frac{\partial \hat{H}_y^s}{\partial x} \right) + \frac{\partial}{\partial z} \left( \frac{1}{k_e^2} \frac{\partial \hat{H}_y^s}{\partial z} \right) - \hat{H}_y^s + \frac{k_y}{\omega\mu} \left[ - \frac{\partial \left( \frac{1}{k_e^2} \right)}{\partial x} \frac{\partial \hat{E}_y^s}{\partial z} + \frac{\partial \left( \frac{1}{k_e^2} \right)}{\partial z} \frac{\partial \hat{E}_y^s}{\partial x} \right] \\ = \frac{\partial}{\partial x} \left( \frac{\sigma_a}{k_e^2} \hat{E}_z^p \right) - \frac{\partial}{\partial z} \left( \frac{\sigma_a}{k_e^2} \hat{E}_x^p \right). \end{aligned} \quad (108)$$

If equations (107) and (108) are solved for  $\hat{E}_y^s$  and  $\hat{H}_y^s$ , the other electric and magnetic field components can be calculated using the field expressions (102) through (105). However, further errors will be introduced by numerical differentiation. Notice that equations (107) and (108) reduce to the 2-D TE and TM equations (48) and (49) if  $k_y$  is zero.

Alternatively, we might formulate the 2-D/3-D problem in terms of the magnetic field and solve for  $\hat{H}_x^s$ ,  $\hat{H}_y^s$ , and  $\hat{H}_z^s$ , or in terms of the vector and scalar potentials  $\hat{A}_x$ ,  $\hat{A}_y$ ,  $\hat{A}_z$ , and  $\hat{V}$ . At this writing it is not clear what approach is best; much more research is required.

For the 2-D/3-D case the  $y$  integration in the integral equation (27) is a convolution. Thus, after Fourier transformation, equation (27) becomes

$$\hat{\mathbf{E}}(x, k_y, z) = \hat{\mathbf{E}}_p(x, k_y, z) + \int_s \hat{\mathbf{G}}(x, z; x', z', k_y) \sigma_a(x', z') \hat{\mathbf{E}}(x', k_y, z') dx' dz'. \quad (109)$$

Although the integral is now over a surface, the unknown still is a vector, and the Green's function is a tensor. No integral-equation solutions have been published, but they would be useful both for checking DE solutions and for computing model catalogs, due to the efficiency of the IE method.

## Three-Dimensional Modeling

Volume integral-equation methods, first formulated in Raiche (1974), Hohmann (1975), and Weidelt (1975), have been more successful than differential-equation methods for 3-D modeling, because it is only necessary to calculate the electric field in small anomalous regions rather than throughout the earth. However, differential-equation techniques are required for simulating complex subsurface distributions of resistivity, and they will be developed when advances in available computing power permit.

### Volume integral-equation method

Numerical results for DC and EM cases in exploration, obtained by solving equation (27) using pulse basis and delta weighting functions, were first published in Hohmann (1975). Results for magnetotellurics were first published in Weidelt (1975) and Ting and Hohmann (1981). A prismatic body is divided into  $N$  cubic cells of dimension  $\Delta$  and the scattering current,  $\mathbf{J}_s = \sigma_a \mathbf{E}$ , is assumed constant in each cell. Then the integral equation is approximated by the finite summation

$$\mathbf{E}(\mathbf{r}) = \mathbf{E}_p(\mathbf{r}) + \sum_{n=1}^N \int_{v_n} \mathbf{G}(\mathbf{r}, \mathbf{r}') d\mathbf{v}' \cdot \mathbf{J}_s^n, \quad (110)$$

where  $\mathbf{G}$  is the half-space tensor Green's function (Hohmann, 1975; Wannamaker et al., 1984) that accounts for layering in the earth.

The primary field  $\mathbf{E}_p$  is just the layered-earth field that would be present at  $\mathbf{r}$  if there were no inhomogeneity. It is found by evaluating Hankel transform integrals numerically.

The integration over the tensor Green's function can be carried out numerically (Meyer, 1976) or analytically over the volumes and surfaces of the cells (Hohmann, 1975) to obtain the equation

$$\frac{1}{\sigma_a} \mathbf{J}_s(\mathbf{r}) = \mathbf{E}_p(\mathbf{r}) + \sum_{n=1}^N \mathbf{\Gamma}(\mathbf{r}, \mathbf{r}_n) \cdot \mathbf{J}_s^n, \quad (111)$$

where  $\mathbf{J}_s^n$  is the scattering current in cell  $n$ , and  $\mathbf{\Gamma}$  is the integrated tensor Green's function for a small volume of current, unlike  $\mathbf{G}$ , which applies to an infinitesimal current element. Care must be taken in deriving  $\mathbf{\Gamma}$ , because  $\mathbf{G}$  is singular at  $\mathbf{r} = \mathbf{r}'$  (VanBladel, 1961).

To improve the solution, we now derive equation (111) in a manner similar to that described in Hohmann (1975), except that, following Harrington (1968), we approximate the derivatives of the scalar potential in the expression (23) with differences (Hohmann, 1983). Also, instead of concentrating the charge [the  $\nabla \cdot \mathbf{J}_s$  term in equation (25)] at the boundaries between cells, we distribute it uniformly over a volume extending from the center of one cell to the center of the next cell. As various authors have indicated, approximating derivatives with differences provides accuracy similar to that of higher-order basis functions but is much easier to implement on a computer. See Miller and Deadrick (1975) and Butler and Wilton (1975).

Figure 11 illustrates the calculation of the  $x$  component of secondary electric field at the center of cell  $m$  due to the  $x$  component of current in cell  $n$ . Denoting the center of cell  $m$  as  $\mathbf{r}_m$ , the  $x$  component of the vector potential from equation (24) becomes

$$A_x^{mn} = A_x(\mathbf{r}_m) = J_x^n \int_n G(\mathbf{r}_m, \mathbf{r}') d\mathbf{v}', \quad (112)$$

which is the volume current contribution.

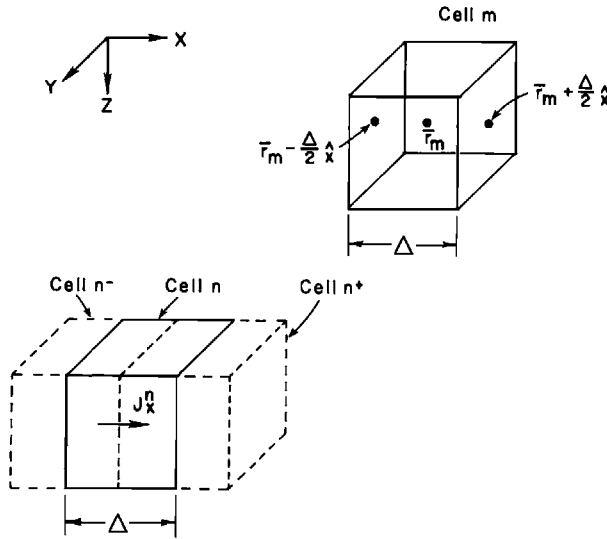


FIG. 11. Illustration of geometry for calculating the matrix element  $Z_{xx}^{mn}$ .

The charge contribution to the electric field is derived from the scalar potential in equation (25). The derivative at the current discontinuity between cell  $n$  and cell  $n+1$  is approximated by

$$\frac{\partial J_x}{\partial x} \approx \frac{J_x^{n+1} - J_x^n}{\Delta}, \quad (113)$$

and is distributed uniformly in a cubic cell, denoted  $n^+$  in Figure 11, extending from the center of cell  $n$  to the center of cell  $n+1$ . The charge at the other end of cell  $n$  is similarly distributed over cell  $n^-$ . Then the potentials  $V_{x+}^{mn}$  and  $V_{x-}^{mn}$  at points  $\mathbf{r}_m + \Delta/2 \mathbf{u}_x$  and  $\mathbf{r}_m - \Delta/2 \mathbf{u}_x$  due to  $J_x^n$  are given by equation (25), which becomes

$$V_{x+}^{mn} = \frac{J_x^n}{\sigma_* \Delta} \left[ - \int_{n^-} G\left(\mathbf{r}_m + \frac{\Delta}{2} \mathbf{u}_x, \mathbf{r}'\right) dv' + \int_{n^+} G\left(\mathbf{r}_m + \frac{\Delta}{2} \mathbf{u}_x, \mathbf{r}'\right) dv' \right], \quad (114)$$

and

$$V_{x-}^{mn} = \frac{J_x^n}{\sigma_* \Delta} \left[ - \int_{n^-} G\left(\mathbf{r}_m - \frac{\Delta}{2} \mathbf{u}_x, \mathbf{r}'\right) dv' + \int_{n^+} G\left(\mathbf{r}_m - \frac{\Delta}{2} \mathbf{u}_x, \mathbf{r}'\right) dv' \right]. \quad (115)$$

Finally,  $E_{xs}^{mn}$  is given by expression (23), which becomes

$$E_{xs}^{mn} = -i\omega\mu_0 A_x^{mn} - (V_{x+}^{mn} - V_{x-}^{mn})/\Delta. \quad (116)$$

In terms of the method of weighted residuals, this solution is equivalent to using pulse functions for both current and charge and approximating the operator. To obtain  $\Gamma$  in equation (111), we need to evaluate the integrals in equations (112), (114), and (115) for each cartesian component of current. The integrals all have the same form: the scalar Green's function integrated over a cubic cell.

We can write  $\Gamma$  as the sum of two components representing current and charge sources:

$$\Gamma = \Gamma_A + \Gamma_V, \quad (117)$$

where, for illustration, the  $x$  component of secondary electric field at the center of cell  $m$  due to the  $x$  component of scattering current in cell  $n$  is given by

$$E_{xs}^{mn} = [(\Gamma_A^{mn})_{xx} + (\Gamma_V^{mn})_{xx}] J_x^n. \quad (118)$$

From equations (112) and (116),

$$(\Gamma_A^{mn})_{xx} = -i\omega\mu_0 \int_n G(\mathbf{r}_m, \mathbf{r}') dv', \quad (119)$$

while from equations (114), (115), and (116),

$$\begin{aligned} (\Gamma_V^{mn})_{xx} = & -\frac{1}{\sigma_* \Delta^2} \left[ - \int_{n-} G\left(\mathbf{r}_m + \frac{\Delta}{2} \mathbf{u}_x, \mathbf{r}'\right) dv' + \int_{n+} G\left(\mathbf{r}_m + \frac{\Delta}{2} \mathbf{u}_x, \mathbf{r}'\right) dv' \right. \\ & \left. - \int_{n-} G\left(\mathbf{r}_m - \frac{\Delta}{2} \mathbf{u}_x, \mathbf{r}'\right) dv' + \int_{n+} G\left(\mathbf{r}_m - \frac{\Delta}{2} \mathbf{u}_x, \mathbf{r}'\right) dv' \right]. \end{aligned} \quad (120)$$

The other elements of the tensor Green's function can be derived by analogy.

For our case of a body in the earth we divide  $\Gamma_A$  and  $\Gamma_V$  into primary and secondary parts, where the secondary parts account for the earth-air interface and any other layers, as described in Hohmann (1975) and Wannamaker et al. (1984).

The integrals in equations (119) and (120) only need to be evaluated for the primary parts of the Green's function, and they all have the same form:

$$I = \int_v \frac{e^{-ik_*|\mathbf{r}_m - \mathbf{r}'|}}{4\pi|\mathbf{r}_m - \mathbf{r}'|} dv'. \quad (121)$$

The shape of the cell is not important for this volume integration, so we can replace the cube by a sphere of the same volume and integrate analytically as described in Hohmann (1975). When the field point,  $\mathbf{r}_m$ , is at the center of the sphere we can integrate through the singularity to obtain

$$I = \frac{1}{k_*^2} [(ik_*a + 1)e^{-ik_*a} - 1],$$

where  $a$  is the radius of the sphere.

When  $\mathbf{r}_m$  is outside the sphere,

$$I = \frac{e^{-ik_*R}}{k_*^3 R} [\sin(k_*a) - k_*a \cos(k_*a)],$$

where  $R = |\mathbf{r}_m - \mathbf{r}_c|$ , with  $\mathbf{r}_c$  the center of the sphere.

In more concise notation, equation (111) becomes

$$\frac{1}{\sigma_a} \mathbf{J}_s^m = \mathbf{E}_p^m + \sum_{n=1}^N \boldsymbol{\Gamma}_{mn} \cdot \mathbf{J}_s^n, \quad (122)$$

where  $\mathbf{J}_s^m$  and  $\mathbf{J}_s^n$  are the scattering currents in cells  $m$  and  $n$ , respectively.

Rearranging equation (122) yields

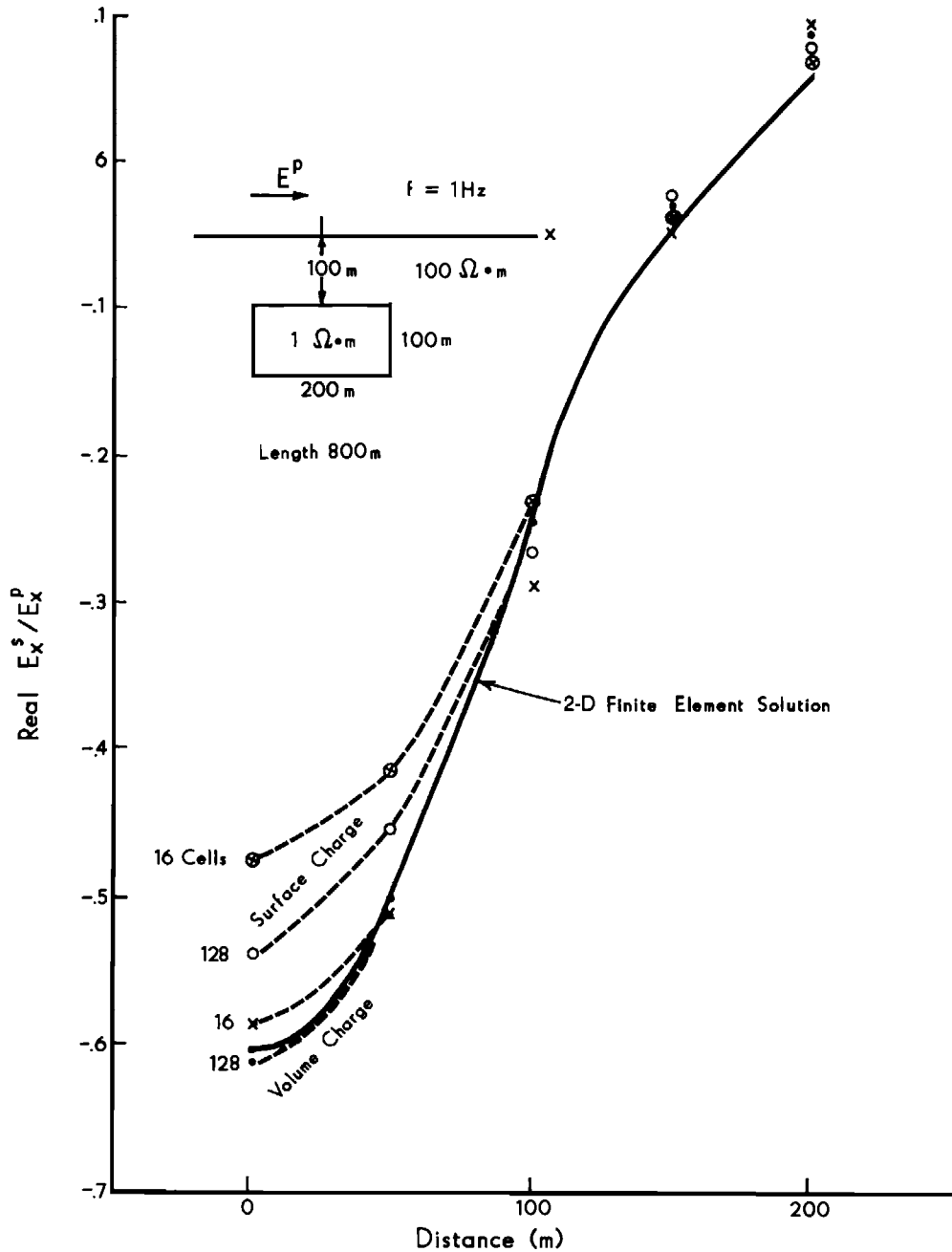


FIG. 12. Improvement in 3-D integral-equation solution resulting from using a vector-scalar potential formulation and charge-smearing.

$$\sum_{n=1}^N \left[ \frac{1}{\sigma_a} \delta_{mn} - \Gamma_{mn} \right] \cdot \mathbf{J}_s^n = \mathbf{E}_p^m, \quad (123)$$

in which

$$\delta_{mn} = \begin{cases} \mathbf{I} & \text{for } m = n \\ \mathbf{0} & \text{for } m \neq n \end{cases}$$

where  $\mathbf{I}$  is the  $3 \times 3$  identity tensor and  $\mathbf{0}$  is the null tensor.

Writing equation (123) for each of the  $N$  values of  $m$  yields a partitioned matrix equation,

$$\mathbf{Z} \cdot \mathbf{J}_s = \mathbf{E}_p, \quad (124)$$

to solve for the scattering current in the body. The elements of the impedance matrix  $\mathbf{Z}$  are themselves  $3 \times 3$  matrices, given by

$$Z_{mn} = \frac{1}{\sigma_a} \delta_{mn} - \Gamma_{mn}. \quad (125)$$

Figure 12 shows the improvement in the 3-D integral equation resulting from distributing the charge over a volume rather than concentrating it on the surface of a cell, and from approximating the derivative of the scalar potential by a difference. The source is a plane wave at 1 Hz, with electric field normal to the long axis of a prismatic conductor, so the response is primarily due to current channeling. Because the effects of the ends of the body are small for this source polarization, near the body the 3-D results should be close to the 2-D profile shown. Note the much improved agreement for the new formulation.

The impedance matrix is full, with dimension  $3N \times 3N$ , where  $N$  is the number of cells into which the body is divided. Because the cell size must be less than a skin depth in the body and less than the depth to the top of the cell, matrix computation time and storage can be excessive. However, as Tripp and Hohmann (1984) show, the impedance matrix for a body with two vertical symmetry planes can be block diagonalized using group theory. The similarity transformation that block diagonalizes  $\mathbf{Z}$  is the same as the one that diagonalizes the group representation matrices  $\mathbf{R}$ . The diagonalized matrix  $\mathbf{R}'$  is given by

$$\mathbf{R}' = \mathbf{U} \mathbf{Z} \mathbf{U}^T, \quad (126)$$

where  $\mathbf{U}$  is easily derived using group theory. Then the block diagonalized impedance matrix is given by

$$\mathbf{Z}' = \mathbf{U} \mathbf{Z} \mathbf{U}^T. \quad (127)$$

In the new basis, the scattering problem becomes

$$\mathbf{Z}' \mathbf{J}'_s = \mathbf{E}'_p, \quad (128)$$

which is much easier to solve than equation (124). The scattering current in the original basis is given by back transforming:

$$\mathbf{J}_s = \mathbf{U}^T \mathbf{J}'_s. \quad (129)$$

Since the basis transformation is inexpensive, this procedure is superior to a direct solution.

The block-diagonalized impedance matrix is composed of four submatrices, each with dimension  $3N/4 \times 3N/4$ . Thus the transformed matrix requires only a fourth of the storage required by the original matrix. The number of operations required for inversion is smaller

by a factor of 12. Because it is only necessary to store one of the four submatrices in core at a time, core storage is reduced by a factor of 16. Matrix formation time for a symmetric body, including the similarity transformation, is about one-third of that for a general body. These savings are significant, because they result in greater accuracy and/or greatly reduced computation costs.

In many cases the IE solution can be improved further by subdividing the body into rectangular prisms rather than cubes, as discussed in Wannamaker et al. (1984). Modifying the basic solution is simple; integration over a prism can be treated as a summation over cubic sub-cells. Rectangular cells are useful for approximating an elongated body, because the scattering current varies more rapidly in the short direction of the body.

Figure 13 illustrates such a case and shows the accuracy that can be obtained for a purely inductive response. The source is a plane wave with the electric field in the long direction of the body, which has a conductivity contrast of 1 000 with its half-space host. Since the body is about 10 skin depths long (in the host), the 3-D results should be the same as those for a 2-D body of the same cross-section. The 2-D and 3-D horizontal magnetic field results for a profile over the center of the body shown in Figure 13 are in good agreement, particularly for the finer discretization. The finer discretization consisted of 168 cells (504 unknowns) per quadrant of the body in plan view, and the results were computed in about 70 hours on a Prime 400 computer. The coarser discretization required only 7 hours.

A major problem with the integral-equation technique, at least for controlled-source applications, arises from the disparity in sizes of the current and charge terms in equation (117) for low but nonnegligible host conductivity. The basic integral equation (27) can be written

$$Z(\mathbf{J}_s) = \mathbf{E}_p, \quad (130)$$

where the impedance operator  $Z$  is given by

$$Z(\mathbf{J}_s) = R(\mathbf{J}_s) + L_A(\mathbf{J}_s) + L_v(\mathbf{J}_s), \quad (131)$$

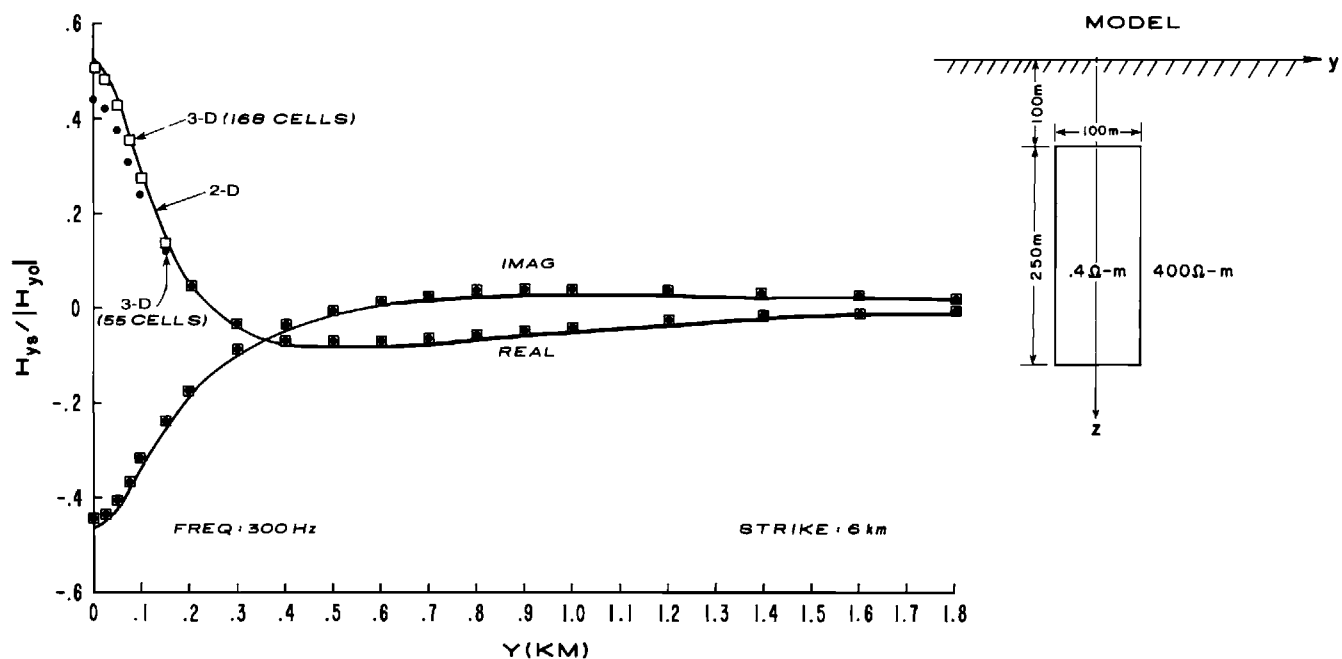


FIG. 13. Comparison between 2-D finite-element results and 3-D integral-equation results with two discretizations. The source is a plane wave with electric field in the  $x$  di-

with

$$R(\mathbf{J}_s) = \frac{1}{\sigma_a} (\mathbf{J}_s), \quad (132)$$

$$L_A(\mathbf{J}_s) = i\omega\mu_0 \int_v G(\mathbf{r}, \mathbf{r}') \mathbf{J}_s(\mathbf{r}') dv', \quad (133)$$

and

$$L_v(\mathbf{J}_s) = -\frac{1}{\sigma_*} \nabla \int_v G(\mathbf{r}, \mathbf{r}') \nabla \cdot \mathbf{J}_s(\mathbf{r}') dv'. \quad (134)$$

To investigate the relative sizes of the operators  $R$ ,  $L_A$ , and  $L_v$ , consider a 1 S/m sphere of radius 50 m in a 0.001 S/m whole space, at 100 Hz. Then to a first-order approximation, considering the current in the sphere to be constant,  $R$  and  $L_A$  are of order 1, while  $L_v$  is of order 300, obtained from the following:

$$R \sim \frac{1}{\sigma_b},$$

$$L_A \sim \omega\mu_0 a^2,$$

and

$$L_v \sim \frac{1}{3\sigma_*}.$$

Thus, the important information contributed by the induction operator  $L_A$  is lost when it is added to  $L_v$ .

### Thin-sheet solutions

Lajoie and West (1976) avoided the disparate-operator problem by solving for curl-free and divergence-free scattering currents on a thin 3-D plate in a conductive half-space. Their results provided important new insight into EM responses of 3-D bodies. Understanding the relation between galvanic and vortex responses, based largely on their work, has been a major breakthrough in EM applications. Figure 14 shows a typical result from their work. The model is a 3-D plate in a conductive half-space excited by a large source loop. Even with a half-space resistivity as high as 3 000  $\Omega \cdot \text{m}$ , the response is quite different from the free-space ( $\rho = \infty$ ) response. As the half-space resistivity decreases, the EM response of the plate changes completely, with the imaginary part changing sign at 200  $\Omega \cdot \text{m}$ . In another approach, Hanneson and West (1984) were able to model thin 3-D plates at relatively high conductivity contrasts by using full-domain (global) basis functions constrained so that no current flows through the edges of the plate.

Dawson and Weaver (1979) discussed an integral-equation solution for an inhomogeneous thin-sheet representing the upper crust. Their solution is very useful for interpreting geomagnetic and MT data. Ranganayaki and Madden (1980), Park (1985), and Vasseur and Weidelt (1977) also developed inhomogeneous-thin-sheet solutions.

Recently Das and Verma (1982) and Wannamaker et al. (1984) presented numerical results, based on similar volume integral-equation solutions, for a 3-D body in a layered earth. The former results are for magnetic-dipole excitation and the latter for plane-wave excitation.

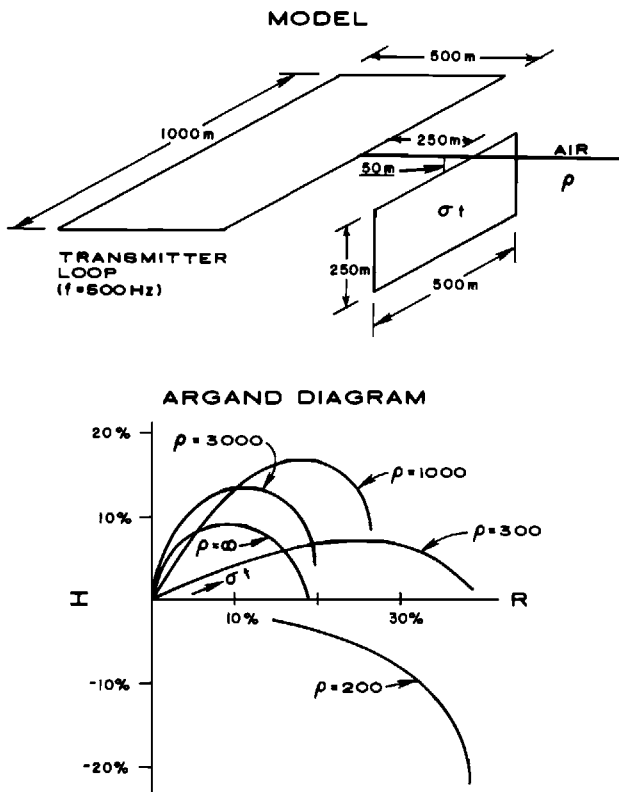


FIG. 14. EM response of a thin 3-D plate in a conductive half-space: (a) model; (b) real (R) and imaginary (I) vertical magnetic field as a percent of free-space field, as a function of plate conductance ( $\sigma t$ ) and half-space resistivity ( $\rho$ ).

Considerations pertaining to the numerical solution are the same as those described above; the only change is that the tensor Green's function is more complicated. Wannamaker et al. are able to keep the computer time about the same as for a homogeneous half-space host by computing the Hankel transforms on a table and interpolating them during matrix formation.

#### Transient calculations

The frequency-domain system function  $H(\omega)$  for an electromagnetic field component and the time-domain impulse response  $h(t)$  for the same component are related by the Fourier transform pair

$$H(\omega) = \int_0^\infty h(t)e^{-i\omega t}dt, \quad (135)$$

and

$$h(t) = \frac{1}{2\pi} \int_{-\infty}^{\infty} H(\omega)e^{i\omega t}d\omega, \quad (136)$$

since the impulse response is causal. Hence, if numerical values of  $H(\omega)$  are available, the time-domain response can be calculated by approximating the inverse Fourier transform of equation (136).

Although the inverse Fourier transform can be approximated by a discrete Fourier transform using an FFT algorithm, the number of frequency-domain data points necessary for accurate estimation of  $h(t)$  is large and their calculation is expensive when they stem from

a 3-D numerical solution. As Lamontagne (1975) observed, simple interpolation of a sparse set of  $H(\omega)$  values does not solve the problem; the discrete inverse Fourier transform of interpolated field values is sensitive to the particular interpolant used, and the calculated impulse response may not be causal.

These problems can be circumvented by treating equation (135) as an inverse problem for  $h(t)$  and utilizing the powerful stabilizing techniques of geophysical inversion theory, as shown in Lamontagne (1975). In a more recent work, Tripp (1982) shows that the impulse response can be written in terms of a decay spectrum  $A(k)$ :

$$h(t) = \int_0^{\infty} A(k)e^{-kt} dk. \quad (137)$$

Thus equation (135), a Fredholm integral equation of the first kind, can be solved by the method of weighted residuals, utilizing exponential basis functions and delta weighting functions. Approximate  $h(t)$  by

$$\hat{h}(t) = \sum_{n=1}^N A_n e^{-k_n t}, \quad (138)$$

where  $k_n$  is the  $n$ th decay constant (reciprocal of the time constant). Substituting equation (138) in equation (135) yields

$$H(\omega) = \sum_{n=1}^N \frac{A_n}{k_n + i\omega}. \quad (139)$$

Incorporating delta weight functions,

$$w_m(\omega) = \delta(\omega - \omega_m),$$

gives

$$\sum_{n=1}^N \frac{1}{k_n + i\omega_m} A_n = H(\omega_m). \quad (140)$$

Writing equation (135) for each of the  $M$  values of  $m$  yields a matrix equation

$$\mathbf{KA} = \mathbf{H} \quad (141)$$

for determining the  $N$  values of  $A_n$ . Then the impulse response is given by equation (138), and the response for any transmitter waveform is given by convolution. In general,  $N$  must be greater than  $M$ , and, because equation (135) is ill-posed, a generalized-inverse or ridge-regression solution is required. For many cases, ten frequency-domain values are sufficient.

In order to avoid the computer interaction and subjectivity involved in the decay-spectrum method, Newman et al. (1986) developed a Fourier transformation technique for 3-D responses based on approximating sine and cosine transforms using the digital filter technique. Equation (136) is rewritten as

$$h(t) = \frac{2}{\pi} \int_0^{\infty} \text{Im}[H(\omega)] \sin(\omega t) d\omega, \quad (142)$$

and

$$s(t) = -\frac{2}{\pi} \int_0^{\infty} \frac{1}{\omega} \text{Im}[H(\omega)] \cos(\omega t) d\omega, \quad (143)$$

for impulse and step responses, respectively.

These sine and cosine transforms are evaluated using a fast digital filtering technique described as lagged convolution in Anderson (1975, 1982). Usually the imaginary part of the 3-D frequency response  $H(\omega)$  must be computed at 20 to 40 frequencies (5 to 8 points per decade). Then the frequency response is replaced by a cubic spline interpolating function, after values at low and high frequencies are calculated using asymptotic techniques.

Annan (1974) developed an elegant method of calculating the frequency- and time-domain EM responses of a thin 3-D plate in free-space. Classically the response of a body whose surface coincides with a constant-coordinate surface, such as a sphere, is calculated in terms of analytic eigenfunctions, with no numerical solution required. Each mode in the eigenfunction expansion is decoupled from the other modes, so that the impedance matrix is diagonal. In contrast, for bodies of arbitrary shape, the impedance matrix for the IE numerical solution links the expansion function coefficients for the scattering currents with those for the primary electric field by a full matrix.

By diagonalizing the IE impedance matrix, Annan formulated a solution for a general body in terms of real eigencurrents expanded in the full-range expansion functions of his numerical solution. He found that for a body in free-space the eigencurrent geometries are the same for all frequencies, and that each eigencurrent has the same frequency response as that of a simple loop circuit. Thus each mode contributes a single exponential decay in the time domain, and it is easy to calculate TEM responses by summing the decays for the first few modes.

Tripp (1982) investigated a similar modal solution for a body in a conductive half-space. He found that the eigencurrent patterns change with frequency, so that the modal solution has no advantage over a direct numerical solution. However, it still may be possible to formulate the problem in terms of complex modes that diagonalize the impedance matrix and that simplify calculations.

Along similar lines, Lee (1981) calculated the TEM response of a sphere in a layered earth by inverse Fourier transforming IE results. He computed the frequency-domain response by expanding the primary and total electric fields in terms of the natural modes of a sphere, terming his solution a “mode-matching” solution. Lee found that he could ignore higher-order modes in computing the transient response.

The TEM integral equation corresponding to equation (27) in the frequency domain is

$$\mathbf{e}(\mathbf{r},t) = \mathbf{e}_p(\mathbf{r},t) + \int_v \int_0^t \mathbf{g}(\mathbf{r},\mathbf{r}';t-t') \cdot \mathbf{e}(\mathbf{r}',t') \sigma_a(\mathbf{r}') dt' dv', \quad (144)$$

where, for a whole space, e.g., the tensor Green's function is derived using the time-domain version of equation (23)

$$\mathbf{e}_s = -\mu_0 \frac{\partial \mathbf{a}}{\partial t} - \nabla v, \quad (145)$$

with, from the expressions (24) and (25)

$$\mathbf{a}(\mathbf{r},t) = \int_v \int_0^t \mathbf{j}_s(\mathbf{r}',t) g(\mathbf{r},\mathbf{r}';t-t') dt' dv', \quad (146)$$

and

$$v(\mathbf{r},t) = -\frac{1}{\sigma_*} \int_v \int_0^t \nabla \cdot \mathbf{j}_s(\mathbf{r}',t') g(\mathbf{r},\mathbf{r}';t-t') dt' dv'. \quad (147)$$

The time-domain scalar Green's function  $g(\mathbf{r},\mathbf{r}';t)$ , obtained by inverse Fourier transforming equation (26), is (Ward and Hohmann, this volume).

$$g(\mathbf{r}, \mathbf{r}'; \tau) = \frac{\theta_*}{4\pi^{3/2}\tau} e^{-\theta_*^2 |\mathbf{r} - \mathbf{r}'|^2}, \quad (148)$$

with

$$\theta_* = \left( \frac{\mu_0 \sigma_*}{4\tau} \right)^{1/2}.$$

Other terms must be added to account for the earth-air interface and any other horizontal layers.

Recently San Filipo and Hohmann (1985) developed a time-domain 3-D solution based on equation (144). By incorporating a set of divergence-free basis functions consisting of closed tubes of current in addition to the usual pulse basis functions, they achieved a time-stepping solution that is valid at high conductivity contrasts. As shown in Figure 15, the evolution of the electric field in time at any point in the body after the current in the transmitter is shut off is approximated as a piece-wise linear function. Then the electric field at time  $n\Delta t$  is given by

$$\mathbf{e}_n = \mathbf{e}_n^p + \sigma_a \int_v \sum_{i=1}^n \int_{(i-1)\Delta t}^{i\Delta t} g(n\Delta t - t') \mathbf{e}(t') dt' dv', \quad (149)$$

where  $\Delta t$  is the time-step, which usually is on the order of 0.1 ms.

The time integrals can be carried out to obtain an integral equation,

$$\mathbf{e}_n(\mathbf{r}) = \mathbf{e}_n^p(\mathbf{r}) + \sigma_a \int_v \Gamma_0(\mathbf{r}, \mathbf{r}') \mathbf{e}_n(\mathbf{r}') dv' + \sigma_a \sum_{j=1}^{n-1} \int_v \Gamma_j(\mathbf{r}, \mathbf{r}') \mathbf{e}_{n-j}(\mathbf{r}') dv', \quad (150)$$

to be solved for the electric field at time  $n\Delta t$ . Expressions for the time-integrated tensor Green's functions  $\Gamma_0$  and  $\Gamma_j$  are given in San Filipo and Hohmann (1985). The terms involving  $\Gamma_j$  in equation (150) can be considered feedback terms, because they involve the previous, known electric field in the body.

In order to deal with the problem of disparate induction and galvanic operators discussed above, spatial discretization is carried out by writing the electric field in terms of two sets of basis functions as

$$\mathbf{e}_n(\mathbf{r}) \approx \sum_{i=1}^N \mathbf{e}_i^0 p_i(\mathbf{r}) + \sum_{i=1}^M c_i \mathbf{q}_i(\mathbf{r}), \quad (151)$$

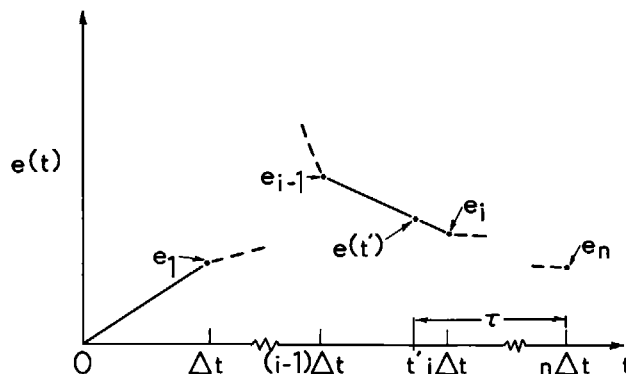


FIG. 15. Piecewise linear approximation of the evolution of the electric field in time at a point in the body.

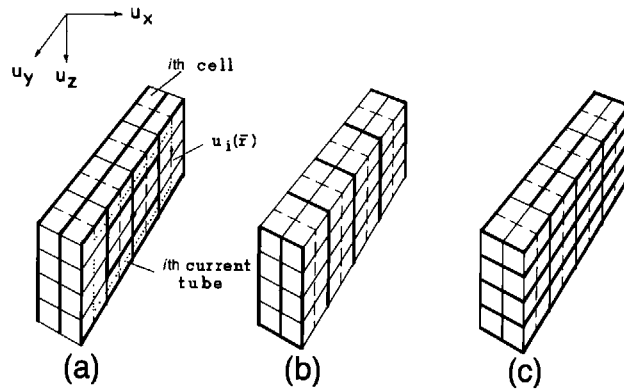


FIG. 16. A prismatic body divided into 32 cells (8 cells/quadrant), each built out of 2 cubic subcells, defining the pulse functions  $\{p_i(\mathbf{r})\}_1^N$ , and the combination of cells for (a) 4 closed current tubes normal to  $u_x$ , (b) 4 normal to  $u_y$ , and (c) 4 normal to  $u_z$ . An example of a current tube with unit direction vector  $\mathbf{u}_i(\mathbf{r})$  is shown in (a).

where the  $p_i$  are the usual pulse basis functions defined by

$$p_i(\mathbf{r}) = \begin{cases} 1 & \text{for } \mathbf{r} \text{ in } i^{\text{th}} \text{ cell} \\ 0 & \text{otherwise.} \end{cases} \quad (152)$$

The divergence-free basis functions  $\mathbf{q}_i$  describing current tubes are illustrated graphically in Figure 16. Mathematically they are given by

$$\mathbf{q}_i(\mathbf{r}) = \begin{cases} \frac{\mathbf{u}_i(\mathbf{r})}{a_i(\mathbf{r})} & \text{for } \mathbf{r} \text{ in } i^{\text{th}} \text{ tube} \\ \mathbf{0} & \text{otherwise} \end{cases}, \quad (153)$$

where  $\mathbf{u}_i$  is the unit vector in the direction of current flow, and  $a_i$  is the (variable) cross-sectional area of the current tube.

The numerical solution for  $\mathbf{e}_n(\mathbf{r})$  is best illustrated by writing equation (150) in operator notation as

$$\mathbf{e}_n + L_a(\mathbf{e}_n) + L_v(\mathbf{e}_n) = \mathbf{e}_n^\rho - \sum_{k=1}^{n-1} [L_a(\mathbf{e}_{n-k}) + L_v(\mathbf{e}_{n-k})] = \mathbf{f}_n, \quad (154)$$

where  $L_a$  is the induction operator from equation (146), and  $L_v$  is the galvanic operator from equation (147). Then a Galerkin solution employing weighting functions that are the same as the basis functions yields the following coupled equations for the  $3N + M$  unknowns  $\{\mathbf{e}_j^0\}_1^N$  and  $\{c_j\}_1^M$ :

$$\sum_{j=1}^N (\langle p_i, p_j \rangle + \langle p_i, (L_a + L_v)p_j \rangle) \mathbf{e}_j^0 + \sum_{j=1}^M (\langle p_i, \mathbf{q}_j \rangle + \langle p_i, L_a \mathbf{q}_j \rangle) c_j = \langle p_i, \mathbf{f}_n \rangle$$

$$i = 1, 2, \dots, N, \quad (155)$$

and

$$\sum_{j=1}^N (\langle \mathbf{q}_i, p_j \rangle + \langle \mathbf{q}_i, L_a p_j \rangle) \mathbf{e}_j^0 + \sum_{j=1}^M (\langle \mathbf{q}_i, \mathbf{q}_j \rangle + \langle \mathbf{q}_i, L_a \mathbf{q}_j \rangle) c_j = \langle \mathbf{q}_i, \mathbf{f}_n \rangle$$

$$i = 1, 2, \dots, M. \quad (156)$$

Because  $\mathbf{q}_j$  is divergence-free, the dominant galvanic operator  $L_v$  does not appear in the second sums in equations (155) and equations (156). Furthermore,  $L_v$  is eliminated from the first sum in equation (156), because taking the inner product of  $\mathbf{q}_i$  and  $L_v p_j$  implies integrating the gradient of a scalar around a closed loop, which is zero by Stokes theorem. The result is a stable numerical solution that is accurate for any host conductivity, including that of free-space.

Finally, the matrix equation for time-stepping is given by

$$\begin{bmatrix} \mathbf{K}_{pp} & \mathbf{K}_{pq} \\ \mathbf{K}_{qp} & \mathbf{K}_{qq} \end{bmatrix} \begin{bmatrix} \mathbf{e}_n^0 \\ c_n \end{bmatrix} = \begin{bmatrix} \langle p_i, \mathbf{e}_n^p \rangle \\ \langle \mathbf{q}_i, \mathbf{e}_n^p \rangle \end{bmatrix} + \sum_{j=1}^{n-1} \begin{bmatrix} \mathbf{F}_j^{pp} & \mathbf{F}_j^{pq} \\ \mathbf{F}_j^{qp} & \mathbf{F}_j^{qq} \end{bmatrix} \begin{bmatrix} \mathbf{e}_{n-j}^0 \\ c_{n-j} \end{bmatrix}, \quad (157)$$

where the sum on the right-hand side involves the feedback terms.

From Faraday's law, the time derivative of the magnetic induction is given by

$$\frac{\partial \mathbf{b}}{\partial t} = \frac{\partial \mathbf{b}^p}{\partial t} + \sigma_a \int_v \int_0^t \mathbf{g}_b(\mathbf{r}, \mathbf{r}', t - t') \mathbf{e}(\mathbf{r}', t') dt' dv', \quad (158)$$

where  $\mathbf{g}_b$  is the tensor Green's function for magnetic induction.

While we have illustrated the solution for a whole-space host for simplicity, the principles are the same for a half-space host. Remarkably, time steps on the order of 0.1 ms produce good results; time steps for differential equation solutions are on the order of a microsecond.

Figure 17 compares transient results computed using the numerical solution described above with results for a sphere (Lee, 1981), for a coincident-loop array. The agreement is good, but it was necessary to use a cube 90 m on a side, whereas a cube of the same volume as the sphere is about 80 m on a side. The smaller cube results in a time constant about 20 percent smaller. The sphere results are not valid at very early times, due to the neglect of higher-order modes.

The effect of increasing the host resistivity from 1 000  $\Omega \cdot \text{m}$ , and to the free-space limit is shown in Figure 17. A galvanic response is evident at early times, when the currents induced in the host are concentrated near the body. The secondary field is substantially greater than the free-space response at times earlier than 0.5 ms for the 100  $\Omega \cdot \text{m}$  host, but with a 1 000  $\Omega \cdot \text{m}$  host the galvanic response has disappeared by 0.1 ms. After 0.2 ms the secondary field of the body in a 1 000  $\Omega \cdot \text{m}$  half-space is the same as that of the body in free-space. Hence, simple superposition applies: the total response is the sum of the background (half-space) response and the response of the body in free-space. However, for a 100  $\Omega \cdot \text{m}$  half-space simple superposition only gives a rough approximation to the total response at late times.

### Differential equation solutions

Finite-difference formulations for 3-D scattering are discussed in Lines and Jones (1973) and in Zhdanov et al. (1982). Instead of equations (15), Lines and Jones approximated the equation

$$\nabla^2 \mathbf{E} - \nabla(\nabla \cdot \mathbf{E}) + k^2 \mathbf{E} = 0, \quad (159)$$

for a plane-wave source. Jones and Vozoff (1978) presented MT results based on a finite-difference solution of equation (141).

Zhdanov et al. (1982) recommend solving equation (15) rather than equation (159) by the finite-difference method. Then it is possible to use a seven-point scheme for the finite-difference approximation, and, furthermore, the second term in equation (15) vanishes in regions where conductivity is constant. However, they did not show any 3-D numerical results.

Reddy et al. (1977) published 3-D MT results based on a finite element (FE) solution of equation (159). They used the Galerkin technique with linear basis and weight functions in

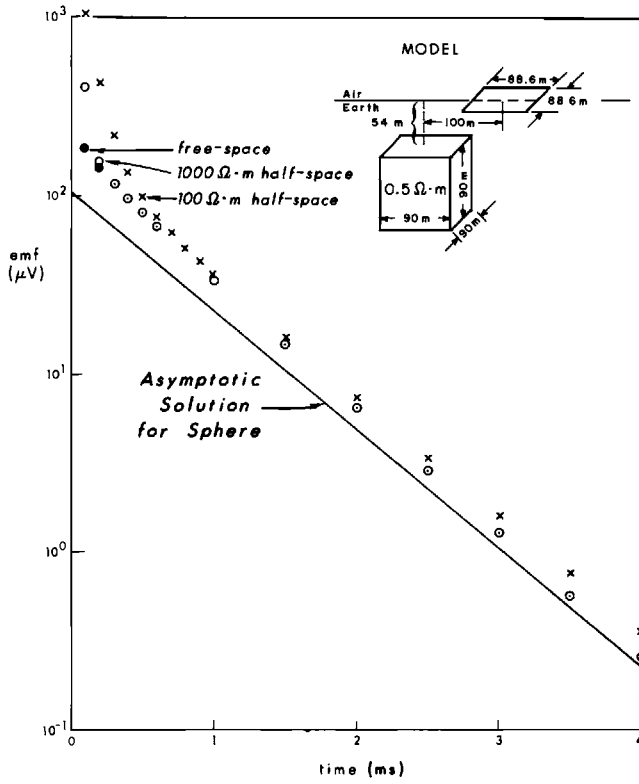


FIG. 17. Comparison between results computed with a time-domain integral-equation solution and with T. Lee's solution for a  $0.5 \Omega \cdot \text{m}$  sphere of radius 50 m with center 100 m deep in a  $100 \Omega \cdot \text{m}$  half-space. Secondary field response for a coincident-loop system. Also shown are the integral-equation responses for the cube in a  $1000 \Omega \cdot \text{m}$  half-space, and in free-space. The free-space results coincide with the  $1000 \Omega \cdot \text{m}$  half-space results after the first two values.

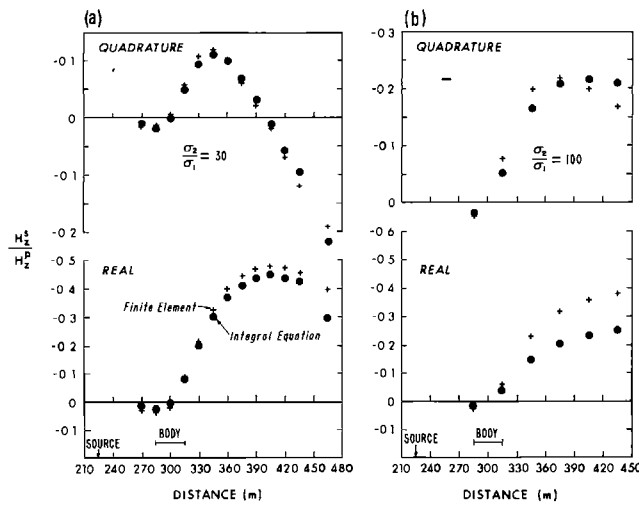


FIG. 18. Comparison between integral-equation and finite-element results for a 3-D conductor in the earth; (a)  $\sigma_b/\sigma_* = 30$ ; (b)  $\sigma_b/\sigma_* = 100$ .

hexahedral elements. They alleviated the problem of discontinuous normal electric fields by specifying smooth, rather than abrupt, conductivity boundaries. Thus the second term in equation (159) results in a volume-charge rather than a surface-charge distribution, as in the integral equation approach discussed above. However, they found that conductivity contrasts greater than 10 result in errors greater than 10 percent up to three node spacings from a conductivity boundary.

Pridmore et al. (1981) presented a 3-D FE solution for controlled-source EM applications. They formulated the problem by minimizing a functional, but since the Galerkin approach yields the same equations, that probably is an unnecessary complication. They used tetrahedral elements for the dc problem and hexahedral elements for the EM problem, and, to reduce storage requirements, they solved the system of equations using a point-successive over-relaxation method. The optimum over-relaxation factor  $W$  can be determined by observing the behavior of certain nodal values during iteration. Typically, a dc problem requires 100 iterations, while EM problems require more.

Figure 18 shows a comparison between FE results of Pridmore et al. (1981) and results computed using the frequency-domain IE solution with only pulse basis functions described above. The model is a conductive prism 30 m deep with 30 m width, 120 m length, 90 m depth extent, and  $1 \Omega \cdot \text{m}$  resistivity, which is a standard test model proposed in Braham et al. (1978). The transmitter is a fixed vertical magnetic dipole with moment  $4\pi \text{ A}\cdot\text{m}^2$  operating at 1 000 Hz, and profiles of the secondary vertical magnetic field are shown for half-space resistivities of 30 and  $100 \Omega \cdot \text{m}$ .

The IE solution, which used 96 cells and did not take advantage of symmetry, took only 5 minutes CPU time on a Univac 1108 computer. By comparison, the FE solution took about 3 hours for 200 iterations, although slightly less accurate results could be calculated in half the time. Since the FE equations are solved iteratively, computations for two transmitter positions would require double the amount of computer time. However, IE results for other source positions can be calculated with little additional computer time.

In Figure 18a, the IE and FE results for a conductivity contrast of 30 are in good agreement. However, the agreement deteriorates for a contrast of 100, particularly for the real part of the field, as shown in Figure 18b. As Pridmore et al. (1981) show, the agreement is very poor for a contrast of 1 000, again especially for the real component. Probably both solutions are invalid at high contrasts.

### Hybrid solutions

Three-dimensional DE solutions with boundary conditions imposed at great distances have not been very successful. The large grids required result in unreasonable amounts of computer time and storage. Thus recent DE research has focused on hybrid approaches, combining DE and IE solutions, as a means of limiting mesh size.

Finite-element discretization of equation (15) inside one of the meshes in Figure 19 yields a matrix equation for the electric field:

$$\mathbf{L}\mathbf{E} = \mathbf{0}. \quad (160)$$

For either of the hybrid cases shown in Figure 19 we can partition equation (160) into

$$\begin{bmatrix} \mathbf{L}_{vv} & \mathbf{L}_{vb} \\ \mathbf{L}_{bv} & \mathbf{L}_{bb} \end{bmatrix} \cdot \begin{bmatrix} \mathbf{E}_v \\ \mathbf{E}_b \end{bmatrix} = \mathbf{0}, \quad (161)$$

where subscript  $v$  denotes electric fields in the interior (volume) of the mesh, and subscript  $b$  denotes electric fields at the boundary nodes. From equation (161)

$$\mathbf{L}_{vv}\mathbf{E}_v = -\mathbf{L}_{vb}\mathbf{E}_b. \quad (162)$$

However, we can calculate the field on the boundary in terms of the field inside the mesh using the expression (27), which becomes

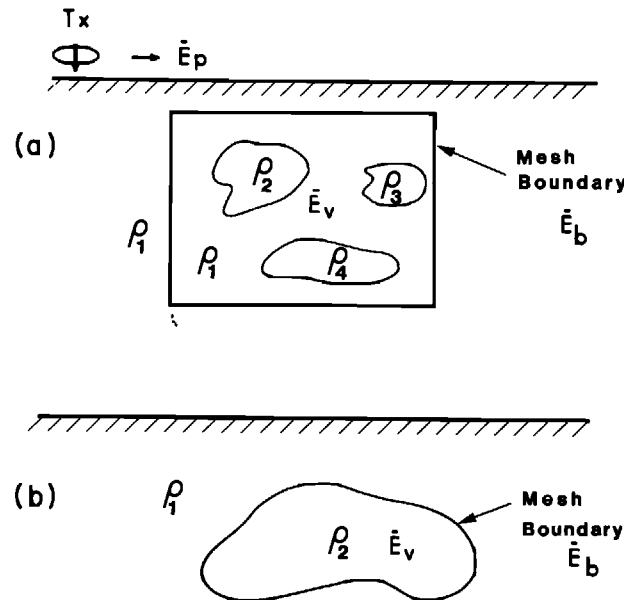


FIG. 19. Geometries for hybrid techniques.

$$\mathbf{E}_b(\mathbf{r}) = \mathbf{E}_b^p(\mathbf{r}) + \int_v \mathbf{G}(\mathbf{r}, \mathbf{r}') \cdot \mathbf{E}_v(\mathbf{r}') \sigma_a(\mathbf{r}') d\mathbf{v}'. \quad (163)$$

The matrix version of equation (163) is

$$\mathbf{E}_b = \mathbf{R}\mathbf{E}_v + \mathbf{E}_b^p, \quad (164)$$

where  $\mathbf{R}$  is  $M \times N$ , with  $M$  the number of boundary nodes and  $N$  the number of interior nodes.

Substituting equation (164) in equation (162),

$$(\mathbf{L}_{vv} + \mathbf{L}_{vb}\mathbf{R})\mathbf{E}_v = -\mathbf{L}_{vb}\mathbf{E}_b^p. \quad (165)$$

In the direct hybrid method, equation (165) is solved for  $\mathbf{E}_v$ , and then equation (163) and the corresponding equation for magnetic field are used to calculate the fields outside the mesh. The matrix  $\mathbf{L}_{vv} + \mathbf{L}_{vb}$  is full, asymmetric and  $N \times N$ .

The advantage of the hybrid scheme illustrated in Figure 19a is that the integral in equation (163) is not singular:  $\mathbf{r}$  is never equal to  $\mathbf{r}'$ . However, the FE solution inside the mesh still is plagued by the problem of discontinuous electric fields at conductivity boundaries. On the other hand, for the hybrid scheme of Figure 19b the FE solution operates in a homogeneous region, but evaluation of equation (163) at singular points on the surface of the mesh is very difficult.

Lee et al. (1981) developed an iterative hybrid solution, by assuming an initial guess for  $\mathbf{E}_b$ , the boundary field, calculating  $\mathbf{E}_v$ , then finding a new  $\mathbf{E}_b$  using equation (163), and proceeding iteratively. Their results agree with the FE and IE results shown in Figure 18 for a low-contrast ( $\sigma_b/\sigma_* = 30$ ) model. However, their MT results for a body with a conductivity contrast of 200 do not agree with IE results, which appear to be correct based on comparison with 2-D results.

More recently, Best et al. (1985) developed a hybrid solution based on solving for secondary magnetic fields. Their secondary field is defined as the difference between the total field and the static field, and their mesh is of the type shown in Figure 19a. Comparison with analytical results for a sphere in a half-space shows that the hybrid results of Best et

al. are valid for a high conductivity contrast of 1 000. Thus 3-D, DE solutions for magnetic fields appear to be superior to those for electric fields. However, as Pridmore et al. (1981) found, problems arise if the finite-element mesh crosses the air-earth interface in the case of a magnetic-field solution. Such is not the case for a hybrid solution or for an explicit time-stepping solution.

## Acknowledgment

I am grateful to Craig Beasley, Nancy Butterworth, Marcus Flis, Cynthia Furse, Sheryl Howard, Jeffrey Johnston, Misac Nabighian, Louise Pellerin, Arthur Raiche, and Luiz Rijo for helpful reviews of this paper. Holly Baker expertly typed the manuscript through several revisions.

## References

- Adhidjaja, J. I., Hohmann, G. W., and Oristaglio, M. L., 1985, Two-dimensional transient electromagnetic responses: *Geophysics*, **50**, 2849–2861.
- Anderson, W. L., 1975, Improved digital filters for evaluating Fourier and Hankel transform integrals: *Nat. Tech. Inf. Serv. Rep. PB-242-800*.
- , 1982, Fast Hankel transforms using related and lagged convolutions: *Assn. Comp. Mach. Trans. on Math. Software*, **8**, 344–368.
- Annan, A. P., 1974, The equivalent source method for electromagnetic scattering analysis and its geophysical application: Ph.D. thesis, Memorial Univ. of Newfoundland.
- Best, M. E., Duncan, P., Jacobs, F. J., and Scheen, W. L., 1985, Numerical modeling of the electromagnetic response of three-dimensional conductors in a layered earth: *Geophysics*, **50**, 665–676.
- Braham, B., Haren, R., Lappi, D., Lemaire, H., Payne, D., Raiche, A., Spies, B., and Vozoff, K., 1978, Lecture notes from the U.S.-Australia electromagnetic workshop: *Bull. Austral. Soc. Explor. Geophys.*, **9**, 2–33.
- Brewitt-Taylor, C. R., and Weaver, J. T., 1976, On the finite difference solution of two-dimensional induction problems: *Geophys. J. Roy. Astr. Soc.*, **47**, 375–396.
- Butler, C. M., and Wilton, D. R., 1975, Analysis of various numerical techniques applied to thin-wire scatterers: *Inst. Elect. and Electron. Eng., Trans. on Ant. and Prop.*, **AP-23**, 534–540.
- Coggon, J. H., 1971, Electromagnetic and electrical modeling by the finite element method: *Geophysics*, **36**, 132–155.
- Das, U. C., and Verma, S. K., 1982, Electromagnetic response of an arbitrarily shaped three-dimensional conductor in a layered earth-numerical results: *Geophys. J. Roy. Astr. Soc.*, **68**, 55–56.
- Dawson, T. W., and Weaver, J. T., 1979, Three-dimensional induction in a non-uniform thin sheet at the surface of a uniformly conducting earth: *Geophys. J. Roy. Astr. Soc.*, **59**, 445–462.
- DuFort, E. C., and Frankel, S. P., 1953, Stability conditions in the numerical treatment of parabolic differential equations: *Math. tables and other aids to computation (former title of Mathematics of computation)*, **7**, 135–152.
- Emeran, S. H., Schmidt, W., and Stephen, R. A., 1982, An implicit finite-difference formulation of the elastic wave equation: *Geophysics*, **47**, 1521–1526.
- Fox, R. C., Hohmann, G. W., Killpack, J. J., and Rijo, L., 1980, Topographic effects in resistivity and induced-polarization surveys: *Geophysics*, **45**, 75–93.
- Goldman, M. M., and Stoyer, C. H., 1983, Finite-difference calculations of the transient field of an axially symmetric earth for vertical magnetic dipole excitation: *Geophysics*, **48**, 953–963.
- Hannesson, J. E., and West, G. F., 1984, The horizontal loop electromagnetic response of a thin plate in a conductive earth: Part 1—Computational method: *Geophysics*, **49**, 411–420.
- Harrington, R. F., 1968, Field computation by moment methods: The Macmillan Publ. Co., Inc.
- Hohmann, G. W., 1971, Electromagnetic scattering by conductors in the earth near a line source of current: *Geophysics*, **36**, 101–131.
- , 1975, Three-dimensional induced polarization and electromagnetic modeling: *Geophysics*, **40**, 309–324.
- , 1983, Three-dimensional EM modeling: *Geophys. Surv.*, **6**, 27–83.
- Howard, A. Q., 1972, Electromagnetic fields of a subterranean cylindrical inhomogeneity excited by a line source: *Geophysics*, **37**, 975–984.
- Jones, F. W., and Price, A. J., 1971, Geomagnetic effects of sloping and shelving discontinuities of earth conductivity: *Geophysics*, **36**, 58–66.
- Jones, F. W., and Vozoff, K., 1978, The calculation of magnetotelluric quantities for three-dimensional conductivity inhomogeneities: *Geophysics*, **43**, 1167–1175.

- Kuo, J. T., and Cho, Vong-heng, 1980, Transient time-domain electromagnetics: *Geophysics*, **45**, 271–291.
- Lajoie, J. J., and West, G. F., 1976, The electromagnetic response of a conductive inhomogeneity in a layered earth: *Geophysics*, **41**, 1133–1156.
- Lamontagne, Y., 1975, Applications of wideband, time-domain electromagnetic measurements in mineral exploration: Ph.D. thesis, Univ. of Toronto.
- Lapidus, L., and Pinder, G. F., 1982, Numerical solution of partial differential equations in science and engineering: John Wiley & Sons, Inc.
- Lee, K. H., 1978, Electromagnetic scattering by a two-dimensional inhomogeneity due to an oscillating magnetic dipole: Ph.D. thesis, Univ. of California, Berkeley.
- Lee, K. H., and Morrison, H. F., 1985a, A numerical solution for the electromagnetic scattering by a two-dimensional inhomogeneity: *Geophysics*, **50**, 466–472.
- \_\_\_\_\_, 1985b, A solution for TM-mode plane waves incident on a two-dimensional inhomogeneity: *Geophysics*, **50**, 1163–1165.
- Lee, K. H., Pridmore, D. F., and Morrison, H. F., 1981, A hybrid three-dimensional electromagnetic modeling scheme: *Geophysics*, **46**, 796–805.
- Lee, T. J., 1981, Transient electromagnetic response of a sphere in a layered medium: PAGEOPH, **119**, 309–338.
- Lines, L. R., and Jones, F. W., 1973, The perturbation of alternating geomagnetic fields by three-dimensional island structures: *Geophys. J. Roy. Astr. Soc.*, **32**, 133–154.
- Meyer, W. H., 1976, computer modelling of electromagnetic prospecting methods: Ph.D. thesis, Univ. of California, Berkeley.
- Miller, E. K., and Deadrick, F. J., 1975, Some computational aspects of thin wire modeling, in R. Mittra, Ed., Numerical and asymptotic techniques in electromagnetics: Springer-Verlag.
- Newman, G. A., Hohmann, G. W., and Anderson, W. L., 1986, Transient electromagnetic response of a three-dimensional body in a layered earth: *Geophysics*, **51**, 1608–1627.
- Oristaglio, M. L., and Hohmann, G. W., 1984, Diffusion of electromagnetic fields in a two-dimensional earth: A finite-difference approach: *Geophysics*, **49**, 870–894.
- Park, S. K., 1985, Distortion of magnetotelluric sounding curves by three-dimensional structures: *Geophysics*, **50**, 785–797.
- Parry, J. R., and Ward, S. H., 1971, Electromagnetic scattering from cylinders of arbitrary cross-section in a conductive half-space: *Geophysics*, **36**, 67–100.
- Pridmore, D. F., Hohmann, G. W., Ward, S. H., and Sill, W. R., 1981, An investigation of finite-element modeling for electrical and electromagnetic data in three dimensions: *Geophysics*, **46**, 1009–1024.
- Raiche, A. P., 1974, An integral equation approach to 3D modeling: *Geophys. J. Roy. Astr. Soc.*, **36**, 363–376.
- \_\_\_\_\_, 1978, Green's functions for modelling the EM response of a target near a dipping contact: *Geophys. J. Roy. Astr. Soc.*, **55**, 507–511.
- Ranganayaki, R. P., and Madden, T. R., 1980, Generalized thin sheet analysis in magnetotellurics: An extension of Price's analysis: *Geophys. J. Roy. Astr. Soc.*, **60**, 445–457.
- Reddy, I. K., Rankin, D., and Phillips, R. J., 1977, Three-dimensional modelling in magnetotelluric and magnetic variational sounding: *Geophys. J. Roy. Astr. Soc.*, **51**, 313–325.
- Richtmyer, R. D., and Morton, K. W., 1967, Difference methods for initial value problems: John Wiley & Sons, Inc.
- Rijo, L., 1977, Modeling of electric and electromagnetic data: Ph.D. thesis, Univ. of Utah.
- SanFilipo, W. A., and Hohmann, G. W., 1985, Integral equation solution for the transient electromagnetic response at a three-dimensional body in a conductive half-space: *Geophysics*, **50**, 798–809.
- Silvester, P., and Haslam, C. R. S., 1972, Magnetotelluric modelling by the finite element method: *Geophys. Prosp.*, **20**, 872–891.
- Snyder, D. D., 1976, A method for modeling the resistivity and IP response of two-dimensional bodies: *Geophysics*, **41**, 997–1015.
- Stoyer, C. H., and Greenfield, R. J., 1976, Numerical solutions of the response of a two-dimensional earth to an oscillating magnetic dipole source: *Geophysics*, **41**, 519–530.
- Swift, C. M., Jr., 1971, Theoretical magnetotelluric and turam response from two-dimensional inhomogeneities: *Geophysics*, **36**, 38–52.
- Ting, S. C., and Hohmann, G. W., 1981, Integral equation modeling of three-dimensional magnetotelluric response: *Geophysics*, **46**, 182–197.
- Tripp, A. C., 1982, Multi-dimensional electromagnetic modeling: Ph.D. thesis, Univ. of Utah.
- Tripp, A. C., and Hohmann, G. W., 1984, Block diagonalization of the electromagnetic impedance matrix of a symmetric buried body using group theory: *Inst. Elect. and Electron. Eng., Trans. Geoscience and Remote Sensing*, **22**, 62–69.
- VanBladel, J., 1961, Some remarks on Green's dyadic for infinite space: *Inst. Radio Eng., Trans. Ant. and Prop.*, **9**, 563–566.
- Vasseur, G., and Weidelt, P., 1977, Bimodal electromagnetic induction in non-uniform thin sheets with an application to the northern Pyrenean induction anomaly: *Geophys. J. Roy. Astr. Soc.*, **51**, 669–690.
- Wannamaker, P. E., 1983, Resistivity structure of the northern Basin and Range: *Geoth. Res. Counc., Spec. Rep.* **13**, 345–362.
- Wannamaker, P. E., Hohmann, G. W., and San Filipo, W. A., 1984, Electromagnetic modeling of three-dimensional bodies in layered earths using integral equations: *Geophysics*, **49**, 60–74.
- Ward, S. H., Peebles, W. J., and Ryu, J., 1973, Analysis of geoelectromagnetic data, in Bolt, B. A., Ed., Methods in Computational Physics, Academic Press Inc.

- Weaver, J. T., and Brewitt-Taylor, C. R., 1978, Improved boundary condition for the numerical solution of E-polarization problems in geomagnetic induction: *Geophys. J. Roy. Astr. Soc.*, **54**, 309–317.
- Weidelt, P., 1975, Electromagnetic induction in three-dimensional structures: *J. Geophys.*, **41**, 85–109.
- Won, I. J., and Kuo, J. T., 1975a, Representation theorems for multiregional electrodynamic diffraction: Part I. Theory: *Geophysics*, **40**, 96–108.
- , 1975b, Representation theorems for multiregional electrodynamic diffraction: Part II. Applications: *Geophysics*, **40**, 109–119.
- Zhdanov, M. S., Golubev, N. G., Spichak, V. V., Varentsov, I. M., 1982, The construction of effective methods for electromagnetic modelling: *Geophys. J. Roy. Astr. Soc.*, **68**, 589–607.



---

---

**6**

**Electromagnetic Physical  
Scale Modeling**

---

---



---

---

**6**

---

---

## Electromagnetic Physical Scale Modeling

*F. C. Frischknecht\**

### Introduction

Physical scale modeling is an important technique for obtaining the electromagnetic response of a large variety of geologic models. In physical or analog scale modeling the geometry of the model is reproduced in the laboratory at a scale usually between 1:100 and 1:10<sup>6</sup>. Generally, the electrical properties of the laboratory model also must be scaled. Measurements are made using miniaturized loops or electrode arrays. By use of appropriate scale factors the scale model measurements can be translated to be equivalent to those that would be obtained for idealized full-size models. As indicated elsewhere in this volume, analytical solutions for electromagnetic response exist only for a relatively small number of conductive structures. Numerical methods for solving two- and three-dimensional problems have been available only for a short time and their use is limited because of computational difficulties and the extensive computer time required. For many years albums of scale model results for finite structures have been one of the chief aids in interpretation of electromagnetic profiling data. However, scale model results are seldom used directly in interpretation of soundings because data that cannot be fit with layered earth models are not interpreted quantitatively and because development of analytic solutions and computational techniques for determining the response of a layered earth have kept up with the development of suitable sounding equipment.

Early model studies were confined to measurements of the response of metal sheets placed in air at one or, at most, a few frequencies. Advances in instrumentation in the last two decades have made broadband frequency and time-domain measurements routine. The wide variety of materials, some of them relatively new products, that are now available make it possible to construct a variety of complex models.

### Theory of Electromagnetic Scale Modeling

For scale model results to represent the desired field model results it is, in general, necessary to scale the electrical properties of the model, the frequency or time range used, and

\*This paper was prepared by an agency of the U.S. Government. U.S. Geological Survey, Branch of Geophysics, Denver, CO 80225.

the intensity of the electric and magnetic fields. In practice this scaling is usually simple; in most modeling the only requirement is that the induction numbers of the field and scale model system be the same. However, if impedances or certain other quantities are measured there are further requirements. The theory to develop the scaling relationships for special cases and to indicate problems and limitations in physical scale modeling is developed in some detail in the next paragraphs.

Scale models can generally be made of any linear electromagnetic system (Sinclair, 1948). Models that contain nonlinear materials or instruments that are nonlinear must be excluded. Systems which obey Maxwell's equations can be modeled since the equations are linear. Following the classic work of Sinclair (1948) and the work of subsequent authors such as Frischknecht (1971) and Spies (1976), use the coordinates  $x, y, z$  to locate any point in the full scale or field system and the coordinates  $x', y', z'$  to locate any point in the model system. Using  $p$  for the length scale factor, the systems are related by the transformations:

$$x = px', \quad y = py', \quad z = pz'. \quad (1)$$

For isotropic media in source free regions Maxwell's curl equations are:

$$\nabla \times \mathbf{E} (x, y, z, t) = -\mu \frac{\partial \mathbf{H}}{\partial t} (x, y, z, t), \quad (2)$$

$$\nabla \times \mathbf{H} (x, y, z, t) = \sigma \mathbf{E}(x, y, z, t) + \epsilon \frac{\partial \mathbf{E}}{\partial t} (x, y, z, t), \quad (3)$$

In general, it is necessary to scale  $\mathbf{E}$ ,  $\mathbf{H}$ , and  $t$  in order that these equations remain invariant under the transformation (1). Thus,

$$\mathbf{E} (x, y, z, t) = a \mathbf{E}' (x', y', z', t'), \quad (4)$$

$$\mathbf{H} (x, y, z, t) = b \mathbf{H}' (x', y', z', t'), \quad (5)$$

$$t = ct', \quad (6)$$

where  $a$ ,  $b$ , and  $c$  are scale factors for electric field, magnetic field, and time, respectively. Equations (2) and (3) for the model system are then

$$\nabla' \times \mathbf{E}' (x', y', z', t') = -\mu' (x', y', z', t') \frac{\partial \mathbf{H}'}{\partial t'} (x', y', z', t'), \quad (7)$$

$$\nabla' \times \mathbf{H}' (x', y', z', t') = \sigma' (x', y', z', t') \mathbf{E}' (x', y', z', t') + \epsilon' (x', y', z', t') \frac{\partial \mathbf{E}'}{\partial t'} (x', y', z', t'), \quad (8)$$

where  $\nabla'$  means that derivatives are calculated using the coordinates of the model system. The properties of the media in the model system are  $\mu'$ ,  $\sigma'$  and  $\epsilon'$  and their relationships to the properties of the full scale system must be determined in terms of the scale factors  $a$ ,  $b$ ,  $c$ , and  $p$ . Equations (7) and (8) can be transformed into equations (2) and (3) using the transformations (1), (4), (5), and (6). To transform the left hand side of equations (7) and (8) note that

$$\frac{\partial E'_z}{\partial y'} = \frac{\partial E'_z}{\partial y} \frac{\partial y}{\partial y'} = \frac{p}{a} \frac{\partial E_z}{\partial y}, \quad \frac{\partial E'_y}{\partial z'} = \frac{p}{a} \frac{\partial E_y}{\partial z}$$

and similarly for other components of  $\nabla' \mathbf{x} \mathbf{E}'$  and  $\nabla' \mathbf{x} \mathbf{H}'$  so that

$$\nabla' \mathbf{x} \mathbf{E}' = \frac{p}{a} \nabla \mathbf{x} \mathbf{E}, \quad (9)$$

$$\nabla' \mathbf{x} \mathbf{H}' = \frac{p}{b} \nabla \mathbf{x} \mathbf{H}. \quad (10)$$

To transform the right hand side of equations (7) and (8), equations (4) and (6) are used to obtain

$$\frac{\partial \mathbf{E}'}{\partial t'} = \frac{\partial \mathbf{E}'}{\partial t} \frac{\partial t}{\partial t'} = \frac{c}{a} \frac{\partial \mathbf{E}}{\partial t} \quad (11)$$

and equations (5) and (6) are used to obtain

$$\frac{\partial \mathbf{H}'}{\partial t'} = \frac{c}{b} \frac{\partial \mathbf{H}}{\partial t}. \quad (12)$$

Then equations (7) and (8) may be written as:

$$\frac{p}{a} \nabla \mathbf{x} \mathbf{E} (x, y, z, t) = -\mu' (x', y', z') \frac{c}{b} \frac{\partial \mathbf{H}}{\partial t} (x, y, z, t) \quad (13)$$

$$\frac{p}{b} \nabla \mathbf{x} \mathbf{H} (x, y, z, t) = \sigma' (x', y', z', t') \frac{1}{a} \mathbf{E}(x, y, z, t) + \frac{c}{a} \epsilon' (x', y', z', t') \frac{\partial}{\partial t} \mathbf{E} (x, y, z, t). \quad (14)$$

For equations (13) and (14) to be equivalent to equations (2) and (3), the following relationships between the properties of the media in the scale model and the full scale system must hold:

$$\sigma' = \frac{pa}{b} \sigma, \quad (15)$$

$$\epsilon' = \frac{pa}{bc} \epsilon, \quad (16)$$

$$\mu' = \frac{pb}{ac} \mu. \quad (17)$$

Models in which the relationships (15), (16), and (17) are obeyed and in which  $a$  and  $b$  are established separately were called "absolute" models by Sinclair. In absolute models, power levels as well as the morphology of the fields are simulated. In principle, a model system can be constructed to represent any field system using arbitrary choices for the scale factors  $a$ ,  $b$ ,  $c$ , and  $p$  provided equations (15), (16), and (17) are satisfied. In general, model materials having suitable electrical and other properties cannot be found to satisfy any arbitrary set of scale factors. In modeling airborne, surface, and surface to borehole electromagnetic systems, the model must basically be an inhomogeneous conductive half-space with an insulating space above the surface. To allow the source and receiver to be moved about easily, the media in the nonconductive half-space must be air or possibly a liquid. If air is used and if it is assumed that the electrical properties of the air are the same as those of free space, which is a good assumption for the range of frequencies used in induction prospecting in either model or full scale systems, then the dielectric constant and magnetic permeability must be the same in both systems:

$$\epsilon' = \epsilon, \quad (18)$$

$$\mu' = \mu. \quad (19)$$

With these assumptions:

$$\frac{pa}{bc} = 1, \quad (20)$$

$$\frac{pb}{ac} = 1, \quad (21)$$

so that

$$a = b, \quad (22)$$

$$p = c, \quad (23)$$

$$\sigma' = p\sigma. \quad (24)$$

In using relationships (22), (23), and (24) we do not preclude use of model materials in the conductive half-space for which  $\epsilon \neq \epsilon_0$  and  $\mu \neq \mu_0$  but these properties must be the same in the model as in the full scale system. If a specific value is assigned to  $a$  and  $b$ , the model is still an absolute model. However, if only the ratio  $a/b = 1$  is specified, the model is a "geometric" model and power levels of the full scale system are not simulated.

The problem of finding suitable model materials is ameliorated by using equations (22), (23), and (24) rather than equations (15), (16), and (17); nevertheless, it is difficult to always find materials that satisfy equation (24) and to use frequencies or times such that equation (23) is satisfied. Fortunately, even less restrictive scaling relationships can be employed if displacement currents are not significant in the full scale system. If we ignore displacement currents by neglecting equation (18) and if we let  $\mu' = \mu$  as before, equations (17) and (15) become, respectively,

$$\frac{a}{b} = \frac{p}{c}, \quad (25)$$

$$\sigma' = \frac{p^2}{c} \sigma. \quad (26)$$

It is convenient to remember equation (26) in the form of induction numbers for frequency and time-domain modeling, respectively:

$$\sigma' f' \ell'^2 = \sigma f \ell^2, \quad (27)$$

$$\frac{\sigma' \ell'^2}{t'} = \frac{\sigma \ell^2}{t}, \quad (28)$$

where  $\ell$  is any characteristic dimension in the full scale system and  $\ell'$  is the corresponding dimension in the model system. The criteria for selection of model materials are then:

1. The magnetic permeability must be the same in the model as in the full scale system; usually  $\mu$  is made equal to  $\mu_0$ .
2. The conductivity, dimensions, and frequency or time must be scaled so that the induction

number for the model system is the same as the induction number for the full scale system.

3. Values of electric permittivity in the model are arbitrary, provided they are small enough that displacement currents in the model are negligible over the range of frequencies or times used.

Requirements (1), (2), and (3) are sufficient to completely specify models for electromagnetic methods in which the ratios of components or normalized components of the magnetic field are measured. However, if other quantities such as impedance are measured, there are further requirements for translating scale model data into full scale data. As an example, to obtain the relationship between voltages in the model and in the full scale system, consider the voltage developed at the terminals of an open circuited square model loop with side  $S$ , due to a uniform time harmonic magnetic field that intersects the loop:

$$V' = i\mu_0 \omega' S'^2 \mathbf{H}' = i\mu_0 \omega c \frac{S^2}{p^2} \frac{\mathbf{H}}{b}.$$

Similarly, for the full scale loop with side  $S$ :

$$V = i\mu_0 \omega S^2 \mathbf{H}.$$

Thus,

$$V' = \frac{c}{p^2 b} V = \frac{V}{ap}. \quad (29)$$

Similarly, we can obtain the relationship for current densities,  $\mathbf{J}$ , from Ohm's law

$$\begin{aligned} \mathbf{J}' &= \sigma' \mathbf{E} = \frac{p^2}{c} \sigma \frac{\mathbf{E}}{a} \\ \mathbf{J} &= \sigma \mathbf{E} \\ \mathbf{J}' &= \frac{p^2}{ac} \mathbf{J} = \frac{p}{b} \mathbf{J}. \end{aligned} \quad (30)$$

To find the relationship for currents, assume a region bounded by a square isotropic conductive cylinder having dimensions  $w \times w$  in which the current density is uniform along the  $x$  axis which is parallel to the axis of the cylinder; then

$$I'_x = J'_x w'^2 = \frac{p^2}{ac} \frac{J_x w^2}{p^2},$$

and

$$I_x = J_x w^2.$$

Therefore, in the general case

$$\mathbf{I}' = \frac{\mathbf{I}}{ac}. \quad (31)$$

The impedance  $V'/I'$  is important in modeling a number of systems:

$$\frac{V'}{I'} = \frac{c}{p} \frac{V}{I}. \quad (32)$$

For time domain systems,

$$\frac{V'}{I'} = \frac{t}{t'} \frac{\ell'}{\ell} \frac{V}{I} \quad (33)$$

and if the currents are the same in the model and full scale system (Spies, 1976)

$$\frac{V'}{V} = \frac{t}{t'} \frac{\ell'}{\ell}. \quad (34)$$

For magnetotelluric systems the impedance,  $Z$ , is

$$Z' = \frac{V'}{I'} = \frac{f'}{f} \frac{\ell'}{\ell} Z. \quad (35)$$

In modeling thin conductive sheets at relatively small induction numbers it is sufficient to scale only the conductance,  $S$ , of the sheet and not its thickness and conductivity separately so that equations (27) and (28) become:

$$S' f' \ell' = S f \ell. \quad (36)$$

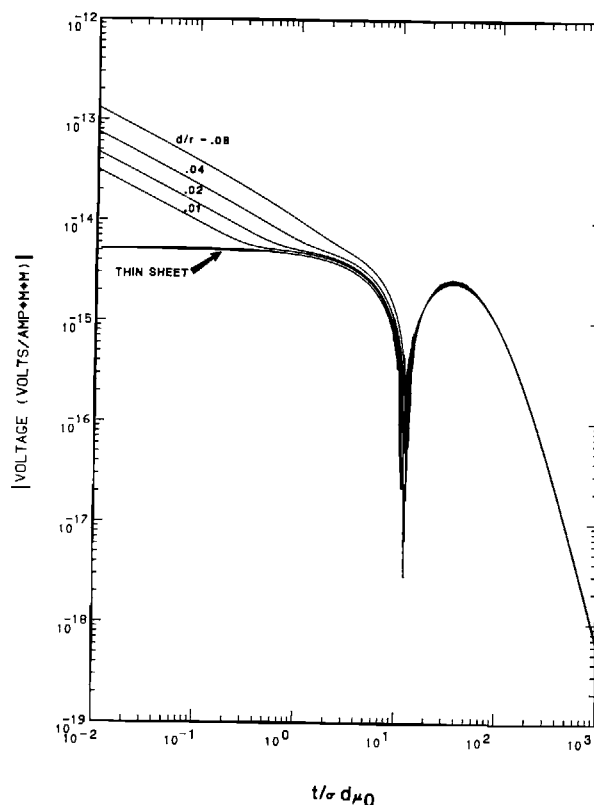


FIG. 1. Transient response for horizontal coplanar loops over infinite horizontal slabs of varying thickness and an infinitesimally thin sheet. The loop spacing is  $r$ . The depth to the center of the slab is  $r/2$  and the thickness of the slab is  $d$ .

$$\frac{S'\ell'}{t'} = \frac{S\ell}{t} \quad (37)$$

Use of equations (36) and (37) rather than equations (27) and (28) allows considerable latitude in choosing materials for modeling thin sheets. However, if measurements are made at large induction numbers such that the skin depth is on the order of the thickness of the sheet, equations (36) and (37) are not valid and the actual thickness of the sheet must be considered. In reviewing his own and earlier work on "thin" and "thick" sheets Bosschart (1964) indicated that equation (36) is applicable provided the thickness of the sheet does not exceed approximately 0.6 skin depths. When the skin depth is less than the thickness of the sheet, the "effective" resistivity of the sheet increases, a well-known phenomenon that is most familiar for its influence on the ac resistance of wires. A number of authors including Heststrom (1940), Parasnis (1962), and Bosschart (1964) give frequency domain model results showing the difference in response between thin and thick sheets. To compare the transient response of thin and thick sheets, calculations were made for infinite horizontal slabs of various thicknesses and for an infinitesimally thin sheet using expressions given in Wait (1956). Results for a specific model (Figure 1) indicate that for this case equation (37) is valid provided  $t/\sigma\mu_0 d$  is greater than approximately 10 and  $d/r < 0.08$ , where  $d$  is the thickness of the sheet and  $r$  is the loop separation.

A summary of the scaling relationships developed plus others which are useful when displacement currents can be neglected are listed in Table 1. The conductivity of the model is completely specified by the distance  $p$  and time  $c$  scale factors. In most modeling, values for  $a$  or  $b$  are not specified. If needed, an arbitrary value for either  $a$  or  $b$  may be selected and then the other parameter is fixed by equation (25), that is,  $a/b = p/c$ .

**Table 1. Scaling relationships when displacement currents are neglected and  $\mu' = \mu^*$**

Quantity	Model system	Full-scale system equivalent
Length	$\ell'$	$\ell/p$
Frequency	$f'$	$cf$
Time	$t'$	$t/c$
Electric field intensity	$\mathbf{E}'$	$\mathbf{E}/a$
Magnetic field intensity	$\mathbf{H}'$	$\mathbf{H}/b$
Electric permittivity	$\epsilon'$	arbitrary
Magnetic permeability	$\mu'$	$\mu$
Electric conductivity	$\sigma'$	$p^2\sigma/c$
Electrical resistivity	$\rho'$	$cp^2/p^2$
Voltage	$V'$	$V/ap$
Current density	$\mathbf{J}'$	$p\mathbf{J}/b$
Current	$I'$	$I/ac$
Impedance	$V'/I'$	$c/p V/I$
Wave impedance	$\mathbf{E}'/\mathbf{H}'$	$c/p \mathbf{E}/\mathbf{H}$
Resistance	$R'$	$c/p R$
Inductance	$L'$	$L/p$
Conductance	$S'$	$p/c S$
Induction number (general)	$B'^2 = \sigma' \mu' \omega' \ell'^2$	$B^2 = \sigma \mu \omega \ell^2$
Induction number (thin sheet)	$\alpha' = S' \mu' \omega' \ell'$	$\alpha = S \mu \omega \ell$
Total power	$P'$	$P/cpa^2$

\*Note that with these assumptions  $a/b = p/c$ .

Physical scale modeling is sometimes used to study problems in induced polarization (IP) and dc resistivity exploration. For resistivity modeling it is convenient to let the time factor  $c$  be unity. Table 1 can be used to design absolute resistivity models. However, in practice, resistivity is usually scaled by an arbitrary factor and the only requirement is that the resistivity contrasts in the scale model must be the same as in the full scale system. As discussed in a later section, there may be serious problems with the behavior of materials used in resistivity and IP modeling.

Rigorous scale modeling of IP response is very difficult. Discrete element models of IP phenomena include resistances and capacitances, some of which are dependent on frequency (Sumner, 1976). Sometimes there is need to allow for EM coupling in the model. Thus IP modeling generally requires the use of equations (22), (23), and (24), as does EM modeling when displacement currents are included. If the possibility of EM coupling is taken into account, it is generally necessary to use a much higher frequency in the laboratory than in the field. Suitable volume polarizable materials that have spectra similar to those of natural IP targets, when scaled by equations (22), (23), and (24), have not been developed. Strong polarization is observed at low frequencies for solid targets in an electrolyte but field IP behavior is not accurately represented by such models (Guptasarma, 1983). An approximate method of IP modeling that is useful for some purposes is to make resistivity measurements using two slightly different contrasts between the targets and surrounding electrolyte. This procedure simulates measurements over a polarizable target at two different frequencies and the results can be expressed as percent frequency effect.

Analog models that are not replicas of the full-scale situation are sometimes used in the study of geoelectric methods. Two-dimensional (2-D) resistivity problems may be modeled rigorously using point electrodes placed on a thin conductive sheet. In practice this type of model may be an adequate approximation where finite line electrodes are used (Parasnis, 1965) or for studying the shapes of anomalies over small elongated conductive structures when point current electrodes are at large distances from the region of interest so that current flow through the region is nearly 2-D. Many authors, including Raby (1966), discuss conductive sheet modeling. In the past, apparatus for conductive sheet modeling was available commercially. Other types of analog models include 2-D and 3-D networks of resistors or resistors and capacitors used to model resistivity and IP problems, respectively. Vine (1966) reviewed the use of impedance networks for solution of Laplace's, Poisson's, and Maxwell's equations.

In a series of papers, Rao and Agnihotru (1984a-f) described modeling 2-D telluric current, resistivity, and magnetic problems through use of a hydrodynamic device termed a "fluid mapper." Nonrotational flow of an incompressible fluid obeys Laplace's equation. In a fluid mapper, flow or streamlines are observed visually by injecting fine streams of dye directly into a chamber made of transparent materials through which a clear fluid is driven. In the absence of targets, the streamlines are straight and they represent flow through a uniform medium. Targets may consist of solid objects of any desired shape placed to partially or completely block part of the flow path. These obstructions represent resistive bodies, if the dye lines are considered flow lines, and they represent conductors, if the dye lines are considered equipotential lines. Alternatively, if the dye lines are considered equipotentials, enlargements in the flow channel may be used to represent insulators.

## Types of Scale Models

Like mathematical models, physical scale models are usually idealized approximations to actual earth structures. The principal elements of a typical model useful in mineral exploration consist of the mineral deposit or deposits, the host rock containing the deposits, and a layer of "overburden" at the surface which may be glacial deposits, alluvium, weathered rock, or other material usually having a lower resistivity than the host rock. The host rock may be layered but generally it is inhomogeneous in both the vertical and horizontal direction and it may contain good conductors, such as graphite bodies or shear zones, that are not of

interest. The conductivity and thickness of overburden usually varies. Topographic variations are a further complication in many field cases. The mineral deposit model is often applicable to other problems where EM methods are applied; for example, EM profiling is useful in exploration for water-filled fracture zones. In models applicable to problems other than massive sulfide exploration, conductivity contrasts are generally smaller.

Most scale models used to study mineral prospecting and similar problems fall into one of four classes representing various degrees of approximation to the field situation. In the first class (Figure 2a), all media except the mineral deposits or other targets are represented by an insulator, air. The targets are usually sheets, blocks, cylinders, or other simple forms made of metal, carbon, or graphite. In special cases, targets are fabricated to approximate the shape of actual conductive structures. Length scale factors ranging from 200 to 2 000 are commonly employed. When metal targets are used, this range of length scale factors causes the time scale factor to be approximately unity for simulation of typical massive sulfide ore bodies. As a consequence, many model studies have been carried out using field instruments modified as necessary to operate with miniature loops. This class of model accurately simulates field situations where the induction numbers for the host rock and overburden are very small. It cannot be used to model situations in which galvanic currents (current gathering) are important or methods in which electric fields are measured. Results from this class of model are most applicable to the interpretation of data taken with older single-frequency equipment operating at short source-receiver separations. As a first approximation, other problems, such as the effect of a coast line on geomagnetic induction measurements, can be studied by this kind of model. To a first order, topography can be accounted for by suitable placement of the source and receiver.

In the next class of models (Figure 2b), conductive sheets are used to represent the overburden but the host rock is represented by air. The instruments and frequencies or times used can be the same as for the first class of models. In some model studies, for example, Villegas-Garcia and West (1983), the thickness of the overburden was varied. In other studies (Olm, 1981) the conductivity of the overburden sheet was varied. This class of model accounts for the response of the overburden itself, the attenuation and phase rotation of fields diffusing through the overburden, and mutual magnetic field coupling between the target and overburden. Many such models are constructed so that the targets are not in contact with the overburden but those models do not accurately represent field cases where galvanic currents flow from the overburden through the target. Electrical contact can be made between the overburden and target to allow current flow between them but such models may not provide quantitatively accurate results due to the difficulty in knowing the degree of electric contact between geologic units, and in duplicating this contact in the model.

In the third class of models (Figure 2c), conductive or insulating targets are placed in a homogeneous medium without a layer of overburden. Most commonly, the homogeneous medium is a conductive solution such as brine; however, Spies (1979, 1980) used large blocks of type metal, in which copper targets were placed during casting; attempts have been made

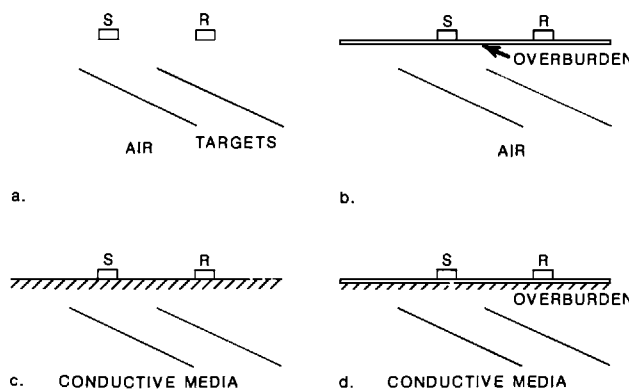


FIG. 2. Typical models indicating various degrees of completeness.

to use other media such as metal shavings. A principal advantage of using liquid over a solid material is that the targets can easily be repositioned. The principal disadvantage of using liquids is that, at best, they are not very conductive so relatively large tanks and relatively high frequencies or short times are required in order that the induction number for the medium can be made sufficiently large. The advantage of using type metal is that relatively small volumes are required and the operating frequencies need not be very high. Avoidance of high surface impedances between conductive targets and the surrounding medium due to electrochemical reactions or oxide coatings on metal surfaces is one of the significant problems in models which include host rock. If this problem is avoided, galvanic currents flowing between the host rock and targets are properly included in these models. Methods using galvanic sources, or those in which electric fields are measured, can easily be studied with such models. In modeling methods that depend on a distant source of energy (MT, AMT, VLF), use of a medium is generally mandatory for realistic modeling due to the importance of galvanic currents in these methods.

A few model studies have been made in which targets are placed in a conductive medium overlain by a more conductive overburden, although until recently it has been difficult to find suitable materials for the overburden (Figure 2d). For many purposes such models are sufficiently complete representations of field problems, particularly if the conductance of the overburden can be varied. However, in some cases, vertical or lateral changes in the conductivity of the host rock should be included. Techniques to easily simulate such variations in the host rock or topography have not been fully developed.

In nonmineral applications of EM methods there is generally more emphasis on horizontal layering than in most mineral exploration problems. For instance, the basic model needed in a magnetometer array study may consist of a number of horizontal layers, some of which are truncated, representing layers in the crust and upper mantle, and long cylindrical or dike shaped conductors representing suture zones or other causes of array anomalies. Due to the availability of rapid computer methods there is little need to study uniform horizontally layered media by scale modeling. However, model studies can be used effectively to study distortions in sounding curves caused by sharp lateral changes in layering or other 2-D or 3-D features. As discussed in the chapter on electromagnetic sounding, the loop-loop and wire-loop response of horizontally layered media depends only on the horizontal conductance and not on the vertical conductance. Therefore, some problems involving horizontally layered media, such as changes in conductance of a thin conductive layer, can be studied using a stack of sheets that are not necessarily in contact with each other. However, lateral variations in layering or the presence of a finite region of higher or lower conductivity in a section will generally cause a vertical component of current flow. Thus the usefulness of models consisting of stacks of metal sheets that are not in good electrical contact with each other is limited. Models consisting of finite sheets in a conductive host, such as a brine tank, can be used to study this class of problem, provided a uniform host is appropriate for the field problem.

Scale modeling has been extensively used in electrical engineering and physics to study problems such as scattering from radar targets and the influence of nearby structures on antenna characteristics. Sometimes modeling is used in communication engineering (King et al., 1981) to study the propagation of signals through the earth or the effects of the earth on communication antennas. Generally the structures to be modeled are variants of a layered earth, for example, the waveguide which may be formed in the lower crust between the conductive rocks of the upper crust and the mantle (Brown and Gangi, 1963) or the transition from sea to land (King and Maley, 1966). Because displacement currents must be included in propagation studies, they are not directly applicable to induction studies. However, where the models are appropriate, the results are relevant to radar, hole-to-hole tomography, and other applications of high frequency EM techniques.

## Physical Facilities

### Supporting structures

Physical facilities for model measurements range from very simple to elaborate. For measurements over targets in air, the coils may be placed on a table marked with a suitable grid pattern for convenience in manual positioning of the coils. The targets should be supported beneath the table in such a way that they can be readily raised, lowered, or reoriented (Woods and Crone, 1980). Profile measurements can be expedited by mounting the moving coils on a carriage which is drawn along a track such as that shown in Figure 3. In some scale model facilities, means are provided also for remotely controlling the lateral position of the carriage and the vertical position of the coil assembly on the carriage. In modeling moving source methods with targets placed in air, the coils can be fixed and the target may be placed on a moving carriage which moves by the coils. This is a particularly good arrangement for modeling airborne systems where great sensitivity is required and where motion of the coils may introduce noise. The carriage can move on rollers or slides. Generally it is drawn by a cord or belt from stationary draw works. In some systems the draw works are powered by stepping motors controlled by a computer (Bays and Duckworth, 1983, Villegas-Garcia and West, 1983). In other systems, the carriage is moved by a variable speed motor and the position is determined by means of high resolution multiturn potentiometers or angle encoders connected to the drive mechanism or by photoelectric sensors.

The "working region" of a model facility is defined as the region within which the source and receiver may be moved plus the region within which models may be placed. To avoid extraneous EM responses, large metallic parts or other conductive materials should not be used in construction of the mechanical parts of the system that are within or near the working region. It is good practice to construct carriages, tracks, and other structures mostly of wood, plastic, concrete, and other insulating materials. The use of small metallic fasteners and some larger metallic parts, if they are not near the coil assembly and if they do not form large closed paths for eddy currents is generally acceptable. In particular, care should be taken in construction of the coil assembly and carriage. Measuring instruments should be placed far enough from the track that their metal cases and chassis do not produce a response. Extraneous responses from elements other than the coil assembly and carriage can generally be detected by moving the coil assembly about over the working region with all models removed. It may be possible to identify responses from the coil assembly itself, or from the

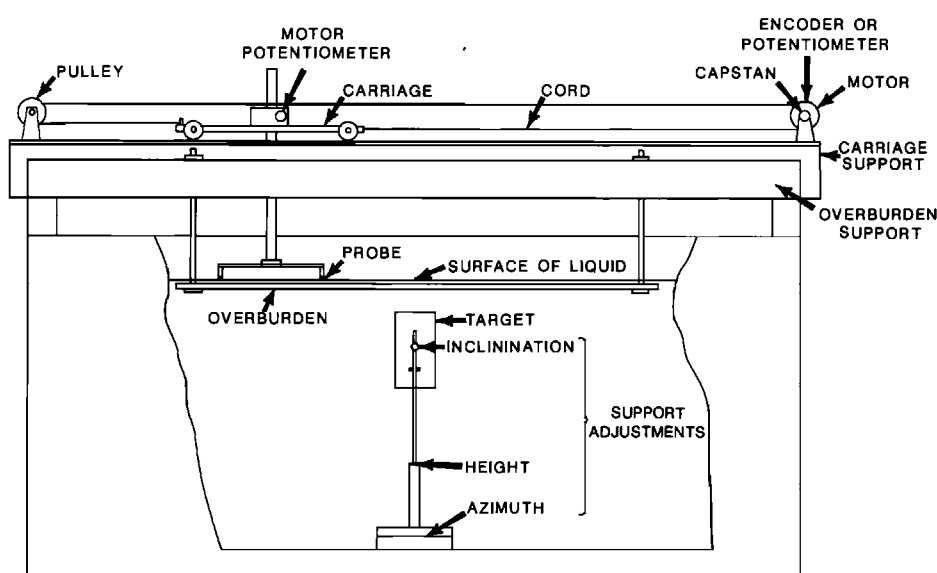


FIG. 3. Sketch of tank, carriage, and model supports.

carriage, by changing the orientation of the coils.

Depending on the configurations and techniques to be used, it may be necessary to design the coil holders so that the orientation and spacings of the coils can be easily changed. Alternatively, the carriage may be designed so that coil assemblies for different configurations are readily mounted or dismounted. To directly model methods in which the direction of the field is measured, the receiving coil may be mounted so that it can be rotated about the proper axis. A clinometer must be attached so that the angle can be read once the system is nulled. Operation of such a system is slow and it is difficult to make the coil assembly and clinometer as small as desirable. As an alternative, the components of the field can be measured using fixed vertical and horizontal coils and the angles can be computed. When an electrolyte is used in modeling surface EM methods, it is generally desirable to seal the coils and their mounts so that they can be half submerged to more accurately simulate loops on the surface of the ground.

### Design of tanks

Tanks for brine or other conductive liquids are commonly used when a conductive half-space is to be included in the model. Generally the tank should be constructed of wood, plastic, concrete, or similar material rather than of metal; the effect of the walls and bottom will generally be less if they are insulating rather than conductive. The size and shape of the tank needed depends on the methods to be modeled, the sensitivity of the system, the specific models to be placed in the tank, the required working region, and the mechanical and time scale factors. The simplest and least stringent criterion by which to determine the necessary dimensions of the tank is that its response should be approximately that of a half-space when it does not contain models or other structures. Consider the design of tanks for modeling frequency-domain electromagnetic (FEM) methods using dipole sources. In modeling airborne systems or other highly sensitive systems operating at low induction numbers, the effect of the bottom and sides of the tank depends on the ratios,  $r_i/\ell$ , where  $r_i$  is the distance from the  $i$ th boundary to the center of the configuration and  $\ell$  is the loop separation. In modeling FEM systems operating only at large induction numbers, the effect of the boundaries depends primarily on the induction number  $r_i/\delta$ , where  $\delta$  is the skin depth in the medium. At intermediate induction numbers, both the geometric ratio and the induction number must be considered.

The effect of an insulating bottom of a tank on a sensitive system operating at low induction numbers can be calculated readily from expressions given in McNeil (1980). For the horizontal coplanar (HCP) configuration,

$$\frac{H_s}{H_{SH}} = 1 - \left[ 4 \left( \frac{d}{\ell} \right)^2 + 1 \right]^{-1/2}, \quad (38)$$

where  $H_s$  is the secondary field of the tank,  $H_{SH}$  is the secondary field of the corresponding half-space,  $d$  is the depth of the fluid in the tank, and  $\ell$  is the loop spacing. The induction number for loop-loop configurations on a half-space is  $B = (\sigma\mu_0\omega/2)^{1/2}r$ , where  $r$  is the loop spacing; to be in the low induction number range  $B$  should be less than about 0.02.

As an example, if  $d/\ell = 10$ , the error due to the bottom of the tank is 4.99 percent. For the vertical coplanar (VCP) configuration the error is the same when  $d/\ell = 5.0$ . A simple expression for the error caused by the sides of the tank at very low induction numbers is not available but model studies indicate that the distance from the configuration to the sides must be several times the loop spacing to keep the error under 5 percent. Fortunately, source-receiver separations can be small in modeling in the very low induction number range so tanks do not necessarily have to be extremely large. A practical loop spacing is 5 to 10 cm; to keep the error due to the effect of the bottom under 5 percent, the tank need be only 0.5 to 1 m deep.

Modeling FEM systems having ordinary sensitivities is less demanding than modeling high-sensitivity systems. To illustrate this point, the difference in amplitude and phase between the response of a conductive slab and a homogeneous earth, for the induction number at

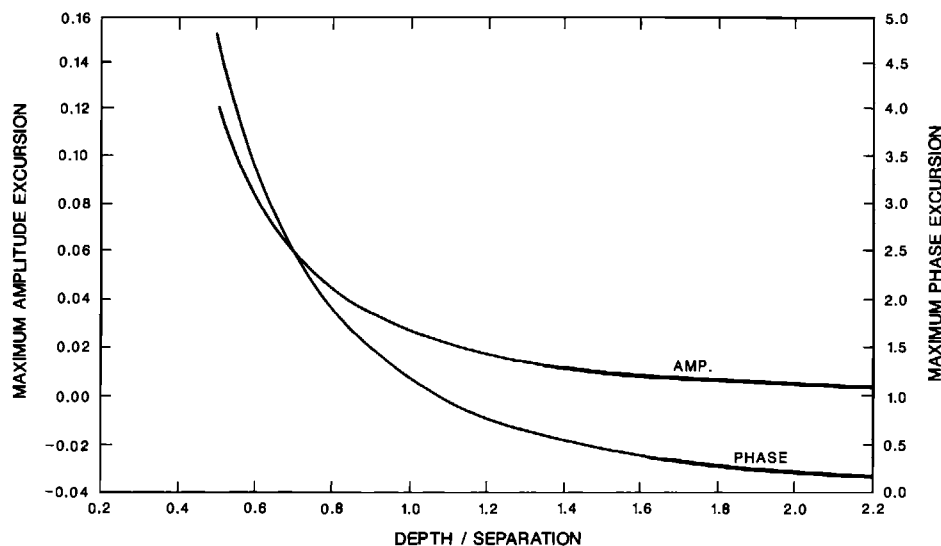


FIG. 4. Maximum difference between response of a conductive slab and a homogeneous Earth as a function of the ratio of depth to separation for a FEM horizontal coplanar loop configuration.

which these differences are largest, is plotted in Figure 4 for a HCP loop-loop configuration. Suppose the objective is to keep the absolute error in the amplitude of the secondary field under 1 percent when modeling this system. For  $d/\ell = 1.5$ , the maximum error in amplitude is only about 0.7 percent, which occurs at a value of  $B$  of about 0.48, and the maximum error in the phase is only about 0.3 degrees, at a somewhat larger value of  $B$ . Precise information is not available but from existing model studies it appears that to keep the error under 1 percent the center of the configuration, when aligned normally to the side of a tank, should be no closer than about  $1.5 \ell$ . As the side of the tank is approached the error would be a little larger than that estimated due to the cumulative affect of the side and the bottom. To compensate for this error the vertical or horizontal dimensions should be made a little larger than those indicated. The actual horizontal dimensions of the tank must, of course, be equal to the dimensions of the working area over which the array is moved plus the necessary distances from the working area to the sides of the tank. The same procedure can be followed to determine the size of tank required for use with other configurations.

If modeling is to be done only at large induction numbers, the dimensions of the tank can be smaller than for either case just described. Suppose that in modeling a HCP loop-loop system, induction numbers smaller than 1 will not be used. Then for  $d/\ell = 1.0$  the maximum error in the amplitude due to the bottom of the tank is only 1 percent; whereas, it is as large as 2.3 percent for smaller induction numbers. At large induction numbers the response of the sides also will be correspondingly less than at intermediate induction numbers.

Similar considerations apply to modeling FEM systems using large loop or grounded wire sources; although, somewhat larger tanks may be required than in modeling dipole source systems because the source occupies a larger area and because the fields fall off more slowly with distance. On the other hand, the desired accuracy in measurement may be less.

In modeling magnetotelluric or other methods that require a uniform field or plane wave source the design of the tank is not easily considered separately from the design of the source. However, regardless of the type of source used, complete and accurate modeling of these methods requires that the dimensions of the tank be equal to more than a skin depth in the medium at the lowest frequency to be employed. It is very easy to determine the working depth of the tank required to meet any required criterion. The maximum difference in surface apparent resistivity between an infinite conductive slab on an insulating or a conductive half-space and a homogeneous earth is plotted in Figure 5. The results show that for the effect

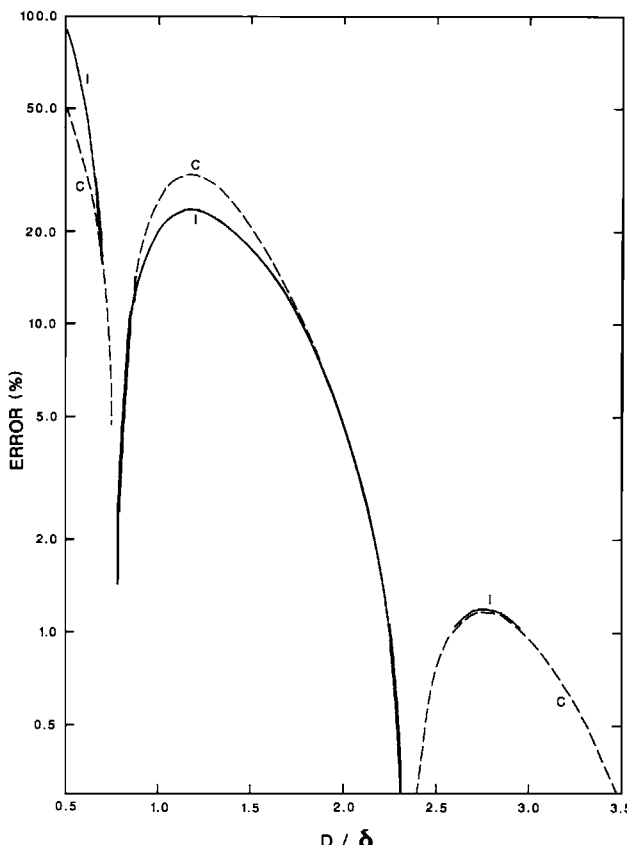


FIG. 5. Normalized error in apparent resistivity at the surface of a tank due to a conductive bottom (solid curve) or insulating bottom (dashed curve).

of the bottom of the slab to be 2 percent or less, the depth must be  $2.16 \delta$  ( $\delta$  = skin depth) or greater and that for the effect to be less than 1 percent, the depth must be  $2.97 \delta$  or greater. In the range of interest there is little difference between the effect of a conducting and an insulating bottom. The required distance between the working area and the sides of the tank, if vertical, can be estimated from calculations for a single vertical contact (d'Erceville and Kunetz, 1962). To keep the error in apparent resistivity at less than 2 percent for the TM mode, the required distance is about  $1.4 \delta$  and to keep the error in phase at less than 5 degrees the distance is about  $1.56 \delta$ .

Modeling transient electromagnetic (TEM) methods is perhaps even more difficult than modeling high sensitivity FEM methods. Not only must small secondary fields be measured accurately, but most TEM systems are broadband whereas existing high sensitivity FEM methods use a limited range of frequencies. In TEM modeling the necessary dimensions of the tank depend on the scale factor for time and the range of times over which measurements must be made. If measurements are made at sufficiently late times the boundaries will always have a substantial effect on the measurements. To accurately include the effect of a half-space in TEM modeling, measurements must be made at times before the disturbances from the boundaries are sensed at the receiver. It is convenient to use the smoke ring concept suggested in Nabighian (1979). According to Lewis and Lee (1978), Nabighian (1979), and Hoversten and Morrison (1982) the position of the maximum electric field moves off from a loop source at an angle of about 30 degrees from the surface. However, the position of the fictitious current filament that would produce the observed magnetic field moves at an angle of 47 degrees (Nabighian, 1979). Nabighian gave approximate formulas for the downward velocity and radius of this fictitious current filament; its depth  $D$  and radius  $R$  and the corresponding times  $t_D$  and  $t_R$  are

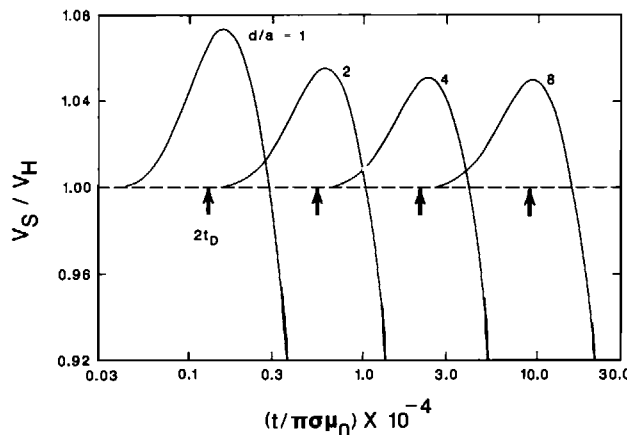


FIG. 6. Ratio of voltage over a conductive slab to that over a homogeneous Earth for a central loop TEM configuration as a function of time and slab thickness.

$$D \simeq 4 \left( \frac{t}{\pi \sigma \mu_0} \right)^{1/2}, \quad t_D \simeq \frac{\pi \sigma \mu_0 D^2}{16}, \quad (39)$$

$$R \simeq 2.09 \left( \frac{t}{\sigma \mu_0} \right)^{1/2}, \quad t_R \simeq 0.229 \sigma \mu_0 R^2. \quad (40)$$

Calculations for a homogeneous earth indicate that these formulas are accurate over a large range of times, provided time is measured from an appropriate point on the advancing diffuse wavefront. To illustrate, the ratio  $V_S/V_H$ , where  $V_S$  is the voltage observed with a central loop configuration at the surface of an infinite conductive slab and  $V_H$  is the corresponding voltage observed on a half-space, is plotted as a function of time for five different ratios of slab thickness  $d$ , to loop radius  $a$  (Figure 6). Except for  $d/a = 1.0$ , all of these curves are nearly the same in shape and magnitude; the deviation of the results for  $d/a = 1.0$  can be attributed to the use of a finite source loop rather than a dipole. For the central loop configuration it is reasonable to assume that the time required for the effect of the bottom of the slab to be observed at the surface is  $2t_D$ . This quantity, as calculated from equations (39), is indicated by an arrow for each value of  $d/a$ . The calculated times fall at almost identical points on each curve demonstrating that equations (39), if properly interpreted, are very accurate. If these equations are used without modification to determine the latest time at which measurements can be made, the maximum error is about 5 percent. From Figure 6, it is apparent that if errors of about 5 percent over a rather large range of times are acceptable, measurements can be made as late as  $4t_D$ .

Forward calculations for a dipole source on a homogeneous earth show that the radius at which the vertical component of  $dB/dt$  at the surface goes through zero is dependent on the square root of time. However, to obtain the actual distance at which  $dB/dt$  goes through zero from measured values of time,  $R$ , as calculated by equation (40), should be increased by the factor 1.2:

$$R_e = 1.2 R. \quad (41)$$

A vertical conductivity boundary would, of course, begin to disturb the advancing field at a somewhat earlier time than that given by equation (41). The time required for the effect to reach the receiver depends on its position. For a central loop configuration, the time would be roughly twice that given by equation (41), less some allowance for the distribution of current ahead of the imaginary filamentary current.

Spies (1979) studied the response of a central loop system over a number of metal blocks and cylinders and from the results developed guidelines for the required thicknesses of slabs to represent a homogeneous earth. Spies' numbers are somewhat more restrictive than those just given, probably because the sides of the blocks had a significant effect.

Not only do the sides and bottom have an influence on the response of the tank but the response of targets may be affected significantly by the tank boundaries. The criteria discussed in the last few paragraphs provide an adequate size tank only if the targets are near the surface and if they do not extend beyond the working area for the source and receiver. If a target is too near a side or the bottom of the tank, the fields exciting the target will be substantially incorrect. To illustrate this point, Figures 7a and 7b show the magnetic and

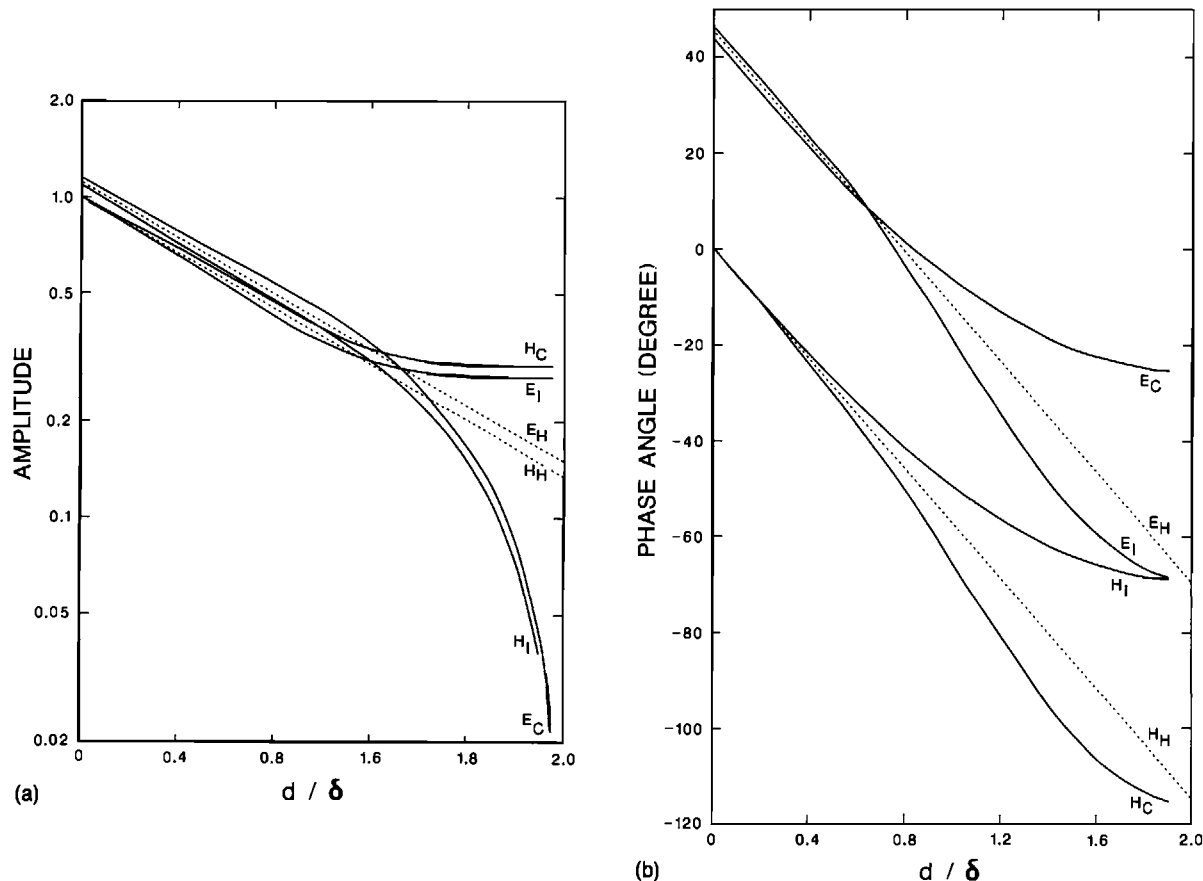


FIG. 7. Variation of electric  $E$  and magnetic fields  $H$  in a slab two skin depths thick (solid curves) placed on a perfectly insulating  $I$  or conductive  $C$  region and a half space (dotted curves); (a) is amplitude and (b) is phase.

electric fields as a function of depth for a plane wave incident on a slab two skin depths thick. Results for an insulating bottom and a nearly perfectly conducting bottom are compared with those for a half-space. For  $d/\delta < 1.2$ , the maximum error in the amplitude for any case is about 8 percent. The error in all of the fields becomes larger as the bottom of the slab is approached. Amplitude errors are largest in the electric field for a conductive bottom and in the magnetic field for an insulating bottom. The maximum error in the phase angle is about 12 degrees for  $d/\delta < 1.2$  but the maximum phase error near the bottom of the tank is about 45 degrees. In plane wave methods, the electric field will generally be more important than the magnetic field in exciting currents in an inhomogeneity; that is, galvanic currents are generally more important than vortex currents when a uniform primary field is employed. Thus, to minimize the error in both amplitude and phase of the electric field in the media, it is preferable to use a tank with an insulating bottom.

If a target is placed too close to a boundary, the errors in the fields in the media, as calculated previously, are not the only source of error. The boundary also modifies the secondary field of the target, just as it modifies the field of the primary source. Estimation of the influence of the tank boundaries is difficult because generally we do not know the secondary field from the target, even in a homogeneous half-space. In rigorous modeling of plane wave methods, or in modeling other methods at high frequencies or short times, it is generally adequate to keep the target 1.5–2 skin depths from the boundary of the tank. Assuming that the exciting fields are correct, the effect of the tank boundaries on the secondary field of a target is small for measurements made in the vicinity of the target and larger for measurements made at a long distance from the target. Let  $r_{tb}$  be the distance between a small target and the nearest boundary and  $r_{tr}$  be the distance between the target and receiver. Then, to be conservative the ratio  $r_{tb}/r_{tr}$  should be nearly as large as the corresponding ratio  $r_t/\ell$ , as determined for the tank without targets. In magnetotelluric modeling of "static effects," where the dimensions of inhomogeneities are much less than a skin depth, the effect of the bottom on the secondary fields of the inhomogeneities is the only important criterion in determining the necessary depth of the tank.

In particular circumstances, errors due to tank boundaries can be reduced by placing conductive structures on the walls and bottom. Goudswaard (1957) experimented with the use of brass plates and grids of brass wire on the walls of a tank used for resistivity modeling. He concluded that use of the wire grid increased the usable surface area of the tank. Some of his results may be inconclusive due to the surface impedance between the brass plates and wires and the NaCl solution used. In studies of the geomagnetic method by Ramaswamy et al. (1975) and in subsequent studies at the University of Victoria, the ends of the tank normal to the direction of the primary electric fields were lined with stainless steel sheets. The two sheets were connected by a heavy copper wire to permit current flow between the ends. This measure, in effect, increased the length of the tank.

In tank modeling, consideration must be given to the structures which support the targets or other model materials. First, the supports should be designed so the depth and other parameters of targets such as dip and strike can be changed while the tank is filled with electrolyte. Second, the effect of the supports on the measurements should be negligible. Ideally, the conductivity of the supports should be the same as that of the liquid in the tank; in practice this is not feasible and insulating materials are used in preference to metals. In designing the supports, they can be thought of as insulating targets. To make their effect negligible, they should be skeletal structures that cause minimal obstruction of currents flowing in the tank and they should not be placed near the working positions of either the source or receiver. The direct response of the supports can readily be determined by making measurements over the working area with all targets removed from the tank. A possibly serious effect of the supports, which is not as easily identified as the direct effect of the supports, is blockage or distortion of current flow between conductive targets and the electrolyte. Model supports should be designed so that they do not cover appreciable areas of the surface of the targets. This is particularly important for regions such as the ends and the upper edge of tabular inhomogeneities. Targets can often be attached to their supports by using small pins or screws placed in holes in the target rather than by clamping. The supports may be anchored to the bottom or sides of the tank, or to a structure above the tank. A system in which targets are

supported from the bottom of the tank and overburden sheets are supported from above is illustrated in Figure 3. If possible, provisions should be made for remote positioning of the target, particularly when an overburden is used.

### Shielding against noise

Model studies are generally carried out in urban environments where electromagnetic noise levels from power systems, radio transmitters, and other devices are high. Model facilities are sometimes shielded to reduce the influence of external noise. Shields can be made of high conductivity metal, such as copper or aluminum, or high permeability metal such as mumetal, or a combination of both. Generally, when an electromagnetic wave impinges on a shield some of the energy is reflected (reflection loss) and some is dissipated in ohmic losses (absorption loss) in diffusing through the shield. A second reflection occurs at the inside surface of the shield. Regardless of its conductivity, a high permeability shield shunts magnetic fields around the shielded region.

The effectiveness of a shield depends on the ratio of the electric to the magnetic field (wave impedance) and the direction of the fields. Except for the effects of local scatterers, radio frequency (RF) fields from broadcast and other transmitters can be regarded as plane waves with a wave impedance close to that of free space, which is 377 ohms. Fields from nearby sources such as fluorescent lights will have a higher wave impedance and will be nonuniform. Fields from nearby electric machinery such as motors and transformers will have a lower wave impedance and will also be nonuniform.

Absorption loss is proportional to the thickness of the shield, inversely proportional to the skin depth, and is somewhat dependent on the geometry of the field. It should be remembered that skin depth,  $\delta = (2/\sigma\mu\omega)^{1/2}$ , depends on magnetic permeability; therefore, the absorption loss for steel can be much greater than for copper. Reflection loss depends on the wave impedance of the source and on the characteristic impedances,  $(\mu\omega/\sigma)^{1/2}$ , of the medium on either side of the reflecting boundary. A high impedance wave has a greater reflection loss.

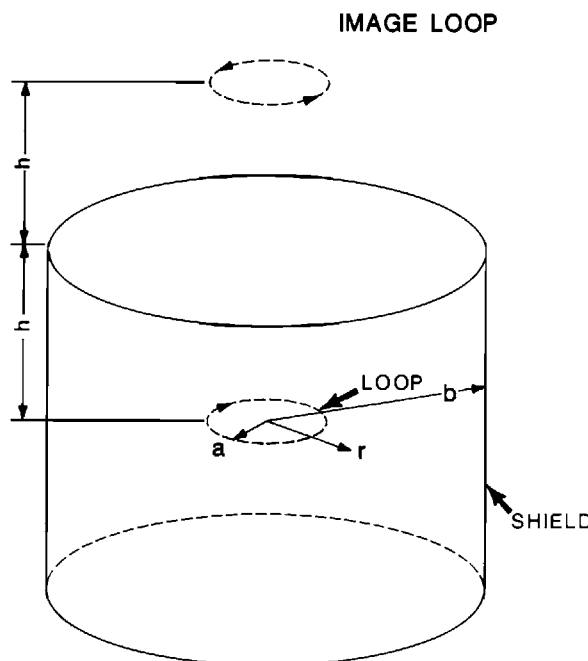


FIG. 8. Large horizontal loop source of radius  $a$  surrounded by shield of radius  $b$  and height  $2h$ .

than a plane wave and a low impedance wave has a lower loss than a plane wave. Reflection losses are highest for low permeability, high conductivity materials. Very thin shields provide a high reflection loss for electric fields but not for magnetic fields, due to the reflection from the inside surface of the shield.

Substantial shielding of the magnetic field at power frequencies depends on use of very thick conductive or high permeability shields that are expensive and heavy. Generally, shielding is not the most practical means of dealing with low-frequency magnetic fields. However, a thin conductive shield, which is effective in reducing electric fields at low frequencies and both electric and magnetic fields at radio frequencies, may be worthwhile. At radio frequencies, the effectiveness of a shield can be seriously reduced if attention is not paid to the size and placement of holes in the shield and to the bonding between various sections of the shield and to the door. A complete discussion of shielding theory and practices is given in a number of sources such as Ott (1976).

In designing a shield for a scale-model facility the effect of the shield on the measurements must be considered. Rigorous treatment of this problem depends on knowing all of the details of the specific shield as well as all of the parameters of the model system. However, guidelines for the effect of shields on model measurements can be developed from some simple approximations. Consider the shield to be a round pillbox and the source to be a coaxial loop at the center of the pillbox (Figure 8), with dimensions as shown. Neglect mutual coupling between the top and bottom and the sides of the pillbox. The top and bottom should be considered as finite conducting disks but they will be approximated here as infinite thin sheets. If the frequency and the conductivity of the sheet are sufficiently high, the effect of the top or bottom can be represented by an image loop a distance  $h$  above or below the sheet. At distances small compared with a wavelength, the near fields of a circular loop are (Smythe, 1968)

$$H_r = \frac{I}{2\pi r[(a+r)^2+z^2]^{1/2}} \left[ -K(k^2) + \frac{a^2+r^2+z^2}{(a-r)^2+z^2} E(k^2) \right], \quad (42)$$

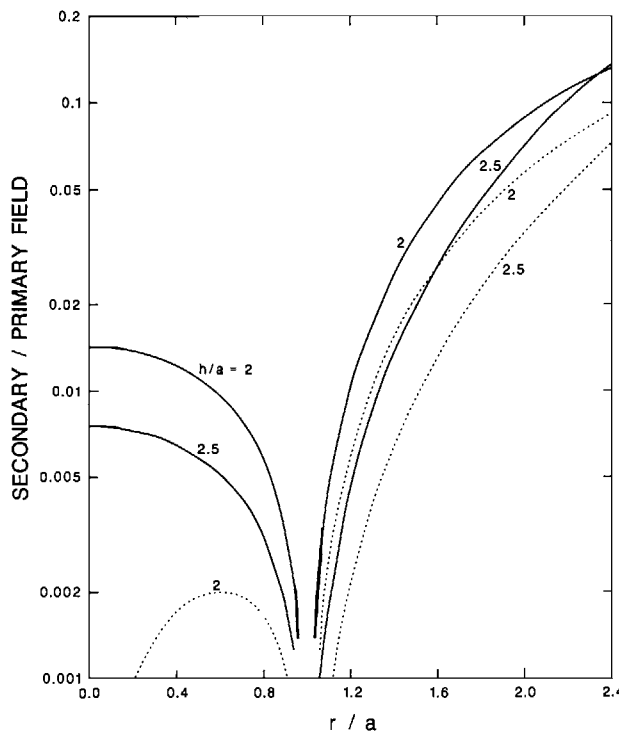


FIG. 9. Ratio of vertical (solid curve) and horizontal (dashed) secondary field of top or bottom of shield to primary field of loop as a function of  $r/a$  and  $h/a$ .

$$H_z = \frac{I}{2\pi} \frac{1}{[(a+r)^2 + z^2]^{1/2}} \left[ K(k^2) + \frac{a^2 - r^2 - z^2}{(a-r)^2 + z^2} E(k^2) \right],$$

$$k^2 = \frac{4ar}{(a+r)^2 + z^2}, \quad (43)$$

where  $K(m)$  and  $E(m)$  are the complete elliptic integrals of the first and second kinds. The primary field in the plane of the loop is calculated by setting  $z = 0$  in equations (42) and (43) and the secondary field due to the image loop in a sheet is obtained by letting  $z = 2h$  and changing the sign of the current. The ratios  $|H_r/H_z^P|$  and  $|H_z/H_z^P|$  are plotted as a function of  $r/a$  in Figure 9. Inside the loop the maximum value of  $|H_z/H_z^P|$  is about 1.5 percent and the maximum value of  $|H_r/H_z^P|$  is about 0.2 percent when  $h/a = 2.0$ . Outside the loop both quantities increase rapidly as  $r/a$  is increased. Large values of  $|H_r/H_z^P|$  are particularly serious because they change the direction of the field exciting the targets. Neglecting mutual coupling between the top and bottom sheets, the effect of the second sheet is to double the vertical component of the secondary field, which opposes the primary field inside the source loop and aids it on the outside. However, the horizontal fields from the top and bottom sheets are in opposite directions so that the horizontal field in the plane of the source loop is zero. Thus, it is desirable, although awkward, to design a large facility so that the source loop is midway between a shielded floor and shielded ceiling, to take advantage of cancellation of horizontal fields.

The effect of the sides of the shield can be viewed as that of a shorted turn coupled to the source loop. From circuit theory, the ratio of the current,  $I_2$ , in the shield to the current in the source loop,  $I_1$ , is

$$\frac{I_2}{I_1} = \frac{M}{R_s + L_s} \quad (44)$$

where  $M$  is the mutual inductance between loops, and  $R_s$  and  $L_s$  are the resistance and inductance of the shield viewed as a shorted turn. The mutual inductance between the source and the shield is approximated by the mutual inductance between two concentric filamentary loops, which is given in Johnk (1975) as,

$$M = \mu_o \sqrt{ab} \left[ \left( \frac{2}{k} - k \right) K(k^2) - \frac{2}{k} E(k^2) \right]$$

$$k^2 = \frac{4ab}{(a+b)^2}, \quad (45)$$

where  $a$  is the radius of the source loop and  $b$  is the radius of the shield.

At low frequencies the external self-inductance of a circular metal ribbon is given in Grover (1946) as:

$$L_s = \mu_o a \left[ \ln \frac{8b}{2h} - \frac{1}{2} \right] \quad (46)$$

where  $2h$  is the width of the ribbon. The resistance  $R_s$  will be neglected. Then equation (44) can be evaluated using equations (45) and (46). From equations (43) and (44) the ratio  $|H_z/H_z^P|$ , where  $H_z$  is the secondary field due to the shield and  $H_z^P$  is the primary field due to the source, was calculated for two different values of  $b/a$  (Figure 10). The effect of the shield is quite large at distances on the order of  $2a$ ; the field from the source loop falls off rapidly with distance outside the loop whereas the field of the shield is rather uniform in its central region.

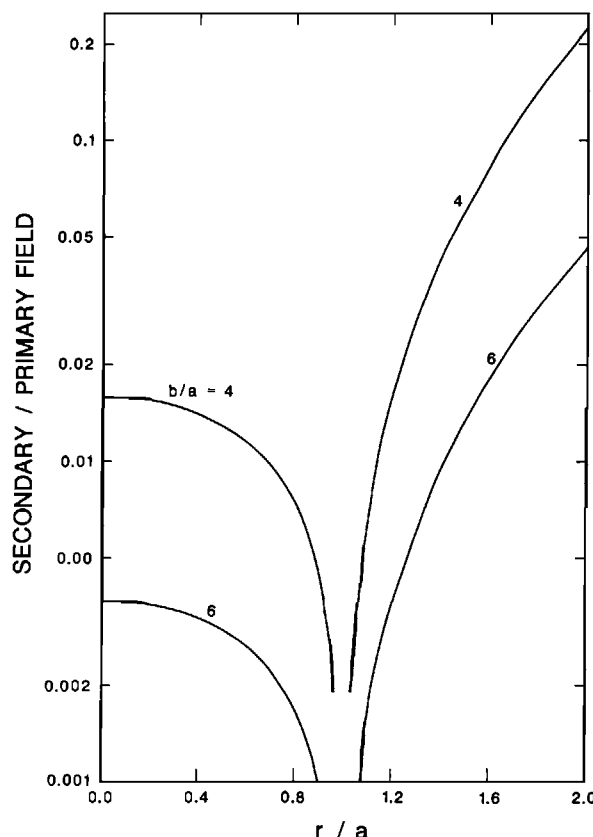


FIG. 10. Ratio of secondary field of side of shield to primary field of loop as a function of  $r/a$  and  $b/a$ .

These results are only rough approximations due to the simplified models used. For instance, at high frequencies the current distribution in the ribbon representing the sides of the shield will be nonuniform with more current flowing near either edge of the ribbon. Although equations (45) and (46) are only rough approximations of the actual model, more rigorous calculation of the effects of a shield would be justified only if parameters such as shape, bonding between sections, material, frequency, and source loop were known. The approximate results given indicate that the response of a shield placed too close to the source and working area of a model can be a problem. The most serious effect is the change in direction of the fields intersecting the models. Thus, the shield and the layout of the source and working area should be designed to minimize changes in direction of the total field. If the secondary field due to the shield is in the same direction as the primary field, model results will be almost correct provided the measurements are normalized by the sum of the primary field and the secondary fields of the shield at the model. Generally, there will be a frequency dependent phase shift between the secondary field of the shield and the primary field. In principle, the undesired secondary field of the shield can be canceled by use of a system of compensating loops driven by properly phase shifted current from the transmitter.

In indoor studies of propagation problems, waves are reflected from the walls and ceiling of the room regardless of whether they are conductive or insulating. A solution to this problem is to line the room with material that has the same surface impedance as that of free space (377 ohms) and that is thick enough to absorb the RF energy before it reaches the structural walls. Such materials are readily available commercially. Of course, the absorbtant material also serves as a shield against external waves. The bottom and sides of an electrolytic tank present a similar problem if the tank is not large enough (Annan et. al., 1975). King et. al. (1981) discuss various absorbtent materials that can be used to prevent reflections from boundaries of tanks.

## Sources

### Finite sources

The design of antennas and transmitters for modeling most controlled source EM systems is generally straightforward. The design of sources for uniform source or far-field measurements introduces special problems and will be considered separately. Some of the important factors to be considered in design of sources for near-field measurements are:

- Dimensions of antennas;
- Source moment over frequency range of interest;
- Power dissipation and thermal characteristics;
- Stability of characteristics; and
- Freedom from extraneous fields.

Most of the following criteria that are used to determine the size of transmitting antennas apply equally well to receiving antennas. This follows from the principle of reciprocity since the response is the same if the functions of the source and the receiving antenna are interchanged. For field systems in which large loops or long grounded wires are used, the model antennas must be scaled by the length scale factor  $p$  which generally presents no serious problem. However, scaling antennas used in dipole-dipole systems by  $p$  is generally not feasible; for example, if  $p$  were 1 000, a 1 mm diameter model loop would be required to simulate a 1 m diameter field loop. Such a small model loop would be difficult to fabricate and its moment would probably be inadequate. Fortunately, it is generally possible to relax the requirements for scaling antennas for dipole-dipole systems. In EM sounding (see Spies and Frischknecht, 1988), it is usually assumed that loops are an adequate approximation to dipoles if their radius is no more than one-tenth of the loop separation. This criterion is more than adequate for modeling airborne systems but may be adequate for modeling surface EM systems in which one or both of the loops are placed very near an inhomogeneity. The worst case is when a conductive target that behaves as a dipole or multipole scatterer is very near a loop. Fortunately, such targets are usually not of great interest; more typical targets are elongated sheets and prisms. The secondary field near the upper edge of a thin sheet is roughly the same as would be caused by a current filament and the secondary field near the upper surface of a thick dike is roughly the same as would be caused by a pair of filaments in which the directions of current flow are opposite. The latter source may be termed a "dipole line."

Let  $x$  be the distance between the center of an infinitesimally thick circular loop of radius  $a$ , and (1) a coplanar line source, (2) a pair of line sources separated an infinitesimal distance (dipole line), or (3) a dipolar loop source. By integration of the flux density through the loop for the first two sources and the use of equation (43) for a dipole, the ratio of the voltage  $V_f$  induced in a finite circular loop to the voltage  $V_i$  induced in an infinitesimal loop having the same turns-area product and located at the center of the finite loop can be calculated:

$$\frac{V_f}{V_i} = \frac{2x[x - (x^2 - a^2)^{1/2}]}{a^2}, \quad \text{line source}; \quad (47)$$

$$\frac{V_f}{V_i} = \frac{2x^2}{a^2} \left[ \frac{x}{(x^2 - a^2)^{1/2}} - 1 \right], \quad \text{dipole line}; \quad (48)$$

$$\frac{V_f}{V_i} = \frac{2x^3}{\pi a^2 (x + a)} \left[ K(k^2) + \frac{a^2 - x^2}{(a - x)^2} E(k^2) \right], \quad \text{dipole}; \quad (49)$$

$$k^2 = \frac{4ax}{(a + x)^2}.$$

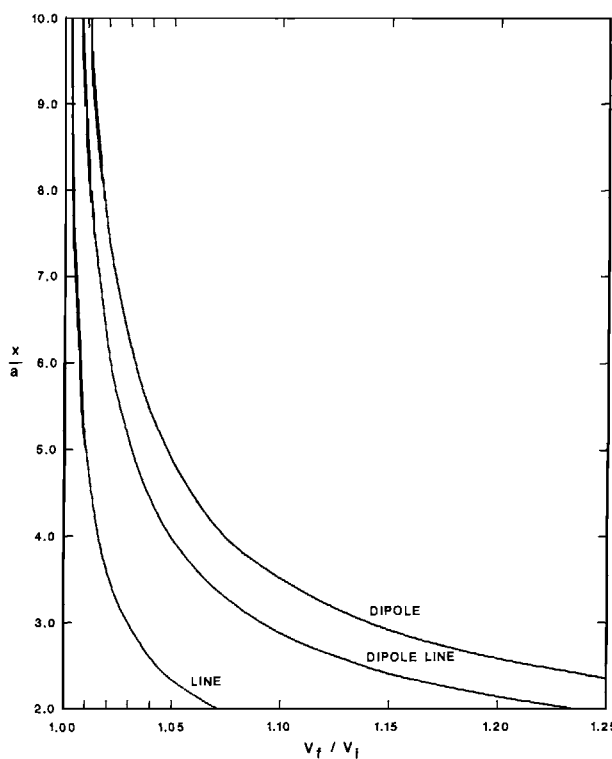


FIG. 11. Ratio of voltage  $V_f$ , induced in a finite loop of radius  $a$ , to voltage  $V_i$ , induced in an infinitesimal loop for coplanar line, dipole line, and dipole sources as a function of  $x/a$  where  $x$  is the separation between source and loop.

In Figure 11 the ratio,  $V_f/V_i$  is plotted as a function of  $x/a$  for each of the three sources. The error for a dipole is about 50 percent greater than for a dipole line source and several times as great as for a line source. Even for  $x/a = 10$ , the error for a dipole source is greater than 1 percent. Use of a finite square loop with these sources would lead to significantly greater error than use of a circular loop. However, a rectangular loop with its short dimension parallel to the gradient can be used to reduce the error when the field distribution is approximately 2-D. It should be noted that, generally, the use of finite loops introduces errors in both phase and amplitude that depend on the orientation and position of the loop with respect to the sources. Thus, the calculations given provide only guidelines for the general case. Also, it should be noted that approximate corrections for a finite loop can be made if the approximate gradient of the field is known. Tesche (1951) developed correction factors for finite receiving loops at an arbitrary position with respect to a dipolar source.

A primary concern in the design of sources is providing enough signal to overcome noise. Possible sources of noise in scale model measurements include internal noise generated in the receiving antenna, preamplifier, and other parts of the system; external noise fields sensed by the antenna; and external noise that may be introduced into the system other than through the receiving antenna. In scale modeling, thermal and semiconductor noise in the antenna and preamplifier typically are small compared with external noise. Excluding the antenna, external noise induced in the system can generally be eliminated through proper layout, shielding, and grounding. Unless the working area of the model is shielded, with the attendant problems described in a previous section, the experimenter generally has little control over most external electromagnetic noise fields. Thus the noise at the output of the system is generally dependent on the source strength and the signal processing capabilities of the receiver as well as the intensity of the noise fields. In principle, very narrow bandwidths or long stacking or averaging times can improve the signal-to-noise (S/N) ratio at the output to any desired degree. In practice the time required to make measurements is an important consideration in model studies so that it is generally desirable to strive for high source strengths.

To provide adequate signals over the desired ranges of frequency or time, attention must be paid both to the transmitter and the antenna. For most purposes an air core loop or coil transmitting antenna can be represented as a three element circuit consisting of an inductor  $L$ , and resistor  $R$ , in series, paralleled by a capacitor representing the distributed capacitance between coil windings. At very low frequencies the impedance depends primarily on the dc resistance of the wire. At higher frequencies the inductive reactance,  $\omega L$ , generally dominates the impedance. At some frequency the impedance of the capacitance equals that of the inductor; the coil is then self-resonant and the impedance is very high. As the frequency is raised above the self-resonant frequency the impedance depends primarily on the capacitor and it decreases with increasing frequency. All of the parameters are somewhat dependent on the frequency. At high frequencies, skin effect causes the current in the wire to flow mostly near the surface, thereby increasing the effective resistance of the wire. Also, eddy currents induced in the wire from adjacent turns represent another form of loss and increase the effective resistance; the ac resistance may be an order of magnitude or more higher than the dc resistance. The properties of ferromagnetic cored coils are similar but there are additional sources of frequency dependent loss such as hysteresis and eddy currents in the core material. However the core may increase the inductance enough to make the quality factor,  $\omega L/R$ , higher than for air cored coils. Ferromagnetic cored coils are generally long and slender to make effective use of the core material; in modeling most ground EM systems it is preferable to achieve the same sensitivity with shorter coils having a larger radius. Additional information on the properties of induction coils is given in Welsby (1960) and Snelling (1969).

To achieve a large moment in a coil that is to approximate a dipole source, it is advantageous to make the diameter as large as possible without introducing excessive error due to the finite size. The moment of the coil depends on the square of the radius, whereas, at low frequencies and for a fixed number of turns, the resistance depends on the radius. If the cross section of the winding is small compared with the diameter of the coil and if the inductance is ignored, at low frequencies the moment  $m$  can be expressed in the form,

$$m = \pi a^2 n I = \frac{VA_w a \sigma}{2} \quad (50)$$

where  $I$  is the current through the coil,  $V$  is the applied voltage,  $n$  is the number of turns,  $a$  is the mean radius of the winding,  $A_w$  is the cross sectional area of the wire, and  $\sigma$  is the conductivity of the wire. The number of turns does not appear in the final expression because the moment depends directly on the current which, in turn, is inversely proportional to the number of turns. Under the same assumptions the power  $P$  dissipated is

$$P = \frac{V^2}{R} = \frac{V^2 A_w \sigma}{2 \pi a n} \quad (51)$$

Since noise is generally most severe at the low end of the operating range, emphasis is usually placed on achieving a large moment at low frequencies. Typically, coils are designed so that their resistance is larger than their inductance at low frequencies. If skin effect could be neglected, an ideal low frequency coil would consist of one turn of heavy wire. In practice, the resistance would be so low that the coil would be a poor load for the transmitter. The wire size and number of turns should be selected to provide a reasonable load for the amplifier. Although maximum power is transferred when the impedance of the load is the complex conjugate of the source impedance, most amplifiers function best when the load resistance is larger than the output resistance of the amplifier. As a compromise, the actual load may generally be somewhat smaller than the optimum load for the amplifier when it is fully driven.

A function generator or signal generator, having adjustable amplitude and frequency, followed by a power amplifier are used to supply current to the transmitting coil. Laboratory or sound system amplifiers that can deliver more than enough power from dc to perhaps 100 kHz are readily available. Smaller current booster and power operational amplifiers are avail-

able which can generally supply adequate power at higher frequencies. Audio amplifiers are usually designed to drive impedances of about 8 ohms. However, at low frequencies, the impedance of a small coil may be less than 1 ohm. If necessary, a step-down transformer may be used at low frequencies to improve the impedance match. When a current booster or operational amplifier is used, precautions may have to be taken to avoid overloading and damaging the device. At high frequencies, the impedance of a coil is likely to be much higher than the intended amplifier load. A step-up transformer can be used to increase the voltage across the coil. The impedance, as seen by the transmitter, can be lowered by use of a series tuning capacitor but this is awkward because a different capacitor is needed for each substantial change in frequency. Generally, source loops are not used near or above their self-resonant frequency.

Many pulse generators are available that can supply suitable waveforms for transient measurements. However, for measurements using rectangular pulses, commercially available power amplifiers generally are not adequate because they are not capable of rapid turnoff of the loop current. If time is scaled to be considerably shorter than in the corresponding field measurements, the experimenter may need to develop a special switcher for transient measurements.

If the depth and width of the winding are small compared with the mean radius of the winding and if skin effect in the wire is negligible, the inductance  $L$  of an  $n$ -turn air core loop is approximately (Johnk, 1975):

$$L \approx n^2 a \mu_0 \left[ \ln \frac{8a}{b} - 2 + \frac{1}{4n} \right], \quad (52)$$

where  $a$  is the mean radius of the winding and  $b$  is the radius of the wire itself. Generally it is desirable to keep  $L$  as small as possible to minimize the impedance of high frequencies. This is most easily done by keeping the number of turns as small as possible.

Regardless of the capability of the transmitter, two factors limit the amount of current that can be driven through a coil. At high frequencies the voltage required to drive the desired current through the coil may be excessively high for the insulation that can reasonably be provided within the coil or between the feed wires. Also, high voltages may constitute a safety hazard, particularly when a brine tank is used. The amount of current that can be driven through a coil at any frequency is limited by thermal considerations. If the temperature becomes too high, the electric insulation, water seal, or other parts of the coil may be damaged. Even if damage is not incurred, excessive temperatures may cause substantial changes in the characteristics of the coil. For example, thermal expansion of the coil may cause excessive drift in a sensitive airborne system. Quantitative data on acceptable power dissipation in scale model loops is not available. However, some idea of allowable dissipation in coils can be obtained by comparing coils with commercially available chokes of about the same size; manufacturers commonly provide power ratings for their chokes.

Coil forms are generally constructed of stable plastic or composite materials such as Delrin or fiber loaded phenolic. If the coil is to be used only at relatively high frequencies, the inductive reactance will usually dominate the impedance and there is little reason not to use fine wire. Large coils that are to be used at low frequencies contain many feet of wire. To achieve a large moment with reasonable voltages, it is necessary to use relatively heavy wire in such coils, and the depth and width of the winding are a substantial fraction of the radius of the coil.

When grounded wires are used as sources, some attention must be given to design of the electrodes. The chief concern is to achieve good electric contact with the brine or other medium without making the electrodes so large that error is introduced because of their finite size. Sunde (1949) and other authors give the resistance to earth for a number of configurations. Assuming that the contact resistance is negligible, the resistance of a single vertical rod is approximately

$$R \approx \frac{1}{2\pi\sigma\ell} \left( \ln \frac{4\ell}{a} - 1 \right), \quad \ell \gg a, \quad (53)$$

where  $\ell$  and  $a$  are the length and the diameter of the rod, respectively, and  $\sigma$  is the conductivity of the medium. In field measurements, arrays of vertical or horizontal wires, rods, or plates are frequently used to reduce the resistance below that for a single element. An array can be used in model measurements but it is simpler to use one large electrode. The ideal resistance of a hemispherical electrode of radius  $a$  is simply,

$$R = \frac{1}{2\pi\sigma a}. \quad (54)$$

As an example, the resistance of a vertical rod having a length of 1 cm and a radius of 0.05 cm is .538 ohm, when immersed in a medium having a resistivity of one S/m. The resistance of a hemispherical electrode having a radius of 0.5 cm and immersed in the same medium is only .318 ohm. The distribution of current around the hemispherical electrode will be the same as that at an equivalent distance from a point electrode, although the potential will be different. Thus the hemispherical electrode has a lower resistance and causes less error than the vertical rod electrode. It must be remembered that the resistances given by equations (53) and (54) must be multiplied by two to account for the second electrode.

In practice, equations (53) and (54) may not yield accurate results due to the complex impedance at the interface between the electrode and the solution (see the section on properties of materials). At high frequencies the interface impedance may be negligible because of the double layer capacitance. At low frequencies the impedance may be minimized by using electrodes such as carbon or platinum. The best electrodes are "platinized" or coated with spongy black platinum which provides a large surface area that is relatively inert. Dearth (1978) studied the impedance in sea water of several materials that might be used as electrodes for submerged low frequency electric field antennas. He recommended consideration of silver-silver chloride, platinum-platinum black, and carbon. Note that the surface areas of the electrodes in the examples given are  $.322 \text{ cm}^2$  for the rod and  $1.5707 \text{ cm}^2$  for the hemisphere. If the contact impedance is very large, the grounding resistance (or impedance) may be essentially independent of the shape of the electrode and depend only on the surface area of the electrode. In this respect, the hemispherical electrode is again superior to the rod electrode.

At frequencies used in modeling induction systems, the inductance of grounded wire antennas generally can be neglected. Due to the electrode impedance, the impedance of a grounded wire may be somewhat frequency dependent; but, usually the characteristics of a grounded wire will change much less than those of a coil. Thus, there are few problems in coupling a transmitter to a grounded wire.

Ideally, driving current through a coil generates a magnetic field which, in free space, has the same form as the field due to a mathematical dipole or finite current loop. The electric field due to the coil should be the same as that which would be calculated from the magnetic field using Maxwell's equation for a current free region; that is,

$$\frac{\partial \mathbf{E}}{\partial t} = \frac{1}{\epsilon} \Delta \mathbf{x} \mathbf{H}.$$

In practice, extraneous or spurious fields may be generated so that the actual magnetic or electric fields deviate from the ideal fields. Generally there is little spurious magnetic field due to the coil itself. However, the wires or cable driving the coil may be a source of extraneous field unless they are well twisted and the terminals on the coil are placed close together. The transmitter can be a source of spurious magnetic fields if it is placed too near the receiving loop. Unless the transmitter is well shielded, care should be taken to avoid large loops in the internal wiring and the use of solenoidal inductors or transformers. Extra-

neous electric fields are more likely to be a problem than extraneous magnetic fields. The voltage across the terminals of the coil is one source of spurious electric field; this field can be minimized by placing the terminals close together and by using low impedance coils and large currents. Another source of extraneous electric field is common mode voltage that may be developed along the feed line between the coil and the transmitter. This can be minimized by using a balanced coil and feed line. For high frequency measurements a "Faraday shield", which is a thin shield that greatly attenuates electric fields but has little effect on magnetic fields, is generally placed around the coil. For operation below about 100 kHz shielding may not be necessary.

### Plane wave or uniform sources

Modeling magnetotelluric (MT), audiagnetotelluric (AMT), very low frequency (VLF), and other "plane wave" methods generally requires establishment of a uniform horizontal magnetic field at the surface of the electrolytic tank or whatever medium is used. The source of energy for the AMT and VLF methods can be represented with little error as a plane wave at grazing incidence with the magnetic field horizontal; whereas, the magnetic field for MT measurements is often incident at much steeper angles. However, when displacement currents in the earth are negligible, the fields diffuse downward in a direction almost normal to the surface, regardless of the angle of incidence. A variety of techniques can be used to establish a nearly uniform magnetic field; but, establishment of a close approximation to an actual plane wave is difficult for most geophysical applications.

Rigorous modeling of the CSAMT method is readily carried out by placing a grounded wire source at the properly scaled distance from the area of investigation. Since the fields will be greatly attenuated at the area of investigation, high source strengths may be required. As indicated in Table 2, modeling the CSAMT method over a wide range of frequencies requires use of a relatively large tank and high frequencies, otherwise the targets and receiver will not always be in the wave zone (see Spies and Frischknecht, 1988). When the medium has a conductivity of 2 S/m, the effect of displacement currents becomes significant at frequencies a little greater than  $10^7$  (see Models Materials discussion Section 10 and Figure 12). Unless the horizontal dimensions of the tank are several meters, the conductivity of the medium must be at least several S/m to be able to vary frequency over two decades and still not violate the requirement that measurements should be made at a distance of several skin depths from the source. Of course, if this condition is violated in the field measurements, it should be similarly violated in the model measurements.

**Table 2. Required source receiver separation for CSAMT modeling**

$f$	$\sigma = 2 \text{ S/m}$		$\sigma = 20 \text{ S/m}$	
	$\delta$	$5\delta$	$\delta$	$5\delta$
$10^4$	3.56 m	17.8 m	1.13 m	5.63 m
$10^5$	1.13	5.63	.356	1.78
$10^6$	.356	1.78	.113	.563
$10^7$	.113	.563	.0356	.178

Natural field AMT, MT, and VLF methods also can be modeled using a grounded source provided measurements are made in the wave zone and provided the targets or structures of interest are small compared with the source-target distance. If the targets are not small, errors will be introduced because the direction, intensity, and phase angle of the source field will vary significantly across the target. Most modeling of natural field and VLF methods is carried out using arrays of wires or large coils to generate a nearly uniform horizontal field at the surface. An ideal source would be a very large "current sheet" placed just above the tank. However, a solid sheet would be cumbersome and at high frequencies the current distribution becomes nonuniform in a finite sheet. The low frequency field of a current sheet can easily be approximated by a planar array of wires. At low frequencies the tangential component of the magnetic field at the point  $P(x_o, y_o, z_o)$  due to a single wire  $2\ell$  in length,

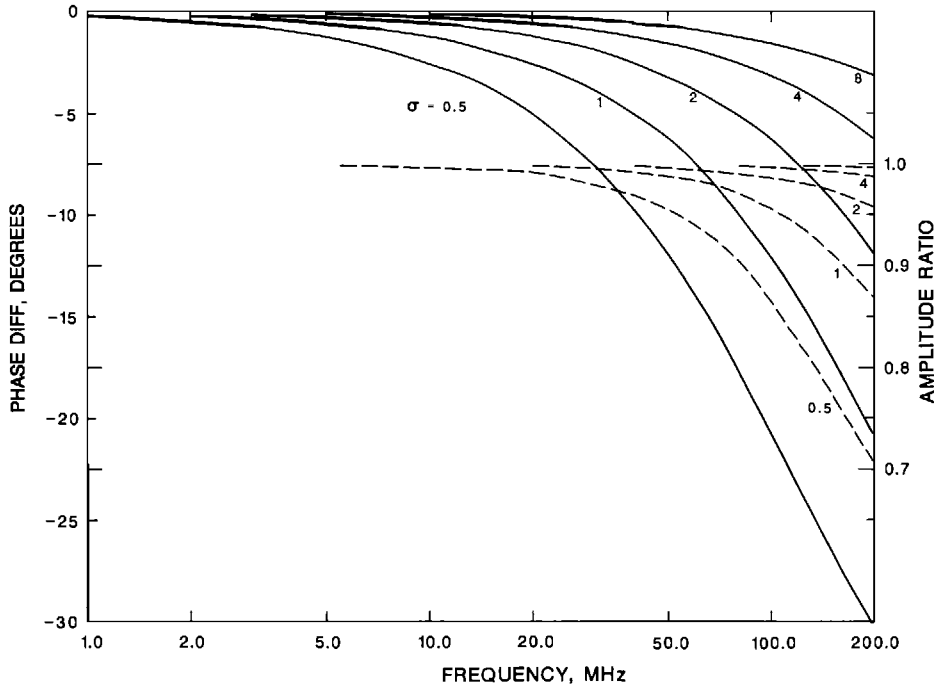


FIG. 12. Amplitude ratio (dashed) and phase difference (solid) between surface impedances for a medium having dielectric constants of 80 and a medium having a dielectric constant of 1 as a function of conductivity and frequency.

which is located in the  $xy$  plane (Figure 13) and which carries a current  $I$ , is

$$H_t = \frac{I}{4\pi\rho} \left\{ \frac{\ell - y_o}{[\rho^2 + (\ell - Y_o)^2]^{1/2}} + \frac{\ell + y_o}{[\rho^2 + (\ell + y_o)^2]^{1/2}} \right\}$$

$$\rho^2 = (x - x_o)^2 + z_o^2 \quad (55)$$

This expression is valid provided the distance between  $P(x_o, y_o, z_o)$  and the wire is much less than a free space wavelength. The field of an array of wires can be determined by calculating the horizontal ( $=H_t z_o / \rho$ ) and vertical ( $=H_t (x - x_o) / \rho$ ) components of the field of each wire using equation (55) and then summing the results; the field of a finite sheet can be obtained by integrating the components in the  $x$  direction (Frischknecht, 1973). The horizontal component of the field due to a finite sheet or an array of closely spaced wires is not uniform over the surface of the tank unless the dimensions of the sheet or array are much larger than those of the tank. Also, the vertical component of the field is substantial except near the center of the tank unless the array is much larger than the tank. To achieve a nearly uniform field distribution in the direction parallel to the wires they should be made as long as possible. The finite width of an array can be partly compensated for by driving more current through the outer wires than the inner wires. This can be accomplished by placing adjustable impedances in series with each individual wire to adjust the phase and amplitude of the current (Frischknecht, 1971, 1973). The use of individual impedances for each wire may be necessary also at high frequencies to compensate for differences in the phase angles of the currents caused by mutual coupling between the wires. Unfortunately, the impedances must be changed when the frequency is changed. Ultimately the array of wires is only one part of a current path that includes the transmitter. The part of the current path external to the array should be arranged so that it does not have a significant effect of the total field at the tank.

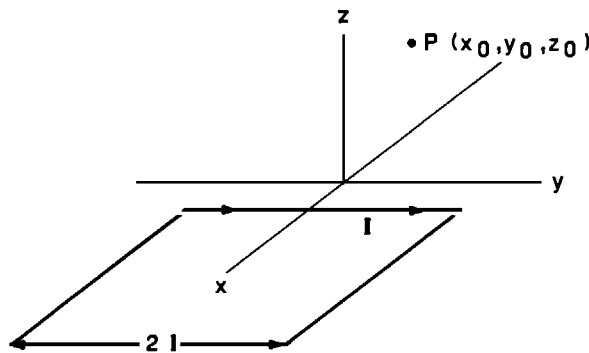


FIG. 13. Sketch of coordinate system for calculation of field of finite wire.

There is an electric field in air associated with a source array. If the electrolyte is emptied from the tank, the ratio of the electric to the magnetic field (wave impedance) at the position of the surface will be much less than for a plane wave in free space but generally it will be greater than the proper surface impedance when the tank is filled. However, when the tank is filled with conductive fluid the correct surface impedance is established, provided the frequency is sufficiently high (Frischknecht, 1973). Also, when it is filled, the vertical component of the magnetic field becomes negligible at the surface in the central region of the tank.

In principle, it should be possible to establish proper electric and magnetic fields in a rectangular tank by driving current through it from electrodes placed at either end. At very low frequencies the current distribution would be uniform if the electrodes covered either end of the tank. This represents the desired condition for modeling the effects of near-surface inhomogeneities having dimensions much smaller than a skin depth. At higher frequencies, currents would tend to concentrate in the outer regions of tanks but, if the tank were large enough, the fields would behave properly in the central region of the tank. By using several electrodes and adjusting the current in each, it should be possible to improve the degree to which the desired field distribution is achieved. In modeling the telluric method Roy (1973) used two sets of electrodes on the sides of a tank to generate a circularly polarized, low-frequency electric field in the central portion of the tank.

Edwards (1980) suggested using one or more long vertical wires grounded at the surface of the tank as a source. A single such wire produces a tangential magnetic field but current flows in vertical planes in the tank. However, if the frequency and conductivity are sufficiently large, the correct surface impedance is established at short distances from the wire. Edwards suggested using four wires, two serving as sources and two as sinks. Let the distances between the two source or two sink wires be  $2d$  and the distance between a source and a sink wire be  $2\sqrt{3}d$ . Edwards showed that if  $d$  is equal to two skin depths in the tank, the apparent resistivity over the working region ( $2d \times 3d$ ) differs from the true resistivity

by no more than 1.5 percent. For a deep tank, the error in the apparent resistivity at a depth of one skin depth under the center of the working region is only about 3 percent when  $d$  is two skin depths. Wait (1981) discussed a problem in using this technique when the media is stratified with a resistive intermediate layer.

Large Helmholtz and other types of coils have been used for specialized purposes in modeling. Helmholtz coils are particularly useful in establishing a uniform field in air or at extremely low frequencies in a tank. Their use is not warranted when the frequency is high enough to establish proper impedance relationships due to induction.

In studying geophysical methods that employ propagating waves or in studying the effects of earth structures on radio waves, it is generally necessary to work in the far field rather than the near field zone of the antenna. This requires that the antenna be at least three free-space wavelengths or more from the working region of the model facility. If such a model facility is placed outdoors it is possible to use relatively low frequencies. For example, a frequency of 10 MHz can be used if the separation between the source and receiving antennas is about 100 m. However, suppose that a propagating wave is to be used in an indoor facility and that displacement currents are to be negligible. These conditions could be met by using a medium having a conductivity of 20 S/m and a frequency of 200 MHz (see Figure 12). The separation between the source antenna and the working area of the tank should be at least 5 m and the room to house this system would have to be on the order of 8 to 10 m long. Wide band measurements would not be possible because, if the frequency were substantially increased, displacement currents would become important and, if the frequency were substantially decreased, a larger tank and room would be needed. Also, note that a skin depth in a 20 S/m medium is only 0.8 cm at 200 MHz. Extremely small targets and impractically small receiving antennas would be required for modeling most structures under these conditions. Thus, when displacement currents must be negligible, indoor use of a propagating wave from an ordinary antenna is almost impossible unless a medium with a lower dielectric constant or higher conductivity than concentrated NaCl ( $\approx 20$  S/m) is used.

When a distant antenna or an array of wires is used to excite a model tank, it is generally advantageous to place a conductive shield at the bottom of the tank to prevent diffusion of fields up from the bottom. Although, as discussed previously, a conductive bottom generally causes a greater disturbance than an insulating one for downward diffusing fields, a tank without a shielded bottom must be about twice as deep as a shielded one if there are substantial fields below the tank. In some cases, shielding part of the sides also may be appropriate.

## Probes

Small loops are used as receiving antennas or probes for measurement of magnetic fields in scale model studies. The most important factors to consider in the design of receiving loops are size, sensitivity, stability of characteristics, insensitivity to extraneous electric fields, and disturbance of the normal fields due to the loop itself. With a few exceptions, the receiving loops employed in field systems can be considered as dipoles. Criteria for the permissible size of model receiving loops are generally the same as those given for transmitting loops in the previous section. The desired sensitivity depends on the noise characteristics of the preamplifier, the level of magnetic field noise, and the source strength. If the sensitivity of the receiving loop is too low, very high gains in the amplifiers will be needed and intrinsic noise in the preamplifier will cause degradation of the S/N ratio at the output of the system. Generally, it is both desirable and feasible to make the sensitivity of the loop sufficiently high that preamplifier noise is smaller than the noise due to extraneous magnetic fields.

In field systems, receiving loops are sometimes made to function as magnetometers by use of current amplifiers or feedback circuits. Such techniques are more difficult to implement in scale model systems so that generally loops are used as ordinary induction coils in scale modeling. For most purposes, a five or six element circuit (Figure 14) is adequate to describe

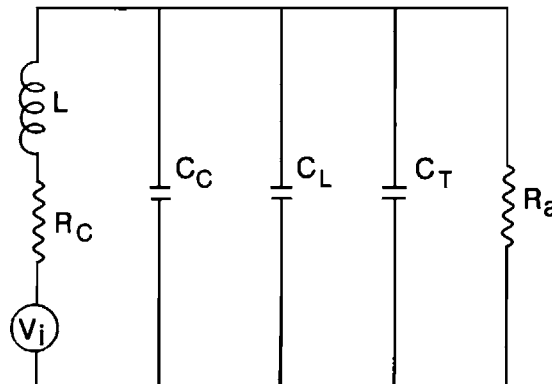


FIG. 14. Equivalent circuit for receiving loop connected to a preamplifier. The inductance, resistance, and capacitance of the loop are  $L$ ,  $R_c$  and  $C_c$  and the open circuit voltage induced in the loop is  $V_i$ . The combined capacitance of the line connecting the loop and preamplifier and the preamplifier input is  $C_L$ . The capacitance  $C_t$  is for tuning the loop and  $R_a$  is the input resistance of the preamplifier.

the behavior of a receiving coil connected to a preamplifier. The parameters  $L$ ,  $R_c$ , and  $C_c$  of the coil itself are the same as those described for transmitting coils in the previous section. The input resistance of the preamplifier  $R_a$ , may be essentially infinite or it may be made low enough, through use of a shunt, if necessary, to load the receiver coil, particularly if transient measurements are made. The capacitor  $C_L$  is the combined capacitance of the cable between the coil and preamplifier and the input capacitance of the preamplifier and  $C_t$  is the capacitor that may be deliberately added to form a parallel resonant circuit with the coil. The voltage  $V_i$  induced in the coil is

$$V_i(t) = n \frac{d\phi}{dt} = nA \frac{dB}{dt} \quad (\text{time domain}) \quad (56)$$

or

$$V_i(\omega) = i\omega nAB, \quad (\text{frequency domain}), \quad (57)$$

where  $n$  is the number of turns,  $A$  is the area enclosed by the mean turn of the winding, and  $B$  is the component of magnetic intensity along the axis of the coil. Combining the capacitors into one equivalent capacitor  $C$ , the ratio of the voltage  $V_a$ , at the input of preamplifier, to  $V_i$  is

$$\frac{V_a}{V_i} = \frac{R_a}{R_a + R_c + s(L + R_a R_c C) + s^2 R_a L C}, \quad (58)$$

where  $s = i\omega$ . If  $R_a$  is much larger than any of the other impedances

$$\frac{V_a}{V_i} \cong \frac{1}{1 + sR_c C + s^2 LC}. \quad (59)$$

At the low end of the operating range, the resistance  $R_c$ , and the reactance  $\omega L$ , of the coil are likely to be much smaller than  $R_a$  and the impedance of the capacitor  $1/\omega C$ , is likely to be much larger so that  $V_a/V_i = 1$ . At higher frequencies the impedances of the coil and capacitor must be considered. When the impedances of the coil and capacitor are equal,  $s^2 LC = -1$ , and equation (59) becomes

$$\frac{V_a}{V_i} = \frac{1}{sR_cC} = \frac{-i\omega L}{R_c} = -iQ, \quad (60)$$

where  $Q$  is the quality factor for the coil. The value of  $Q$  for an air core model coil may be 10 or higher for much of the operating range; by tuning the coil the voltage at the input of the amplifier can be increased considerably. Also, tuning narrows the bandwidth, thereby providing noise rejection. However, since a different value of tuning capacitance is required for each frequency, tuning is impractical in broadband measurements. Tuning also magnifies the effects of changes in coil parameters. Even if the coil is not deliberately tuned, the capacitances  $C_c$  and  $C_L$  will tune the coil at some high frequency. The capacitance  $C_L$  can be minimized by placing the preamplifier near the coil and using a low-capacitance line. However, at some frequency all coils become self-resonant because of their distributed capacity. Sensitivity is particularly likely to drift when a coil is operated near self-resonance. If a finite value for  $R_a$  is used,  $V_a/V_i$  is reduced, particularly when the coil is at or near resonance. However, use of a finite value for  $R_a$  also reduces the sensitivity of  $V_a/V_i$  to changes in the coil parameters  $R_c$  and  $L$ . Thus, it may be desirable to load the coil with a relatively low value of resistance if it is to be operated near resonance. When transient measurements are made, high frequencies associated with turn-off of the transmitter current may cause a damped oscillation or ringing in the coil at its self-resonant frequency. If time is scaled so that model measurements are made at much shorter times than in field measurements, it is usually necessary to make  $R_a$  sufficiently small that coil ringing ceases before the time of the first measurement. For most transient measurements the coil should be critically damped or slightly undamped; excessive damping will distort the measured transient.

Factors that are likely to cause changes in coil parameters are changes in temperature or humidity that may cause expansion or contraction of the coil form or winding and electrical loading of the coil by proximity to conductive material. Changes in coil parameters can be minimized by using stable materials in construction of the coil and by controlling temperature and humidity in the model facility. Both the resistance and the inductance of a loop are changed appreciably when it is brought in close proximity to conducting material. This change in impedance will not cause a significant error if the loop is untuned, connected to a high impedance load, and operated well below its self-resonant frequency. However, significant errors in both phase and amplitude may result if the loop is tuned, since the resonant frequency will change when the load changes.

Any coil or other probe causes some disturbance of the field which is being measured. If this disturbance is substantial only in the immediate vicinity of the probe, correct measurements can be obtained by calibrating the probe. However, correct measurements are not obtained if the probe significantly disturbs the fields in the vicinity of the model media; that is, if the probe behaves as a secondary source. To reduce the disturbance it causes, the probe should be as small as possible and currents flowing in the probe should be minimized. The current in a receiving coil will be almost nil if it is operated well below its resonant frequency and if it is connected to a high impedance preamplifier. If the currents in the shield and the windings of a receiving coil are known, its distant field can be calculated readily by assuming the coil to be one or more small current loops. If the currents cannot be estimated, the maximum possible in-phase field of a loop can be calculated by assuming it to be a perfectly conducting sphere having the same radius. The moment of such a sphere in a uniform field is  $2\pi R^3 H_0$ , where  $H_0$  is the exciting field. For a conductive layered half-space the disturbance due to an arbitrarily oriented dipole may readily be determined. Wait (1968) analyzed a similar problem for magnetic dipole excitation. For more complicated earth models, some approximate method of evaluating the effect of the loop must be used.

Many of the considerations that are important in the construction of dipolar source loops apply also to receiving loops. Ordinarily, more turns are used for receiving loops than for source loops and maintaining the self-resonant frequency above the operating range may be a problem. From the standpoint of minimizing self-capacitance, the most efficient shape of winding for a solenoidal coil is a flat disk (Welsby, 1960). If more turns than can be placed in one such section are required, two or more separated sections connected in series may be

used. Given a particular shape and winding volume, self-capacitance can be minimized by (1) increasing the distance between adjacent turns and (2) reducing the voltage difference between adjacent turns. Wave windings (Welsby, 1960), in which the turns in adjacent layers are not parallel, are sometimes employed to reduce self-capacitance; however, coils for use in modeling are likely to be too small to employ these types of windings. A random or "scramble" winding is probably the most practical to use in making coils for use in model studies. A number of investigators including Becker et al. (1972) and Ghosh (1972) have used commercially available RF chokes in model studies.

Electric fields exist in model systems, particularly when modeling distant source or plane wave methods. Receiving coils may behave as electric field antennas, thereby causing extraneous voltages at the input of the preamplifier. Elimination of these unwanted voltages requires careful design of both the source and receiver, and the transmission path between the receiving probe and the measuring equipment. When fairly high frequencies are used, it is generally necessary to use a balanced loop connected to a receiver with a balanced input, or to put a Faraday shield around the loop, or both. Balanced loops are easily made using two sections, one wound clockwise and the other counterclockwise. The outside ends of the windings, when connected, place the voltages induced in each section in series and serve as the center-tap of the loop. If a shield is used on a balanced loop, it should be constructed so that it is symmetric with respect to the windings and the center of the shield should be connected to the center-tap of the loop. If a single-section shielded loop is used, the shield should be connected to the outside end of the winding to minimize the additional capacitance added to the loop by the shield. All shields must have a small open region to avoid forming a shorted turn around the loop. To reduce eddy currents in the shield, the shield should be made of a very thin sheet of tin or other foil or conductive paint which should be applied in strips or cuts should be made to reduce the size of eddy current paths.

In modeling most geophysical problems, the diameter of the receiving loop must be very much smaller than a free-space wavelength. Under these conditions a properly designed loop and measuring apparatus sense only the magnetic field as intended. However, in modeling propagation problems using ultra high frequency (UHF) or microwave frequencies, it may, from a practical standpoint, be necessary to make the dimensions of the loop a significant fraction of a wavelength. Then the loop, even if shielded, may respond, in part, to electric as well as to magnetic fields. Whiteside and King (1964), King and Harrison (1969), and King et al. (1981) analyzed the behavior of loops under such conditions and discussed double loading and other means of minimizing electric field response.

In most geophysical methods, the only electric field of interest is the horizontal component at the surface of the earth. When a tank is used it is much easier to measure the electric field immediately below the surface of the electrolyte than just above. This can be done with two small electrodes spaced a short distance apart and immersed a slight distance into the electrolyte. If the model study requires a solid inhomogeneity to be placed at the surface, it is usually permissible to cover the inhomogeneity with a thin layer of electrolyte so that the electrode array can be moved across the surface and still make contact. If contact cannot be made by use of a layer of electrolyte, it is feasible, but very tedious, to use sharp electrodes and press them into the solid or to fasten electrodes directly to the solid with conductive paint.

Ordinarily, a third electrode is placed midway between the two principal electrodes and connected to the preamplifier ground. If the impedance of the transmission line and measuring apparatus is sufficiently high, the electrodes may be made of almost any metal; otherwise platinized platinum or other material having a very low electrode impedance should be used. In practice, it is never desirable to draw much current through the electrodes since this can alter significantly the current distribution and corresponding fields in the media. Unless the probe is designed so that the wire connecting the electrodes is at the surface of the media and unless the connecting wires are well twisted, a loop is formed which is sensitive to magnetic fields. One of the probes I used (Frischknecht, 1973) contained such a loop and some of the electrical field results are in error.

Measurement of electric fields in air usually is much more difficult than measurement of electric fields in a solution. At UHF and microwave frequencies it may be possible to use

scaled-down conventional thin wire, resonant, electric dipole antennas connected to short sections of matching transmission lines (Annan et al., 1975; Bansal, 1985). At lower frequencies the impedance of such dipoles is very high compared with even a short section of transmission line. For instance, the capacitance to space of a small wire 4 cm long and loaded at the end with a disk 1 cm in radius is only about 1.4 pF. The capacitance between two such elements is less than 1 pF. Such an antenna might be connected to a high impedance preamplifier located several centimeters from the antenna by means of an open-wire transmission line. However, such an open-wire line would act as an antenna and also would distort the field being measured. One solution to some of these problems is to place a preamplifier inside the antenna. This technique was used by Greene (1967) in making a field strength meter for near field measurements and by Frischknecht (1971, 1973) in scale modeling. A relatively thick dipole is required, of course. Greene (1975) described the design and calibration of small electric dipole and loop antennas for measuring intense fields at frequencies greater than 10 MHz.

Distortion of electric fields in air by a probe is much more likely to be serious than the corresponding distortion of the magnetic field. For an electric field antenna in a uniform electric field at a height  $h$  above a flat conducting surface, the error due to its proximity to the surface can be calculated by assuming the presence of an image antenna at a depth  $h$  beneath the surface. Using results obtained in Harrison and Lewis (1965) the error caused by a 4 cm long antenna at a height of 6 cm above the surface would be about 2 percent. The error could, of course, be larger if the undisturbed field were not homogeneous.

## Transmission Lines

Measuring and recording apparatus is always bulky and must be placed at some distance from the probes. The system used for transmitting signals from the probe to the measuring apparatus is a potential source of error in measurement. An ordinary cable or transmission line can disturb the field in the vicinity of the probe and in the region of the model media and, in effect, it can act as an antenna. If not properly twisted the line may act as a loop and sense magnetic fields. Parallel components of electric fields induce voltages in each line that are about equal and that are called "common mode" voltages. However, imbalances in the line or the measuring equipment may cause undesired conversion of common mode voltages to differential mode voltages. In modeling loop-loop induction methods at low frequencies or long times, electric fields are small and very little error is introduced by connecting the receiving loop directly to the measuring apparatus with a conventional cable, provided certain precautions are taken. A small diameter cable should be selected and run directly away from the loop; otherwise, eddy currents induced in the cable may cause small errors. The cable will, of course, distort the electric fields which exist in air but this is not likely to cause a significant error because the common mode current is small. If the loop-loop system is operated at relatively high frequencies or short times, part of the common mode voltage induced in the loop and along the cable is likely to be converted to a differential mode voltage and detected by the receiving apparatus. A good way to reduce this effect is to use a balanced center-tapped receiving loop, a two conductor shielded cable, and a differential preamplifier having a ground terminal. The shield of the cable is connected to the center tap of the loop and the ground of the amplifier. The shielding eliminates most of the common mode voltage from the signal conductors and the differential amplifier provides further rejection of common mode voltages. Additional improvement can be made by using a similarly balanced transmitting loop and transmitter for the source and by using balanced shields connected to the center tap of the loop winding.

This same technique may be satisfactory in modeling magnetotelluric and other methods using uniform field sources, provided the frequency is not too high and provided the exciting field is primarily a magnetic field. If electric fields in air are excited or are to be measured at frequencies of a few MHz, the use of a direct cable connection between probes and the

receiving apparatus is generally not satisfactory. In addition to problems with common mode voltages, the cable distorts the electric fields in air and it may carry enough common mode current to cause a substantial extraneous magnetic field.

The effect of the connection between probes and measuring apparatus is eliminated most effectively by not using a conventional transmission line or other conductive link. The signal can be telemetered directly from the probe to the measuring apparatus by a radio or optical link. If a radio link is used it must function at frequencies outside the operating frequencies of the model facility. At high frequencies, phase information can be telemetered by simply doubling the operating frequency in the receiving probe and transmitting this signal to the measuring apparatus. However, since the probe is moved about, the amplitude of the radio frequency carrier cannot be used to transmit useful information. Frequency modulation or another modulation scheme is required to transmit both phase and amplitude.

It appears a major if not impossible task to place a satisfactory radio telemetry system inside a probe small enough for scale model studies. However, a telemetry transmitter could be placed on the carriage relatively near the probe. The connection between the probe and transmitter would still tend to disturb the fields but not as much as a connection running all the way to the measuring apparatus. The transmitter would, of course, have to be powered by batteries or another source of power that does not involve running power leads to the transmitter.

Transmission of the signal through an optical fiber link is probably a better solution. Just as for radio transmitters, the transmitter for an optical system must be placed near the probe and powered by batteries. The receiver may be located at any desired distance from the working area of the model. Because optical fibers are nonmetallic, they do not act as antennas and do not significantly distort electric fields. Optical fiber systems are now available for transmission of analog signals with sufficient accuracy and bandwidth for most purposes. If desired, simple signal processing could be done near the probe and an optical link could be used to transmit digital results in serial form. A second fiber link would be required to transmit phase information from the transmitter to the signal processor on the carriage.

At microwave frequencies, electric fields can be measured using backscattering techniques that do not require a conductive path between transmitter and receiver (King, 1965, 1978). A small electric dipole at the observation point is modulated at an audio frequency using a high impedance link. A small amount of modulated microwave energy, which is proportional to the square of the field at the receiver antenna, is backscattered. Because it is modulated, the backscattered field can be separated from the transmitted field. Measurement of the backscattered signal then gives the field at the receiving dipole.

There are several means of reducing the effect of a metallic transmission line between the probe and measuring equipment. First, it is generally possible to place most of the transmission line along an equipotential path, at least in the region where electric fields are most intense. Second, conductive lines that present a high impedance to common mode voltages can be designed.

In measuring the vertical electric field strength of VLF waves, Harrison and Lewis (1965) placed a receiver at the base of a monopole antenna. The RF signal was converted into a 1 kHz signal and transmitted by a 300-ohm twin-line to high-impedance measuring apparatus located at some distance from the antenna. Resistors having a value of 2 megohms were inserted in both sides of the line at three different points to impede the flow of RF current. By thus limiting the flow of RF current, the disturbance caused by the line was only about 2.5 percent. In the design of probes for use near transmitting antennas, Greene (1967, 1975) converted the RF to a proportional dc voltage and transmitted it to a high-impedance differential voltmeter using a conductive plastic line having a common mode resistance of about 30K ohms per meter. Unfortunately, phase information cannot be transmitted using these methods.

If the phase of the signal is to be measured, RF must be transmitted along the line. Accordingly, the line must present a very high impedance to currents common to both conductors and to the shield, if any, and at the same time transmit the differential mode signal applied between the conductors. At RF it is impractical to achieve this result by placing high values of resistance in the line because the capacity between lines and the input capacitance

of the measuring equipment cause excessive attenuation of differential mode signals in a resistive line.

Transformers can be used to greatly increase the impedance of a metallic line to common mode voltages and still transmit differential mode signals with little attenuation. Transformers used for this purpose must have very low capacitance between primary and secondary windings and must be constructed or shielded so that they do not pick up external magnetic fields. Transformers having extremely low capacitance between primary and secondary windings are available commercially. However, their low capacitance is achieved by placing a complete shield between the windings and connecting it to ground; if the shield is not grounded it is not as effective in lowering the capacitance. In a model facility there is no suitable place to ground the shield and, if there were, common mode currents flowing in the low impedance path to ground would represent a source of extraneous magnetic fields. Small transformers having relatively low capacitance between windings can be constructed by placing the windings on opposite sides of toroids made of high resistivity ferrite. However, such transformers act as loop antennas for external magnetic fields and must be shielded, which increases the capacitance between primary and secondary windings.

Another method for raising the common mode impedance of a metallic line is to insert bifilar wound inductors, sometimes called longitudinal chokes (Ott, 1976). The method of construction is indicated in Figure 15; toroidal cores are probably most convenient but pot cores or other types could be used. Such devices present a high impedance to voltages common to the two strands but a very low impedance to voltages applied between the strands; also, they are insensitive to external fields. One of the chief concerns in constructing such devices is achieving a high inductance while keeping the self-resonant frequency above the operating range. If operated near self-resonance, the parameters of the inductor will be unstable and if operated at frequencies above self-resonance the device will act as a capacitor. For operation at a single frequency, very high impedances can be achieved by tuning the inductor through use of a tuning winding and tuning capacitor, as indicated in Figure 15. At resonance, the common mode impedance of such a device is approximately  $Z_{cm} = \omega^2 K_m^2 L_1 L_2 / R_2$ , where  $K_m$  is the coefficient of coupling between the windings,  $L_1$  and  $L_2$  are the self-inductances of the two windings, and  $R_2$  is the resistance of the tuning winding (Frischknecht, 1973).

The techniques just described for reducing the effect of transmission lines apply principally to frequency domain methods. The limited dynamic range of fiber optic links may complicate their use in transient systems and the waveform distortion caused by transformers and other devices may preclude their use. At present, there are no transient methods that use uniform field sources so conventional metallic lines can generally be used.

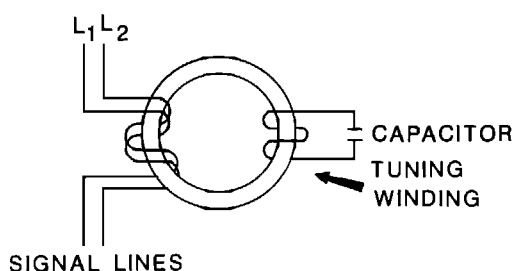


FIG. 15. Sketch of tuned longitudinal choke.

## Signal Processing and Data Acquisition

A thorough discussion of signal processing techniques, as applied in making electromagnetic field measurements, is given in the chapter on instrumentation and will not be repeated here. Most of the theory and techniques applied in acquisition of field data are relevant in scale model studies; but, there are differences in noise spectra in the two cases. Also, commercially available laboratory equipment that is too bulky or not sufficiently rugged for field use can be used in scale modeling.

In the past many model studies of electromagnetic profiling methods such as slingram and turam were carried out using the same frequencies and measuring equipment that were used in the field. Such equipment may still be employed for limited studies of targets placed in air. Generally, matching circuits are required to adapt field equipment for use with model loops. In the past two decades, a large variety of broadband laboratory equipment that can be used for frequency and time domain measurements has become available. For frequency domain measurements several of the required functions are commonly combined in one unit known as a lock-in-amplifier. A block diagram of a system for making loop-loop measurements at frequencies up to 100–200 kHz using a lock-in-amplifier is shown in Figure 16; the bandpass filter, the preamplifier, and the dc offset circuit are not necessarily a part of the lock-in-amplifier. For a signal,  $V_s \cos(\omega t + \phi)$ , where  $\omega$  is the same in the signal and reference channels, the phase sensitive or synchronous detectors produce dc or low-frequency outputs, proportional to  $V_s \cos \phi$  for the in-phase channel and  $V_s \sin \phi$  for the quadrature channel. Superimposed on the desired output signals are noise components having frequencies  $\omega = |\omega_r - \omega_n|$ , where  $\omega_r$  is the reference frequency and  $\omega_n$  is the noise frequency. The purpose of the low pass filter is to eliminate unwanted ac signal and noise voltages in the output. The bandwidth of the filter must be wide enough not to affect the very low-frequency components in the desired signals. In a scale model system these low frequencies are the anomalies as the probes are moved across the region of the target.

The reference channel contains circuits for shifting the phase of the reference channel and for generating two reference signals having a phase relationship of 90 degrees with respect to each other. Also, the reference channel is generally designed to remove phase noise from the input reference signal and to produce clean square-wave reference signals for the phase sensitive detectors. The latter function is not important in scale model measurements where the reference signal is inherently clean.

Since the in-phase detector rejects quadrature noise and the quadrature detector rejects in-phase noise, synchronous detection inherently results in improving the S/N ratio by a factor of two, even without the bandpass filter (Meade, 1983). Without considering this improvement the noise bandwidth of a lock-in amplifier is  $2B_0$ , where  $B_0$  is the bandwidth of the lowpass filter, because frequencies above and below the reference frequency are transmitted. The final result is that the effective noise bandwidth through the system is  $B_0$  (Meade, 1983). The phase sensitive detector is a linear device, that is, signals and noise are superimposed or added together in the output. Thus, in principle a very slowly varying signal can be extracted from an arbitrarily large noise input if the bandwidth of the low pass filter is made small enough. In practice, the dynamic range of the phase sensitive detectors and preceding stages cannot be large enough to handle extremely small signals without becoming overloaded or saturated when large noise components are present. Unless the frequencies of the noise are centered closely around the signal frequency, a bandpass filter can be used before the phase detectors to reduce the input noise, thereby preventing saturation of the system. Most phase-sensitive detectors employ square-wave reference signals which cause them to respond to voltages that are odd harmonics of the reference frequencies; a second reason for employing a bandpass filter is to eliminate spurious harmonic responses. Many early lock-in amplifiers included a bandpass filter; because of improvements in dynamic range to avoid saturation, most later units do not contain such filters. In applications where harmonic response is a problem, frequency translation or heterodyning is sometimes now used.

Often there is a need to measure small variations superimposed on a constant level. Many lock-in amplifiers provide dc offset circuits that allow suppression of such constant levels in the output.

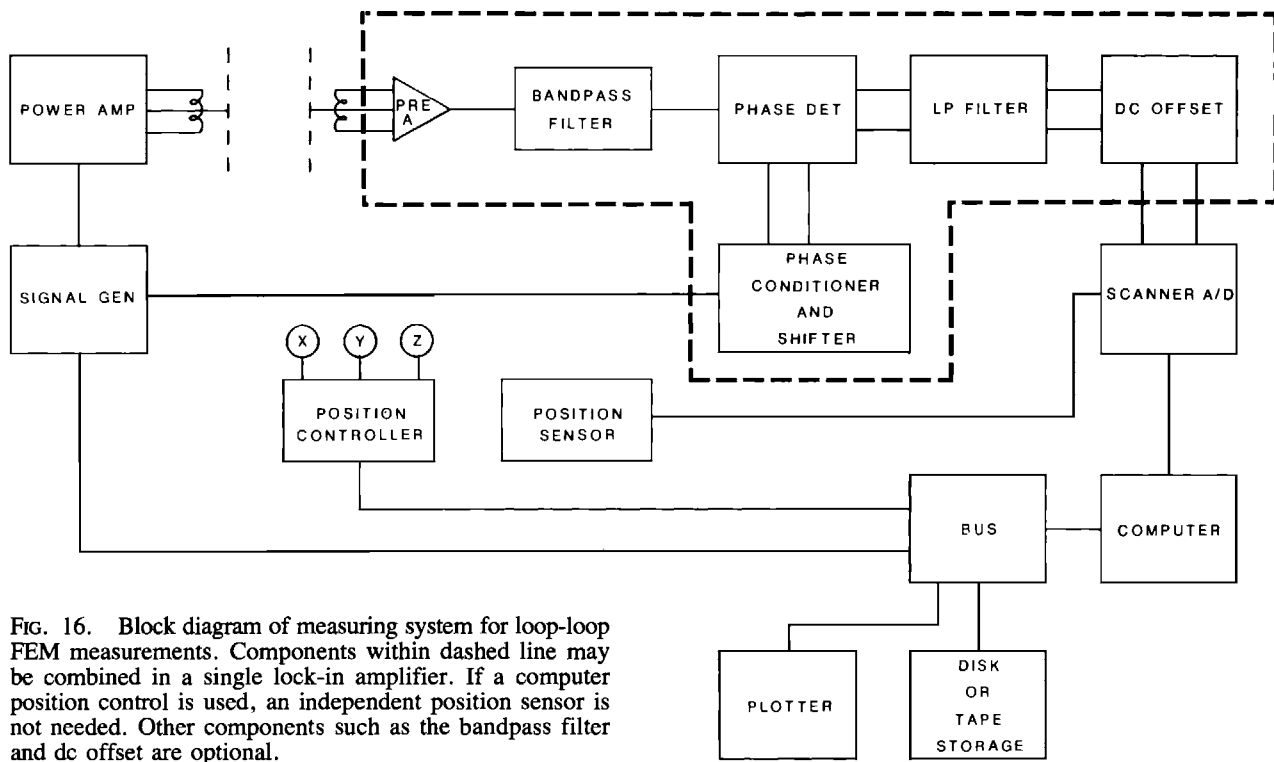


FIG. 16. Block diagram of measuring system for loop-loop FEM measurements. Components within dashed line may be combined in a single lock-in amplifier. If a computer position control is used, an independent position sensor is not needed. Other components such as the bandpass filter and dc offset are optional.

At frequencies up to about 200 kHz, it is feasible to connect a receiving coil directly to the differential input preamplifier provided with most lock-in amplifiers. If an external bandpass or rejection filter is required, then a separate preamplifier will be required. At frequencies above 100–200 kHz, the capacity of the line is likely to be great enough to tune the coil. At high frequencies, particularly if plane wave methods are being modeled, it is generally necessary to locate the preamplifier near the probe and to use an optical or high impedance transmission line.

External preamplifiers placed near a probe should be shielded and should be made as small as possible. To estimate their effect on the field at the probe they may be considered as conductive spheres or cylinders having equivalent dimensions. Generally, the preamplifier should have both a differential input and output; if it is used to drive an optical link a single ended output may be used. A few monolithic amplifiers are made that can be used as complete differential input and output amplifiers but generally it will be necessary to use a pair of monolithic amplifiers in the usual instrumentation amplifier configuration. If necessary, a second stage can be added. Many operational amplifiers are incapable of driving long lines due to their capacitance; a pair of transistors or small current boosters can be used as line drivers if necessary. To achieve good common mode rejection, care must be taken in selecting components and in the physical layout of the amplifier. Differences in capacitance between components and between the shield and the two sides of the amplifier can unbalance the circuits and thus be a cause of poor common mode rejection at high frequencies. The amplifier may be powered from a supply through a high impedance line using longitudinal chokes or it may be battery powered. Unfortunately, operational amplifiers having high bandwidths generally consume much more power than those having smaller bandwidths.

One of the chief advantages of using a lock-in-amplifier is that a high quality preamplifier, an effective signal processor, and dc offset for high resolution measurements are combined in one unit, thereby minimizing construction of special circuits and interfaces by the experimenter. There are, however, many alternatives to the use of a standard lock-in-amplifier that may be attractive, particularly if a separate preamplifier is required or if measurements are to be made above 100–200 kHz, which exceeds the range of most lock-in-amplifiers.

One possibility for high frequency measurements is to translate or heterodyne the signal

and the reference to a lower frequency where they can be processed by a conventional lock-in-amplifier or other measuring scheme. This can be an effective technique but care is required in design of the mixers to avoid overall nonlinear behavior of the system. If the S/N ratio in the system is high enough, synchronous detection may not be required and an ordinary high-frequency voltmeter and a phase meter can be used for measurement. Newer phase sensitive voltmeters use fast Fourier transform (FFT) signal processing to measure the fundamental component and some of its harmonics in either cartesian or polar form. Waveform processors and spectrum analyzers with similar capabilities are available. Some of these instruments can provide accurate results throughout the range of interest for geophysical model studies. Of course, such systems inherently reject noise except at the frequency of interest.

Digital oscilloscopes and waveform processors are used for transient measurements. Cultural noise is likely to be a much more serious problem in transient measurements than in frequency-domain measurements at selected discrete frequencies. To be suitable for model studies, time-domain processing equipment should be capable of stacking many transients to improve the S/N ratio. A trigger pulse is used to synchronize the oscilloscope or processor sweep to the transmitter. In making short-offset transient electromagnetic method (TEM) measurements, the range in amplitude of single transients may exceed the dynamic range of fast oscilloscopes and processors. The time range of interest can be covered by using low preamplifier gain for early times and a higher preamplifier gain for late times, provided the oscilloscope is protected from overload or can recover rapidly from overload when high preamplifier gain is used. Ketelaar and Pronker (1985) show an example of merging three short time windows to obtain a single long window.

As an alternative to use of lock-in-amplifiers, phase sensitive voltmeters, waveform processors, oscilloscopes, and similar devices, the signals may be amplified and digitized by a data acquisition system, and processed by a microcomputer (Burgett et al., 1981, Saito, 1984). Such systems can be developed relatively easily for low-frequency model measurements but sampling techniques are required for high-frequency measurements, due to the limited rate at which data can be transferred into a microcomputer and processed. Even if not used as a primary means of processing raw data, a microcomputer is an essential part of a model facility when a substantial quantity of data are collected. In the system outlined in Figure 16, a computer is used to collate, annotate, format, and store data. The computer can also drive a plotter that makes visual results rapidly available; and be used to control positioning and other components of the system such as the signal generators with computer interfaces that are designed for computer control. When the computer is used for position control, the independent position sensor shown in Figure 16 is redundant.

If the noise fields are relatively uniform throughout the working area of the model facility and a nearby location, noise cancellation can be used to improve the S/N ratio and to reduce the necessary dynamic range of the receiver system. Strangway (1966b) employed two coils, one of which was remote from the working area of the model. The circuits were designed so that the noise voltage induced in the remote coil canceled part of the noise voltage induced in the receiving coil. Spies (1979) used a remote coil in TEM model studies to reduce voltage spikes and external interference. Such cancellation techniques have not been widely used, perhaps because of a lack of spatial uniformity of noise fields in model facilities. Also, cancellation of high-frequency noise fields is likely to be difficult due to differing phase shifts in the signal and remote channels.

The stability and resolution of systems, such as the system illustrated in Figure 16 which electronically senses and measures the sum of the primary and secondary fields, has not previously been adequate for modeling high resolution airborne systems. Instrumentation for model studies of high resolution systems employs some of the techniques used in their field counterparts. One such technique is to employ a compensating or bucking loop placed near the receiving loop (Ghosh, 1972). The compensation loop is fed by current derived directly from the transmitter circuit. Passive circuits are used to adjust the current in the compensation loop so that the voltage induced in the receiving loop due to the primary field is completely canceled. This leaves only voltages due to the secondary field to be measured by the electronic circuitry.

Specific operational procedures must be developed for each model system. To illustrate

possible procedures, consider operation of a lock-in-amplifier system, such as that illustrated in Figure 16, for slingram modeling. First the coil assembly is positioned laterally or above the models or tank such that secondary fields are negligible. The signal generator is set to the desired frequency and the phase of the reference channel is adjusted so that the output from the quadrature channel is zero. Next the preamplifier gain and signal generator level are adjusted until the output of the in-phase channel reads positive full-scale, or another suitable reference value. If the reference is set at full scale and dc offset is then added to bring the reading back to zero, the instrument will measure  $Z/Z_0 - 1$  (see Frischknecht, 1988) over the range -1 to 1, which is adequate for most modeling. If greater resolution is desired, the preamplifier gain may be increased by a factor of, say 10, after the dc offset is adjusted, so that the range is now -0.1 to 0.1. It may be possible to increase the gain by 100 to operate over the range -0.01 to 0.01; generally lock-in-amplifiers are not sufficiently stable to operate with greater resolution. If dc offset is not available in the amplifier used, a reference value of one-half full scale may be used. To correspond to slingram readings, the measurements are divided by two, and one (or 100 percent) is subtracted from the result. Generally one or more traverses are made and then the setup procedure is repeated to make measurements at a new frequency. If the system is sufficiently stable, it may be possible to use predetermined phase and amplitude settings for each frequency. If computer control is available, adjustments of phase and amplitude can be made rapidly without direct operator intervention.

When a half-space or overburden is used in modeling loop-loop moving source systems, the range of vertical motion of the coil assembly may be insufficient to place the coil assembly out of range of conductive media. In this case the response of the half-space or overburden can be calculated using its measured conductivity and the system can then be adjusted to read this response when the targets are removed or when the coil assembly is moved laterally out of range of the targets. Similar procedures, in which the response of the half-space is calculated, can be used in modeling methods that employ fixed loop or wire sources, or uniform field sources.

The procedures outlined are quite efficient in obtaining profile data at a few frequencies but are tedious if measurements are to be made at many frequencies at only a few positions. If the system is very stable, measurements may be made at a number of frequencies without resetting. Later the data must be normalized at each frequency by the response obtained when the system is out of range of conductive material.

## Testing and Calibration

To ensure that accurate high quality data are collected, model systems must be tested and calibrated. First, individual components should be tested and calibrated to meet the manufacturers or experimenters specifications. Then the entire system should be tested and calibrated. Some problems, such as incompatibility between components or a poor S/N ratio, will be obvious when the system is assembled and tested. Other problems, such as generation of spurious fields or sensitivity to common mode voltages, may not be as obvious. In systems using a fixed source or a distance source, the primary fields should be carefully mapped throughout the working volume of the facility and compared with the expected fields. The sensitivity of the magnetic field sensors and measuring circuitry to spurious electric fields can be checked empirically by touching the coil and other components of the measuring system; little if any change in response should be seen.

Once initial testing is complete and any identified problems corrected, system performance should be verified by making measurements over models for which the response is known from calculations or from previous, calibrated, model measurements. For loop-loop systems a horizontal slab in air is a good model to use in checking the response at many frequencies, provided the horizontal dimensions are large enough for the slab to appear to be infinite for measurements made near its center. The resistivity of the slab must be known or measured

so that the response can be determined by calculation or from tables, such as those given for dipole sources in Frischknecht (1967). A thin metal sheet will serve as a slab if it is supported so that it is flat; but, to avoid small errors due to the finite thickness of the coils, it is best not to put the coils directly on the sheet. If the coils are placed on the surface of a thick slab, allowance should be made for the thickness of the coils; available programs for calculation of the response of a layered earth do not allow for coils with finite thickness. As a first approximation, the calculated position of the coils may be taken as the center of the actual coils. A thin vertical sheet or plate is another useful model. Profiles can be run above the sheet to make sure that the response varies correctly with distance. The response for a perfectly conducting vertical half-plane can be calculated from equations developed in Wesley (1958), or Grant and West (1965), or taken from results given in Grant and West (1965) or Ketola and Puranen (1967). Further information on the response of perfectly conducting half-planes and plates with finite conductivity is given in Frischknecht et al., 1988.

A conductive sphere is another model with known response that can be used to check a model system. Unfortunately spheres are somewhat difficult to machine or to construct by other methods. A long circular cylinder is a useful model if the primary field is uniform or if the source is approximately a line source. The responses of spheres and cylinders are discussed in the chapter on theory.

Frischknecht (1971, 1973) used a shorted loop in calibration of a uniform field system. If the axis of a closed circular single-turn loop is placed in the direction of a uniform field, the field at the center of the loop is

$$H = H_o - \frac{I}{2r}, \quad (61)$$

where  $H_o$  is the primary field,  $I$  is the current induced in the loop, and  $r$  is the radius. The current depends on the induced voltage  $i\mu\omega\pi r^2 H_o$ , and the loop impedance  $Z_\ell$ , so that

$$\frac{H}{H_o} = 1 - \frac{i\pi\mu_0\omega r}{2Z_\ell}. \quad (62)$$

The external inductance of a single turn loop is

$$L_{\text{ext}} = r\mu_0 \left[ \ln \frac{8r}{a} - 2 \right], \quad (63)$$

where  $a$  is the radius of the wire used. If the frequency is low enough for the current to be uniformly distributed the internal inductance is

$$L_{\text{int}} = \frac{\pi a \mu_0}{4\pi} \quad (64)$$

and the impedance of this element is  $i\omega L_{\text{int}}$ . If the frequency is sufficiently high for most of the current to be concentrated at the surface, the internal impedance of the wire is dependent on the skin depth  $\delta$ , and it has a resistive component,

$$Z_{\text{int}} = \frac{1 + i}{2\pi a \sigma \delta}. \quad (65)$$

At intermediate frequencies more general formulas involving Bessel functions must be used (see equation 72). The internal impedance is generally small compared to the external impedance and either equation (64) or (65) may be used with little error. The total loop impedance is

$$Z_\ell = i\omega L_{\text{ext}} + Z_{\text{int}} + Z, \quad (66)$$

where  $Z$  is the impedance of a resistor, inductor, or capacitor that may be placed in the loop to modify the current. The impedance of any added elements must be known at the frequencies that are used.

In some cases it may be necessary to calibrate a modeling system absolutely. An isolated loop or a long wire are suitable sources for which the primary magnetic field can be readily calculated. It is particularly easy to determine the response of a system to magnetic fields by placing the receiving coil at the center of a large loop driven with a known current. Electrode arrays for measuring electric fields in tanks may be calibrated by placing a known, isolated, voltage across the electrodes. Probes for measuring electric fields in air may be calibrated by placing them between two large metal plates and applying a known voltage across the plates. The separation between plates should be several times as great as the length of the probe. If the dimensions of the plate are much larger than their separation  $D$ , the field  $E$  near the center is almost  $E = V/D$ , where  $V$  is the applied voltage.

## Model Materials

### Properties of materials

As discussed previously, in most geophysical modeling, displacement currents should be negligible so the condition,  $\sigma >> \epsilon\omega$  or  $\sigma >> \epsilon/t$  must hold in all of the model materials over the range of frequencies and times used. Also, the magnetic permeability of model materials must be close to  $\mu_0$  unless high permeability targets are to be studied. Fortunately, it is seldom difficult to satisfy these two requirements in modeling induction prospecting systems. The principal concern in selecting materials for most modeling is finding materials with a wide range of conductivities so that the required conductivity contrasts in the model can be achieved. Generally, the materials should be electrically isotropic and linear and their conductivity should not vary with frequency or time over the ranges used. Important secondary criteria in the selection of model materials are strength, the ease with which the material can be formed, stability of properties with time and temperature, corrosive or toxic properties (particularly for liquids), and the cost.

Table 3 lists typical values for the conductivity of a number of modeling materials. Where only one value for a metal is listed, it represents the pure metal. The conductivity of alloys, carbon and graphite, and the various composites can vary considerably from the ranges of values or single values listed. Unless pure metals are used or the manufacturer can supply accurate information, the experimenter must measure the conductivity of model material.

For models in which country rock and overburden are neglected, metals are commonly used to simulate ore bodies or other good conductors. Aluminum is often used because it is light, fairly rigid, and is readily available in foil and a variety of stock sizes including sheets of large dimensions. Aluminum is highly conductive and may require the use of excessively low frequencies, unless used as thin sheets. Brass and bronze are less conductive than aluminum, are more malleable, and can be soldered or brazed readily to make complex models. Lead is roughly an order of magnitude less conductive than aluminum, is more malleable, and can be soldered when fabricating models from several pieces. However, lead is so heavy and soft that thin models made of lead may not support their own weight. To reduce the weight of 3-D models, Ketola and Puranen (1967) used hollow aluminum targets with walls several skin depths thick at the lowest frequency used; this technique is also particularly suitable for large lead models. Stainless steel is readily available in large sheets, as is aluminum, but it is much less conductive and is more rigid. So-called nonmagnetic stainless steels have relative magnetic permeabilities of about 1.001 to 1.003 which, for most purposes, is not significantly different from one. By using available metals, scale factors between 200 and 1000, and a frequency range of 100 to 20 000 Hz, the full range of induction numbers generally encountered in prospecting for conductive ore bodies in highly resistive surroundings can be covered.

**Table 3. Conductivity of model materials**

Material	Conductivity
Metals	S/m × 10 <sup>7</sup>
Aluminum	3.77
Aluminum, EC alloy (used for wire)	3.6
Aluminum, commercial alloys	1.22–3.60
Bismuth	.083
Brass, yellow (35% Zn)	1.56
Brass, red (15% Zn)	2.12
Bronze, phosphor	0.91–1.04
Copper	5.96
Copper, Int. Annealed Copper Standard	5.80
Lead	0.485
Magnesium	2.38
Manganese, $\alpha$	0.063
Manganin	2.27
Mercury	0.10
Solder (50/50)	0.68
Steel (0.63% C)	0.56
Steel, nonmagnetic stainless	1.35–2.34
Tin	0.91
Titanium	0.185
Type metal	0.31–0.50
Woods metal	0.23
Zinc	1.68
<b>Carbides, borides, semiconductors</b>	S/m
Carbon, petroleum coke	1.3–4.4 × 10 <sup>4</sup>
Chromium boride	4.8 × 10 <sup>6</sup>
Germanium	2 × 10 <sup>3</sup>
Graphite	0.7–1.6 × 10 <sup>5</sup>
Graphite, "Super Graph"	1.3–1.7 × 10 <sup>6</sup>
Molybdenum carbide, $\alpha$	2.2 × 10 <sup>6</sup>
Silicon	0.017–10
<b>Composites and mixtures</b>	
Aluminum foam	5 × 10 <sup>5</sup>
Epoxy, commercial silver loaded	1 × 10 <sup>5</sup> –1 × 10 <sup>6</sup>
Epoxy, commercial copper loaded	2.5 × 10 <sup>4</sup>
"Lay-up" resin, graphite flake loaded	0.0–2.0 × 10 <sup>3</sup>
Epoxy, graphite fiber loaded (along fibers)	1–1.5 × 10 <sup>4</sup>
Epoxy, graphite fiber loaded (across fibers)	0.5–70 × 10 <sup>2</sup>
Foam, graphite flake loaded	4 × 10 <sup>4</sup>
Grease, silver loaded	1 × 10 <sup>4</sup>
Grease, carbon loaded	1
Portland cement, graphite flake loaded	0–3.5 × 10 <sup>2</sup>
Wax, bronze loaded	100–1.25 × 10 <sup>4</sup>
Silicone rubber, silver loaded	1.3 × 10 <sup>5</sup>
<b>Liquids (S/m at 18°C)</b>	
Liquid	Weight percent
	5    10    15    20    25
NH <sub>4</sub> Cl	9.2    17.8    25.9    33.7    40.3
HCl	39.4    62.9    74.7    76.4    72.5
H <sub>2</sub> SO <sub>4</sub>	20.9    39.2    54.4    65.4    72.0
NaCl	6.7    12.0    16.4    19.6    21.4
CuSO <sub>4</sub>	1.9    3.2    4.2
NaOH	19.7    31.2    33.4    32.7    27.2

Sources: Handbook of chemistry and physics, 65th ed; Chemical Rubber Press, Electronic engineers handbook, 2nd ed; McGraw Hill, Spies (1980), and various manufacturers specifications.

Commercially available carbon or graphite may be used in place of metals. For the same mechanical scale factor the frequency must be increased by one or two orders of magnitude to account for the lower conductivity of these materials when they are used in place of metals. Large, tabular blocks and circular cylinders are available; sheets can be cut from large blocks. One serious disadvantage of carbon and graphite is that usually they are somewhat anisotropic, although some manufacturers can supply isotropic material. Typically, carbon and graphite tend to be isotropic in one plane and to have a different conductivity in the direction normal to this plane. In this respect they are similar to many rocks and, for some purposes, this property can be used to advantage in modeling. If we define the longitudinal or larger conductivity as  $\sigma_\ell$  and the transverse or smaller conductivity as  $\sigma_t$ , the coefficient of anisotropy  $\lambda$ , is

$$\lambda = \left( \frac{\sigma_\ell}{\sigma_t} \right)^{1/2}. \quad (67)$$

For cubes cut from extruded carbon cylinders, Forbes (1957) found values for  $\lambda$  ranging from 1.12 to 1.17 and Frischknecht (1973) found values ranging from 1.09 to 1.21. Although  $\lambda$  can be very large in natural samples, brochures indicate that it ranges between 1.1 and 2.2 in most industrial graphite. Forbes estimated the conductivity at 200 kHz of the carbon plates he used to be almost 25 percent less than at dc. Frischknecht (1971) found the conductivity of petroleum-coke carbon to vary no more than a few percent from dc to 500 kHz.

There are a number of other carbides and borides that have higher conductivities than graphite and carbon. Their cost probably excludes their use except for very small models.

A variety of other products are available that range in conductivity from about  $10^6$  S/m to essentially zero; most of them involve use of plastics. In the past decade much progress has been made in developing polymers that are inherently conductive (Seymour, 1981, Mascone, 1984, Chidsey and Murray, 1986). By doping with various ions, conductivities ranging from  $5 \times 10^2 - 10^6$  S/m have been achieved (Young, 1984). Polyacetylene, one of the first conductive polymers developed, shows considerable promise for application in light-weight batteries. Such materials are probably not readily available for use in the model laboratory now but offer considerable future promise.

There are many conductive materials that are best described as mixtures or composites. If a suitable plastic binder is loaded with enough conductive particles or fibers, some of the particles or fibers will touch each other and form continuous conducting paths through the material. Pritchett (1955) used bronze grindings in a mixture of red sealing wax and a high melting wax, and obtained a fairly uniform model having a conductivity of about  $1.25 \times 10^4$  S/m. With time the resistivity changed considerably, probably due to cold flow of the wax that allowed the bronze particles to separate from each other. Ordinary Portland cement and powdered or flaked graphite are suitable materials for making blocks of rather low conductivity. When sufficient graphite is used to make the conductivity greater than about 50 S/m, the material is very soft and flakes too easily to be of much use.

A variety of plastic materials including polyester, polyurethane, epoxy, polycarbonate foam, nylon, rubber, silicone, and ABS can be used as binders. Conductive particles or flakes may be made of silver, silver coated copper, copper, aluminum, nickel, stainless steel, carbon, and graphite. Conductive fibers are commonly carbon, graphite, aluminum, and boron/boron tungstate; the latter are not very conductive and may not be of interest in scale modeling. Conductive plastics are used commercially in adhesives, gaskets, RF shields and absorbers, enclosures for electronic equipment, and in high strength panels and other structural members.

There are a number of commercially available silver, copper, or nickel loaded epoxies that have conductivities in the same range as graphite and carbon. These materials are useful for joining pieces of graphite, carbon, and metal but are too expensive to use in making complete models. Rubber, vinyl, and silicone based materials loaded with carbon particles generally have conductivities under 100 S/m. They are available in sheets and are particularly useful in high-frequency modeling. Graphite fiber-epoxy composites are used to make high strength

panels for aircraft and structural members for a variety of purposes. Many authors including Volpe (1980), Bull et al. (1981) and Tse et al. (1981) have studied the electrical properties of these materials. The panels are particularly useful in scale modeling as rigid sheets having a much lower conductivity than metal sheets and a higher conductivity than conductive rubber or vinyl. Conductive materials used in electronic instrument cases, such as metal-loaded ABS, are probably not readily available to modelers in small quantities.

Large blocks of conductive plastic can be made by the experimenter without need for special facilities. Frischknecht (1971) used polyester resin ("lay-up" resin), such as is used in making fiberglass reinforced plastic structures, and flake or powdered graphite to produce conductive blocks and slabs ranging in conductivity from about  $10^1$ – $10^3$  S/m. In the process used, the resin was first mixed with its catalyst and then thoroughly stirred into the graphite with a "beater" attached to an electric drill. It was then tamped or pressed into a mold and allowed to set. Mylar sheet or PVC mold release was placed in the mold to avoid sticking. With some resins the normal proportion of catalyst to resin had to be greatly increased over normal use for the material to set up properly. Before it set up, the material was a very viscous sticky slurry if a relatively small amount of graphite was used; but it resembled sticky wet sand when a relatively large amount of graphite was added. Under compression the material became cohesive. The overall conductivity and the homogeneity of the final models depended strongly on the physical treatment in placing the material in the mold. In initial experiments, the material was tamped into molds by hand. The resulting models had a high conductivity rim around the edges of the mold and were rather inhomogeneous within the central part. In later work a press was used to squeeze the material into the mold and the central part of finished models was uniform in conductivity within 5 to 10 percent. The high-conductivity rim was cut away and all the surfaces sanded to remove the surface glaze before the model was used.

Duffin and Drinkrow (1976) carried out experiments using polyurethane and polyester resin as binders and zinc dust, graphite powder, and graphite flakes as conductive particles. Polyurethane was found to be unsuitable because it completely wet the particles and prevented electric contact between them. The zinc dust particles were apparently too small to establish adequate contact. Graphite powder and polyester resin produced conductive material that tended to be unstable under stress. Satisfactory models having conductivities ranging from 50 to 550 S/m were made using casting resin and "coarse" ground graphite. The models were cured under a pressure of about 7 kPa. A thin graphite-depleted and a thinner graphite-enriched layer were formed along the outer surfaces. After these layers were ground away the models were homogeneous and isotropic. In making resin-epoxy models at the University of California, Morrison et al. (1982) and W. D. Hansen (pers. comm., 1980) found that use of pressures as high as 10 000 kPa improved the conductivity and homogeneity of models.

A common feature of all plastics loaded with conductive particles is that once enough particles are used to establish conducting paths, the conductivity increases nonlinearly with particle content. Bigg (1979) and Davenport (1981) pointed out that fibers with a large length to cross-section ratio are much more effective in establishing conducting paths than short fibers or nearly equidimensional particles. However, long fibers may be broken in the fabrication process, thereby reducing their efficiency. In some composite materials the conductivity may change significantly with time, probably due to flexing and relaxation of the binder (Galli, 1982). Significant changes in resin loaded with graphite flakes have not been reported. When metal particles are used, oxide coatings must be removed before mixing with the binder to avoid high resistivity contacts between particles. Silver is often used for demanding applications because of its high conductivity and because clean surfaces can be maintained during fabrication. For the same reason silver plated copper particles and stainless steel fibers and particles are used.

Another possible approach to making models having conductivities less than that of metals is to use an aggregate of small metal spheres or disks that are insulated from each other. Tesche (1951) used spherical flasks filled with lead shot of various sizes to simulate spheres of various conductivities. He found that current flow between spheres was negligible due to the high contact resistance, and that the response of such an aggregate is then due to eddy currents induced in each shot. Mutual coupling between individual pellets was important and

was estimated by Tesche. Forbes (1957) used a planar array of small foil disks glued to a plastic sheet to make a poorly conducting thin sheet. These techniques are probably suitable only for modeling small spheres, disks, or similar objects; it has not been demonstrated that distribution of currents among small elements would produce the same magnetic fields as would eddy currents flowing in large paths were the elements connected. Forbes also made artificial thin sheets using rectangular arrays of resistance wire soldered at each joint. This technique has been extended to making artificial 3-D models. By making the structure sufficiently fine, such models are satisfactory for simulating conductors in the absence of host rock but this model is not satisfactory in tank modeling since it does not present the same surface impedance to the fluid as does the equivalent solid sheet or block.

Targets intended to simulate perfect insulators can be made of concrete, wood, plastic, or other materials. Porous material should be sealed to prevent changes in dimensions or conductivity when placed in the electrolyte. When placed in a conductive liquid, porous materials such as sand or plastic foam provide models having a conductivity less than that of the liquid itself.

Conductivities ranging from essentially zero to about 80 S/m can be obtained by use of aqueous solutions of salts or acids (Table 3). Acids have been used for modeling special shapes by placing the solution in a suitable container such as a tray or a spherical flask. Ammonium chloride solution was used by Goldstein (1971), Goldstein and Strangway (1975), and dilute hydrochloric acid solution was used by Gaur et al. (1972) and Leppin and Boldt (1978) to simulate a conductive half-space. Acid solutions are very corrosive and toxic so most investigators have used aqueous solutions of commercial salt (primarily NaCl) to simulate conductive half-spaces. Although less conductive than several other solutions, NaCl brine is not toxic or highly corrosive and is very inexpensive. Dry salt is most easily mixed by placing it in a relatively small container and pumping water through the container. If the salt is simply poured in a large tank, it requires a long time to dissolve. The temperature coefficient of NaCl brine is about 3 percent/ $^{\circ}\text{C}$ . This is not usually a serious problem except during the time required for a tank of freshly mixed brine to come to equilibrium with the laboratory conditions. Temperature gradients from top to bottom of the tank are likely to occur, and it is necessary to stir or circulate the solution to maintain uniform conductivity.

The dielectric constant of NaCl brine is nearly that of fresh water ( $\sim 80$ ) except at very high concentrations (King et al. 1981). If displacement currents in brine are to be negligible, the operating frequency must be limited. The allowable frequency depends both on the conductivity of the brine and the EM method being modeled. If displacement currents are included, the ratio of the electric to the magnetic field, or surface impedance, for a plane wave normally incident on a half-space is

$$\frac{E}{H} = Z_s = \left( \frac{i\mu_o\omega}{\sigma + i\epsilon\omega^2} \right)^{1/2}. \quad (68)$$

If displacement currents are negligible,

$$Z_{so} = \left( \frac{i\mu_o\omega}{\sigma} \right)^{1/2}. \quad (69)$$

The ratio  $Z_s/Z_{so}$  and the phase difference between  $Z_s$  and  $Z_{so}$  are plotted in Figure 12 for various values of conductivity. If, for example, the phase error is to be kept under 1 degree the frequency should not exceed 4 MHz for brine with a conductivity of 0.5 S/m, or 15 MHz for a conductivity of 2 S/m. Somewhat higher frequencies may be used before equivalent errors in amplitude are encountered. The converse is true for horizontal coplanar loop-loop measurements. Results for a horizontal coplanar configuration with a spacing of 20 cm are plotted in Figure 17 (see also Spies and Frischknecht et al., 1988). For a conductivity of 2 S/m, the error in amplitude exceeds 1 percent for induction numbers as small as  $B = 2$  (12.7 MHz) and is several percent or more at most higher frequencies. The phase error is small at  $B = 2$  but becomes large for values of  $B$  greater than about 4 (50.7 MHz). Curves

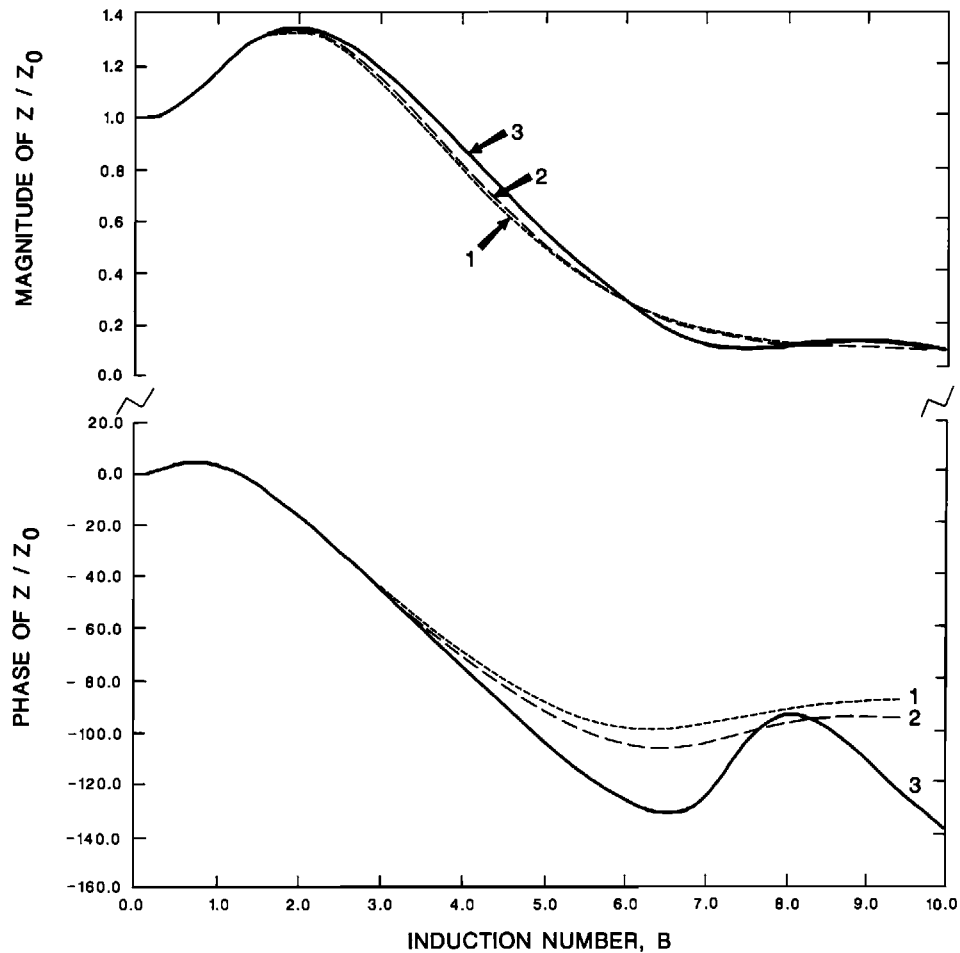


FIG. 17. Amplitude and phase of  $Z/Z_0$  for horizontal co-planar loop system at the surface of a half space having a conductivity of 4 S/m and dielectric constants of 1 (1) and 80 (2) and a half-space having a conductivity of 2 S/m and a dielectric constant of 80 (3).

for conductivities of 0.5 and 1.0 S/m were calculated but not included in Figure 17 because they fluctuate wildly. It is apparent that if displacement currents are to be negligible and if measurements at large induction numbers in the medium must be made using brine tanks, relatively high conductivities must be used.

In modeling problems where displacement currents are important and in which air is one of the media in the model, the dielectric constants of the model media must, according to equation (18), be the same as those of the full scale system. At radio frequencies the dielectric constant of aqueous solutions is generally higher than that of most earth materials. Annan et al. (1975) used an oil which had a lower dielectric constant (2.16) than most earth materials; in some experiments the oil was doped to increase its conductivity. There is a large variety of organic liquids which have dielectric constants in the range 4 to 30. However, most of these materials are probably too toxic or too expensive for use in large quantities in model studies.

The characteristics of the interfaces between materials of differing conductivity are a potential source of error in modeling. The interface between metallic conductors and electrolytes is more likely to be a problem than the interface between solid conductors. Although many aspects of the electrical behavior of the contact between metallic minerals and electrolytes have been understood for many years, the implications for geophysical scale modeling have often been ignored. The nature of the interface when metals or graphite are involved has

been studied extensively by electrochemists. Geophysical researchers have made extensive studies of interface phenomena when one side is a metallic mineral. In modeling resistivity and electromagnetic methods the interface between electrolytes and targets can be represented by a complex, frequency-dependent impedance paralleled by a double-layer capacitance (Sumner, 1976). The impedance and the capacitance are inversely and directly proportional, respectively, to the surface area of the contact. At the low current densities that are likely to exist in most model tanks (except near current electrodes) the electrical characteristics of interfaces are linear. If a sufficiently high-frequency is used, the combined impedance across the interface is small and can be ignored. At low frequencies the interface impedance is not necessarily small and its effect must be considered.

Electrolytic tanks have been used extensively for the study of boundary value problems in a number of disciplines where the fields obey Laplace's or Poisson's equations. Vitkovitch (1966) reviewed sources of error in using electrolytic tanks and described the work of a number of other authors in this field. A rigorous quantitative evaluation of the effect of interface impedance on scale model results would be more difficult than solving the original problem by numerical methods. In a study of interface impedance or electrode polarization and its effect on modeling, Einstein (1951) suggested expressing the voltage drop across the interface in terms of the thickness of a layer of electrolyte, having the same area as the interface, that would cause an equivalent voltage drop. He defined a "factor-of-merit" for electrode-electrolyte combinations as:

$$F = \frac{1}{d} = \frac{\text{electrolyte resistivity}}{\text{polarization impedance/unit area}}. \quad (70)$$

In resistivity modeling the surface of a metal or graphite target is approximately an equipotential surface and the direction of current flow near the surface is almost normal to the surface. Thus  $d$ , if a real quantity, is the distance by which the surface of the solid should be contracted to yield a smaller equivalent model, having zero contact impedance, that would produce the same galvanic response as the real model having finite contact impedance. Of course,  $d$  is generally a complex quantity and, in EM modeling, the surfaces of solid conductors are not necessarily equipotential surfaces. Nevertheless, comparison of the electrode impedance with the resistivity of a layer of the solution a useful concept.

Electrode impedance and capacitance depend on the composition of the solid and the electrolyte, the roughness of the solid, and the presence of oxide, grease, or other films on the surface of the solid. Reported values of interface capacitance (Delahay, 1965, Brodd and Hackerman 1957, McMullen and Hackerman, 1959) range from less than 1 to more than 100  $\mu\text{F}/\text{cm}^2$ ; most reported measurements are made under ideal conditions using weak electrolytes and may not be directly applicable to modeling problems. Frischknecht (1971) measured the impedance of the interfaces between graphite loaded epoxy and brine and carbon and brine using brine having a conductivity of about 4.20 S/m. Over the range of frequencies used, 20 Hz–40 kHz, the quadrature part of the impedance was larger than the in-phase part and both components decreased monotonically with frequency; at the highest frequency both components for both graphite-epoxy and carbon were less than 1 ohm/cm<sup>2</sup>. In resistivity modeling, high resistivity solutions should be used to make  $F$  (equation 70) as large as possible. In electromagnetic modeling, low resistivity solutions must be used to achieve sufficiently large induction numbers and  $F$  can be controlled only through proper selection of the solid materials.

Guptasarma (1983) made a study of polarization as it relates to resistivity modeling (see also Apparao, 1984, and Duckworth, 1984). He showed that, at low frequencies, an aluminum cylinder immersed in tap water behaves as an insulator rather than a conductor. He measured the amplitude and phase response over aluminum, copper, and stainless steel spheres and cylinders using a Wenner array. The results were expressed in terms of the characteristic frequency  $f_c$ , at which the phase response is a maximum and the ratio  $A_0/A_\infty$ , where  $A_0$  and  $A_\infty$  are the low-frequency and the high-frequency asymptotes of the magnitude of the apparent resistivity. Generally,  $f_c$  was considerably lower for copper than for the other two metals.

The value of  $f_c$  decreased with decreasing model size but not in direct proportion to model size. Guptasarma recommended that frequency dependence be investigated as part of resistivity modeling and that operating frequencies higher than  $20 f_c$  should be used. Unfortunately, if metals are used it may be difficult to satisfy this criteria and also keep the induction number for the targets negligibly small, as required in resistivity modeling.

Often there is a need to join various metal, graphite, carbon or composite models to make structures having complex shapes or internal resistivity contrasts. A good electric connection between parts can be achieved by soldering, brazing, or welding, when feasible, or by use of conductive epoxies or adhesives. However, if not properly formed, the joint itself may influence the results. To join blocks, the matching surfaces should be machined so that they fit closely together and then a thin layer of adhesive or solder should be used to establish electrical connection. The conductivity of the solder or adhesive need not closely match the conductivity of the blocks provided the connecting layer is much thinner than the blocks. Gaps in the film of solder or adhesive are, however, a potential source of error. Small screws or pins can be used for strengthening the assembly without introducing significant errors. If the structure is used in a solution, plastic screws are generally preferable to metal ones. Joining thin sheets is more difficult. If the edges are overlapped, the double thickness plus the solder or adhesive may allow a significant concentration of current unless the width of the splice is very small and only small amounts of additional material are used. Welding may cause a wider zone of discontinuity in properties than the use of adhesives and should not be employed unless the conductivity of the welded zone approximately matches the conductivity of the metal on one side or the other.

In modeling some problems it is desirable to use large volumes of rather low conductivity media in various regions in a tank. This can be done by using liquids of differing conductivity, provided they can be kept from mixing. Two or more immiscible liquids such as methyl-isobutyl-ketone and brine can be used to obtain a horizontally stratified medium. If nonhorizontal boundaries are required, solid barriers must be used to separate the liquids; ideally the barrier should have the same conductivity as the liquid on one side. Conductive rubber can be used as a barrier although it tends to develop a high surface impedance (Vitkovitch, 1966). Barriers consisting of rigid insulating sheets, which contain a grid of metal pins or rivets running completely through the sheet to provide conducting paths, have been used in electrolytic tank field plotting (Vitkovitch, 1966). Goldstein and Strangway (1975) used a metal fiber loaded epoxy sheet as a conductive boundary between two quarter-spaces. Benvenuti and Guzzon (1974) studied the effect of a vertical aluminum dike separating a region containing brine from a region containing clay saturated with brine. Possible problems with electrode impedance should be considered when barriers containing metal or graphite are used. Agar-agar gel can be used for one of the regions in a tank provided use of a semisolid is acceptable. Iizuka (1968, 1971) constructed a layer having varying conductivity by diffusing NaCl into the agar-agar.

### Measurement of properties of model materials

Unless accurate data are supplied by the manufacturer, the properties of model materials must be measured by the experimenter. In most geophysical modeling, the only electrical parameter of interest is the conductivity, although, for nonmetallic materials it may be necessary to determine if displacement currents are significant or if the conductivity is constant in the frequency range of interest. Stainless steels and brasses should be checked to make certain that they are nonmagnetic.

The simplest means of measuring the conductivity of materials such as graphite is to cut small bars from the model material. Measurements on bars cut in different directions, can be used to determine whether or not the material is anisotropic. In dealing with carbon, graphite and composite materials the directions of greatest and least conductivity are usually known. Bars can then be cut accordingly to measure the maximum and minimum conductivity. If the principal axes cannot be determined beforehand, use of expressions given by Kalenov (1957) can determine the parameters of a cube having faces cut at arbitrary angles with respect to the principal axes. To eliminate the effect of contact resistance, it is generally

necessary to use a four-terminal method.

Current may be supplied to the bar from a signal generator using wires attached to the ends of the bar with silver paint or other conductive adhesive. To make the current distribution more uniform near the ends of the bar, the entire end should be coated with a conductive film and, for large bars, several parallel wires should be attached. The current can be determined by measuring the voltage drop across a low-value resistor connected between the signal generator ground and one end of the bar. At low frequencies, the potential difference may be measured between one or more pairs of wires attached to the side of the bar using a battery operated voltmeter isolated from ground. If it is necessary to use high frequencies, potentials can be measured between wires placed at various distances along the block and a wire attached to the signal generator ground. The difference between these potentials is used in calculating the conductivity according to the formula

$$\sigma = \frac{I\ell}{A\Delta V}, \quad (71)$$

where  $I$  is the current through the bar,  $\Delta V$  is the potential difference between a pair of potential electrodes,  $\ell$  is the corresponding distance between potential electrodes, and  $A$  is the cross-sectional area of the bar. Step-down transformers are useful in driving large currents through low resistance models. If a sufficiently low frequency is used, the resistivity of entire elongated models that have uniform cross-sections can be measured by this technique. For equation (71) to be correct, the frequency must be low enough, in proportion to the size and conductivity of the bar, that skin effect and the inductance of the bar are negligible. The ratio of the ac impedance  $Z$ , to the dc resistance  $R_0$ , of a round bar of radius  $a$  is (Johnk, 1975)

$$\frac{Z}{R_0} = \frac{iq}{2} \left[ \frac{\text{ber}(q) + i \text{bei}(q)}{\text{ber}'(q) + \text{bei}'(q)} \right] \quad (72)$$

where  $q = \sqrt{2} a/\delta$ , ber and bei are the Kelvin functions of order zero, and ber' and bei' are their derivatives. The ratio  $|Z/R_0|$  does not exceed about 1.01 provided the induction number  $a/\delta$  is less than 0.7. However, if the phase of  $Z$  is measured to determine whether or not the material behaves as a pure conductor, the induction number must be considerably smaller than 0.7 or corrections using equation (72) must be made to avoid significant error.

The conductance of thin sheets, such as graphite cloth, can be measured by the same technique. For a long strip of width  $w$  the conductance  $S$  is

$$S = \frac{I\ell}{w\Delta V}. \quad (73)$$

Since sheets are often used in modeling, a technique devised by van der Pauw (1958, 1958–59) for measuring the conductivity of disks of uniform thickness, but arbitrary shape, is very useful. Four line electrodes are attached to the edge of the disk at arbitrary locations m, n, o, and p. Define the resistance  $R_{mn,op}$  as the potential difference  $V_p - V_o$ , between electrodes p and o, per unit current flowing between m and n. Define  $R_{no,pm}$  in a similar manner. Then the following relationship holds:

$$\exp(-\pi d\sigma R_{mn,op}) + \exp(-\pi d\sigma R_{no,pm}) = 1, \quad (74)$$

where  $d$  is the thickness of the disk.

Curves to aid in solving for  $\sigma$  from equation (74) are given in the papers by van der Pauw. For the special case where the disk has a line of symmetry, the conductivity can be obtained from a single measurement. Electrodes m and o are placed on the line of symmetry and n and p are placed symmetrically with respect to this line. For this case van der Pauw (1958–59) showed that

$$\sigma = \frac{\ln 2}{\pi d R_{mn,op}}. \quad (75)$$

Besides making measurements on small bar or disk samples of model materials, four-terminal measurements can be made directly on edges of flat surfaces of some models. By using electrode arrays with a small spacing, it is possible to determine the degree of homogeneity of the model. Of the various electrode configurations that might be used, the Wenner array is probably the most satisfactory for model measurements because  $\Delta V$  is larger and the ratio of the electrode contact area to electrode spacing is smaller than for other common arrays. Using the Wenner array with point electrodes, the "apparent" conductivity is defined as

$$\sigma_a = \frac{I}{2\pi a \Delta V}, \quad (76)$$

where  $a$  is the spacing between electrodes and where dc or a sufficiently low frequency ac current is used. For a homogeneous, isotropic, half-space, the apparent conductivity is the true conductivity. The Wenner array, using line electrodes rather than point electrodes, is useful in making measurements along flat edges of large slabs and sheets. The apparent conductivity for this array is

$$\sigma_a = \frac{2I \ln 2}{\pi \Delta V}, \quad (77)$$

where  $I$  is the current per meter length of the electrodes, or slab thickness, rather than the total current. Again, the apparent conductivity, given by equation (77), is the same as the true conductivity for infinite line electrodes on the surface of a half-space or for line electrodes across the edge of a semiinfinite slab.

Since models do not have infinite dimensions, either use sufficiently small electrode spacings so that equations (76) and (77) give the true conductivity without significant error, or apply correction factors to determine the true conductivity. For point electrode measurements made on the surface of an infinite, homogeneous, slab of thickness  $d$ , the true conductivity is given by

$$\sigma = \sigma_a M(a/d), \quad (78)$$

where  $M$  is a disturbing factor that depends on the parameter  $a/d$ . This disturbing factor may be calculated, if a program for Wenner resistivity sounding is available, or it may be taken from tables in many publications such as Keller and Frischknecht (1966).

For a line electrode Wenner array on one edge of a rectangular slab having an infinite length and finite width, the true conductivity is found, using results given in Peters and Bardeen (1930), to be

$$\sigma = \frac{2I}{\pi \Delta V} \ln \left[ \frac{\sinh(\pi a/d)}{\sinh(\pi a/2d)} \right]. \quad (79)$$

The ratio of apparent to true conductivity was calculated from equation (79) and is plotted in Figure 18 together with the equivalent curve for point electrodes on an infinite slab. These results can be used to determine the true resistivities for measurements made on slabs. It is important to note that the line electrode array is influenced significantly by the bottom of the slab at much smaller electrode spacings than is the point electrode array.

It is necessary to consider lateral boundaries as well as the bottoms of slabs. For a point electrode Wenner array oriented normally to the edge of a quarter space, the true conductivity is found by use of image theory to be

$$\sigma = \frac{I}{2\pi a \Delta V} \left[ 1 + \frac{1}{\frac{2x}{a} + 1} + \frac{1}{\frac{2x}{a} + 5} - \frac{1}{\frac{2x}{a} + 2} - \frac{1}{\frac{2x}{a} + 4} \right], \quad (80)$$

where  $x$  is the distance between the edge and the nearest electrode.

For a line electrode array oriented normally to a quarter space

$$\sigma = \frac{2I}{\pi \Delta V} \left( \ln 2 + \frac{1}{2} \left[ \ln \frac{\frac{2x}{a} + 2}{\frac{2x}{a} + 1} - \ln \frac{\frac{2x}{a} + 5}{\frac{2x}{a} + 4} \right] \right). \quad (81)$$

The ratio  $\sigma_a/\sigma$  was calculated from equations (76), (77), (80), and (81) for point and line electrodes and is plotted in Figure 19.

For a point electrode Wenner array oriented parallel to the edge of a quarter space at a distance  $x$ , the conductivity is

$$\sigma = \frac{I}{2\pi a \Delta V} \left[ 1 + \frac{2}{\left[ 1 + 4\left(\frac{x}{a}\right)^2 \right]^{1/2}} - \frac{2}{\left[ 4 + 4\left(\frac{x}{a}\right)^2 \right]^{1/2}} \right]. \quad (82)$$

If a point electrode Wenner array is oriented parallel to the edge of a very thin sheet the conductivity is

$$\sigma = \frac{I}{\pi \Delta V} \left( \ln 2 + \ln \left[ \frac{\left[ 4 + 4\left(\frac{x}{a}\right)^2 \right]^{1/2}}{1 + 4\left(\frac{x}{a}\right)^2} \right] \right). \quad (83)$$

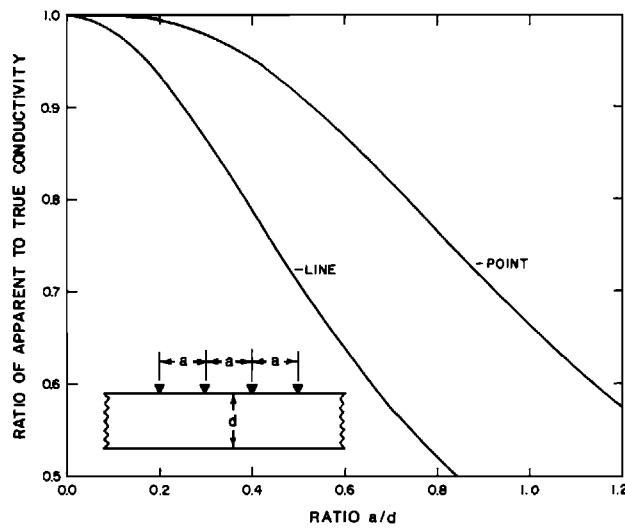


FIG. 18. Ratio of apparent to true conductivity for Wenner point and line electrode arrays on surface of a slab.

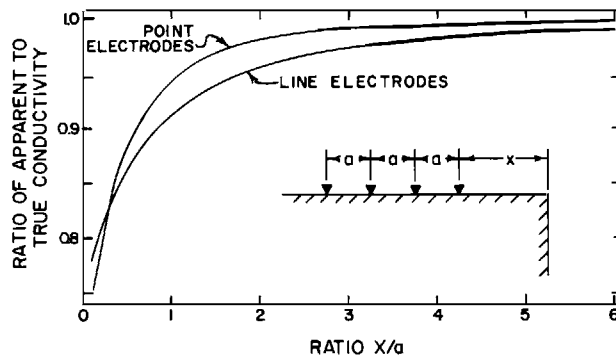


FIG. 19. Ratio of apparent to true conductivity for Wenner point and line electrode arrays normal to edge of a quarter space.

The ratio of apparent to true conductivity for these later two cases is plotted in Figure 20. For a point electrode array oriented parallel to the edge of a thick sheet, the conductivity is intermediate between the results given by equations (82) and (83). Equation (83) does not account for the effect of the opposite edge of a finite sheet. It should be noted that for an electrode array located along the midplane of a strip  $2x$  wide, the effect of two edges is more than twice the effect for one edge. In this case, two infinite sets of images must be considered. Smits (1958) gives correction factors for measurements made on rectangular and circular sheets and Uhlir (1955) gives correction factors for arrays placed near the corner of a sheet of finite thickness, for an array on one face of a square filament, and for other complicated problems.

Four-terminal measurements made on the face or edge of an anisotropic slab are, in general, a function of both the longitudinal and transverse conductance. For a slab, the longitudinal conductivity  $\sigma_\ell$  can be determined directly from line electrode measurements made along an edge. If a point electrode Wenner array is used on the surface of a homogeneous half-space having a conductivity  $\sigma_\ell$ , in the direction parallel to the surface, and a conductivity  $\sigma_t$ , in the transverse direction, the apparent conductivity depends on the coefficient of anisotropy  $\lambda$  (Keller and Frischknecht, 1966)

$$\sigma_a = \sigma_\ell / \lambda. \quad (84)$$

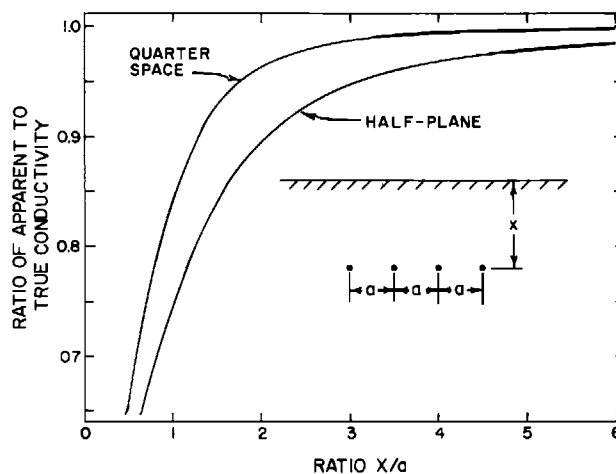


FIG. 20. Ratio of apparent to true conductivity for Wenner point electrode array parallel to edge of a quarter space and a half plane.

If measurements are made at sufficiently short electrode spacings for the slab to appear to be infinite in thickness,  $\sigma_a$ , for a slab can be calculated from measured values of  $\sigma_a$  and  $\sigma_\epsilon$  using equation (84). Alternatively, the electrode configuration may be expanded and  $\sigma_a$  plotted as a function of electrode spacing. Then by curve matching or computer inversion, the values for  $\sigma_a$ , corresponding to measurements made on an anisotropic half-space having the same conductivity as the slab, and  $d_a$  the apparent thickness of the slab, can be determined. The apparent thickness of the slab is related to  $\lambda$  by the expression

$$\lambda = d_a/d. \quad (85)$$

Thus,  $\lambda$  may be determined either from the apparent and true thickness of the slab or from the apparent and longitudinal conductivities.

The conductivity of a liquid in a tank can be measured readily by using a Wenner array at the surface. The same precautions should be observed as for measurements on solid samples. The use of electrodes that are too large or placing them too far into the solution can lead to significant error. The impedance of the voltmeter used for potential measurements must be high enough to not draw a significant amount of current through the electrodes. Commercial cells and equipment are available for measuring the conductivity of samples; both galvanic and induction techniques are used. Lacking a commercial cell and measuring apparatus, a simple cell can easily be constructed. A plastic or glass tube about one centimeter in diameter and several centimeters long is fitted with plates at each end for current electrodes. Two fine wires, suitably spaced, are run through the tube to serve as potential electrodes. The tube is fitted with liquid and measurements are made in the same manner as described earlier for a solid bar.

If the response of a simple conducting target such as a sphere, cylinder, or plate is known as a function of frequency, its conductivity can be determined directly from the scale model measurements. Electromagnetic soundings can be made over the center of a horizontal slab and then inverted to determine the longitudinal conductivity. The response for vertical half-planes and plates is also well known and can be used to determine their conductivity. If a uniform field is employed, the conductivity of long cylinders can readily be determined from model measurements (Frischknecht, 1973).

Most of the methods just described can be applied only at low frequencies, although they can be used on small bars at frequencies up to a few MHz. Generally these methods meet most needs in modeling induction systems. There is a large variety of radio frequency methods that can be used at higher frequencies to measure the properties of "lossy" dielectrics. At frequencies up to about 100 MHz the classical approach is to use two or three terminal capacitance cells and RF bridges. At higher frequencies, samples are placed in wave-guides or cavities and the resultant disturbances in transmission or resonant properties are measured using various microwave techniques. Microwave measurements are also sometimes made on samples in free space. Older high-frequency methods are described in Von Hippel (1954a,b). Afsar et al. (1986) reviewed current and older techniques and provided an extensive bibliography on RF and microwave measurements.

## Review of Model Studies

### Historical development

The use of scale model studies dates from the early years of electromagnetic exploration. Slichter (1932) measured the response of a spherical-shell and thin sheets in experiments conducted outdoors. Sundberg (1931) made measurements over a variety of metal and graphite models employing a large rectangular source loop and Sundberg and Hedstrom (1934) used scale model experiments to help develop interpretation techniques for a sounding method. A number of private and government organizations in Scandinavia and elsewhere made model studies during the 1930's and 1940's in support of exploration and research programs. Only a small amount of the early work was published, which continues to be true for more recent

work. The principles of electromagnetic similitude were known and employed in early studies; later the most commonly used references were Stratton (1941) and Sinclair (1948).

Starting in the early 1950's the amount of available scale model information, much of it in the form of post graduate theses, began to increase. Tesche (1951) developed instrumentation for operation at 200 kHz, made measurements over spheres and plates in free space, and analyzed some of the sources of errors in model measurements. Wait (1951) studied the coupling between grounded wires on a half-space at frequencies up to 5 MHz using a brine tank. Hansen (1953) studied the response of insulating cylinders in brine, and Forbes (1957) made measurements over conductors in brine. Forbes' measurements over a wire in brine clearly demonstrated the role of galvanic current, or current gathering in elongated conductors.

In the late 1950's and 1960's, a number of results for airborne EM systems were published (Hedstrom and Parasnis, 1958; Boyd and Roberts, 1961; and Patterson, 1961). These studies were made using models in air, except for a study by Gaur (1963) who measured response of the airborne "quadrature" system over carbon models immersed in a brine tank. Several sets of results useful in the interpretation of ground EM data were published in the 1960's. Examples are the work of Swanson (1961) for the vertical loop tilt-angle method; the work of Frischknecht and Mangan (1960), West (1960), Lowrie and West (1965), Strangway (1966a, 1966b), Ketola and Puranen (1967), and Nair et al. (1968) for the slingram method; the work of Bosschart (1964) for the turam method; and the work of Lin (1969) for the shootback method. In a chapter on electromagnetic methods, Ward (1967) included model curves for several methods taken in part from several unpublished studies by private organizations.

Starting in the mid 1960's, interest increased in the modeling of magnetotelluric and geomagnetic induction methods. Some of the model structures were metal sheets in air (Roden, 1964, Hermance, 1968). Rankin et al. (1965) and Dosso (1966) used brine tanks to simulate a half-space. As indicated by the list of References for General Reading, Dosso and co-workers have continued to make extensive use of scale model results in interpretation of geomagnetic induction data. Beginning in the early 1970's a number of papers on the slingram response of various targets in a conductive half-space were published (Frischknecht, 1971; Guptasarma and Maru, 1971; and Gaur et al., 1972).

One of the first model studies of a time domain method was that of Yost et al. (1952); they measured the response of a two-loop system over a stack of metal sheets. Model studies of the airborne INPUT method were carried out by Becker et al. (1972), Palacky (1972), Palacky and West (1973), Nelson (1973), and others. Spies (1977, 1980) studied coincident and two-loop transient methods using a variety of models including copper targets cast into type metal blocks. Burgett, et al. (1981) made time domain studies using a wire grounded to the model overburden as a source. Miles (1985) measured the transient response of carbon and graphite targets in brine using a large loop source.

Examples of available results for borehole EM are those in Woods (1975) and Woods and Crone (1980) for a transient method with a fixed source at the surface, those in Drinkrow and Duffin (1978) for a frequency domain moving-source probe, and those in Nevitt et al. (1985) for VLF system.

The studies mentioned in the preceding paragraphs are representative of what has been done and indicate some trends in model studies. However, a large number of other important and useful publications were not mentioned, including most of those not in English and many theses and reports not widely distributed. A number of papers and reports that contain model data but which are not specifically referenced in the text are listed as References for General Reading. Generally, papers in languages other than English were not included unless a suitable English abstract or translation is available.

### Examples of instrumentation and facilities

To illustrate implementation of some described techniques, salient aspects of a few specific model facilities are discussed and draw heavily on systems with which I have been involved. A sketch of the tank and source array used in Farstad (1970) and Frischknecht (1971, 1973) for VLF/MT studies is shown in Figure 21. Current from two different sources was driven in opposite directions through each array to generate a horizontal magnetic field in the region

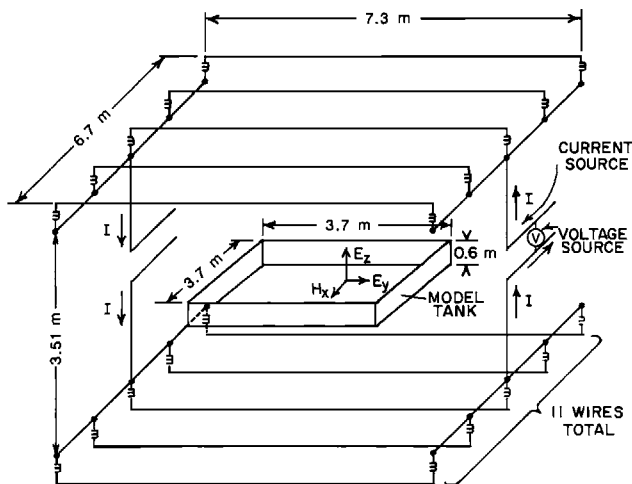


FIG. 21. Sketch of model tank and source arrays.

occupied by the tank. Inductor-resistor networks were placed in series with each wire so that the magnitude and phase of the current could be adjusted. More current was driven through the outer wires than the inner wires to improve the uniformity of the field. At the midplane between the two arrays, the vertical component of the primary field was zero and it was very small elsewhere in the vicinity of the tank. Along most of the path between the transmitter and the arrays, the feed lines for both arrays were run together so that their magnetic fields canceled. The vertical portions of the feed lines, illustrated in Figure 21, generated a non-uniform horizontal field that caused a variation of about 3 percent in the primary field over a distance of 2 m near the center of the tank.

The facility was located in a large two-story room in a reinforced concrete building. Noise from external sources was relatively low at frequencies of interest due to shielding by the steel reinforcing in the concrete. A small secondary field due to currents induced in the wall nearest the tank was observed. The horizontal component of this secondary field was of little significance but the vertical field was a nuisance even though its amplitude was less than 1 percent of the primary field. A single turn loop was placed on the supports for the array at the midplane of the tank and driven with a current of proper magnitude and phase to cancel most of the extraneous vertical field.

For most measurements, the bottom of the tank was lined with metal sheets to prevent fields from diffusing upward from the bottom. When filled with brine the surface impedance was constant within measurement error over the central  $2 \times 2$  m part of the tank. Farstad (1970) verified that the magnetic field behaved correctly with depth. Generally the conductivity of the brine was high enough to make the tank at least 2.5 skin depths deep. Although the impedance at the surface of the tank was correct, the horizontal electric field above the tank decreased rapidly toward the current array. This complicated measurements of horizontal electric field anomalies in air.

The vertical electric field is of some importance in VLF measurements, principally as the phase reference in airborne measurements. Locally the vertical field is distorted near the surface by topography but it is not much affected by changes in resistivity. For study of the vertical electrical field, a vertical electric field was generated simultaneously with the horizontal magnetic field by applying a voltage between the two arrays. In effect, the arrays acted as the plates of a capacitor. While this arrangement permitted study of perturbations in the electric field due to topography or changes in conductivity, it did not provide a true propagating wave. In the absence of targets, the phase of both the horizontal magnetic field and the vertical electric field were constant across the surface of the tank; whereas, the phase of a propagating wave would have varied.

All magnetic field measurements were made with a single receiving loop that could be

Downloaded 06/23/14 to 134.153.184.170. Redistribution subject to SEG license or copyright; see Terms of Use at <http://library.seg.org/>

oriented horizontally or vertically. The loop was 0.91 cm in diameter and 0.76 cm long, was wound with two pies of 40 turns each, and was shielded to produce a balanced coil as described in Section 6. The self-resonant frequency was about 20 MHz without leads attached. The probe for measuring electric fields at the surface of the tank consisted of three short, equally spaced, platinum wires attached to an acrylic tube. At 2 MHz the impedance between two electrodes was less than 100 ohms when the brine had a conductivity of about 3 S/m. Preamplifiers for the magnetic and electric probes consisted of single  $\mu$ A 733 differential input-output amplifiers in a shielded housing placed several centimeters from the probes.

A variety of designs were tested in developing a probe for measurements of electric fields in air. Problems were encountered with common mode voltages and the fact that dielectric materials as well as conductive materials distort electric fields in air. The best probe developed consisted of a  $\mu$ A 733 amplifier placed in a very small shield at the center of an 8 cm long dipole. The ends of the dipole were "loaded" with 1 cm diameter disks to increase the capacitance and thereby decrease the impedance of the dipole, which far exceeded the input impedance of the amplifier used.

Tuned longitudinal chokes, as described in the Transmission Lines section, were used at strategic locations in the lines between the preamplifiers and the measuring equipment. These chokes were wound with four strands to carry both signal and power wires. The common mode impedance was made greater than  $800 \text{ k}\Omega$  by tuning the chokes after they were installed in the lines. The signal from the line was passed through an isolation transformer and a broadband filter to a voltmeter and a phase meter. A reference signal for the phase meter was derived from a current transformer coupled to one of the wires in the arrays.

If this system were to be updated, an optical fiber link should be used to transmit signals from the preamplifier to the measuring equipment. The preamplifier and transmitter for the optical fiber link would be battery powered. More stable phase measuring equipment is now available. A digital data acquisition system and computer would greatly speed up data acquisition and processing.

In contrast to the source used in this study, many investigators employ a single array of overhead wires to generate uniform fields. Dosso (1966, 1973) and Benvenuti and Guzzon (1974) used large arrays with wires separated 1 cm apart. Later Dosso and coworkers (Ramaswamy et al., 1975) used only two wires, probably reflecting the fact that few wires are required to achieve a sufficiently uniform magnetic field at the surface of a conductive medium. Hermance (1968) employed an overhead coil wound to provide a field with a Gaussian distribution to simulate the equatorial electrojet. Spitta (1973) used a large rectangular coil in a study of the coastline effect using metal sheets in air. Baker and Myers (1979) used large Helmholtz coils as a source.

Most investigators use unshielded tanks. However, Dosso (1966) covered the floor of the tank with a layer of graphite blocks. Benvenuti and Guzzon (1974) covered both the bottom and the walls with thick aluminum plates.

Many MT and geomagnetic induction model studies have been made using frequencies no greater than 100 kHz. Although the medium is often concentrated brine ( $\sigma \approx 20 \text{ S/m}$ ), most tanks are not large enough to simulate a half space without using frequencies greater than 100 kHz. Thus, many available measurements are representative of an Earth in which the lower layer is either a good conductor or an insulator. If the tank is sufficiently deep compared with the dimensions of the targets used, the results are valid at low frequencies when the targets are near the surface and their dimensions are much less than a skin depth. In many low-frequency studies, tank walls may have had an influence on the results.

A concrete tank having dimensions  $3.65 \times 2.75 \times 1.5 \text{ m}$  is used by the U.S. Geological Survey (USGS) for finite source measurements (Frischknecht, 1971). Early measurements were made using a signal generator, power amplifier, and a single-component lock-in amplifier. The output from the amplifier drove the Y axis of an analog X-Y plotter. The X axis was driven by the voltage obtained from a multi-turn potentiometer connected to the carriage drawworks to obtain results in profile form. Olm (1981) used a data acquisition system consisting of a scanner to multiplex the signals from a two-component lock-in amplifier and a positioning potentiometer to a digital voltmeter and a microcomputer. The microcomputer was used to edit, process, and store data. It also drove a plotter to obtain rapid graphical

information. In a study of the two-frequency differencing technique Olm made measurements over multiple conductors in air over the frequency range 1.25–100 kHz.

Currently, the transmitter for FEM measurements in this facility consists of a frequency synthesizer and a pair of power voltage followers; the followers are placed in a small shielded enclosure directly on the carriage. Two two-component, lock-in amplifiers are employed, one for measurements to 100 kHz and the second for measurements between 100 kHz and about 1 MHz. A broadband preamplifier is placed on the carriage. Longitudinal chokes are placed in the signal and power cables between the carriage and the measuring apparatus. The data acquisition system is essentially the same as that used by Olm except that the frequency synthesizer is controlled by the computer and the vertical as well as one horizontal position of the coil assembly are sensed and recorded.

Guptasarma and Maru (1971) designed a phase sensitive system for measurements over the range 10–100 kHz. The horizontal position of the carriage was obtained from interruption of a light beam by a set of wires attached to the rails. A  $1.9 \times 1.13 \times 0.75$  m tank filled with brine was used to study the effect of host rock on the response of conductive targets. Gupta et al. (1980) made measurements using the same system operating at 60 kHz. Gaur et al. (1972) and Verma and Gaur (1975) used a bridge or ratiometer to measure in-phase and quadrature components at 100 kHz. Their tank had dimensions  $1.5 \times 1 \times 0.45$  m and they used a hydrochloric acid solution. The horizontal position was read from a scale attached to the rails.

Drinkrow and Duffin (1978) made in-phase and quadrature measurements for a coaxial borehole system using frequencies of 27 kHz and 90 kHz. A brine tank having dimensions  $3.65 \times 2.65 \times 2.6$  m was employed for some of the measurements. The motion of the probe was controlled by a computer. Measurements were recorded by a two pen X-Y recorder. Verma (1981) studied the response of folded conductors in air using a uniform primary field generated by Helmholtz coils. A compensator was used to remove the primary field and a phase detector measured in-phase and quadrature parts of the secondary field at 500 and 3 000 Hz.

Villegas-Garcia and West (1983) used a specially designed phase component meter capable of operating over the range 60 Hz–25 kHz. The analog voltages from the phase component meter were digitized and transmitted to a microcomputer. Stepping motors controlled by a microcomputer moved the coil assembly in all three directions. All information was transmitted from the microcomputer to a large minicomputer system.

Marcz et al. (1986) (see also Adám et al., 1981), described a system for measuring electric and magnetic fields about grounded electric dipoles and magnetic dipoles over the range 5 kHz to 5 MHz. The received signal was heterodyned down to 10 kHz and its amplitude and phase angle were measured by a voltmeter and phase meter. A photo-electric system provided trigger pulses for A/D conversion as the coil assembly was moved in either horizontal direction. Data were stored and processed using a microcomputer. A brine tank  $4.0 \times 4.0 \times 0.5$  m was used to simulate a half-space.

Miles (1985) made TEM measurements using the USGS tank described previously. The source was a  $60 \times 60$  cm, 5 turn, fixed loop driven by a pair of Darlington power transistors. Peak currents of about 22.5 amps were obtained from a storage battery. Current pulses were 500  $\mu$ s long and the repetition rate was 100 Hz. At turnoff, current fell from 90 percent to 10 percent of peak value in about 2.4  $\mu$ s. Measurements could be made within a few  $\mu$ s of the beginning of current turnoff but generally measurements started at about 16  $\mu$ s. The receiving coils were 1.75 cm in diameter and had 20, 100, or 400 turns depending on the required sensitivity. The coils were balanced and shielded and connected to a differential preamplifier. The feedback resistors in the amplifier were shunted by diodes to decrease the gain at high levels and thereby prevent saturation and slow recovery of the amplifier following turnoff of the primary field.

Measurements were made with a digital oscilloscope and system controller/computer. A scanner and digital voltmeter were used to digitize the outputs of potentiometers that sense the horizontal position and height of the receiving coil. Data for several stacks were averaged together and the results were edited, corrected for amplifier offset, plotted, and stored.

Miles (1985) made measurements over a variety of carbon and graphite targets in air and

over some of these targets placed under a conductive sheet or in a brine solution. For measurements made over brine the tank appeared as a half-space only at times shorter than a few  $\mu$ s. At later times the response of the tank decayed exponentially with a time constant of about 7.7  $\mu$ s. Although Miles scaled distance  $p$ , by a factor of 1 000 and time  $c$ , by a factor of 250, it is apparent that time should be scaled by a much larger factor for a tank of the size used to appear as a half-space over the entire time range of interest. The digital oscilloscope used was capable of working at much shorter times but difficulties with rapid turn-off of the loop current and characteristics of the preamplifier prevented working at shorter times.

Similar TEM measurements using a brine tank have not been reported in readily accessible literature. Spies (1979, 1980) used blocks of type metal to simulate a half-space. Because type metal is orders of magnitude more conductive than brine, a block of reasonable size can simulate a half-space without scaling time by a large factor. Recent TEM studies have been made over targets in air. Ogilvy (1983) used a field system for studies of the single-loop response of sheets and cylinders. Spies and Parker (1984) used a digital oscilloscope in making measurements over vertical aluminum sheets in electrical contact with a graphite slab overburden. In their study time was scaled by a factor of 1.4 to 4.1.

### Examples of results

Examples of scale model studies given in this section illustrate information obtained by physical modeling. The first examples (Figures 22–27) are results for targets in brine using a uniform primary field (Frischknecht, 1973). All of the measurements were made at a frequency of 2 MHz; the conductivity of the brine was about 3.35 S/m giving a skin depth of 19.4 cm.

Half-profiles of the normalized horizontal field at various heights over the center of a long cylinder placed 1 cm below the surface (Figure 22) show that the field attenuates much more rapidly with height above the surface than would the field from a current filament in free space. The reason for this is, although the cylinder carried large galvanic currents, there was a depletion of current in the medium surrounding the cylinder. Note that the effect of the cylinder was readily observed at a horizontal distance of 2.5 skin depths. A contour map of

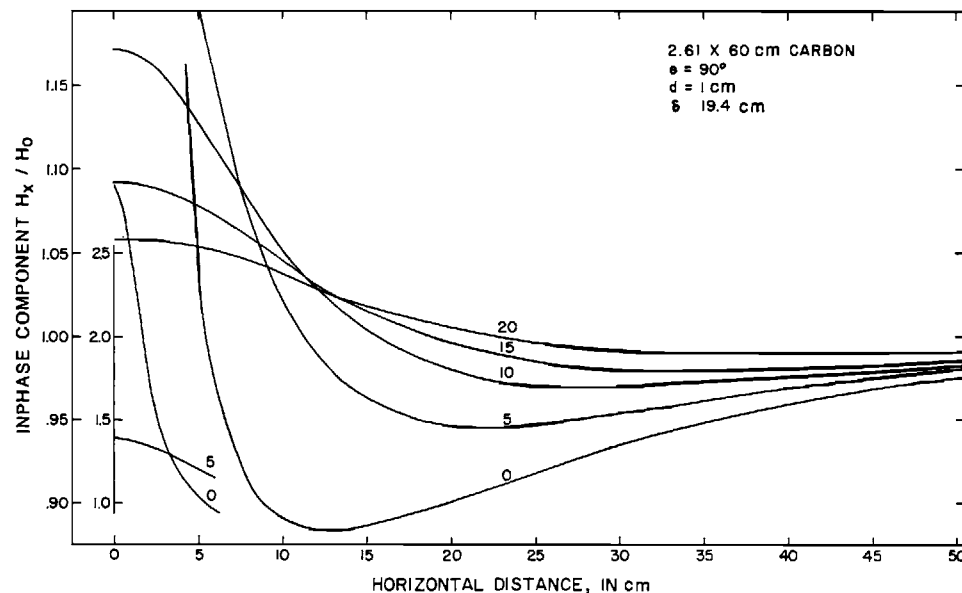


FIG. 22. Half-profiles of in-phase component of normalized horizontal magnetic field at various heights over a 2.61  $\times$  60 cm carbon cylinder 1 cm below surface in medium having a skin depth of 19.4 cm.

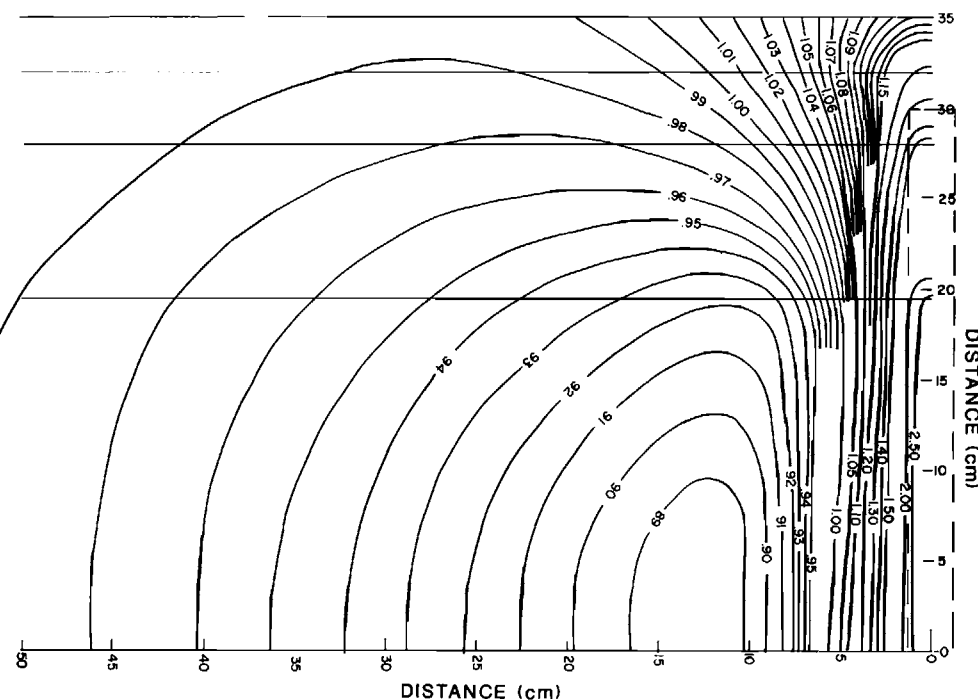


FIG. 23. Contour map of in-phase component of normalized horizontal magnetic field at the surface over a  $2.61 \times 60$  cm carbon cylinder.

the field at the surface (Figure 23) shows that the region of current depletion in the medium was greatest at a distance of more than half of a skin depth from the center of the cylinder. Due to the large current flowing between the medium and the end of the cylinder, the field in the medium near the ends of the cylinder was larger than the undisturbed field. The normalized field at a distance of 1 cm from the surface of the submerged cylinder has a value of nearly three whereas at the surface of a cylinder in air it has a maximum value of two.

Even at a single frequency the anomaly due to an elongated conductor is a complicated function of the length and depth of burial of the cylinder (Figure 24). Observe the difference in the anomaly, principally the phase angle, between the 120 cm and 180 cm long cylinders even though they are about 6 and 9 skin depths long, respectively; when the conductivity contrast is extremely large, a conductor must be extremely long to appear 2-D. Note that the sign of the imaginary component can be positive or negative depending on the conductor length and depth. This phenomenon is sometimes observed in VLF field results. Although the cylinders studied here are too thin to be realistic Earth models, similar behavior was noted for thicker models (Frischknecht, 1973).

In dc methods, saturation of the electric field response is observed at relatively low conductivity contrasts between the medium and the target. That is, if the contrast is large, there is little change in the anomaly if the contrast is increased. However, a study of cylinders of the same size but varying conductivity showed that when an alternating field is used the anomaly in the magnetic field changes over a very wide range of conductivity contrasts (Figure 25). Note that for the cylinder at a depth of 5 cm, the sign of the quadrature anomaly depended on the conductivity. The change in sign would probably occur at different depths for different conductivities of the media.

At the corner of a finite conductor, phenomena characteristic of both TE and TM excitation of a 2-D conductor were observed. In the vicinity of the end of the slab shown in Figure 26, current was diverted into the conductor causing lower than normal values for  $E$ , and corresponding low apparent resistivity. Around the corner where these currents reenter the medium, higher than normal electric fields were observed at the surface. Away from the

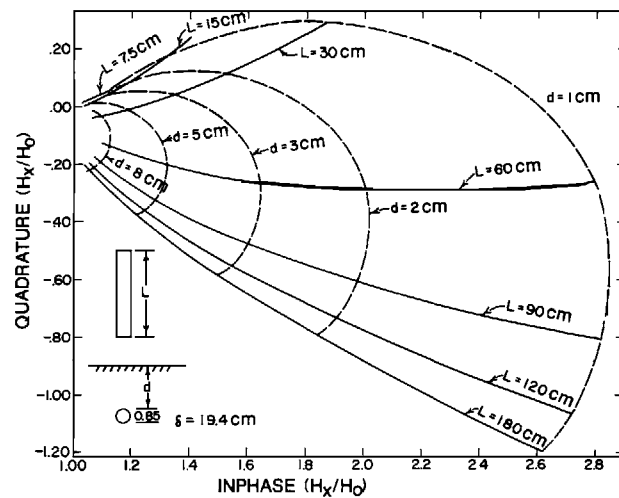


FIG. 24. Phasor diagram of peak values of normalized horizontal magnetic field over brass cylinders as a function of length  $L$  and depth  $d$  of burial.

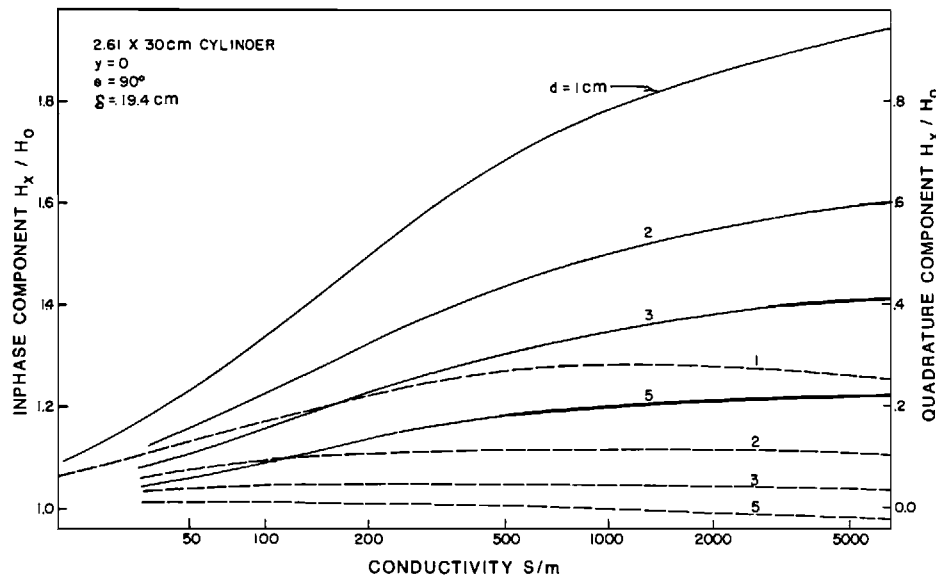


FIG. 25. Variation in in-phase (solid) and quadrature (dashed) horizontal magnetic field over  $2.61 \times 30\text{ cm}$  cylinders as a function of cylinder conductivity and depth.

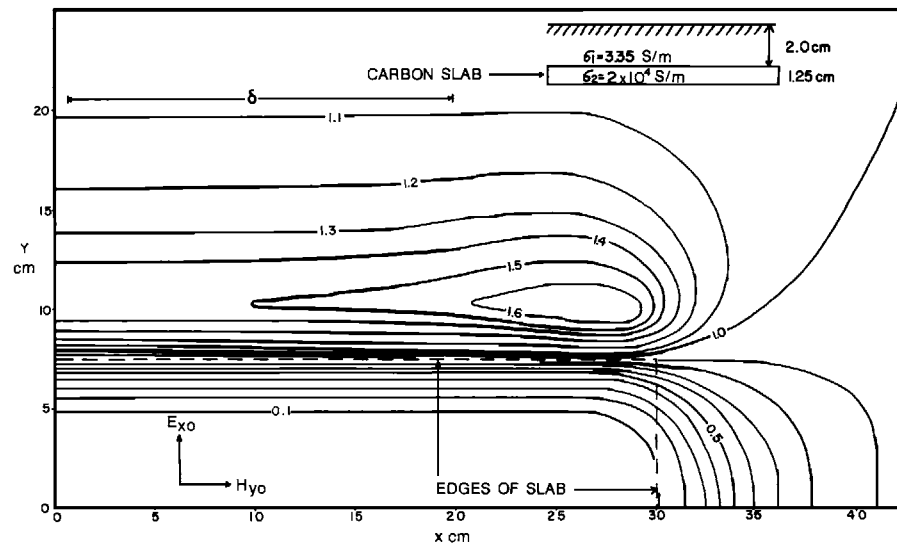


FIG. 26. Contour map of apparent resistivity from  $E_x/H_y$  over a  $1.25 \times 15 \times 60$  cm carbon slab.

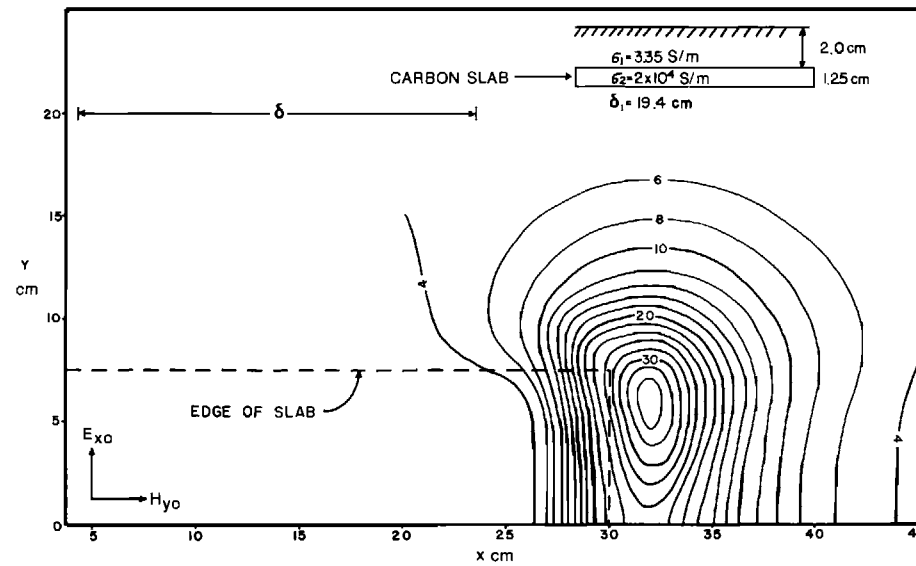


FIG. 27. Contour map of apparent resistivity from  $E_y/H_x$  over a  $1.25 \times 15 \times 60$  cm carbon slab.

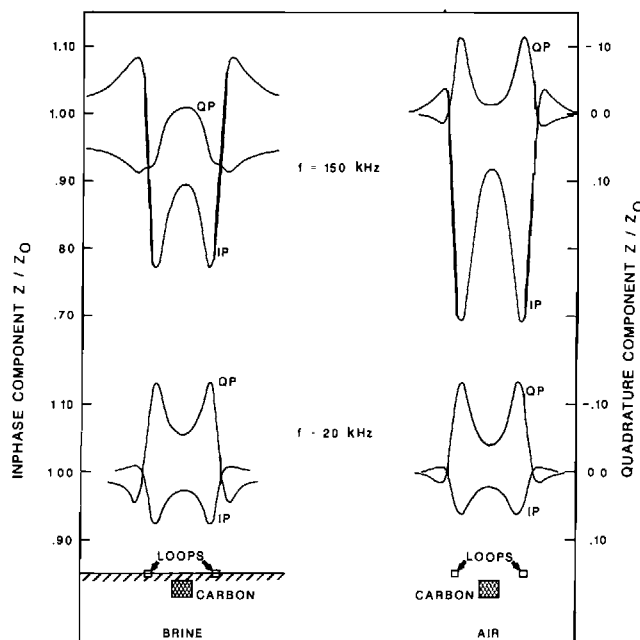


FIG. 28. HCP slingram response for  $5 \times 5 \times 30$  cm carbon prism ( $\sigma = 20,000$  S/m) in air and in a conductive medium (7.3 S/m).

corner of the conductor,  $E_y$  and  $H_x$  were zero. Near the corner both fields exist but  $E_y$  was relatively large compared with  $H_x$ , leading to large values of apparent resistivity based on the ratio  $E_y/H_x$  (Figure 27).

Results obtained using the USGS facility previously described illustrate some differences between plane-wave and finite-source methods. Generally, the importance of galvanic currents relative to vortex currents is less for finite sources than for uniform field sources. When the conductivity contrast between the target and host medium is high and the induction number in the host medium is low, there is little effect from galvanic currents, as indicated by the similarity in the horizontal coplanar (HCP) slingram results for 20 kHz in Figure 28. However, if the induction number in the medium is on the order of 0.3–0.4 or more, the host medium has substantial effect, even if the conductivity contrast is large. At 150 kHz the distribution and the magnitude of the quadrature currents were quite different for the target in a conductive host and in air. The amplitude of the in-phase minima was decreased but the flanking maxima were much larger and broader when the target was in a conductive medium. When the contrast between the host medium and the target is relatively small, the response is much more dependent on the medium. For the model illustrated in Figure 29, a small but easily observable anomaly was obtained when the target was in a conductive medium. However, when the target was in air, the response was less than 1 percent at 150 kHz and was too small to measure at 20 kHz with the system used.

The effectiveness of EM methods is often seriously limited by the presence of conductive inhomogeneous overburden. The problem can be studied using overburdens with controlled or arbitrary variations in conductance. The HCP slingram responses for an arbitrarily inhomogeneous overburden and the same overburden plus a target are shown in Figure 30. At high frequencies the edges of the overburden caused large anomalies; in complex field environments such edge anomalies can be mistakenly attributed to the existence of thin vertical conductors. At 150 kHz the quadrature component provided little evidence of the target. However, an experienced interpreter might recognize the significance of the in-phase anomaly. The situation is much improved by using lower frequencies; the existence of a conductive target should be clearly discerned from the results at 50 kHz and 15 kHz. Aside from shifting the background level of the response, the existence of host rock had little effect on this model

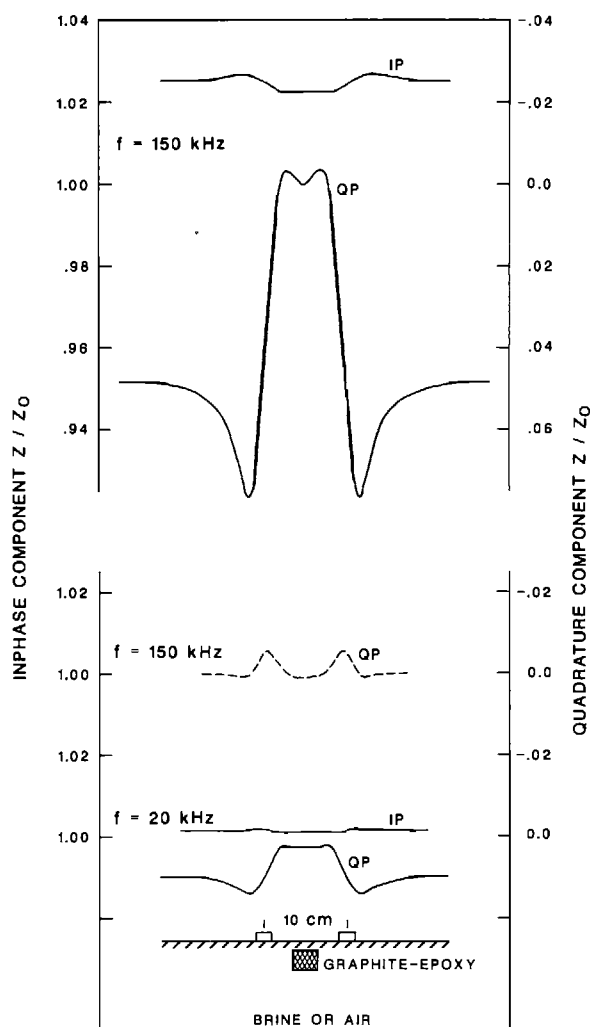


FIG. 29. HCP slingram response for  $5 \times 5 \times 30$  cm epoxy-graphite prism ( $\sigma = 55$  S/m) in air (dashed curve) and in a conductive medium (solid curve).

at low frequencies (Figure 31). At 150 kHz, presence of a host rock decreased the anomalies at the edge of the overburden slightly and increased the anomaly due to the target. In particular, a distinct quadrature anomaly was observed over the target when the host was present.

One of the more valuable uses of physical modeling is to compare results obtained with different methods over the same model. A SIROTEM field instrument (see Nabighian, 1988, appendix) was used to make the time domain measurements in Figure 32 and the system previously described was used to make the HCP slingram measurements. At the two higher frequencies the largest slingram anomaly was due to the edges of the sheet. Although the target produced a substantial slingram anomaly it would be difficult to recognize the target in field profiles if the overburden was somewhat inhomogeneous. The in-phase anomaly at the lowest frequency and the change in direction of the quadrature anomaly, which is characteristic of phase rotation through an overburden, are clues that might point to a correct interpretation. In contrast, the single loop TEM results clearly show the presence of a good conductor at the center of the profile. The edges of the overburden were indicated primarily by the early time profiles.

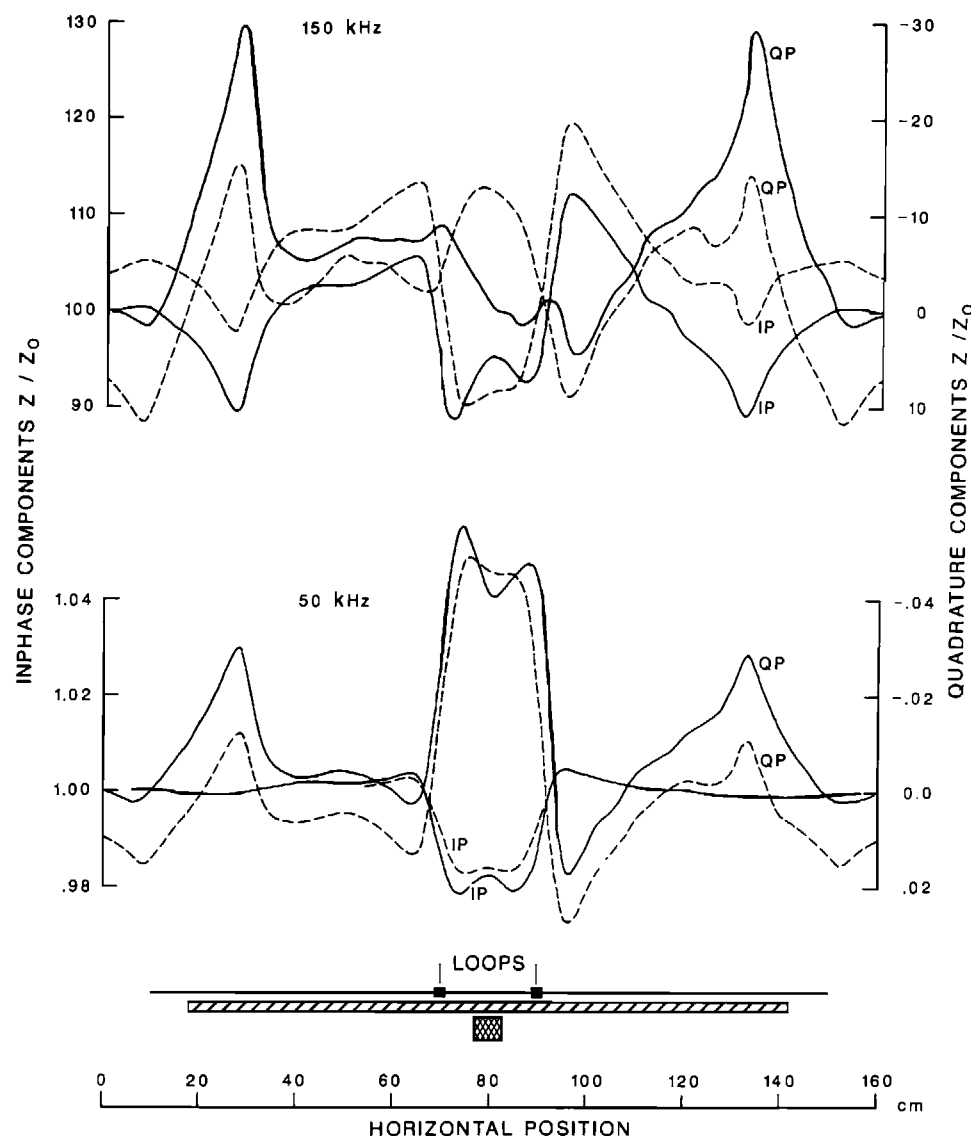


FIG. 30. HCP slingshot response for an inhomogeneous epoxy-graphite overburden (solid curve) and overburden and carbon ( $\sigma = 20\,000 \text{ S/m}$ ) target (dashed curve).

When a fixed source is employed, the response of a target is highly dependent on the position of the source, particularly when a conductive host rock is present. Miles (1985) studied the effects of position and strike length for models in a conductive medium excited by a fixed time domain source. When a cylinder was centered under the source its anomaly was almost the same whether it was in the conductive medium or in air. However, when the center of the source was offset 50 cm from the cylinder, a profound difference in the anomalies for brine and air was observed (Figures 33 and 34). Notice that when a conductive host was used the horizontal component profile at 16  $\mu\text{s}$  was nearly symmetric, indicating large unidirectional galvanic currents in the cylinder. However, when the cylinder was in air, the profile was asymmetric indicating the presence of vortex currents in the cylinder.

The effect on the early time (16  $\mu\text{s}$ ) response of changing the strike length of a long prism is illustrated in Figures 35 and 36. The differences in the anomalies are much greater than the differences in length. At 64  $\mu\text{s}$  the change in the anomaly with length was much smaller, only about 17 percent in going from a length of 100 cm to a length of 50 cm. The response at 64  $\mu\text{s}$  and later time as due primarily to vortex currents.

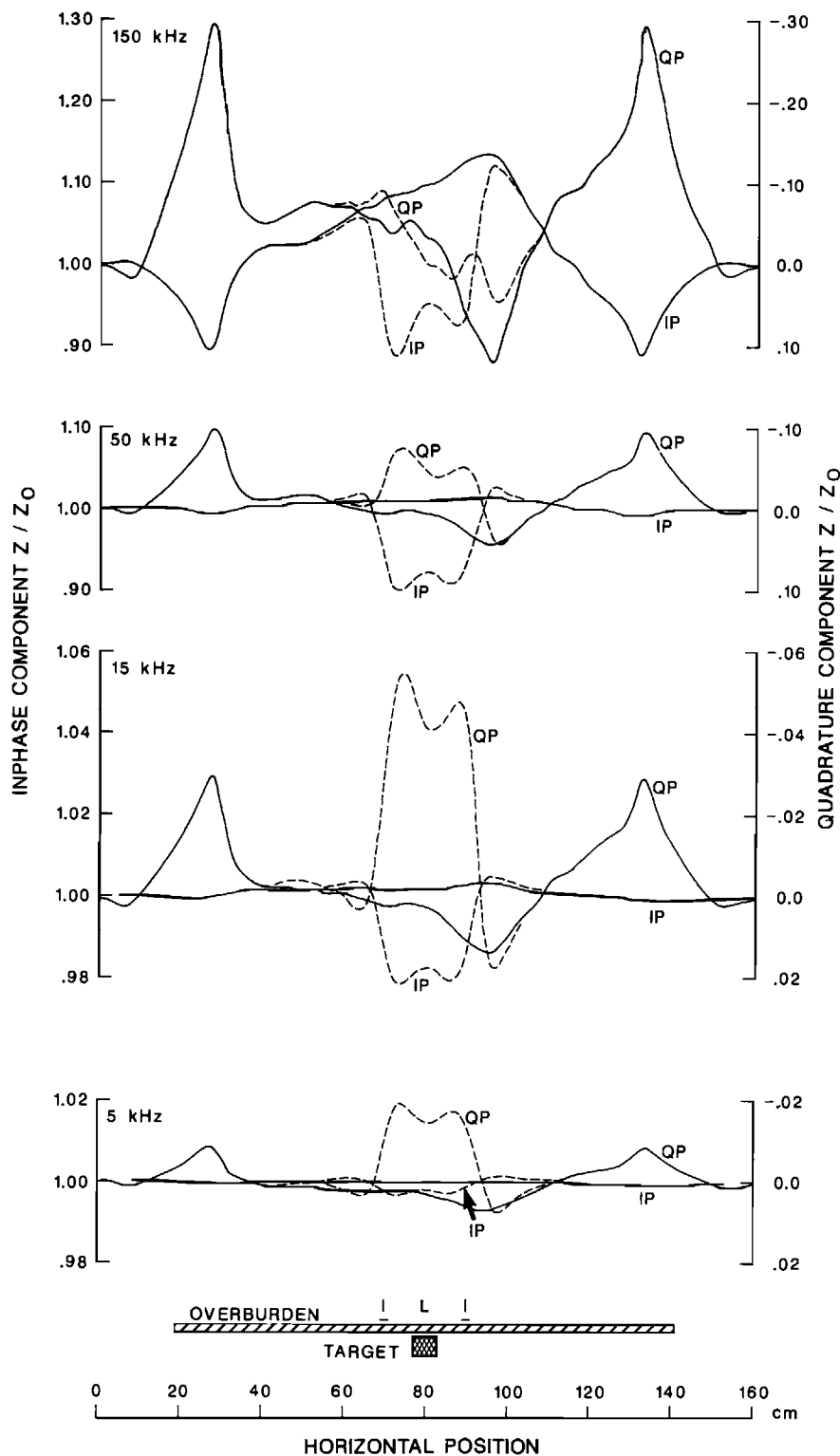


FIG. 31. HCP slingshot response for an inhomogeneous overburden and target without a conductive half-space (solid) and with a conductive ( $7.2 \text{ S/m}$ ) half-space (dashed curve).

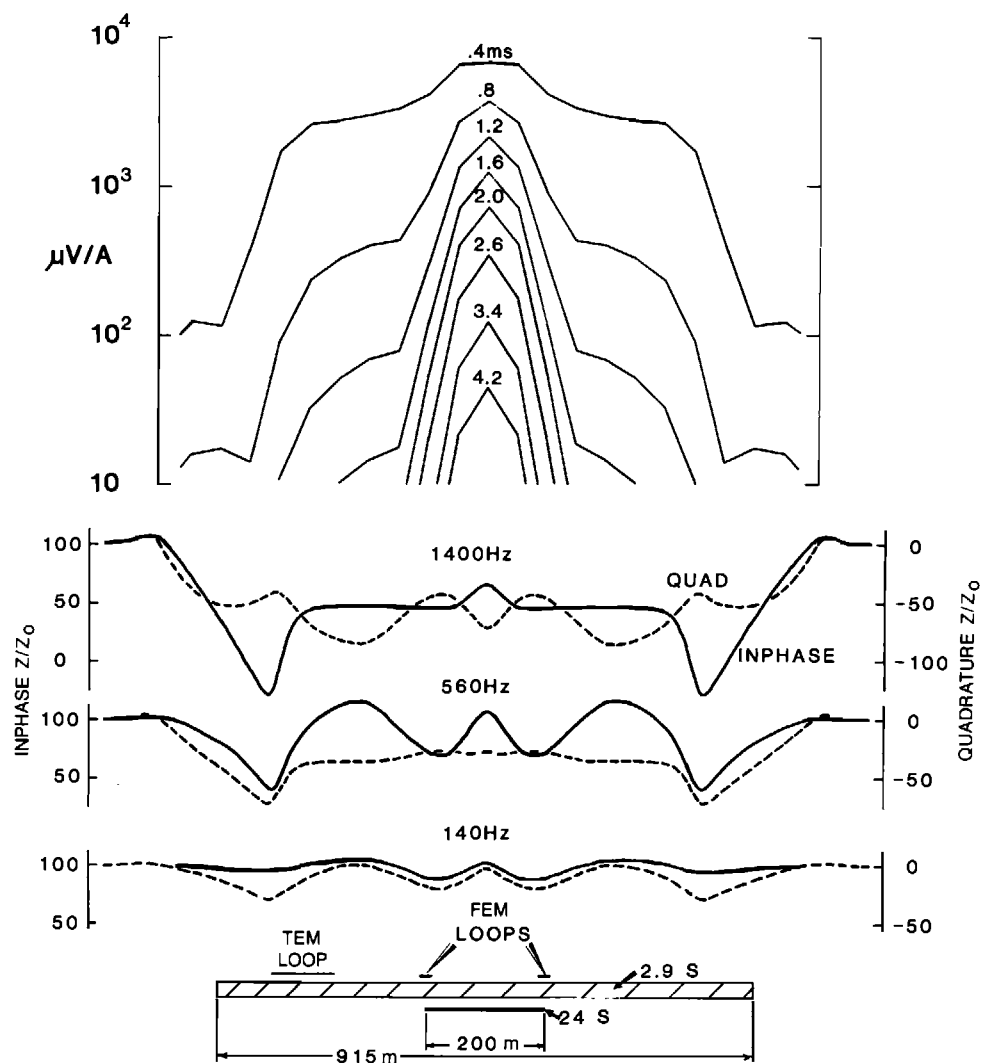


FIG. 32. HCP slingshot and single loop TEM responses over a flat-lying target under a conductive overburden.

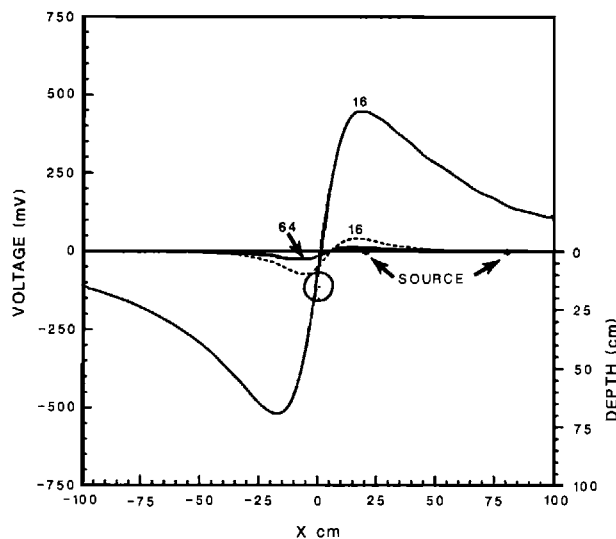


FIG. 33. Profiles of vertical component of  $\text{dB}/\text{dt}$  at 16 and 64  $\mu\text{s}$  over  $10.2 \times 207$  cm graphite cylinder in air (dashed curve) and in 21.4 S/m brine (solid curve).

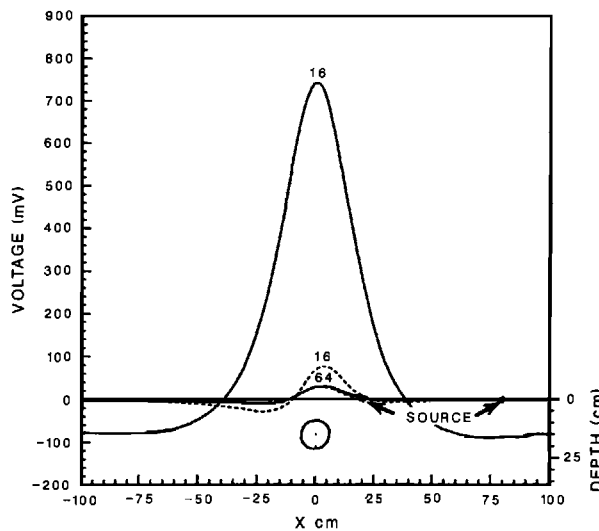


FIG. 34. Profiles of horizontal component of  $\text{dB}/\text{dt}$  at 16 and 64  $\mu\text{s}$  over  $10.2 \times 207$  cm graphite cylinder in air (dashed curve) and in  $21.4 \text{ S/m}$  brine (solid curve).

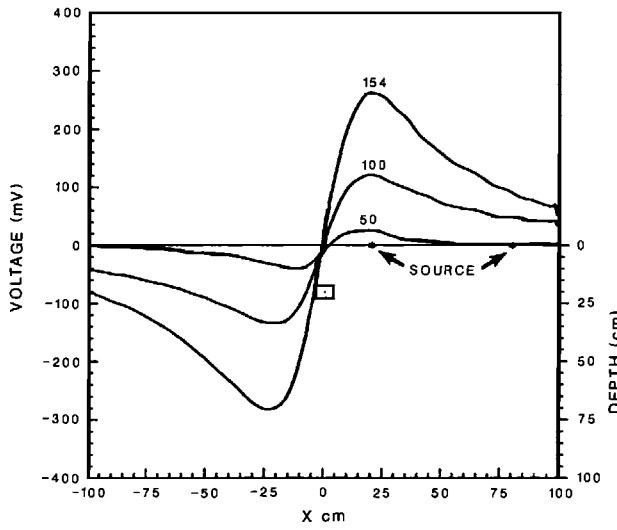


FIG. 35. Profiles of vertical component of  $\text{dB}/\text{dt}$  at 16  $\mu\text{s}$  over graphite prisms with cross sections of  $5.7 \times 8.2$  cm and various lengths in  $21.4 \text{ S/m}$  brine.

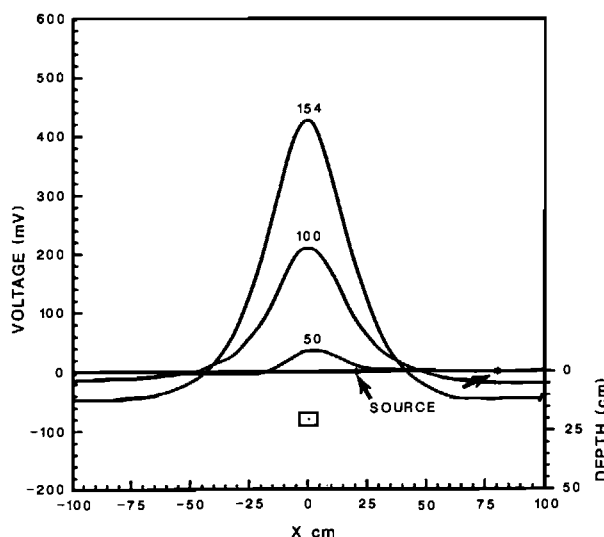


FIG. 36. Profiles of horizontal component of  $\text{dB}/\text{dt}$  at  $16 \mu\text{s}$  over a graphite prism with cross sections of  $5.7 \times 8.2 \text{ cm}$  and various lengths in  $21.4 \text{ S/m}$  brine.

## Discussion

In the last two decades improvements in instrumentation that can be used for scale model measurements have exceeded improvements in instrumentation for field measurements. Coupled with increasing availability of a wide range of model materials, realistic scale modeling of most electromagnetic induction problems of interest can be carried out. The most serious limitations in scale modeling are in simulating a half-space when modeling uniform field and TEM methods.

For many years scale model results for metal sheets in air were the main guides in interpretation of electromagnetic profiling in resistive environments. Scale modeling in which host rock and overburden are included can be very useful in interpretation of results in conductive environments. Unfortunately there are not enough published broadband studies in which overburden and a conductive half-space are included.

Due to the many advances in numerical modeling in the last decade and a half, numerical methods are sometimes more versatile and easier to use than scale model methods. In particular, 2-D structures and half-planes and plates are often more easily modeled by computer methods than by scale modeling. However numerical modeling of 3-D structures is still difficult. High conductivity contrasts, close proximity of boundaries to the source or receiver and odd shapes and attitudes of targets pose many difficulties in numerical modeling. On the other hand, high conductivity contrasts and odd shaped or multiple targets are easily handled in scale modeling. Also, relatively large computer resources, which are not available to many users, are required for 3-D modeling. Thus, 3-D modeling can often be done more easily, accurately, and inexpensively by scale modeling than by computer modeling. Also, scale modeling results are often valuable in checking new numerical results. With expected decreases in the cost of computer resources and improvement of numerical methods, it is likely that numerical modeling will ultimately replace scale modeling. However, scale modeling will probably remain an important technique for many years in solving certain classes of problems and in situations where necessary computer resources are not available.

The capabilities of equipment available for scale model studies will no doubt continue to keep up with the capability of field equipment. The most important advances in scale modeling are likely to be in computer control of the systems to obtain large amounts of data rapidly and in the use of new model materials.

## References

- Ádám, A., Pongrácz, J., Szarka, L., Kardovan, P., Szabadvary, L., Nagy, Z., Zimannyi, I., Kormus, I., and Régini, 1981, Analogue model for studying geoelectrical methods in the Geodetic and Geological Research Institute of the Hungarian Academy of Sciences: *Acta. Geodat. Geophys. et. Montanist.*
- Afsar, M. N., Birch, J. R., and Clark, R. N., 1986, The measurement of the properties of materials: *Proc., Inst. Electr. Electron. Eng.*, **74**, 183–199.
- Annan, A. P., Waller, W. M., Strangway, D. W., Rossiter, J. R., Redman, J. D., and Watts, R. D., 1975, The electromagnetic response of a low-loss, 2-layer dielectric earth for horizontal electric dipole excitation: *Geophysics*, **40**, 285–298. Response of electric dipole-dipole configuration at 5.9 GHz above a layered earth model.
- Apparao, A., 1984, Discussion on: "Effect of surface polarization on resistivity modeling" by D. Guptasarma with reply by author: *Geophysics*, **49**, 1808–1810.
- Baker, H. A., and Myers, J. O., 1979, VLF-EM model studies and some simple quantitative applications to field results: *Geexplor.*, **17**, 55–63. Measurements were made at 17 kHz over metal sheets immersed in brine. The primary field was generated by a submerged Helmholtz coil.
- Bansal, R., 1985, The measurement of the electric field on the surface above conducting objects immersed in a dissipative half-space: *Inst. Electr. Electron. Eng., Trans., Ant. Propagate.*, AP33, 1154–1157. Measurements over a disk in a tank at 300 MHz using electric dipole source and receiver.
- Bays, A. R., and Duckworth, K., 1983, A newly available scale modeling facility: *J. Can. Soc. Explor. Geophys.*, **19**, 67–74. Includes turam results over tabular conductors in brine.
- Becker, A., Gauvreau, C., and Collett, L., 1972, Scale model study of TDEM response of tabular conductors: *Can. Inst. Min. and Metallurg. Bull.*, **65**, 90–96. The response of the airborne INPUT system was studied.
- Benvenuti, G., and Guzzon, M., 1974, A magnetotelluric scale model: preliminary results: *Bollettino di Geofisica Teorica e Applicata*, **16**, 83–99. Measurements of the magnetic and electric field over a thick aluminum dike in a brine tank.
- Bigg, D. M., 1979, Mechanical and conductive properties of metal fiber-filled polymer composites: *Composites*, **10**, 95–100.
- Boschart, R. A., 1964, Analytic interpretation of fixed source electromagnetic prospecting data: Ph.D. thesis, Univ. of Delft. Extensive study of turam method using metal sheets in air.
- Boyd, D., and Roberts, B. C., 1961, Model experiments and survey results from a wing-tip-mounted electromagnetic prospecting system: *Geophys. Prosp.*, **9**, 411–420. Includes model results for a vertical coplanar loop airborne slingram system.
- Brodd, R. J., and Hackerman, N., 1957, Polarization capacity of solid electrodes and true surface area values: *J. of Electrochem. Soc.*, **104**, 704–709.
- Brown, G. L., and Gangi, A. F., 1963, Electromagnetic modeling of lithospheric propagation: *Inst. Electr. Electron. Eng., Trans., Geosci. Elect.*, GE-1, 17–23.
- Bull, D. A., Jackson, G. A., and Smithers, B. W., 1981, Radio frequency characteristics of carbon fibre composite materials: *The Radio Elect. Eng.*, **51**, 505–513.
- Burgett, J., Stoyer, C. H., and James, B., 1981, Modeling TDEM surveys [abs.]: *Geophysics* **46**, 468–469. The response of horizontal and vertical sheets beneath a conductive overburden were measured for a loop and a grounded wire source.
- Chidsey, C. E. D., and Murray, R. W., 1986, Electroactive polymers and macromolecular electronics: *Science*, **231**, 25–31.
- Davenport, D. E., 1981, Metaloplastics-high conductivity materials, in Seymour, R. B., ed., *Conductive polymers*: Plenum Press, 39–47.
- Dearth, L. C., 1978, Investigation of electrode materials for low frequency electric antennas in sea water: M.Sc. thesis, Naval Postgraduate School, available NTIS AD AO 66366.
- Delahay, P., 1965, Double layer and electrode kinetics: Interscience Publishers.
- d'Erceville, I., and Kunetz, G., 1962, The effect of a fault on the Earth's natural electromagnetic field: *Geophysics*, **27**, 651–665.
- Dosso, H. W., 1966, A plane-wave analogue model for studying electromagnetic variations: *Can. J. Physics*, **44**, 67–80.
- , 1973, A review of analogue model studies of the coast effect: *Phys. Earth Plan. Int.*, **7**, 294–302. Includes comparison of scale model and analytical results.
- Drinkow, R. L., and Duffin, R. H., 1978, Scale model results for inductive logging in the region of single and multiple conductive bodies: *Geophysics*, **43**, 804–810. Multi-frequency profiles were made in the vicinity of graphite and graphite-loaded resin models immersed in brine using a coaxial loop-loop configuration.
- Duckworth, K., 1984, Discussion on: "Effect of surface polarization on resistivity modeling" by D. Guptasarma with reply by author: *Geophysics*, **49**, 314–315.
- Duffin, R. H., and Drinkow, R. L., 1976, The construction of bodies of moderate conductivity for electromagnetic scale modeling experiments: *Bull. Austral. Soc. Explor. Geophys.*, **7**, 66–68.
- Edwards, R. N., 1980, A grounded vertical long-wire source system for plane wave magnetotelluric analog modeling: *Geophysics*, **45**, 1523–1529.
- Einstein, P. A., 1951, Factors limiting the accuracy of the electrolytic plotting tank: *J. of Appl. Phys.*, **2**, 49–55.
- Farstad, A. J., 1970, Surface impedance measurements for geophysical prospecting: M.Sc. thesis, Univ. of Colo. Comparison of response of slabs immersed in brine for uniform and dipole sources.
- Forbes, R. F. S., 1957, Modeling of the electromagnetic response of mineral bodies as a function of

- conductivity: Ph.D. thesis, Univ. of Calif., Los Angeles. The response of carbon and wire grid models in air and a few models in brine are given.
- Frischknecht, F. C., 1967, Fields about an oscillating magnetic dipole over a two-layer earth, and application to ground and airborne electromagnetic surveys: Colo. Sch. Mines Quart., **62**, 326.
- , 1971, Electromagnetic scale modeling, in J. R. Wait, ed., *Electromagnetic probing in geophysics*: Golem Press, 265–320.
- , 1973, Electromagnetic scale model study of geophysical methods using a plane wave source: Ph.D. thesis, Univ. of Colo.
- , 1988, Electromagnetic profiling with dipolar source, in Nabighian, M. N., ed., *Electromagnetic methods in applied geophysics*, Vol II: Soc. Explor. Geophys., in preparation.
- Frischknecht, F. C., and Mangan, G. B., 1960, Preliminary report on electromagnetic model studies: U.S. Geol. Surv. Open-File Rept. A collection slingram and turam curves for metal models in air.
- Galli, E., 1982, Carbon blocks: Plastic Compounding, **5**, 22–32.
- Gaur, V. K., 1963, Electromagnetic model experiments simulating an airborne method of prospecting: Bull., Nat. Geophys. Res. Inst., **1**, 167–174. A few curves for the response of the airborne quadrature system over carbon sheets placed in brine are given.
- Gaur, V. K., Verma, O. P., and Gupta, C. P., 1972, Enhancement of electromagnetic anomalies by a conducting overburden: Geophys. Prosp., **20**, 580–604. Results at 100 kHz for HCP, VCP, and VCA configurations over graphite, copper, and perspex sheets and an aluminum sphere in an HCl solution.
- Ghosh, M. K., 1972, Interpretation of airborne EM measurements based on thin sheet models: Ph.D. thesis, Geophysics Laboratory, no. 4, Univ. of Toronto. Includes many results for both helicopter and fixed wing airborne systems.
- Goldstein, M. A., 1971, Magnetotelluric experiments employing an artificial dipole source: Ph.D. thesis, Univ. of Toronto. Includes CSAMT measurements made over the boundary between quarter-spaces and over a block in NH<sub>4</sub>Cl solution.
- Goldstein, M. A., and Strangway, D. W., 1975, Audio frequency magnetotellurics with a grounded wire source: Geophysics, **40**, 669–683. CSAMT measurements for a half-space and two quarter spaces using NH<sub>4</sub>Cl solution and a wire-loaded epoxy separator.
- Goudswaard, W., 1957, On the effect of the tank wall material in geoelectrical model experiments: Geophys. Prosp., **V**, 272–281.
- Grant, F. S., and West, G. F., 1965, *Interpretation theory in applied geophysics*: McGraw Hill Book Company, Inc.
- Greene, F. M., 1967, A new near-zone electric-field-strength meter: J. Res., Nat. Bur. Stands., **71C**, **1**, 51–57.
- , 1975, Development of electric and magnetic near-field probes: Nat. Bur. Stands. Tech. Note 658.
- Grover, F. W., 1946, *Inductance calculations*: D. Van Nostrand Company, Inc.
- Gupta, O. P., Joshi, M. S., and Negi, J. G., 1980, Scale model electromagnetic response to inline and broadside systems at skew traverses of a dipping half plane embedded in a conducting host rock: Geophys. Prosp., **28**, 119–134. Single frequency horizontal coplanar profiles over a stainless steel sheet in air and in brine.
- Guptasarma, D., and Maru, V. M., 1971, A study of some effects of a conducting host rock with a new modeling apparatus: Geophysics, **36**, 166–183.
- Guptasarma, D., 1983, Effects of surface polarization on resistivity modeling: Geophysics, **48**, 98–106.
- Hansen, D. A., 1953, Electromagnetic prospecting with application to ground water problems: Ph.D. thesis, Univ. of Calif., Los Angeles. Contains curves giving the radial field about a horizontal loop over insulating cylinders placed in a conductive solution.
- Harrison, R. P., and Lewis, E. A., 1965, A method for accurately measuring the vertical electric field strength of a propagating VLF wave: Int. Electr. Electron. Eng., Trans. Instr. and Measurement, **IM-14**, 89–97.
- Hedstrom, 1940, Phase measurements in electrical prospecting: Am. Inst. Min. Metalurg., Trans. **138**, 456–472. Includes phasor diagrams for thin and thick sheets using a long wire source.
- Hedstrom, E. H., and Parasnis, D. S., 1958, Some model experiments relating to electromagnetic prospecting with special reference to airborne work: Geophys. Prosp., **6**, 322–341. Gives interpretation curves for rotary field airborne method based on metal models in air.
- Hermance, J. F., 1968, Model studies of the coast effect on geomagnetic variations: Can. J. of Earth Sci., **5**, 515–522.
- Hoversten, G. M., and Morrison, H. F., 1982, Transient fields of a current loop source above a layered earth: Geophysics, **47**, 1068–1077.
- Iizuka, K., 1968, An agar-agar chamber for the study of electromagnetic waves in an inhomogeneous medium: Tech. Rep. 565, Div. Engr. Appl. Phys. Harvard Univ.
- , 1971, An agar-agar chamber for the study of electromagnetic waves in an inhomogeneous medium: Int. Electr. Electron. Eng. Trans., Ant. Propag. AP-**19**, 365–377.
- Johnk, C. T. A., 1975, *Engineering electromagnetic fields and waves*: John Wiley & Sons.
- Kalenov, E. N., 1957, Interpretation of vertical electric sounding curves (in Russian): Gostoptekhizdat.
- Keller, G. V., and Frischknecht, F. C., 1966, *Electrical methods in geophysical prospecting*: Pergamon Press.
- Ketelaar, A., and Pronker, W., 1985, A simple time-domain EM modelling system: First Break, **3**, 17–21.
- Ketola, M., and Puranen, M., 1967, Type curves for the interpretation of slingram (horizontal loop) anomalies over tabular bodies: Geol. Surv. of Finland Rep. of Invest. 1. Contains extensive results for the slingram method for metal sheets placed in air.

- King, R. J., 1965, An amplitude and phase measuring system using a small modulated scatterer: *The Microwave J.*, **8**, 51, 95–98.
- , 1978, *Microwave homodyne systems*: Peter Peregrinus Ltd.
- King, R. J., and Maley, S. W., 1966, Model experiments on propagation on groundwaves across an abrupt boundary at oblique incidence: *Radio Sci.*, **1**, 111–115.
- King, R. W. P., and Harrison, C. W., 1969, *Antennas and waves: A modern approach*: The M.I.T. Press.
- King, R. W. P., and Smith, G. S., with Owens, M., and Wu, T. T., 1981, *Antennas in matter*: The M.I.T. Press.
- Leppin, M., and Boldt, B., 1978, Modellversuche zur elektromagnetischen induktion in langgestreckten strukturten: *J. Geophys.*, **44**, 557–566. Measurements of apparent resistivity and induction arrows over graphite cylinder in HCl solution.
- Lewis, R., and Lee, T., 1978, The transient electric fields about a loop on a halfspace: *Bull. Austr. Soc. of Explor. Geophys.*, **9**, 173–177.
- Lin, W., 1969, A model study of the Crone Shootback EM method: Thesis, Univ. of Calif., Berkeley. Gives multi-frequency measurements for shootback method over sheets, disks, and cylinders placed in air.
- Lowrie, W., and West, G. F., 1965, The effect of a conducting overburden on electromagnetic prospecting measurements: *Geophysics*, **30**, 624–632. Phasor diagrams and profiles for the slingram method using an aluminum sheet to simulate a conducting overburden.
- März, G., Pongracz, J., and Szarka, L., 1986, Electromagnetic scale modelling instrument for geological prospecting: *Scientific Instrumentation*, **1**, 119–133.
- Mascone, C. F., 1984, Progress sparks interest in conductive plastics: *Chem. Eng.*, **91**, 25–29.
- McMullen, J. J., and Hackerman, Norman, 1959, Capacities of solid metal-solution interfaces: *J. of Electrochem. Soc.*, **106**, 341–346.
- McNeil, D., 1980, Electromagnetic terrain conductivity measurements at low induction numbers: Geonics Ltd., Technical Note TN-6.
- Meade, M. L., 1983, Lock-in amplifiers: principles and applications: Peter Peregrinus Ltd.
- Miles, T. O., 1985, Physical model studies of the turam time domain electromagnetic method in mineral exploration: M.Sc. thesis, Colo. Sch. Mines.
- Morrison, H. F., Clarke, A. J., Hansen, W. D., and Becker, A., 1982, A versatile EM scale modeling system (abs): *Geophysics*, **47**, 435.
- Nabighian, M. N., 1979, Quasi-static transient response of a conducting half-space—An approximate representation: *Geophysics*, **44**, 1700–1705.
- , 1988, Time domain electromagnetic prospecting methods, in Nabighian, M. N., ed., *Electromagnetic methods in applied geophysics*, Vol. II: Soc. Explor. Geophys., in preparation.
- Nair, M. R., Biswas, S. K., and Mazumdar, K., 1968, Experimental studies on the electromagnetic response of tilted conducting half-planes to a horizontal-loop prospecting system: *Geoexploration*, **6**, 207–244. Extensive results for the slingram method for large metal sheets placed in air.
- Nelson, P. H., 1973, Model results and field checks for a time-domain airborne EM system: *Geophysics*, **39**, 845–853. Frequency domain measurements were made over metal sheets in air and transformed into time domain results.
- Nevitt, C. E., Kantaris, E., and Waller, M. D., 1985, Model studies of VLF-EM borehole prospecting system: *Trans. Inst. Min. Metallurg. (Sect. B: Appl. Earth Sci.)*, **94**, B-6-B-11. Measurements were made over copper sheets in a brine tank placed inside a set of Holmholtz coils.
- Ogilvy, R. D., 1983, A model study of the transient electromagnetic coincident loop technique: *Geoexplor.*, **21**, 231–264. Sets of curves for thin and thick dikes, a sphere, and cylinders in air using a field instrument.
- Olm, M. C., 1981, Electromagnetic scale model study of the dual frequency differencing technique: M.Sc. thesis, Colo. Sch. Mines. Includes slingram results for carbon and graphite targets under homogeneous and inhomogeneous overburden.
- Ott, H. W., 1976, *Noise reduction techniques in electronic systems*: John Wiley & Sons.
- Palacky, G. J., 1972, Computer assisted interpretation of multichannel airborne electromagnetic measurements: Ph.D. thesis, Univ. of Toronto. Includes many model results for airborne INPUT system.
- Palacky, G. J., and West, G. F., 1973, Quantitative interpretation of INPUT AEM measurements: *Geophysics*, **38**, 1145–1158. Model results over thin sheets and ribbons using model INPUT system.
- Parasnis, D. S., 1962, *Principles of applied geophysics*: Wiley and Sons.
- , 1965, Theory and practice of electric potential and resistivity prospecting using linear current electrodes: *Geoexplor.*, **3**, 1–69.
- Patterson, N. R., 1961, Experimental and field data for the dual frequency phase-shift method of airborne electromagnetic prospecting: *Geophysics*, **26**, 601–617. Gives interpretation curves, based on model results for metal disks in air, for the quadrature airborne method.
- Peters, L. J., and Bardeen, J., 1930, The solution of some theoretical problems which arise in electrical methods of geophysical exploration: Bull., Univ. of Wisconsin, Eng. Exper. Station Ser. No. 71.
- Pritchett, W. C., 1955, A low-frequency electrical earth model: *Geophysics*, **20**, 860–870.
- Raby, K. F., 1966, Conductive-sheet analogues in Vitkovitch, D., ed., *Field analysis*: Van Nostrand Co. Ltd., 186–204.
- Ramaswamy, V., Nienaber, W., Dosso, H. W., Jones, F. W., and Law, L. K., 1975, Numerical and analogue model results for electromagnetic induction for an island situated near a coastline: *Phys. Earth Plan. Int.*, **11**, 81–90.
- Rankin, D., Garland, G. D., and Vozoff, K., 1965, Analog model for the magnetotelluric effect: *J. Geophys. Res.*, **70**, 1939–1945.
- Rao, S. H., and Agnihotru, K., 1984-a-f, “Fluid mappers” and their application for the computation of geophysical anomalies, I–VI: *Gerlands Beitr. Geophysik*, **93**, 287–302, 303–313, 356–368, 357–

- 378, 436–448, 449–462. III, IV, V, and VI include results for telluric current profiling and resistivity profiling with line electrodes.
- Roden, R. B., 1964, The effect of an ocean on magnetic diurnal variations: *Geophys. J.*, **8**, 375–388.
- Roy, K. K., 1973, Model studies on electro-telluric interpretation problems of some geological inhomogeneities: *Pure Appl. Geophys.*, **102**, 105–119. Measurements were made over insulating anticlines and a conductive.
- Saito, A., 1984, Development of transient electromagnetic physical modeling for geophysical exploration: Ph.D. thesis, Colo. Sch. Mines. Includes model measurements over plates in air.
- Seymour, R. B., 1981, New horizons in conductive polymers, in Seymour, R. B., ed., *Conductive polymers*: Plenum Press, 1–5.
- Sinclair, G., 1948, Theory of models of electromagnetic systems: *Proc. Inst. Radio Eng.*, **36**, 1364–1370.
- Slichter, L. B., 1932, Observed and theoretical electromagnetic model response of conducting spheres: *Trans., Am. Inst. Min. Metallurg. Petr. Eng., Geophys. Prosp.*, 443–459. Multifrequency measurements of dip and strike angles over spherical shells and a sheet.
- Smits, F. M., 1958, Measurement of sheet resistivities with the four-point probe: *Bell System Tech. J.* **37**, 711–718.
- Smythe, W. R., 1968, *Static and Dynamic Electricity*: 3rd ed., McGraw-Hill Book Co.
- Snelling, E. C., 1969, *Soft ferrites properties and applications*: Chemical Rubber Co. Press.
- Spies, B. R., 1976, The derivation of absolute units in electromagnetic scale modeling: *Geophysics*, **41**, 1042–1047. Includes transient decay curves over various cylinders.
- , 1977, Absolute electromagnetic scale modeling and its use in interpretation of TEM response: *Bur. Min. Res., J. Austral. Geol. Geophys.*, **2**, 89–95. Includes results for a model of the Woodlawn massive sulfide deposit.
- , 1979, Scale model studies of a transient electromagnetic prospecting system using an interactive minicomputer: *Int. Electr. Electron. Eng., Trans. Geosci. Elect.*, GE-17, 24–33.
- , 1980, The application of the transient EM method in Australian conditions-field example and model studies: Ph.D. thesis, Macquarie Univ.
- Spies, B. R., and Parker, P. D., 1984, Limitations of large-loop transient electromagnetic surveys in conductive terrains: *Geophysics*, **49**, 902–912.
- Spies, B. R., and Frischknecht, F. C., 1988, Electromagnetic sounding, in Nabighian, M. N., ed., *Electromagnetic methods in applied geophysics*, Vol. II: Soc. Explor. Geophys., in preparation.
- Spitta, P., 1973, Scale model experiments using solid conductors: *Phys. Earth Plan. Int.*, **7**, 445–449. Measurements over aluminum sheets and cylinders in air using a Helmholtz coil as a source.
- Strangway, D. W., 1966a, Electromagnetic parameters of some sulfide ore bodies, in *Mining Geophysics*, V. I, Soc. Explor. Geophys., 227–242. Gives Argand diagrams for the slingram method based on model data for sheets placed in air.
- , 1966b, Electromagnetic scale modeling, in Runcorn, S. K., ed., *Methods and Techniques in Geophysics*: Interscience Publ., 1–31. Contains several Argand diagrams and other results for the slingram method obtained by the author as well as a review of some other model results.
- Stratton, J. A., 1941, *Electromagnetic theory*: McGraw Hill Book Co., Inc.
- Sumner, J. S., 1976, *Principles of induced polarization for geophysical exploration*: Elsevier.
- Sundberg, K., 1931, Principles of the Swedish geo-electrical methods: *Beiträge zur Geophysik*, Band 1, 298–361.
- Sundberg, K., and Hedstrom, F. H., 1934, Structural investigations by electromagnetic methods: *Proc., World Petr. Congress*, V. B., part 4, 102–110.
- Sunde, E. D., 1949, Earth conduction effects in transmission systems: D. Van Nostrand Co.
- Swanson, H. E., 1961, Model studies of an apparatus for electromagnetic prospecting: *Trans., Am. Inst. of Min. Metallurg. Petr. Eng.*, **220**, 234–238. Contains model curves for the dip angle method including results for anisotropic media using metal sheets placed in air.
- Tesche, F. R., 1951, Instrumentation of electromagnetic modeling and applications to electromagnetic prospecting: Ph.D. thesis, Univ. of Calif., Los Angeles.
- Tse, K. W., Meyer, C. A., and Arajs, S., 1981, Electrical conductivity of graphite fiber-epoxy resin composites: *Materials Sci. Engr.* **49**, 41–46.
- Uhlir, A. J., 1955, The potentials of infinite systems of sources and numerical solutions of problems in semiconductor engineering: *Bell System Tech. J.*, **34**, 105–128.
- van der Pauw, L. J., 1958, A method of measuring specific resistivity and Hall effect of discs of arbitrary shape: *Phillips Res. Rep.* **13**, 1–9.
- , 1958–59, A method of measuring the resistivity and Hall coefficient of lamellae of arbitrary shape: *Phillips Tech. Rev.*, **20**, 220–224.
- Verma, O. P., 1981, Electromagnetic response of fold models in a uniform field: *Geophys. Prosp.*, **29**, 451–461. Profiles and phasor diagrams of the vertical field for inverted vee shaped metal sheets in air using a vertical axis Helmholtz coil as a source.
- Verma, O. P., and Gaur, V. K., 1975, Transformation of electromagnetic anomalies brought about by a conducting host rock: *Geophysics*, **40**, 473–489. An extension of work by Gaur et al. (1972) with emphasis on dipping sheets.
- Villegas-Garcia, C. J., and West, G. F., 1983, Recognition of electromagnetic overburden anomalies with horizontal loop electromagnetic survey data: *Geophysics*, **48**, 42–51. Results for graphite slabs shaped to simulate conductive overburden containing ramps, ridges, and valleys.
- Vine, F., 1966, Impedance networks in Vitkovitch, D., ed., *Field analysis*: D. Van Nostrand Co., 265–356.
- Vitkovitch, D., 1966, The electrolytic tank analogue in Vitkovitch, D., ed., *Field analysis*: D. Van Nostrand Company.
- Volpe, V., 1980, Estimation of electrical conductivity and electromagnetic shielding characteristics of

- graphite/epoxy laminates: *J. Composite Materials*, **14**, 189–197.
- Von Hippel, A. R., 1954a, Dielectrics and waves: M.I.T. Press.
- ed., 1954b, Dielectric materials and applications: M.I.T. Press.
- Wait, J. R., 1951, A basis of electrical prospecting methods employing time varying fields: Ph.D. thesis, Univ. of Toronto. In addition to many theoretical solutions of prospecting problems, it contains model results for grounded arrays using a brine tank.
- 1956, Shielding of a transient electromagnetic dipole field by a conductive sheet: *Can. J. Physics*, **34**, 890–893.
- 1968, Electromagnetic induction in a small conducting sphere above a resistive half-space: *Radio Sci.*, **3**, 1030–1034.
- 1981, Discussion on: "A grounded vertical long-wire source system for plane wave magnetotelluric analog modeling" by R. H. Edwards with reply by author: *Geophysics*, **46**, 934–936.
- Ward, S. H., 1967, The electromagnetic method, in *Mining Geophysics*, v. II, Theory, Chapter II: Soc. Explor. Geophys., 224–372. Contains many type curves for a variety of ground and airborne methods.
- Welsby, V. G., 1960, The theory and design of inductance coils: Great Britain, John Wiley & Sons, Inc.
- Wesley, J. P., 1958, Response of a dyke to an oscillating dipole: *Geophysics*, **23**, 128–133.
- West, G. F., 1960, Quantitative interpretation of electromagnetic prospecting measurements: Ph.D. thesis, Univ. of Toronto. Contains theoretical and model slingram and dip angle curves for a half plane in air.
- Whiteside, H., and King, R. W. P., 1964, The loop antenna as a probe: *Int. Electr. Electron. Eng., Trans. Ant. Propag.*, AP-**12**, 291–297.
- Woods, D. V., 1975, A model Study of the Crone borehole pulse electromagnetic (PEM) system: M.Sc. thesis, Queens Univ. Contains extensive results for metal sheets in air.
- Woods, D. V., and Crone, J. D., 1980, Scale model study of a borehole pulse electromagnetic system: *Can. Min. Metalurg. Bull.*, **73**, 817, 96–104. Includes many response curves for thin sheets in air using surface transmitter loops and a downhole receiver loop.
- Yost, W. J., Caldwell, R. L., Beard, C. I., McClure, C. D., and Skomal, E. N., 1952, The interpretation of electromagnetic reflection data in geophysical exploration, Part II—Metallic model measurements: *Geophysics*, **27**, 806–826. Unique model studies of a transient two-loop method.
- Young, R. J., 1984, conducting polymer-plastic metals?: *Plastics and Rubber Internat.*, **9**, 29–32.

## References for General Reading

- Abdul-Malik, M. M., Myers, J. O., and McFarlane, J., 1985, Model studies of topographic noise VLF-EM data: Accounting for the direction of morphological strike relative to survey line and magnetic field directions: *Geoexplor.*, **23**, 217–225. Sets of curves for vertical and dipping thin sheets.
- Apparao, A., Reddy, B. S., and Sarma, V. S., 1983, Model tank experiments on comparative performance of different electrode arrays in I. P. (Induced Polarization) and resistivity profiling, in Proc. of Symp. on Explor. Geophys. in India: 1945–1978, Calcutta: Geol. Surv. India Spec. Pub. Series No. 2, v. II, 479–493. Measurements were made over aluminum sheets in water.
- Apparao, A., Roy, A., and Mallick, K., 1969, Resistivity model experiments: *Geoexplor.*, **7**, 45–54. Gives resistivity profiles over thick sheets made of graphite and cement immersed in water.
- Apparao, A., and Roy, A., 1971, Resistivity model experiments 2: *Geoexplor.*, **9**, 195–205. Extension of previous work by Apparao and Roy (1969) including results for five electrode configurations.
- Apparao, A., 1979, Model tank experiments on resolution of resistivity anomalies obtained over buried conducting dykes—in line and broadside profiling: *Geophys. Prosp.*, **27**, 835–847. Resistivity profiles over one and two aluminum sheets in water using two electrode and Wenner configurations.
- Berdichevskiy, M. N., Kobzova, V. M., and Morozov, I. P., 1980, Physical modeling of the magnetotelluric field above a non-uniform asthenosphere: *Izvestia, Earth Physics*, **16**, 633–635. Magnetotelluric soundings over a metal disc under an electrolytic tank containing a long metal cylinder over the range 100 kHz–10 MHz.
- Chan, E., Dosso, H. W., Law, L. K., Auld, D. R., and Nienabor, W., 1983, Electromagnetic induction in the Queen Charlotte Islands region: analogue model and field station result: *J. Geomag. Geoelectr.*, **35**, 501–516.
- Clark, A. R., and Mungal, A. G., 1951, Scale model experiments in electromagnetic methods of geophysical exploration: *Can. J. Physics*, **29**, 285–293. Amplitude and phase were measured over a variety of metal targets using a large circular loop source.
- Clay, C. S., Greischer, L. L., and Kon, T. K., 1974, Matched filter detection of electromagnetic transient reflections: *Geophysics*, **39**, 683–691. Includes results for concentric loops over horizontal Al plates.
- Coney, D. P., 1977, Model studies of the VLF-EM method of geophysical prospecting: *Geoexplor.*, **15**, 19–35. Sets of single frequency measurements over dipping thin sheets; a horizontal sheet is included as overburden in one model. The primary field was provided by a Helmholtz coil.
- Daev, D. S., Sordinov, A. I., and Tarkhov, 1963, Model simulation of problems bearing upon the method of radio-wave sounding: *IZV. Geophys. Ser. G*, 936–945. Measurements were made over sheets, cylinders, spheres, and discs immersed in water at a frequency of 100 MHz and greater.
- Dosso, H. W., 1966a, Model measurements for EM variations near a fault or dike: *Can. J. of Earth Sci.*, **3**, 287.
- 1966b, Analogue model measurements for electromagnetic variations near a coastline: *Can. J. of Earth Sci.*, **7**, 917–936. The effect of a coastline on geomagnetic measurements is studied by model measurements.

- Dosso, H. W., Nienaber, W., and Hutton, V. R. S., 1980, An analogue model study of electromagnetic induction in the Eastern Coastal region of North America: *Phys. Earth Plan. Inter.*, **23**, 13–20.
- Dosso, H. W., Nienaber, W., and Parkinson, W. D., 1985, An analogue model study of electromagnetic induction in the Tasmania region: *Phys. Earth Plan. Int.*, **39**, 119–133.
- Drinkrow, R. L., 1975, Scale model studies of a down-hole EM probe: *Investigation Rep. 108*, CSIRO Div. of Min. Physics. Response of a coaxial loop-loop probe for sheets, tabular bodies, and discs in air.
- Drinkrow, R. L., and Duffin, R. H., 1976, Scale model type curves for downhole electromagnetic logging in a conductive environment: *Investigation Rept. 120*, CSIRO Div. of Min. Physics. Response of coaxial loop-loop probes for graphite and graphite loaded resin slabs immersed in brine.
- Duckworth, K., 1975, Electromagnetic depth sounding using a source orientation mode: *Geophys. Prosp.*, **23**, 139–155. Includes model results for edges of metal sheets in air for source orientation sounding method.
- Douloff, A. A., 1960, The response of a disk in a dipole field: *Geophysics*, **26**, 452–464. Contains model results for a finitely conducting disk as well as computed results for a perfectly conducting disk—applicable to airborne and ground measurements.
- Ethington, E. F., 1985, Resistivity and induced-polarization modeling for a buried resistive dike and buried resistive cylinder: M.Sc. thesis, Univ. of Arizona. Resistivity measurements were made over a resistive target in electrolytes having different resistivities and percent frequency effect was calculated.
- Fraser, D. C., and Ward, S. H., 1967, Analytic and model studies of a rotatable field electromagnetic prospecting system: *Geophysics*, **32**, 899–917. In addition to many calculated results for spheres and cylinders, model results for a sphere beneath a conducting sheet and other more complicated models are given.
- Gaur, V. K., and Verma, O. P., 1973, Enhancement of electromagnetic anomalies by a conducting overburden II: *Geophys. Prosp.*, **21**, 159–184. An extension of work by Gaur et al. (1972) including results for the rotary field method.
- Hall, S. H., Kelley, M. J., and Davis, J., 1978, Modeling the rotating current dipole method of EM prospecting: *Bull. Austral. Soc. Explor. Geophys.*, **9**, 55–61. Results for aluminum and graphite models in 55 S/m NaCl solution.
- Haren, R. J., 1981, Slingram scale modeling of the Woodlawn Orebody, in *Geophysical case study of the Woodlawn Orebody New South Wales, Australia*, R. J. Whitley, ed.: Pergamon Press, 206–217. Measurements were made over aluminum and lead models of the Woodlawn orebody in air and in brine.
- Herbert, D., Dosso, H. W., and Nienaber, W., 1983, Analogue model study of electromagnetic induction in the Newfoundland region: *Phys. Earth. Plan. Int.*, **32**, 65–84.
- Herbert, D., Wright, J. A., Dosso, H. W., and Nienaber, W., 1983, Comparison of analogue model and field station results for the Newfoundland region: *J. Geomag. Geoelectr.*, **35**, 673–682.
- Howland-Rose, A. W., Linford, G., Pitcher, D. H., and Seigel, H. G., 1980, Some recent magnetic induced-polarization developments—Part I: Theory: *Geophysics*, **45**, 37–54. The effect of horizontal layering and the effect of a vertical contact on magnetic and electric field IP methods was studied using salt solutions stabilized with agar to represent various regions.
- Hu, W. B., Nienaber, W., and Dosso, H. W., 1984, Analogue model magnetic field responses of an ocean channel, an island, and a seamount in the Hainan Island region: *J. Geophys.*, **55**, 222–227.
- Jones, B., and Wong, J., 1975, Some thin sheet responses to a model dipole-dipole prospecting system: *Geoexplor.*, **13**, 187–196. Response of finite vertical sheets and horizontal ribbons in air for horizontal coplanar and perpendicular configurations.
- Joshi, M. S., Gupta, O. P., and Negi, J. G., 1983, Electromagnetic model studies simulating conductive overburden with non-uniform thickness, in *Proc. of Symp. on Explor. Geophys. in India: 1945–1978*, Calcutta: Geo. Surv. India Spec. Publ. Series 2, II, 469–478. Includes slingram measurements over overburden and vertical half-plane in air.
- , 1984, Scale-model response of a thin vertical conductor below a conductive, inductive, or laterally inhomogeneous overburden layer: *Geophysics*, **49**, 2159–2165.
- Kabra, S., and Rao, I. B. R., 1984, Interpretation of dipole-dipole transient technique data for steeply dipping sheet conductor: *Geophys. Res. Bull.*, **22**, 1–6. Measurements were made over Al sheets in air.
- Karwotowski, J., and Halberjam, G. M., 1981, A tunnel resolution investigation using an automated resistivity tank analog: *Geophys. Prosp.*, **26**, 891–905. Description of equipment and results of a study of response of one and two parallel trends using square resistivity array.
- Ketelaar, A. C. R., and De Vente, C. P., 1976, Interpretation graph for vertical tabular conductors in E.M. in-line dip-angle measurements: *Geophys. Prosp.*, **24**, 670–671. Interpretation graph based on multi-frequency measurements for case when angle between profile and strike of plate is 45°.
- Ketola, M., 1968, The interpretation of slingram (horizontal loop) anomalies by small-scale model measurements: Geological Survey of Finland, Rep. of Investigations, **2**, 35. Includes scale model results for multiple thin sheets, wide dikes, folded conductors and magnetic bodies.
- Koefoed, O., and Struyk, A. P., 1969, The electrical current pattern induced by an oscillating magnetic dipole in a semi infinite conductive thin plate: *Geophys. Prosp.*, **27**, 182–195. Model studies interpreted to give the distribution of current near the edge of a thin sheet.
- Kuznetsov, A. N., 1986, The features of an electromagnetic field from multiple-frequency-sounding and transient sounding over a horst structure: *Izvestiya*, **21**, 524–530. The vertical and horizontal magnetic fields and the impedance were measured over a horst at the bottom of an electrolyte tank using an electric dipole source.
- Kuznetsov, A. N., and Doshchitsa, S. A., 1983, Transient electromagnetic sounding of horizontally inhomogeneous media: *Izvestia, Earth Physics*, **19**, 644–648. Measurements in the range 0.1–5  $\mu$ s over insulating structures in a layer of 20 S/m electrolyte.

- Majumdar, R. K., 1985, Simulation of surface percentage frequency effect and metal factors over thin dykes using physical modeling: *Geoexplor.*, **23**, 183–192. Includes measurements over graphite loaded resin targets in an NaOH solution.
- Matias, M. J. S., and Habberjam, G. M., 1986, The effect of structure and anisotropy on resistivity measurements: *Geophysics*, **51**, 964–971. A brine tank was used to measure the response of the square array over wide homogeneous and anisotropic dikes.
- Moroz, I. P., 1983, Physical modeling of magnetotelluric fields: *Geophys. J. (Gordon-Breach Science Publ.)*, **5**(6), 932–938.
- Negi, J. G., 1973, Mathematical and experimental models in induction prospecting: *Geophys. Res. Bull.*, **11**, 285–317. Review paper including examples of published scale model results.
- Negi, J. G., and Gupta, O. P., 1968, Models in applied geo-electromagnetics: *Earth-Science Reviews*, **4**, 219–241.
- , 1982, Analog models in geoelectromagnetism: *Nat. Geophys. Res. Inst. Bull.*, **20**, 329–343. A review of analog modeling at NGRI.
- Negi, J. G., Joshi, M. S., and Gupta, O. P., 1977, Some recent advances in numerical and analog modelling of evaluating the electromagnetic response modification due to conducting host rock: *J. Ind. Geophys. Union*, **14**, 31–40.
- Nienaber, W., Dosso, H. W., Law, K. K., Jones, F. W., and Ramaswamy, V., 1976, An analog model study of electromagnetic induction for island—continent ocean channels: *Phys. Earth Plan. Int.*, **13**, 169–183.
- , 1979a, An analogue model study of electromagnetic induction in the Vancouver Island region: *J. Geomag. Geoelectr.*, **31**, 115–132.
- , 1979b, Electromagnetic induction in the Vancouver Island region—field station and analogue model results: *J. Geomag. Geoelectr.*, **31**, 599–613.
- Nienaber, W., Hebert, D., and Dosso, H. W., 1983, Induction arrows for a buried conducting plate: *Phys. Earth Plan. Int.*, **32**, 306–311. In phase and quadrature induction arrows were measured over a 50 × 100 cm graphite plate.
- Palacky, G. J., 1975, Interpretation of INPUT AEM measurements in areas of conductive overburden: *Geophysics*, **50**, 490–502. Model results for thin sheets in air including simulation of overburden by horizontal sheets.
- , 1976, Use of decay patterns for the classification of anomalies in time-domain AEM measurements: *Geophysics*, **41**, 1031–1041. Includes model results for thin strips and sheets for INPUT system.
- Papamastorakis, I., and Haerondol, G., 1983, An analogue model of the geomagnetic induction in the South Indian Ocean: *J. Geophys.*, **52**, 61–68. A copper sheet in air was used to represent the ocean and equatorial and magnetospheric sources were represented by driving current through metal bands.
- Parry, J. R., 1965, A theoretical and experimental investigation of finite thin dykes in a uniform electromagnetic field: Thesis, Univ. of Calif., Berkeley. Model data for sheets placed in air are compared with calculations based on current loops.
- Poddar, M., and Bhattacharya, P. K., 1966a, On the electromagnetic response of conductors in the inductive method of prospecting (model studies): *Geophys. Prosp.*, **24**, 470–486. Experimental results for a sphere, a plate, and a disk in the fields of a uniform, a line, and a point source are given.
- , 1966b, On the response of conducting plates to an inducing dipolar field (model studies): *Geoexplor.*, **4**, 93–106.
- Poddar, M., 1975, Some experimental studies on the effect of a screen on the electromagnetic response of a cylinder: *Geoexplor.*, **13**, 57–67. Multi-frequency measurements over a metal cylinder with a concentric metal shell.
- Poddar, M., Lahiri, A. K., and Deb, B. K., 1976, Electromagnetic response of a broken ore-vein (model studies): *Geophys. Prosp.*, **24**, 255–264. Fixed source measurements over a single and two non-contacting coplanar metal sheets in air.
- Ramaprasada, I. B., and Bhimasankaram, V. L. S., 1973, Electromagnetic modeling of sheet-like bodies by the combined-loop version of the transient pulse induction method: *Geoexplor.*, **11**, 87–95. Single-loop transient measurements over vertical and dipping thin aluminum sheets placed in air.
- Ramaswamy, V., Dosso, H. W., and Winter, R., 1983, An electromagnetic scale model study of the Rhinegraben Anomaly: *J. Geomag. Geoelectr.*, **35**, 17–27.
- Rao, I. B. R., and Kabra, S., 1983, Model results for a dipole-dipole transient electromagnetic technique: *Bull. Austral. Soc. Explor. Geophys.*, **14**, 72–74. Curves for the response of a metal sheet in air.
- Roy, K. K., and Elliott, H. M., 1980, Model studies on some aspects of resistivity and membrane polarization behavior over a layered earth: *Geophys. Prosp.*, **28**, 759–775. The Wenner configuration was used to make resistivity and time-domain IP measurements on layers of water, sand, and clay.
- Savin, A. P., 1977, Screening effect of surface deposits on anomalies of inductive dipole profiling: *Izvestiya, Earth Physics*, **12**, 734–739. Includes results for spheres and vertical plates beneath a horizontal plate.
- Spiegel, R. J., Sturdvant, V. R., and Owen, T. E., 1980, Modeling resistivity anomalies from localized units under irregular terrain: *Geophysics*, **45**, 1164–1183. Pole-dipole measurements were made over a long insulating prism immersed in water.
- Spies, B. R., 1980, TEM model studies of the Elura deposit, Cobar, New South Wales: *Bur. Min. Res. J. Austral. Geol. Geophys.*, **5**, 77–85.
- Spitta, P., 1977, Electromagnetic scale model experiments for the coastline effect of geomagnetic variations: *J. Geophys.*, **42**, 507–520. Magnetic field measurements over aluminum plates in air excited by a large rectangular coil.

- Srinivas, D., Rao, I. B. R., Nagendra, R., and Bhimasankaram, V. L. S., 1980, Effect of profile angle and strike extent of the vertical sheet in one loop transient induction method (modelling): *Bull. Austral. Soc. Explor. Geophys.*, **11**, 52–53. Curves for the response of a metal sheet in air.
- Sumi, F., 1956, Geoelectric exploration of inclined thin beds and ore veins: *Geophys. Prosp.*, **4**, 194–204. Scale model measurements made over a conducting cylinder and a thin plate in water are compared with theoretical calculations.
- Vedrintsev, G. A., 1966, Problems in conducting and interpreting electrical sounding surveys in an area where there is sharp relief in the basement surface: in Keller, G. V., translator, Dipole methods for measuring earth conductivity, 147–177. Contains many resistivity curves obtained by model measurements.
- Ward, S. H., O'Brien, D. P., Parry, J. R., and McKnight, B. K., 1968, AFMAG interpretation: *Geophysics*, **33**, 621–644. Compares model results with theoretical results for disks and wire loops in a uniform field.
- Ward, S. H., Ryu, J., Glenn, W. E., Hohmann, G. W., Day, A., and Smith, B. D., 1974, Electromagnetic methods in conductive terranes: *Geoexplor.*, **12**, 121–183. Includes results for aluminum targets in NaCl for the turam method.
- Won, I. J., 1980, A wide-band electromagnetic exploration method—some theoretical and experimental results: *Geophysics*, **45**, 928–940. The response of a graphite slab in 12 S/m brine was studied using a signal swept logarithmically from 4KHz to 4MHz.
- Yogadish, D., McFee, J. E., and Chesney, R. H., 1984, Time domain response of a sphere in the field of a coil; theory and experiment: *Int. Electr. Electron. Eng., Trans. Geosc. Rem. Sens.*, GE22, 360–367. Measurements were made over aluminum and steel spheres in air using a concentric loop configuration.



---

---

# 7

## **Detection of Repetitive Electromagnetic Signals**

---

---



---

---

---

7

---

---

## Detection of Repetitive Electromagnetic Signals

*A. Becker and G. Cheng\**

The principle of increasing the accuracy in the measurement of a given quantity by averaging repeated determinations of its magnitude is probably as old as experimental science itself. Considerable advances in electronics were required, however, before this simple principle could be directly incorporated into signal detectors used in physics and chemistry. With the advent of solid state devices, builders of geophysical equipment for electrical and electromagnetic measurements quickly saw the advantages of analog averaging detectors and included them in their designs. Thus virtually all geophysical equipment built after 1970 uses a detector that coherently samples and averages the observed repetitive electrical signal. Since 1980, the availability of reliable, compact, digital microprocessors has resulted in an upgrading of the analog equipment to full or partial digital status. In modern equipment the analog to digital conversion takes place right at the sensor output and all the subsequent signal processing is done digitally.

A qualitative discussion of electronic signal averaging techniques is given in Hieftje (1972). More recently Neelakantan and Dattagupta (1978, 1980) did a quantitative analysis of signal enhancement by a boxcar integrator and a lock-in amplifier, two of the most commonly used signal averaging detectors. In spite of the popular use of such detectors in geophysical equipment only two articles on the subject [San Filipo and Hohmann (1983) and Macnae et al. (1984)] have appeared in scientific journals dedicated to geophysics. While each article concerns a specific subject, namely low frequency EM data acquisition by San Filipo and Hohmann and noise processing techniques for the UTEM3 equipment by Macnae et al., both articles contribute much to our understanding of specialized detectors for the sensing of electrical signals used in geophysical exploration.

Here we provide a tutorial overview of the principles of synchronous detection of repetitive signals. Starting with the early analog devices and continuing to state-of-the-art digital equipment we discuss the spectral transfer function, the equivalent white noise bandwidth, and the step function response or the dynamic characteristics of each device. The last section is devoted to the use of synchronous detectors on a moving platform such as an aircraft. In this application, the signal strength is time dependent and the equipment used to detect it can be optimally defined.



\*Engineering Geoscience, University of California-Berkeley.

### The Boxcar Integrator

Use of this classical device for detecting a periodic unipolar signal was first reported in 1955 by Holcomb and Norberg (Blume, 1961) in connection with their work on nuclear magnetic resonance. The detector basically consists of an analog gate which opens for a given duration every time a signal is received, followed by a classical RC low-pass filter for averaging the sampled signal. For proper operation the time delay between the onset of the signal and the opening of the gate must be maintained constant. Figure 1 shows a synoptic diagram for the boxcar integrator and the timing for the gate operation. A solid state version of this type of equipment is described in Collins and Katchinoski (1973).

Before proceeding to derive a frequency domain transfer function for the repetitive boxcar integrator we establish the transfer function for each operation of the gate. Suppose the input voltage appearing at the gate is given by

$$V_{in} = Ae^{j\omega t}, \quad (1)$$

the gate is closed at time  $t_0 - \Delta$  and is again opened at time  $t_0$ . The voltage that will appear at the output terminals at the conclusion of this operation will be

$$V_{out} = \int_{t_0-\Delta}^{t_0} V_{in}(s)h(t-s)ds. \quad (2)$$

Here,

$$h(s) = \frac{e^{-s/RC}}{RC} = \frac{e^{-s/\tau}}{\tau} \quad (3)$$

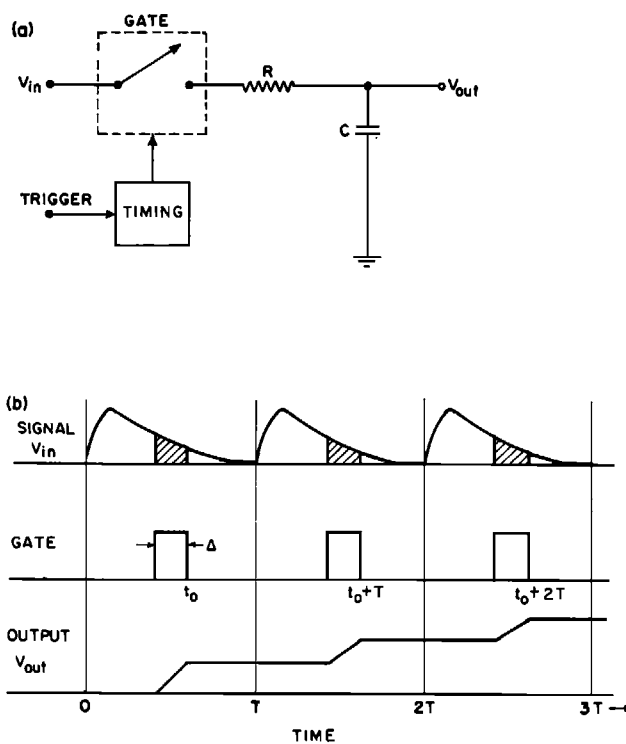


FIG. 1. (a) Simplified schematic diagram for the boxcar integrator. (b) Synopsis of signal processing for the boxcar integrator.

is the impulse response of the RC low-pass network which is activated by a source with zero output impedance while the gate is closed. The required convolution integral can be readily evaluated to yield

$$V_{\text{out}} \Big|_{t=t_0} = Ae^{j\omega t_0} \left[ \frac{1 - e^{-\Delta/\tau} e^{-j\omega\Delta}}{1 + j\omega\tau} \right] \quad (4)$$

$$= V_{\text{in}} \Big|_{t=t_0} [g(\omega, \Delta, \tau)]. \quad (5)$$

The complex gate transfer function can be rationalized to obtain the required amplitude-frequency characteristic for this operation. Thus,

$$|g|^2 = gg^* = \frac{(1 - e^{-\Delta/\tau})^2 + 4e^{-\Delta/\tau} \sin^2 \omega \frac{\Delta}{2}}{(1 + \omega^2\tau^2)}. \quad (6)$$

Usually the duration of the gate on time  $\Delta$  is much shorter than the filter network time constant  $\tau$  which in turn is usually much longer than the period of the signal being detected. Let us then examine the case where

$$\Delta/\tau \ll 1$$

and

$$\omega\tau \gg 1.$$

Under these conditions, the gate transfer function can be simplified to read:

$$|g| = \frac{\Delta}{\tau} \operatorname{sinc} \left( \omega \frac{\Delta}{2} \right). \quad (7)$$

As expected, the gate output is the average value of the signal during its on time multiplied by the dc response factor of the RC network.

We can now derive the frequency domain transfer function for the usual repetitive mode of operation of the boxcar integrator. Let  $T$  be the period with which the input signal is repeated. Then, as shown, at the end of the first gate closure the output voltage will be

$$V_1 = gAe^{j\omega t_0}. \quad (8)$$

One signal period later, at the completion gate closure, the output voltage will be

$$V_2 = V_1 e^{-\Delta/\tau} + gAe^{j\omega(t_0+T)} = gAe^{j\omega(t_0+T)} [e^{-j\omega T} e^{-\Delta/\tau} + 1]. \quad (9)$$

Similarly, we find that after  $N$  successive closures of the gate the output voltage is

$$V_N = V_{N-1} e^{-\Delta/\tau} + gAe^{j\omega[t_0+(N-1)T]}. \quad (9a)$$

Here the first term represents the leakage of the charge previously stored on the capacitor while the second term is the voltage due to the charge acquired during the last operation of the gate. Expanding the first term into its constituents shows that

$$\begin{aligned} V_{\text{out}|_{t=t_0+(N-1)T}} &= g(Ae^{j\omega[t_0+(N-1)T]}) \times [S_N(j\omega T, \Delta/\tau)] \\ &= V_{\text{in}|_{t=t_0+(N-1)T}} \times [g(\omega, \Delta, \tau) \times S_N(j\omega T, \Delta/\tau)]. \end{aligned} \quad (10)$$

Here,

$$S_N(j\omega T, \Delta/\tau) = e^{-(N-1)u} + e^{-(N-2)u} + \dots + e^{-2u} + e^{-u} + 1$$

with  $u = (\Delta/\tau + j\omega T)$ . This geometric progression can be readily summed to obtain

$$S_N(u) = \frac{1 - e^{-Nu}}{1 - e^{-u}}. \quad (11)$$

Because of the short gate activation time, a large number of signal samples are required to establish an equilibrium between the input and output voltages. In other words, we must have

$$N\Delta \gg \tau. \quad (12)$$

In this case the numerator in equation (11) is reduced to unity and the equilibrium transfer function for the boxcar integrator is given by

$$G_\infty = g \times S_\infty = \frac{1 - e^{-\Delta/\tau} e^{-j\omega\Delta}}{1 + j\omega\tau} \times \frac{1}{1 - e^{-\Delta/\tau} e^{-j\omega T}}. \quad (13)$$

Again the amplitude transfer function for this device can be best examined by forming,

$$|G_\infty|^2 = \frac{1}{1 + \omega^2\tau^2} \left[ \frac{(1 - e^{-\Delta/\tau})^2 + 4e^{-\Delta/\tau} \sin^2 \omega\Delta/2}{(1 - e^{-\Delta/\tau})^2 + 4e^{-\Delta/\tau} \sin^2 \omega T/2} \right]. \quad (14)$$

Although the above expression is fairly complicated, it can be demonstrated that equation (14) describes a comb filter with a window at dc and windows centered on all the harmonics of the signal repetition frequency ( $f = 1/T$ ). Figure 2 shows the frequency dependence of the equilibrium transfer function for some common parameter values. It is instructive, however, to further examine some limiting forms of this transfer function.

Let us first consider the behavior near dc. As before, we take  $\Delta \ll \tau$  and  $\omega T \ll 1$ .

Under these conditions equation (14) can be simplified to read:

$$|G_\infty|_{dc}^2 \approx \frac{1}{1 + \omega^2\tau_e^2} \frac{[\Delta^2/\tau^2 + \omega^2\Delta^2]}{[\Delta^2/\tau^2 + \omega^2T^2]} \approx \frac{1}{1 + \omega^2\tau_e^2}, \quad (15)$$

with

$$\tau_e = \tau T / \Delta. \quad (16)$$

Equation (15), which describes the behavior of the transfer function for very low frequencies, shows that the first spectral window of the boxcar integrator is formed by a very narrow low-pass filter with a half power point at

$$\omega_L = 1/\tau_e = \Delta/T\tau.$$

To evaluate the transfer function (14) near the center of any other spectral window put

$$\omega = \omega_n \pm \Omega$$

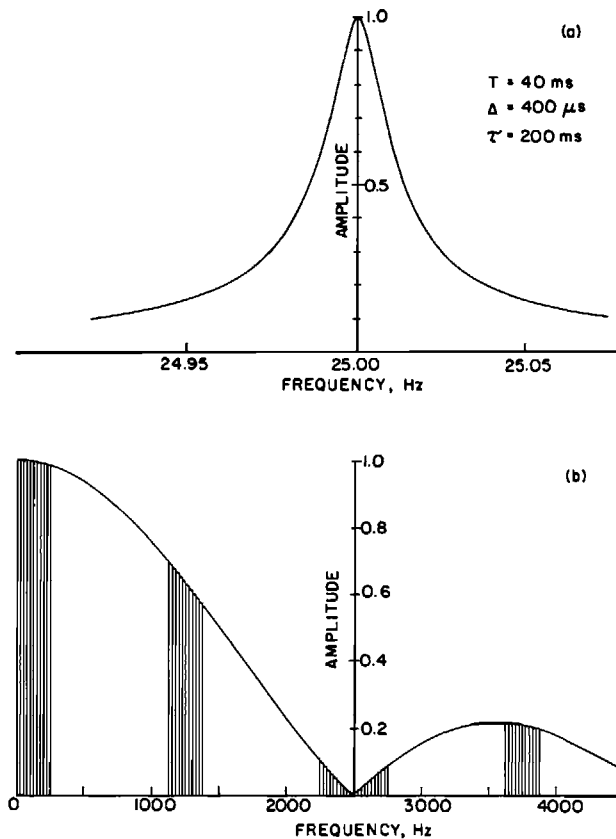


FIG. 2. Transfer function for boxcar integrator: Base frequency 25 Hz; gate width 400  $\mu\text{s}$ ; RC product, “ $\tau$ ” 200 ms (a) Detailed description of the first spectral window. (b) Envelope of spectral window amplitudes. Selected spectral lines are shown explicitly.

$$= \frac{2\pi n}{T} \pm \Omega$$

where  $n$  = an integer and  $\Omega T \ll 1$ . As usual, take  $\Delta \ll T \ll \tau$  and  $\omega_n \tau \gg 1$ .

In that case equation (14) can be reduced to read,

$$|G_\infty|_{\omega_n}^2 \approx \frac{4 \sin^2 \frac{\omega_n \Delta}{2}}{\left( \frac{\Delta^2}{\tau^2} + 4 \sin^2 \frac{\Omega T}{2} \right) (\omega_n^2 \tau^2)}. \quad (17)$$

Rearranging we get

$$|G_\infty|_{\omega_n}^2 \approx \operatorname{sinc}^2 \frac{\omega_n \Delta}{2} \times \frac{1}{1 + \Omega^2 \tau_e^2} \quad (18)$$

with  $\tau_e = \tau T / \Delta$  as before. Each window then has the form of a band-pass filter whose gain is determined by the sinc function and whose width at the half-power points is defined by the effective time constant  $\tau_e$ .

Before evaluating the noise reduction properties of the boxcar integrator we consider its response time to any coherent signal. Equation (18) indicates that at the window frequencies the device acts as a filter with a response time (time constant) equal to  $\tau_e$ . That this intuitive

deduction is correct may be seen by returning to equation (10). If we put

$$t_0 = 0,$$

and

$$\omega_n = 2n\pi/T,$$

and substitute for  $g$  and  $S_N$  from equations (7) and (11) we get,

$$|V_{\text{out}}| = A \operatorname{sinc} \frac{\omega_n \Delta}{2} (1 - e^{-N\Delta/\tau}). \quad (19)$$

Now put  $t = (N - 1)T$ ;  $\tau_e = \tau \cdot T/\Delta$  so that,

$$|V_{\text{out}}| = A \operatorname{sinc} \frac{\omega_n \Delta}{2} (1 - e^{-\Delta/\tau} e^{-t/\tau_e}). \quad (20)$$

For  $\omega_n \Delta \ll \pi$  and  $\Delta \ll \tau$

$$|V_{\text{out}}| = A(1 - e^{-t/\tau_e}). \quad (21)$$

To prove the noise reduction feature of the boxcar integrator we find the noise bandwidth for this device. By definition the required quantity is given by

$$B = \int_0^\infty |G_\infty|^2 df. \quad (22)$$

This integral is difficult to evaluate if we use the exact transfer function (14) as the integrand. If, however, we are only interested in the narrow window case, then we can use the approximate form for  $|G_\infty|^2$  given by equation (18). In that case

$$\begin{aligned} B &= \int_0^{f_{1/2}} \frac{df}{1 + \Omega^2 \tau_e} + \sum_{n=1}^{\infty} \frac{\operatorname{sinc}^2 n\pi\Delta}{T} \int_{(fn+fn-1)/2}^{(fn+fn+1)/2} \frac{df}{1 + \Omega^2 \tau_e} \\ &= \frac{1}{2\tau_e} \left[ \frac{1}{2} + \sum_{n=1}^{\infty} \operatorname{sinc}^2 \frac{n\pi\Delta}{T} \right]. \end{aligned}$$

The summation can be evaluated in closed form (Jolley, 1961) to yield

$$B = \frac{1}{2\tau_e} \left[ \frac{1}{2} + \frac{\pi}{2\pi} \frac{T}{\Delta} - \frac{1}{2} \right], \quad (23)$$

or simply

$$B = 1/4\tau.$$

From equations (21) and (23) we immediately define the output signal-to-noise ratio (S/N) for the boxcar integrator when the input consists of a repetitive signal immersed in wideband noise. If the noise density is  $\eta_0 V^2/\text{Hz}$  then the output S/N ratio will be given by

$$\text{S/N}_{\text{out}} = A^2 / \eta_0 B = 4\tau A^2 / \eta_0. \quad (24)$$

We can now calculate the improvements in the signal-to-noise ratio derived from the use of the boxcar integrator. This quantity is derived by comparing the signal-to-noise ratio after taking only one sample with that given by equation (24). From equation (7) the output voltage at any coherent frequency will be

$$V_{\text{out}} = A \frac{\Delta}{\tau}, \quad (25)$$

provided as usual we take  $\omega_n \Delta < \pi$  and  $\Delta \ll \tau$ . The noise bandwidth for a single opening of the gate is given by

$$b = \int_0^\infty |g^2| df = \int_0^\infty \left( \frac{\Delta^2}{\tau^2} + 4 \sin^2 \omega \frac{\Delta}{2} \right) \frac{df}{1 + \omega^2 \tau^2}. \quad (26)$$

The integral can be evaluated (Gradshteyn and Ryzhik, 1965) to yield

$$b = \frac{\Delta}{2\tau^2} \left( 1 + \frac{\Delta}{2\tau} \right) \approx \frac{\Delta}{2\tau^2}. \quad (27)$$

Thus the signal-to-noise ratio, after one signal sample is taken, is

$$\text{S/N}_{\text{in}} = \frac{A^2 \Delta^2 / \tau^2}{\eta_0 b} = \frac{2A^2 \Delta}{\eta_0}. \quad (28)$$

Finally, comparing equations (24) and (28) we obtain the signal-to-noise improvement ratio (SNIR) for the boxcar

$$\text{SNIR} = \left( \frac{\text{S/N}_{\text{out}}}{\text{S/N}_{\text{in}}} \right)^{1/2} = \left( 2 \frac{\tau}{\Delta} \right)^{1/2}. \quad (29)$$

Although a number of approximations were made in deriving expression (29), it is in complete agreement with a more formal derivation of this result in Neelakantan and Datta-gupta (1978). Note that in addition to obtaining the boxcar SNIR for white noise these authors also indicate a procedure for obtaining the boxcar SNIR when the noise is colored (e.g. pink or  $1/f$ ).

Before concluding the discussion of the boxcar integrator we note that the spectral content of the noise at the input differs from that at the output of this device. In fact, because of severe aliasing by the sampling gate, all the noise at the output of the boxcar integrator appears in a limited frequency range defined by

$$0 < f < \frac{1}{2T}. \quad (30)$$

Figure 3 shows a folding diagram that illustrates the frequency translation properties of this device. Here all the harmonics of the signal frequency are translated to the origin and appear as dc. Although the highest frequency component present in the output is limited to one half of the signal frequency, the spectral content of the output is effectively limited to

$$f_{\text{max}} \approx \frac{1}{2\pi\tau_e} = \frac{\Delta}{2\pi T} \quad (31)$$

which is much smaller than the limiting value indicated by inequality (30) above. The actual spectral density for the output noise deduced from expressions (15) and (23) is

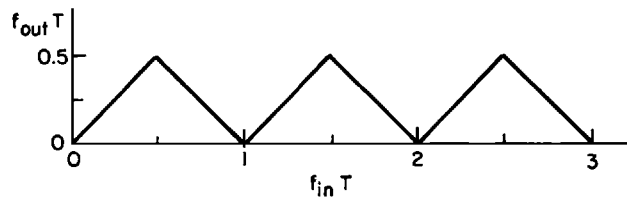


FIG. 3. Frequency translation diagram for the boxcar integrator.

$$S(\omega) = \eta_0 \frac{T/\Delta}{1 + \omega^2 \tau_e^2} \quad 0 < \omega < \frac{\pi}{T}. \quad (32)$$

Thus noise reduction and improvement in the signal-to-noise ratio takes place at the expense of spectral compression and long response times. All the signal appears as a spectral line at dc and the residual noise appears in a narrow frequency band defined by equation (31).

## Analog Detection of Geophysical Signals

### General purpose equipment

To avoid the influence of low frequency noise and instrumental drift in the first amplification stages, all geophysical signals are transmitted with alternating polarity. Thus, as shown in Figure 4, one period of signal transmission consists of a positive pulse followed by a negative one. Synchronous detection is accomplished by adding a reversing switch to the circuitry for a boxcar integrator. With the exception of the reversing switch, which operates in concert with the reversals of the transmitted pulse, the geophysical detector functions exactly the same way as the boxcar integrator. However, note one other difference: whereas the boxcar integrator is essentially a single channel device, the detection of geophysical signals is usually done with a number of gates activated sequentially. The averaged output of each gate constitutes one channel of information related to the detected signal. A geophysical detector usually has from six to twenty channels. Gate widths and positions are set to fully recover the expected signal. A circuit diagram for a six-channel analog device is given in Lazenby and Wondergem (1974) and a modified version that has seen much use, the Mark VI INPUT detector, is described in Lazenby and Wondergem (1975).

Now we can proceed to derive the signal processing and noise rejection characteristics for the geophysical detector. As before, the frequency domain transfer function for the gate is given by equation (6), the summation formula (11), however, must be amended to reflect the action of the reversing switch and the fact that two signal samples are taken during each signal period. The resultant summation function can be derived from first principles by following steps in equations (8) through (11). The required relationship is given by

$$S_N(v) = \frac{(1 - e^{-v/2})}{1 - e^{-v}} (1 - e^{-Nv}), \quad (33)$$

with

$$v = \frac{2\Delta}{\tau} + j\omega T,$$

and,

$N$  = number of signal periods sampled.

To get the equilibrium frequency domain transfer function for the geophysical detector, we evaluate equation (33) for large  $N$  and multiply it by the gating function  $g$ . Again, in this case,

$$G_\infty = g \cdot S_\infty = \frac{1 - e^{-\Delta/\tau} e^{-j\omega\Delta}}{1 + j\omega\tau} \cdot \frac{1}{1 + e^{-\Delta/\tau} e^{j\omega T/2}}. \quad (34)$$

This expression is now rationalized to obtain

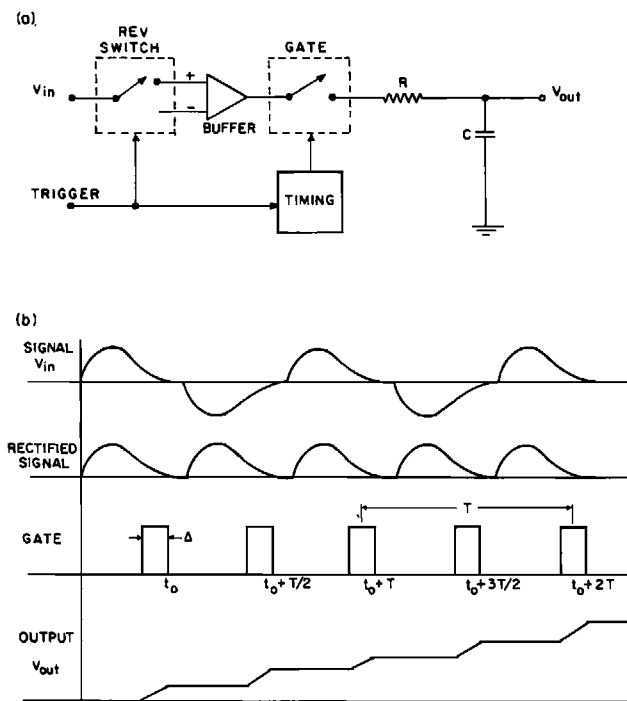


FIG. 4. (a) Simplified schematic diagram for the geophysical detector. (b) Synopsis of signal processing for the geophysical detector.

$$|G_\infty|^2 = \frac{1}{(1 + \omega^2 \tau^2)} \left[ \frac{(1 - e^{-\Delta/\tau})^2 + 4e^{-\Delta/\tau} \sin^2 \omega \Delta / 2}{(1 + e^{-\Delta/\tau})^2 - 4e^{-\Delta/\tau} \sin^2 \omega T / 4} \right]. \quad (35)$$

To inspect the behavior of this function, we can examine limiting values of this expression under the same assumptions used to establish equations (15 through 18). In so doing we find

$$\begin{aligned} |G_\infty|_{dc}^2 &= \frac{\Delta^2}{4\tau^2}, \\ |G_\infty|_{\omega_n}^2 &\approx \frac{\text{sinc}^2 \omega_n \Delta / 2}{1 + \Omega^2 \tau_e^2}, \end{aligned} \quad (36)$$

with

$$\Omega = \pm \left( \omega - \frac{2n\pi}{T} \right),$$

$n = \text{an odd integer}$  and  $\tau_e = \tau T / 2\Delta$ .

Figure 5 shows that the transfer function takes the form of a comb filter which blocks any dc and passes only the odd harmonics of the fundamental signal frequency. The width of each spectral window however is now twice as large as it was for the boxcar integrator because the effective time constant  $\tau_e$  has been reduced by a factor of two. This change is a direct consequence of sampling the signal twice during each full period. The shortening in the effective time constant also results in a relatively shortened step response which is given by equation (21).

Turning to the noise rejection properties of the geophysical detector we proceed to evaluate its noise bandwidth. Using a result that can be derived by applying Parseval's theorem to the Fourier series for an alternating square wave i.e.,

$$\sum_{n=1,3,5,\dots}^{\infty} \text{sinc}^2 nx = \frac{\pi}{4} x; \quad (37)$$

we readily find,

$$B = \int_0^{\infty} |G_\infty|^2 df = 1/4\tau. \quad (38)$$

Surprisingly, the noise bandwidth for the geophysical detector which has windows only at the odd harmonics of the signal frequency is the same as that for the boxcar integrator with windows at all the harmonics. The apparent inconsistency is immediately resolved by noting that the windows of the geophysical detector are twice as wide as those of the boxcar integrator.

Finally, we note that because the gating functions and the noise bandwidth for the geophysical detector and the boxcar integrator are the same, the signal-to-noise improvement ratio for these two devices is the same and is given by equation (29). As in the case of the boxcar detector the output noise is severely band limited to a frequency range

$$f_{MAX} \approx \frac{\Delta}{\pi\tau T} \approx \frac{1}{2\pi\tau_e}. \quad (39)$$

A spectral compression diagram for the geophysical detector is shown in Figure 6. As in the

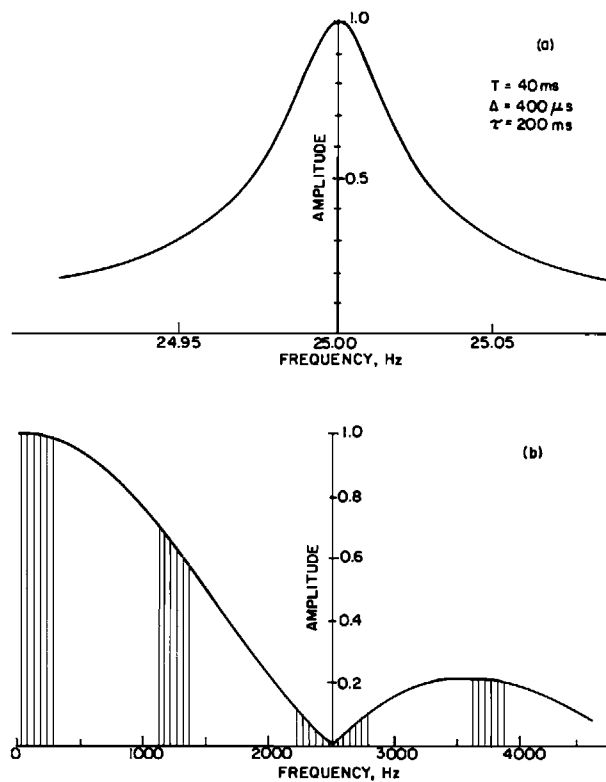


FIG. 5. Transfer function for the geophysical detector: Base frequency 25 Hz; gate width 400  $\mu\text{s}$ ; RC product “ $\tau$ ” 200 ms. (a) Detailed description of the first spectral window. (b) Envelope of spectral window amplitudes. Selected odd spectral lines are shown explicitly.

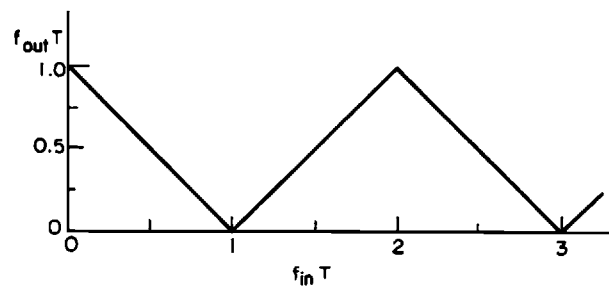


FIG. 6. Frequency translation diagram for the geophysical detector.

boxcar integrator all the odd signal harmonics are translated to d.c. but d.c. and noise at the even harmonics (where there is virtually no transmission) appear at the fundamental frequency of the signal.

### Lock-in amplifier

The lock-in amplifier (Meade, 1983) is a specific implementation of the geophysical detector. Because it is only used to sense sinusoidal continuous wave signals, the gate width  $\Delta$  is fixed and is made to equal one-half of the signal period. Under this condition, the equilibrium frequency domain transfer function (35) becomes

$$|G_\infty|^2 = \frac{1}{(1 + \omega^2 \tau^2)} \left[ \frac{(1 - e^{-T/2\tau})^2 + 4e^{-T/2\tau} \sin^2 \omega T/4}{(1 + e^{-T/2\tau})^2 - 4e^{-T/2\tau} \sin^2 \frac{\omega T}{4}} \right]. \quad (40)$$

For  $\omega_n = 2n\pi/T$ ,  $n =$  an odd integer, we have

$$|G_\infty|_{\omega_n}^2 = \frac{\coth^2 T/4\tau}{1 + 4\pi^2 n^2 \tau^2/T^2}. \quad (41)$$

If additionally we allow  $\tau \gg T$ , then

$$|G_\infty|_{\omega_n} \approx \frac{2}{\pi n}. \quad (42)$$

Thus, we see that the output of the lock-in amplifier at any odd harmonic of the signal frequency is exactly that harmonic's amplitude averaged over a half-period of the fundamental. All the other relationships derived for the geophysical detector apply here. In particular the response time  $\tau_e$  equals the time constant  $\tau$  of the averaging circuit. The signal-to-noise improvement ratio for white noise is also given by equation (29) i.e.,

$$\text{SNIR} = (4\pi/T)^{1/2}.$$

This result is in agreement with that given in Neelakantan et al. (1980) which points out that the SNIR for colored noise is a much more complex function of  $T$  and  $\tau$ .

The lock-in amplifier is used on all frequency domain electromagnetic exploration systems. In its usual configuration two gates are used. One gate is opened the instant that the primary field crosses zero while the second gate is opened  $T/4$  or  $90^\circ$  later. The averaged output of the first gate then detects the inphase component of the secondary field, while the averaged output of the second gate is proportional to the quadrature component. The noise bandwidth of the lock-in amplifier can be further reduced by incorporating a narrow band-pass filter tuned to the signal frequency in the signal channel. The additional circuitry is not very effective for white noise because it only results in a 20 percent reduction of the noise bandwidth. It does, however, prevent the detection of any harmonics of the signal frequency and reduces cross-talk in multi-frequency systems.

## Digital Detection of Geophysical Signals

Makers of geophysical instruments were among the first to take advantage of new digital technology which became available fifteen years ago. Initially, because of slow speed and poor resolution, the technology was only used in airborne instrumentation for data logging. In these applications the signal was processed by an analog detector of the type just described but the detector output was digitally recorded on magnetic tape. The advent of high-speed,

high-resolution analog-to-digital converters and microprocessors however can be expected to render analog detection of electromagnetic signals obsolete.

A typical geophysical detector consists of an antialiasing filter with a high frequency cutoff defined by the required signal bandwidth, a fast, high resolution analog to digital converter, and a minicomputer or microcomputer for processing the acquired data. The detector output is then fed to an appropriate display device and to a digital recording device that stores the acquired data for further processing. Figure 7 (a) shows a synoptic diagram for a typical digital detector.

The signal acquisition process for the digital detector follows closely the sequence used in analog equipment. First the signal is sampled at a rate consistent with the bandwidth (BW) of the antialias filter and the data is then gated by averaging groups of  $n$  adjacent samples. The data groups are then coherently sorted into channels with each channel containing a subset of the acquired data. Two data groups spaced by half the period of the signal repetition frequency are taken during each cycle of the signal. As shown in Figure 7b the acquisition timing is synchronized with the transmitted primary field so that the delay between the commencement of the signal cycle and the positioning of a given data group is constant. The sorting or windowing process is then followed by rectification consistent with the signal polarity changes that occur during each half cycle and averaging of the rectified data. Usually these two processes are combined into a single digital filtering operation. Note also that the subdivision of the acquired data into channels effectively results in a number of data streams each containing only two data points per signal cycle. Thus the spectral compression process shown for the analog geophysical detector in Figure 6 equally applies here.

Before describing a number of different digital filtering procedures, we consider the frequency domain transfer function for the windowing process. Consider a stream of samples taken every  $\epsilon$  seconds. To properly sample the signal which is band-limited to a width (BW) by the antialias filter we must have

$$\epsilon = 1/(2(BW)). \quad (44)$$

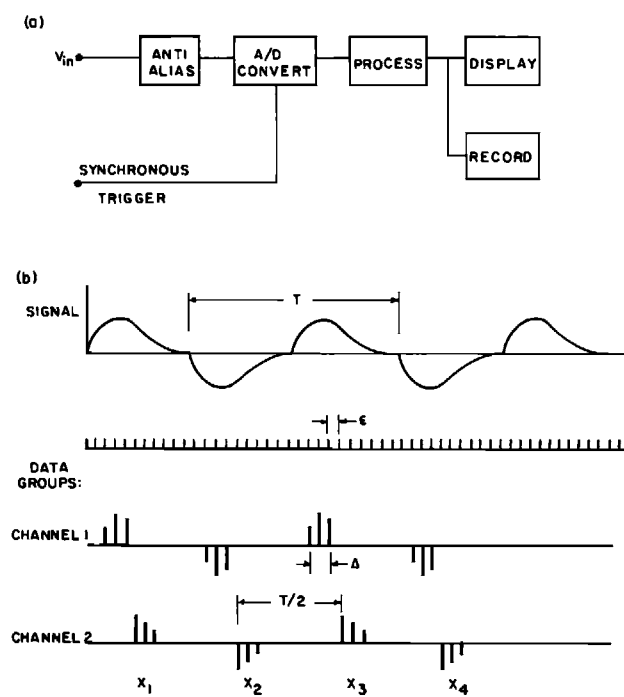


FIG. 7. (a) Simplified block diagram for a digital detector. (b) Synopsis of signal processing for the digital detector.

As shown in Lee (1960, p. 316) the averaging of  $n$  contiguous samples in a group results in a transfer function given by

$$|g|^2 = \frac{\sin^2 n\omega\varepsilon/2}{n^2 \sin^2 \omega\varepsilon/2}. \quad (45)$$

Substituting

$$\Delta = n\varepsilon \quad (46)$$

and assuming  $\omega\varepsilon \ll 1$ , we find that

$$|g| \approx \text{sinc} \frac{\omega\Delta}{2}, \quad (47)$$

an expression quite similar to equation (7) (apart from a factor of  $\Delta/\tau$ ) that was obtained for the gating of the boxcar integrator.

### The digital analogy detector

The digital analogy detector derives its name from the fact that its mode of operation is entirely analogous to that ascribed to the general purpose equipment discussed. Signal averaging in this case, however, is accomplished with the aid of a recursive digital filtering algorithm instead of a gate and an analog low pass filter. The algorithm used is given by

$$y_n = \left(\frac{\alpha - 1}{\alpha}\right)^2 y_{n-2} - \left(\frac{1}{\alpha}\right)\left(\frac{\alpha - 1}{\alpha}\right)x_{n-1} + \left(\frac{1}{\alpha}\right)x_n. \quad (48)$$

Here the symbol  $y_i$  denotes the output of the filter while the symbol  $x_i$  corresponds to the input. Because “ $\alpha$ ” is a number that defines the time constant of the filter, it must be greater than one but otherwise may be set as desired. The frequency domain transfer function for this filter can be written according to a general relationship for recursive filters given in Hamming (1977, p. 181) as,

$$S(\omega) = \frac{1}{\alpha} \left[ \frac{1 - \left(\frac{\alpha - 1}{\alpha}\right)e^{-j\omega T/2}}{1 - \left(\frac{\alpha - 1}{\alpha}\right)^2 e^{-j\omega T}} \right] = \frac{1}{\alpha} \frac{1}{1 + \left(\frac{\alpha - 1}{\alpha}\right)e^{-j\omega T/2}}. \quad (49)$$

Here  $T$  denotes the signal repetition period. The significance of the filter variable  $\alpha$  is immediately available by comparing equation (49) with its analog equivalent equation (33) evaluated for large  $N$ . In that case we have

$$S_\infty(v) = \frac{1}{1 + e^{-v/2}} = \frac{1}{1 + e^{-\Delta/\tau} e^{-j\omega T/2}}.$$

For  $\Delta \ll \tau$  we have

$$e^{-\Delta/\tau} \approx 1 - \Delta/\tau \equiv 1 - \frac{1}{\alpha} \quad (50)$$

or

$$\alpha = \frac{\tau}{\Delta}$$

and

$$\alpha T/2 = T \cdot \tau/2\Delta = \tau_e. \quad (51)$$

Thus we begin to suspect that the digital filtering process described is indeed analogous to the analog geophysical detector, providing we set the filter variable  $\alpha$  to equal twice the effective time constant of the analog device divided by the signal repetition period.

The amplitude dependence on frequency of the overall transfer function of the device can now be established by rationalizing equation (49) and multiplying by equation (45). We then have

$$|G|^2 = |g|^2 \cdot |s|^2 = \frac{\sin^2 n\omega\varepsilon/2}{n^2 \sin^2 \varepsilon\omega/2} \cdot \frac{1}{1 + 4\alpha(\alpha - 1) \cos^2 \omega T/4}. \quad (52)$$

This transfer function is entirely similar to that for the analog geophysical detector as given by equation (36). To confirm this put

$$\omega_m = 2m\pi/T \quad m \text{ odd}$$

$$\Omega = \omega - \omega_m$$

$$\tau_e = \sqrt{\alpha(\alpha - 1)} T/2 \approx \alpha T/2$$

$$n\varepsilon = \Delta$$

$$\omega_m \varepsilon \ll 1$$

to get

$$|G|^2 \approx \operatorname{sinc}^2 \frac{\omega_m \Delta}{2} \frac{1}{1 + \Omega^2 \tau_e^2}. \quad (53)$$

As shown in Figure 8 the transfer function (52) takes on the familiar form of a comb-filter that passes only the odd harmonics of the fundamental frequency. The width of each spectral window is identical and is given by

$$\Delta f = \frac{1}{\pi \tau_e} = \frac{2}{\pi \alpha T}. \quad (53a)$$

We now show that the step response of the recursive digital filter is approximately exponential with the effective time constant given by equation (51). To do this we return to equation (48) and use as the input  $x_i$  a series of coherently alternating samples of unit amplitude.

Putting  $x_i = (-1)^{i+1}$  we obtain from equation (48)

$$(y_n - y_{n-2}) = \left( -\frac{2}{\alpha} + \frac{1}{\alpha^2} \right) y_{n-2} + \frac{1}{\alpha} \left( 1 - \frac{1}{\alpha} + 1 \right) \approx \frac{2}{\alpha} (1 - y_{n-2}) \quad (54)$$

or

$$\frac{(y_n - y_{n-2})}{T} \approx \frac{2}{\alpha T} (1 - y_{n-2}).$$

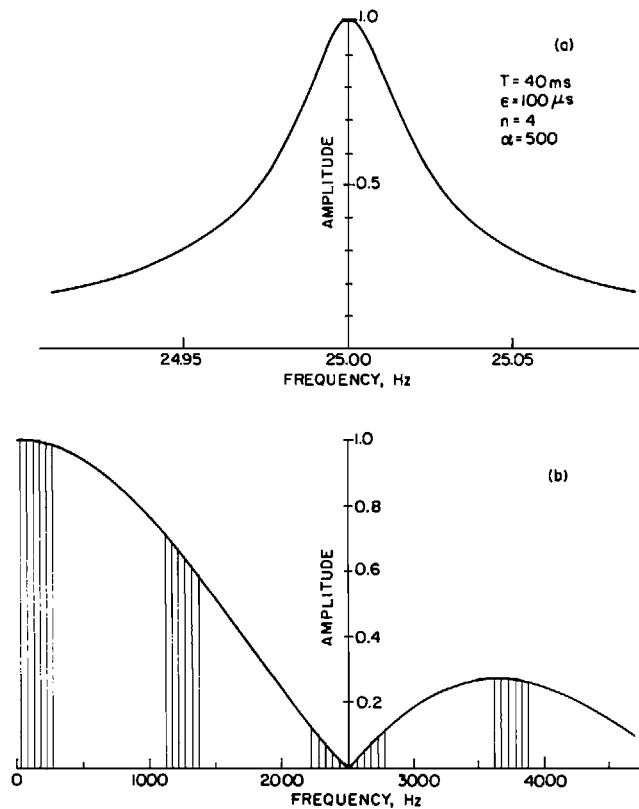


FIG. 8. Transfer function for the digital analogy detector: Base frequency 25 Hz; sampling interval 100  $\mu\text{s}$ ; window width 4 samples; filtering coefficient "a" equals 500. (a) Detailed description of the first spectral window. (b) Envelope of spectral window amplitudes. Selected odd spectral lines are shown explicitly.

Now, approximate the difference on the left hand side by a derivative to get

$$\frac{dy}{dt} \approx \frac{2}{\alpha T} (1 - y) \quad (55)$$

and

$$y(t) \approx (1 - e^{-t/\tau_e})$$

Here

$$\tau_e = \frac{\alpha T}{2}$$

as before.

To obtain the signal-to-noise improvement ratio for the digital analogy device we inspect the reduction in the output variance at each step in the process. Initially for white noise with spectral density  $\eta_0$  and bandwidth BW the variance is given by

$$\sigma_x^2 = \eta_0(BW). \quad (56)$$

Averaging  $n$  contiguous samples reduces the variance by a factor of  $n$ . Thus

$$\sigma_{xx}^2 = \frac{\sigma_x^2}{n}. \quad (57)$$

Finally, assuming uncorrelated noise, it can be shown from first principles that the recursive filtering process reduces the output variance further by a factor of

$$p = \alpha^2 - (\alpha - 1)^2 = (2\alpha - 1). \quad (58)$$

Thus the overall reduction is given by

$$\sigma_y^2 = \frac{\sigma_x^2}{n[(\alpha^2 - (\alpha - 1)^2)]. \quad (59)}$$

This corresponds to an SNIR of

$$\text{SNIR} = \frac{\sigma_x}{\sigma_y} \approx \sqrt{2n\alpha} \quad (60)$$

for  $\alpha \gg 1$ .

Note that the noise reduction factor  $p$  is in agreement with that given in Oliver (1984) for the exponential smoothing of a time series with no sign reversals in adjoining samples.

### Uniform stacking detector

If the available computing equipment is optimized or if a very high rejection of coherent interference (e.g. powerline harmonics) is needed, it is useful to follow the initial gating process given by equation (45) with a uniform nonrecursive averaging process. In this case, simply average each gate output over  $N$  repetitions of the primary field cycle. This procedure can be written as

$$y_{n+M} = \frac{1}{(M + 1)} \sum_{k=0}^M (-1)^k x_{n+k}, \\ M = 2N - 1. \quad (61)$$

Here  $y_i$  corresponds to the output while the  $x_i$  constitutes the input data. As shown in San Filipo and Hohmann (1983) and in Macnae et al. (1984) the frequency domain transfer function for the linear averaging process is also a comb filter with windows positioned at the odd harmonics of the signal repetition frequency. Unlike the digital analogy process, however, the transfer function also has points of zero transmission. These can be positioned at will by a suitable choice of signal repetition frequency and the number of cycles to be averaged. Both authors cited use the convolution theorem to derive a frequency domain transfer function for the filtering process described by equation (61). Proceeding in this manner the result is a solution in terms of an infinite series. A simpler equivalent result however, may be obtained by returning to first principles and using the method proposed in Lee (1960, p. 316) or in Hamming (1977, p. 31) to derive the required transfer function. In that case, the relationship sought can be written in closed form as

$$S_1(\omega) = \left( \frac{1 - e^{-j\omega T/2}}{2N} \right) \left( \frac{1 - e^{-j\omega NT}}{1 - e^{-j\omega T}} \right) \quad (62)$$

where  $N$  = number of cycles averaged and  $T$  = signal repetition period. The complete frequency domain transfer function for the uniform stacking detector is obtained by rationalizing equation (62) and multiplying it by equation (45). We then have

$$|G|^2 = |g|^2 |S_1^2| = \frac{\sin^2 n\omega\varepsilon/2}{n^2 \sin^2 \omega\varepsilon/2} \cdot \frac{1}{4N^2} \cdot \frac{\sin^2 N\omega T/2}{\cos^2 \omega T/4}. \quad (63)$$

As shown in Figure 9, equation (63) defines a comb filter with windows positioned at the odd harmonics of the signal repetition frequency. To verify this put

$$\omega_m = 2m\pi/T, \quad m \text{ odd}$$

$$\Omega = \omega - \omega_m,$$

$$n\varepsilon = \Delta,$$

$$\omega_m\varepsilon \ll 1.$$

Then for

$$\Omega T \ll 1$$

$$|G^2| = \operatorname{sinc}^2 \frac{\omega_m \Delta}{2} \operatorname{sinc}^2 N\Omega T/2. \quad (64)$$

The width of each spectral window is approximately given by

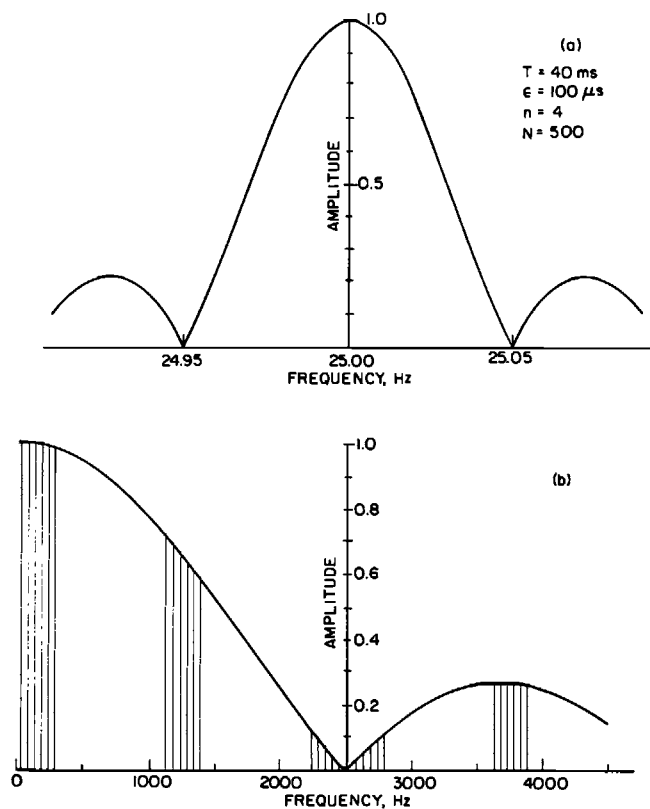


FIG. 9. Transfer function for the uniform stacking detector: Base frequency 25 Hz; sampling interval 100  $\mu$ s; window width 4 samples; stack length N 500 cycles. (a) Detailed description of the first spectral window. (b) Envelope of spectral window amplitudes. Selected odd spectral lines are shown explicitly.

$$\Delta f = 2\sqrt{2}/\pi NT. \quad (64a)$$

Unlike the digital analogy detector the step response of the uniform stacking detector is linear in time and is given by,

$$\begin{aligned} h(t) &= t/NT & 0 < t < NT \\ &= 0 & t > NT. \end{aligned} \quad (65)$$

Finally, as shown in San Filipo and Hohmann (1983), it is easy to demonstrate that the variance of the input noise is reduced by a factor of  $2Nn$  using the linear stacking process. In this case a signal-to-noise improvement ratio is given by

$$\text{SNIR} = \frac{\sigma_x}{\sigma_y} = \sqrt{2nN}. \quad (66)$$

### Digital lock-in

Either the digital analogy detector or the uniform stacking detector may be operated as a digital lock-in amplifier. San Filipo and Hohmann (1983) point out, however, that to detect a single frequency signal it is best to eliminate the spectral windows at the odd harmonics of the signal frequency by cross correlating the input with a sinusoid. The result is then averaged over N cycles of the signal. The required operation is defined by

$$y(t) = \frac{i}{NT} \int_{t-NT}^t x(\tau) e^{-i\omega_0[\tau-(t-NT)]} d\tau. \quad (67)$$

where  $T$  = signal period and  $\omega_0 = 2\pi/T$ . The frequency domain transfer function for this process is given by

$$|G|^2 = \text{sinc}^2 \frac{NT}{2} \left( \omega - \frac{2\pi}{T} \right). \quad (68)$$

This transfer function has only one window at the signal frequency. Its SNIR is given by

$$\text{SNIR} = NT(BW), \quad (69)$$

where  $BW$  = is the input bandwidth.

## Optimization of Dynamic Systems

On the basis of the material presented, we conclude that in stationary applications the signal-to-noise ratio can be improved without limit. To a large extent this is true, nevertheless, for very low frequency signals long data acquisition periods may turn out to be impractical and other supplementary means of noise reduction should be used. These include filtering (San Filipo et al., 1983), spike rejection or tapered window stacking (Macnae et al., 1984), and remote reference noise cancellation (Wilt et al., 1983). In the last case care must be taken with the telemetry so no additional digitizing noise is introduced. (San Filipo et al., 1983).

In the case of dynamic data acquisition when the signal is observed from a moving platform the maximum possible signal-to-noise improvement ratio is finite. It depends on the target, the vehicle velocity, and the effective time constant of the signal detector. This matter was first examined by Li and Cao (1982).

Thus consider the detection of a vertical tabular orebody with a large scale, towed-bird airborne electromagnetic system. To a first coarse approximation the static anomaly for this type of configuration is given by

$$V(x) = \frac{V_0(S, f, h)}{2} \left[ 1 + \cos \pi \frac{x}{h} \right], \quad -h < x < h,$$

$$= 0 \quad \text{elsewhere.} \quad (70)$$

Here,

- $V(x)$  = Anomaly amplitude
- $x$  = distance along traverse wrt ore body,
- $h$  = depth of deposit below aircraft,
- $V_0$  = amplitude factor,
- $S$  = conductance of deposit,
- $f$  = primary field frequency.

If the aircraft traverses the orebody with a constant velocity " $v$ ," the observable static anomaly as a function of time " $t$ ," is given by

$$V(t) = \frac{V_0}{2} \left[ 1 + \cos \pi \frac{t}{b} \right],$$

with

$$x = vt,$$

and

$$b = h/v.$$

Now when this anomaly is observed with a detector whose step response is governed by a time constant " $\tau_e$ " and equals

$$h(t) = 1 - e^{-t/\tau_e}, \quad (71)$$

then the observed dynamic anomaly will be given by

$$V^1(t) = V(t) * \frac{d}{dt} h(t) = \frac{V_0}{2\tau_e} \int_{-b}^t \left[ 1 + \cos \left( \frac{\pi y}{b} \right) \right] e^{-(t-y)/\tau_e} dy. \quad (72)$$

Carrying out the required integration we get

$$V^1(t) = 0 \quad \text{for } t < -b,$$

$$V^1(t) = \frac{V_0}{2} \left\{ 1 + \frac{1}{1 + \beta^2} [\cos \beta t^1 + \beta \sin \beta t^1 - \beta^2 e^{-(t^1 + \pi/\beta)}] \right\}$$

$$= \frac{V_0}{2} y(t^1, \beta) \quad \text{for } -b < t < b, \quad (73)$$

and

$$V^1(t) = V_0 \frac{\beta^2}{1 + \beta^2} \sinh\left(\frac{\pi}{\beta}\right) e^{-t^1} \quad \text{for } t > b.$$

Here,

$$\beta = \frac{\pi \tau_e}{b},$$

and

$$t^1 = t/\tau_e.$$

Figure 10 compares the static anomaly ( $\beta = 0$ ) with the filtered anomaly for a number of detector time constants. For low values of the time constant the static anomaly is observed virtually undistorted and with little reduction in amplitude. As the time constant is increased, however, the filtered anomaly is distorted, its maximum is delayed, and its amplitude is severely diminished. Thus in the presence of noise we see a conflict between reducing the noise, which calls for a large detector time constant, and faithfully reproducing the anomaly, which requires a low value for the detector time constant. This conflict of interest can be resolved by realizing that it is possible to choose a detection time constant that yields an optimum value for the signal-to-noise ratio.

Recall that for an analog detector the noise bandwidth is given by

$$B = 1/4\tau$$

while the effective time constant is given by

$$\tau_e = \tau T / 2\Delta.$$

Thus, in the presence of white noise defined by a spectral density " $\eta_0$ ," the noise power that

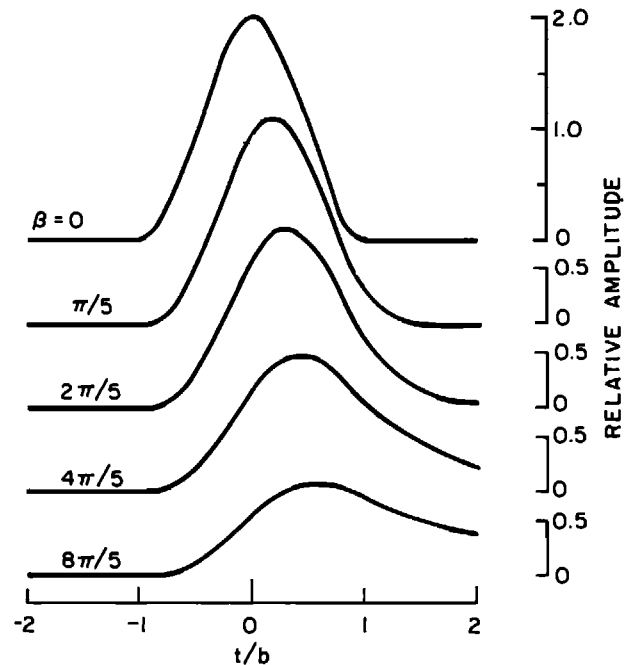


FIG. 10. Effect of low-pass filtering on a typical geophysical anomaly.

appears at the detector output will be

$$\eta_0 B = \frac{\eta_0}{4\pi} = \frac{\eta_0}{8\tau_e} \times T/\Delta. \quad (74)$$

If  $V_0^1(\beta)$  is the maximum anomaly observed when the effective value of the detector time constant is  $\tau_e$ , then the S/N ratio is given by

$$S/N = [V_0^1(\beta)]^2 / \eta_0 B, \quad (75)$$

or

$$S/N = \left( \frac{2V_0^2}{\eta_0} \right) \left( \frac{\Delta b}{\pi T} \right) [\beta y_m^2(\beta)],$$

where all the symbols stand as defined and  $y_m(\beta)$  is the maximum value of  $y(t^1, \beta)$  and is obtained from a numerical evaluation of equation (73). Once this is done we can readily compute the function

$$\mu(\beta) = \beta y_m^2(\beta).$$

As shown in Figure 11, this function has a well defined maximum that occurs at

$$\beta = \pi\tau T v / 2\Delta h = 2.65$$

$$\mu_m = 0.94 \quad (76)$$

Thus, for white noise,

$$S/N_{MAX} = 0.6 \frac{V_0^2 \Delta b}{\eta_0 T} = 0.6 \frac{(V_0^2 \Delta) h}{\eta_0 v T} \quad (77)$$

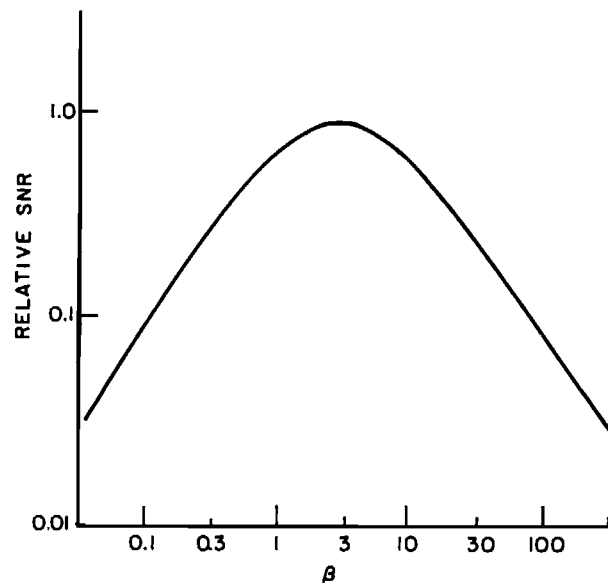


FIG. 11. Variation of the signal-to-noise ratio with the detector time constant.

Equation (77) shows that for a given static anomaly amplitude and a given white noise density the maximum possible S/N ratio that can be obtained with an analog geophysical detector is defined by the detector channel gate width and the number of primary field pulses that are transmitted while traversing the anomaly. Of course in any realistic situation the maximum static anomaly amplitude  $V_0$  is a function of the signal repetition period  $T$ , and some minimal value of this last parameter is needed to detect a given type of deposit. Furthermore, once a particular aircraft is chosen to carry the airborne system, the transit velocity is defined so that the only free variable in equation (76) is the low pass filter time constant which can be set to a value that will result in an optimal S/N ratio.

Finally, we must note that the object of this discussion of detector optimization is to introduce a concept rather than to present a recipe. A similar approach can be used to derive optimal parameter values ( $\alpha$  and  $N$ , respectively) for the digital analogy detector and uniform stacking detector. Furthermore this type of analysis need not be restricted to the case of white noise but may be applied numerically in other cases where the actual noise spectrum for a given installation can be obtained experimentally.

## Summary

We have demonstrated the comb-filter characteristics of geophysical detectors. This property arises directly from the process of coherent periodic sampling of the signal. The width of the transmission windows depends on the duty cycle (gate width to signal period ratio) and the parameter (time constant or number of cycles averaged) that defines the averaging process. These two quantities also define the effective time constant of the detector and the signal-to-noise improvement ratio. The gate width for a given detector channel also has a relatively minor role in determining the height of the comb-filter windows. Its principal effect is the suppression of high-frequency noise. The parameters of a geophysical detector may be set at will, depending on the detector's exact properties. In the case of stationary applications these are determined by the desired signal-to-noise improvement ratio. In the case of dynamic applications, however, the detector parameters can be optimized as a function of the system used, the vehicle it is installed in, and the exact spectral characteristics of the noise.

## Acknowledgments

This work was partially funded by a grant from the Selco Division of British Petroleum, Canada.

## References

- Blume, R.J., 1981, Boxcar integrator with long holding times: *Rev. Sci. Inst.*, **32**, No. 9, 1016–1018.  
 Collins, F.G. and Katchinoski, R., 1973, Boxcar attachment for oscilloscopes useful for low level signals: *Rev. Sci. Inst.*, **44**, No. 9, 1178–1181.  
 Gradshteyn I.S. and Ryzhik I.M., 1965, Tables of integrals, series and products: Academic Press, N.Y.  
 Hamming, R.W., 1977, Digital filters: Prentice-Hall, Inc. N.J.  
 Hietje, G.M., 1972, Signal to noise enhancement through instrumental techniques, Part I: *Anal. Chem.*, **44** No. 6, 81A–88A. Part II, *Annal. Chem.*, **44**, No. 7, 69A–78A.  
 Jolley, L.B.W., 1961, Summation of series: Dover Publ. Inc., N.Y.  
 Lazenby, P.G. and Wondergem, H.M., 1974, Apparatus for the remote detection of conducting bodies: Canadian Patent # 941015, iss. Jan. 29, 1974.  
 ——Apparatus for analyzing transients in a periodic sequence of signals: Canadian Patent No. 970471, iss. July 1, 1975.  
 Lee, Y.W., 1960, Statistical theory of communication: John Wiley & Sons, N.Y.  
 Li, M., and Cao, M., 1982, On the selection of sampling frequency in airborne digital pulsed EM systems: *Journal of Changchun College of Geology*, Vol. 1, 105–112.

- Neelakantan K. and Dattagupta, S., 1978, Analysis of signal-to-noise enhancement of Box-Car averagers: *Pramana* **11**, No. 3, 295–306.
- Neelakantan, K., Dattagupta, S., and Rajappan, K.P., 1980, Signal-to-noise enhancement of lock-in amplifiers: *Rev. Sci. Inst.*, **51** No. 2, 251–252.
- Macnae, J.C., Larmontagne, Y., and West, G.F., 1984, Noise processing techniques for time-domain EM systems: *Geophysics*, **49**, 934–948.
- Meade, M.L., 1983, Lock-in amplifiers: principles and applications: Peter Peregrinus Ltd., London.
- Oliver, R.M., 1984, Exponential smoothing-I: *Operations Res. Ctr. Rept.* 84-5. University of California, Berkeley.
- San Filipo, W.A., and Hohmann, G.W., 1983, Computer simulation of low-frequency electromagnetic data acquisition: *Geophysics* **48**, 1219–1232.
- Wilt, M., Goldstein, N.E., Stark, M., Haught, J. R., and Morrison, H.F., 1983, Experience with the EM-60 electromagnetic system for geothermal exploration in Nevada: *Geophysics*, **48**, 1090–1101.



This page has been intentionally left blank

---

---

**8**

**Inversion of Controlled-Source  
Electromagnetic Data**

---

---



---

---

---

**8**

---

---

## Inversion of Controlled-Source Electromagnetic Data

*Gerald W. Hohmann\**  
*and*  
*Arthur P. Raiche‡*

Given a set of geophysical measurements, we want to determine all information possible about the geologic structure that gave rise to the data. There are two aspects. First, because we use electrical and electromagnetic (EM) methods of exploration we want to determine the geolectric structure of the earth; i.e., the conductivity and/or the permittivity as a function of depth and lateral distance. If we can do this, then the second aspect will relate the geolectric structure to the geologic structure. In some cases, a one-to-one relationship exists between the two; in others, there may be only a partial but useful overlap. This chapter addresses the first aspect—determining the geoelectrical structure based on controlled-source electromagnetic (CSEM) data.

The earliest inversion methods can be described as trial-and-error exercises. Starting with a general model, such as a layered earth or a thin dike, and then adjusting the parameters of the model we achieve a best-fit to the data. The parameters in this case are the physical dimensions and conductivities of the structures. Basically the exercise consists of running a number of forward models, and systematically adjusting the important parameters until the response matches the observed data within the noise level of the measurements.

Model-fitting by trial-and-error is still the most common interpretation technique for multidimensional models, but there are problems with the approach:

1. There is an a priori restriction to classes of models for which a relatively fast forward solution exists.
2. Because relatively simple models can have several parameters, some of which may be strongly correlated, the trial-and-error process may involve a prohibitive amount of time.
3. Fitting an assumed physical model to observed data involves a high degree of subjectivity.  
It is important to estimate confidence intervals for the various parameters and for other statistical measures that provide insight into how appropriate the model is. The trial-and-error approach does not provide this information.

A more satisfactory method of interpretation is inversion where properties of the earth are calculated directly or indirectly from the data. Inversion, which is more objective than curve

\*Department of Geology and Geophysics, University of Utah, Salt Lake City, Utah 84112 USA  
‡CSIRO, Division of Mineral Physics, P.O. Box 136, North Ryde, NSW, Australia 2113

fitting, also provides information on resolution and reliability of interpreted models. However, the inverse problem for EM is complicated greatly because it is nonlinear.

The fundamental inverse problem for EM consists of estimating conductivity as a function of position (Parker, 1980). We consider this problem for a one-dimensional (1-D) earth in the first section of this chapter. Because the solution must be based on a finite data set, the inverse problem is underdetermined. Of more use in practical interpretation problems, however, is model fitting by optimization: computing the parameters of an assumed model that is supposed to represent that portion of the earth under consideration. Normally the model fitting problem is overdetermined, i.e., there are fewer parameters than data. This latter approach, developed in detail for the 1-D sounding case in the second section of the chapter, alleviates some of the inherent nonuniqueness by constraining the interpreted model based on geological knowledge and other geophysical data. Central to either approach is appraisal: assessing the reliability of the interpretation. Finally, we consider inversion for multidimensional models, which is an extremely important research topic given the inadequacy of 1-D models in most cases. 

## The Electromagnetic Inverse Problem

This section considers the fundamental inverse problem for EM: determining the conductivity as a function of position based on measurements of one or more components of the EM field. The measurements may be made as a function of position or as a function of time or frequency. For simplicity, we consider frequency-domain measurements only, and specifically the 1-D case.

### Integral equation formulation

The fundamental and conceptually simplest formulation of the EM inverse problem is based on the integral equation

$$\mathbf{E}(\mathbf{r}_0, \omega) = \mathbf{E}_p(\mathbf{r}_0, \omega) + \int_{\Omega} \mathbf{G}(\mathbf{r}_0, \mathbf{r}; \omega) \mathbf{E}(\mathbf{r}, \omega) \sigma_a(\mathbf{r}) d\mathbf{v}, \quad (1)$$

derived by Hohmann (this volume). As illustrated in Figure 1,  $\mathbf{r}_0$  denotes an observation point, and the conductivity  $\sigma(\mathbf{r})$  in a domain  $\Omega$  is to be estimated based on measurements of  $\mathbf{E}(\mathbf{r}_0)$  or  $\mathbf{H}(\mathbf{r}_0)$ , or both.

The anomalous conductivity,  $\sigma_a = \sigma - \sigma_*$  in equation (1), is the difference between the actual conductivity  $\sigma$  in  $\Omega$  and the reference conductivity  $\sigma_*$ . Here  $\mathbf{G}$  is the tensor Green's function for electric field based on the reference model. For the situation illustrated in Figure

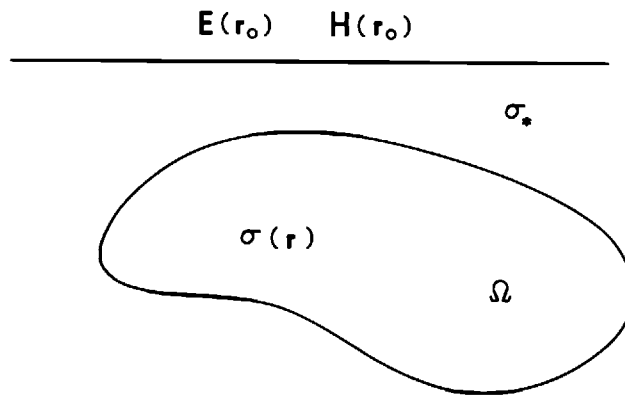


FIG. 1. Configuration for EM inverse problem.

1, the tensor Green's function accounts for the earth-air interface. The primary or reference field  $\mathbf{E}_p$  is the field that would exist if  $\sigma_*$  were equal to  $\sigma$  in  $\Omega$ . In another situation the reference medium might be free space instead of a half-space, in which case the Green's function would be the simple free-space Green's function.

Applying Faraday's law to equation (1) results in an analogous equation for magnetic field measurements:

$$\mathbf{H}(\mathbf{r}_0, \omega) = \mathbf{H}_p(\mathbf{r}_0, \omega) + \int_{\Omega} \mathbf{G}_H(\mathbf{r}_0, \mathbf{r}; \omega) \mathbf{E}(\mathbf{r}, \omega) \sigma_a(\mathbf{r}) d\mathbf{v}, \quad (2)$$

where  $\mathbf{G}_H$  is the tensor Green's function for the magnetic field.

If the electric field in  $\Omega$  were known, equations (1) and (2) would be simple, linear, Fredholm integral equations of the first kind to solve for the anomalous conductivity  $\sigma_a$ . One possible approach is to set  $\mathbf{E}$  to  $\mathbf{E}_p$ , the known primary electric field, in  $\Omega$  and determine an approximate  $\sigma_a$ , a procedure known as Born inversion. In seismology Born inversion produces useful results, because changes in the sought physical property (velocity) are small. In fact, Cheng and Coen (1984) show that results from Born inversion of seismic data are directly related to those produced by migration. However, because conductivity varies over orders of magnitude, Born inversion is not sufficient for EM data. For example, if  $\sigma \gg \sigma_*$ , then  $\mathbf{E} \ll \mathbf{E}_p$ .

For simplicity, we consider only 1-D inverse problems now and discuss multidimensional models later. To conserve space, we consider electric field measurements and equation (1); analogous results apply for magnetic field measurements and equation (2). For a 1-D earth, equation (1) can be written

$$\begin{aligned} \mathbf{E}(x_0, y_0, z_0) &= \mathbf{E}_p(x_0, y_0, z_0) \\ &+ \int_0^{\infty} \int_{-\infty}^{\infty} \int_{-\infty}^{\infty} \mathbf{G}(x_0 - x; y_0 - y; z_0, z) \mathbf{E}(x, y, z) dx dy \sigma_a(z) dz, \end{aligned} \quad (3)$$

where dependence on frequency is implicit.

### Uniqueness

Even with error-free data, the inverse problem for  $\sigma(z)$  based on equation (3) does not have a unique solution. The conductivity is a continuously defined function, which cannot be determined uniquely from a finite collection of data (Parker, 1977). When random noise is added, the situation might seem hopeless; however, geophysical inverse theory provides a means of deducing what can be determined about the Earth based on the data. For example, we might find properties of  $\sigma(z)$ , such as averages, that are shared by all reasonable solutions and hence are unique properties of the Earth. Furthermore, the class of possible solutions can be reduced by constraining the conductivity based on geologic knowledge.

Nevertheless, establishing that an inverse problem has a unique solution for perfect data (error-free and known at all positions or at all frequencies) is an important exercise. Such a uniqueness proof lends credence to a solution that satisfies all available data, and indicates that the solution can be improved by acquiring additional data. In other areas of EM, important uniqueness proofs were given in Bailey (1970) for geomagnetic deep sounding and in Weidelt (1972) for magnetotelluric sounding.

Three uniqueness proofs have been presented for the inversion of controlled-source electromagnetic (CSEM) data over a 1-D half-space. Schlichter (1933), using the uniqueness theorem for Hankel transforms and a method of deriving  $\sigma(z)$  from the kernel function, showed that the geometric sounding problem has a unique solution if the vertical or horizontal magnetic field due to an oscillatory magnetic source is known everywhere on the surface of the half-space at one frequency. Fullager (1984) presented a uniqueness proof for horizontal-loop parametric soundings, where the magnetic field at a point is known at all frequencies.

Finally, Vidberg and Riska (1985) showed that if surface data for dipole sources are known at two frequencies and all transmitter-receiver separations over a 1-D earth, then the permittivity, permeability, and conductivity profiles can be determined uniquely.

### Construction of a solution

Each uniqueness proof discussed in the previous section is based on a method of constructing a solution from perfect data. However, as discussed in Weidelt (1972), such construction methods are not very useful in practice due to their inherent instability. Small changes in the data due to random or geologic noise lead to large changes in the estimated conductivity. Practical methods of constructing solutions must deal both with nonuniqueness due to incomplete data, and with instability in the face of random noise and geologic noise resulting from the inadequacy of simplified models of the earth.

One way to proceed is to use the result from Born inversion as the first approximation in an iterative solution. At each iteration, a new approximation to the electric field in the earth can be calculated based on the current estimate of the conductivity. The background medium can be assumed to be a free space or a half-space, so that the Green's function is a simple expression. This approach appears to be a promising method of attacking the multidimensional inverse problem, and is discussed later in this chapter.

Traditionally, nonlinear, 1-D inverse problems have been solved by linearization using the Fréchet derivative, and iterative improvement of a starting model, as discussed, e.g., in Backus and Gilbert (1968) and in Parker (1977). Fullager and Oldenburg (1984) discuss such a solution for horizontal-loop EM soundings in the frequency domain.

The basic equation for iterative construction of a conductivity profile  $\sigma(z)$  from  $N$  data points  $d_n$  is

$$\delta d_n = \int_0^\infty D_n [\sigma(z), z] \delta\sigma(z) dz \quad n = 1, 2, \dots, N, \quad (4)$$

where terms of order

$$\delta\sigma^2 = \int_0^\infty [\sigma(z)]^2 dz$$

have been neglected. The functional in equation (4) that relates small changes in conductivity  $\delta\sigma$  to small changes in the data  $\delta d_n$  is termed the Fréchet derivative, while the functions  $(D_n)_1^N$  are called the Fréchet kernels. Notice that the Fréchet kernels are functions of conductivity, which is characteristic of a nonlinear inverse problem and which necessitates an iterative solution.

Chave (1985) shows that the EM response functions for both TM and TE modes are Fréchet differentiable, i.e., that the neglected terms in equation (4) are of order  $\delta\sigma^2$ . He also illustrates how the Fréchet kernels (really sensitivity functions) can be used to qualitatively assess resolving capability and depth of exploration. In the sea-floor cases studied in Chave (1985), the TM mode provided superior resolution, but unfortunately the TM-mode magnetic field vanishes at the surface of the earth.

Let us look specifically at a circular, horizontal-loop source. Fullager and Oldenburg (1984) derive the Fréchet kernels by the usual method of perturbing a differential equation. However, we begin with equation (3), rewritten in terms of the departure of the conductivity  $\delta\sigma(z)$  from some reference model  $\sigma(z)$ . Because there is only a  $\phi$  component of the electric field, and it is circularly symmetric, equation (3) can be written

$$E^+(r_0, z_0) = E(r_0, z_0) + \int_0^\infty \int_0^\infty G_\phi(r_0, r, z_0, z) E^+(r, z) dr \delta\sigma(z) dz, \quad (5)$$

where  $E$  is the  $\phi$  component of electric field for the model  $\sigma(z)$ , and  $E^+$  is the  $\phi$  component of electric field for the model  $\sigma(z) + \delta\sigma(z)$ . Here  $G_\phi$  is the electric field at  $r_0, z_0$  due to a

loop of current of unit amplitude and radius  $r$  at depth  $z$  in the earth.

Taking the Hankel transform of order 1 with respect to  $r_0$ , equation (5) becomes

$$\tilde{E}^+(\lambda, z_0) = \tilde{E}(\lambda, z_0) + \int_0^\infty \int_0^\infty \tilde{\Gamma}(\lambda, z_0, z) r J_1(\lambda r) \tilde{E}^+(r, z) dr \delta\sigma(z) dz, \quad (5a)$$

where  $\tilde{\Gamma}$  is the result of factoring from  $\tilde{G}_\phi$  terms associated with the radius  $r$  of the loop of current in the earth. Now the inner integral in equation (5a) defines the Hankel transform of  $E^+$ , so we can write

$$\tilde{E}^+(\lambda, z_0) = \tilde{E}(\lambda, z_0) + \int_0^\infty \tilde{\Gamma}(\lambda, z_0, z) \tilde{E}^+(\lambda, z) \delta\sigma(z) dz. \quad (6)$$

Substituting  $\tilde{E}^+ = \tilde{E} + \delta\tilde{E}$  and neglecting higher-order terms, we have

$$\delta\tilde{E}(\lambda, \omega) = \int_0^\infty \tilde{\Gamma}(\lambda, z, \omega) \tilde{E}(\lambda, z, \omega) \delta\sigma(z) dz, \quad (7)$$

where we have assumed that the observations are taken at the surface of the earth where  $z_0 = 0$ , and where we have denoted explicitly the frequency dependence. Because  $E^+$  is the field in the earth due to a loop of radius  $a$  at the surface of the earth, we can utilize reciprocity to write

$$\tilde{\Gamma}(\lambda, z, \omega) = \tilde{E}(\lambda, z, \omega) / Ia J_1(\lambda a). \quad (8)$$

After performing the inverse Hankel transform,

$$\delta E(r, \omega) = \int_0^\infty \left[ \int_0^\infty \frac{\hat{E}^2(\lambda, z, \omega)}{Ia J_1(\lambda a)} \lambda J_1(\lambda r) d\lambda \right] \delta\sigma(z) dz. \quad (9)$$

Hence, by analogy with equation (4) the Fréchet kernel is

$$D(r, z, \omega) = \int_0^\infty \frac{\hat{E}^2(\lambda, z, \omega)}{Ia J_1(\lambda a)} \lambda J_1(\lambda r) d\lambda. \quad (10)$$

Applying Faraday's law to equation (9) results in the following Fréchet kernels for the horizontal and vertical components of the magnetic field:

$$D_r(r, z, \omega) = \frac{1}{i\omega\mu_0} \int_0^\infty \tilde{D}(\lambda, z, \omega) \lambda^2 J_1(\lambda r) d\lambda, \quad (11)$$

and

$$D_z(r, z, \omega) = -\frac{1}{i\omega\mu_0} \int_0^\infty \tilde{D}(\lambda, z, \omega) \lambda^2 J_0(\lambda r) d\lambda, \quad (12)$$

where  $\tilde{D}(\lambda, z, \omega)$  is given by the kernel of equation (10).

Fréchet kernels for measurements other than in-phase and quadrature, for example wave tilt and ellipticity, can be derived from equations (11) and (12), as shown in Fullager and Oldenburg (1984).

It is computationally expedient to assume a piecewise uniform conductivity (layered model), in which case equation (4) becomes a system of equations to solve for the conductivities in  $M$  layers:

$$\delta d_n = \sum_{m=1}^M D_{nm} \delta \sigma_m \quad n = 1, 2, \dots, N, \quad (13)$$

with discrete kernel

$$D_{nm} = \int_{\Delta z_m} D_n(\sigma, z) dz. \quad (14)$$

Fullager and Oldenburg show how to efficiently compute the discrete kernels defined by equation (14).

Iterative construction of a solution begins with equations (13) and an initial guess;  $\sigma_m^j$ ,  $m = 1, 2, \dots, M$ ; for the conductivity structure. Then let

$$\delta d_n = d_n - d_n^j, \quad (15)$$

where  $d_n$  is the  $n$ th observed datum, and  $d_n^j$  is the  $n$ th predicted datum based on the  $j$ th conductivity structure. Generally it is necessary to normalize both sides of equations (13) by the assumed standard deviation of the error of the  $n$ th datum. This normalization both deemphasizes observations with large uncertainties, and accounts for disparate data due to the

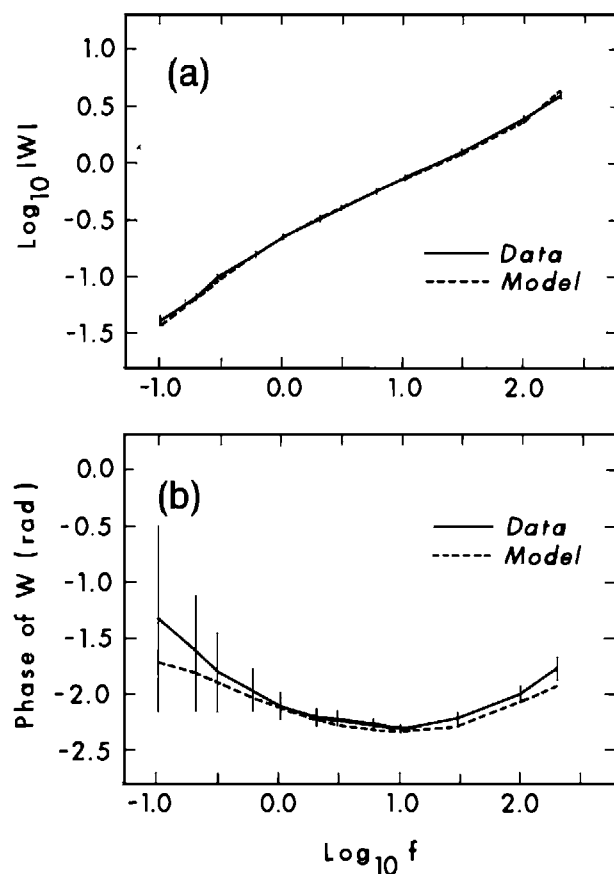


FIG. 2. Sounding curves from Grass Valley, Nevada: (a) wavetilt amplitude and (b) wavetilt phase. Receiver 1 004 m from horizontal loop transmitter with radius 50 m.

large dynamic range of EM data and due to the joint use of different kinds of data such as amplitude and phase.

In matrix notation equation (14) becomes

$$\delta\mathbf{d} = \mathbf{D}\delta\sigma. \quad (16)$$

However, due to the neglect of higher-order terms, noise in the data, and the inadequacy of the 1-D model in actual situations, it is not appropriate to solve equation (16) exactly. In general the solution is given by

$$\delta\sigma = \mathbf{D}^+ \delta\mathbf{d}, \quad (17)$$

where  $\mathbf{D}^+$  is a stable pseudoinverse defined, e.g., by the Marquardt or singular value decomposition procedures discussed later in the section on model fitting. Fullager and Oldenburg (1984) minimize the length of an extended vector of unknowns consisting of  $\delta\sigma$  and the differences between observed and predicted data, resulting in a pseudoinverse similar to that of the Marquardt technique.

The next approximation to the conductivity structure is given by

$$\sigma^{j+1} = \sigma^j + \delta\sigma, \quad (18)$$

where  $\sigma^j$  and  $\sigma^{j+1}$  are vectors of layer conductivities at successive iterations. Because of the approximations involved, the solution must proceed iteratively until a conductivity vector is found that produces predicted data that fit the observed data at an acceptable level. Inevitably, the solution will depend to a greater or lesser extent on the initial guess, and, of course, on the choice of the number of layers.

As an example, Fullager and Oldenburg (1984) inverted horizontal-loop, frequency-sounding data taken in Grass Valley, Nevada by a team from the University of California at Berkeley. The data, shown in Figure 2, consist of the amplitude and phase of the wavetilt  $W$ , the ratio of the horizontal to vertical magnetic field, at 12 frequencies. They show how to derive Fréchet kernels for such data from those of the magnetic field components. The error bars in Figure 2 define the assumed one-standard-deviation envelope, including allowances for coil misalignment, an important source of system noise. The effects of misalignment are most pronounced in the phase data at low frequencies.

The construction of an acceptable model for the Grass Valley soundings is documented in Figure 3. The starting model was a  $10 \Omega \cdot m$  half-space, and the number of layers was increased to a maximum of 24 in the course of the iterations. During any one iteration no individual layer conductivity was permitted to increase or decrease by a factor of more than 1.65; when restrained in this way the construction algorithm was stable in the sense that it converged to an acceptable model without operator intervention.

Data misfit at the  $j$ th iteration is quantified by the relation

$$\chi^2 = \sum_{n=1}^N (d_n - d_n^j)^2 / q_n^2, \quad (19)$$

where  $q_n^2$  is the assumed variance of the  $n$ th datum. In this example, Fullager and Oldenburg considered  $\chi^2 = 24$  to be an acceptable fit to the data, and they stopped the iterations when  $\chi^2$  fell below that value. Of course, the convergence criterion is somewhat subjective due to the approximations involved in estimating the mean of  $\chi^2$ . Correlated geologic noise due to lateral conductivity variations can seriously bias the solution and should be taken into account when designing convergence criteria.

The principal features of the acceptable model in Figure 3d can be summarized as follows: (1) a relatively resistive zone ( $>10 \Omega \cdot m$ ) extending from the surface to about 500 m depth; (2) a conductive zone ( $<2 \Omega \cdot m$ ) between 500 and 1 000 m. The conductivities assigned at depths greater than 1 km can be safely disregarded since, as shown below, the effective depth of penetration of the survey was approximately 1 km.

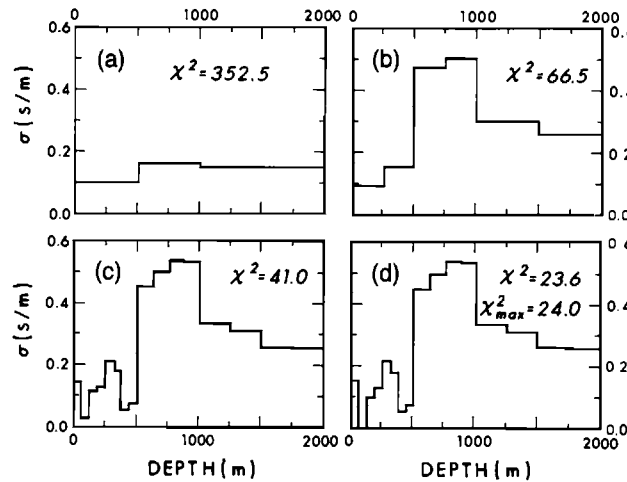


FIG. 3. Model construction for the Grass Valley data. Estimates depicted after (a) 1; (b) 4; (c) 8; and (d) 13 iterations.  $\chi^2$  is the squared misfit defined in equation (19) and  $\chi^2_{\max}$  is its maximum acceptable value.

### Appraisal

Due to the inherent nonuniqueness and instability of the geophysical inverse problem, simply finding an acceptable solution such as that of Figure 3d is not sufficient. Just as important is solution appraisal: finding unique properties of all solutions that fit the data at an acceptable level. These unique properties usually take the form of averages. They are strictly unique in linear inverse problems, but in the nonlinear case these averages are unique only to solutions that are linearly close; i.e., to solutions for which equation (4) is a good approximation.

Suppose we have found a conductivity function  $\sigma_1(z)$  that fits the data. Let  $\sigma_2(z)$  be another solution fitting the data and linearly close to  $\sigma_1$ . Then from equation (4),

$$\int_0^\infty D_n(z)\sigma_1(z)dz = \int_0^\infty D_n(z)\sigma_2(z)dz, \quad (20)$$

where  $D_n(z)$  is evaluated for either  $\sigma_1$  or  $\sigma_2$ . Generalizing, for any model  $\sigma$  fitting the data and linearly close to  $\sigma_1$ , the conductivity average

$$\bar{\sigma} = \int_0^\infty D_n(z)\sigma(z)dz \quad (21)$$

is approximately the same.

Multiplying equation (21) by the undetermined coefficient  $\alpha_n(z_0)$  and summing,

$$\bar{\sigma}(z_0) = \int_0^\infty A(z, z_0)\sigma(z)dz, \quad (22)$$

where the linear combination of Fréchet kernels,

$$A(z, z_0) = \sum_{n=1}^N \alpha_n(z_0)D_n(z), \quad (23)$$

is the Backus and Gilbert (1967, 1968) averaging function or resolving kernel. We attempt to choose the coefficients  $\alpha_n(z_0)$  in such a way that  $\bar{\sigma}(z_0)$  represents a meaningful average of the conductivity at  $z_0$ .

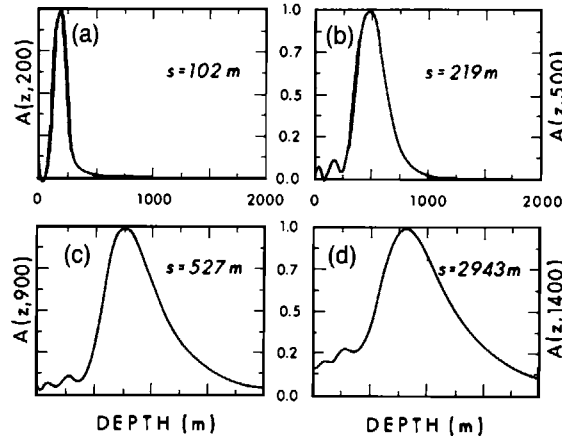


FIG. 4. Averaging functions for the Grass Valley data at depths (a) 200 m, (b) 500 m, (c) 900 m, and (d) 1400 m computed with equation (24) for a standard deviation  $\epsilon$  of 0.05 S/m.

Ideally,  $A(z, z_0)$  should resemble a delta function centered at  $z_0$ . The usual means of producing a delta-like averaging function is to choose the  $[\alpha_n(z_0)]_1^N$  in such a way that they minimize the spread  $s(z_0)$  based on the quadratic criterion

$$s(z_0) = 12 \int_0^\infty (z - z_0)^2 A^2(z, z_0) dz, \quad (24)$$

with unimodularity constraint

$$\int_0^\infty A(z, z_0) dz = 1. \quad (25)$$

The factor of 12 is included in equation (24) so that, if  $A(z, z_0)$  were a pulse function of width  $w$  and amplitude  $1/w$ ,  $s$  would be equal to  $w$ . The constrained minimization problem defined by equations (24) and (25) can be solved for  $(\alpha_n)_1^N$  using the method of Lagrange multipliers.

If the resulting averaging function  $A(z, z_0)$  is centered at  $z_0$  and if the spread  $s(z_0)$  is small, then  $\bar{\sigma}(z_0)$  is a good estimate of the conductivity at  $z_0$ . The numerical value of  $s(z_0)$  is a measure of the attainable resolution at that depth. On the other hand, if  $A(z, z_0)$  is not centered at  $z_0$  or if  $s(z_0)$  is large,  $\bar{\sigma}(z_0)$  is not meaningful.

In practice, however, the averaging function with minimum spread is rarely used, because the variance of the corresponding average usually is unacceptably high. From equations (4) and (21), an estimate of the variance of  $\bar{\sigma}(z_0)$  is given by

$$\epsilon^2 = V[\bar{\sigma}(z_0)] = \sum_{n=1}^N \alpha_n^2(z_0) q_n^2, \quad (25a)$$

assuming uncorrelated data errors with variances  $q_n^2$ . As usual in physical problems, a decrease in variance can be achieved only at a sacrifice of resolution. A plot of variance versus spread at a particular depth is known as a trade-off curve; it provides a convenient summary of the range of possible averages at that depth.

Averaging functions at four depths for the Grass Valley model of Figure 3d are shown in Figure 4. These averaging functions were computed for a standard deviation  $\epsilon$  in equation (25a) of 0.05 S/m using the Fréchet kernels for the reference model in Figure 3d. As seen

in Figures 4a and 4b,  $A(z, 200)$  and  $A(z, 500)$  are concentrated near their nominal depths, so the resulting averages are meaningful indicators of the conductivity near depths 200 and 500 m, respectively. In contrast, the averaging function for  $z_0 = 1400$  m (Figure 4d) peaks near 800 m; hence the associated average is a very poor indicator of the conductivity close to 1400 m. When  $z_0 = 900$  m, the peak of the averaging function is slightly offset from the nominal depth (Figure 4c), but the discrepancy is not so severe as to prevent the conductivity in the vicinity of 900 m from influencing the resulting average appreciably. Evidently the data contain relatively detailed information about the ground conductivity only for depths less than about 1 km, i.e., the effective depth of exploration is approximately 1 km. Over this interval the averages quite possibly reflect the variations of the actual conductivity with depth.

As shown in Figure 4, the computed spreads are 102, 219, 527, and 2943 m at depths of 200, 500, 900, and 1400 m, respectively. Hence, the fine details of the model in Figure 3d are not resolvable based on the sounding data alone.

Unfortunately, in a nonlinear inverse problem such as this, the Backus-Gilbert averages may not be unique. There may be other models that fit the data but that are not linearly close to the solution found. In order to engender confidence in the averages, Fullager and Oldenburg (1984) used the reference model in Figure 3d to generate a suite of acceptable models. They used linear programming to maximize and minimize the conductivities of particular layers.

Averages with standard deviation 0.05 S/m for many acceptable models generate the envelope shown in Figure 5a. The deviations of the averages from the reference model averages are indicated in Figure 5b, from which we conclude that (with allowance for random error)

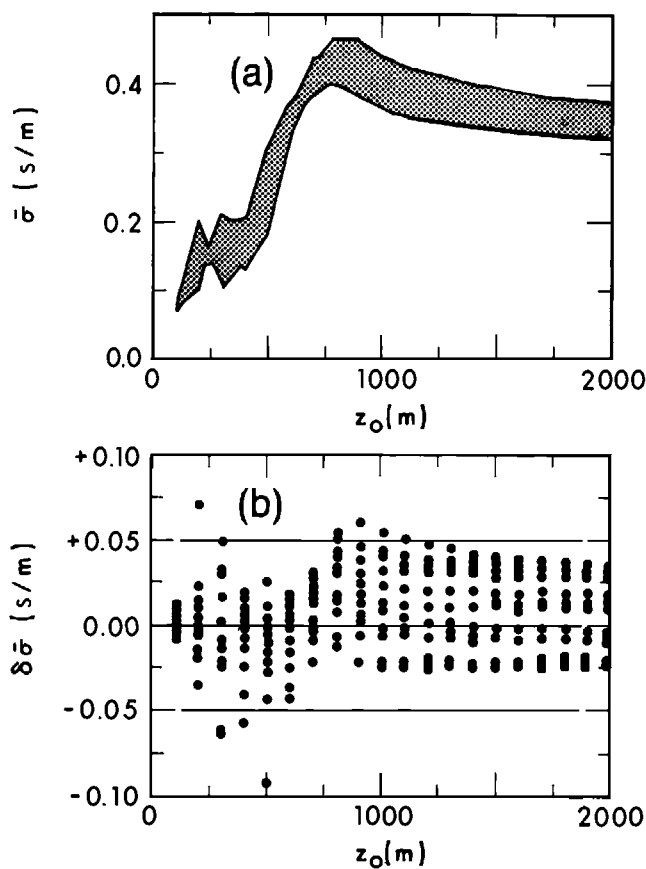


FIG. 5. (a) Envelope of Backus-Gilbert averages for several acceptable models obtained by maximizing and minimizing conductivities of particular layers in model of Figure 3d. (b) Residuals after subtraction of the reference model averages from those in (a).

all the models give rise to the same averages at all nominal depths considered.

From Figures 4 and 5 we conclude that the conductivity increases steadily for the first 800 m below the surface, from 0.1 S/m to 0.5 S/m. However, without the incorporation of constraints based on geologic reasoning or on other types of geophysical data, not much can be inferred about the conductivity at depths greater than 1 km.

This example points out both the strengths and weaknesses of unconstrained solution of the inverse problem. The Backus-Gilbert technique is an elegant means of determining what can be learned about the conductivity structure from the EM sounding data alone. However, a priori constraints, based on geologic knowledge should be incorporated if possible to improve the interpretation (Jackson, 1979; Whittall, 1986). One method of incorporating constraints is to estimate the parameters of a simple but realistic model, such as a layered earth, as discussed in the next section.

## Model Fitting by Nonlinear Optimization

For most applied EM problems, model fitting is a more useful technique than solving the unconstrained inverse problem previously discussed. By model fitting we mean estimating the parameters of an assumed, simplified model of the earth, a technique often called discrete inversion. Incorporation of constraints based on geological or geophysical information is an inherent part of choosing the model and contributes to the efficacy of the method. The technique has been very successful in applied geophysics.

We consider here a layered (1-D) earth, which is the most common interpretation model due to its simplicity. Over small regions the Earth actually may resemble a horizontally layered structure. More complex models can be built by combining these localized 1-D interpretations. More importantly, 1-D interpretations can be used as starting points in finding two-dimensional (2-D) and three-dimensional (3-D) models. As shown in the previous section, the problem is complicated because the data are nonlinear functionals of the model parameters.

The use of 1-D model fitting to interpret controlled-source EM sounding data was first discussed in Glenn et al. (1973). Later Glenn and Ward (1976) elaborated on the method, emphasizing experiment design: customizing a field survey based on an assumed model to maximize the information content of the data. Ward et al. (1976) illustrated the use of the techniques in a groundwater problem, comparing results obtained from the use of horizontal- and vertical-loop sources with those from electrical (Schlumberger) sounding. Then Tripp et al. (1978), Gomez-Trevino and Edwards (1983), and Raiche et al. (1985) discussed model fitting techniques and applications further, in each case demonstrating the enhanced resolution engendered by joint inversion of electrical and EM soundings. Other publications illustrating the applications of 1-D model fitting for controlled-source EM are Frishknecht and Raab (1984), Spies and Frishknecht (Volume II), and Kaufman and Keller (1983).

### Parameter estimation

Suppose an EM or electrical survey has been completed which requires a model with  $M$  parameters,  $p_1, p_2, \dots, p_M$  be fit to  $N$  data values,  $d_1, d_2, \dots, d_N$ . The problem can be represented mathematically as follows:

$$d_n = F(p_1, p_2, \dots, p_M, S_n) \quad n = 1, 2, \dots, N \quad (26)$$

where  $S_n$  represents the measurement system parameters such as frequency, delay time, transmitter-receiver location, etc. The functional  $F$  represents the forward model.

For example, suppose we want to fit a thin sheet in a half-space to a slinger frequency-domain survey with measurements made at three frequencies at each of 20 transmitter-receiver (Tx-Rx) locations. Each of the 60  $S_n$  represents a different combination of frequency and Tx-Rx locations incorporated in a forward model of plate response. Each of the  $d_n$  represents an output voltage measured for each  $S_n$ . We then want to determine parameters  $p_m$

that make equation (26) true. There are ten such parameters necessary to specify the model. For example,  $p_1$  could be the resistivity of the half-space,  $p_2$ , the conductance of the sheet, and  $p_3, p_4, p_5$ , the strike, dip, and plunge, respectively, of the sheet. Further,  $p_6, p_7$ , and  $p_8$  might correspond to the  $x, y, z$  coordinates of a point on the sheet. Lastly,  $p_9$  and  $p_{10}$  could correspond to the length and width of the sheet. Thus,  $M = 10$ .

Alternatively, we might wish to fit a two-layer model to a coincident-loop transient EM sounding with 20 delay times. In such a case,  $N = 20$ , with each of the 20  $S_n$  corresponding to a different delay time. We would need to find three parameters: the resistivity and thickness of the overburden (say  $p_1$  and  $p_3$ ) and the resistivity of the basement,  $p_2$ . Once again, we wish to find  $p_1, p_2$ , and  $p_3$  that make equation (26) true.

In general, we cannot satisfy equation (26) exactly because of noise in the data and also because our model is only an approximation to the real earth. Let  $y_n$  be the result of a forward model calculation for a given choice of earth model parameters;  $p_1, p_2, \dots, p_M$ ; corresponding to  $S_n$  and  $d_n$ .

The inversion procedure, called optimization or parameter estimation, consists of trying to find a set of earth model parameters  $p_1, p_2, \dots, p_M$  that minimize the difference between the field data  $d_n$  and the predicted data  $y_n$ . If we adopt the usual least squares procedure, we would look for a minimum in the two-norm, defined as

$$E_2 = \left[ \sum_{n=1}^N (d_n - y_n)^2 \right]^{1/2}. \quad (27)$$

Alternatively, we could minimize the one-norm, defined as

$$E_1 = \sum_{n=1}^N |d_n - y_n|. \quad (28)$$

In general, the parameter values that minimize  $E_2$  will not be the same as those which minimize  $E_1$ . The latter will be less affected by outlying data points than the former. Most workers use the least squares norm,  $E_2$ , because a whole range of statistical procedures have been developed for it and outliers can be culled from the data before inversion.

Equation (26) is linearized by expanding in a Taylor series and ignoring higher-order terms as follows:

$$d_n = y_n + \frac{\partial F_n}{\partial p_1} \delta p_1 + \frac{\partial F_n}{\partial p_2} \delta p_2 + \cdots + \frac{\partial F_n}{\partial p_M} \delta p_M, \\ n = 1, 2, \dots, N; \quad (29)$$

where

$$y_n = F(p_1, p_2, \dots, p_M, S_n).$$

Defining

$$J_{nm} = \frac{\partial F_n}{\partial p_m} = \frac{\partial F(p_1, \dots, p_M, S_n)}{\partial p_m}, \quad (30)$$

equation (30) can be expressed in matrix notation as

$$\mathbf{d} - \mathbf{y} = \mathbf{J}\boldsymbol{\delta}\mathbf{p}, \quad (31)$$

where

$$\mathbf{d} = (d_1, d_2, \dots, d_N)^T$$

is the vector of observed data,

$$\mathbf{y} = (y_1, y_2, \dots, y_N)^T$$

is the vector of predicted data, and

$$\mathbf{p} = (p_1, p_2, \dots, p_M)^T$$

is the parameter vector.

The element  $J_{nm}$  of the Jacobian matrix  $\mathbf{J}$ , defined in equation (30), is called a sensitivity coefficient, because it is a measure of the sensitivity of the  $n$ th data value to the  $m$ th parameter. We can calculate a vector parameter correction step by

$$\delta\mathbf{p} = \mathbf{J}^+ \boldsymbol{\varepsilon}, \quad (32)$$

where  $\mathbf{J}^+$  is a pseudoinverse, and  $\boldsymbol{\varepsilon} = \mathbf{d} - \mathbf{y}$  is the residual. Then an updated parameter vector is given by

$$\mathbf{p}^{\text{new}} = \mathbf{p}^{\text{old}} + \delta\mathbf{p}, \quad (33)$$

This new set of parameters is incorporated in the forward model calculation to produce new predicted data,  $\mathbf{y}^{\text{new}}$ , a new residual  $\boldsymbol{\varepsilon}^{\text{new}} = \mathbf{d} - \mathbf{y}^{\text{new}}$ , and a new Jacobian, which in turn is used to produce a new vector parameter correction step, etc. The process continues until one of three things happens:

1. The most recent estimate of the standard error,

$$\hat{\sigma} = \left[ \frac{1}{N - M} \sum_{n=1}^N \varepsilon_n^2 \right]^{1/2}, \quad (34)$$

- is within the noise level of the measurements;
2. A relative minimum is reached; i.e. subsequent iterations do not produce a noticeable decrease in the error; or
  3. The number of iterations exceeds a preset value.

### Generalized inverse of a matrix

In order to satisfy equation (32) it is necessary to find a pseudoinverse of the matrix  $\mathbf{J}$ , which has dimensions  $N \times M$ , where in general  $N > M$ .

Using  $T$  to denote the transpose of a matrix,  $\mathbf{J}^T$  and  $\mathbf{J} \mathbf{J}^T$  are  $M \times M$  and  $N \times N$  matrices, respectively. In the ordinary least squares solution, equation (31) can be written

$$\mathbf{J}^T \boldsymbol{\varepsilon} = \mathbf{J}^T \mathbf{J} \delta\mathbf{p},$$

so that

$$\delta\mathbf{p} = [\mathbf{J}^T \mathbf{J}]^{-1} \mathbf{J}^T \boldsymbol{\varepsilon}. \quad (35)$$

Hence the ordinary least-squares pseudoinverse is

$$\mathbf{J}^+ = [\mathbf{J}^T \mathbf{J}]^{-1} \mathbf{J}^T. \quad (36)$$

In the nonunique, underdetermined case where  $N < M$ , we would use another pseudoinverse

$$\underline{\mathbf{J}}^+ = \underline{\mathbf{J}}^T [\underline{\mathbf{J}} \underline{\mathbf{J}}^T]^{-1}, \quad (37)$$

which minimizes the length of the solution vector.

To alleviate instability, it is common to compute a generalized inverse for the overdetermined problem based on the singular value decomposition.

$$\underline{\mathbf{J}} = \underline{\mathbf{U}} \underline{\mathbf{S}} \underline{\mathbf{V}}^T, \quad (38)$$

where  $\underline{\mathbf{U}}$  is an  $N \times M$  matrix,  $\underline{\mathbf{S}}$  is a diagonal  $M \times M$  matrix containing the ordered eigenvalues of  $\underline{\mathbf{J}}$ , and  $\underline{\mathbf{V}}$  is an  $M \times M$  matrix. The matrices  $\underline{\mathbf{U}}$ ,  $\underline{\mathbf{S}}$  and  $\underline{\mathbf{V}}$  are derived from the singular value decompositions of  $\underline{\mathbf{J}} \underline{\mathbf{J}}^T$  and  $\underline{\mathbf{J}}^T \underline{\mathbf{J}}$ .

Since  $\underline{\mathbf{J}}^T \underline{\mathbf{J}}$  is a symmetric  $M \times M$  matrix, it can be decomposed as

$$\underline{\mathbf{J}}^T \underline{\mathbf{J}} = \underline{\mathbf{V}} \underline{\Lambda}_M \underline{\mathbf{V}}^T, \quad (39)$$

where  $\underline{\Lambda}_M$  is an  $M \times M$  diagonal matrix containing the  $M$  nonnegative eigenvalues  $\lambda_1, \lambda_2, \dots, \lambda_M$ . For convenience we assume that the eigenvalues are arranged in descending order such that  $\lambda_m \geq \lambda_{m+1}$ . The  $\underline{\mathbf{V}}$  matrix, whose columns are the normalized eigenvectors of the system, is orthogonal, i.e.,

$$\underline{\mathbf{V}}^T \underline{\mathbf{V}} = \underline{\mathbf{V}} \underline{\mathbf{V}}^T = \underline{\mathbf{I}}_M, \quad (40)$$

where  $\underline{\mathbf{I}}_M$  is the  $M \times M$  identity matrix. Since  $\underline{\mathbf{J}} \underline{\mathbf{J}}^T$  is a symmetric  $N \times N$  matrix of rank  $R \leq M$ , it can be decomposed as

$$\underline{\mathbf{J}} \underline{\mathbf{J}}^T = \underline{\mathbf{W}} \underline{\Lambda}_N \underline{\mathbf{W}}^T, \quad (41)$$

where  $\underline{\Lambda}_N$  is an  $N \times N$  diagonal matrix containing the same nonnegative eigenvalues  $\lambda_1, \lambda_2, \dots, \lambda_M$ , plus  $N - M$  zero eigenvalues, i.e.

$$\underline{\Lambda}_N = \begin{bmatrix} \lambda_1 & & & & & & \\ & \lambda_2 & & & & & \\ & & \lambda_3 & & & & \\ & & & \ddots & & & \\ & & & & 0 & & \\ & & & & & \ddots & \\ & & & & & & 0 \\ & & & & & & & 0 \\ & & & & & & & & 0 \end{bmatrix}$$

or

$$\underline{\Lambda}_N = \begin{bmatrix} \underline{\Lambda}_M & \mathbf{0} \\ \mathbf{0} & \mathbf{0} \end{bmatrix}. \quad (42)$$

The  $\underline{\mathbf{W}}$  matrix contains the eigenvectors of  $\underline{\mathbf{J}} \underline{\mathbf{J}}^T$  so that  $\underline{\mathbf{W}}^T \underline{\mathbf{W}} = \underline{\mathbf{W}} \underline{\mathbf{W}}^T = \underline{\mathbf{I}}_N$ , the identity matrix of rank  $N$ . Because the last  $N - M$  eigenvalues of  $\underline{\Lambda}_N$  are identically zero, we can rewrite equation (41) using  $\underline{\Lambda}_M$  and the  $N \times M$  matrix  $\underline{\mathbf{U}}$  which consists of the  $M$  leftmost columns of  $\underline{\mathbf{W}}$

$$\underline{\mathbf{J}} \underline{\mathbf{J}}^T = \underline{\mathbf{U}} \underline{\Lambda}_M \underline{\mathbf{U}}^T. \quad (43)$$

Note that  $\underline{\mathbf{U}}^T \underline{\mathbf{U}} = \underline{\mathbf{I}}_M$ , but in general  $\underline{\mathbf{U}}^T \underline{\mathbf{U}} \neq \underline{\mathbf{I}}_N$ . By substitution, it can be confirmed that the decomposition of  $\underline{\mathbf{J}}$  defined in equation (38) is consistent with equations (39) and (41) if  $\underline{\mathbf{A}} \underline{\mathbf{L}} = \underline{\Lambda}_M^{1/2}$ .

For convenience, we define an  $M \times M$  diagonal matrix  $\underline{\mathbf{S}}$  such that

$$S_{jj} = s_j = \sqrt{\lambda_j / \lambda_1}, \quad (44)$$

where the convention  $\lambda_1 \geq \lambda_2 \geq \dots \geq \lambda_M$  is maintained and where  $S_j$  is nonnegative. Equation (31) then becomes

$$\boldsymbol{\epsilon} = \sqrt{\lambda_1} \mathbf{U} \mathbf{S} \mathbf{V}^T \boldsymbol{\delta p}. \quad (45)$$

Equation (45) is a complicated expression relating the difference between the predicted and the observed data and the parameter correction that will decrease the difference. We can simplify the relationship by defining the eigenparameter of the system

$$\mathbf{q} = \mathbf{V}^T \boldsymbol{\delta p}. \quad (46)$$

We then write the parameter correction vector  $\boldsymbol{\delta p}$  in terms of an eigenparameter correction vector  $\boldsymbol{\delta q} = \mathbf{V}^T \boldsymbol{\delta p}$ . Equation (45) is premultiplied on both sides by  $\lambda_1^{-1/2} \mathbf{U}^T$ . We then define the transformed residual vector  $\mathbf{r}$  as

$$\mathbf{r} = \lambda_1^{-1/2} \mathbf{U}^T \boldsymbol{\epsilon}. \quad (47)$$

The result is an uncoupled system of equations which relates components of the eigenparameter correction step to those of the transformed error vector

$$\mathbf{r} = \mathbf{S} \boldsymbol{\delta q} \quad (48)$$

or

$$\delta q_i = s_i^{-1} r_i. \quad (49)$$

The eigenparameters and the  $\mathbf{Y}$  matrix are quite useful in analyzing the roles of individual parameters in an inversion.

It appears the problem has been solved. We first selected a model applicable to the observed data and for which an algorithm to compute synthetic data exists. We then made guesses for the unknown parameters and used these in the selected algorithm to calculate model data and a Jacobian. The error between the observed data and model data was calculated and used to generate correction steps for each of the parameters. New model data were calculated and the iterative process continued until some sort of convergence was achieved.

However, if the Jacobian matrix,  $\mathbf{J}$  is ill-conditioned, the iterative process can be very erratic, leading to spurious convergence or divergence. An ill-conditioned matrix will produce  $s_i$  ranging from one down to or close to zero. From equation (49), the small  $s_i$  values will produce large  $\delta q_i$ , resulting in large erratic oscillations in the value of  $q_i$  from iteration to iteration.

Because the physical parameters  $p_j$  are linear combinations of the eigenparameters  $q_i$ , ( $p_j = \sum_{i=1}^M v_{ji} q_i$ ), wild oscillations in any of the  $q_i$  can have deleterious effects on determining the  $p_j$ .

We can view this in a different but equivalent way. The Jacobian, which is sometimes called the sensitivity matrix, is defined as

$$J_{ij} = \frac{\partial y_i}{\partial p_j}, \quad (50)$$

where  $y_i$  is the  $i$ th predicted datum. If a small change is made in the value of the  $j$ th parameter and it produces a significant change in at least some of the model data points, then it can be said that  $p_j$  is an important parameter. If a fairly large change in  $p_j$  produces only a minimal change in a few of the predicted data, then  $p_j$  is an unimportant parameter. If a large change in  $p_j$  has no effect on any of the model data points, then  $p_j$  is an irrelevant parameter.

As an example, consider a transient, coincident loop, sounding taken over the four layer

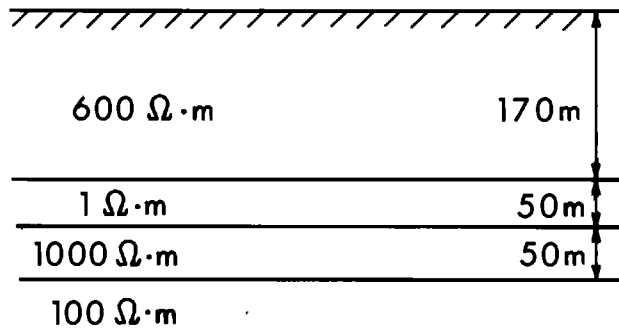


FIG. 6. Four-layer model for nonlinear inversion test.

model shown in Figure 6. A 10 percent change in the resistivity, thickness, or depth of the  $1 \Omega \cdot \text{m}$  conducting layer would produce considerable changes in the transient electromagnetic (TEM) data. Hence these parameters are important. However, changing the resistivity of the top layer by 50 percent would have only a marginal effect upon the data, so the parameter is unimportant. The thin, resistive third layer would be invisible to this TEM system, so its thickness and resistivity are irrelevant parameters.

Returning to equation (50), if one of the  $p_j$  were irrelevant, then the  $j$ th column of the Jacobian would be zero, which in turn would produce a zero eigenvalue. If one of the parameters were unimportant, at least one of the eigenvalues would be very small.

We therefore need to modify our inversion scheme so irrelevant parameters are eliminated, and the oscillations of unimportant parameters are damped. This can easily be done by incorporating a damping factor,  $t_i$ , into equation (49), so that

$$\delta q_i = \frac{t_i}{s_i} r_i, \quad (51)$$

with

$$t_i = \frac{s_i^{2k}}{s_i^{2k} + \mu^{2k}}, \quad (52)$$

where  $\mu$  is called the relative singular value threshold, and  $k$  is the order of damping. Remember that  $(0 \leq s_i \leq 1)$ . Figure 7 shows a plot of  $t_i$  versus  $\gamma_i$  for four different values of  $k$ , where  $\gamma_i = (\mu/s_i)^2$  and  $t_i = (1 + \gamma_i^k)^{-1}$ .

One strategy employed to overcome the problem of unimportant and irrelevant parameters is truncation, i.e., ignoring all eigenvalues less than  $\mu$ , which corresponds to  $k = \infty$ . As seen in Figure 7, truncation corresponds to using equation (49) for  $s_i > \mu$  and setting  $\delta q_i = 0$  for  $s_i < \mu$ . In essence, parameters are classified as either important or irrelevant.

Another technique is the Marquardt method, which amounts to setting  $k = 1$ . As can be seen from Figure 7, the effects of all but the largest eigenvalues are damped. The amount of damping can be modified by changing the value of  $\mu$ .

Recent work has sought to combine damping and truncation, and at the same time reduce

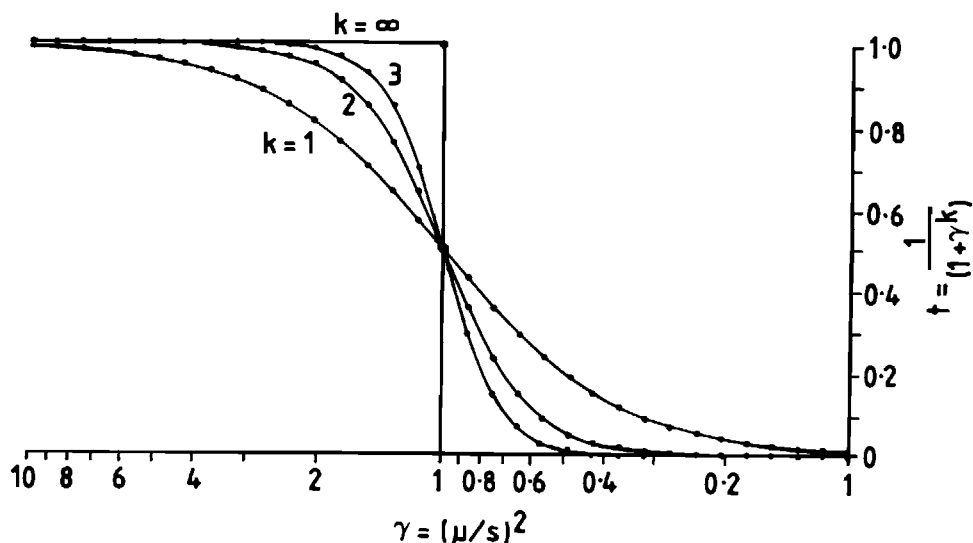


FIG. 7. Damping factor as a function of normalized eigenvalues.

the breadth of the damping. For example, Jupp and Vozoff (1977) chose a value  $k = 2$  with the refinement that  $t_i = 0$  for  $s_i < \mu^2$ .

The use of a damping factor biases the solution such that a true error minimum is not found. Because we have represented a very nonlinear process by a linear approximation, no serious problem exists in the early iterations. However, the closer we come to the correct values of the parameters, the more valid the linear approximation becomes. Thus, in the final iteration, all damping factors should be as close to one as possible in order to achieve a true error minimum. This corresponds to reducing the value of the relative singular value threshold  $\mu$  to zero.

From a practical point of view, we interpret the above as follows. First, obtain good estimates of the most important parameters and then, try to gradually modify the less important parameters in a stable fashion.

An inversion procedure should reflect that it will not be possible to resolve irrelevant parameters or unimportant parameters, due to noise in both the observed and predicted data. Noise in the predicted data arises because any theoretical model is an idealization of the underlying geoelectric section and because inaccuracies are present in calculations.

A practical inversion procedure might be conducted as follows. To initially estimate only the most important parameters,  $\mu$  is set to a high level, say  $\mu = 0.1$ . If the resulting parameter estimates decrease the error,  $\mu$  would be decreased, say by half, to allow more parameters to come into play. At any stage where the error increased,  $\mu$  would be increased in order to reset the important parameters and to damp the destabilizing effects of the less important ones. If  $\mu$  has to be continually increased or if it is not possible to decrease it below 0.1, one or more of the following applies:

1. The model is inappropriate,
2. Poor initial guesses have been made,
3. The noise to signal ratio (NSR) is so high that any inversion results should be regarded with caution.

When the error decreases after an iteration,  $\mu$  should also be decreased until it reaches the NSR. This decrease reflects the constraints imposed by noisy data upon parameter determination. The NSR is defined as the inverse square root of the familiar  $F$  statistic, i.e.,

$$\text{NSR} = \left\{ \frac{\frac{1}{N-M} \sum_{n=1}^N (d_n - y_n)^2}{\frac{1}{N-1} \sum_{n=1}^N (y_n - \bar{y})^2} \right\}^{1/2}, \quad (53)$$

where  $\bar{y}$  is the mean of the predicted data. This statistic is a measure of how well variations in the predicted data account for variations in the observed data.

Because this statistic is calculated at the end of an inversion, we must set the minimum value of  $\mu$  equal to an estimate of NSR. For a good inversion, the NSR should not be above a few percent. In many cases it will be below 1 percent. Thus, an initial estimate for the minimum allowed value of  $\mu$  might be 0.01 or 0.02. If, at the end of the inversion, the calculated NSR is appreciably different, then a second inversion should be run with the minimum allowed value of  $\mu$  set equal to the calculated NSR.

### Mathematical representation of data and parameters

The important question of how to represent data and parameter values during an inversion is now discussed. Consider the transient EM sounding curve shown in Figure 8, where the voltages range over five orders of magnitude. A 2 percent residual at the first delay time has 100 000 times the effect of a 2 percent residual at the last delay time if the data values are not weighted. These scaling problems occur for most electrical methods: voltages and apparent resistivities typically range over several orders of magnitude.

Because the inversion method uses a linearized model, it is reasonable to assume that the residual also has the linear form

$$\varepsilon_n = \alpha y_n + \beta, \quad (54)$$

where it is hoped that  $\alpha$  and  $\beta$  are normally distributed. It is usually assumed that  $\beta$  is important only at low signal levels.

If equation (54) is accepted as a reasonable error model, then it is important to scale observed and model data values so that a given percent error will have the same effect regardless of signal level. Moreover, it is important to balance the Jacobian matrix so that the sums of squares of the elements in different rows are of the same order of magnitude. This

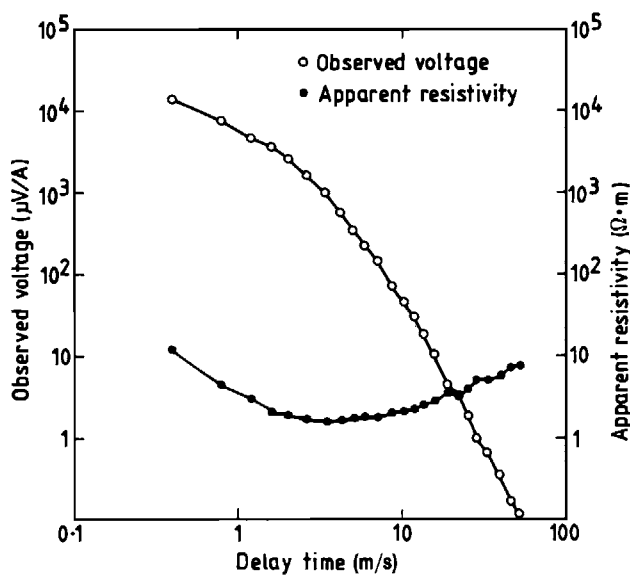


FIG. 8. Coincident-loop TEM decay curves.

tends to improve the condition of the matrix.

One device is to define an  $N$  dimensional weighting matrix  $\mathbf{W}$  whose elements are  $w_{mn} = |d_n|^{-1}$ , in which case equation (31) has the form

$$\mathbf{W}\boldsymbol{\epsilon} = \mathbf{W}\mathbf{J}\delta\mathbf{p}. \quad (55)$$

Although this scaling balances the rows of the Jacobian, a disadvantage is that it discriminates between the predicted data and the observed data. For example, suppose at the  $n$ th data point  $d_n = 1$  mV and  $y_n = 0.5$  mV. Thus, the implicit error definition of  $\epsilon_n = (d_n - y_n)/d_n$  would produce an error of 50 percent. If the values were reversed, the error would be -200 percent.

Keep in mind that an inversion philosophy which forces a model onto a data set must not distinguish between error in the predicted data and error in the observed data without a priori information. Therefore, it is desirable that the residual be antisymmetric with respect to interchange between  $y_n$  and  $d_n$ . Thus, a better solution to the scaling problem would be to work with the logarithms of the data values. Use of the logarithms produces the desired antisymmetric error behavior and scales the Jacobian; i.e.,

$$\epsilon_n = \ln(d_n/y_n) = -\ln(y_n/d_n), \quad (56)$$

and

$$J_{nm} = \lim_{\Delta p_m \rightarrow 0} \frac{\Delta y_n}{y_n} (\Delta p_m)^{-1}. \quad (57)$$

This solution will work very well as long as  $y_n$  and  $d_n$  have the same sign. A refinement which accommodates different signs and allows the introduction of the constant term in equation (54) is the use of the stitched logarithm

$$y_n = \begin{cases} \ln(y_n/DT) & \text{for } y_n > DT \\ 0 & \text{for } |y_n| < DT \\ -\ln(-y_n/DT) & \text{for } y_n < -DT. \end{cases} \quad (58)$$

$D_n$  is similarly defined in terms of  $DT$ , the data threshold level. For the stitched representation,

$$\epsilon_n = D_n - Y_n \quad (59)$$

$$J_{nm} = \lim_{\Delta p_m \rightarrow 0} \frac{\Delta y_n}{y_n} \Delta p_m^{-1} \text{ for } |y_n| > DT. \quad (60)$$

If  $\beta$  in equation (54) can be estimated, then  $DT$  might be given a value  $DT = 0.5\beta$ . Otherwise, a more conservative approach would set  $DT$  equal to some fraction of the minimum allowable data value.

Geophysical parameters such as resistivities, body dimensions, and target location can vary over several orders of magnitude. Thus, in any inversion procedure which strives to fit several parameters simultaneously, it is important to scale these parameters so that their variations will be over the same range of magnitude. Another way of expressing this is that the Jacobian will have a more stable inverse if the sums of squares of the elements of the columns are of the same order of magnitude.

An obvious scaling procedure is to invert for the logarithms of the parameters. Not only does the use of logarithms scale the parameters, but it restricts them to positive values. Using this transformation, the Jacobian of equation (57) has the form

$$J_{nm} = \lim_{\Delta p_m \rightarrow 0} \left( \frac{\Delta y_n}{y_n} \right) \left( \frac{\Delta p_m}{p_m} \right). \quad (61)$$

In some cases, it can be difficult to calculate the derivatives in a fast, stable fashion. When this is the case, the Jacobian can be calculated numerically as the difference between two forward models; i.e.,

$$J_{nm} = \frac{y_n[(1 + \alpha)p_m] - y_n(p_m)}{\alpha y_n(p_m)}, \quad (62)$$

where  $\alpha$  is a number on the order of  $10^{-3}$ .

An important exception to the use of  $\ln$  (parameter) occurs when an inversion with respect to angles is needed; e.g., strike, dip, or plunge of a target. If one inverted with respect to  $\ln$  (angle), then an error of 5 degrees could yield an error term of 5 percent or 500 percent depending upon how the coordinate system is defined. Thus it is better to use a linear scaling rather than a logarithmic scaling for angles. In particular, if the angles are expressed in radians, inverting on the angles themselves will yield variations similar to those of the logarithms of other parameters.

### Measuring inversion performance

We have developed a procedure for recovering parameters of a geoelectric model from survey data which involved the following subjective choices:

1. A specific physical model was chosen.
2. Initial parameter guesses were made which determined the choice of relative minimum.
3. The assumption was made that the best model would be achieved by minimizing the sum of squares of the errors.

The obvious question is how much confidence can be placed in the inversion results. Short of drilling, we cannot verify the inversion results completely, but we can monitor a number of aspects, such as estimated standard error

$$\hat{\sigma} = \left[ \frac{1}{N - M} \sum_{n=1}^N (D_n - Y_n)^2 \right]^{1/2}, \quad (63)$$

and the noise to signal ratio,

$$\text{NSR} = \frac{\hat{\sigma}}{\left[ \frac{1}{N - 1} \sum_{n=1}^N (Y_n - \bar{Y})^2 \right]^{1/2}}. \quad (64)$$

Note that equations (63) and (64) are now expressed in terms of the scaled data values,  $Y_n$  and  $D_n$  rather than in the unscaled values  $y_n$  and  $d_n$ . A standard error of a few percent usually implies a good fit. A standard error greater than 20 percent usually implies severe problems with the inversion.

The NSR is a measure of how well variations in the observed data are taken up by variations in the model data. A good inversion should result in an NSR of less than 2 percent. An NSR greater than 10 percent would indicate an inappropriate model.

The individual residuals should be somewhat randomly distributed about zero. If they all have the same sign or if their order of magnitude is not consistent, there are either bad data points or the model is inappropriate.

**Confidence Intervals.**—Confidence intervals for the parameters can be calculated using the estimated standard error  $\hat{\sigma}$ , and the Cramer-Rao multipliers  $\beta_m$  (Bard, 1974) where

$$\beta_m = \left[ \sum_{k=1}^N t_k (V_{mk}/S_k)^2 \right]^{1/2}. \quad (65)$$

Then, assuming that the inversion has been performed with respect to the logarithms of the parameters, the confidence interval is

$$p_m^\pm = p_m \exp (\pm 1.96 \beta_m \hat{\sigma}). \quad (66)$$

Otherwise

$$p_m^\pm = p_m \pm 1.96 \beta_m \hat{\sigma}, \quad (67)$$

where  $p_m^\pm$  are the upper and lower bounds of a 95 percent confidence interval for the parameter  $p_m$ . For 90 percent confidence intervals, the factor 1.96 would be replaced by 1.65. It should be noted that these are the damped error bounds. Thus, a given parameter may be unimportant but it could have tight confidence bounds because it is severely damped. That is, the confidence bounds reflect how the inversion procedure would let the parameter vary regardless of the "true" uncertainty of its value. Thus, in practice, we calculate undamped error bounds using  $s_k^{-2}$  rather than  $t_k/s_k^2$  in equation (65). In the case of a thin layer equivalence problem for a dc inversion, the resulting bounds are ridiculously large. For important parameters, the  $t$ 's are close to 1, so there is little difference between damped and undamped estimates.

**Eigenvector Analysis.**—One of the most useful tools in examining parameter resolution is the  $\mathbf{V}$  matrix, which relates the physical parameters to the eigenparameters. Usually inversions are performed with respect to parameter logarithms so we define  $P_m = \ln(p_m)$  and  $Q_m = \ln(q_m)$ . In the case of angles  $P_m = \ln(\exp \theta_m)$  where  $\theta_m$  represents an angle parameter. Equation (46) can then be expressed

$$\mathbf{P} = \mathbf{V}\mathbf{Q}. \quad (68)$$

$V_{ij}$  is a measure of the relative contribution of physical parameter  $P_i$  to  $Q_j$ . Thus, each column of  $\mathbf{V}$ , corresponding to an eigenparameter  $Q_j$ , is a linear combination of physical parameters  $P_i$ . Any combination of  $P_i$  corresponding to a  $Q_j$  with a damping factor  $t_j = 1$  will be well resolved. Similarly, any combination corresponding to a  $Q_j$  with  $t_j \ll 1$  will be poorly resolved.

If we were to perform an inversion on dc data for a structure containing a thin conductive layer, we would find that one of the  $Q_j$  would mostly consist of  $[\ln(h) - \ln(\rho)]$ , i.e., the conductivity-thickness product, where  $h$  is the thickness and  $\rho$  is the resistivity of the thin layer. This parameter could be well resolved. Another parameter would consist of  $[\ln(h) + \ln(\rho)]$ , i.e. the resistivity-thickness product. This parameter would be poorly resolved. Thus the  $\mathbf{V}$  matrix would tell us that we could resolve the ratio  $h/\rho$  but not either  $h$  or  $\rho$  alone. So far, this is not startling; the more commonly used correlation matrix could have given us the same result.

But if we were to do a joint transient EM—dc inversion, the  $\mathbf{V}$  matrix would tell us that both  $ph$  and  $h/\rho$  would be well resolved, i.e. we could resolve both  $\rho$  and  $h$ . The correlation matrix, on the other hand, would still only show a high correlation between  $\rho$  and  $h$ . An illustration is given in the next section.

**Appropriate Number of Parameters.**—When fitting models to data, there is often the question of how many parameters to use. If our model were a sheet in a half-space, the number of parameters would be fixed. But if the model included layers, we would question how many layers to use. For a more general inversion the question would be how many discrete bodies to use.

In principle, the more parameters used, the lower the two-norm of the error. However, it is best not to create fictitious structures that result from fitting the noise.

One of the most useful statistics in finding the most parsimonious model consistent with the data is the average predicted residual error (APRE). Consider the problem of fitting a model to  $N$  data points. Suppose one data point is removed and a model is fitted to the remaining  $N-1$  points. We use this model to calculate a value for the eliminated point. The difference between the calculated point and the original data point is the predicted residual error. If each of the  $N$  points is deleted in turn and a model is fitted to the remaining  $N-1$  points, APRE is the root-mean-square predicted residual error. Instead of requiring  $N$  inversions, an approximation to APRE can be calculated using the  $\mathbf{U}$  matrix and the equation

$$H_n = \left[ 1 - \sum_{m=1}^M U_{nm}^2 \right]^{-1}, \quad (69)$$

and

$$\text{APRE} = \left[ \frac{1}{N} \sum_{n=1}^N H_n \epsilon_n^2 \right]^{1/2}, \quad (70)$$

where  $\epsilon_n = D_n - Y_n$ . This estimate is exact when the model is linear.

In practice, APRE will show a sharp minimum for the most parsimonious model because the increase in  $H_n$  is faster than the decrease in  $\epsilon_n$  when the model becomes more complex than is justified by the data. For models that are not sufficiently complex, the  $\epsilon_n$  become sufficiently large to give large values of APRE. It has been found in practice that an appropriate model fit to good data will yield a value of APRE just slightly larger than the standard error. Inappropriate models or bad data will result in a value of APRE much larger than the standard error.

**Use of the Sensitivity Matrix.**—So far we have concentrated on what parameters we can use to fit the data. We can also consider the question of how to change the data set to resolve the parameters. The  $j$ th column of the Jacobian is a measure of how much each data point would be affected by a change in the  $j$ th parameter. If a substantial number of elements in the  $j$ th column have relatively high values, then there is sufficient data to resolve the parameter. If there are few or no relatively high values, then the data set is useless in trying to determine the  $j$ th parameter. From observing the trend in the column as parameters of the exploration system are changed (delay times, frequencies, spacings, etc.), it will become obvious in many cases as to what new measurements are needed to increase the resolution of a given parameter. This same procedure can be used to identify redundant data points and hence cut the costs of a survey.

#### An example of joint inversion and the use of inversion statistics

We have now developed a stable least-squares inversion scheme, as well as the tools to analyze its performance. However, we still do not know how close to being unique our answer is, nor do we even know which of the potential relative minima is the best answer. We need to find a procedure that can help eliminate relative minima associated with erroneous models.

One method is to jointly invert compatible data sets. For example, if we had reason to believe that the seismic velocity structure and the geoelectric structure were reasonably coincident, we could jointly invert the EM and seismic data. However, in most cases, the seismic velocity structure is not directly related to the geoelectric section, so a joint inversion would produce an unacceptable compromise between the two.

Another choice would be to jointly invert EM data and resistivity data. If the same earth volume were illuminated by the two survey types, the data from each survey type would be the result of the same earth structure. However, because the fields from resistivity methods behave quite differently from those due to EM methods, they provide complementary information.

To show the benefits of joint inversion explicitly and to illustrate the use of inversion

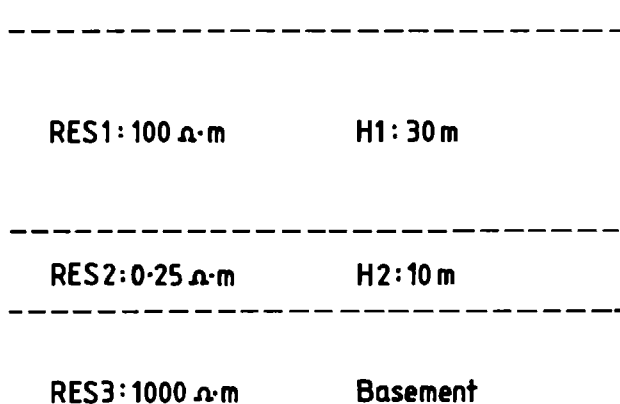


FIG. 9. Model for joint inversion test.

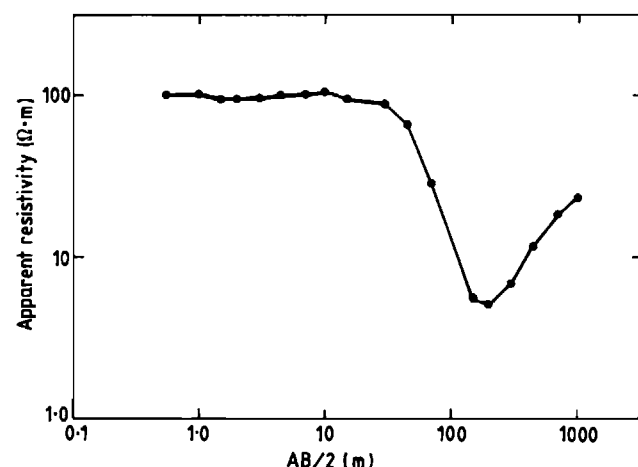


FIG. 10. Schlumberger data for joint inversion test.

statistics, the layered model shown in Figure 9 was used to generate model data for a 100-m coincident-loop transient EM survey and a Schlumberger survey. Random Gaussian noise was added to each data set: 10 percent to the TEM data, and 5 percent to the dc data. The resulting artificial data sets are shown in Figures 8 and 10.

Initial guesses for resistivities were made from the apparent resistivities. Inversions were run for dc data only, TEM data only, and joint data. The results are contained in Table 1.

These results are consistent with our initial expectations. The dc inversion provided good estimates for top-layer parameters and the conductivity-thickness product of the middle layer. Individual estimates of resistivity and thickness for this layer are out by a factor of four.

TEM inversion provided reasonable estimates for the middle conducting layer as well as depth to the top of this layer. The top-layer resistivity is greatly in error because most of the energy had already propagated through it by the time the first measurement was made.

Joint inversion effectively combined the resolution powers of each method. Estimates for the parameters of the upper two layers are quite good. Because the array dimensions and delay times were not sufficiently extensive to resolve the basement, the resistivity estimate is in error for all inversions. The fact that the joint estimate for basement resistivity is more in error than those for single techniques is irrelevant since this parameter is unresolved by all techniques.

We were able to judge the performance of the inversions in this case because we knew the true model. In practice, we usually do not have this information. However, we can use the damping factors, the  $\mathbf{Y}$  matrix, and calculated error bounds to monitor the inversion performance. For example, the dc inversion produced the  $\mathbf{Y}$  matrix and associated damping factors shown in Table 2.

The columns correspond to the eigenparameters (EP) and the rows to the logarithms of the physical parameters resistivity and thickness. A damping factor above 0.9 indicates that the

Table 1. Results of  $H$ -model inversion.

Parameter	DC inversion		TEM inversion		Joint inversion	
	Final model	Starting model	Final model	Starting model	Final model	Starting model
RES1	101.0	100	22.2	15	100.0	100
RES2	1.04	5	0.186	1	0.298	1
RES3	650.0	30	241.0	15	530.0	30
H1	29.8	50	34.4	50	30.3	50
H2	41.4	50	7.34	50	11.9	50

associated eigenparameter is well resolved. Damping factors less than around 0.8 imply that the resolution of the eigenparameter is quite shaky. Damping factors of less than 0.1 imply that the eigenparameter is completely unresolved. Clearly EP1, EP2, and EP3 are well resolved. EP4 is shaky and EP5 is not resolved. Since each of these eigenparameters is a linear combination of logarithms of physical parameters, we can estimate the resolution of different aspects of the final model.

For example, EP1 has relatively large positive entries in the first and fourth rows so it consists of the resistivity-thickness product of the top layer. EP3 has large, roughly equal entries of opposite sign in rows one and four so it consists of the resistivity-thickness quotient of the top layer. Since EP1 and EP3 have damping factors of 1.0, they are well resolved. Since both the product and quotient of the top layer resistivity and thickness are known, each of these is known separately.

Similarly EP2 consists of the conductivity-thickness product of the second layer. EP5 consists of the resistivity-thickness product of the second layer. The former is well resolved, the latter is not. Hence we cannot say anything separately about the resistivity or thickness of that layer.

EP4, the basement resistivity, is of questionable reliability. Hence,  $\mathbf{Y}$  matrix analysis has given us a good measure of the inversion performance. This is also born out in the confidence intervals shown in Table 3.

**Table 2.  $\mathbf{Y}$  Matrix and damping factors for dc inversion.**

	EP1	EP2	EP3	EP4	EP5
Log (RES1)	0.571	-0.437	0.695	-0.001	0.001
Log (RES2)	0.275	0.629	0.169	-0.076	0.703
Log (RES3)	0.004	0.012	0.005	0.996	0.094
Log (H1)	0.726	-0.127	-0.676	0.003	-0.008
Log (H2)	-0.267	-0.630	-0.177	-0.057	0.705
Damping factors	1.0	1.0	1.0	0.105	$3.0 \times 10^{-4}$

**Table 3. Error bounds for dc inversion.**

	Bound (1)		Bound (2)	
<i>Layer resistivities—95 percent confidence interval</i>				
(undamped)				
RES 1	101.0	97.5		104
RES 2	1.04	0.0000	76	261
RES 3	650.0	13.7	30	701
<i>Layer thicknesses—95 percent confidence interval</i>				
(undamped)				
H 1	29.8	26.2		33.8
H 2	41.4	0.0005	3 159	380

**Table 4.  $\mathbf{Y}$  Matrix and damping factors for TEM inversion.**

	EP1	EP2	EP3	EP4	EP5
Log (RES1)	0.026	-0.023	0.091	-0.121	-0.988
Log (RES2)	0.678	0.015	-0.727	-0.101	-0.037
Log (RES3)	0.008	0.006	0.136	-0.982	0.133
Log (H1)	0.118	-0.989	0.086	0.011	0.032
Log (H2)	-0.725	-0.148	-0.661	-0.107	-0.063
Damping factors	1.0	1.0	0.96	0.0094	$4.5 \times 10^{-4}$

A similar analysis can be applied to the TEM inversion (Table 4). EP1 and EP3 consist of the second layer resistivity-thickness quotient and product, respectively, so the resistivity and thickness of the second layer are each well resolved. EP2 shows that the depth to the conductive layer is well resolved. EP4 and EP5 have very low damping factors. Consequently basement and overburden resistivity are not at all resolved. Once again this is born out by the calculated 95 percent confidence intervals shown in Table 5.

As expected, the  $\mathbf{V}$  matrix for the joint inversion (Table 6) shows a much more complete resolution. EP1 and EP4 show resolution of the second layer parameters. EP2 and EP3 show resolution of top layer thickness and resistivity, respectively. EP5 shows that the basement resistivity is unresolved. This is also indicated by the error bounds given in Table 7.

We conclude this section with an illustration of the use of the APRE statistic. We calculated the Schlumberger response of a five-layer model, added random noise, and then performed inversion for 2, 3, 4, 5, 6, and 7 layer models. We calculated the APRE, standard error (SE), NSR and general cross-validation (GCV). All of these statistics showed that the data best supported a four-layer model. This was expected because regardless of what the underlying "true" model was, the data were such that only a four-layer fit could be justified, i.e. there was not sufficient information in the data to support a fifth layer. See Vozoff and Jupp (1977) for a discussion of this point.

**Table 5. Error bounds for TEM inversion.**

	Bound (1)	Bound (2)
<i>Layer resistivities</i> —95 percent confidence interval (undamped)		
RES1	22.2715	0.0024
RES2	0.1863	0.0911
RES3	240.7881	2.9151
<i>Layer thicknesses</i> —95 percent confidence interval (undamped)		
H 1	34.3544	25.1844
H 2	7.3392	3.1302

**Table 6.  $\mathbf{V}$  Matrix and damping factors for joint inversion.**

	EP1	EP2	EP3	EP4	EP5
Log (RES1)	0.012	-0.351	0.936	-0.033	0.000
Log (RES2)	0.684	0.035	-0.031	-0.729	-0.013
Log (RES3)	0.004	0.002	0.002	0.022	-1.000
Log (H1)	0.135	-0.924	-0.345	0.092	0.000
Log (H2)	-0.717	-0.146	-0.070	-0.678	-0.018
Damping factors	1.0	1.0	1.0	0.99	0.021

**Table 7. Error bounds for joint inversion.**

	Bound (1)	Bound (2)
<i>Layer resistivities</i> —95 percent confidence interval (undamped)		
RES1	99.6462	95.6303
RES2	0.2983	0.2433
RES3	530.1002	42.0494
<i>Layer thicknesses</i> —95 percent confidence interval (undamped)		
H 1	30.2803	29.1282
H 2	11.9281	9.8383

**Table 8.** Comparison of model resolution statistics.

Number of layers	APRE (%)	SE (%)	NSR (%)	GCV
2	10.1	10.2	8.98	2.6
3	7.06	6.85	8.49	1.90
4	0.79	0.54	0.79	0.16
5	4.32	0.55	0.95	0.18
6	14.75	0.69	1.33	0.26
7	47.45	0.84	1.75	0.38

From Table 8, we see that the APRE statistic is a much more focused indicator of the most parsimonious model than are the other statistics.

This description of the APRE statistic concludes this theoretical section on parametric inversion, the process by which we use one or more data sets to estimate the parameters of a given physical model which will best support that model. The precisely defined mathematical procedures are the result of subjective choices. At their worst, they offer a systematic refinement on running forward models in a curve fitting exercise. At their best, they can be highly effective in identifying the salient features of the geoelectric section.

### Field example

Raiche et al. (1985) presented a field example of joint coincident-loop TEM and Schlumberger electrical inversion, from a semiarid area in South Australia. There is virtually no outcrop and the visible surface cover consists of stable sand dunes. Apart from the rise and fall of the dunes, the general topography is flat. Beneath the sand are tertiary deposits consisting of sands, clays, and a fairly continuous lignite layer. Bedrock, at an average depth of 80 m, is of Proterozoic granites, schists, gneisses, and amphibolites.

As indicated in Figure 11, the eight coincident-loop soundings were taken at 200 m spacings from 700 east to 700 west. Schlumberger soundings were available at 300 west and 200 east. When the TEM data were converted to apparent resistivities, the result appeared to be a classic H-type model with a resistive top layer, a thin intermediate conductive layer, and a resistive basement. The dc apparent resistivities indicated the presence of an additional layer above the thin conductive layer. Thus, the initial inversion effort was a joint inversion using a four-layer model. The dc sounding at 200 east was combined with the four eastern TEM soundings. The dc sounding at 300 west was combined with the western TEM soundings.

The final results are shown in Figure 11 with the estimated standard errors of the data and the APRE values given below each TEM station. These relate very well with the known geology. The top two layers are fairly consistent across the eight sections. The more conductive top layer consists of feruginous sand dunes with a maximum crest-to-trough amplitude of 10 m. These lie upon a thicker, more resistive sequence of old sand. The conductive lignite, which also extends across the traverse, is initially thin at the eastern end and thickens until about 100 east. The depth of the lignite layer at 300 west (75–90 m) was verified by the single drill hole at that point. Note that the depths are relative to the dune surface. There appears to be some geologic event at the east-west contact with the basement interface rising by 20 m from east to west.

Using the  $\mathbf{Y}$  matrix analysis presented above, Raiche et al. (1985) found that, of the seven parameters implicit in a four-layer model, only the basement resistivity was not well resolved. Resolution of this parameter would require either later delay time of the TEM sounding or wider array spacings for the Schlumberger sounding. In order of importance, the well-re-

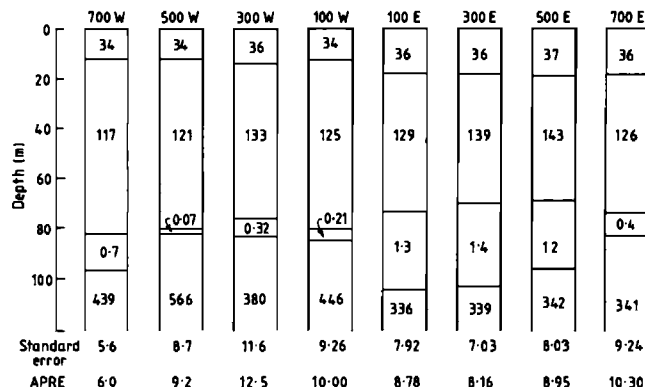


FIG. 11. Resistivity-depth section based on 1-D inversions of field data at 8 locations.

solved eigenparameters were:  $h_3/\rho_3$ ,  $h_2$ ,  $\rho_1$ ,  $\rho_2$ ,  $h_1$ ,  $\rho_3 h_3$  where  $\rho_i$  and  $h_i$  denote the resistivity and thickness, respectively, of the  $i$ th layer.

The NSR values were generally less than 0.5 percent. The standard errors and the APRE values were very low, indicating that a four-layer model is a good representation of the data. Attempts to fit three-layer and five-layer models to the joint data set produced considerably worse statistics.

## Multidimensional Inversion

Interpretations based on 1-D inversions can be erroneous or misleading if the data are affected by lateral conductivity changes. In some cases it may not be possible to fit the data using a 1-D model, while in other cases the parameters of an assumed 1-D model or a continuous conductivity profile may be seriously biased. Ideally, a series of 1-D inversions along a profile would serve as a starting point for 2-D or 3-D inversions, but development of multidimensional inversion techniques is still in its infancy. Model-fitting methods and approximate inverse methods based on simple models appear to be the most promising in a practical sense.

### Simple models

In principle, the parameters of any interpretation model can be estimated using the non-linear model-fitting technique illustrated in the previous section. In practice, however, the required partial derivatives with respect to the parameters, usually based on numerical differences, may be prohibitively time consuming to compute.

Pelton et al. (1978) developed an efficient way of computing partial derivatives for simple 2-D resistivity and induced polarization (IP) models. Their method is based on computing forward solutions by interpolating within a data bank containing solutions for the entire range of expected parameter combinations for a 2-D prism. Such an approach may be useful in EM interpretation, once a reliable forward solution is developed for a 2-D model excited by a 3-D source.

In an entirely different approach, Zhdanov and Varentsov (1983) presented a method of determining the position and shape of a deep, 2-D conductor from geomagnetic data. The conductivity of the anomalous zone must be assumed. Such an approach may have applications in interpreting controlled-source EM data.

Based on experience with forward solutions for plate-like conductors in free space, Barnett (1984) developed an approximate inverse technique for time-domain EM data. At each measurement time the conductor is replaced by a circular or rectangular current filament. As time progresses, the estimated current migrates from an initial position of maximum primary field

coupling to a final position centered on the conductor. During this migration, the current filament remains in the plane of the conductor, as shown by experiments with synthetic data.

At late times the eddy current distribution in a plate can be closely approximated by an equivalent current filament that traces a path about 30 percent in from the edge and encompasses half the area of the conductor (Nabighian, pers. comm.). Hence, if the environment is not so conductive that galvanic effects, which are not taken into account, dominate the response at all times, the method solves the practical inverse problem of estimating the position, size, and attitude of a conductor.

This general concept of tracking equivalent current filaments is an exciting new approach to transient EM inversion. It has proven very useful for efficient, approximate, 1-D inversion (Macnae and Lamontagne, 1986; Eaton and Hohmann, 1986). The velocity of an equivalent current filament at a point provides an estimate of the conductivity at that point. In principle the technique can be applied to 2-D and 3-D inversion, although galvanic effects complicate the problem.

### Differential equation methods

Numerical solutions of differential equations using a finite-difference or finite-element technique can form the basis for 2-D or 3-D inversion. In principle, an inverse technique can determine continuous conductivity models defined by interpolation of nodal values of resistivity on a grid, as discussed in Swanger et al. (1983) for 2-D MT interpretation. Some form of smoothing is a requirement for success with such a scheme.

In practical exploration problems, it may be more useful to estimate the parameters of a number of blocks of aggregated elements, with the blocks defined to incorporate geologic constraints. Jupp and Vozoff (1977) presented a 2-D MT inversion technique based on such a model-fitting approach.

Smith and Vozoff (1984) and Tripp et al. (1984) discussed differential-equation methods for 2-D inversion of dipole-dipole resistivity data. Both methods use a model-fitting approach: estimation of the resistivities of blocks of elements. Because the source is 3-D, the problem is more complicated than that of 2-D MT inversion discussed above. No inversion technique has been developed yet for CSEM for the case of a 2-D model and a 3-D source, let alone for the full 3-D problem.

However, Oristaglio and Worthington (1980) presented an inversion technique based on the finite-element method for the CSEM case of a 2-D earth excited by a line source of current. They used a model-fitting approach rather than inverting for each nodal value of conductivity separately, and solved the nonlinear parameter estimation problem in the manner described above for 1-D models.

**Partial Derivatives.**—Rodi (1976) first discussed simplified methods of calculating the required partial derivatives for nonlinear inversion when forward calculations must be made by computationally intensive numerical solution of a differential equation. As described in Hohmann (this volume), the forward solution in the finite element method is given by solving the matrix equation

$$\mathbf{G}\mathbf{f} = \mathbf{s}, \quad (71)$$

where  $\mathbf{G}$  is the so-called stiffness matrix,  $\mathbf{f}$  is the vector of unknown nodal values of the field, and  $\mathbf{s}$  is the source vector. Because  $\mathbf{G}$  is symmetric, the equation can be solved by decomposing  $\mathbf{G}$  as

$$\mathbf{G} = \mathbf{L}\mathbf{D}\mathbf{L}^T, \quad (72)$$

where  $\mathbf{L}$  is lower triangular;  $\mathbf{D}$  is diagonal; and  $\mathbf{L}^T$ , the transpose of  $\mathbf{L}$ , is upper triangular. The solution for  $\mathbf{f}$  is obtained by forward reduction and back substitution, i.e., by solving the three systems

$$\mathbf{L}\mathbf{z} = \mathbf{s}, \quad (73)$$

$$\underline{\mathbf{D}}\mathbf{z}' = \mathbf{z}, \quad (74)$$

and

$$\underline{\mathbf{L}}^T \mathbf{f} = \mathbf{z}'. \quad (75)$$

The key to efficient calculation of partial derivatives is to store  $\underline{\mathbf{L}}$  and  $\underline{\mathbf{D}}$  as they are calculated during Gaussian elimination. Then equation (71) can be solved for other source vectors with little additional computation.

The model is characterized by the conductivities  $\sigma_m$  of  $M$  2-D blocks, each composed of many elements. Because the source is independent of the model parameters, differentiating equation (71) yields

$$\mathbf{G} \frac{\partial \mathbf{f}}{\partial \sigma_m} = -\frac{\partial \mathbf{G}}{\partial \sigma_m} \mathbf{f}. \quad (76)$$

Thus, the derivative of the field with respect to parameter  $\sigma_m$  can be expressed as a column vector that satisfies the same matrix equation as the field itself, but with a different right hand side (RHS). This new source term is the product of the derivative of the stiffness matrix with respect to parameter  $\sigma_m$  and the column vector of the fields for the particular model  $\sigma$ .

There are two key observations regarding equation (76). First, because  $\mathbf{G}$  is the sum of simple element matrices, its derivative with respect to parameter  $\sigma_m$  can also be assembled from the appropriate derivatives of the element matrices: In this case, the parameters are the conductivities of the elements. The derivative of a particular element stiffness matrix with respect to conductivity  $\sigma_m$  is identically zero unless  $\sigma_m$  is the conductivity of that element. Consequently the matrix  $\partial \mathbf{G} / \partial \sigma_m$  will be very sparse, having nonzero entries only in positions corresponding to the element or group of elements whose conductivity is being varied.

The second important point concerning equation (76) is that the matrix  $\mathbf{G}$  has already been factored, and the factors were stored when the fields were calculated. The solution to equation (76) is obtained through the simple process of forward-reduction and back-substitution with the new RHS. The solution is the partial derivative of the vector potential; its curl gives the derivatives of the magnetic fields. The entire process is repeated for each parameter, filling in the Jacobian matrix a column at a time.

Apart from the finite-element approximation, equation (76) is an exact analytical equation for the partial derivatives. As outlined its solution is very stable numerically. Thus the partial derivatives are calculated as accurately as the fields themselves, and this accuracy is the same both for very high and very low conductivities. The process is also fast in terms of computer time. For the Oxford ICL 1906a computer Oristaglio and Worthington used, assembling and factoring the matrix  $\mathbf{G}$  for a large ( $25 \times 29$ ) finite element grid required about 65 s of CPU time. The solution was then given in approximately another 5 s by forward reduction and back substitution. Thus a Jacobian matrix of 30 columns, corresponding to 30 separate conductivities, can be calculated in just over twice the time it takes to compute the fields themselves. This is an excellent ratio for such a large set of complex, nonlinear equations. The above method is similar to that used in Rodi (1976).

**Example.**—Figure 12 shows a model that Oristaglio and Worthington (1980) used to test their technique. A good conductor lies at depth beneath variably conducting overburden. The transmitter is a line source of current, and the data consist of vertical and horizontal magnetic field measurements at a single frequency of 300 Hz. The dimensions and conductivities of the model correspond to those of a typical massive sulfide exploration problem. However, intuitive interpretation for such a case would be difficult because of the great depth of the conductor and because of geologic noise due to the change in overburden conductivity.

The inversion model is shown in Figure 13. The local region of the earth (dimension 350 × 175 m) is divided into 36 blocks of constant conductivity, which have been numbered in the diagram for future reference. Each of the 40 m × 40 m blocks in the top three layers, i.e. blocks 1–27, comprise 8 linear triangular elements, the 40 m × 60 m blocks in the

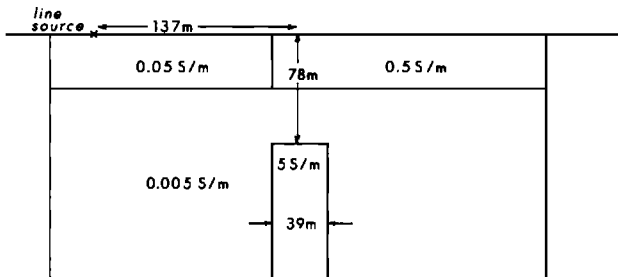


FIG. 12. Model for 2-D inversion test (after Oristaglio and Worthington, 1980).

lowest layer (blocks 28–36) comprise 12 triangular elements. The local region is embedded in an infinite half-space, whose conductivity is held to its true value of 0.005 S/m. This inverse model is able to represent the true model exactly; in Figure 13 the anomalous regions of the true model are outlined. Blocks 1–4 and blocks 5–9 correspond to the two sections of the overburden, and blocks 23 and 32 represent the conducting vein. In real applications, the question of whether the inverse model has sufficient detail to represent the physical situation adequately is generally difficult to answer, and is closely related to the experimenter's assumptions about the errors and resolving power in the data.

For this simulation, the fields are calculated at a single frequency at equally spaced points along a profile on the surface perpendicular to strike. For the first inversion, synthetic data were calculated at 16 points along the surface of the earth, every 20 m starting from the middle of block 3 and extending to the edge of block 9. Thus there were four readings at each point (real and quadrature components of  $H_x$  and  $H_z$ ), yielding a total of 64 data values. The fields were rounded to two decimal places, introducing approximately 1 percent error into each data point.

Given the data and a starting model in which the conductivities of all blocks were set at 0.001 S/m (thus no block had its true conductivity in the starting model), the inverse algorithm required 36 iterations to converge to the final model shown in Figure 14. In this and all other inversions, the algorithm was defined to have converged when either (a) the average change in the logarithm of the conductivity of the blocks in two successive iterations was less than 0.005, or (b) the decrease in the sum of squares error in two successive iterations was less than 0.1 percent of its current value.

The rms error for the final model was 0.011, mainly due to rounding the fields to two decimal places, thus the model fits the data very well. Comparing the inverted model with the true model, however, shows that while the conductivities of the surface blocks have attained their true values, the conductivities of the blocks below the surface differ greatly from their exact values. Blocks 23 and 32, which define the conducting vein, also have the highest conductivities in the inverse model, but the conductivity of block 32 is 100 times its true value. Furthermore, the anomalous region is ill-defined, because blocks in the region surrounding the dike all have relatively high conductivities (e.g., blocks 24, 33, and 34).

Figure 15 shows how the conductivities of representative blocks varied during iteration. Parameter values are plotted versus iteration number for blocks from each region of the model: the surface layer, the dike, and host rock surrounding the dike.

The most striking feature of the plots is the strong correlations between the parameter changes in adjacent blocks. The correlations show why the inversion goes wrong in the sense that it does not converge to the true model, even though it manages to fit the data very well. For example, block 24, which in the true model is part of the resistive host rock, is at each step assigned nearly the same conductivity as block 23, which is part of the highly conducting vein. It is obvious that the surface data alone are not sensitive enough to resolve these blocks separately. However, Oristaglio and Worthington show that the conductor is well resolved if data from a borehole alongside it, through blocks 6, 15, 24, and 33, are incorporated into the inversion.

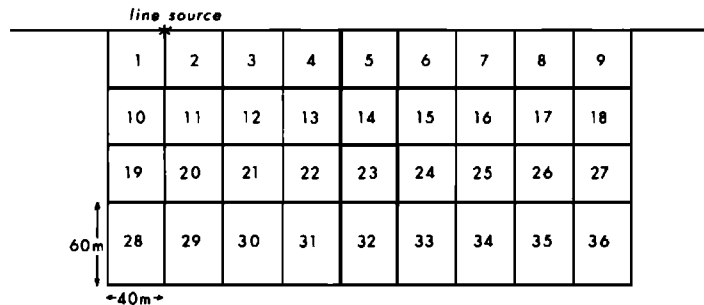


FIG. 13. Inversion model defining blocks of constant conductivity for 2-D inversion test (after Oristaglio and Worthington, 1980).

This model-fitting technique could be quite useful in practice if two line sources are used to represent the front and back of a large loop, if the earth surrounding the conductor is not too conductive, and if the length of the conductor is on the order of the loop size. However, if the surrounding earth is conductive, galvanic effects may severely bias the inversion results.

### Integral equation methods

General integral equation formulations for inversion were previously given in equations (1) and (2) for electric-field and magnetic-field data, respectively. Although no 2-D or 3-D inverse solutions based on integral equation formulations have been reported for CSEM, the technique has been applied in geomagnetic studies.

Weidelt (1975) inverted theoretic and field geomagnetic data in terms of 2-D models. He used the 2-D version of equation (9),

$$\delta E(\mathbf{r}_0) = \int_S G(\mathbf{r}_0, \mathbf{r}) E(\mathbf{r}) \delta \sigma(\mathbf{r}) ds, \quad (77)$$

and its magnetic-field counterpart. In equation (77)  $E$  is the component of electric field in the strike direction,  $S$  is the cross-section of the earth under consideration, and frequency dependence is implicit.

To formulate the inverse problem, take  $\delta E$  to be the difference between the observed and calculated data at a certain iteration and  $\delta \sigma$  to be the difference in conductivity between one iteration and the next. Equation (77) thus is in the format of the general inverse problem in equation (4), with Fréchet kernel

$$D(\sigma, \mathbf{r}) = G(\mathbf{r}_0, \mathbf{r}) E(\mathbf{r}), \quad (78)$$

where  $\mathbf{r}_0$  denotes an observation point.

.05	.055	.054	.051	.479	.440	.490	.512	.512
.002	.001	.001	.001	.102	.047	.009	.007	.003
.002	.001	.001	.003	3.8	1.9	.012	.004	.003
.005	.005	.009	.07	501.	.29	3.6	.013	.005

FIG. 14. Conductivities estimated by 2-D inversion technique (after Oristaglio and Worthington, 1980). Compare with true model in Figure 12.

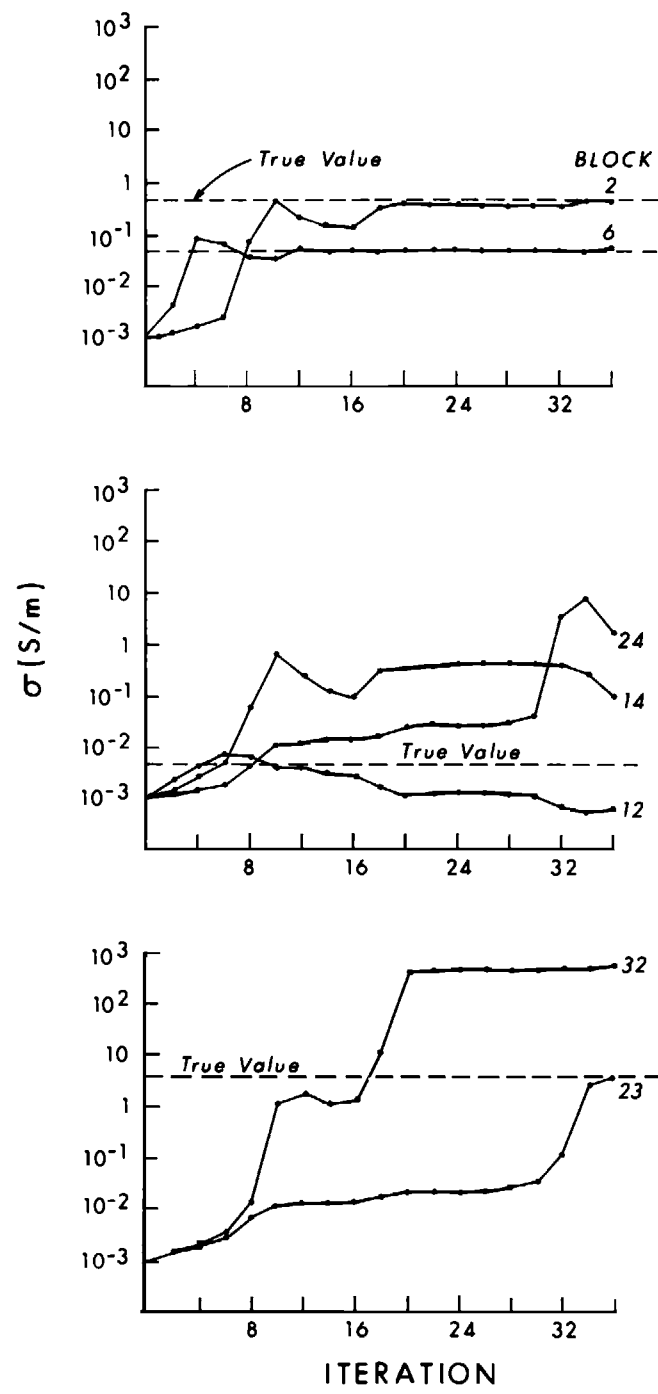


FIG. 15. Convergence of conductivities for several blocks of the 2-D inverse model of Figure 13 (after Oristaglio and Worthington, 1980).

Weidelt (1975) set up the inverse problem by dividing the cross-section beneath the anomaly into cells of constant conductivity and constant electric field. The anomalous conductivity thus is approximated by a piecewise-uniform, 2-D function in a technique similar to that used in Fullager and Oldenburg (1984) for 1-D inversion. Equation (77) then becomes, in the notation of equation (13),

$$\delta E_n = \sum_{m=1}^M D_{nm} \delta \sigma_m \quad n = 1, 2, \dots, N, \quad (79)$$

with discrete kernel

$$D_{nm} = \int_m G(\mathbf{r}_n, \mathbf{r}) ds, \quad (80)$$

which is an integral over cell  $m$ , with  $\mathbf{r}_n$  the position of the  $n$ th data point.

The solution proceeds in a manner similar to that discussed earlier for 1-D inversion. One problem with this formulation is that the Green's function pertains to the current estimate of the 2-D model, rather than to a homogeneous or layered earth. Hence, unless it can be approximated, the Green's function must be computed by solving an integral equation.

A better approach for 2-D and 3-D geometries, at least for low contrasts, may be to begin with a solution based on the Born approximation and proceed iteratively. The integral equation for Born inversion of magnetic field data is, from equation (2),

$$\mathbf{H}(\mathbf{r}_0) = \mathbf{H}_p(\mathbf{r}_0) + \int_{\Omega} \mathbf{G}_H(\mathbf{r}_0, \mathbf{r}) \mathbf{E}_p(\mathbf{r}) \sigma_a(\mathbf{r}) d\mathbf{v}, \quad (81)$$

where  $\sigma_a$  is the difference between the actual conductivity in domain  $\Omega$  and the conductivity of the reference model. The reference model might be a homogeneous earth, a layered earth, or free space. Here  $\mathbf{H}(\mathbf{r}_0)$  is the magnetic field measured at position  $\mathbf{r}_0$ , while  $\mathbf{H}_p(\mathbf{r}_0)$  is the magnetic field of the reference model at  $\mathbf{r}_0$ . The unknown electric field in  $\Omega$  is approximated by  $\mathbf{E}_p$ , the electric field in the reference model. Hence, equation (81) is a simple, linear integral equation to solve for the anomalous conductivity in a manner similar to that of a gravity or magnetic problem.

However, in most EM cases, Born inversion is not sufficient:  $\mathbf{E}_p$  is a poor approximation to the electric field. The solution must proceed iteratively, with a new approximation to the electric field in  $\Omega$  calculated using equation (1).

In the only published test of the method, Barthes and Vasseur (1978) inverted synthetic geomagnetic data in terms of an inhomogeneous horizontal thin sheet embedded in a layered earth. Their test model is shown in Figure 16; an inhomogeneous thin sheet lies at 2 000 m depth, with conductivities above and below of 0.02 S/m and 0.001 S/m, respectively. For this case, equation (81) becomes

$$\mathbf{H}(\mathbf{r}_0) = \mathbf{H}_p(\mathbf{r}_0) + \int_{\Omega} \mathbf{G}_H(\mathbf{r}_0, \mathbf{r}) \mathbf{E}_p(\mathbf{r}) \tau_a(\mathbf{r}) ds, \quad (82)$$

where  $\tau_a$  is the anomalous conductance of the sheet, and  $\Omega$  denotes its surface.

As shown in Figure 16, the anomalous zone was divided into 25 square cells, in each of which  $\tau_a$  and  $\mathbf{E}$  are assumed constant. In the shaded cells  $\tau$  differs from its normal value of 10 S. The source is a plane wave, and the synthetic data consist of 49 measurements of the real and imaginary components of  $H_x$  at 1 Hz at the surface of the earth, as shown by the dots in Figure 16. Thus the problem is overdetermined, with 98 data points and 25 unknown conductances.

Figure 17 illustrates the convergence of the inverse solution for resistive (0.1S) and conductive (1 000S) inhomogeneities. Convergence is rapid in the former case, but slow in the latter.

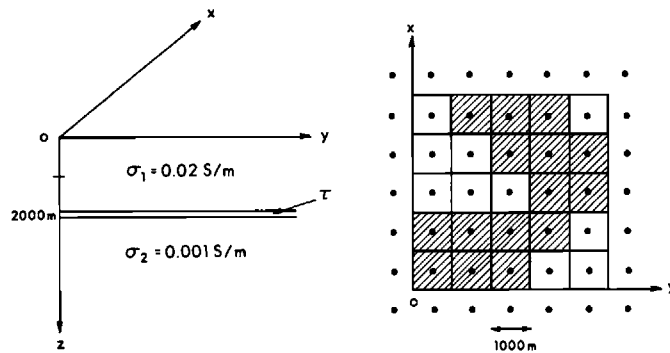


FIG. 16. Model for integral equation inversion to determine conductance of an inhomogeneous thin sheet (After Barthes and Vasseur, 1978).

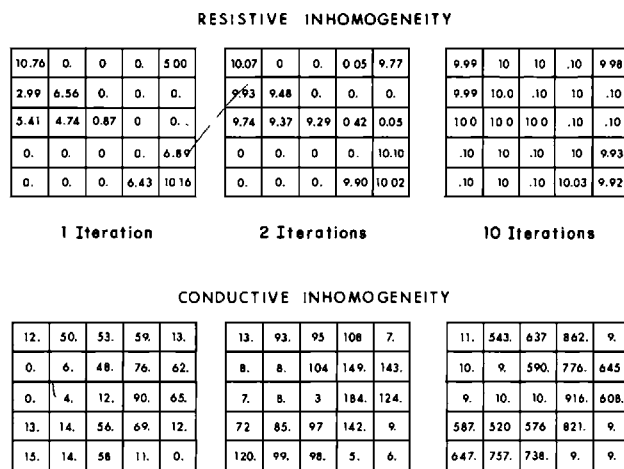


FIG. 17. Convergence of inverse solution for the model of Figure 16 with resistive and conductive inhomogeneities (After Barthes and Vasseur, 1978).

Much more work needs to be done to investigate the effectiveness of this type of inversion, but in some cases it may be a useful alternative to inversion based on differential equation solutions.

## References

- Backus, G. E. and Gilbert, J. F., 1967, Numerical applications of a formalism for geophysical inverse problems: *Geophys. J. Roy. Astr. Soc.*, **13**, 247–276.  
 ———, 1968, The resolving power of gross earth data: *Geophys. J. Roy. Astr. Soc.*, **16**, 169–205.  
 Bailey, R. C., 1970, Inversion of the geomagnetic induction problem: *Proc. Roy. Soc.*, **315**, 185–194.  
 Bard, Y., 1974, Non-linear parameter estimation: Academic Press Inc.  
 Barnett, C. T., 1984, Simple inversion of time-domain electromagnetic data: *Geophysics*, **49**, 925–933.  
 Barthes, V. and Vasseur, G., 1978, An inverse problem for electromagnetic prospection: in P. C. Sabatier, ed., *Applied Inverse Problems, Lecture Notes in Physics*, **85**, 325–329.  
 Chave, A. D., 1985, The Fréchet derivatives of electromagnetic induction: *J. Geophys. Res.*, **89**, 3373–3380.  
 Cheng, G. and Coen, S., 1984, The relationship between Born inversion and migration for common-midpoint stacked data: *Geophysics*, **49**, 2117–2131.  
 Eaton, P. A. and Hohmann, G. W., 1986, A technique for rapidly estimating the resistivity of the earth from transient electromagnetic soundings: *Expanded Abstracts, 56th Ann. Internat. Soc. Explor. Geophys. Mtg.*  
 Frischknecht, F. C. and Raab, P. V., 1984, Time-domain electromagnetic soundings at the Nevada

- Test Site, Nevada: *Geophysics*, **49**, 981–992.
- Fullagar, P. K., 1984, A uniqueness theorem for horizontal loop electromagnetic frequency soundings: *Geophys. J. Roy. Astr. Soc.*, **77**, 559–566.
- Fullagar, P. K. and Oldenburg, D. W., 1984, Inversion of horizontal loop electromagnetic frequency soundings: *Geophysics*, **49**, 150–164.
- Glenn, W. E. and Ward, S. H., 1976, Statistical evaluation of electrical sounding methods. Part I: Experiment design: *Geophysics*, **41**, 1207–1221.
- Glenn, W. E., Ryu, J., Ward, S. H., Peebles, W. J., and Phillipps, R. J., 1973, The inversion of vertical magnetic dipole sounding data: *Geophysics*, **38**, 1109–1129.
- Gomez-Trevino, E. and Edwards, R. N., 1983, Electromagnetic soundings in the sedimentary basin of southern Ontario—A case history: *Geophysics*, **48**, 311–326.
- Jackson, D. D., 1979, The use of a priori data to resolve non-uniqueness in linear inversion: *Geophys. J. Roy. Astr. Soc.*, **57**, 137–157.
- Jupp, D. L. B. and Vozoff, K., 1977, Two dimensional magnetotelluric inversion: *Geophys. J. Roy. Astr. Soc.*, **50**, 333–352.
- Kaufman, A. A. and Keller, G. V., 1983, Frequency and transient soundings: Elsevier Scientific Publ. Co.
- Macnae, J. and Lamontagne, Y., 1986, Imaging quasi-layered conductive structures by simple processing of transient electromagnetic data: *Geophysics*, **52**, 545–554.
- Oristaglio, M. L. and Worthington, M. H., 1980, Inversion of surface and borehole electromagnetic data for two-dimensional electrical conductivity models: *Geophys. Prosp.*, **28**, 633–657.
- Parker, R. L., 1977, Understanding inverse theory: *Ann. Rev. Earth Planet. Sci.*, **5**, 35–64.
- \_\_\_\_\_, 1980, The inverse problem of electromagnetic induction: existence and construction of solutions based on incomplete data: *J. Geophys. Res.*, **85**, 4421–4425.
- Pelton, W. H., Rijo, L., and Swift, C. M., Jr., 1978, Inversion of two-dimensional resistivity and induced-polarization data: *Geophysics*, **43**, 788–803.
- Raiche, A. P., Jupp, D. L. B., Rutter, H., and Vozoff, K., 1985, The joint use of coincident loop transient electromagnetic and Schlumberger sounding to resolve layered structures: *Geophysics*, **50**, 1618–1627.
- Rodi, W. L., 1976, A technique for improving the accuracy of finite element solutions for magnetotelluric data: *Geophys. J. Roy. Astr. Soc.*, **44**, 483–506.
- Schlichter, L. B., 1933, An inverse boundary value problem in electrodynamics: *Physics*, **4**, 411–418.
- Smith, N. C. and Vozoff, K., 1984, Two-dimensional DC resistivity inversion for dipole-dipole data: *Inst. Electr. and Electron. Eng., Trans. Geosci. and Remote Sensing*, **22**, 21–28.
- Swanger, J. H., Rodi, W. L., and Minster, J. B., 1983, An interactive system for two-dimensional magnetotelluric interpretation: Expanded abstracts, 53rd Annual Internat. Soc. Explor. Geophys. Mtg.
- Tripp, A. C., Hohmann, G. W., and Swift, C. M., Jr., 1984, Two-dimensional resistivity inversion: *Geophysics*, **49**, 1708–1717.
- Tripp, A. C., Ward, S. H., Sill, W. R., Swift, C. M., Jr., and Petrick, W. R., 1978, Electromagnetic and Schlumberger resistivity sounding in the Roosevelt Hot Springs KGRA: *Geophysics*, **43**, 1450–1469.
- Vidberg, H. J. and Riska, D. O., 1985, The inverse scattering problem for reflection of electromagnetic dipole radiation from Earth with vertical variation: *J. Geophys.*, **56**, 183–191.
- Vozoff, K., and Jupp, D. L. B., 1977, Effective search for a buried layer: *Bull., Austral. Soc. Explor. Geophys.*, **8**, 6–15.
- Ward, S. H., Smith, B. D., Glenn, W. E., Rijo, L., and Inman, J. R., 1976, Statistical evaluation of electrical sounding methods. Part II: applied electromagnetic depth sounding: *Geophysics*, **41**, 1222–1235.
- Weidelt, P., 1972, The inverse problem of geomagnetic induction: *Z. Geophys.*, **38**, 257–289.
- \_\_\_\_\_, 1975, Inversion of two-dimensional conductivity structures: *Phys. Earth. and Plan. Int.*, **10**, 282–291.
- Whittall, K. P., 1986, Inversion of magnetotelluric data using localized conductivity constraints: *Geophysics*, **51**, 1603–1607.
- Zhdanov, M. S., and Varentsov, I. M., 1983, Interpretation of local two-dimensional electromagnetic anomalies by formalized trial procedure: *Geophys. J. Roy. Astr. Soc.*, **75**, 623–638.



This page has been intentionally left blank

# INDEX

- Abitibi, Canada
  - clay belt, 55, 65
  - clays, 105
  - greenstone belt, 57, 65, 72, 102
- admittivity, 134
- airborne EM, 63, 65
  - selection of anomalies, 68
  - survey statistics, 65
- Aitkowan, Ontario research area, 105
- Alberta, Canada coal prospecting, 110
- Alfred, Ontario resistivity soundings, 104
- Alfred/Hawkesbury airborne area, 105
- Alps temperate glaciers, 122
- alternating magnetic dipole, 296
- alternating magnetic field, 252
- aluminum, source of, 54
- alunite, 97
- Ampere's law, 281
- amphibolite, 75, 83, 84, 88, 95
- amplitude, 141
- analog
  - detection, 450
  - models, 372
- andesite, 71
- Andhra Pradesh, India, Vikarabad area, 82
- angular frequency, 194
- anisotropic, 14
- anomalous potential, 257
- Antarctica, 122
- antenna
  - adequate signals, 374, 388, 394
  - design of, 386, 394, 398
  - grounded wire, 390
  - in VLF, 398, 399
  - receiving coils, 394, 397
- Aphebian age rocks, 87
- apparent resistivity map, 106, 115, 118
- applied potential, 255
- aqueous solution, 410
- aquifer
  - freshwater, 56, 115, 121,
  - mapping, Mombasa, Kenya, 115
  - saltwater, 56, 61
- Archean rock and sediments, 62
- Archean granites, 83, 89
- Archie's law, 40
- Arctic
  - permafrost mapping, 56
  - resistivity soundings, 122
- Argillite, conductivity of, 100
- Arles, 115
- arsenopyrite, 68
- Athabasca basin, Saskatchewan, 87, 88
- audiomagnetotelluric
  - data, 183
  - EM method, 96
  - plane-wave method, 391
- Australia
  - arid areas, 73
  - bauxite deposits, 90
- average predicted residual error, 490
- axially symmetric component, 271
- backscattering, 399
- Bakony Hills bauxite deposits, 91
- Bakonyjako horst, 92
- balanced coil, 421
- balanced loops, 397, 398
- barite, 57, 68
- basalt
  - flows, 77, 81
  - structure, 83
  - weathered, 82
- Basin and Range province, Utah, 96
- basis functions, 321
- Bathrust Camp, New Brunswick, 57, 65
- bathymetric charting, 112, 113
- bauxite deposits
  - Arkansas secondary, 91
  - Bakony Hill, 91
  - formation, 90
  - Guinea secondary, 91
  - Guyana buried, 91
  - Malaysia, 91
  - Papavar Hungary, 92
  - unconformity related, 72
- Bells Corners, Ontario, 86
- Belo Horizonte, Brazil, 81
- Bessel functions, 253
- Bessel's equation, 253
- Besshi deposits, Japan, 57, 67
- binding energy, 32
- black cotton soil, 82
- black shales, 57, 60, 70
- blue ground, 93
- Bois-de-Cene, France, 84
- borehole
  - EM examples, 419
  - coaxial system, 422
- Born inversion
  - procedure, 471
  - equation, 501
- boundary
  - conditions, 148
  - value problems, 131
- Bowen's reaction series, 75
- boxcar integrator, 443
- Brazil
  - bauxite deposits, 90
  - Carajas, 70
  - deep weathering area, 72
  - Itapicuru greenstone belt, 83
  - Minas Gerais, 70
  - State of Bahia, 106
- breccia
  - and tuff, 71
  - conglomerate, 68
  - form of ore, 69

- Brewster angle, 183  
 brine, 423  
 Broken Hill Mine, New South Wales, 68  
 Burundi, Bujumbura, Africa, 93  
 Burkina Faso, Africa, 95
- calculus of residues, 272  
 Canabrava, Goias, Brazil, 77  
 Canada  
     Abitibi greenstone belt, 65  
     chemical pollution surveys, 118  
     conductive clay layers, 102  
     geological survey, 85  
     glaciolacustrine sediments, 55  
     resistivity soundings, 103  
     thick weathered layers, 73  
 Canadian Shield, 67  
 canga, duricrust, 75  
 Cape Breton Island, Nova Scotia, 113  
 Cape Cod Bay, Massachusetts, 113  
 Captain Flats, NSW, 58  
 Carajas, Brazil, 70  
 carbonaceous shale, 109  
 cassiterite, 68, 82  
 Central Europe, 73  
 central loop configuration, 220, 221  
 chalcopyrite, 57, 58, 63, 66, 68  
 changes in coil parameters, 396  
 characteristic impedances, 382  
 chemical pollution, 112  
 chemical pollution plumes testing  
     Canada, 118  
     Netherlands, 118  
     USA, 118  
 chemical weathering, 73, 89, 90  
 Chert, 63, 68, 71  
 Chester mine, Zeehan, Australia, 63, 64  
 Chibougamau, Canada sulfide deposit, 67  
 chloride plume, Las Vegas, Nevada, 121  
 chloride, 76  
 chloritization zone, 74  
 Cigar Lake, Canada orebody, 88, 89  
 circular  
     functions, 287  
     loop, 218  
 clathrates, 30  
 clay  
     composition, 101  
     conductivity, 55  
     frozen, 122  
     impermeable layer, 118  
     intercalations, 114  
     lithology, 107  
     minerals, 76  
     thickness, 103  
     thin layers, 124  
 coal  
     prospecting, 110  
     seam, 109  
     span, 100  
 cobalt, 90  
 Cobar, NSW, 61  
 Cocorobo, Brazil, 106  
 coefficient of anisotropy, 408, 417  
 coil  
     assembly, 404  
     current, 389, 390, 391  
     dipole source, 388  
     form construction, 389, 396  
     Helmholtz, 394  
     impedance, 389  
     multiple, 403  
     placement, 375  
     thickness, 405  
     transmitting antenna, 388  
 coincident-loop, 220  
 Cole-Cole plot, 20  
 Colombia, South America, 92  
 comb-filter, 465  
 common mode  
     impedance, 400, 421  
     rejection, 402  
     voltage, 398, 399, 404, 421  
 complementary error function, 289  
 complementary solution, 203  
 complex  
     resistivity measurements, 121  
     wave number, 194  
 conductance  
     anomalies, 93  
     definition, 47  
     determination of, 67  
     high, 65  
     thickness, 55  
 conduction currents, 136  
 conductive  
     composites, 408  
     fibers, 408  
     particles, 408  
 conductive materials area, Nantes, France, 84  
 conductivity  
     electrical parameter, 413  
     of modeling materials, 406  
 confidence intervals, 488, 492  
 conglomerate, 55, 87, 100, 106  
 constitutive  
     equations, 13  
     relations, 131  
 controlled source EM, 386  
 convolution, 251  
 copper  
     magmatic deposits, 69  
     production percentage, 57, 58, 63  
     zinc, 57  
 Cramer's rule, 261  
 Cretaceous basalt, 82  
 Cretaceous-Tertiary, 110  
 Crone system, 62, 63  
 CSAMT, 90, 391  
 Cuba lateritic nickel deposits, 92  
 cuirasse duricrust, 75  
 cylinder  
     centered, 429  
     conducting target, 418  
     elongated, 423, 424  
     functions, 253  
     single loop response, 423  
 cylindrical coordinates, 252  
 Cyprus copper zinc deposits, 57
- Debye potentials, 300  
 decay spectrum, 353  
 Deccan Trap, 82  
 deep weathering area  
     Africa, 73  
     Australia, 73  
     Brazil, 73  
     Guyanas, 73  
     India, 73  
 Deepem, 89  
 degrees of approximation, 373  
 detection of electromagnetic signals, 443  
 Detour deposit, Quebec, 65, 66  
 Devonian, 58, 61  
 diabase, 76  
 diamagnetic, 35

- dielectric  
 constant, 410  
 displacement, 132  
 EM studies of ice, 183  
 permittivity, 14, 26, 30, 133  
 susceptibility, 142  
 Dighem system, 60, 62, 99, 106  
 digital  
 analogy detector, 456  
 detection, 454  
 filtering, 250, 455  
 dimensionless time, 290  
 Diojon, France, 106  
 diorite, 76  
 dipolar line sources, 255  
 dipole-dipole systems, 386  
 direct current  
 equations, 319  
 methods, 424  
 point source, 172  
 resistivity, 372  
 dispersion, 140  
 displacement current  
 important, 411  
 less than conduction current, 136  
 negligible, 391, 394, 406, 410, 413  
 significant, 413  
 disseminated sulfides, 62  
 dolomite, 55, 87, 100  
 Dominican Republic, 92  
 drumlins, 101  
 dunite, 81  
 duricrust  
 canga, 75  
 conductivities, 80  
 cuirasse, 75  
 formation, 75  
 resistive, 55, 62, 81
- E-phase, 101  
 East Bull Lake, Massey, Ontario, 103  
 East Pacific Rise, 57  
 East Perenjori, Western Australia, 118  
 eigencurrents, 354  
 eigenparameter, 483, 491  
 eigenvector analysis, 489  
 electrostatic, 277  
 electric  
 charge density, 133  
 conductivity, 133  
 current, 144  
 current density, 133  
 dipole, 173  
 field intensity, 132  
 permittivity, 369  
 sources, 258  
 electrical  
 properties of earth materials, 53  
 prospecting, 138  
 unit of distance, 18  
 electrodes  
 impedance, 390, 412, 413  
 use of, 389, 390, 393, 397, 418, 421  
 electrolyte, 397  
 electrolytic  
 conduction, 25  
 polarization, 46  
 tank, 385, 412  
 tank field, 413  
 electromagnetic  
 coupling, 372  
 field, 252
- inverse problem, 470  
 theory, 131  
 electronic signal averaging, 443  
 electrostatic field, 255  
 Elura deposit, New South Wales, 61  
 electromagnetic  
 coupling, 372  
 surveys, 97  
 Eocambrian, 67  
 equations  
 differential, 314, 357  
 diffusion, 137  
 integral, 314  
 time-domain, 314  
 error  
 bounds, 493  
 due to bottom of tank, 376  
 due to tank boundaries, 381  
 function, 289  
 in electrical field results, 397  
 source of, 398  
 esker, 101, 103  
 estimate of standard error, 378, 481  
 Esperance, Western Australia, 110
- factor-of-merit, 412  
 factorial, 253  
 Fairbanks, Alaska, 122  
 far field, 386, 394  
 Faraday shield, 391, 397  
 Faraday's law, 271  
 Faro, Yukon, Canada, 68  
 felsic  
 rocks, 57, 76  
 volcanism, 57, 58  
 FEM  
 measurements, 422  
 methods, 378  
 system, 376, 377  
 ferromagnetism, 35  
 ferruginous zone, 74, 80  
 fiber optic links, 400  
 fields, 140  
 finite  
 difference solution, 334  
 element technique, 324  
 loop, 387  
 source, 203, 428  
 Finland surveying, 68  
 Flin Flon, Manitoba, Canada, 57, 66  
 Flying Fox, Australia, 70  
 flysch, 58  
 Fourier transform, 132, 167, 204  
 Fox, Alaska, 122  
 fractures, 94  
 France  
 buried deposits, 91  
 nuclear power plants, 106  
 Frechet  
 derivative, 472  
 kernel, 472, 499  
 free-space, 141  
 frequency domain  
 electromagnetic (FEM), 376  
 equations, 134, 317  
 methods, 400  
 freshwater-saltwater interface, 114, 115  
 Fresnel equations, 183
- gabbro-associated Ni-Cu-Pt deposits, 69, 76  
 galena

- in sulfides, 58, 62, 63  
 ore minerals, 57  
 with sphalerite, 68, 69  
 zone, 57  
 galvanic response, 357  
 gamma function, 253  
 generalized inverse, 482  
 geomagnetic induction, 419, 421  
 Geonics, 63, 121  
 geophysical equipment, 443  
 geotechnical studies, 56, 94, 106  
 geothermal exploration, 96  
 glaciolacustrine  
     clays, 100, 101  
     sediments, 54, 65, 72, 102  
 Gloucester Landfill Site, Canada, 121  
 Gneiss, 75, 80, 95  
 goethite, 62, 71  
 Goias, Brazil, 80  
 gold, 54, 57, 58, 65, 72  
 gold mining towns  
     Kirkland Lake, Canada, 65  
     Rouyn-Noranda, Canada, 65  
     Timmins, Canada, 65  
     Val d'Or, Canada, 65  
 Goldstream deposit, B.C., 57, 67  
 gossan, 62, 63  
 grade  
     copper-zinc sulfide orebodies, 57  
     lead and zinc orebodies, 69  
     platinum-group deposits, 69  
     zinc, copper, lead deposits, 57  
     zinc and lead deposits, 68  
 granite  
     biotite, 122  
     covered by regolith, 89  
     hydrothermally altered tertiary, 97  
     in-situ resistivity, 76  
     Permo-Carboniferous, 81  
     Rapadama survey, 95  
     tertiary, 97  
 graphite, 54  
 graphitic  
     metapelite, 88, 89  
     schist, 66, 83  
     shale, 66  
 gravel, 55, 100, 101, 121  
 Green's function, 167  
 Greenland, 122  
 greenstone belts, 57  
     Abitibi, Canada, 57, 65, 72, 102  
     Rice Lake, Canada, 86  
     Whim Creek, Australia, 62  
 greywacke, 100  
 ground EM, 63, 82, 83, 90, 124  
 grounded wire, 237  
 groundwater  
     exploration, 56, 94, 106  
     prospecting, 106  
  
 half-planes, 433  
 half-plates, 433  
 half-space  
     conductive, 376, 415, 419, 433  
     simulating, 433  
     surface impedance, 415  
 Hall effect, 16  
 Hankel functions, 253  
 Hankel transform, 282  
 hardebank, 93  
 Hawaiian basalts, 76  
 HCP loop-loop system, 377  
 HCP slingram, 427  
  
 Heath Steele mine, 65  
 helicopter AEM, 71, 67, 99, 106, 113  
 Helmholtz  
     coils, 394, 421, 422  
     equations, 136  
 hematite, 62, 70, 74  
 Hilbert transform, 202  
 homogeneous earth, 197, 210  
 horizontal  
     coplanar configuration, 376, 410  
     electric dipole, 229  
     magnetic dipole, 223  
 horizontal-loop EM, 95, 96  
 Horne, Quebec orebodies, 57  
 host rock, 422, 429, 433  
 Hungary  
     bauxite exploration, 91  
     buried bauxite, 91  
 hybrid solutions, 359  
 hydrothermal  
     activity, 57, 68  
     alteration, 72, 89, 96  
     solutions, 57  
     systems mapping, Nevada, 99  
 hyperbolic functions, 287  
  
 Iberian Pyrite Belt (Spain, Portugal), 57  
 igneous rocks, 54, 69, 76, 93  
 Illisarvik, NWT, 123  
 ilmenite, 94  
 imaginary part, 141  
 impedivity, 134  
 Imperial Valley California, 99  
 impulsive fields, 140  
 in-phase, 141  
 incident fields, 268  
 Indonesia lateritic nickel deposits, 92  
 induced polarization, 15, 46, 47, 68, 142, 372  
 induction  
     number, 366, 368, 376, 377  
     regime, 18  
     systems, 390  
 Ingham, Queensland, Australia, 81  
 Input  
     helicopter AEM survey report, 67, 83  
     location of AEM anomalies, 84  
     survey results, 86, 105, 113, 118  
     tests, 62  
     use, 102, 110, 115  
 instrumentation examples, 419  
 insulators, 22, 25  
 integral equation  
     formulations for inversion, 318, 499  
     method, 345  
     solutions, 282  
 interface impedance, 412  
 interfacial polarization, 45  
 intrinsic impedance, 195  
 inverse  
     Fourier transform, 352  
     Laplace transform, 271  
 inversion statistics, 490  
 inward and outward propagating waves, 295  
 ion exchange process, 40  
 Ireland EM surveys, 69  
 iron  
     detection of formations, 70, 71  
     formation types, 70  
 irrelevant parameter, 484  
 isotropic minerals or rocks, 14  
 itabirite, 70  
 Itapicuru greenstone belt

Araci, Brazil, 83  
Bahia, Brazil, 83

Jacobian matrix, 481  
jaspilite, 70  
joint inversion, 490, 494

Kalgoorlie, Australia, 70  
Kambalda, Western Australia  
camp, 70  
deposits, 69  
kames, 101, 103  
Kangaroo Hills, Australia, 81  
kaolin, 72, 90  
kaolinite, 74, 88, 97, 107  
Keretti, Finland, 57  
Kidd Creek, Ontario, 57, 66  
kimberlites, 72, 93  
Kitchener-Milton, 110  
Known Geothermal Resource Area, 96  
Kuroko Green Tuff Belt, 57  
Kuroko-type deposits, 60

Labrador Trough, Quebec, 66, 71, 87  
Lachlan Fold Belt Australia, 57  
Lake Agasiz, Manitoba, 102  
Lake Champlain, Ottawa, 102  
Lake Ojibwe-Barlow, Ontario-Quebec, 102  
Lake Superior type iron formation, 70  
Laplace's equation, 200  
large horizontal loop, 217  
Lassen National Park, California, 99  
lateritic nickel deposits, 92  
Colombia, 92  
Cuba, 92  
Domenico Republic, 92  
Indonesia, 92  
New Caledonia, 92  
lateritic soils, Quatipuru, Brazil, 80  
laterization, 75  
Lavras do Sul, Brazil, 71  
layered half-space, 203  
leachate plume, 121  
leached zone, 75, 80, 88, 91  
leaching, 75, 90  
lead, 57, 58, 63, 68  
least-squares pseudoinverse, 481  
Legendre  
associated Legendre functions, 293  
equation, 278  
polynomial, 278  
lignite, 100, 110  
limestone  
and bauxite contrast, 91  
coastal reef, 115  
Jurassic, 106  
Late Sillurian deposit, 58  
layer confined plume, 121  
Paleozoic, 105  
resistive, 55, 100, 106  
line electrode, 372, 415, 416  
line source, 178, 252, 269  
lineaments, 72, 94, 105, 112  
linearization, 472  
lock-in amplifier  
advantages of, 402, 403  
alternative to, 403  
dc offset circuits, 401  
definition, 401

operation, 404  
signal averaging detector, 443  
use of two-component, 422  
with receiving coil, 402  
loess, 84  
logarithmic mixing rule, 44  
longitudinal  
chokes, 400, 402, 421, 422  
inducing field, 264  
loop  
air core, 388, 389  
receiving, 394, 396, 397, 398, 420  
transmitting, 394  
Lorentz conditions, 146  
loss  
factor, 18  
tangent, 141

Mackenzie Delta, NWT, 123  
mafic  
minerals, 76  
rocks, 76  
volcanic, 58  
magmatic deposits, 69  
magnetic  
association, 65, 67, 70  
current, 144  
dipole, 175, 285  
field intensity, 132  
induction, 132  
permeability, 15, 133, 368, 382  
signature, 94  
sources, 258  
susceptibility, 71, 142  
magnetite, 57, 70, 71, 94  
magnetostatic problems, 277  
magnetostatic field, 252  
magnetotelluric  
induction, 419, 421  
measurement interpretation, 90  
modeling, 377, 391, 398  
one-dimensional data interpretation, 183  
systems, 370  
techniques, 100  
Magusi River, Iso, New Inco, Canada, 65  
Mali resistivity range, 95  
Manitoba Pioneer project, 86  
map of apparent resistivity, 97  
marcasite, 68  
marine clays, 84  
marl, 106  
Marquardt method, 484  
massive sulfide  
deposits, 56  
form of ores, 69  
in Pyritic ore, 62  
pyrotite, in, 65  
resistivities, 60  
typical anomaly, 67  
Matheson, Ontario, 102  
Mattagami Syndicate, 65  
Maxwell's equations, 131  
McArthur River-type orebodies, 69  
McCLean, Canada orebody, 88, 90  
Merensky Reef mines, South Africa, 69  
mesozoic  
basement, 106  
shale, 83  
Tucano Basin, 106  
metals, 22  
metamorphic rocks, 54, 79  
method  
of moments, 321

- of weighted residuals, 321  
 microcomputer, 403, 422  
 Minas Gerais, Brazil, 70, 80, 81  
 mineral  
   exploration, 94  
   prospecting, 65  
 Missouri  
   Old Lead Belt, 69  
   Viburnum Trend District, 69  
 mobility of ions, 39  
 Mobrun, Canada, 65  
 mode decomposition, 132  
 model  
   fitting, 479  
   operational procedures, 403  
 model materials  
   conductivity of, 406  
   criteria for selection, 368  
   modified Bessel functions, 253, 286  
   molecular polarization, 30  
   monopolar line sources, 255  
   Mons Cupri, Western Australia, 62, 65  
   montmorillonite, 76, 93, 97, 98  
   most parsimonious model, 490  
   mottled zone, 55, 74, 80, 81  
   Mount Isa, Queensland, 68, 69  
   mudstone, 58  
   multidimensional inversion, 495  
   mutual impedance  
     of grounded wires, 240  
     of loops, 228
- natural field AMT, MT, and VLF, 391  
 near field, 386, 394  
 Neumann function, 253  
 Newmont system, 62  
 nickel, 54, 69, 72, 90, 93  
 nickel deposit, Musongati, Burundi, Africa, 77, 93  
 nickel sulfide deposits, Mt. Keith, Australia, 70  
 Nigeria duricrust, 80  
 noise  
   to avoid, 382, 388  
   bandwidth, 443  
   causes of, 387  
   processing techniques, 443  
   system rejection, 403  
 noise to signal ratio, 485, 488  
 nonglacial unconsolidated sediments, 106  
 Noranda district, Canada, 65  
 Norilsk, USSR, 69  
 normal incidence, 191  
 normal potential, 257  
 Nova Lima, Brazil, 80, 81  
 nuclear fuel waste management program, 105  
 nuclear fuel waste research areas  
   Aitkohan, Ontario, 105  
   East Bull Lake, Massey, 105  
   Whiteshell, Manitoba, 105  
 numerical  
   integration, 250  
   modeling, 433
- oblique incidence, 198  
 Old Lead Belt District, Missouri, 69  
 Onakawana, Canada, 110  
 one-dimensional earth, 202  
 Ontario, Canada, 53, 65, 110  
 ophiolite, 57  
 optical fiber link, 399, 402, 421  
 optimization, 461, 479  
 Ordovician age, 110  
 orebodies, Mt. Isa, Australia, 69  
 Ottawa, Ontario, Canada, 86, 121  
 Ouagadougou, Africa, 95  
 Outokumpu, Finland, 57  
 outward traveling wave, 294, 295  
 overburden, 404, 406, 423, 429, 433
- paleo-saprolite  
   layers, New Brunswick, 85, 86  
   paleoweathered layers, 84, 90  
 paleozoic, 87  
 paramagnetic, 35  
 parameter estimation, 479  
 Pechenga, USSR, 69  
 pentlandite and chalcopyrite, 69  
 peridotite, 70, 77, 86  
 permafrost, 56, 112, 122  
 Permian, 109  
 permitivity of water, 30  
 phase of conductivity, 141  
 physical  
   facilities, 375  
   property factor, 257  
   scale modeling, 365, 366, 372, 423  
   weathering, 73  
 piezoelectric  
   polarization, 15  
   properties, 37  
 Pilbara, Australia, 62  
 Pine Point, NWT, Canada, 69  
 Pioneer project, 86  
 pipe mine, 69  
 plane of constant phase, 138  
 plane of incidence, 189  
 plane wave  
   methods, 397, 427  
   sources, 376, 391  
 platinum, 69  
 plutonic complex, Winnipeg River, 86  
 point electrode, 372, 415, 416  
 Polaris Mines, NWT, Canada, 69  
 polarization  
   resistivity modeling, 412  
   vector, 131, 142  
 polluted water, 121  
 pollution plume, 56, 121  
 polymetallic  
   base metal deposits, 58  
   ore, 58  
 pore fluid, 100, 112  
 porosity, 55, 100, 107, 112  
 potentials, 144  
 power reflection coefficients, 192  
 Precambrian  
   age, 71  
   basement, 110  
   granite and gneiss, 87  
   greenstone belt, 67, 69  
   shields, 55  
   topography, 110  
 primary potential, 215  
 profiling, 110  
 properties of model materials, 406, 413  
 pyritic ore, 62  
 pulse basis functions, 322  
 pyrite  
   conductivity, 66, 69  
   in lens, 58  
   massive sulfide, 62  
   ore mineral, 68  
   zone, 57, 63, 97  
 pyrrhotite  
   conductivity, 67, 69

- content, 62, 67  
 in massive sulfide deposits, 65, 68  
 in Ni-Cu magmatic deposits, 70  
 zone, 57, 65
- quadrature, 141  
 quartz, 68, 71, 76  
 quartzite, 88, 89  
 quasi-static  
     approximation, 200, 210, 225  
     case, 171  
 quaternary, 92, 100, 104, 106, 110  
 Quebec, Canada  
     Abitibi greenstone belt, 65  
     conductivity data, 66  
     government policy, 68  
 Queensland, Australia, 68, 69
- Rabbit Lake, Canada, uranium deposit, 88  
 radar antenna, 374  
 radial magnetic dipole, 301  
 radio frequencies, 382, 383, 418  
 radio link, 399  
 Rammelsberg, Meggen, Germany, 68  
 Rapadama, Africa, 95  
 real component, 141  
 receiving  
     coil, 397, 402  
     loop, 394, 396, 397  
 reciprocity, 181, 226  
 rectangular loop, 217  
 reflected waves, 184  
 reflection of plane waves, 183  
 reflection coefficient, 188, 191, 302  
 refraction of plane waves, 183  
 regolith, 74, 87, 88, 89  
 relative dielectric permittivity, 141  
 relative magnetic permeability, 141  
 remote coil, 403  
 repetitive signals, 443  
 research area, Whiteshell, Manitoba, 105  
 resistivity  
     logs, 77, 87, 101  
     maps, 92, 97, 99, 110  
     modeling, 412  
     profiling, 92, 110  
     ranges, 54, 60, 83  
     section, 103, 123  
     soundings, 77, 80, 83, 95, 103, 106, 110, 114, 124  
     surveys, 97  
     use, 55, 81, 83, 95, 106, 114  
 resolving kernel, 476  
 reviews of model studies, 418  
 radio-frequency energy, 385, 399, 418  
 Rhone delta, France, 115  
 rhyolite, 97  
 Rio Grande do Sul, Brazil, 71, 83  
 Roosevelt Hot Springs, Arkansas, 96  
 Rosebery, Australia, 65
- Sahel, Africa, 95  
 saline water, 118  
 salinity, 112, 114  
 salinization, 115  
 Salt Creek, Australia, 62  
 salt pans, 118  
 saltwater-freshwater interface, 112  
 sand, 55, 100, 104, 106, 107, 114, 118, 121, 124  
 sandstone, 58, 71, 87, 100, 105, 106, 107, 115  
 Santa Fe, Goias, Brazil, 80  
 Saone River, France, 106  
 saprolite  
     conductive, 62, 70, 81, 112  
     layers, 66, 74, 84, 88, 106  
     leaching, 90  
     resistivity of, 55, 82  
     response, 62  
     water saturated zone, 76  
 Saskatchewan, Canada, 87, 101  
 scalar potential, 151  
 scale model, 394, 572  
 scale model studies, 423, 433  
 scale modeling, 372, 433  
 scaling relationships, 366  
 Scandinavia  
     glaciated areas, 55  
     thick weathered layers, 73  
 scattered fields, 268  
 Schelkunoff potentials, 132, 144  
 schists, 80, 84  
 Scott orebody, Canada, 67  
 sea ice, 56  
 seawater, 55, 112, 113, 115  
 sediment hosted sulfide deposits, 68  
 sedimentary rocks, 100, 106  
 Selebi-Pikwe, Botswana, Africa, 69  
 selection of AEM anomalies, 68 (see also airborne EM,  
     selection of anomalies)  
 selection of targets, 65  
 semiconductors, 22  
 Sennecey, France, 106  
 sensitivity coefficient, 481  
 sensitivity matrix, 490  
 serpentinite dikes, 84, 86  
 shale, 61, 100, 105, 107, 109, 110, 115  
 shallow-water bathymetry, 56, 112  
 shear zones, 54  
 shears, 94  
 sheet, 392, 405, 414, 423  
 Sherman Mine, Canada, 71  
 shield design, 382, 383  
 shielded  
     loop, 397, 421  
     magnetic field, 382, 383  
     preamplifier, 402  
     tank bottom, 394  
     transmitter, 390  
 shielding, 398  
 signal detectors, 443  
 signal-to-noise ratio, 387, 394, 401, 403, 404, 450,  
     461  
 siliceous layer, 63  
 siliceous ore, 61  
 siltstone, 58, 61, 110  
 Silurian  
     deposits, 58  
     dolomite, 110  
     silver, 57, 58, 68  
 Silvermines, Tynagh, Ireland, 68  
 singular value decompositions, 482  
 Sirotem system, 62, 428  
 skin depth, 17, 138  
 slab, 404, 405, 415  
 slate, 58, 100  
 Slingram, 401, 404, 419, 428  
 Snell's law, 183  
 solution appraisal, 373  
 source  
     array, 419  
     loops, 396  
 sources in unbounded media, 167  
 spectral transfer function, 443  
 sphalerite, 57, 58, 62, 63  
     and galena, 68, 69

- spherical  
 coordinates, 276, 279  
 cylinder functions, 282
- Spiekeroog, Germany, 114
- step function response, 443
- stratabound orebodies, Mississippi Valley, 69
- submarine volcanic rocks, 57
- Sudbury, Ontario, Canada, 69
- sulfide deposit, Whistle, Ontario, Canada, 53
- Sullivan, British Columbia, 68
- superparamagnetic effect, 134
- surface impedance, 197
- survey steps  
 data interpretation, 53  
 data processing, 53  
 surveying, 53
- Sydney Basin, Australia, 107
- syenite, 76
- synchronous detection, 443
- taconite, 70, 71
- tank  
 boundary response, 380, 381  
 concrete, 421  
 design of, 376, 377, 392, 394  
 electric field, 393, 397  
 empty, 393  
 position to coil assembly, 404  
 rectangular, 393  
 sketch, 419
- Tanzania, Africa, 82, 94
- Tasmania, Australia, 63
- Tasmania, Que River, 64
- TE mode, 132, 205
- telluric method, 96, 393
- TEM. (see transient electromagnetic)
- Temagami, Ontario, Canada, 71
- Tennessee, East District, 69
- Tensor Green's functions, 180
- Tertiary, 57, 91, 97, 106, 110
- testing and calibration, 404
- Teutonic Bore, Western Australia, 63, 80
- Thalanga deposit, Queensland, 63
- thin sheet, 370, 372, 386, 405, 414, 416
- thin-sheet solution, 351
- Thompson deposit, Manitoba, Canada, 69
- three-dimensional modeling, 345
- till, 55, 90, 101, 104, 110
- tilt-angle, 419
- time constant, 465
- time domain  
 electromagnetic, 63, 107, 114, 123, 132  
 equations, 314  
 Green's function, 169  
 Maxwell's equation, 132  
 method, 419  
 response, 352  
 source, 429  
 systems, 370  
 3-D solution, 355
- Timmins, Ontario, Canada, 65, 66
- tin, 54
- TM mode, 132
- tonnage of deposits, 57
- total reflection, 183, 192
- transfer matrix, 196
- transformers, 400
- transient  
 calculations, 352  
 electric dipole, 174  
 electromagnetic method, 378, 403, 423, 428, 433  
 fields of a large loop, 221  
 Green's function, 170
- line source, 180
- magnetic dipole, 177, 305
- measurements, 389, 422
- response, 287
- transmission line, 397, 398, 399, 400
- transmitted waves, 184
- transmitter, 386, 387, 389, 390, 398
- transmitting loops, 394
- transverse inducing field, 259
- transverse magnetic dipole, 296
- Triassic, 91, 107
- Tridem, 105, 115
- Trondheim, Norway, 57
- Tuktoyaktuk, Canada, 123
- Turam, 401, 419
- Tverfjell, Killingal, Norway, 57
- two-dimensional model, 322  
 and three-dimensional source, 341
- ultra high frequency (UHF), 397
- ultramafic-associated Ni-Cu deposits, 65, 69
- unconformity-related uranium deposits, 88
- unconsolidated sediments, 100, 106, 121, 122
- uniform  
 field, 421, 433  
 plane wave, 138  
 source, 386, 390  
 stacking detector, 459
- unimportant parameters, 484
- uniqueness, 471
- unshielded tanks, 421
- uranium, 72, 88, 89, 90  
 deposit, Rabbit Lake, Canada, 88
- Utrecht, The Netherlands, 118
- Val Gagne, Ontario, 103
- vector potentials, 146
- vehicle-borne EM, 65
- vertical  
 EM loop, 69  
 magnetic dipole, 208
- Viburnum Trend District, Missouri, 69
- Vikarabad area, Andhra Pradesh, India, 82
- very low frequency  
 field results, 424  
 measurements, 420  
 methods, 391  
 studies, 419  
 surveys, 92, 95  
 techniques, 95  
 waves, 399
- volcanic-associated massive sulfide deposits, 54, 57, 62, 65, 66, 67
- volume polarization, 30
- Wadena, Saskatchewan surveys, 101
- Warburg impedance, 47
- waste disposal, 118
- water  
 saturation, 55, 100  
 table, 55, 74, 90, 106
- Watson Lake, 65
- wave  
 equation, 131, 276  
 functions, 132  
 impedance, 183, 382, 393  
 length, 17, 18, 285  
 number, 16, 18, 137  
 transformation, 291

- weathered layer  
composition, 54, 62, 63, 66, 82, 88, 95  
electric response, 106  
prospecting, 70  
resistivity, 72, 80, 83  
weathering,  
alteration, 72  
process, 75  
profile, 74, 76, 80, 90  
weighting functions, 321  
well-logging, 60, 100, 106, 107, 123  
Wenner array, 415, 416, 418  
Westarm deposit, Flin Flon, Manitoba, 66  
Western Australia deposits  
Mt. Isa, 69  
Mt. Keith, 69, 70  
Kambalda, 69  
whole space, 276  
Woodlawn, Australia deposit, 57, 60  
world class orebodies, New Caledonia, 92  
yellow ground, 93  
Yilgarn Block, Western Australia, 70  
Yugoslavia  
bauxite deposits, 91  
buried, 91  
residual, 91  
zinc, 57, 58, 63, 68  
zone of fractured rock, 76

This page has been intentionally left blank